GEOLOGY, STRUCTURE, PETROGENESIS, AND HYDROTHERMAL ALTERATION RECONSTRUCTION OF THE MING VOLCANOGENIC MASSIVE SULPHIDE DEPOSIT, BAIE VERTE PENINSULA, NEWFOUNDLAND, CANADA

by

© Jean-Luc Pilote

A thesis submitted to the School of Graduate Studies

in partial fulfillment of the requirements for the degree of

Doctor of Philosophy

Department of Earth Sciences

Memorial University of Newfoundland

February 2018

St. John's, Newfoundland and Labrador

Abstract

The Cambro-Ordovician Ming volcanogenic massive sulphide (VMS) deposit, Newfoundland Appalachians consists of stratiform and elongated semimassive to massive sulphide lenses (1807, 1806, Ming North, and Ming South zones) enriched in Cu, Zn, Ag, and Au that are underlain by a discordant Cu-rich stockwork zone (Lower Footwall zone). The host successions consist of highly fractionated FI-/FII-type rhyodacitic coherent to volcaniclastic rocks, which were deposited within a synvolcanic fault-controlled nested basin. The disposition of the sulphide lenses and the stockwork zone were controlled by the same synvolcanic faults. Deformation and greenschist metamorphic overprint have remobilized (≤20 m) less competent sulphide assemblages locally, but original stratigraphic relationships are preserved. Enclosed precious metal-rich sulphide clasts in a mafic polymictic breccia, which immediately overlies the deposit, support a syngenetic introduction of Au and associated tellurides at the Ming deposit. From regional geology and geochemical affinities, the felsic host successions are likely derived from direct partial melting of an island arc tholeiite at depths exceeding garnet stability zones (≥30 km). These types of magmas share many affinities to modern adakites formed in juvenile environments and may be more conducive to Au transport than previously thought. Ten distinct alteration assemblages are associated with the ore-forming hydrothermal fluids, grouped as chlorite-, sericite-, and (Mn-)carbonate-rich facies. The distribution and chemistry of the alteration assemblages are strongly controlled by the hosting lithologies. Most mass changes are restricted to the upper ~100 m of the stratigraphy, within the permeable volcaniclastic lithofacies. The Cu-rich stockwork is hosted by a chlorite-rich assemblage, reflecting high temperature fluids (≥300°C) that mixed with seawater at the

coherent-fragmental interface, decreasing Cu solubility and resulting in the precipitation of chalcopyrite. Gold, Ag, sulfosalts and other magmatophile elements are enriched in sulphide zones that are immediately underlain by coherent rocks. The less diffusive potential of the coherent rocks may have increased the efficiency of metal precipitation in these zones and could explain the heterogeneity of metal grades at Ming. The paragenetic evolution indicates that the introduction of precious metals is spatially and temporally associated with the quartz-sericite-sulphides assemblage, which is considered to reflect the overprint of acidic and low temperature (≤250°C) fluids in the waning stage of the hydrothermal system.

Acknowledgements

I would like to extend my sincere gratitude to my supervisor Steve Piercey for his support, guidance, and mentorship during this thesis project. Steve has allowed me to take the necessary risks to reach the independence of a researcher, to pursue ideas, and test hypotheses that I believed were deemed fundamentally important. You trusted me, knowing very well that mistakes or re-adjustments had to be made along the way. You also insisted to *keep it real*, which I believe is a state of mind that would benefit all of us. Thank you and I look forward to continuing working closely with you in the future on other exciting projects.

This thesis has received important contributions via discussions from many individuals, including Greg Dunning, John Hanchar, Sébastien Castonguay, Tom Skulski and other faculty members of the department at MUN. I would also like to extend my sincere appreciation to John Hanchar who has been there as a mentor and for giving me the opportunity to broaden my geological knowledge outside the island. Patrick Mercier-Langevin and Toby Rivers served as thesis committee members and are acknowledged for their comments throughout the years. I would particularly like to thank Patrick Mercier-Langevin for his help over the course of this journey and for his numerous encouragements.

Dave Grant, Pam King, Lakmali Hewu, Sherri Strong, and Wanda Aylward of CREAIT are thanked for their technical support during the various analytical techniques used over the course of this project. Industry colleagues Larry Pilgrim, Paul Legrow, and Peter Mercer of Rambler Metals and Mining Ltd., are thanked for their constant support throughout the summers that I have spent in Baie Verte. Their trust in me and the opportunities they have given me outside this project helped me grow as a researcher and I will always be grateful for this.

Friends, colleagues, and officemates of the department, thank you for your time, support (e.g., babysitting my dog, Charlotte), jokes, and patience. I would like to thank in particular my good friends Giorgio Ruberti, Stefanie Brueckner, Nicolas Lachance, and Shannon Gill. I enjoyed the time we have had together and I hope to spend more time with you in the future.

Five years or so of near constant focus can only be achieved with the countless support and encouragement from some amazing people. My family and extended family have been there for me every minute of the way. Thank you for your time, understanding, and kind words. I owe you a lot. Marie-Ève Lajoie, I do not know how you do it, but you have continuously found the right words to help me put my head back in the game. I think it would also be appropriate to acknowledge my dog, Charlotte; an introvert golden retriever, who has been a loyal supporter since day one.

My sister, Amélie, left us in the last year of completing this thesis. The difficult times that followed were dampened by the heartfelt support from my family, friends, and close colleagues. She is deeply missed and I wish to have spent more time with her. I would like to dedicate this thesis to my parents, Céline and Hermel, and my brothers, Anthony and Gérémy, who have shown and continue to show great resilience and strength. I am proud of you.

Table of Contents

Chapter 2. Volcanic and Structural Reconstruction of the Deformed and Metamorphosed Ming Volcanogenic Massive Sulfide Deposit, Canada: Implications for Ore Zone Geometry and Metal Distribution

List of Tables

List of Figures

List of Appendices

Co-authorship Statement

This thesis has received contribution from a number of authors. The design of the research project is attributed to Stephen (Steve) Piercey and Jean-Luc Pilote. The identification of specific questions to be examined was refined by Jean-Luc Pilote during the course of the study with the guidance of Steve Piercey and Patrick Mercier-Langevin. Field work was predominantly planned and carried out by the thesis author and Steve Piercey. A number of samples collected by Steve Piercey in 2010 were reanalyzed by the thesis author and included in this thesis. Early visits from Steve Piercey and Patrick Mercier-Langevin in the study area were used as occasions to plan and examine and discuss the preliminary results with the thesis author.

Chapters 2 through 5 were written with the intention to publish in various scientific journals. The paper which constitutes Chapter 2 was published in *Economic Geology* as a regular paper and was co-authored by Steve Piercey and Patrick Mercier-Langevin. The co-authors provided editorial guidance and helped the principal author in shaping ideas. This paper was reviewed by journal editor and reviewers Paul Spry (Iowa State), Alan Bailes (Bailes Geoscience), and Suzanne Paradis (GSC).

A scientific communication was published in *Economic Geology*, which comprises Chapter 3. The co-authors include Steve Piercey, Stefanie Brueckner (Auburn), and Dave Grant (CREAIT – MUN). Dr. Piercey provided editorial guidance and helped in refining the scientific methods; Dr. Brueckner contributed in providing key photomicrographs from her study and guidance on the Au-Te association; Dr. Grant provided technical assistance during SEM-MLA analyses. The paper was reviewed by

journal editor and reviewer Paul Spry (Iowa State) and Dave Huston (Geoscience Australia).

A paper that comprises Chapter 4 has been submitted to *American Journal of Science*, which is pending reviews. This paper is co-authored by Steve Piercey, which has contributed editorially and helped in shaping ideas. This paper was informally reviewed by Greg Dunning (MUN). Samples from previous field seasons by Steve Piercey were included in this study.

Lastly, a paper that constitutes mostly Chapter 5 is expected to be submitted to the journal Mineralium Deposita or Ore Geology Reviews. This paper is co-authored by Steve Piercey and Patrick Mercier-Langevin, both of whom have contributed editorially. This paper also includes samples collected by Dr. Piercey during previous field seasons.

In Appendices 1 to 3 are papers that were published by the GSC as *Current Research* or open files and represent progress reports written at the end of each field season. Appendix 1 was published as a *Current Research* report by the GSC and was co-authored by Steve Piercey, who provided editorial guidance. This report was reviewed internally by Jan Peter (GSC) and Patrick Mercier-Langevin. Appendix 2 represents a *Current Research* report published by the GSC and is co-authored by Steve Piercey and Patrick Mercier-Langevin, both of whom have provided editorial guidance. This paper was reviewed internally by Jan Peter. Appendix 3 represents a summary report published as a chapter in a compiled report, part of the Targeted Geoscience Initiative (TGI)-4 program. This paper is also co-authored by Steve Piercey and Patrick Mercier-Langevin, who have contributed editorially. This paper was reviewed by Pierre-Simon Ross (Institut National de la Recherche Scientifique – INRS) and Jan Peter.

Chapter 1
Introduction to the thesis

1.1. Scope and location of the study area

The eastern portion of the Baie Verte Peninsula is host to some of the most complex geology of the Canadian Appalachians and to significant mineral deposits, including volcanogenic massive sulphide (VMS), and orogenic Au deposits hosted in both mafic rocks and iron formations. Because of its endowment in base and precious metals, the peninsula represents an important contributor to the economy for the province of Newfoundland and Labrador. This eastern portion of the peninsula is composed of a series of dissected Cambro-Ordovician ophiolites that formed during the closing stages of the Humber (also known as the Taconic) seaway, a realm developed at the paleo-margin of Laurentia (Fig. 1.1). In recent years, geologists have provided geological, geochemical, and geochronological evidence to reliably correlate all the ophiolites across the peninsula, which has delivered crucial contributions to the tectonic reconstruction of the area (Skulski et al., 2010; 2015 and references therein).

Although they once formed a single sheet of oceanic crust (i.e., Baie Verte oceanic tract), each sliver has a distinct name, including (from east to west) the Betts Cove, Pacquet, Pointe Rousse, and Advocate complexes (Fig. 1.1; Hibbard, 1983; Skulski et al., 2015). A cover sequence, namely the Snooks Arm Group, has also been correlated across the peninsula (Skulski et al., 2015). Of particular importance to this thesis has been the detailed regional work carried out in the late 1990s through early 2010s on all ophiolitic complexes (e.g., Bédard, 1999; Bédard et al., 1996; 1998; Castonguay et al., 2009; 2014; Skulski et al., 2010; 2015), which has proven to be a productive period in the

overall understanding of the geological setting. However, many questions remained unanswered at the local scale, particularly regarding the genesis and setting of numerous mineral deposits. It is well known that a proper understanding of the regional metallogenic framework can greatly benefit regional to orogenic-scale geological and tectonic reconstructions, and vice versa (e.g., Swinden and Thorpe, 1984; Swinden et al., 1988; 1997; van Staal, 2007).

This thesis centers on the ca. 487 Ma Ming VMS deposit, a ~30 Mt Cu-Zn-Ag-Au deposit that is hosted in the uppermost section of the Pacquet complex (Fig. 1.2). Whereas the Pacquet complex predominantly consists of rocks of mafic compositions, within the limits of the Ming deposit, the host rocks are entirely felsic (Rambler Rhyolite formation). The Ming deposit was discovered in 1970 and has been in operation intermittently since 1971. Since its discovery, it has been the focus of only a few studies (Gale, 1971; Tuach, 1976; Tuach and Kennedy, 1978; Weick et al., 1990; Bailey, 2002) that were limited by sample numbers and/or access. Only recently has there been detailed work. For example, Brueckner et al. (2011; 2014; 2015; 2016) carried out a comprehensive study on the sulfide mineralogy at Ming, providing key elements to the understanding of the distribution and paragenesis of the metals and the fluid conditions that are associated with the formation of the ore zones. While these authors were successful in advancing our general knowledge of the deposit, many fundamental questions remained unanswered. Because of its current operation and accessible drill core and underground workings, the Ming deposit provided an excellent laboratory to study the relationships between the mineralization and aspects enumerated below (objectives).

In the following section are an overview of VMS deposits, the objectives and methodology of this study, and an outline of the structure of this thesis.

1.2. Overview of volcanogenic massive sulphide deposits

Volcanic- and magmatic-associated hydrothermal events in ancient and present submarine environments are subject to the formation of stratabound accumulations of sulphide minerals referred to as seafloor massive sulfide (SMS) or volcanogenic massive sulphide (VMS). They form at or near the seafloor in various tectonic settings (e.g., mid ocean rifts, arcs, back-arcs) and consequently in a variety of host-rock lithologies (e.g., Franklin et al., 1981, 2005; Hannington et al., 1999). The formation of VMS deposits depends on various factors such as the presence of a heat source (subvolcanic intrusion), deep and shallow fractures, which allow the interaction between heated seawater (hydrothermal fluid) and the wall rock, and the water:rock ratio or the metal endowment in the wall rock (e.g., Lydon, 1984, 1988, 1996; Franklin, 1993, 1996). The hydrothermal activity resulting in the formation of VMS deposits as observed on modern analogues on the seafloor (e.g., black and white smokers; Herzig and Hannington, 1995; German and von Damm, 2003; Hannington et al., 2005) can be compared to a plumbing system (Franklin, 1993, 1996). They typically form stratiform semi-massive to massive sulphide horizons of various shapes (Large, 1992) overlying a stockwork zone (Lydon, 1984). The stockwork zone is usually intensely altered to chlorite and/or quartz with associated sulphide-bearing stringers, which reflect pathways of metals in fluids that reached disequilibrium due to, for example, mixing with infiltrated seawater.

Large (1992) presented a variety of VMS styles based on the relationship between shape, metal content, types of mineralization, and related footwall alteration from Australian deposits. This generalization can be applied to VMS deposits worldwide and shows the variability in morphology of VMS deposits. Volcanogenic massive sulphides usually have aspect ratios (maximum lateral extent: thickness) ranging between 10:1 and 3:1 (Lydon 1984, 1996), and in plan-view, elongate to lobate shapes. The elongated bodies may reflect transported ore (e.g. debris flow), fissure-controlled hydrothermal discharge, or post-burial tectonic deformation (e.g., Lydon, 1996; Bleeker, 1999).

Volcanogenic massive sulphide deposits have been classified by their metal content (Franklin et al., 1981; Lydon, 1984; Large, 1992), their host rock assemblages (Barrie and Hannington, 1999; Franklin et al., 2005), and their tectonic setting (Franklin et al., 2005; Huston et al., 2010). The latter two classifications are commonly used mutually since the host rock lithological assemblages are controlled by geodynamic processes (e.g., Barrie and Hannington, 1999). The lithological classification considers five main assemblages based on their respective proportions: 1) mafic, 2) bimodal-mafic, 3) siliciclastic-mafic or pelitic-mafic, 4) siliciclastic-felsic, and 5) bimodal-felsic. This five-fold classification is described in more detail in Barrie and Hannington (1999) and Franklin et al. (2005) with the addition of the high-sulfidation bimodal-felsic type by Galley et al. (2007), a hybrid between bimodal-felsic VMS deposits and high-sulfidation epithermal deposits.

Fertile rock sequences forming VMS deposits are tightly controlled by their tectonic environment. This implies that the tectonic setting is the primary controlling factor to their formation, irrespective of the VMS classification (i.e., metal classification

or host-rock lithology). However, lithostratigraphic and lithogeochemical associations can be assigned to specific tectonic settings, collectively used to characterize volcanic terranes for their potential for VMS formation (Franklin et al., 2005). It is well known that VMS deposits are formed in extensional regimes (Lydon, 1988, 1996) and consequently associated with bimodal magmatism (Lesher et al., 1986; Lentz, 1998) with variable proportions (hence Barrie and Hannington's (1999) classification). These include: (1) intra-oceanic back-arcs, (2) sedimented mid-ocean ridges, transform or back-arcs, (3) rifted oceanic arcs, (4) continental margin arcs and related back-arcs, (5) mature epicontinental back-arcs, and (6) ocean spreading centres (Fig. 1.3; e.g., Gibson et al., 2007; Franklin et al., 2005; Hannington et al., 2005). More complex and/or rare settings exist, and these include: (7) transtensional regime related to oblique collision, (8) post-collisional extension, (9) plume or hot spot-related, and (10) off-axis volcanoes (Hannington et al., 2005; Huston et al., 2010). Since it has been widely accepted that the Baie Verte oceanic tract was formed in a supra-subduction-related setting and more specifically in a fore-arc system (Bédard et al., 1998; Bédard, 1999; van Staal and Barr, 2012), it holds the foundation of many of the hypotheses that were formulated over the course of this thesis. Extension in supra-subduction zones may result from slab roll-back of the subducted slab, convection in the upper mantle wedge induced by the descending slab, or slab break-off (Hannington et al., 2005 and references therein).

1.3. Objectives

The broad goals of this research are to better understand the setting of the Ming VMS deposit, the petrologic evolution of the host rocks and their association with the

mineralization, and to characterize the alteration associated with the hydrothermal processes genetically associated with deposit formation. Within these broad goals are a number of specific thematic interests, including an improved understanding of: 1) the stratigraphy and physical volcanology of the host successions; 2) the underlying controlling factor(s) for the current geometry of the sulphide lenses and the underlying stockwork zone; 3) the timing of the introduction of Au in the Ming deposit (i.e., syngenetic vs. epigenetic); 4) the role of deformation on sulphide and metal remobilization; 5) the petrogenesis of the felsic rocks that are host to the Ming VMS deposit and their role in the formation of the deposit; 6) the provenance and petrogenesis of the sedimentary and volcanic/volcaniclastic rocks that immediately overly the Ming deposit in order to, together with the petrotectonic attributes of the Rambler Rhyolite formation and its underlying geology, provide insights into the tectonic evolution of this peri-Laurentian domain; and 7) the nature, distribution, paragenesis, and controlling factors of the hydrothermal alteration. Resolving these various aspects helps elucidate some of the remaining knowledge gaps that exist in other similar VMS environments globally.

1.4. Methodology

1.4.1. Mapping and petrography

Field portions of this study were carried out during the summers of 2012 through 2014. Detailed mapping at a scale of 1:20 and sampling were undertaken in various underground workings, mostly in the northwest portion of the Ming deposit. Additionally, a series of historical to recent surface and underground diamond drill cores were

described with representative and/or systematic samples collected throughout the deposit for various petrographic, lithogeochemical, hyperspectral, and isotopic analyses. Samples selected for regular polished thin sections were sent to Vancouver Petrographics Ltd. for preparation. All petrographic work was done on a Nikon Eclipse LV100POL diascopic and episcopic microscope at Memorial University of Newfoundland.

1.4.2. Whole-rock lithogeochemistry

Whole-rock lithogeochemistry constitutes an important aspect of this thesis and was used to understand the magmatic affinity of the various rock units that are host to, overlying, and cross-cutting the Ming deposit. It was also employed as a tool to characterize and understand element mobility due to the hydrothermal alteration associated with the formation of the Ming deposit. Selected samples were sent to Activation Laboratories Ltd. in Ancaster, Ontario for major and some trace elements, which were determined by inductively coupled plasma emission-mass spectrometry (ICP-ES). Returned powders were analyzed for an extended suite of trace and rare earth elements by inductively coupled plasma-mass spectrometry (ICP-MS) at Memorial University of Newfoundland. Details on the methodology and quality controls are presented in Appendix A4.2.

1.4.3. Nd isotope geochemistry

The main goal for using Nd isotope geochemistry is to determine the relative involvement of juvenile and evolved components during magma genesis. Neodymium isotope geochemistry was performed on all units of the felsic host successions, the

immediately overlying units, and on the cross-cutting mafic dykes. This method complements the use of trace element geochemistry, which can also help to elucidate similar questions. Neodymium analyses were done at the Department of Earth Sciences of Memorial University of Newfoundland on representative samples using the same powders that were used for whole-rock geochemistry. Further details on the method and quality controls are presented in Appendix A4.2.

1.4.4. Mineral liberation analyzer (MLA)-secondary electron microscopy (SEM)

The combination of MLA and SEM provides a powerful tool to identify the textural and mineralogical assemblages in samples. Here it was used to resolve fundamental genetic problems associated with Au at the Ming deposit. This technique is efficient to examine thousands of mineral grains, it provides a statistically representative analysis of the mineral composition of a sample, and it allows the ability to distinguish extremely fine-grained or complexly intergrown minerals at submicroscopic levels that are often very difficult to determine using conventional reflected light microscopy and SEM. The analyses were done at Memorial University of Newfoundland and further details on the method are presented in Chapter 3.

1.4.5. Hyperspectral reflectance spectrometry

The hyperspectral reflectance spectrometry is used in this study as a complementary method to the whole-rock geochemistry. The technique is based on the principle that certain minerals associated with alteration absorb light at specific ranges of

wavelengths, diagnostic to the composition of the mineral of interest. Analyses were mostly done systematically on drill cores (intervals of 3 to 5 m) or on specific samples collected underground. Further details on the method are presented in Chapter 5.

1.4.6. Electron probe micro-analyzer (EPMA)

The composition of key minerals associated with hydrothermal alteration can help in understanding some of the fluid conditions (e.g., temperature, acidity, redox conditions). All mineral composition determinations were done at the Department of Earth Sciences of Memorial University of Newfoundland using the electron probe micro-analyzer. Further details on the method are presented in Chapter 5.

1.5. Presentation of the thesis

The thesis is divided in six chapters, four (Chapters 2 to 5) of which have been written as manuscripts for publication in refereed scientific journals. As stated above, this collection of manuscripts are in various stages of publication and each paper addresses a unique geological problem associated with the Ming deposit. Overlaps between chapters are unavoidable but efforts were made within each chapter to provide a unique rendering of some of the repetitive geological or geochemical aspects presented in accordance to the main topic discussed.

Chapter 2 documents the stratigraphy, physical volcanology, and primary and secondary structures of the Ming deposit. It provides, for the first time, a detailed reconstruction of the stratigraphic host successions at Ming and their relationships to the mineralization. It also shows the abrupt lateral changes in the host rocks that are likely to

be expressions of synvolcanic faulting. These faults are shown to have controlled volcanic eruptions, hydrothermal fluids, and sulphide precipitation. This chapter provides details on the post-mineralization deformation evolution and evidence for sulphide remobilization in response to deformation. This chapter is critical to this research as it sets the geological foundation to the other chapters.

Chapter 3 examines the implications of precious metals-enriched sulphide clasts in a mafic polymictic breccia that immediately overlies part of the Ming deposit. By using a standard petrographic microscope and the MLA-SEM to identify the distribution of metal phases in the sulphide clasts, the results are then used to: 1) constrain their provenance, and to 2) discuss their implications in the timing of Au introduction in the massive sulphides at the Ming deposit. The results convincingly show that based on the textural relationships and mineral assemblages, the sulfide clasts originated from the underlying massive sulfides lenses, that the Au and associated trace metals are enclosed in the clasts, and that the Au is syngenetic.

Chapter 4 is a geochemical and Nd isotopic study on the felsic host successions at the Ming deposit, their immediately overlying rocks, and the different generations of cross-cutting mafic to intermediate intrusions. In this paper, emphasis is placed on the FI- and FII-type felsic volcanic rocks that are host to the Ming deposit and their petrogenesis. It investigates the various possible source(s) and/or process(ses) responsible for the formation of FI- and FII-type rhyolites and their relationships, or lack thereof, with the underlying boninitic crust. Modeled melting products derived from a variety of source compositions (mineralogical and geochemical) determined that the most likely source to form the highly geochemically fractionated felsic rocks includes the direct contribution of

an island arc tholeiite. The results of this model are interpreted to reflect the direct involvement of subducted crustal material that was originally formed in a supra-subduction zone, thus providing key elements to the complex Cambro-Ordovician tectonic evolution of the peri-Laurentian realm. The chapter also poses a possible link between FI-(FII-)type rhyolites and adakites formed in primitive settings such as in the Bonin arc and their involvement into the formation of Au-enriched VMS deposits. The paper also questions the composition of the mantle at the time of the formation of Ming, its interaction with the rising felsic magmas, and the transition to the less depleted cover sequence (i.e., base of the Snooks Arm Group).

Chapter 5 documents the various hydrothermal alteration assemblages associated with the formation of the Ming deposit. It provides a detailed reconstruction and paragenesis of these assemblages from field observations, petrography, geochemistry, hyperspectral analyses, and mineral chemical analyses. The results provide evidence of a synvolcanic and volcanological control on fluid chemistry and the distribution of these fluids. Waxing of the hydrothermal system to culminating temperatures is contemporaneous with the deposition of the Cu-rich stockwork zone of the deposit, which is also spatially controlled by the coherent-volcaniclastic interface in the upper Rambler Rhyolite formation. The paper also provides evidence that the waning stage of the hydrothermal system is likely coeval with the deposition of the precious metals at Ming. From the detailed mapping, these areas are immediately underlain by coherent facies, thus providing some indications that the volcanic rocks had a direct control on the fluid that carried precious metals. The paper also discusses the implication of the compositions of some of the minerals found associated with the alteration at the Ming deposit.

Lastly, chapter 6 presents the overall conclusions of the thesis with recommended directions for future research that could solve some of the outstanding geological problems at the Ming deposit and its vicinity.

1.6. References

Bailey, J., 2002, Chemostratigraphy surrounding the Ming Mine VMS mineralization in the northern Pacquet Harbour Group (PHG) and correlations with the southern PHG, Baie Verte Peninsula, Newfoundland: Unpublished B.Sc. thesis, Memorial University of Newfoundland, 125 p.

Barrie, C.T., and Hannington, M.D., 1999, Classification of volcanic-associated massive sulfide deposits based on host-rock composition: Reviews in Economic Geology, v. 8, p. 1-11.

Bédard, J.H., 1999, Petrogenesis of boninites from the Betts Cove ophiolite, Newfoundland, Canada: Identification of subducted source components: Journal of Petrology, v. 40, p. 1853-1889.

Bédard, J.H., Lauzière, K., Sangster, A., Boisvert, E., Tellier, M., Tremblay, A., and Dec, T., 1996, Geological map of the Betts Cove ophiolitic massif and its cover rocks: Geological Survey of Canada, Canadian Geoscience Map 3271, scale 1:20 000. doi:10.4095/208188

Bédard, J. H., Lauzière, K., Tremblay, A., and Sangster, A., 1998, Evidence for forearc seafloor-spreading from the Betts Cove ophiolite, Newfoundland: oceanic crust of boninitic affinity: Tectonophysics, v. 284, p. 233-245.

Bleeker, W., 1999, Structure, stratigraphy, and primary setting of Kidd creek volcanogenic massive sulfide deposit: A semiquantitative reconstruction, In Hannington, M.D., and Barrie, C.T., eds., The Giant Kidd Creek volcanogenic massive sulfide deposit, western Abitibi Subprovince, Canada: Economic Geology Monograph, v. 10, p. 71-121.

Brueckner, S., Piercey, S., Layne, G., Piercey, G., and Sylvester, P., 2015, Variations of sulphur isotope signatures in sulphides from the metamorphosed Ming Cu(−Au) volcanogenic massive sulphide deposit, Newfoundland Appalachians, Canada: Mineralium Deposita, p. 1-22.

Brueckner, S.M., Piercey, S.J., Pilote, J.-L., Layne, G.D., and Sylvester, P.J., 2016, Mineralogy and mineral chemistry of the metamorphosed and precious metal-bearing Ming deposit, Canada: Ore Geology Reviews, v. 72, p. 914-939.

Brueckner, S.M., Piercey, S.J., Sylvester, P.J., Maloney, S., and Pilgrim, L., 2014, Evidence for syngenetic precious metal enrichment in an Appalachian volcanogenic massive sulfide system: The 1806 Zone, Ming Mine, Newfoundland, Canada: Economic Geology, v. 109, p. 1611-1642.

Brueckner, S.M., Piercey, S.J., Sylvester, P.J., Pilgrim, L., Maloney, S., Hyde, D., and Ogilvie, G., 2011, Stratigraphy, mineralogy, geochemistry, and genesis of an Au-rich volcanogenic massive sulfide (VMS) system from the Baie Verte Peninsula, NW Newfoundland, Canada: The 1806 Zone as an example from the Ming Mine, Rambler Camp, In Deschênes, G., Dimitrakopoulos, R., and Bouchard, J., eds., World Gold 2011: Montreal, QC, Canada, Canadian Institute of Mining, Metallurgy and Petroleum, p. 899-911.

Castonguay, S., Skulski, T., van Staal, C.R., and Currie, M., 2009, New insights on the structural geology of the Pacquet Harbour group and Point Rousse complex, Baie Verte peninsula, Newfoundland: Newfoundland and Labrador Department of Natural Resources, Geological Survey, Current Research, Report 09-1, p. 147-158.

Castonguay, S., van Staal, C.R., Joyce, N., Skulski, T., and Hibbard, J.P., 2014, Taconic metamorphism preserved in the Baie Verte Peninsula, Newfoundland Appalachians: Geochronological evidence for ophiolite obduction and subduction and exhumation of the leading edge of the Laurentian (Humber) margin during closure of the Taconic seaway: Geoscience Canada, v. 14, p. 459-482.

Franklin, J. M., 1993, Volcanic-associated massive sulphide deposits, In Kirkham, R.V., Sinclair, W.D., Thorpe, R.I., and Duke, J.M., eds., Mineral Deposit Modeling, Geological Association of Canada, Special Paper 40, p. 315-334.

Franklin, J.M., 1996, Volcanic-associated massive sulphide base metals, In Eckstrand, O.R., Sinclair, W.D., and Thorpe, R.I., eds., Geology of Canadian Mineral Deposit Types, Geological Survey of Canada, v. 8, p. 158-183.

Franklin, J.M., Gibson, H.L., Jonasson, I.R., and Galley, A.G., 2005, Volcanogenic massive sulfide deposits, In Hedenquist, J.W., Thompson, J.F.H., Goldfarb, R.J., and Richards, J.P., eds., Economic Geology 100th Anniversary Volume, 1905-2005, Society of Economic Geologists, p. 523-560.

Franklin, J.M., Lydon, J.W., and Sangster, D.F., 1981, Volcanic-associated sulfide deposits, In Skinner, B.J., ed., Economic Geology Seventy-Fifth Anniversary Volume, Society of Economic Geologists, p. 485-627.

Gale, G.H., 1971, An investigation of some sulphide deposits in the Rambler area, Newfoundland: Unpublished Ph.D. thesis, Durham, England, University of Durham, 137 p.

Galley, A., Hannington, M., and Jonasson, I., 2007, Volcanogenic massive sulphide deposits, In Goodfellow, W.D., ed., Mineral Deposits of Canada: A synthesis of major deposit-types, district metallogeny, the evolution of geological provinces, and exploration methods, Special Publication No. 5, Geological Association of Canada, Mineral Deposits Division, p. 141-161.

German, C.R., and von Damm, K.L., 2003, Hydrothermal processes, In Holland, H.D., and Turekian, K.H., eds., The Oceans and Marine Geochemistry. Treatise on Geochemistry, Vol. 6, p. 181-222.

Gibson, H.L., Allen, R.L., Riverin, G., and Lane, T.E., 2007, The VMS model; advances and application to exploration: Proceedings - Decennial International Conference on Mineral Exploration, v. 5, p. 713-730.

Hannington, M.D., de Ronde, C.E.J., D.R., and Petersen, S., 2005, Sea-floor tectonics and submarine hydrothermal systems, Economic Geology 100th Anniversary Volume, p. 111-141.

Hannington, M.D., Poulsen, K.H., Thompson, J.F.H., and Sillitoe, R.H., 1999, Volcanogenic gold in the massive sulfide environment: Reviews in Economic Geology, v. 8, p. 325-351.

Herzig, P.M., and Hannington, M.D., 1995, Polymetallic massive sulfides at the modem seafloor: A review: Ore Geology Reviews, v. 10, p. 95-115.

Hibbard, L.J., 1983, Geology of the Baie Verte Peninsula, Newfoundland, Department of Mines and Energy, Government of Newfoundland and Labrador, Memoir 2, 279 p.

Huston, D.L., Pehrsson, S., Eglington, B.M., and Zaw, K., 2010, The geology and metallogeny of volcanic-hosted massive sulfide deposits: Variations through geologic time and with tectonic setting: Economic Geology, v. 105, p. 571-591.

Large, R.R., 1992, Australian volcanic-hosted massive sulfide deposits; features, styles, and genetic models: Economic Geology, v. 87, p. 471-510.

Lentz, D.R., 1998, Petrogenetic evolution of felsic volcanic sequences associated with Phanerozoic volcanic-hosted massive sulphide systems: the role of extensional geodynamics: Ore Geology Reviews, v. 12, p. 289-327.

Lesher, C.M., Goodwin, A.M., Campbell, I.H., and Gorton, M.P., 1986, Trace-element geochemistry of ore-associated and barren, felsic metavolcanic rocks in the Superior Province, Canada: Canadian Journal of Earth, v. 23, p. 222-237.

Lydon, J.W., 1984, Volcanogenic massive sulphide deposits, Part 1: A descriptive model: Geoscience Canada, v. 11, p. 195-202.

Lydon, J.W., 1988, Volcanogenic massive sulphide deposits, Part 2: Genetic models: Geoscience Canada, v. 15, p. 43-65.

Lydon, J.W., 1996, Characteristics of volcanogenic massive sulphide deposits; interpretations in terms of hydrothermal convection systems and magmatic hydrothermal systems: Boletin Geologico y Minero, v. 107, p. 215-264.

Pilgrim, L., 2009, Mineral resource estimate for the Ming Mine, Newfoundland, Canada: Rambler Metals and Mining Canada Ltd., Technical Report NI43-101, 114 p.

Skulski, T., Castonguay, S., McNicoll, V., van Staal, C., Kidd, W., Rogers, N., Morris, W., Ugalde, H., Slavinski, H., Spicer, W., Moussallam, Y., and Kerr, I., 2010, Tectonostratigraphy of the Baie Verte oceanic tract and its ophiolite cover sequence on the Baie Verte Peninsula: Current Research, Newfoundland and Labrador Department of Natural Resources, Geological Survey, Report 10-1, p. 315-335.

Skulski, T., Castonguay, S., Kidd, W.S.F., McNicoll, V.J., van Staal, C.R., and Hibbard, J.P., 2015, Geology, Baie Verte and parts of Fleur de Lys, Newfoundland and Labrador, NTS 12-H/16 and part of NTS 12-I/1: Geological Survey of Canada, Canadian Geoscience Map 159, scale 1:50 000. doi:10.4095/295865

Swinden, H.S., Jenner, G.A., and Szybinski, Z.A., 1997, Magmatic and tectonic evolution of the Cambrian-Ordovician Laurentian margin of Iapetus; geochemical and isotopic constraints from the Notre Dame Subzone, Newfoundland: Memoir - Geological Society of America, v. 191, p. 337-365.

Swinden, H.S., Kean, B.F., and Dunning, G.R., 1988, Geological and paleotectonic settings of volcanogenic sulphide mineralization in Central Newfoundland, In Swinden, H.S., and Kean, B.F., eds., The volcanogenic sulphide districts of Central Newfoundland: A guidebook and reference manual for volcanogenic sulphide deposits in the early Paleozoic oceanic volcanic terranes of Central Newfoundland: Geological Association of Canada, Mineral Deposits Division, p. 5-26.

Swinden, H.S., and Thorpe, R.I., 1984, Variations in style of volcanism and massive sulfide deposition in Early to Middle Ordovician island-arc sequences of the Newfoundland Central Mobile Belt: Economic Geology, v. 79, p. 1596-1619.

Tuach, J., 1976, Structural and stratigraphic setting of the Ming and other sulphide deposits in the Rambler area, Newfoundland: Unpublished M.Sc. thesis, Memorial University of Newfoundland, Canada, 128 p.

Tuach, J., and Kennedy, M.J., 1978, The geologic setting of the Ming and other sulfide deposits, consolidated Rambler mines, Northeast Newfoundland: Economic Geology, v. 73, p. 192-206.

van Staal, C.R., 2007, Pre-Carboniferous tectonic evolution and metallogeny of the Canadian Appalachians, In Goodfellow, W.D., ed., Mineral deposits of Canada: A synthesis of major deposit-types, district metallogeny, the evolution of geological provinces, and exploration methods, Special Publication No. 5, Geological Association of Canada, Mineral Deposits Division, p. 793-818.

van Staal, C.R., and Barr, S.M., 2012, Lithospheric architecture and tectonic evolution of the Canadian Appalachians, in Percival, J.A., Cook, F.A., and Clowes, R.M., eds.,

Tectonic Styles in Canada Revisited: the LITHOPROBE perspective: Geological Association of Canada Special Paper 49, p. 41-95.

Weick, R.J., Wilson, M., and Swinden, S., 1990, Mineralization and alteration study of the Main Orebody, Consolidated Rambler Mines, Baie Verte, Newfoundland: Canada, Newfoundland. Mineral Development Division : St. John's, NL, Canada, p. 217-225.

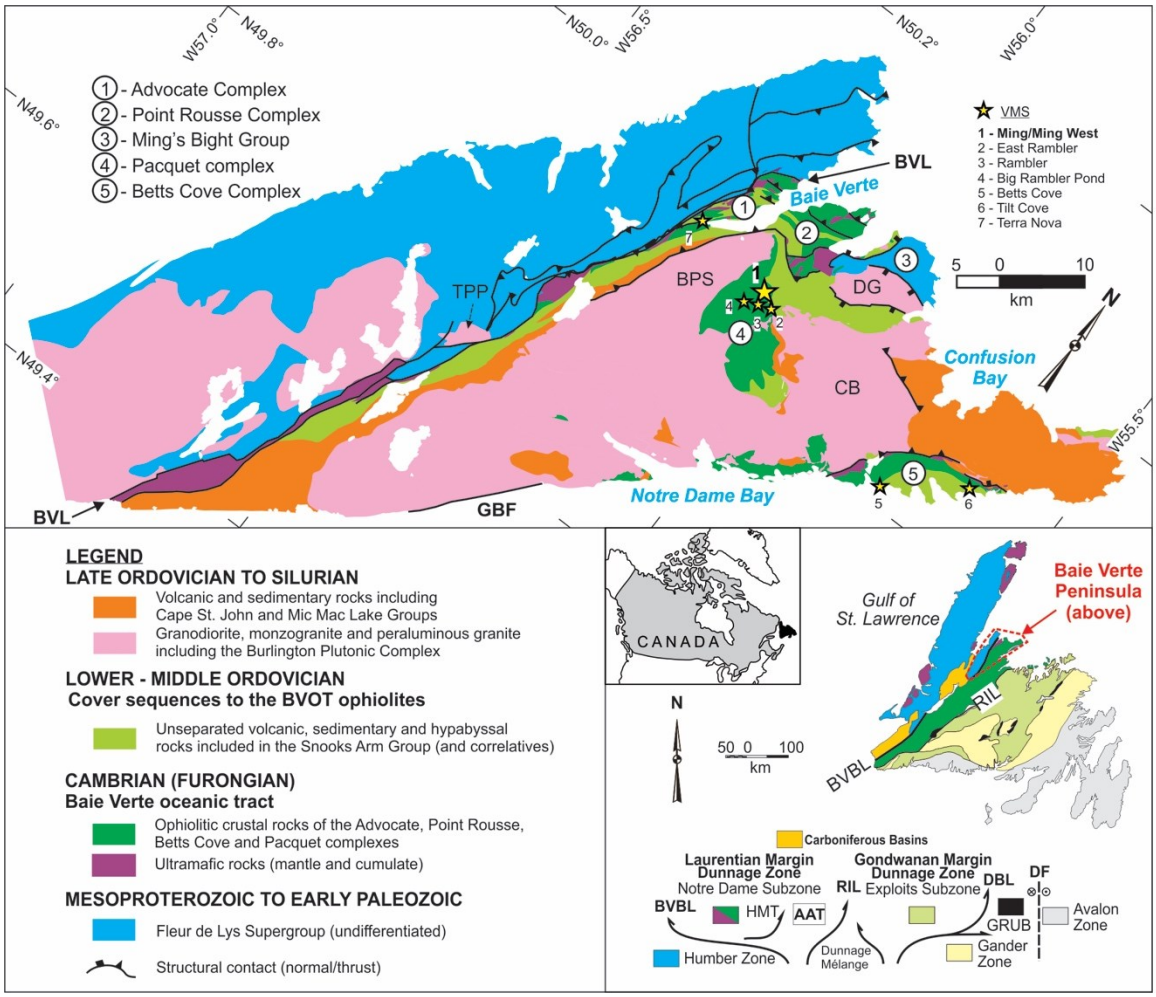

Fig. 1.1. Simplified geology of the Baie Verte Peninsula with major tectonostratigraphic zones that form the Appalachian orogenic belt in Newfoundland (modified from Castonguay et al., 2014 and references therein). Location of major VMS deposits as yellow stars. AAT = Annieopsquotch Accretionary Tract, BPS = Burlington plutonic Suite, BVBL = Baie Verte-Brompton Line, BVL = Baie Verte Line, CB = Cape Brulé, DBL = Dog Bay Line, DF = Dover Fault, DG = Dunamagon Granite, GBF = Green Bay Fault, GRUB = Gander River Ultramafic Belt, TPP = Trap Pond pluton, RIL = Red Indian Line, HMT = Hungry Mountain Thrust.

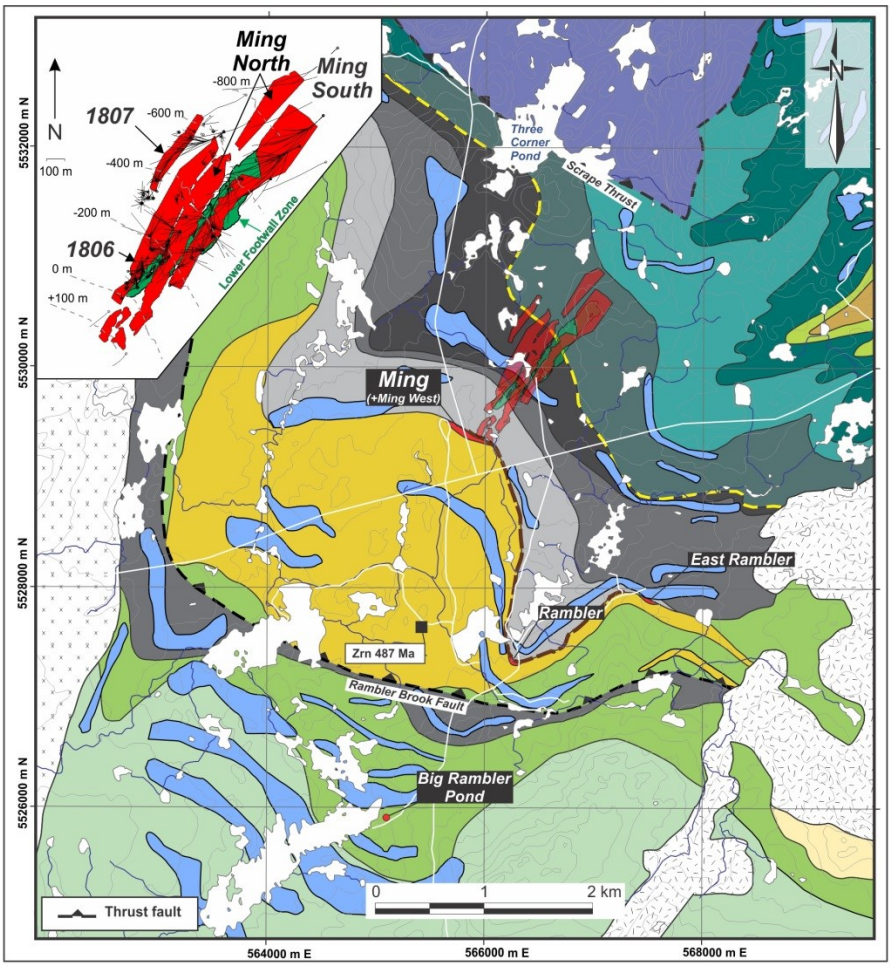

Silurian Cape St. John Group (unseparated)

Clastic, pink-red sedimentary rocks, mafic and/or felsic volcanic rocks.

Burlington Granodiorite (434 - 430 Ma)

Cape Brulé Porphyry (430 Ma)
Porphyritic granodiorite, quartz-feldspar porphyry.

Early-Middle Ordovician Snooks Arm Group (479-467 Ma)

Tholeiitic gabbro sills/dikes, include plagioclase-phyric to fine-grained gabbro. Minor medium-grained equigranular diorite.

Basalm Bud Cove Formation

Volcanogenic turbidite, siltstone, felsic tuffs, basalts.

Calc-alkaline felsic tuff, lapilli tuff.

Venam's Bight Formation
Tholeiitic pillowed basalt, porphyritic and vesicular basalt, siliceous mudstone.

Bobby Cove Formation
Chert, iron formation, volcanogenic sedimentary rocks, minor felsic tuffs.

Mafic tuff, lapilli tuff, epiclastic rocks, interbedded basalt flows.

Clinopyroxene-phyric crystal tuff, lapilli tuff, and tuff breccia (Prairie Hat member).

Calk-alkaline plagioclase-phyric pillow basalt and andesite.

Scrape Point Formation
Mafic volcaniclastic rocks, tuff, lapilli tuff, epiclastic sandstone, shale, interbedded pillow basalt.

Pillowed, massive, amygdaloidal, plgioclase-phyric basalt flows. Tholeiitic affinities.

Magnetite-rich iron formation, chert beds, volcanogenic siltstone (Nugget Pond horizon).

Cambro-Ordovician Pacquet Complex

Rambler Rhyolite formation (487 Ma)
Quartz-phyric rhyolite to rhyodacite flows interbedded with intermediate to felsic tuff, lapilli tuffs, and tuff breccia.

Mt. Misery Formation
Plagioclase- and pyroxene-phyric pillow basalt with tholeiitic affinities, interbedded with boninite.

Betts Head Formation
Spherulitic, amygdaloidal, porphyritic boninitic pillow lavas with aphanitic dark-green groundmass.

Point Rousse ophiolite (490 Ma)

Undifferentiated serpentinized ultramafic rocks with tholeiitic and boninitic affinities.

Fig. 1.2. Geological map of the study area, Baie Verte Peninsula, with Ming VMS orebodies projected to surface (also in the inset) and shown in light red and light green (Lower Footwall Zone = stockwork). Datum is UTM 21N NAD 83. Map compiled and modified from Tuach and Kennedy (1978), Hibbard (1983), Castonguay et al. (2009), Pilgrim (2009), and Skulski et al. (2010). The U-Pb zircon (Zrn) age is from Skulski et al. (2015).

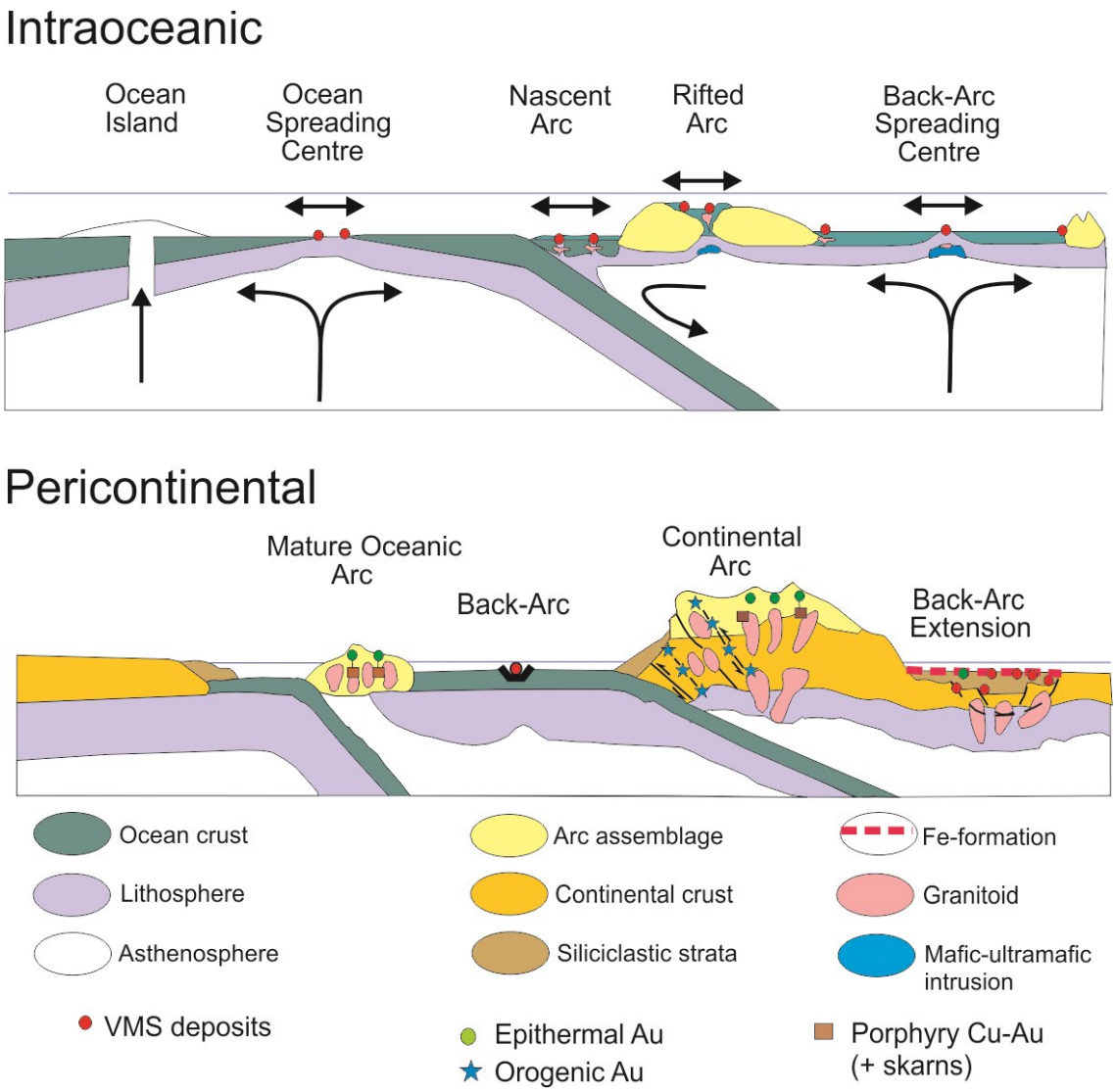

Fig. 1.3. Different intraoceanic (juvenile) and pericontinental (mature) tectonic settings in which VMS deposits can form. Other types of deposits can form associated to certain types of tectonic settings (i.e. epithermal Au, orogenic Au, and porphyry Cu-Au (+skarns)). Diagrams modified from Galley et al. (2007) and reference therein.

Chapter 2
Volcanic and Structural Reconstruction of the Deformed and Metamorphosed Ming Volcanogenic Massive Sulfide Deposit, Canada: Implications for Ore Zone Geometry and Metal Distribution

2.1. Abstract

The Ming volcanogenic massive sulfide deposit (28 Mt at 1.48 wt % Cu, 0.06 wt % Zn, 1.99 g/t Ag, and 0.26 g/t Au) is part of the Baie Verte oceanic tract located in the northeast Canadian Appalachian orogen. The deposit is hosted in a northeast dipping volcanic succession (~487 Ma Rambler Rhyolite formation) composed of rhyodacitic to rhyolitic volcanic and volcaniclastic rocks that form the uppermost part of the Pacquet ophiolite complex.

The deposit consists of four elongated, stratiform semimassive to massive sulfide lenses (1807, 1806, Ming North, and Ming South zones) averaging 3 m in thickness, 50 m in width, and 500 m to 1 km in length, all spaced 50 m apart from each another. The four semimassive to massive sulfide lenses are underlain by discordant stringers transitioning from sphalerite-rich to chalcopyrite-rich assemblages with stratigraphic depth. The chalcopyrite-rich stringer zone (Lower Footwall Zone) defines a 26 Mt mineral resource, oriented subparallel to the Ming North and 1806 zones.

Three units host the Ming deposit with the lowermost (unit 1.1) consisting of quartz-phyric to aphyric coherent rhyodacitic flows with marginal in situ massive hyaloclastite and peperite of similar compositions. Unit 1.1 is overlain by <200 m thick felsic quartz-bearing volcaniclastic sequences (unit 1.2) with localized quartz-phyric to megacrystic rhyodacite flows at the top, which forms a flow-dome complex, immediately underlying the semimassive to massive sulfide of the 1806 Zone. A coeval volcanic

sequence, consisting of quartz-phyric to -megacrystic rhyodacite (unit 1.3a) and quartz-bearing tuff (unit 1.3b), host superimposed stratiform massive sulfide lenses in the Ming South Zone, representing the waning stages of Rambler Rhyolite formation-related volcanism. The succession hosting the Ming deposit is overlain by sedimentary and mafic volcanic and volcaniclastic rocks of the ≤479 Ma Snooks Arm Group.

Synvolcanic faults are recognized at Ming by abrupt lateral changes in lithofacies. Subsidence of unit 1.1 and coeval deposition of unit 1.2 as a result of these synvolcanic faults occurred prior to the onset of the hydrothermal convection system responsible for the formation of the Lower Footwall Zone and associated semimassive to massive sulfide lenses. The faults, which are interpreted to have been conduits for the metal-rich hydrothermal and magmatic fluids that deposited the metal-rich sulfide deposits, continued to be active until the deposition and eruption of unit 1.3, which is restricted to the Ming South Zone.

Four major deformation events (D_1 to D_4) are recognized at the Ming deposit, with D_2 the most intense. Penetrative fabrics related to D_2 are commonly oriented north-northeast, dipping east, with Cu-Au-rich semimassive to massive sulfides locally transposed and/or remobilized into these structures, together with drag folds, sphalerite exsolution layers, and boudinaged mafic dikes. Piercement structures of Cu-Au-rich sulfides associated with D_2, commonly perpendicular to S_2, are accentuated by D_3 and D_4 structures, representing significant targets for exploration and production.

The results presented here suggest that the linear distribution of the semimassive to massive sulfide zones relates to the original volcanic architecture (synvolcanic fault control) despite the previous interpretation of them being entirely controlled by structural

elongation parallel to a regional stretch lineation; hence, this illustrates the importance of detailed reconstructions of lithostratigraphy, volcanic facies, and structure to the understanding of primary depositional controls on volcanogenic massive sulfide (VMS) mineralization in deformed orogenic belts. Furthermore, this study illustrates the effects of post-VMS deformation and metamorphism on the geometry of the ore lenses and on metal distribution in response to remobilization at various scales (secondary controls). A better understanding of primary and secondary controls on the nature and style of VMS has implications for exploration and development of deposits in ancient orogenic belts.

2.2. Introduction

Volcanogenic massive sulfide (VMS) and seafloor massive sulfide (SMS) deposits represent predominantly stratabound accumulations of polymetallic sulfide minerals at or near the seafloor that form due to interaction between metal-bearing hydrothermal ± magmatic fluids and seawater (Franklin et al., 1981, 2005; Lydon, 1996; Barrie and Hannington, 1999; Large et al., 2001). These deposits are generally interpreted to be spatially, temporally, and genetically associated with synchronous volcanism (Franklin et al., 2005). Although the volcanostratigraphy and volcanic lithofacies hosting VMS deposits are well understood at the district scale, detailed studies regarding the character of the host successions are lacking for many, particularly those in strongly deformed VMS districts. Because rock types, architecture, and lithofacies of the host volcanic succession exert a significant control on the composition and style of the VMS mineralization and alteration (Gibson et al., 1999; Doyle and Allen, 2003; Franklin et al., 2005; Ross and Mercier-Langevin, 2014), understanding the volcanostratigraphy and

physical volcanology of VMS deposits provide a framework for developing better genetic and exploration models.

In addition to synvolcanic controls on the composition and styles of VMS deposits, their geometry, ore distribution, and metal content are also strongly influenced by post-mineralization sulfide remobilization (chemical and/or mechanical) during deformation and metamorphism (Gilligan and Marshall, 1987; Marshall and Gilligan, 1987, 1993; Larocque et al., 1993; Zheng et al., 2012; Caté et al., 2014). For example, these processes can lead to localized enrichment of sulfides (e.g., chalcopyrite, sphalerite, and galena), sulfosalts (e.g., tennantite-tetrahedrite), and precious metals (Au, Ag). Despite many VMS deposits exhibiting deformation, the recognition and understanding of the relationship between deformation and sulfide remobilization is poorly documented and understood globally.

The Baie Verte Peninsula in Newfoundland, Canada, is host to six producing and past-producing VMS deposits. One of them, the Ming deposit, locally contains up to 2.96 g/t Au (Table 2.1 and Fig. 2.1; Brueckner et al., 2014, 2016). Recent work by Brueckner et al. (2014, 2016) and Pilote et al. (2016) reported a syngenetic Au-enrichment with a magmatic source for the elements of the epithermal suite and precious metals at the Ming deposit. However, the broader volcanic architectural controls on the distribution of mineralization and the remobilization of mineralization by post-VMS deformation and metamorphism were, prior to this study, poorly understood and yet to be determined. Although the Ming deposit contains significantly lower production grades and tonnage (Table 2.1) than world-class Au-rich and auriferous deposits globally (Mercier-Langevin et al., 2011), it has a number of important attributes that make it worthy of careful study.

These include availability of a complete stratigraphic sequence to study, excellent preservation state in a well constrained tectonic setting (e.g., van Staal and Barr, 2012), and extensive underground access (core and mine workings) to different parts of the deposit. This makes the Ming deposit an ideal natural laboratory for improving our understanding of precious metals-enrichment processes, the volcanostratigraphic controls on VMS deposit genesis, and the effects of post-VMS deformation and metamorphism on the remobilization of sulfide mineralization.

The objectives of this paper are to: (1) document the volcanic lithofacies, including lateral and vertical variations, in order to determine the possible controls on the composition and styles of mineralization and site(s) of VMS-related hydrothermal upflow zones; (2) determine the deformation controls on the geometry and metal distribution of the Ming orebodies; and (3) provide key geological features to be used as exploration guidelines and applied to other VMS deposits. This study shows that a reconstruction from careful examination of the host volcanic and volcaniclastic successions is possible in deformed and metamorphosed VMS deposits globally. This, together with a detailed structural study, permits distinction between primary and deformation features and allows an accurate constraint on the controlling factors for ore characteristics and geometry.

2.3. Regional Geology

The Ming deposit is located in the Baie Verte Peninsula, northern Newfoundland (Fig. 2.1). The rocks that form the peninsula straddle the boundary between the Humber Zone to the west and a series of ophiolitic slivers and their cover rocks to the east, separated by the northeast striking and steeply dipping Baie Verte Line (BVL; Fig. 2.1;

Hibbard, 1983). The ophiolites comprise mainly suprasubduction zone rocks of mafic to ultramafic composition, including boninites (e.g., Skulski et al., 2010; 2015). These include the ca. 490 Ma (Dunning and Krogh, 1985; Cawood et al., 1996; Skulski et al., 2010) Advocate Complex (Bursnall, 1975), the Pointe Rousse Complex (Norman and Strong, 1975), the Betts Cove Complex (Bédard et al., 1998; Bédard, 1999), and rocks within the southern informally named Pacquet complex (Hibbard, 1983; Piercey et al., 1997; Skulski et al., 2015). Collectively, the ophiolites form the Baie Verte oceanic tract (BVOT; van Staal, 2007) and basement to the para-conformably to disconformably overlying volcano-sedimentary cover sequences of the ≤479 Ma Snooks Arm Group (Upadhyay, 1973; Jenner and Fryer, 1980; Hibbard, 1983; Skulski et al., 2010; 2015).

The Ming deposit host successions are part of the Pacquet complex. The base of the Pacquet complex consists of low-Ti boninite flows intercalated with thin (<50 m) beds of felsic tuff and rhyodacitic flows of the Betts Head Formation, which hosts the Big Rambler Pond, the Tilt Cove, and Betts Cove VMS deposits (Figs. 2.1, 2.2; Hibbard, 1983; Piercey et al., 1997; Skulski et al., 2010). The Betts Head Formation is overlain by intermediate-Ti boninite, island arc tholeiitic pillow basalt and breccia, and minor felsic tuff belonging to the Mount Misery Formation (Skulski et al., 2010). The upper part of this sequence is structurally repeated in the hanging wall of the Rambler Brook thrust fault (Fig. 2.2; Castonguay et al., 2009) where the 2.5 km-wide Rambler Rhyolite formation and massive sulfide lenses of the Ming deposit occur. The Rambler Rhyolite formation consists of a deformed, dome-shaped succession of felsic coherent volcanic and volcaniclastic rocks (Skulski et al., 2010). A sample of coherent felsic flow immediately stratigraphically below the nearby Rambler Main deposit has a U-Pb zircon age of 487±4

Ma (Fig. 2.2; V. McNicoll, unpub. data, reported in Skulski et al., 2015). This age is similar to coeval rocks in the Betts Cove Complex (ca. 489 Ma; Dunning and Krogh, 1985) and the 489-487 Ma age is the likely age of VMS mineralization within the Baie Verte oceanic tract. The Rambler Rhyolite formation is locally overlain by thin lenses of basalt of island-arc affinity, which are chemically similar to those of the Mount Misery Formation (Skulski et al., 2010). The latter are overlain by the ca. 479-467 Ma Snooks Arm Group (Skulski et al., 2010, 2015). The base of the Snooks Arm Group consists of a thin (<1 m) sequence of chert, magnetite-rich mudstone to siltstone, and sandstone (Nugget Pond horizon), which is laterally extensive and present throughout the Baie Verte Peninsula (Skulski et al., 2010). Overlying this unit are thin (<1 m) to thick (>100 m) alternating sequences of volcaniclastic monomictic to polymictic conglomerate, epiclastic wacke, iron formations, high-Ti tholeiitic to calc-alkaline basalt, and mafic to felsic volcaniclastic rocks (Hibbard, 1983; Skulski et al., 2010; 2015). The Snooks Arm Group is truncated to the north by the north-dipping Scrape Thrust (Fig. 2.2), juxtaposing the cover sequence with serpentinized ultramafic rocks of the Point Rousse Complex.

The Rambler Rhyolite formation is host to three VMS deposits (Table 2.1; Rambler, East Mine, and Ming) as well as numerous smaller VMS occurrences (Hibbard et al., 1983). These deposits are stratiform and spatially related to the intermediate-felsic volcanic and volcaniclastic rocks. The Big Rambler Pond deposit is stockwork-type mineralization (Tuach and Kennedy, 1978) hosted by the Mount Misery Formation (Fig. 2.2).

Multiple generations of mafic to intermediate dikes, which may be cogenetic tholeiitic feeders to units higher in the Snooks Arm Group, cross-cut the Pacquet

complex. In addition, several large, Late Ordovician to Early Silurian granitoid plutons intrude the Baie Verte oceanic tract and its cover sequence, including the ca. 445-433 Ma Burlington granodiorite, the ca. 429 Ma Cape Brulé porphyry, and the ca. 427 Ma Dunamagon granite (Figs. 2.1, 2.2; Skulski et al, 2012; 2015).

2.3.1. Regional deformation and metamorphism

Multiple deformation and associated metamorphic events affect rocks of the Baie Verte Peninsula (e.g., Castonguay et al., 2009, 2014). Metamorphic grade in rocks of the Pacquet complex does not exceed upper greenschist facies mineral assemblages, except near the Ordovician-Silurian intrusive bodies where contact metamorphism has locally produced amphibolite facies mineral assemblages (Tuach and Kennedy, 1978). Four (and locally five) deformation events are recognized in rocks of the Baie Verte oceanic tract. Castonguay et al. (2014) attribute the first deformation event, D_1, to the obduction of the ophiolite; this event is poorly developed east of the Baie Verte Line. The penetrative D_2 and D_3 events are regionally recognized as Wenlockian-Ludlovian (ca. 428-423 Ma; Castonguay et al., 2014) tectonometamorphic events. D_4 includes late fabrics which are associated with a dextral strike-slip regime during the Late Silurian-Early Devonian Acadian orogeny (Waldron et al., 1998; Anderson et al., 2001).

2.4. Geology of Host Successions of the Ming deposit

The stratigraphic host successions to the Ming deposit, which consist of several discrete zones (Fig. 2.3), are described in part by Tuach and Kennedy (1978), Pilote and Piercey (2013), and Pilote et al. (2014, 2015). Brueckner et al. (2016) describes the

detailed mineralogical and chemical assemblages of the semimassive and massive sulfide lenses at the Ming deposit. This study emphasizes the host successions that stratigraphically underlie and overlie the orebodies (see summary in Table 2.2). Cross-sections (Figs. 2.4-2.6) and detailed maps (Fig. 2.7) were constructed using underground and drill core observations. A composite of stratigraphic columns representative for each zone is illustrated in Figure 2.8. Although deformation affected the deposit and host rocks, primary volcanic features are preserved in low strain zones and can be traced both laterally and vertically. The geochemistry of the host successions and a detailed description of the hydrothermal alteration will be addressed in subsequent papers.

2.4.1. Terminology

The Ming deposit consists of five subparallel discrete zones, the 1807, 1806, Ming North, Ming South, and Lower Footwall (Fig. 2.3). The *zones* refer to spatially and economically defined orebodies (e.g., 1807 Zone; Pilgrim, 2009). We use the term volcaniclastic as defined by White and Houghton (2006), to encompass clastic rocks composed exclusively or partly of volcanic material and which may include pyroclastic, autoclastic, hyaloclastic, peperitic deposits, and their resedimented, syneruptive equivalents. Distinctions among volcaniclastic rocks are made using the non-genetic granulometric nomenclature of White and Houghton (2006) and references therein. Although rocks of the Rambler Rhyolite formation vary from rhyodacite to rhyolite in composition (J.-L. Pilote, unpublished data, 2016), we retain the designation Rambler Rhyolite consistent with past nomenclature for this formation.

2.4.2. Coherent lithofacies (unit 1.1)

The lowermost unit of the Ming deposit succession, which consists mainly of coherent rhyodacite, has a minimum thickness of 500 m (Figs. 2.4-2.6, 2.8). It underlies the entire deposit and is locally found in contact with the massive sulfide lens in the down-dip section of the 1807 Zone (Fig. 2.4). Rocks of this unit are massive, light grey to dark purple blue, aphyric to quartz- and plagioclase-phyric with an aphanitic quartz-rich groundmass. More than 80 vol.% of the unit is aphyric and where porphyritic, phenocrysts make up less than 10 vol.% of the rock. The quartz-rich groundmass has a polygonal mosaic texture due to metamorphic recrystallization. The least-altered rocks contain 2 to 5 mm subhedral to anhedral quartz phenocrysts, 2 to 5 mm subhedral to euhedral plagioclase phenocrysts or both (Fig. 2.9A). Plagioclase crystals are intermediate in composition (optically positive = An_{40-75}; Nesse, 2000) and typically poorly preserved due to hydrothermal alteration (Pilote et al., 2015). Round-shaped and tube-like (5 to 10 mm long) elongated vesicles (pipe vesicles) are present but uncommon in this unit.

Distinct flows composed of coherent volcanic rocks are recognized in drill core. They are typically bounded by irregular but sharp intrusive contacts and are generally more than 50 m thick (Fig. 2.8, 2.9B). In the upper part of the unit, flows are also bounded by in situ hyaloclastite and peperite, sharing similar textures to their coherent equivalent. Hyaloclastite lithofacies locally forms the 1-5 m upper part of some flows, defined by juvenile jigsaw-fit blocks of 2-5 cm long and 2-3 cm thick (Fig. 2.9C). The juvenile blocks are locally bounded by sulfide, rhodochrosite (Mn-carbonate), magnetite and/or chlorite-epidote. The peperite is characterized by irregular fluidal fragments of

rhyodacite in contact with a fine-grained chlorite-altered material (volcaniclastic debris, hyaloclastite, or sediments) (Fig. 2.9D).

2.4.3. Volcaniclastic-dominated lithofacies (unit 1.2)

An up to 200 m-thick succession (Figs. 2.4-2.6) of felsic volcaniclastic and minor coherent volcanic rocks (unit 1.2) immediately overlies the coherent rhyodacite of unit 1.1. The base of unit 1.2 consists of rhyodacitic monomictic tuff breccia grading into a lapilli tuff. The tuff breccia is matrix-supported with bomb size fragments of aphyric rhyodacite, whereas the lapilli tuff is clast- to matrix-supported with irregular, poorly-sorted aphyric rhyodacite lapilli-sized fragments (Fig. 2.9E). The lapilli tuff is overlain by alternating sequences of tuff breccia and bedded tuff, which is in turn overlain by a laminated quartz-barren rhyodacitic tuff with isolated sub-rounded bomb-size fragments of coherent aphyric rhyodacite (Fig. 2.9F). The tuff is overlain by a 10 to 30 m-thick distinct sequence of dark grey rhyodacite tuff breccia that contains angular to rounded (locally amoeboidal) fragments consisting of quartz-epidote-altered quartz-phyric rhyodacite (Fig. 2.9G). This tuff breccia sequence is usually found 30 to 40 m stratigraphically below the 1806 and 1807 massive sulfide lenses and extends up-dip for at least 400 m. In level 434 (Fig. 2.9G), it is locally less than 3 m below the 1806 and 1807 zones. This lithofacies is restricted to, or preserved, near the semimassive to massive sulfide of the 1806 and 1807 zones. Exclusive to the 1806 Zone, the upper ~50 m of unit 1.2 is characterized by flows of aphyric to quartz-phyric rhyodacite (Figs. 2.5, 2.9H). Moreover, fluidal juvenile fragments of coherent rhyodacite closely spatially ($\leq$ 2 m) associated with the rhyodacite flows are present at different depths in the 1806 Zone.

The fluidal fragments show irregular or amoeboidal shapes in contact with fine-grained, chlorite altered material, diagnostic of peperitic structures (Fig. 2.10A). These restricted peperitic domains are not common in the host succession, but indicate the presence of an unconsolidated material during emplacement of the coherent rocks (Skilling et al., 2002). Hourglass shaped cylindrical features of 1 to 2 cm in diameter with internal, 1 to 5 mm spaced laminae defined by sericite occur within the coherent facies, are oriented perpendicular to stratigraphy and near the contact with the felsic bedded tuffaceous sediment (Fig. 2.10B). The origin of these structures is uncertain but their formation may be related to the process of dewatering of the underlying unconsolidated material. The uppermost part of the rhyodacite flows (immediately below the semimassive and massive sulfide of the 1806 Zone) consist of massive rhyodacitic hyaloclastite. The hyaloclastite facies is 5 to 7 m thick and displays jigsaw-fit structures transitioning to sparsely to closely packed, well-defined, blocky and splintery, quartz-phyric rhyodacite clasts in a sericite altered quartz-bearing rhyodacitic matrix (Fig. 2.10C). This hyaloclastite facies represents the margin or envelope of the flows underlying the 1806 Zone. The semimassive to massive sulfide horizons of the 1807 and Ming South zones are immediately underlain by bedded to massive quartz-bearing rhyodacitic tuffs and locally lapilli to breccia tuffs with rounded to subrounded fragments of quartz-phyric rhyodacite.

2.4.4. Volcanic and volcaniclastic rocks (unit 1.3)

The down-dip section of the Ming South Zone contains two or more stacked, stratabound and stratiform massive sulfide lenses separated by and within up to three discrete conformable beds of quartz-bearing rhyodacitic tuff, which collectively form a

≤10 m-thick unit (unit 1.3a; Figs. 2.6A, B, 2.8, 2.10D). Stacked sulfide lenses also occur up-dip; however, they are hosted by a ≤10 m-thick light grey to pinkish coherent quartz-megacrystic rhyodacite (unit 1.3b; Figs. 2.6A, 2.8, 2.10E). This coherent quartz-megacrystic facies is also locally found in the 1806 Zone. More than 50% of the quartz crystals in both the tuff beds and coherent facies are blue in color. The contact between the coherent units 1.3b and 1.3a is sharp and conformable, indicating that the tuff beds (unit 1.3b) were deposited during and/or following the formation of the flow dome structure (unit 1.3a). The extent of this unit is restricted to the Ming South (and possibly Ming North; Tuach and Kennedy, 1978) and is continuous down-dip, >50 m beyond the maximum extent of the defined orebody (L. Pilgrim, pers. communication, 2016).

2.4.5. Sulfide-bearing volcaniclastic rocks (unit 2)

Part of the semimassive to massive sulfide horizons in the 1806 and 1807 zones are immediately overlain by a discontinuous 10 m-thick unit of polymictic breccia of mafic to intermediate composition (Figs. 2.4, 2.5; Pilote et al., 2016). This unit contains clasts of different compositions including sulfide-bearing fragments and dark purple to medium grey quartz and quartz-sericite hydrothermally altered coherent rhyodacite clasts (Fig. 2.10F). The sulfide clasts locally make up to 10 vol.% of the rock, whereas the rhyodacite clasts make up to 30 vol.%. The majority of sulfide and silicate clasts are subrounded to subangular, vary in size (≤5 cm), and stretched co-axial to the main stretching lineation (see below). The matrix of the breccia is fine to medium grained, foliated, and composed of an assemblage of recrystallized quartz-plagioclase-epidote-chlorite, with biotite grains forming post-kinematic porphyroblasts, commonly

overprinting chlorite (Fig. 2.10F). Pilote et al. (2016) revealed the presence of Au- and Te-bearing minerals in close association within the sulfide clasts that are similar to the underlying massive sulfide lenses.

2.4.6. Rocks forming the base of the cover sequence (Snooks Arm Group)

The Ming deposit is overlain by a laterally extensive unit (Nugget Pond horizon) composed of quartz-biotite-actinolite-epidote-rich siltstone to very fine sandstone (<1/8 mm) with abundant fine-grained magnetite porphyroblasts (unit 3; Fig. 2.11A). This sedimentary unit is <1 m thick and intercalated with massive basaltic flows, and can be traced along strike at surface for more than 2 km to the south. Rocks overlying the Nugget Pond horizon are predominantly mafic massive, vesicular, and pillowed flows and mafic volcaniclastic rocks. The presence of fine-grained and finely laminated sedimentary rocks and directly overlying pillowed basalt flows indicate that rocks immediately overlying the Ming deposit were deposited in a subaqueous environment. These rocks show no evidence of the hydrothermal alteration observed in rocks associated with the formation of the Ming deposit, although they are overprinted by metamorphism and deformation.

2.4.7. Post-mineralization intrusive rocks

Three generations of mafic to intermediate dikes and sills intruded the Ming deposit, forming up to 30% of the Ming deposit sequence and are distinguished from each other by their different textures, cross-cutting relationships, and geochemistry (Pilote et al., 2014, 2015). Despite the near-complete obliteration and replacement of primary textures

and minerals in these intrusive rocks, clear distinctions can still be made (Table 2.2). The dikes and sills typically dip northeast, subparallel to stratigraphy (i.e., 30-35° dip; Fig. 2.7). They are up to 30 m thick with many were truncated by shearing, concurrent with the remobilization of sulfide minerals. All intrusions show sharp, locally irregular contacts with the host rocks. The first (IN1) and second (IN2) generation intrusions consist of medium- to coarse-grained actinolite-calcite porphyroblastic gabbro and diorite, respectively (Fig. 2.11B). The second dike generation (IN2) contains up to 5 vol. % rutile and ilmenite, which are absent in IN1, and is chilled against IN1 and varies from a coarse-grained equigranular to porphyroblastic near the margins. The third dike generation (IN3) consists of a fine-grained equigranular quartz diorite to granodiorite, locally with bluish green ferro-actinolite porphyroblasts (Fig. 2.11C). The last generation of intrusions also display chilled margins against IN1 and IN2. All three generations of dikes intrude the semimassive to massive sulfide and are overprinted by D_2 deformation, indicating that the dikes have a minimum age of late mid-Silurian (Skulski et al., 2015) and maximum age of Early Ordovician. Preliminary geochemical and isotopic data indicate strong affinities between the dikes and some of the rocks that are part of the Snooks Arm Group (J.-L. Pilote, unpublished data, 2016).

2.4.8. Late quartz-carbonate±epidote±sulfides veins

Late brittle quartz-carbonate±epidote±sulfides veins cut all units of the Ming deposit host succession, including the post-mineralization mafic intrusions. Different generations of veins have been recognized and, despite containing traces of pyrite and chalcopyrite, are not associated with an alteration mineral assemblage. These post-

mineralization, but pre- to syn-deformation veins, are transposed into the main foliation and do not carry precious metals (Pilote et al., 2016).

2.5. Nature and Styles of Sulfide Mineralization

Recent studies by Brueckner et al. (2014, 2016) on the semimassive to massive sulfide orebodies of the Ming deposit provide a thorough description of the nature and styles of mineralization. A brief summary is presented here with readers referred to the aforementioned papers for further details. The Ming deposit consists of discordant sulfide stringers, disseminated sulfides, and stratabound semimassive to massive sulfide lenses. The stratabound massive sulfides are up to 20 m thick, 500 m in length, an average width of 50 m, and occur at the top of unit 1.2, and both within and at the top of unit 1.3 (Fig. 2.12A). Discordant stringers, which occur stratigraphically below and to minimum depth of 300 m below the massive sulfides, are hosted in units 1.1, 1.2, and 1.3. A small proportion of stringers are also found within the immediate hanging wall of the 1806 Zone. Although they are present throughout the footwall of the Ming deposit, the 1807 Zone contains relatively few footwall sulfide stringers (≤1 vol.%) underlying its stratabound lens. Disseminated sulfide mineralization occurs throughout the Ming deposit within alteration assemblages, adjacent to sulfide stringers and proximal to semimassive to massive sulfide mineralization.

2.5.1. Ore mineralogy

The semimassive to massive sulfides are mainly composed of pyrite±chalcopyrite with minor (5-10 vol.%) sphalerite±pyrrhotite. Localized enrichment in chalcopyrite

and/or sphalerite is a result of deformation (see below). Clasts of silicified felsic volcanic rocks occur within the massive sulfide lenses and locally reach up to 30 vol.% (Fig. 2.12B). They average 10 cm in diameter, are elongated and folded by deformation, and are cross-cut by all generations of mafic intrusions, which indicates that they were incorporated within the massive sulfide prior to deformation. For 100 m below the semimassive to massive sulfide lenses of the 1806 and Ming South zones, sulfide stringers are predominantly composed of pyrite-chalcopyrite±sphalerite±pyrrhotite±galena (Fig. 2.12C). The sulfide stringers become rich in chalcopyrite-pyrrhotite±pyrite±cubanite beyond 100 m below the massive sulfide horizon, and are spatially associated with a chlorite-rich alteration assemblage (Fig. 2.12D; Pilote et al., 2015). This lower zone of discordant sulfide stringers delineate the >26 Mt Cu-rich Lower Footwall Zone of the deposit. The Lower Footwall Zone is restricted to the footwall of the Ming South Zone and part of the up-dip section of the 1806 Zone (Fig. 2.5, 2.6A), hence, showing a distribution that is slightly oblique (15-20°) to the orebodies.

In addition to the sulfides, 29 trace minerals (tellurides, selenides, (sulfo-)antimonides, sulfosalts, native metals, and oxides) are present in the Ming deposit (Brueckner et al., 2016). Of the precious metals, electrum is the most common Au-hosting mineral and is found almost entirely within the semimassive to massive sulfide lenses (Brueckner et al., 2016).

2.5.2. Metal distribution

In agreement with observations by Brueckner et al. (2014; 2016), compiled assay data from delineation and exploration drill holes show a good correlation between Ag and Au values (Fig. 2.13A) and Ag+Au and Zn values (Fig. 2.13B). The highest grades in Au (and by association, Ag) and Zn tend to be associated with zones of lower Cu grades (Fig. 2.13B). On the scale of the Ming deposit, the distribution of Cu, Au, Ag, and Zn shows strong variations in grades (Fig. 2.14). The 1807 and the Lower Footwall zones contain the highest grades (>2.89 wt.%; upper 5^{th} percentile) in Cu, whereas Au, Ag, and Zn grades are highest (> 2.05 g/t, 15.27 g/t, 0.57 wt.%, respectively; upper 5^{th} percentile) in the up- and down-dip sections of the 1806 Zone, down-dip section of the 1807 Zone, and locally in the Ming South Zone. Although Cu and Au contents covary in most of the 1807 Zone, the sulfides in the down-dip section become progressively more enriched in Au relative to Cu (Fig. 2.15). These variations reflect sulfide and other trace mineral assemblage distributions reported by Brueckner et al. (2014; 2016). Areas with higher grades in Cu are dominated by chalcopyrite, whereas higher grades in Au, Ag, and Zn are dominated by electrum, Ag-phases (e.g., Ag-Hg ± Au alloy, Ag-bearing sulfosalts), and sphalerite, respectively. Despite deformation, the metal distribution indicates areas with conditions (e.g., temperature) more favorable for certain metals to precipitate and can be linked to the type of rocks (coherent vs. fragmental) that host mineralization, and where the geometry of the deposit (i.e., discrete lenses) provide evidence of separate hydrothermal fluid upflow zones forming characteristically different orebodies.

2.6. Structure and Geometry of the Ming Deposit

Polyphase deformation affects all zones of the Ming deposit. Determination of successive generations of structures is based on overprinting relationships on micro- and mesoscopic scales. A summary of the main structural elements of the deposits is described in Table 2.3. The correlation with recognized regional and local tectonic features builds on previous work by Tuach and Kennedy (1978) and Castonguay et al. (2009).

2.6.1. Early ductile deformation (D_1)

The earliest deformation (D_1) recognized in the Ming deposit is cryptic and only locally preserved in domains within the felsic volcanic and volcaniclastic rocks of the stratigraphic footwall. It consists of a north striking (average of 359°/39°) biotite-quartz-muscovite penetrative foliation (S_1) (Fig. 2.16A). The semimassive to massive sulfides are devoid of any clear D_1 structures, most likely due to the obliteration of them by younger deformation and metamorphic events. D_1 structures are absent in the ophiolite cover sequence (i.e., magnetite-rich siltstone of the base of the Snooks Arm Group and younger rocks; Castonguay et al., 2009) and thus, also absent in the feeder mafic dikes that cross-cut the Ming deposit. The lack of well-preserved strain indicators hinders the interpretation of the kinematics related to D_1. The lack of stratigraphic repetitions indicates that no F_1 folds were developed in the Ming deposit area. Furthermore, considering the continuity of the stratigraphy outside the Ming deposit (Skulski et al., 2015), it is unlikely that the Ming deposit sequence occupies one limb of a large F_1 fold as previously proposed in Tuach and Kennedy (1978).

2.6.2. Main ductile deformation (D_2)

The dominant structural features in the deposit are attributable to the second deformation event (D_2), which is the main tectono-metamorphic episode in the Rambler area (Gale, 1971; Tuach and Kennedy, 1978; Hibbard, 1983; Anderson et al., 2001; Castonguay et al., 2009). Structural features related to D_2 are ubiquitous with many different structural elements and styles of deformation recognized (Table 2.3). An intense, penetrative schistosity (S_2) is present in all rocks underlying and overlying the semimassive to massive sulfides, including the semimassive to massive sulfides themselves and the post mineralization mafic dikes. The ubiquitous S_2 penetrative schistosity is also accompanied by metamorphic differentiation and recrystallization (M_2) (Fig. 2.17A) that produced upper greenschist to lower amphibolite facies mineral assemblages (Hibbard, 1983). The S_2 schistosity dips to the east-southeast with an average dip of 52° (Fig. 2.16A). In the footwall felsic rocks, S_2 planes are defined by domains of sericite-quartz-chlorite-biotite±actinolite±feldspars minerals with varying relative abundances that depend on pre-deformation hydrothermal alteration mineral assemblages. In the mafic dikes, S_2 planes are pervasive and defined by strain-slip planes of chlorite (Fig. 2.17B). Sheafs of elongate actinolite arranged along the S_2 foliation in mafic dikes define a *garbenschiefer* texture (e.g., Spry, 1969). D_2 is also associated with variable degrees of stretching lineation defined by elongated fragments and crystals ($k>>1$; Flinn, 1962). Deformed fragments in lithologies of different competencies (e.g., chlorite-altered vs. quartz-rich fragments) show average aspect ratios varying from 1:1:10 to 1:2.5:100. This stretching lineation (L_2) has an average trend and plunge of 042°/29° and is developed on the northeast striking S_2 fabrics, indicating a northwest-southeast

oriented shortening (Fig. 2.16B). Measured primary stratigraphic contacts (S_0) throughout the deposit show upright open folding with a northeast plunging fold axis (Fig. 2.16C), roughly coaxial with L_2 (Fig. 2.16B). Measured intersection lineation between S_2 and S_0 and S_1 are co-axial to mineral and stretching lineation L_2 (Fig. 2.16C). Moreover, tight to isoclinal overturned folded (F_2) mafic dikes that cross-cut the semimassive to massive sulfide lenses and felsic footwall rocks are co-axial and co-planar to L_2 and S_2, respectively (Fig. 2.17C). These folds are transposed by younger structures and are commonly restricted to or adjacent to the massive sulfides (competency control). North to northeast striking shear zones (≤4 m thick) with consistent kinematics occur in the 1806 and 1807 zones and are defined by well foliated SL-tectonite, coplanar with S_2 (Fig. 2.17D, E). The shear zones (C_2) affect all rock types and are commonly accommodated by co-planar mafic dikes cutting both the semimassive to massive sulfides and felsic footwall rocks.

The fabrics related to D_2 have recorded a dominant reverse sinistral movement (i.e., northwest-directed) as indicated by the S-folds of the mafic dikes within the semimassive to massive sulfides and felsic footwall rocks and the shear zones (Fig. 2.17C-E). Tuach and Kennedy (1978) and Castonguay et al. (2009) defined S_2 as a prominent foliation that generally dips to the northeast at 30° to 40° (Fig. 2.16A). They define D_2 as the main tectono-metamorphic phase of this part of the Baie Verte Peninsula; however, our D_2 structure is not consistent with their kinematics which generally suggests a south-directed movement. It is noteworthy that our observations are limited to a restricted area as opposed to their respective studies. If co-axial and non-coaxial deformation (strain partitioning) is present, then this may add to the deposit-scale

kinematic complexities. More work is necessary to fully correlate the local fabrics with their regional equivalents.

2.6.3. Late ductile deformation (D_3)

The third deformation event (D_3) is ubiquitous in the Ming deposit area and is manifested in discrete domains, commonly associated with northwest striking shear zones in or near the semimassive to sulfide lenses (Fig. 2.16A). Mafic dikes with S_2 foliation are crenulated onto C_{S2} defined predominantly by chlorite minerals (Fig. 2.17B). D_3 structures are not prominent in the footwall felsic volcanic rocks, except in strongly chlorite- and sericite-altered rocks. In the Lower Footwall Zone, an S_3 foliation, defined by a parallel arrangement of chlorite, overprints S_2 and possibly S_1. Most of the measured sulfide stringers of chalcopyrite-pyrrhotite-pyrite in the Lower Footwall Zone are subparallel to S_3 (Fig. 2.16D). Because of the discordant relationship between sulfide stringers and stratigraphy in the least deformed areas of the Ming deposit (and typical for most VMS deposits; e.g., Hannington et al., 2005), their parallel relationship in the Lower Footwall Zone likely reflects a complete transposition of these stringers in to S_3. Minor tight recumbent F_3 folds, in which S_3 is axial planar, are developed in the mafic dikes cutting the massive sulfides and hanging-wall rocks of the Snooks Arm Group (Fig. 2.17F). Most F_3 folds are co-axial to the lineation resulting from the intersection of S_2 and S_3 and also the crenulation affecting the main schistosity (L^C_{S2}). Boudinaged mafic dikes and dismembered folds along the S_3 plane indicate a south- to southeast-directed strike slip to normal movement (Fig. 2.17G). This deformation is consistent with the south-

directed movement along the Scrape and Rambler Brook thrust faults (Fig. 2.2; Hibbard, 1983; Castonguay et al., 2009).

2.6.4. Late brittle deformation (D_4)

A late brittle deformation (D_4) is observed throughout the Ming deposit and is defined by north dipping normal curviplanar faults, locally crenulating S_3 (Fig. 2.16A). The faults show displacement of less than 1 m and commonly contain significant amounts of chalcopyrite (Fig. 2.17H). This deformation indicates a north-south extension and could be the equivalent to the regional D_4 event of Castonguay et al. (2009).

2.6.5. Deformation structures within and near the semimassive to massive sulfides

The ore zones and their host rocks are clearly affected by the deformation events, including flattening/stretching and local F_2 and F_3 folding on a large scale, and, at smaller scale, by piercement structures that are discordant to bedding and/or transecting structural fabrics. Piercement textures are present within, below, and above the semimassive to massive sulfides in different forms. The scale and style of such textures vary but have significant extent to form major ore shoots. Veins of precious metals and base metal sulfides are found within the quartz-rich horizon (Fig. 2.18A; 1806 Zone), altered felsic footwall rocks (Fig. 2.18B) and mafic dikes (Fig. 2.18C), and associated with D_2, D_3, and/or D_4 fabrics. The massive sulfides in the 1807 Zone locally contain domains dominated by chalcopyrite. These occur exclusively in F_2 and F_3 hinges (Fig. 2.17C), in

sheared mafic dikes and sills, and at the margins of the orebodies (Fig. 2.7), indicating remobilization of some of the primary sulfides.

The northwest part of the 1807 Zone is boudinaged and necked co-axially to L_2, resulting in the formation of an extended (or remobilized) Cu-Au-rich massive sulfide zone that is co-planar to C_2 and S_2 (Fig. 2.19). The remobilized section from the main massive sulfide lens is chalcopyrite-rich, coarse grained, contains fragments of the mafic intrusion(s), and contains sphalerite layers that are parallel to S_2 (Fig. 2.18D). The main lens, in comparison, is composed of fine-grained pyrite with granular chalcopyrite and sphalerite, contains quartz-rich fragments, and it is devoid of mafic intrusion fragments. This D_2-induced external remobilization also characterizes the 1806 zone at levels 420 and 431 (e.g. Fig. 2.17E).

2.7. Discussion

2.7.1. Reconstruction of the Ming deposit host successions and volcanic controls on ore genesis

The base of the Ming deposit footwall succession is dominated by coherent felsic rocks (unit 1.1) that are overlain by variable thicknesses of volcaniclastics (unit 1.2). The coherent lithofacies is massive with relatively minor evidence of internal primary volcanic features such as flow banding or vesicles (i.e., low volatile content in magma). The lack of internal fabrics (other than the deformational fabrics) are indicative of emplacement as a devolatilized rhyolitic dome (Gibson et al., 1999). Although the maximum thickness of unit 1.1 is unknown, alternating volcaniclastic units are reported

stratigraphically below the Ming deposit (Figs. 2.4-2.8; Skulski et al., 2015) providing evidence of multiple volcanic events and/or evolving volcanic regime during the emplacement of the Rambler Rhyolite formation. Based on the compositional and textural similarities of unit 1.1 and its distribution below the Ming South, 1806, and 1807 zones, we interpret this unit to have formed as part of the same upper domal structure. A simplified schematic of the sequence of volcanic, tectonic (subsidence) and VMS ore-forming events at the Ming deposit is shown in Figure 2.20.

A rapid change in the style of volcanism is reflected by the sharp contact between units 1.1 and 1.2. The existence of features suggestive of explosive eruption have not yet been observed, but the predominance of in-situ volcanic structures such as hyaloclastite and jigsaw-fit fabrics (quench fragmentation) together with thick successions of massive volcaniclastic rocks indicate that the effusive-style of volcanism is combined with in-situ fragmentation and debris flow deposition of slumped material (Cas, 1992). As illustrated in Figures 2.4 to 2.6 and 2.8, we interpret the abrupt lateral change from coherent rhyodacite lithofacies (unit 1.1) to the thick and nested felsic volcaniclastic lithofacies (unit 1.2) to have been produced by multiple margins of a possibly larger subsidence structure that hosts the Ming deposit. Abrupt lateral changes in thickness in the volcaniclastic lithofacies, as seen across the host successions (Fig. 2.8), are interpreted to reflect their deposition within smaller fault bounded basins, genetically and spatially associated with a series of synvolcanic faults oriented subparallel to the sulfide lenses. The coherent quartz-megacrystic rhyodacite (unit 1.3a) and its lateral eruptive-equivalent tuff beds (unit 1.3b; Fig. 2.20) are restricted to the southeast part of the Ming deposit and lie parallel to the Ming South Zone. Recent drilling down-dip of the Ming South Zone

intercepted tuff beds interpreted to be of the same unit, with sulfide mineralization, providing further constraints on the linear distribution of unit 1.3a (L. Pilgrim, pers. comm., 2016). As demonstrated above, the degree of stretching attributed to D_2 is not constant throughout the deposit, conversely to the suggestions made by Tuach and Kennedy (1978), and alone cannot account for the linear and spatially restricted distribution of unit 1.3. In order to stretch unit 1.3 to a ratio exceeding a length to width ratio of ~10:1 (currently known ratio) with $k>>1$, significant stretching in clasts or porphyroclasts together with boudinaged features should be expected throughout the deposit, which is not the case. The "ruler-shaped" unit 1.3 (and associated massive sulfides) is inconsistent with Tuach and Kennedy's (1978) finite strain ellipsoid analyses, in which case a cigar shape would be expected. Furthermore, assuming that stretching (principal stress) parallels L_2 and that it controlled the current ore zones geometry as suggested by Tuach and Kennedy (1978), the Lower Footwall Zone trends consistently ~15-20° from L_2 (Fig. 2.16B), thus making the argument for a deformation-controlled geometry difficult to support. Therefore, to explain the elongated geometry of the deposit, we propose that the eruption and deposition of units 1.2 and 1.3 were dominantly controlled by synvolcanic faults, consistent with the abrupt lateral changes in lithofacies that are sub-parallel to the ore zones distribution, and persisted during subsidence and development of the hydrothermal fluid convection. Hence, the stacked semimassive to massive sulfide lenses of the Ming South Zone (and possibly Ming North Zone; Tuach and Kennedy, 1978) that are intimately associated with unit 1.3 are interpreted to have formed synchronous to and despite concurrent volcanic activity. The latter is typically considered an impediment to hydrothermal fluid circulation and to the rapid accumulation

of massive sulfides that can take place more easily (without dilution) during pauses in volcanic activity (Gibson et al., 1999).

Based on the lithofacies distribution and volcanic architecture, the host succession of the Ming deposit is characterized by a number of features that are highly favorable for the development of a VMS-forming hydrothermal system and preservation of sulfides. The linear (possibly arcuate and/or connecting) synvolcanic fault system provided a controlled pathway to both the rising magmas and also the upwelling hydrothermal fluids. The asymmetric profile of the basin allowed accumulation of thick layers of volcaniclastic rocks (Fig. 2.20). The timing of sulfide formation at the Ming deposit is interpreted to have occurred in the waning stage of pre-obduction volcanic activity (Skulski et al., 2010). Subsidence and deposition of volcaniclastic sequences had to be synchronous and relatively rapid as evidenced by the intermittent synvolcanic faults (active until the deposition of unit 1.3), the dominance of massive monomictic volcaniclastic rocks in the footwall, and the rapid thickness variations of some lithofacies (e.g., Gibson et al., 2006, 2013). Additionally, the absence of stratiform sulfides or extensive sub-seafloor replacement-style mineralization deeper in the stratigraphy implies that: (1) synvolcanic faults controlled circulation of the hydrothermal fluids; (2) the near continuity of volcanic activity during accumulation of unit 1.2, or lack of a sufficient volcanic hiatus, restricted hydrothermal fluid circulation to initiate only after deposition of unit 1.2 and allowing massive sulfides to accumulate (e.g., Ohmoto, 1996); and (3) the hydrothermal system favored sulfide deposition near or at the seafloor, possibly due to a relatively low-permeability of the volcaniclastic lithofacies (efficient cementation?). These conditions may also apply to the formation of the East and Rambler deposits (Fig.

2) where massive sulfide lies exclusively at the interface between the Rambler Rhyolite formation and the base of the Snooks Arm Group (Gale, 1971; Tuach and Kennedy, 1978).

2.7.1.1. Volcanic controls on metal distribution

Despite deformation, on the scale of the Ming deposit, the distribution of metals within a certain grade range and the distance from low to high metal grades within a single lens (Fig. 2.14) exceed 100 m, which is beyond the maximum distance of the observable massive sulfide remobilization (<20 m) in underground exposures and drill core. Consequently, remobilization alone cannot explain the metal distribution on the scale of the deposit; thus, the metal zoning in the deposit currently is likely close to its original distribution. The differences in metal assemblages and geometries as described above most likely reflect changes in physico-chemical conditions of the hydrothermal fluids during the formation of the Ming deposit. The Lower Footwall Zone is a discordant chlorite-altered zone (Pilote et al., 2015) with Cu-rich stringers that consist of an assemblage of chalcopyrite-pyrrhotite-pyrite±cubanite (Brueckner et al., 2016), which reflect hydrothermal fluid conditions of T>350°C (Lydon, 1988; Large, 1992; Ohmoto, 1996). The reconstruction of the volcanostratigraphy as shown in Figures 2.5 and 2.6 reveals that most of the vertical distribution of this high-temperature Lower Footwall Zone is restricted at or near the coherent-fragmental interface (i.e. near the contact between units 1.1 and 1.2). This implies that in addition to the synvolcanic faults acting as structural controls on the lateral and longitudinal distribution of the hydrothermal fluids, the presence of a volcaniclastic-dominated succession played a fundamental role in the

precipitation of these high-temperature sulfides, at a consistent depth of 50 to 100 m below the massive sulfide horizon. Considering this lithological-mineralization relationship, it is reasonable to suggest that the fragmental nature of unit 1.2 was intrinsically more permeable, and thus the hydrothermal fluids in this unit were likely to have had a higher water/rock ratio and been lower temperature than those in unit 1.1. An abrupt change in temperature of the ascending hydrothermal fluids that has been interpreted to occur at the unit 1.1 to unit 1.2 contact could have controlled the precipitation of the discordant Cu-rich stringer-style Lower Footwall Zone (e.g., Lydon, 1988).

Near the massive sulfide lenses (≤50 m), alteration assemblages are dominated by sericite and/or carbonate minerals with sulfide stringers and semimassive to massive sulfide composed of metal assemblages (e.g., Zn, As, Pb, Bi, Te, Ag, Au) that are most typical of those produced by low temperature (T<300°C) hydrothermal fluids (Pilote et al., 2015; Brueckner et al., 2016). Replacement-style textures (e.g., Piercey, 2015) are negligible at Ming and do not represent an important process during mineralization, further supporting the lack of permeability and/or porosity of the volcaniclastic successions. Although the geometry of the massive sulfide lenses appears to be predominantly controlled by the synvolcanic faults, the distributions of high grade Zn, Ag, and Au are typically in proximity to coherent facies of units 1.1 and 1.2 (Figs. 2.4 and 2.5), rather than the volcaniclastic facies. Previous work by Brueckner et al. (2016) concluded that temperature was the dominant controlling factor for sphalerite and electrum (dominant phase hosting Au and Ag) precipitation in the Ming deposit. The relationship between the coherent nature of the lithology and temperature controlling the

precipitation implies that the decrease in temperature of the hydrothermal fluids, while maintaining constant other physico-chemical parameters (pH, redox state, fS_2; Brueckner et al., 2016), may have occurred by conductive heat transfer with minimum interaction with modified seawater (relatively low water/rock ratio) before reaching the seafloor.

2.7.2. Effect of metamorphism and deformation on the Ming deposit

Structural features associated with D_1 to D_4 affect, to various degrees, the entire Ming deposit and host rocks. The effect of D_1 deformation is cryptic due to the overprint by later deformation events (mainly D_2) and as a result, it is difficult to specify the style of deformation. D_2-related fabrics are ubiquitous and pervasive, although at variable intensity, throughout the deposit and include northeast-striking S_2 fabrics related to northwest-directed thrusting. At the scale of the sulfide lenses, this caused localized thrust imbrications, multiscale sulfide remobilization and, folds, and faulting (e.g., Fig. 2.17). As mentioned above, many of the D_2 fabrics are subparallel to parallel to the geometry of the mineralized zones, which led previous workers to suggest that the current elongated shape of the orebodies is due to stretching parallel to L_2 (Tuach and Kennedy, 1978; Castonguay et al., 2009). Despite a strong L>S fabric in domains near mineralization which likely did accentuate the linearity of the lenses, we propose that the current deposit geometry was largely inherited from the primary volcanic architecture of the host succession. This interpretation can be further substantiated using the following reasoning: (1) under significant macro-scale stretching, boudinaged sulfide lenses would have been expected along with an internal redistribution of metals, particularly an enrichment of Cu in the lens extremities and/or partitions, under upper-greenschist metamorphic conditions

(e.g., Whitten, 1966; Pedersen, 1980; Davies et al., 1983; van Staal and Williams, 1984); these features are not observed at the Ming deposit; and (2) if a simple palinspastic analysis is utilized, applying the 1:1:10 aspect ratio measured from stretched fragments to the entire deposit, would require the pre-deformation thickness of the massive sulfide to have been at least 10 times greater than it is presently. However, displacement of the mafic dikes within the massive sulfides is only on the order of centimetres to meters. Therefore, we argue that the geometry of the deposit was mainly controlled by synvolcanic faults with only localized modifications of the mineralization during deformation.

A D_3 fabric is ubiquitous in the deposit, typically subparallel to stratigraphic contacts (N330°), and is responsible for tight overturned folds near the mineralization. Boudins are also associated with D_3 due to S_3-parallel stretching of mafic dikes within the massive sulfide. Although only present in these latter dikes, thin ($\leq$ 2 mm) chalcopyrite-rich veins are found parallel to S_3. D_4 fabrics are brittle and commonly consist of discrete faults steeply dipping to the north with relatively minor effects on the semimassive to massive sulfide, except for localized remobilization along the faults and parallel discrete chalcopyrite-rich veins (Table 2.3).

2.7.2.1. Sulfide remobilization

Regional metamorphism and deformation can modify the initial mineral assemblage and geometry of a deposit, resulting in an internal or external metal redistribution by liquid- and/or solid-state remobilization (Marshall and Gilligan, 1987, 1993; Marshall and Spry, 1998). In addition, stress can be greatly accommodated in

metamorphosed and deformed VMS deposits by weakly competent semimassive to massive sulfides and associated hydrothermally altered rocks (e.g., Jones et al., 2006; Drown and Downs, 1990; Large et al., 1988; Allen and Barr, 1990). At the Ming deposit, there are multiple lines of field evidence to suggest that there has been significant sulfide remobilization. These include (with maximum extent): (1) development of a concordant chalcopyrite-rich sulfide body along the sheared hanging wall-footwall interface (≤ 20 m) (Fig. 2.19); (2) piercement structures of chalcopyrite-sphalerite-rich massive sulfide into both footwall and hanging wall rocks (≤ 5 m) (Fig. 2.18B); (3) concordant and discordant base metal and precious metal veinlets along transposed foliations (≤ 1 m) (Fig. 2.18A); (4) layers and bands of sphalerite within the massive sulfides that are co-planar to foliation (exsolution within the massive sulfides; Marshall et al., 1998) (Fig. 2.18D); (5) pre-deformation mafic dikes that are dismembered, folded, and boudinaged by deformation (Fig. 2.17C, D, G) ; and (6) localized chalcopyrite-enrichment in fold hinges (Fig. 2.7, 2.17C). Structures (1) to (3) are evidence of external remobilization, whereas features (4) to (6) are intrinsic to the semimassive to massive sulfides (Marshall and Gilligan, 1987, 1993; Marshall et al., 1998; Marshall and Spry, 1998). Moreover, Brueckner et al. (2016) described metamorphic and deformation textures among ore minerals in the semimassive to massive sulfides, including recrystallization, cataclasis, and porphyroblastic growth of pyrite, pyrrhotite, and arsenopyrite. Brueckner et al. (2016) and Pilote et al. (2016) also reported that electrum grains are sporadically found along cataclastic fractures or recrystallized pyrite and arsenopyrite in contact with galena, sphalerite, and less commonly, Bi-tellurides.

The increase in Au and Cu grades in the western part of the 1807 Zone and locally within the 1806 Zone is possibly a combined result of metamorphic liberation and fluid shear zone transfer (Marshall et al., 1998). Although evidence of remobilization is present throughout the deposit at all scales, the western part of the 1807 zone shows the most extensive sulfide remobilization. The western limb of the open F_2 fold in the 1807 zone (Fig. 2.19) is co-planar to S_2 and commonly represents the shear plane for the northwest-directed thrust along the hanging wall-footwall contact. This highly strained zone consists of a favorable horizon for sulfide remobilization due to competency contrasts. This northwest-directed remobilization resulted in distinct increases in Cu and Au grades in the remobilized zones (Fig. 2.19; Pilote et al., 2015). Localized transposition of D_2 fabrics by piercement structures and development of S_3 and S_4 parallel to chalcopyrite and/or electrum veins (Fig. 2.18) indicate that remobilization occurred in various stages (syn- to post-D_2 deformation). This clear association between higher Cu and Au grades in structurally remobilized sulfides provides not only a prime target for production and exploration, but also further evidence that remobilization occurred out of the primary semimassive to massive sulfide lenses and not from external epigenetic process(es) (e.g., Brueckner et al., 2014, 2016; Pilote et al., 2016).

2.7.3. Potential Structural and Economic Implications

This study of the Ming deposit provides numerous observations with potential structural and economic implications globally. One of these observations includes the geometry of the deposit. The long aspect ratio (maximum of 1:7; width:length) of the massive sulfide lenses at the Ming deposit (Fig. 2.2) has long been thought to be a result

of deformation (i.e., stretching). This is based almost entirely on the argument that both the stretching lineation and the plunge directions of the "ruler-shaped" massive sulfide lenses are sub-axial (Tuach and Kennedy, 1978; Castonguay et al., 2009). We show in this study that a detailed reconstruction of the deformed and metamorphosed volcanostratigraphy at the Ming deposit, together with the distribution of discordant mineralization, permits recognition of sub-parallel synvolcanic faults that are interpreted to play a prominent role in controlling the linear distribution of the semimassive to massive sulfide. Synvolcanic fault-control of the geometry of SMS and VMS deposits (e.g. Gibson et al, 1999) has been shown to be responsible for the linearity of sulfide mounds in many deposits. For example, this has been proposed at the Horne deposit, Québec (Barrett et al., 1991), Kidd Creek, Ontario (Bleeker, 1999; Hannington et al., 1999) and for some deposits in the Norwegian Caledonides (Vokes, 1969; Zachrisson, 1984; Grenne, 1989).

Nearly 8% of ancient VMS deposits worldwide (87 out of 1090 deposits) that are deformed and metamorphosed to greenschist to amphibolite facies have aspect ratios of 1:7 (width:length) or less (i.e., greater length relative to width), irrespective of their ages and host rocks (calculated after Mosier et al., 2009). Although a primary stratigraphic depositional control is asserted for most of the VMS deposits (e.g., Mosier et al., 2009), very few authors are able to attribute a possible controlling factor (i.e., primary and/or secondary) that explains their current elongated geometries. This is largely due to the lack of detailed stratigraphic and/or structural work on deposits. However, in the cases where deformation has been suggested as the cause for the "ruler-shape" or "cigar-shape" of the massive sulfide deposits, the predominant stretching lineation is sub- or co-axial to the

length of the deposit (Gilligan and Marshall, 1987 and references therein). We argue, based on our study of the Ming deposit, that in order to fully substantiate the cause(s) of their elongate shapes, it is critical to reconstruct, where possible, the volcanostratigraphy of the deposit. Making the distinction between a synvolcanic or deformation control on the geometry of a VMS deposit has direct economic implications and is critical for vectoring towards potential mineralized targets.

2.8. Conclusions

The Cambro-Ordovician Ming deposit consists of stratiform Cu-Au(-Zn-Ag) semimassive to massive sulfide lenses overlying a discordant chloritic alteration zone with a stringer Cu zone in its core. Three intermediate to felsic units were distinguished (starting from the stratigraphic base): (1) a coherent-dominated lithofacies (unit 1.1), (2) transitioning to a volcaniclastic-dominated lithofacies (unit 1.2) and (3) a synchronous coherent- and tuffaceous-dominated facies at the top (unit 1.3). The massive sulfide occurs above unit 1.2 and within unit 1.3. The genesis and geometry of the semimassive to massive sulfide at the Ming deposit appears to be a function of protracted synvolcanic faults, which developed during extension and acted as pathways for both magmas and hydrothermal fluids. Despite deformation and metamorphism of the Ming deposit at intermediate P-T conditions, we interpret the long aspect ratios of the semimassive to massive sulfide lenses to be mainly due to the linearity of the hydrothermal discharge zones rather than being solely the result of superimposed deformation (i.e., stretching). Primary controls on the distribution of metals and mineral assemblages within the semimassive to massive sulfide are provided by a combination of the thickness of

volcaniclastic rocks and distribution of high level coherent volcanic facies. In addition to the primary controls, deformation-induced remobilization occurred in high strain zones (i.e., along the massive sulfide horizon), thus forming, for example, piercement structures, sphalerite exsolution bands, and fold hinge-enrichment and upgrading significantly (up to 20 times) the remobilized massive sulfide in Cu and Au metals.

This study also shows that a volcanic reconstruction such as that done for the Ming deposit is possible in deformed and metamorphosed VMS deposits worldwide through careful examination of primary volcanic and volcaniclastic features. Moreover, numerous implications derive from these reconstructions, which can provide a critical framework while exploring for potential nearby mineralization.

2.9. Acknowledgements

The authors thank Paul Legrow and Larry Pilgrim, geologists at Rambler Metals and Mining Canada Ltd. for the valuable data, logistics, and access to the mine. S.M. Brueckner, S. Castonguay, and T. Skulski and many other academic and company geologists are acknowledged for their helpful and insightful discussions during the course of this study. This research was funded by grants to S.J. Piercey, including an NSERC Discovery Grant and the NSERC-Altius Industrial Research Chair in Mineral Deposits funded by NSERC, Altius Minerals Inc., and the Research and Development Corporation of Newfoundland and Labrador. This study was also funded in part by the Geological Survey of Canada through the Targeted Geoscience Initiative 4 program and the Volcanogenic Massive Sulphide Ore System, led by J.M. Peter, whom we thank for

support. This paper was significantly improved by constructive reviews by A. Bailes, S. Paradis, P. Spry, and L. Meinert.

2.10. References

Allen, R.L., and Barr, D.J., 1990, Benambra copper-zinc deposits: Australasian Institute of Mining and Metallurgy Monograph Series, v. 14, p. 1311-1318.

Anderson, S.D., 1998, Structure, metamorphism, and uranium-lead and $^{40}Ar/^{39}Ar$ geochronology of the Ming's Bight Group, and the Paleozoic tectonic evolution of the Baie Verte Peninsula, Newfoundland: Unpublished Ph.D. thesis, Halifax, Canada, Dalhousie University, 417 p.

Anderson, S.D., Jamieson, R.A., Reynolds, P.H., and Dunning, G.R., 2001, Devonian extension in northwestern Newfoundland: $^{40}Ar/^{39}Ar$ and U-Pb data from the Ming's Bight area, Baie Verte Peninsula: Journal of Geology, v. 109, p. 191-211.

Barrett, T.J., Cattalani, S., and MacLean, W.H., 1991, Massive sulfide deposits of the Noranda area, Quebec; I, The Horne Mine: Canadian Journal of Earth Sciences, v. 28, p. 465-488.

Barrie, C.T., and Hannington, M.D., 1999, Classification of volcanic-associated massive sulfide deposits based on host-rock composition: Reviews in Economic Geology, v. 8, p. 1-11.

Bédard, J.H., 1999, Petrogenesis of boninites from the Betts Cove ophiolite, Newfoundland, Canada: Identification of subducted source components: Journal of Petrology, v. 40, p. 1853-1889.

Bédard, J.H., Lauzière, K., Tremblay, A., and Sangster, A., 1998, Evidence for forearc seafloor-spreading from the Betts Cove ophiolite, Newfoundland: oceanic crust of boninitic affinity: Tectonophysics, v. 284, p. 233-245.

Bleeker, W., 1999, Structure, stratigraphy, and primary setting of Kidd creek volcanogenic massive sulfide deposit: A semiquantitative reconstruction, *in* Hannington, M. D. and Barrie, C.T., eds., The Giant Kidd Creek volcanogenic

massive sulfide deposit, western Abitibi Subprovince, Canada, 10. Economic Geology Monograph: Boulder, CO, Society of Economic Geologists, p. 71-121.

Brueckner, S.M., Piercey, S.J., Pilote, J.-L., Layne, G.D., and Sylvester, P.J., 2016, Mineralogy and mineral chemistry of the metamorphosed and precious metal-bearing Ming deposit, Canada: Ore Geology Reviews, v. 72, p. 914-939.

Brueckner, S.M., Piercey, S.J., Sylvester, P.J., Maloney, S., and Pilgrim, L., 2014, Evidence for syngenetic precious metal enrichment in an Appalachian volcanogenic massive sulfide system: The 1806 Zone, Ming Mine, Newfoundland, Canada: Economic Geology, v. 109, p. 1611-1642.

Bursnall, J.T., 1975, Stratigraphy, structure and metamorphism west of Baie Verte, Burlington Peninsula, Newfoundland: Unpublished PhD thesis, Cambridge, England, Cambridge University, 337 p.

Butterfield, D.A., Massoth, G.J., McDuff, R.E., Lupton, J.E., and Lilley, M.D., 1990, Geochemistry of hydrothermal fluids from axial seamount hydrothermal emissions study vent field, Juan de Fuca ridge: Subseafloor boiling and subsequent fluid-rock interaction: Journal of Geophysical Research, v. 95, p. 12895-12921.

Cas, R.A.F., 1992, Submarine volcanism; eruption styles, products, and relevance to understanding the host-rock successions to volcanic-hosted massive sulfide deposits: Economic Geology, v. 87, p. 511-541.

Castonguay, S., Skulski, T., van Staal, C., and Currie, M., 2009, New insights on the structural geology of the Pacquet Harbour group and Point Rousse complex, Baie Verte peninsula, Newfoundland: Current Research Newfoundland and Labrador Department of Natural Resources, Geological Survey, Report 09-1, p. 147-158.

Castonguay, S., van Staal, C.R., Joyce, N., Skulski, T., and Hibbard, J.P., 2014, Taconic metamorphism preserved in the Baie Verte Peninsula, Newfoundland Appalachians: Geochronological evidence for ophiolite obduction and subduction and exhumation of the leading edge of the Laurentian (Humber) margin during closure of the Taconic Seaway: Geoscience Canada, v. 41, p. 459-482.

Caté, A., Mercier-Langevin, P., Ross, P.-S. and Simms, D., 2014, Structural controls on geometry and ore distribution in the Lalor auriferous VMS deposit, Snow Lake,

west-central Manitoba (part of NTS 63K16): Preliminary results from underground mapping: Report of Activities 2014, Manitoba Mineral Resources, Manitoba Geological Survey, p. 104–115.

Cawood, P.A., van Gool, J.A.M., and Dunning, G.R., 1996, Geological development of eastern Humber and western Dunnage zones; Corner Brook-Glover Island region, Newfoundland: Canadian Journal of Earth Sciences, v. 33, p. 182-198.

Davies, J.L., Fyffe, L.R. and McAllister, A.L., 1983, Geology and massive sulphides of the Bathurst area, New Brunswick, *in* Scrapter, D.F., ed., Field Trip Guidebook to Stratabound Sulphide Deposits, Bathurst area, New Brunswick, Canada; and West-Central New England, U.S.A.: Geological Survey of Canada Report 36, p. 1-30.

de Wit, M.J., 1972, The geology around Bear Cove, eastern White Bay, Newfoundland: Unpublished Ph.D. thesis, Cambridge, England, University of Cambridge, 232 p.

Doyle, M.G., and Allen, R.L., 2003, Subsea-floor replacement in volcanic-hosted massive sulfide deposits: Ore Geology Reviews, v. 23, p. 183-222.

Drown, C.G., and Downs, R.C., 1990, Deformational style and strain partitioning at the Hellyer volcanogenic massive sulphide deposit [abs.]: Australian Geological Convention, 10th, Hobart, Australia, 1990, Abstract no. 25, p. 176-177.

Dunning, G.R., and Krogh, T.E., 1985, Geochronology of ophiolites of the Newfoundland Appalachians: Canadian Journal of Earth Sciences, v. 22, p. 1659-1670.

Flinn, D., 1962, On folding during three-dimensional progressive deformation: Geological Society of London, Quarterly Journal, v. 118, p. 385-443.

Franklin, J.M., Gibson, H.L., Jonasson, I.R., and Galley, A.G., 2005, Volcanogenic massive sulfide deposits Economic Geology 100th Anniversary Volume, , p. 523-560.

Franklin, J.M., Lydon, J.W., and Sangster, D.F., 1981, Volcanic-associated sulfide deposits Economic Geology 75th Anniversary Volume, p. 485-627.

Gale, G.H., 1971, An investigation of some sulphide deposits in the Rambler area, Newfoundland: Unpublished Ph.D. thesis, Durham, England, University of Durham, 137 p.

Gibson, H.L., Bailey, K., DeWolfe, M., Gilmore, K., Devine, C., Sims, D., Bailes, A., and MacLachlan, K., 2006, Evidence for cauldron subsidence at the Flin Flon Mining Camp: Implications for the location of volcanogenic massive sulphide deposits [abs]: Saskatchewan Industry and Resources Convention, Saskatoon, Saskatchewan, 2006, Program, p. 24.

Gibson, H., Lafrance, B., Pehrsson, S., DeWolfe, M., Gilmore, K., Simard, R.-L., and Pearson, B., 2013, The volcanological and structural evolution of the Paleoproterozoic Flin Flon mining district, Manitoba; the anatomy of a giant VMS system: Canada, Manitoba Resources Division, Manitoba Geological Survey, Winnipeg, MB, Canada., 47 p.

Gibson, H., Morton, R.L., and Hudak, G.J., 1999, Submarine volcanic processes, deposits, and environments favorable for the location of volcanic-associated massive sulfide deposits: Reviews in Economic Geology, v. 8, p. 13-51.

Gilligan, L.B., and Marshall, B., 1987, Textural evidence for remobilization in metamorphic environments: Ore Geology Reviews, v. 2, p. 205-229.

Grenne, T., 1989, The feeder zone to the Lokken ophiolite-hosted massive sulfide deposit and related mineralizations in the central Norwegian Caledonides: Economic Geology, v. 84, p. 2173-2195.

Hannington, M. D., Bleeker, W., and Kjarsgaard, I., 1999, Sulfide mineralogy, geochemistry, and ore genesis of the Kidd Creek deposit: Part I. North, central and south orebodies, in Hannington, M. D. and Barrie, C.T., eds., The Giant Kidd Creek volcanogenic massive sulfide deposit, western Abitibi Subprovince, Canada, 10. Economic Geology Monograph: Boulder, CO, Society of Economic Geologists, p. 163-224.

Hannington, M.D., de Ronde, C.E.J., D.R., and Petersen, S., 2005, Sea-floor tectonics and submarine hydrothermal systems, Economic Geology 100th Anniversary Volume, p. 111-141.

Hannington, M.D., Poulsen, K.H., Thompson, J.F.H., and Sillitoe, R.H., 1999, Volcanogenic gold in the massive sulfide environment: Reviews in Economic Geology, v. 8, p. 325-351.

Hibbard, L.J., 1983, Geology of the Baie Verte Peninsula, Newfoundland: Department of Mines and Energy, Government of Newfoundland and Labrador, Memoir 2, 279 p.

Jenner, G.A., and Fryer, B.J., 1980, Geochemistry of the upper Snooks Arm Group basalts, Burlington Peninsula, Newfoundland; evidence against formation in an island arc: Canadian Journal of Earth Sciences, v. 17, p. 888-900.

Jones, S., Berry, R.F., and Sinclair, B., 2006, Multiple deformation episodes at Myra Falls volcanic-hosted massive sulfide camp, central Vancouver Island, British Columbia, Canada: Canadian Journal of Earth Sciences, v. 43, p. 1711-1732.

Kennedy, M.J., 1971, Structure and stratigraphy of the Fleur de Lys Supergroup in the Fleur de Lys area, Burlington Peninsula, Newfoundland: Geological Association of Canada, Proceedings, v. 24, p. 59–71.

Kerr, D.J., and Gibson, H.L., 1993, A comparison of the Horne volcanogenic massive sulfide deposit and intracauldron deposits of the mine sequence; Noranda, Quebec: Economic Geology, v. 88, p. 1419-1442.

Kidd, W.S.F., 1974, The evolution of the Baie Verte lineament, Burlington Peninsula, Newfoundland: Unpublished Ph.D. thesis, Cambridge, England, University of Cambridge, 294 p.

Large, R.R., McGoldrick, P.J., Berry, R.F., and Young, C.H., 1988, A tightly folded, gold-rich, massive sulfide deposit; Que River Mine, Tasmania: Economic Geology, v. 83, p. 681-693.

Large, R.R., McPhie, J., Gemmell, J.B., Herrmann, W., and Davidson, G.J., 2001, The spectrum of ore deposit types, volcanic environments, alteration halos, and related exploration vectors in submarine volcanic successions: Some examples from Australia: Economic Geology, v. 96, p. 913-938.

Larocque, A.C.L., Hodgson, C.J., and Lafleur, P.-J., 1993, Gold distribution in the Mobrun volcanic-associated massive sulfide deposit, Noranda, Quebec: A preliminary evaluation of the role of metamorphic remobilization: Economic Geology, v. 88, p. 1443-1459.

Lydon, J.W., 1988, Volcanogenic massive sulphide deposits Part 2: Genetic models: Geoscience Canada, v. 15, p. 43-65.

Lydon, J. W., 1996, Characteristics of volcanogenic massive sulphide deposits; interpretations in terms of hydrothermal convection systems and magmatic hydrothermal systems: Boletin Geologico y Minero, v. 107, p. 215-264.

Marshall, B., and Gilligan, L.B., 1987, An introduction to remobilization: Information from ore-body geometry and experimental considerations: Ore Geology Reviews, v. 2, p. 87-131.

Marshall, B., and Gilligan, L.B., 1993, Remobilization, syn-tectonic processes and massive sulphide deposits: Ore Geology Reviews, v. 8, p. 39-64.

Marshall, B., and Spry, P.G., 2000, Discriminating between regional metamorphic remobilization and syntectonic emplacement in the genesis of massive sulfide ores: Reviews in Economic Geology, v. 11, p. 39-79.

Marshall, B., Vokes, F.M., and Larocque, A.C.L., 20008, Regional metamorphic remobilization: Upgrading and formation of ore deposits: Reviews in Economic Geology, v. 11, p. 19-38.

Mercier-Langevin, P., Hannington, M.D., Dubé, B., and Bécu, V., 2011, The gold content of volcanogenic massive sulfide deposits: Mineralium Deposita, v. 46, p. 509-539.

Mercier-Langevin, P., Lafrance, B., Bécu, V., Dubé, B., Kjarsgaard, I., and Guha, J., 2014, The Lemoine auriferous volcanogenic massive sulfide deposit, Chibougamau Camp, Abitibi Greenstone Belt, Quebec, Canada: Geology and Genesis: Economic Geology, v. 109, p. 231-269.

Mercier-Langevin, P., Hannington, M.D., Dubé, B., Piercey, S.J., Peter, J.M., and Pehrsson, S.J., 2015, Precious metal enrichment processes in volcanogenic massive sulphide deposits − A summary of key features, with an emphasis on TIGI-4 research contributions, *in* Peter, J.M. and Mercier-Langevin, P., eds., Targeted Geoscience Initiative 4: Contributions to the Understanding of Volcanogenic Massive Sulphide Deposit Genesis and Exploration Methods Development: Geological Survey of Canada, Open File 7853, p. 117‑130.

Mosier, D.L., Berger, V.I., and Singer, D.A., 2009, Volcanogenic massive sulfide deposits of the world: Database and grade tonnage models, U.S. Geological Survey Open-File Report 2009-1034, 46 p.

Nesse, W.D., 2000, Introduction to mineralogy: New York, Oxford University Press, 442 p.

Norman, R.E., and Strong, D.F., 1975, The geology and geochemistry of ophiolitic rocks exposed at Ming's Bight, Newfoundland: Canadian Journal of Earth Sciences, v. 12, p. 777-797.

Ohmoto, H., 1996, Formation of volcanogenic massive sulfide deposits: The Kuroko perspective: Ore Geology Reviews, v. 10, p. 135-177.

Pedersen, F.D., 1980, Remobilization of the massive sulfide ore of the Black Angel Mine, central West Greenland: Economic Geology, v. 75, p. 1022-1041.

Piercey, S. J., 2015, A semipermeable interface model for the genesis of subseafloor replacement-type volcanogenic massive sulfide (VMS) deposits: Economic Geology, v. 110, p. 1655-1660.

Piercey, S.J., Jenner, G.A., and Wilton, D.H.C., 1997, The stratigraphy and geochemistry of the southern Pacquet Harbour Group, Baie Verte Peninsula, Newfoundland; Implications for mineral exploration: Current Research, Newfoundland and Labrador Department of Natural Resources, Geological Survey, Report 97-1, p. 119-139.

Pilgrim, L., 2009, Mineral resource estimate for the Ming Mine, Newfoundland, Canada: Unpublished Technical Report 43-101, Rambler Metals and Mining Canada Ltd.

Pilote, J.-L., and Piercey, S.J., 2013, Volcanostratigraphy of the 1807 zone of the Ming Cu-Au volcanogenic massive-sulphide deposit, Baie Verte peninsula, northern Newfoundland: Geological Survey of Canada, Current Research, Report 2013-20, 13 p.

Pilote, J.-L., Piercey, S.J., and Mercier-Langevin, P., 2014, Stratigraphy and hydrothermal alteration of the Ming Cu-Au volcanogenic massive-sulphide deposit, Baie Verte peninsula, Newfoundland: Geological Survey of Canada, Current Research, Report 2014-7, 18 p.

Pilote, J.-L., Piercey, S.J., and Mercier-Langevin, P., 2015, Volcanic architecture and alteration assemblages of the Ming Cu-Au-(Zn-Ag) VMS deposit, Baie Verte,

Newfoundland: Implications for Au enrichment processes and exploration: Geological Survey of Canada, Open File 7853, p. 197–210.

Pilote, J.-L., Piercey, S.J., Brueckner, S.M., and Grant, D., 2016, Resolving the relative timing of Au enrichment in volcanogenic massive sulfide deposits using scanning electron microscopy-mineral liberation analyzer: Empirical evidence from the Ming Deposit, Newfoundland, Canada: Economic Geology, v. 111, p. 1495-1508.

Ross, P.-S., and Mercier-Langevin, P., 2014, The volcanic setting of VMS and SMS deposits: A review: Geoscience Canada, v. 41, p. 365-377.

Skilling, I.P., White, J.D.L., and McPhie, J., 2002, Peperite; a review of magma-sediment mingling: Journal of Volcanology and Geothermal Research, v. 114, p. 1-17.

Skulski, T., Castonguay, S., McNicoll, V., van Staal, C., Kidd, W., Rogers, N., Morris, W., Ugalde, H., Slavinski, H., Spicer, W., Moussallam, Y., and Kerr, I., 2010, Tectonostratigraphy of the Baie Verte oceanic tract and its ophiolite cover sequence on the Baie Verte Peninsula: Current Research, Newfoundland and Labrador Department of Natural Resources, Geological Survey, Report 10-1, p. 315-335.

Skulski, T., Castonguay, S., Kidd, W.S.F., McNicoll, V.J., van Staal, C.R., and Hibbard, J.P., 2015, Geology, Baie Verte and parts of Fleur de Lys, Newfoundland and Labrador, NTS 12-H/16 and part of NTS 12-I/1: Geological Survey of Canada, Canadian Geoscience Map 159, scale 1:50 000. doi:10.4095/295865

Skulski, T., McNicoll, V., Whalen, J.B., Moussallam, Y., Dunning, G., Castonguay, S., Cawood, P., Kidd, W.S.F., and van Staal, C., 2012, Subduction to slab-break-off transition recorded in the timing, composition and setting of early Silurian volcano-plutonic complexes, Baie Verte Peninsula, Newfoundland [abs.]: Geological Association of Canada–Mineralogical Association of Canada Annual Meeting, St. John's, Canada, 2012, p. 128.

Spry, A., 1969, Metamorphic textures: Oxford, Pergamon Press, 350 p.

Tuach, J., and Kennedy, M.J., 1978, The geologic setting of the Ming and other sulfide deposits, consolidated Rambler mines, Northeast Newfoundland: Economic Geology, v. 73, p. 192-206.

Upadhyay, H. D., 1973, The Betts Cove ophiolite and related rocks of the Snooks Arm Group, Newfoundland: Unpublished Ph.D. thesis, St. John's, Canada, Memorial University of Newfoundland, 224 p.

van Staal, C.R., 2007, Pre-Carboniferous tectonic evolution and metallogeny of the Canadian Appalachians, *in* Goodfellow, W.D., ed., Mineral deposits of Canada: A synthesis of major deposit-types, district metallogeny, the evolution of geological provinces, and exploration methods, Special Publication No. 5, Geological Association of Canada, Mineral Deposits Division, p. 793-818.

van Staal, C.R., and Barr, S.M., 2012, Lithosperic architecture and tectonic evolution of the Canadian Appalachians and associated Atlantic margin, *in* Percival, J.A., Cook, F.A., and Clowes, R.M., eds., Tectonic Styles in Canada: The LITHOPROBE perspective, Geological Association of Canada, Special Paper 49.

van Staal, C.R., and Williams, P.F., 1984, Structure, origin, and concentration of the Brunswick 12 and 6 orebodies: Economic Geology, v. 79, p. 1669-1692.

Vokes, F.M., 1969, A review of the metamorphism of sulphide deposits: Earth-Science Reviews, v. 5, p. 99-143.

Waldron, J.F.W., Anderson, S.D., Cawood, P.A., Goodwin, L.B., Hall, J., Jamieson, R.A., Palmer, S.E., Stockmal, G.S., and Williams, P.F., 1998, Evolution of the Appalachian Laurentian margin: Lithoprobe results in western Newfoundland: Canadian Journal of Earth Sciences, v. 35, p. 1271–1287.

White, J.D.L., and Houghton, B.F., 2006, Primary volcaniclastic rocks: Geology, v. 34, p. 677-680.

Whitten, E.H.T., 1966, Structural geology of folded rocks: Chicago, Rand McNally, 678 p.

Zachrisson, E., 1984, Lateral metal zonation and stringer zone development, reflecting fissure-controlled exhalations at the Stekenjokk-Levi strata-bound sulfide deposit, central Scandinavian Caledonides: Economic Geology, v. 79, p. 1643-1659.

Zheng, Y., Gu, L., Tang, X., Wang, Z., Wu, C., Zhang, W., and Wu, X., 2012, Sulfide remobilisation from sulfide ore at high temperatures and differential stresses: An experimental approach: Resource Geology, v. 62, p. 174-186.

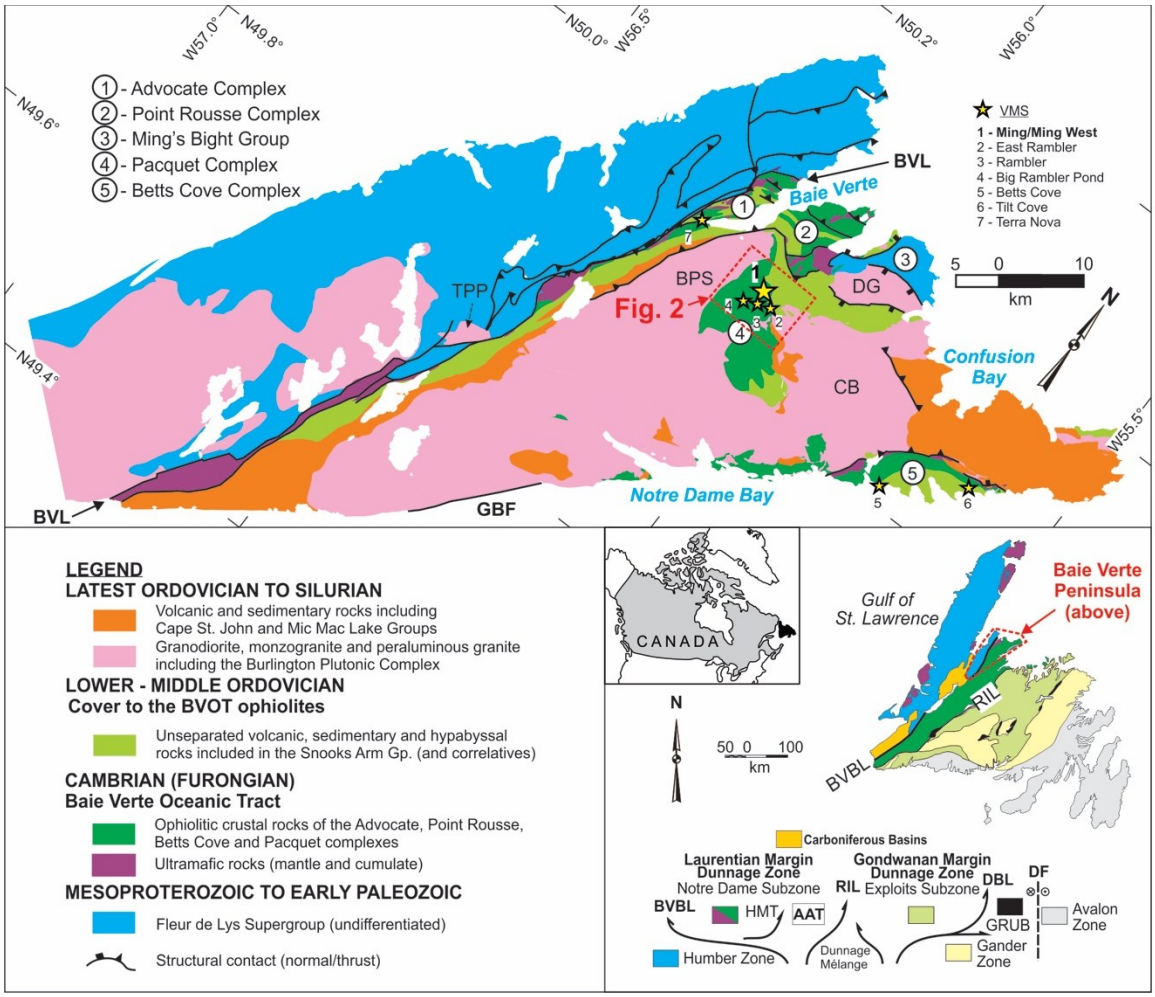

Fig. 2.1. Simplified geology of the Baie Verte Peninsula with major tectonostratigraphic zones that form the Appalachian orogenic belt in Newfoundland (modified from Castonguay et al., 2014 and references therein). Past and currently producing VMS deposits are also shown. AAT = Annieopsquotch Accretionary Tract, BPS = Burlington plutonic Suite, BVBL = Baie Verte-Brompton Line, BVL = Baie Verte Line, CB = Cape Brulé, DBL = Dog Bay Line, DF = Dover Fault, DG = Dunamagon Granite, GRUB = Gander River Ultramafic Belt, TPP = Trap Pond pluton, RIL = Red Indian Line, HMT = Hungry Mountain Thrust.

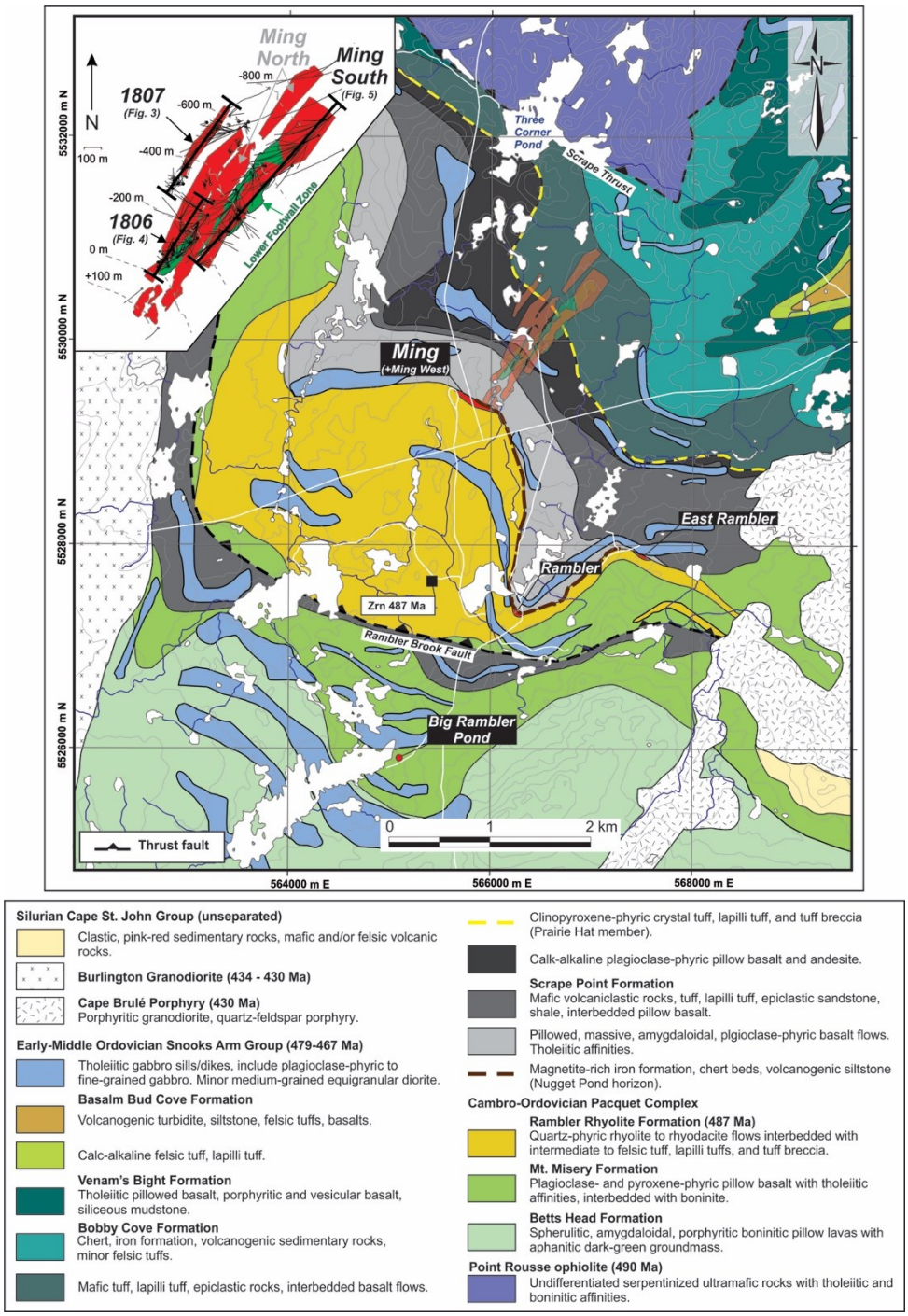

Fig. 2.2. Geological map of the study area, Baie Verte Peninsula, with Ming VMS orebodies projected to surface (also in the inset) and shown in light red and light green (Lower Footwall Zone). Datum is UTM 21N NAD 83. Map compiled and modified from Tuach and Kennedy (1978), Hibbard (1983), Castonguay et al. (2009), Pilgrim (2009), and Skulski et al. (2010). The U-Pb zircon (Zrn) age of the Rambler Rhyolite formation is from Skulski et al. (2015).

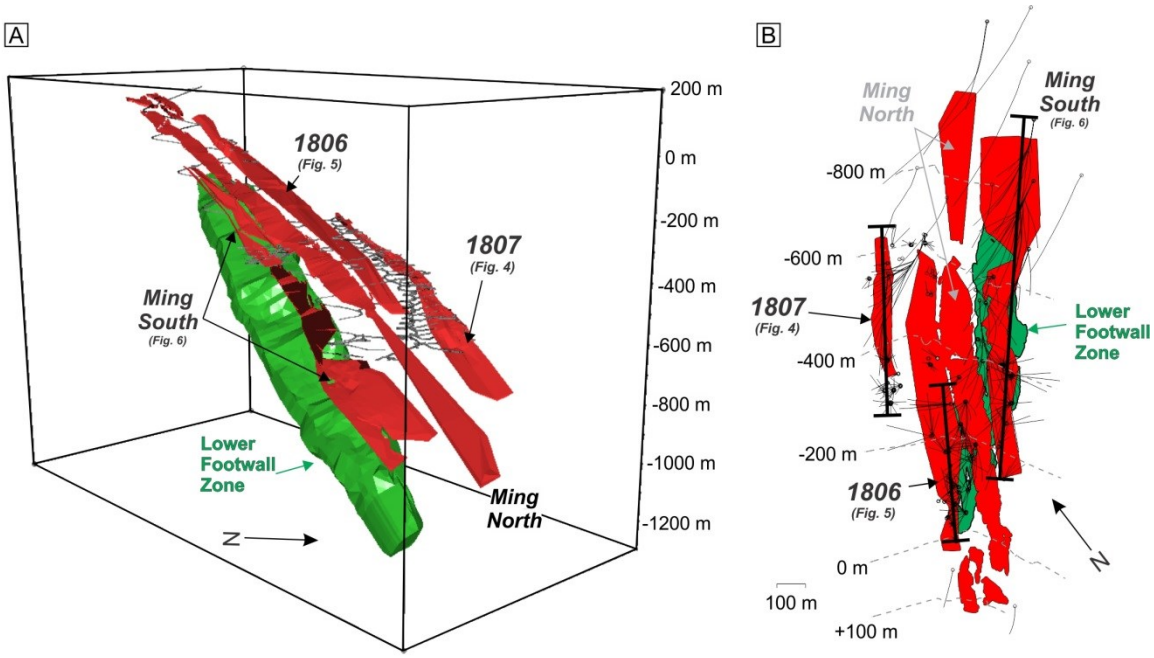

Fig. 2.3. A. Three-dimensional model of the Ming deposit. Shown are the extent of the wireframes for each zone based on resources calculation by Rambler Metals and Mining Ltd. B. Plan view of A). The black strings represent drill holes.

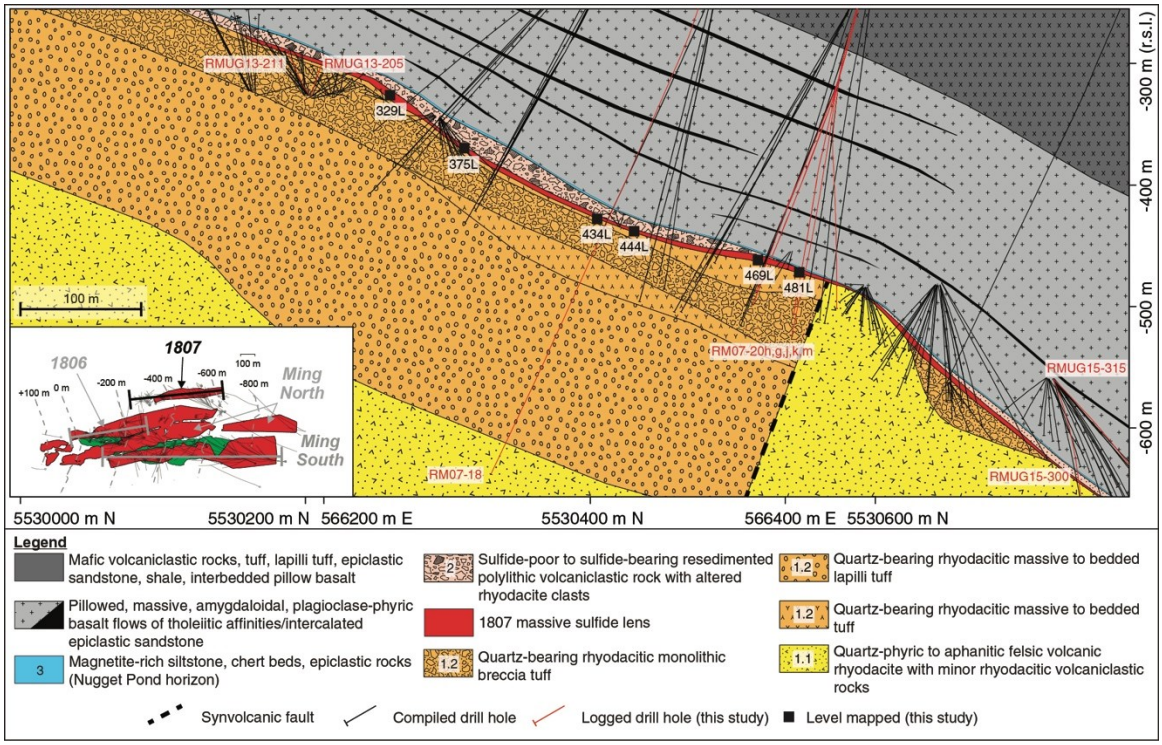

Fig. 2.4. Geological cross-section of the 1807 Zone (looking northwest). The dikes were omitted to simplify the map. Unit names of the Snooks Arm Group are from Skulski et al. (2010). The inset shows the location of the cross section (thick black line).

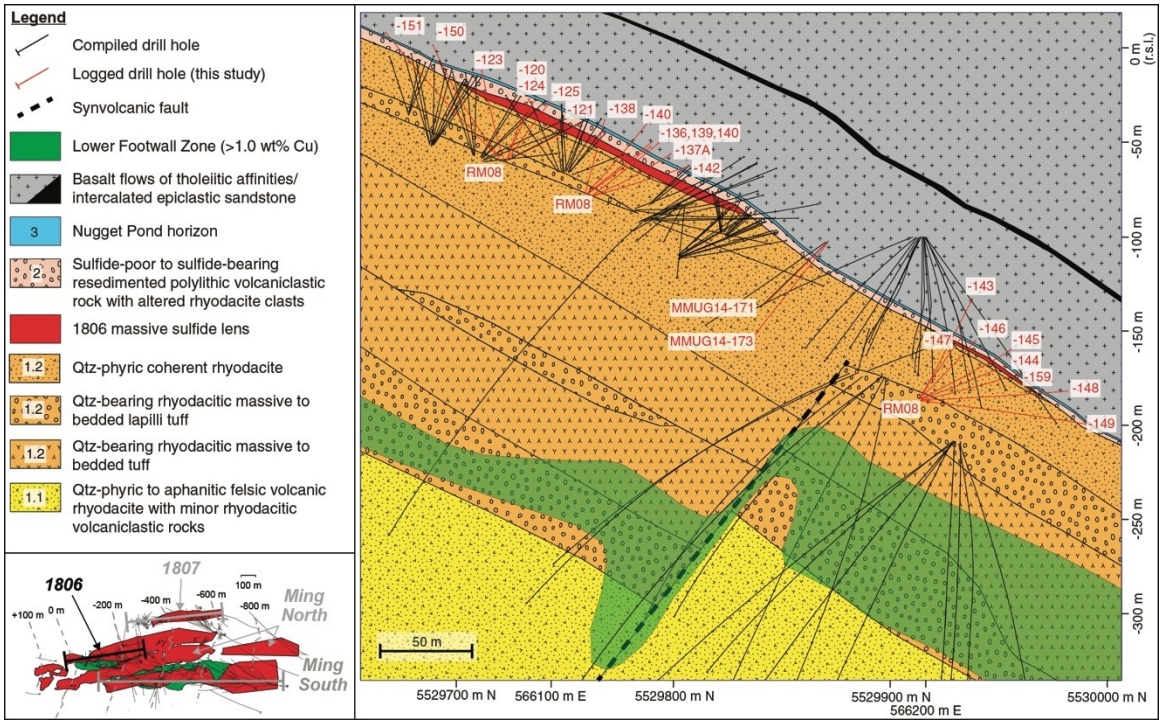

Fig. 2.5. Geological cross-section of the 1806 Zone (looking northwest). The dikes were omitted to simplify the map. Unit names of the Snooks Arm Group are from Skulski et al. (2010). The inset shows the location of the cross section (thick black line).

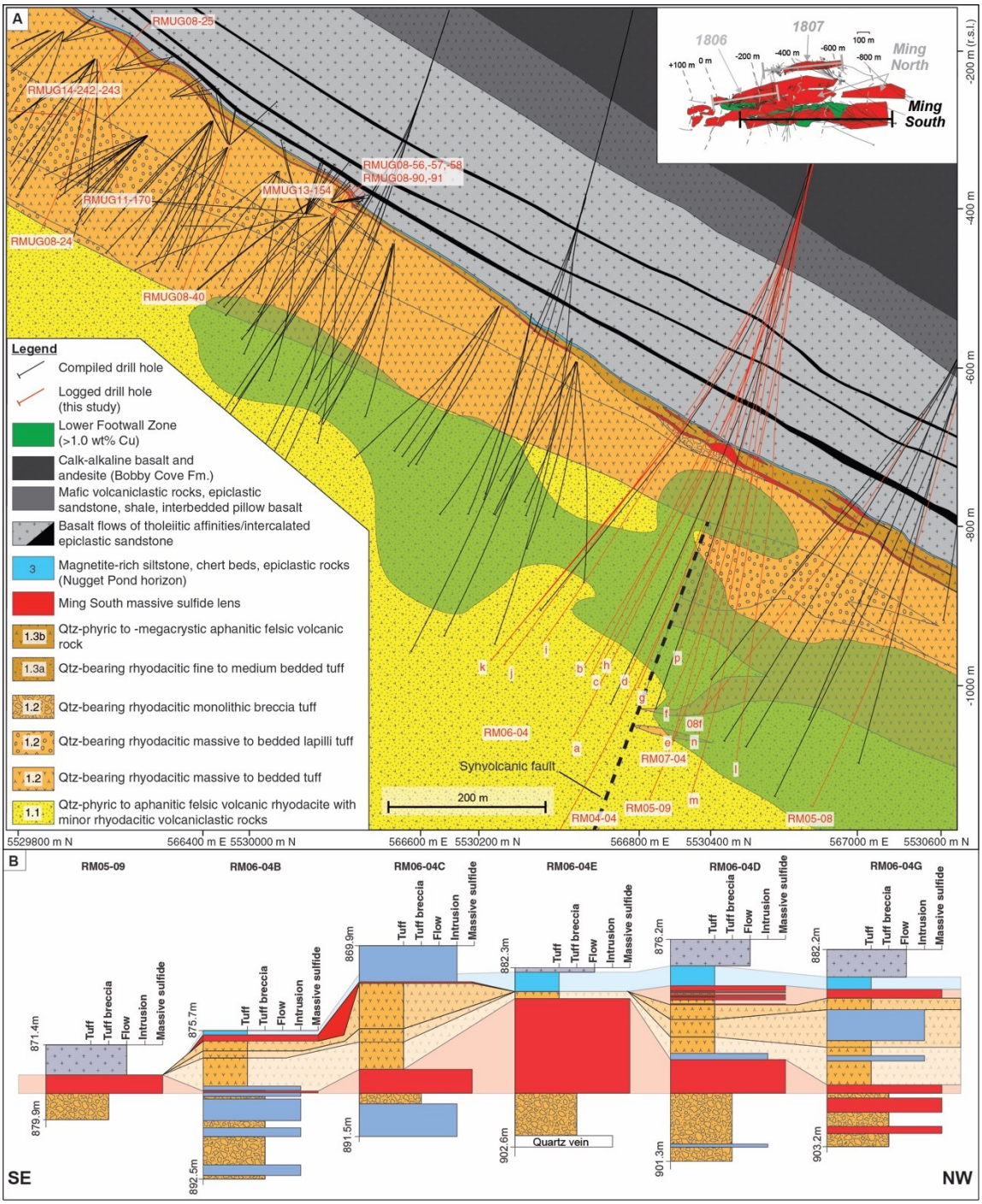

Fig. 2.6. A. Geological cross-section of the Ming South Zone (looking northwest). The dikes were omitted to simplify the map. Unit names of the Snooks Arm Group are from Skulski et al. (2010). The inset shows the location of the cross section (thick black line). B. Graphic logs for representative diamond-drill holes intersecting the Ming South Zone (see line on the inset for location). The drill holes in B) are correlated across (or "hung on") the base of the lower sulfide lens. Undifferentiated mafic dikes are in blue. The relative horizontal positions of the drill holes are not to scale.

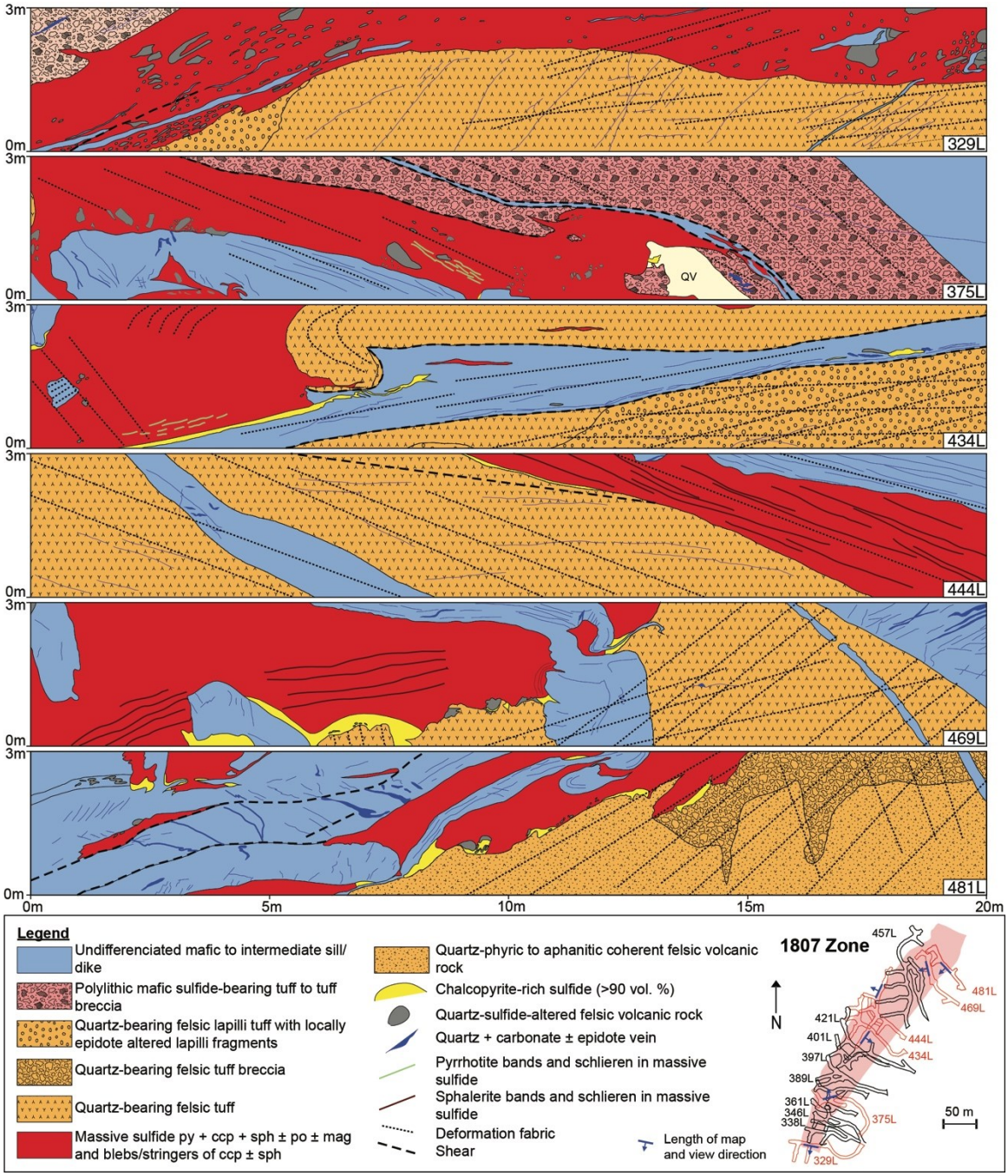

Fig. 2.7. Geological wall maps of selected underground levels in the 1807 Zone. The maps show the relationship between the different lithological units, including the massive sulfide horizon where it is intruded by undifferentiated mafic to intermediate dikes. Mapped walls are shown in the inset (blue lines) with their respective orientation of point-of-view (blue arrow). Ccp = chalcopyrite, Po = pyrrhotite, Py = pyrite, Mag = magnetite, Sp = sphalerite, QV = quartz vein.

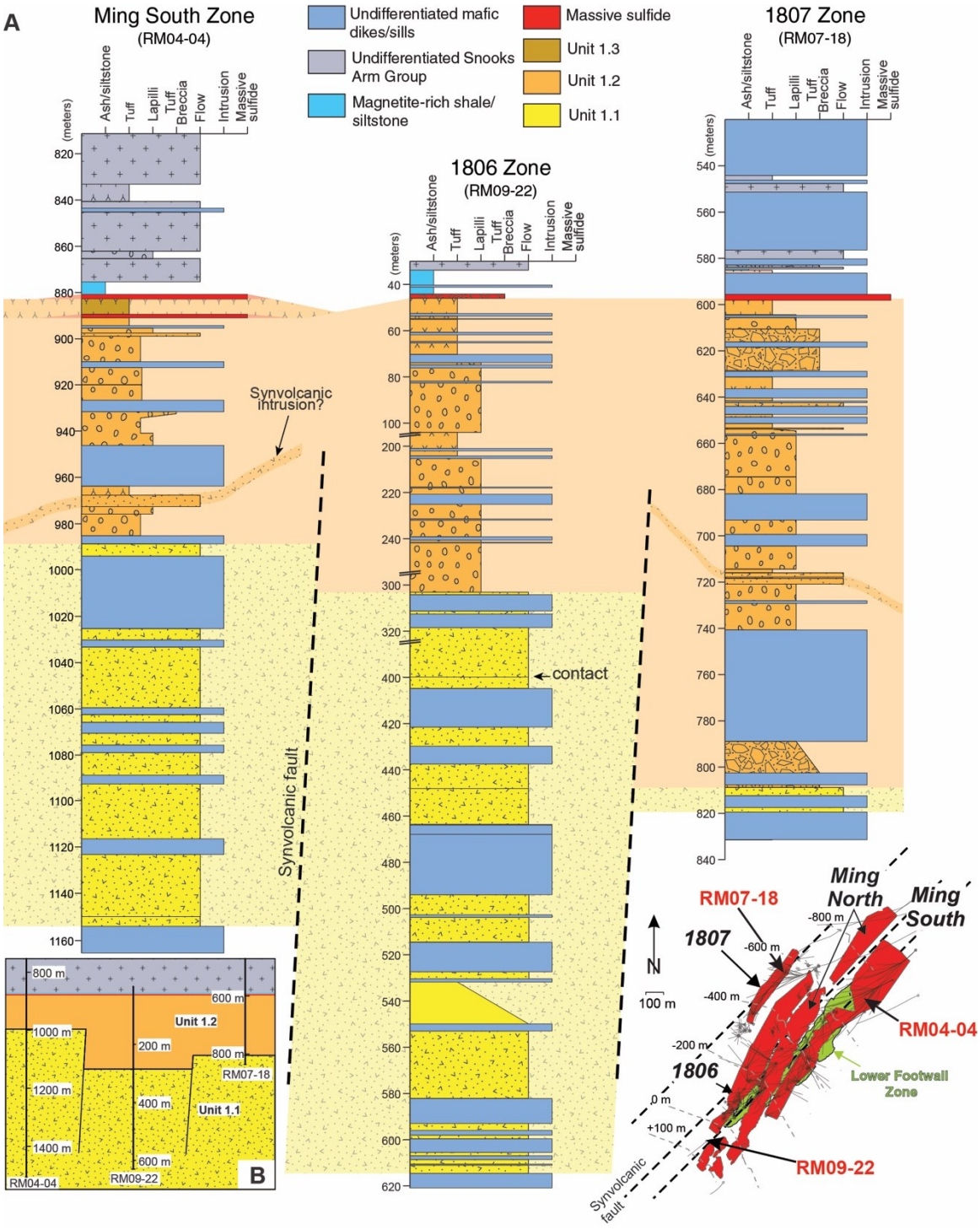
A
Ming South Zone
(RM04-04)
1806 Zone
(RM09-22)
1807 Zone
(RM07-18)
Undifferentiated mafic dikes/sills
Undifferentiated Snooks Arm Group
Magnetite-rich shale/ siltstone
Massive sulfide
Unit 1.3
Unit 1.2
Unit 1.1
Ash/siltstone
Tuff
Lapilli Tuff
Breccia
Flow
Intrusion
Massive sulfide
(meters)
Synvolcanic intrusion?
Synvolcanic fault
contact
800 m
600 m
Unit 1.2
1000 m
200 m
800 m
RM07-18
1200 m
400 m
Unit 1.1
1400 m
600 m
RM04-04
RM09-22
B
Ming North
Ming South
RM07-18
1807
-800 m
-600 m
-400 m
-200 m
1806
0 m
+100 m
N
100 m
RM04-04
Lower Footwall Zone
RM09-22
Synvolcanic fault

(Previous page) Fig. 2.8. A. Composite stratigraphic columns of the Ming South (DDH RM04-04), 1806 (RM09-22), and 1807 (RM07-18) zones. These illustrate the volcaniclastic lithofacies associated with all zones. Note the downhole breaks of lengths in drill hole RM09-22. The synvolcanic faults are interpreted based on the sharp lateral change in lithofacies and on the distribution of the chlorite-rich alteration spatially and genetically associated with the Lower Footwall Zone. B. Simplified cross-section of A. This section shows complete stratigraphic thicknesses (no downhole breaks). Units are as in Figures 4-6 with the addition of undifferentiated mafic dikes (in greyish blue). The red coloured tuff breccia in RM09-22 contains >20 vol.% sulfides. The drill holes are correlated across the sulfide lenses.

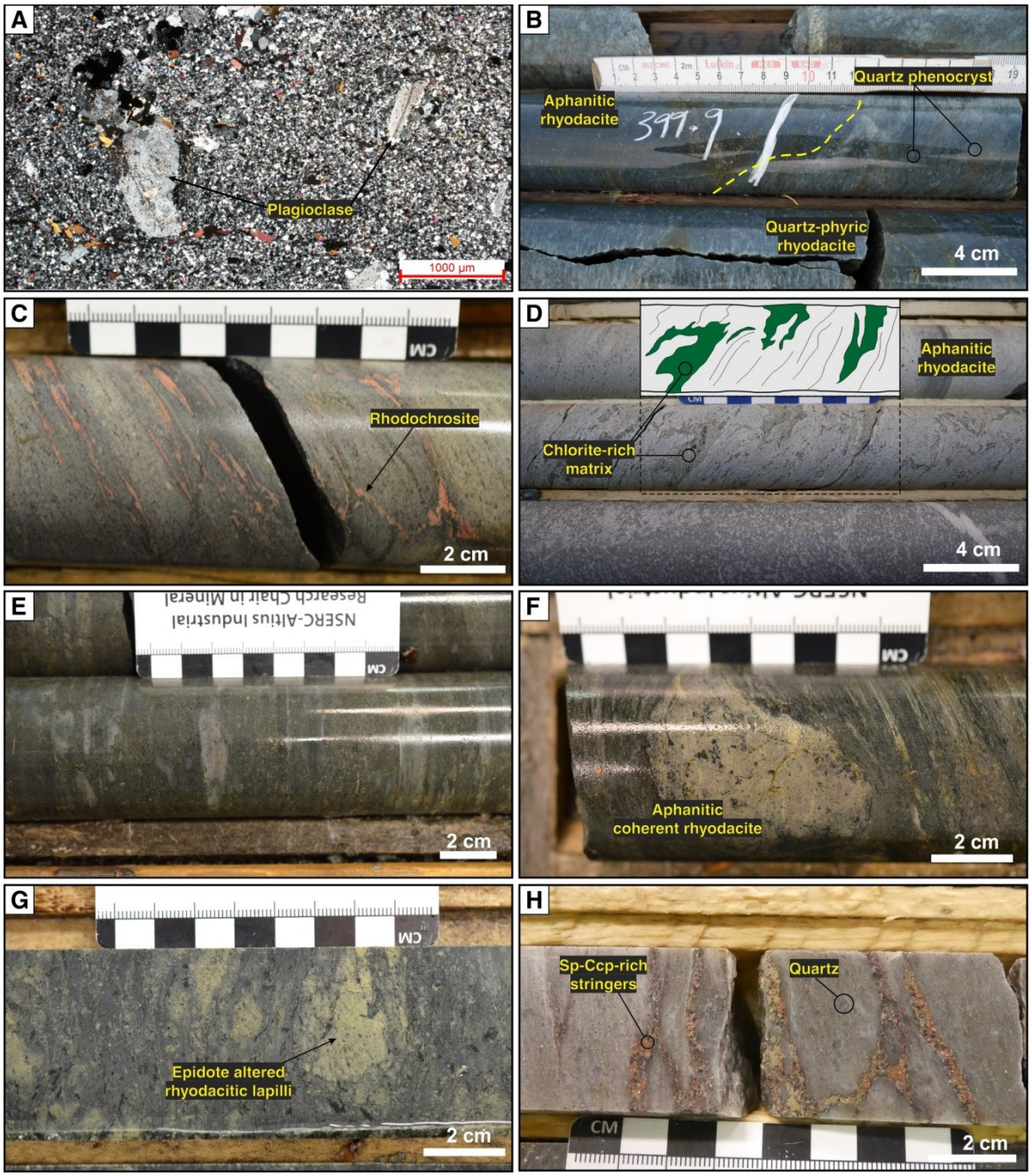
A
Plagioclase
1000 µm
B
Quartz phenocryst
Aphanitic rhyodacite
Quartz-phyric rhyodacite
4 cm
C
Rhodochrosite
2 cm
D
Aphanitic rhyodacite
Chlorite-rich matrix
4 cm
E
2 cm
F
Aphanitic coherent rhyodacite
2 cm
G
Epidote altered rhyodacitic lapilli
2 cm
H
Sp-Ccp-rich stringers
Quartz
2 cm

(Previous page) Fig. 2.9. Representative photographs of host rocks from the Ming deposit. A. Subhedral plagioclase phenocrysts in coherent rhyodacite (1807 Zone). B. Irregular contact between quartz-phyric and aphyric coherent felsic volcanic rocks of unit 1.1 (RM09-22; 400 m downhole). C. Felsic hyaloclastite showing jigsaw-fit structures, replaced by rhodochrosite (Mn-carbonate) (RM07-20M; 675 m downhole). D. Peperitic texture of aphanitic rhyodacite in contact with a fine-grained chlorite-rich tuffaceous sedimentary rock (RMUG15-315; 90 m downhole). E. Representative felsic lapilli tuff with ellipsoidal aphanitic rhyodacite lapilli fragments in a fine-grained chlorite-sericite-quartz matrix. This facies is found near the base of unit 1.2 (RM07-18; 807 m downhole). F. Rounded aphanitic coherent rhyodacite pyroclast in foliated tuff (RM07-18; 718 m downhole). G. Epidote-altered rhyodacitic lapilli in a bedded fine-grained chloritic matrix (RM07-18; 614 m downhole). H. Pyrite-sphalerite-chalcopyrite-quartz stringers in sericite-altered quartz-phyric coherent rhyodacite (MMUG14-173; 40 m downhole).

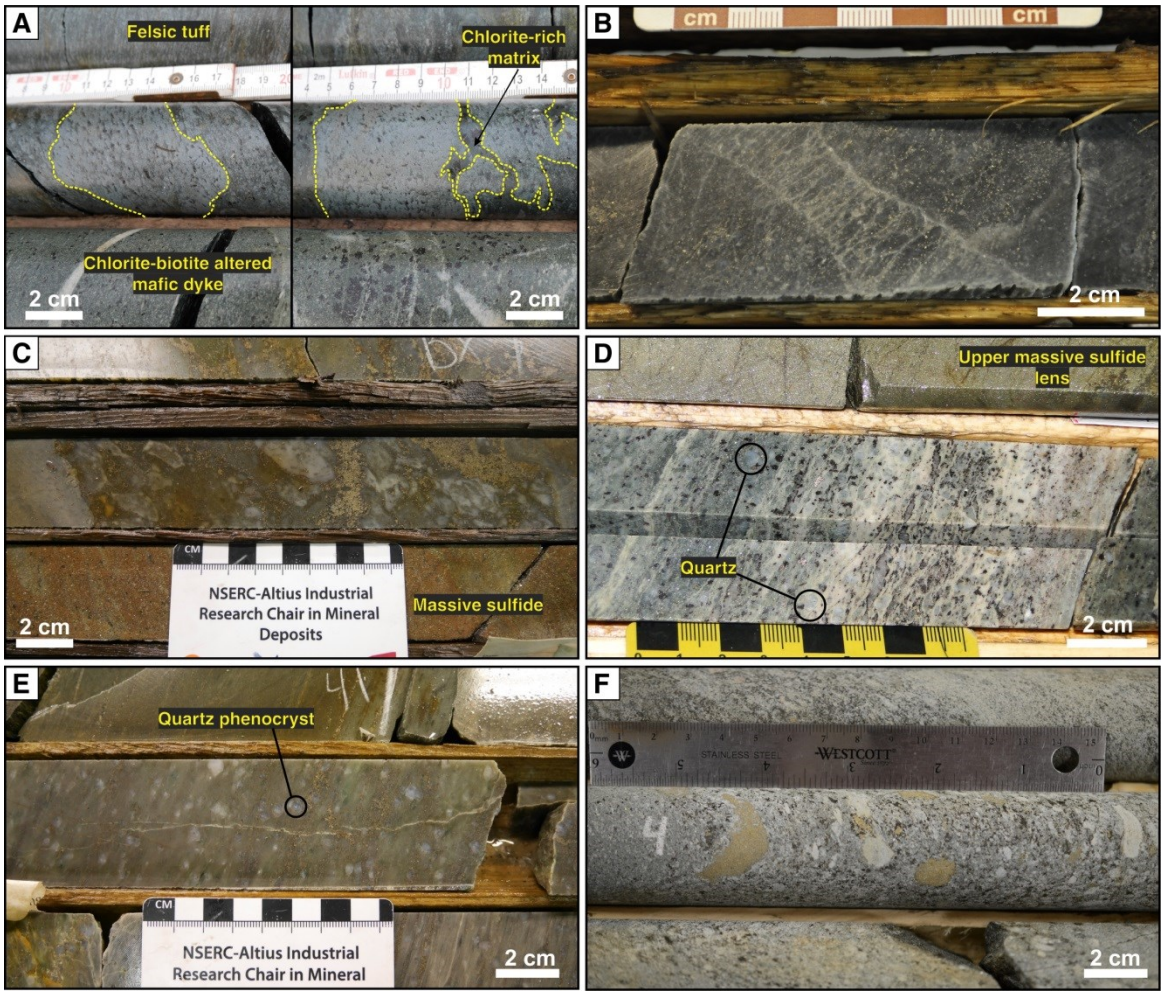

Fig. 2.10. Representative photographs of host rocks from the Ming deposit. A. Fluidal juvenile fragments of coherent rhyodacite closely spatially (≤ 2 m) associated with coherent rhyodacite and laminated rhyodacitic tuff (RM09-22; 230 m downhole). B. Hourglass shaped cylindrical features of 1 to 2 cm in diameter with internal, 1 to 5 mm spaced layers defined by sericite in a coherent quartz-phyric rhyodacite (RMUG08-138; 19 m downhole). C. Sparsely to closely packed, well-defined, blocky and splintery, quartz-phyric rhyodacite clasts in a sericite altered quartz-bearing rhyodacitic matrix, partially replaced by sulfides (RMUG08-138; 42.5 m downhole). D. Representative quartz-bearing rhyodacitic tuff bed located down-dip of the Ming South Zone (RM06-04D; 885 m downhole). E. Quartz-phyric coherent rhyodacite between the lower and upper massive sulfide lenses of the Ming South Zone (RMUG08-25; 42.5 m downhole). F. Mafic polylithic primary to recycled (or lithic) tuff breccia with <10 vol. % pyrite-chalcopyrite-rich sulfide clasts (bronze), minor felsic fragments (white) and fine-grained mafic tuff groundmass (RMUG13-205; 30 m downhole).

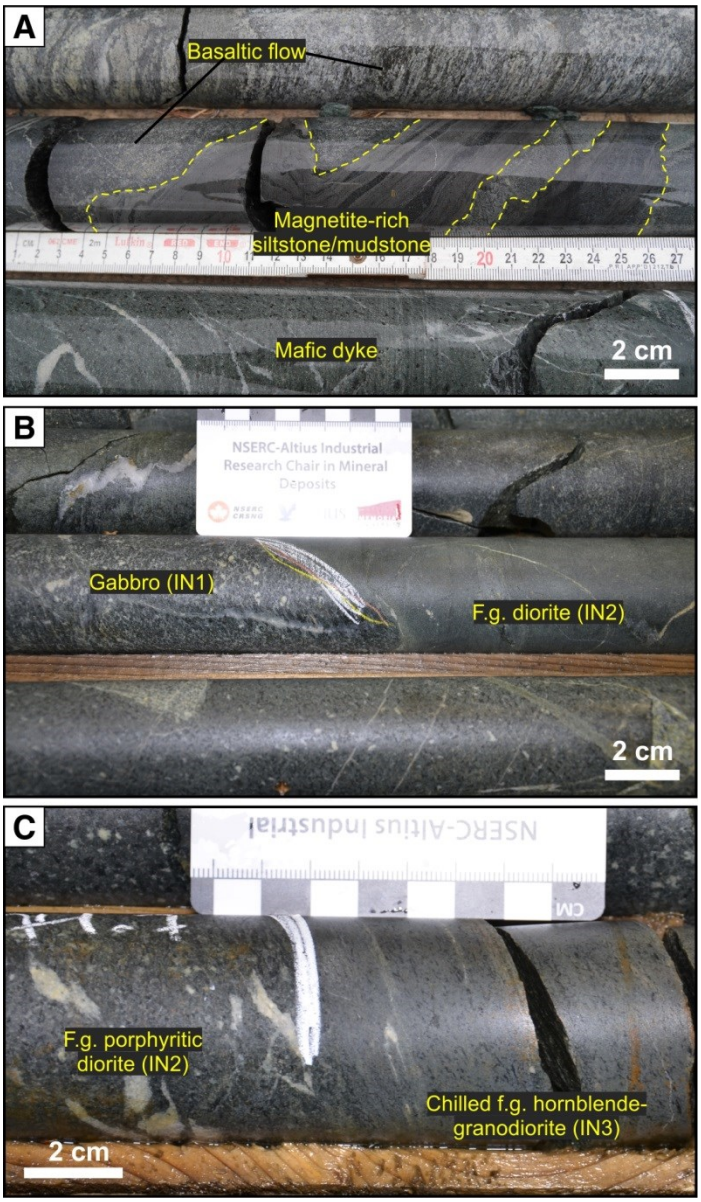

Fig. 2.11. Representative photographs of cover sequence and intrusive rocks from the Ming deposit. A. Folded beds of magnetite-rich siltstone/mudstone intercalated with coarser grain sized sediment and basalt flows. The sedimentary unit represents the base of the Snook Arm Group (Nugget Pond horizon) (RM09-22; 37.5 m downhole). B. Intrusive contact between medium-grained, equigranular gabbro (IN1) and chilled fine-grained diorite (IN2) (RM05-08; 1168 m downhole). C. Intrusive contact between porphyritic diorite (IN2) and chilled fine-grained hornblende-rich granodiorite (IN3) (RM05-08; 1174.7 m downhole).

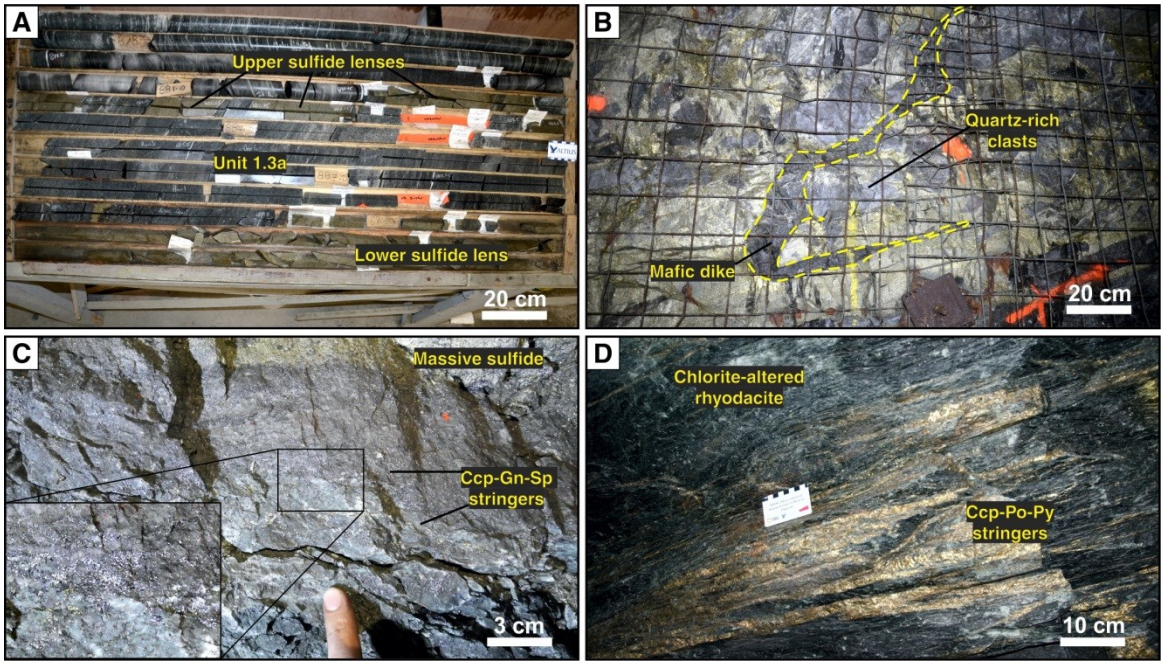

Fig. 2.12. Representative photographs of the mineralization from the Ming deposit. A. Stratiform lower and upper sulfide lenses, separated by quartz-bearing tuff beds of unit 1.3 (RM06-04D; 876.5 m to 893.5 m downhole). B. Folded mafic dike cross-cutting massive sulfide and quartz-rich fragments (looking southwest; 1807 Zone; 329 level). C. Chalcopyrite-galena-sphalerite-rich stringers in a quartz-bearing rhyodacitic tuff at the contact with massive sulfide (looking northeast; 1806 Zone; 431 level). D. Strongly transposed chalcopyrite-pyrrhotite-pyrite stringers onto deformation fabrics in an intensely chlorite-altered rhyodacite (looking southeast; Lower Footwall Zone; 1450 level).

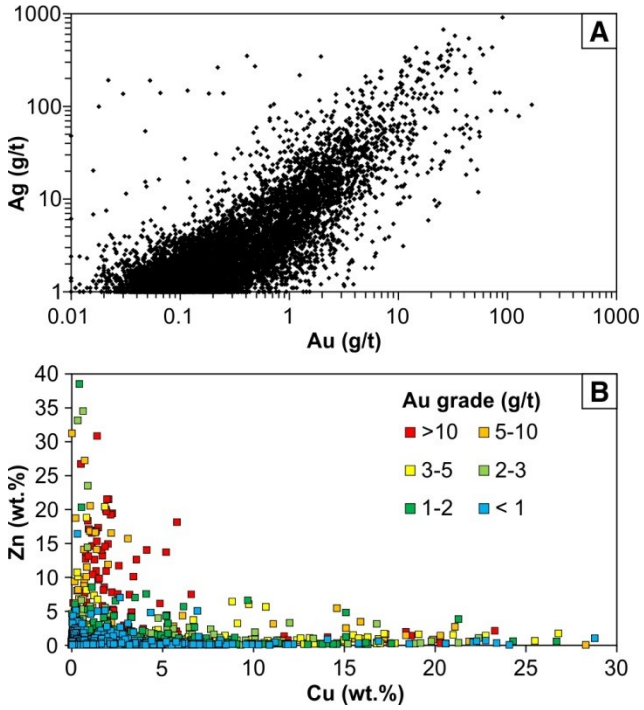

Fig. 2.13. Binary plots of assay data for 19,268 samples from 588 exploration and definition drill-hole intersections at the Ming deposit. A. Log-log plot of Ag (g/t) vs. Au (g/t). B. Cu (wt %) vs. Zn (wt %) as a function of Au grades (g/t). Assay data kindly provided by Rambler Metals and Mining Ltd. (January 2016).

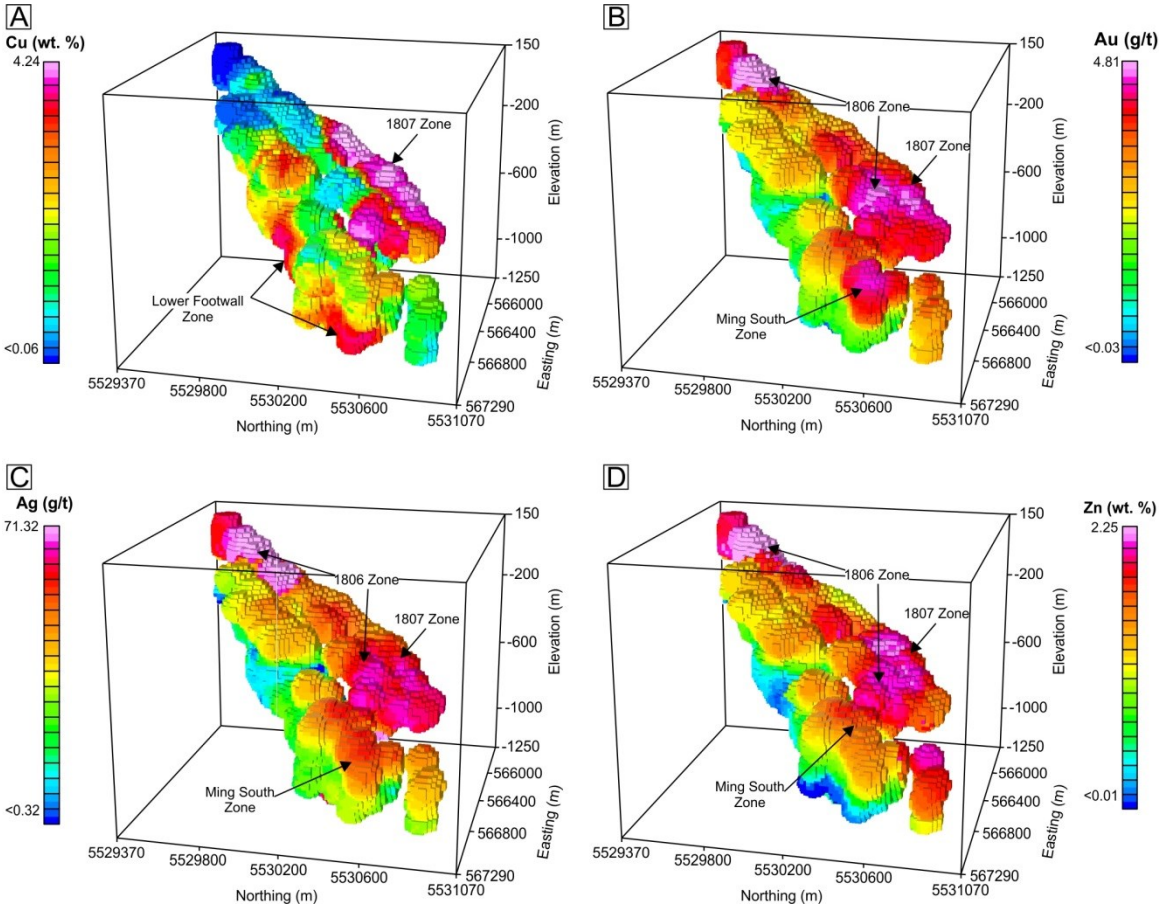

Fig. 2.14. Metal distribution of A. Cu (wt. %), B. Au (g/t), C. Ag (g/t), and D. Zn (wt. %) in the Ming deposit. These images of metals distribution were obtained by the interpolation (3-dimensional kriging; voxel dimensions of 80 m^3) of 588 exploration and definition drill-hole intersections, including up to 19,268 assayed samples. Assay data gracefully provided by Rambler Metals and Mining Ltd. (January 2016).

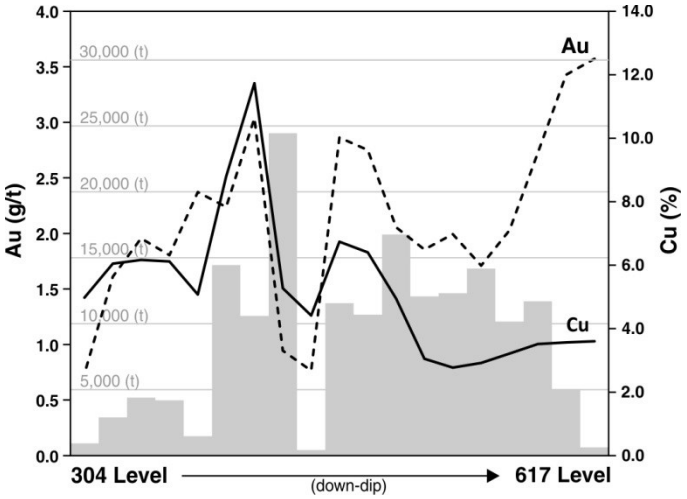

Fig. 2.15. Average Cu and Au grades (line) and ore tonnage (histogram) in the 1807 Zone. The values were calculated and provided by Rambler Metals and Mining Ltd. from systematic sampling of the semimassive to massive sulfide at all levels. Note the decoupling of Au and Cu grades in the deepest levels.

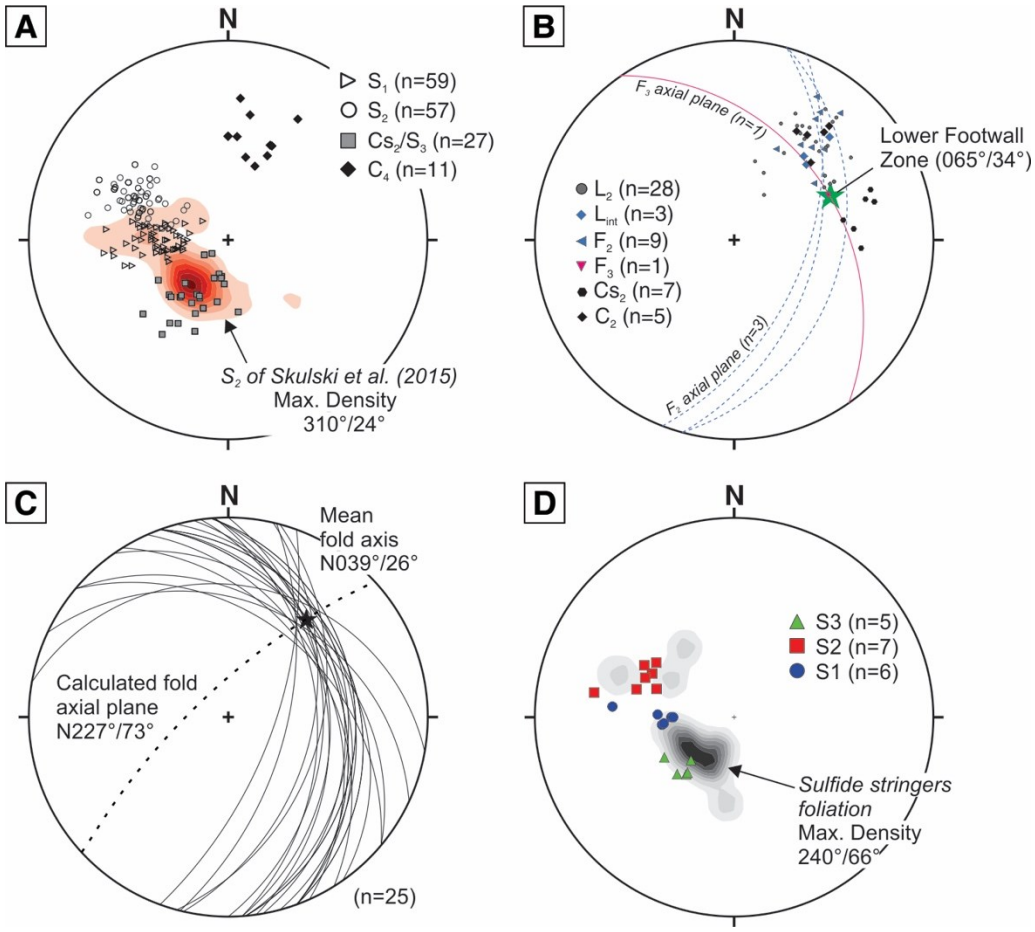

Fig. 2.16. Stereographic projections (Wulff lower hemisphere) of fabrics at the Ming deposit. A. Dominant foliations related to different deformation events. Contours represent the density distribution of poles to S_2 as interpreted by previous studies in the Rambler Rhyolite formation (S. Castonguay, unpub. data, 2016). B. Linear and intersecting features related to different deformation events. C. Deformation of primary stratigraphic contacts (S_0). D. Density distribution of poles to sulfide stringers in the Lower Footwall Zone (LFZ) in relation to S_1, S_2, and S_3.

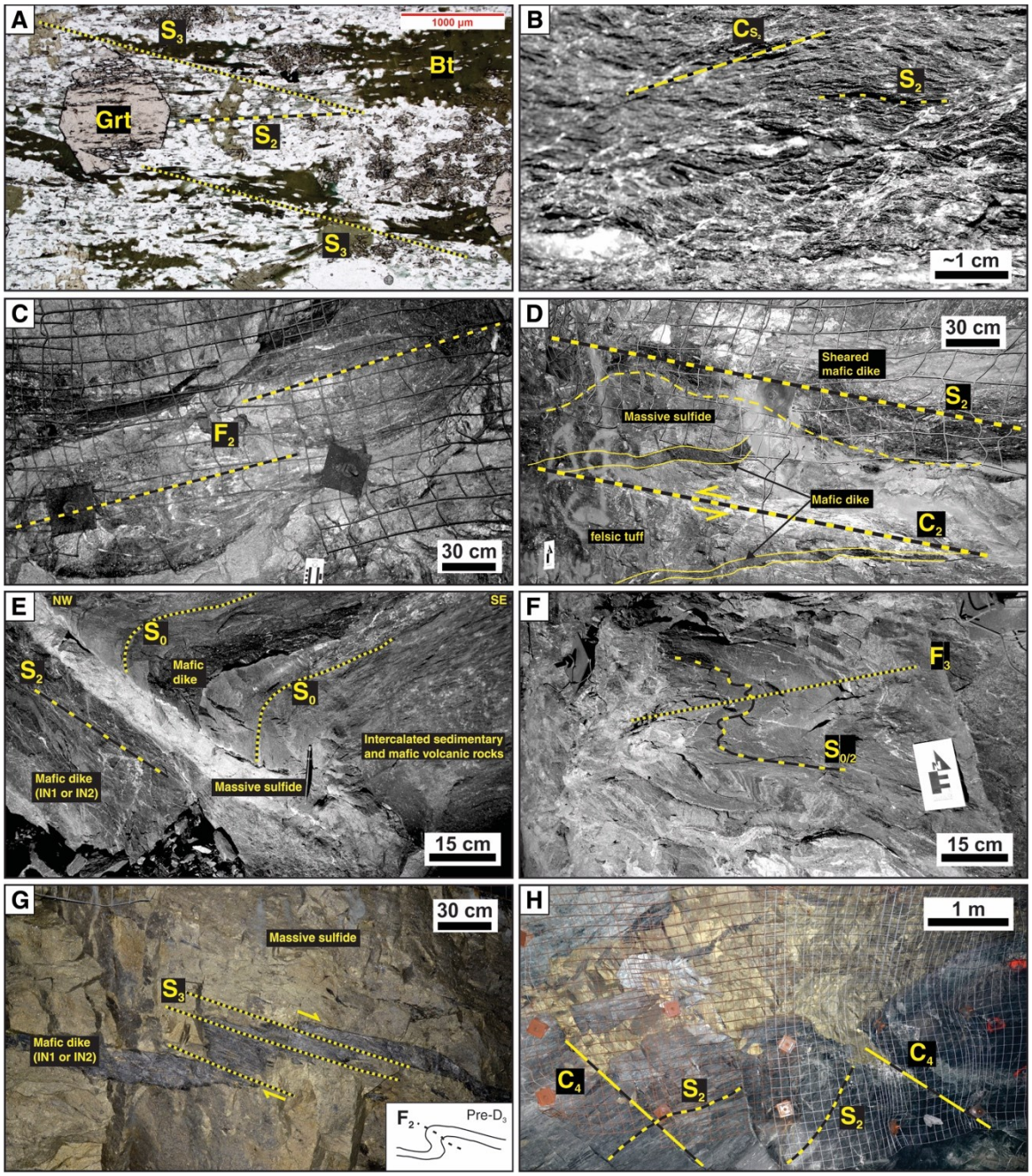
A
S3
1000 µm
Bt
Grt
S2
S3
B
Cs2
S2
~1 cm
C
F2
30 cm
D
30 cm
Sheared mafic dike
S2
Massive sulfide
Mafic dike
C2
felsic tuff
E
NW
SE
S0
Mafic dike
S2
S0
Intercalated sedimentary and mafic volcanic rocks
Mafic dike (IN1 or IN2)
Massive sulfide
15 cm
F
F3
S0/2
15 cm
G
30 cm
Massive sulfide
S3
Mafic dike (IN1 or IN2)
F2
Pre-D3
H
1 m
C4
S2
C4
S2

(Previous page) Fig. 2.17. A. Relationships between the pervasive S_2 foliation, late syn- to post-D_2 garnet and biotite porphyroblasts, and spaced cleavage S_3 fabric. B. Crenulated S_2 fabric in mafic sill by C_{S2}. C. Tight overturned and boudinaged folded (F_2) mafic sill in massive sulfide. D. Sheared mafic dikes, cross cutting the massive sulfide lens, by C_2 with co-planar S_2 foliation. E. Northeast plunging drag fold in in hanging wall cross cut by a massive sulfide and mafic dike piercement structure. The drag fold is co-planar to S_2 and show northwest-directed kinematics. F. Magnetite-rich siltstone folded by F_3 with associated piercement of sulfide in the left part of the photo. G. Folded (F_2) mafic dike in massive sulfide, displaced by northeast-directed normal subhorizontal extensional faults (S_3). H. Extensional C_4 discrete faults in felsic tuff and massive sulfide with remobilized sulfides along the faults.

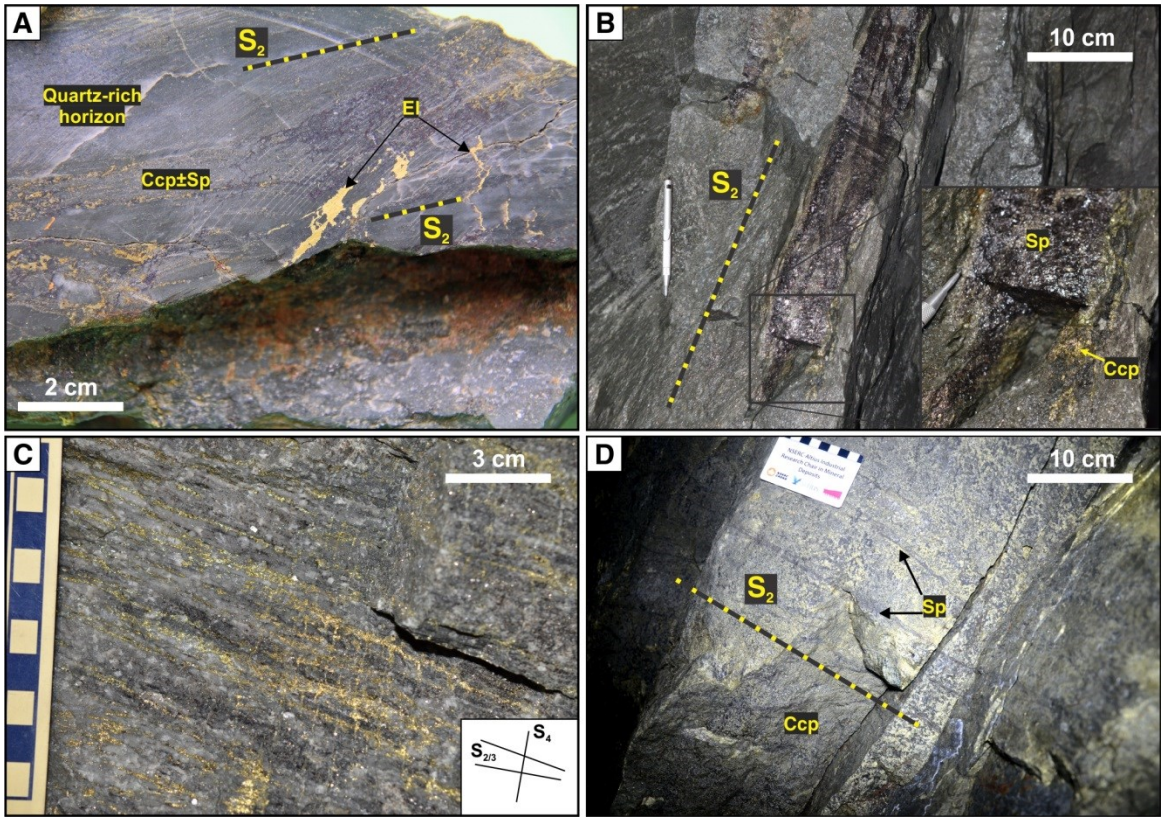

Fig. 2.18. Evidence of sulfide remobilization. A. Electrum veinlets cutting S_2 fabrics in the quartz-rich horizon, immediately overlying the 1806 Zone massive sulfide orebody (1700 level). B. Sphalerite-chalcopyrite piercement structure parallel to S_2 and oblique to the 1806 Zone massive sulfide, located 2 m above. C. Cross-cutting relationship between chalcopyrite-rich veinlets parallel to S_1, S_2, and S_3 in a mafic dike that cuts the massive sulfide (434 level; 1807 Zone). D. Sphalerite exsolution layers in a chalcopyrite-rich remobilized massive sulfide (444 level; 1807 Zone.

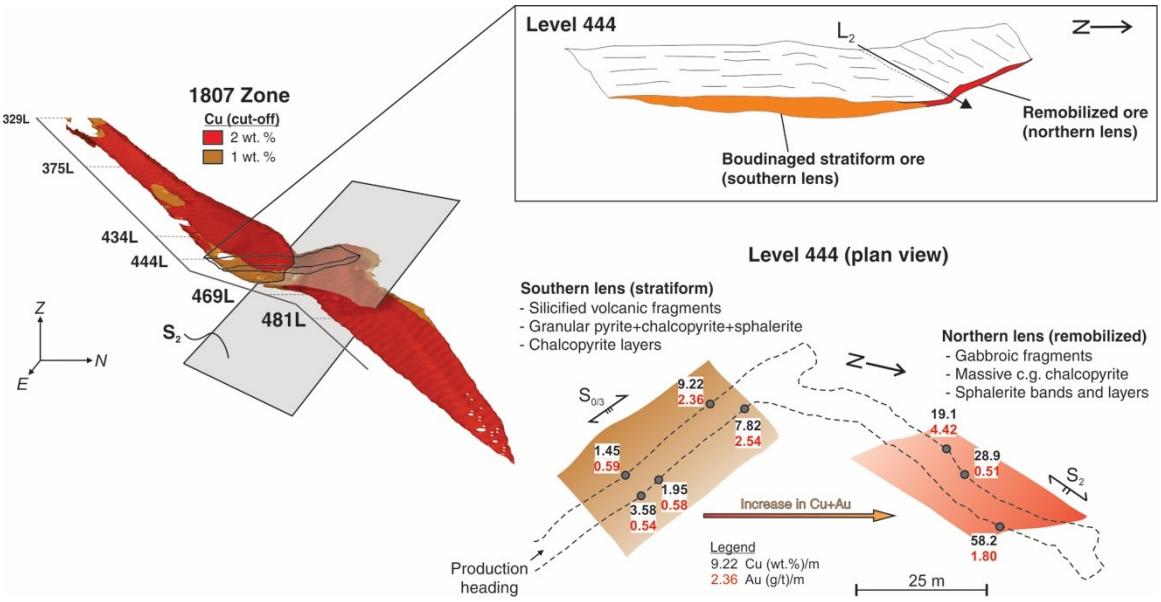

Fig. 2.19. Relationship between the D_2 thrust and the 1807 Zone orebody. The plan view map of level 444 indicates grades, compositional, and textural variations between the parent and daughter sulfide body. A significant increase in Au and Cu grades in observed in the northwest-directed remobilized sulfide lens. Sphalerite layers in the remobilized sulfides are shown in Figure 18D.

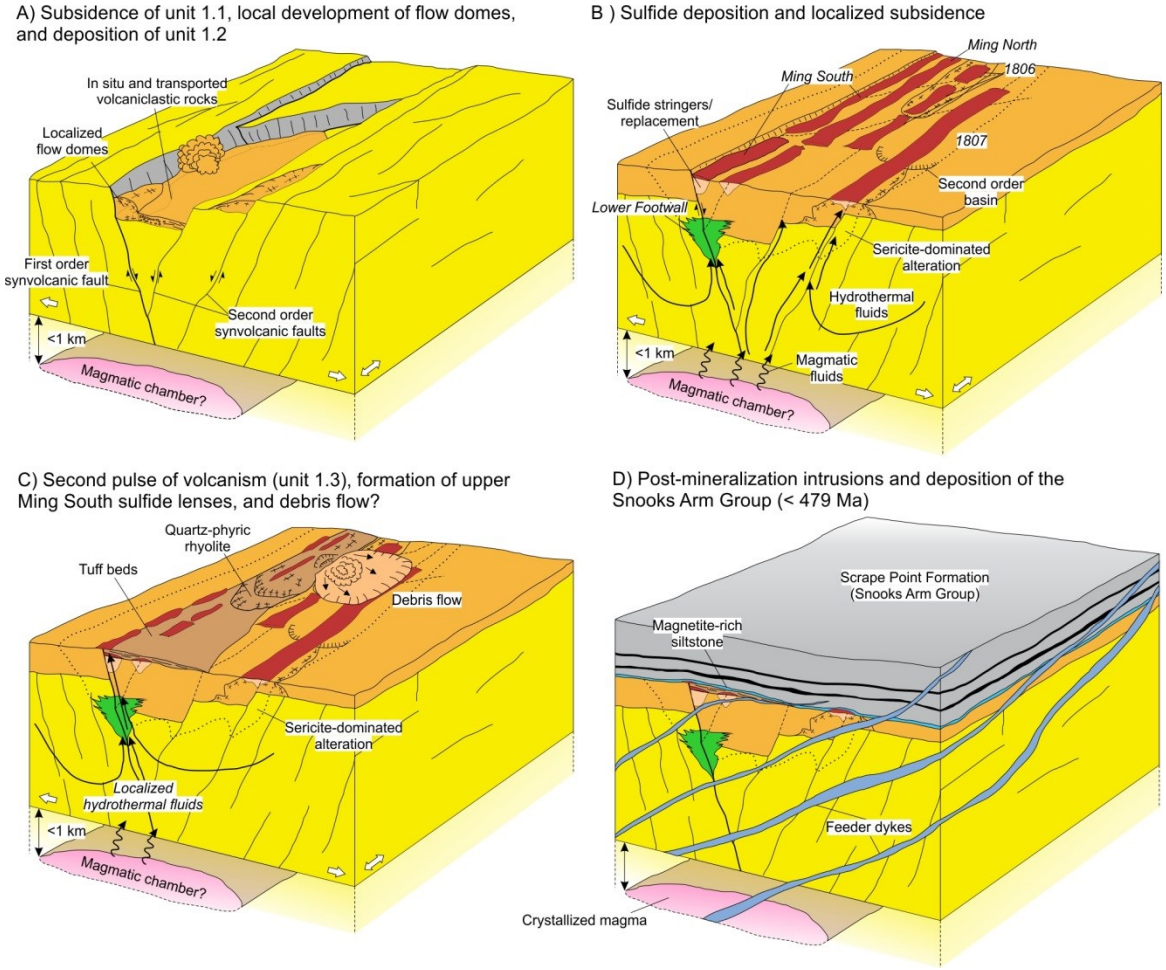

Fig. 2.20. Schematic block diagrams showing the interpreted evolution of the Ming deposit host successions. A. Collapse of the Rambler Rhyolite and eruption of nested rhyolitic domes and volcaniclastic rocks. B. Upflow of metal-rich hydrothermal fluids forming the Lower Footwall Zone and semimassive to massive sulfide lenses and associated alteration assemblages. C. Eruption of the quartz-megacrystic rhyolite and equivalent tuff beds along the reactivated first-order synvolcanic fault, forming the upper sulfide lenses in the Ming South (and North?) Zone. D. Deposition of the magnetite-rich siltstone, cross-cut by mafic to intermediate sills/dikes, possible feeders to the Snooks Arm Group volcanic and volcaniclastic rocks.

Table 2.1. Production and Geologic Resources for all Currently and Past Producing VMS Deposits in the Baie Verte oceanic tract (BVOT)

Mine/orebody	Style of mineralization	Tonnage	Cu		Zn		Ag		Au	
		[t]	[%]	[t]	[%]	[t]	[g/t]	[oz]	[g/t]	[oz]
Ming[1]										
1807 Zone	Massive stratabound (py-ccp-sph±cbn±po±apy±gn)	249,000	3.20	7,968.00	0.66	1,643.40	17.58	140,753.05	2.33	18,654.98
1806 Zone	Massive stratabound (py-ccp-sph±po±apy±gn)	250,000	0.48	1,200	0.64	1,600	15.07	121,141.48	2.96	23,794.21
Ming North[2]	Massive stratabound (py-ccp-sph)	194,000	1.87	3,627.80	0.92	1,784.80	9.60	59,884.24	1.56	9,731.19
Ming South	Massive stratabound (py-ccp-po±sph±apy±gn)	1,291,000	1.64	21,172.40	0.41	5,293.10	9.31	386,469.77	2.19	90,909.65
Lower Footwall Zone	Discordant stringers (ccp-po-py)	25,958,000	1.46	378,986.80	0.02	5,191.60	1.29	1,076,714.47	0.11	91,812.86
Total		27,942,000	1.48	412,955.00	0.06	15,512.90	1.99	1,784,963.02	0.261	234,902.89
Ming West[3]	Massive stratabound (py-ccp-po±bo±sph±ga±tet)	271,000	3.98	10,785.80	-	-	13.69	119,292.28	5.29	46,096.14
Rambler[4]	Massive stratabound (py-sph-ccp-po)	440,000	1.30	5,720	2.16	9,504.00	4.67	66,070.74	26.44[6]	374,084.89
East Rambler[4]	Disseminated stratabound (po-ccp-py)	2,130,854	1.04	22,160.88	-	-	-	-	-	-
Big Rambler Pond[4]	Disseminated (po-ccp-py)	50,000	1.20	600	-	-	-	-	-	-
Betts Cove[5]	Sub-seafloor replacement	130,682	~10	13,068.2[6]	-	-	-	-	-	-
Tilt Cove[5]	Sub-seafloor replacement	7,400,000	1.24	91,760	-	-	-	-	0.179	42,500

[1]Combined measured and indicated resources; after Rambler Metals and Mining Ltd. press release, September 2016.

[2]Down-dip extension of the mined out Ming North Zone (1972-1982)

[3]Total produced (1995-1996); after Canamera Geological Ltd. (1997)

[4]Total produced; after Tuach and Kennedy (1978)

[5]Total produced; after Strong (1984)

[6]Hand-cobbed, increasing by default production grades

Table 2.2. Stratigraphic and Volcanological Summary of the Ming Area

Stratigraphic unit	Thickness/distribution	Lithofacies/description	Inferred volcanic setting
Intusive units			
Gabbro (IN1)	Dykes to sills; ranging in thickness from ~1 m to 50 m; commonly intruding the massive sulfide, parallel to the stratigraphic contacts; in average dipping east to northeast; this unit	Consist of fine- to coarse-grained actinolite-calcite porphyroblastic gabbro	Intrusive; feeder to ophiolite cover sequence
Diorite (IN2)	Similar to IN1	Consist of medium- to coarse-grained actinolite-calcite porphyroblastic gabbro; Contains up to 5 vol. % rutile and ilmenite; IN2 is chilled against IN1; varies from coarse-grained equigranular to porphyroblastic near the margins	Intrusive; feeder to ophiolite cover sequence
Quartz monzodiorite to granodiorite (IN3)	Commonly thin (<1 m) and cross-cut the massive sulfide; dip in average to the northwest	Fine-grained equigranular quartz monzodiorite to granodiorite, locally with bluish green ferro-actinolite porphyroblasts; IN3 shows chilled margins against IN1 and IN2	Intrusive; feeder to ophiolite cover sequence
Nugget Pond horizon (Snooks Arm Group)			
Magnetite-rich siltstone (unit 3)	Base of the cover sequence; Extensive unit forming in average 10-50 cm thick sequences; locally intercalated with mafic volcanic flows (down-dip 1807 Zone)	Dark purple to black magnetite-rich siltstone with minor shale and sandstone. Predominantly consists of an epidote-magnetite-biotite-actinolite-quartz-calcite-muscovite-apatite-rutile assemblage with minor sulfides	Below storm-wave base detrital/volcanogenic sedimentary rock
Rambler Rhyolite formation			
Polymictic breccia (unit 2)	<10 m thick; 600 m x 300 m; sulfide fragments more abundant in the up-dip section of the 1807 Zone	Mafic polylithic juvenile to recycled tuff breccia. Predominantly composed of lapilli (2-64 mm) to bomb size (>64 mm) mafic fragments with minor quartz-bearing to -phyric tuffs and coherent felsic volcanic rocks; Contains up to 10 vol. % pyrite-chalcopyrite-sphalerite-rich sulfide clasts and locally up to 30 vol. % quartz-altered purple coherent felsic volcanic rocks	Subaqueous debris flow from collapse of volcanic edifice or volcanic eruption
Rambler Rhyolite (unit 1.3a)	≤10 m thick; >1 km long; <500 m wide; structurally controlled	Quartz-bearing rhyodacitic to felsic tuff beds (1-3 m thick); light to dark grey; blue to milky quartz varying, all <5 mm in diameter; host to chalcopyrite-pyrite-quartz stringers (<2 vol. % of the rock)	Extrusive, juvenile and composite components; extrusive equivalent of unit 1.3b
Rambler Rhyolite (unit 1.3b)	≤10 m thick; < 1 km long; <500 m wide; structurally controlled	Light grey to light salmon pink quartz-pyrhic to -megacrystic rhyodacite to rhyolite; Quartz phenocrysts are blue to white and together make up to 25 vol. % of the rock	Thin tabular lava flow
Rambler Rhyolite (unit 1.2)	50-150m thick; extends beyond the Ming area; individual lithofacies are ~20 m thick in average and commonly laterally structurally controlled.	Various lithofacies; predominantly volcaniclastic with juvenile massive (in situ) fragments and minor recycled fragments (e.g., epidote-altered lapilli); minor coherent felsic volcanic rocks with up to 25 vol. % quartz phenocrysts; breccia commonly host quartz-sulfide stringers; partly host to ccp-py-po sulfide stringers forming the Lower Footwall Zone	Extrusive; juvenile to recycled components; minor domal features to lava flows
Rambler Rhyolite (unit 1.1)	>1 km thick; >2 km long; >2 km wide	Coherent aphanitic to quartz-phyric (minor plagioclase-phyric) rhyodacite to rhyolite; up to 20 vol. % quartz phenocrysts; locally peperitic near the top of the unit; partly host to ccp-py-po sulfide stringers forming the Lower Footwall Zone.	Part of a larger felsic dome

Table 2.3. Summary of the Main Structural Fabrics Recognized in the Ming Deposit Area

Event	Elements	Description	Distribution	Kinematics (in respect to present coordinates)	Effects on the ore zones nature and geometry
D_1	S_1	Pervasive fabric	Domainal, preserved locally in fold hinges, and distal to massive sulfide in the altered footwall rocks	E-W shortening	Incorporation of quartz-altered fragments in massive sulfide (?); development of sphalerite bands (?)
D_2	S_2	Main schistosity, pervasive	Throughout the deposit; affects all rocks	SE-NW shortening	Overprints massive sulfide; controls the orientation of remobilization
	C_2	Shearing developed along S_2 foliation	Developed in mafic dykes and felsic rocks within and near the massive sulfide	N-NW Sinistral-oblique directed	Localizing remobilized massive sulfide along C planes; Cu-Au-enrichment along these shear planes, commonly accomodated by intruded mafic dykes
	F_2	Tight folding of boudinaged mafic dykes (e.g., levels 329, 434)	Restricted to the massive sufide	SE-NW shortening	Thickening of massive sulfides at fold hinges; Cu-Au enrichment
	L_2	Mineral and stretching lineation	Throughout the deposit; increase of intensity near the massive sulfide	L-tectonite, k>>1, moderately plunging NE axially symmetric extension	No apparent effects
	L_{int}	Intersection lineation between S_1 and S_2	Restricted to near the massive sufide	N/A	No apparent effects
D_3	S_3	Boudinaged mafic dykes	Restricted to the massive sulfide, mafic dykes, and adjacent felsic footwall rocks	N-S shortening	Boudinaged mafic dykes; Development of sulfide piercement structures
	C_{S2}	Secondary cleavage and crenulation of S_2	Restricted to the massive sulfide, mafic dykes, and adjacent felsic footwall rocks	Normal oblique strike-slip S- to SE-directed	Dismembering of the ore zones along the massive sulfide horizon
	L^{C}_{S2}	Intersection lineation of crenulation on the main schistosity S_2	Restricted to the massive sulfide, mafic dykes, and adjacent felsic footwall rocks	N/A	No apparent effects
D_4	C_4	Discrete subvertical open faults and cleavages	1807, 1806, within and near masive sulfide	N-S extension	Remobilization of chalcopyrite-rich massive sulfide along discrete subvertical cleavage cross-cutting earlier deformation fabrics

Chapter 3
Resolving the relative timing of Au-enrichment in volcanogenic massive sulfide deposits using scanning electron microscopy-mineral liberation analyzer: empirical evidence from the Ming deposit, Newfoundland, Canada

3.1. Abstract

The metamorphosed Cambro-Ordovician Ming volcanogenic massive sulfide deposit in northern Newfoundland, Canada, is locally overlain by a unit consisting of mafic to intermediate medium- to coarse-grained volcaniclastic breccia with up to 10 vol.% sulfide clasts. Analysis via mineral liberation analyzer of two sulfide clasts, completed using scanning electron microscope observations, allowed the identification of a number of microscopic and submicroscopic electrum grains. These electrum grains occur in three types of textural settings: (1) electrum grains with tellurides associated with gangue minerals; (2) inclusions of electrum with tellurides in pyrrhotite grains; and (3) free electrum grains with base metal sulfide minerals and tellurides interstitial between base metals and along cataclastic fractures in pyrite. These three textural settings are similar to those in the underlying massive sulfide orebodies that represent very likely sources to the sulfide clasts. The polylithic nature and angularity of the volcaniclastic fragments in the breccia suggest a post-mineralization gravity-controlled debris flow proximal to its source. The mineral assemblage and textures of electrum in the sulfide clasts is evidence of syngenetic and pre-deformation Au introduction in the volcanogenic massive sulfide deposit, and argues against an orogenic overprint as the cause for Au-enrichment.

3.2. Introduction

The origin of Au-enrichment in ancient Au-bearing, metamorphosed massive sulfide deposits is controversial, with some workers arguing for a syngenetic, volcanogenic massive sulfide (VMS)-related origin (Hannington et al., 1986, 1999, 2005; Hannington and Scott, 1989; Larocque et al., 1993; Herzig and Hannington, 1995; Huston, 2000; Dubé et al., 2007a; de Ronde et al., 2011), whereas other workers argue that Au-enrichment is due to a later, orogenic overprint on a pre-existing massive sulfide deposit (e.g., Tourigny et al., 1989; Marquis et al., 1990; Yeats and Groves, 1998). In many deposits, Au-bearing sulfide clasts in volcaniclastic rocks occur stratigraphically above massive sulfide orebodies (e.g., Horne: Kerr and Gibson, 1993, Doyon-Bousquet-Laronde: Dubé et al., 2007b; Mercier-Langevin et al., 2007, Mount Read Volcanics: McPhie and Gemmell, 1992). The setting of Au, the mineral associations, and textural relationships within these clasts provides important insight into the timing of Au emplacement and is central to understanding the origin of Au-enrichment. If Au is found in veins cross-cutting the clasts then it could be syngenetic and remobilized by later deformation, or due to orogenic introduction (i.e., equivocal). In contrast, if Au is found armored in sulfide clasts and has similar mineral assemblages and textures to associated massive sulfide mineralization, it provides supportive evidence for syngenetic Au introduction.

This study was undertaken to examine a well-constrained, intermediate volcaniclastic unit containing sulfide clasts that immediately overlies part of the precious metal-bearing Ming VMS deposit, northern Newfoundland, Canada. The volcaniclastic unit contains assay values of up to 0.9 g/t Au and 3.85 wt.% Cu in the 2.6 m overlying the

massive sulfide (L. Pilgrim, unpublished data, 2013); however, the setting of Au in this unit is yet unclear. Although numerous lines of evidence support a syngenetic Au mineralization at the Ming deposit from recent work exclusively on the (semi-)massive sulfide orebodies (Brueckner et al., 2014, 2016), the results of this study and the setting of Au in this clast-rich unit provide an additional test of the syngenetic versus epigenetic origin for Au-enrichment. Here we use for the first time on samples from a different unit at the Ming deposit the combination of scanning electron microscopy (SEM)-mineral liberation analysis (MLA) to identify the textural and mineralogical setting of Au-bearing minerals. This technique was used for three reasons: (1) it is an efficient technique, at relatively low cost, to examine thousands of mineral grains; (2) it provides a statistically representative analysis of the mineral composition of a sample; and (3) it allows the ability to distinguish extremely fine-grained or complexly intergown minerals at submicroscopic levels that are often very difficult to determine using conventional reflected light microscopy and SEM. The MLA observations were supported by SEM backscattered electron imaging and reflected light microscopy. The integration of field relationships with SEM-MLA, while focused on VMS deposits herein, provides a powerful tool for resolving fundamental genetic problems regardless of deposit type.

The goals of this study are: (1) the identification of Au-bearing minerals inside the sulfide clasts; (2) characterization of their textures and mineral associations; and (3) comparison with the previously studied underlying massive sulfide orebodies (Brueckner et al., 2014, 2016). These results are then utilized to provide insight into Au provenance within the clasts and to assess whether Au-enrichment was syngenetic or epigenetic.

3.3. Geologic Setting

The geology of the Ming deposit and its regional setting are well documented (Tuach and Kennedy, 1978; Hibbard; 1983; Castonguay et al., 2009; Skulski et al., 2010; Pilote and Piercey, 2013; Pilote et al., 2014, 2015), and only a brief summary will be presented here. The Ming deposit is hosted by Cambro-Ordovician (c. 487 Ma) intermediate to felsic rocks of the informally named Rambler Rhyolite formation, Baie Verte Peninsula, Newfoundland (Fig. 3.1; Hibbard, 1983; Skulski et al., 2010). The Rambler Rhyolite formation forms the upper part of the Cambro-Ordovician Pacquet Complex, which is a partial ophiolite sequence (Hibbard, 1983) of the Baie Verte oceanic tract (BVOT; van Staal, 2007). The Pacquet Complex is defined at its base by low-Ti boninites, locally cogenetic felsic tuffs and rhyodacitic flows (Hibbard, 1983; Piercey et al., 1997), and pillowed intermediate-Ti boninites (Skulski et al., 2010). The Pacquet Complex is unconformably overlain by a sequence of the early to middle Ordovician Snooks Arm Group that includes, starting at its base, magnetite-rich siltstone, tholeiitic mafic volcanic rocks, volcaniclastic and epiclastic fragmental rocks and calk-alkaline flows and fragmental rocks (Skulski et al., 2010).

The Rambler Rhyolite formation is defined by a 6 km wide and 2.5 km thick folded dome-shaped sequence of quartz-phyric rhyodacite, quartz-bearing intermediate to felsic tuff, and tuff breccia (Tuach and Kennedy, 1978; Hibbard, 1983; Skulski et al., 2010; Pilote et al., 2015). The Ming deposit, located in the upper part of the Rambler Rhyolite formation, consists of five orebodies that are hosted within variously hydrothermally altered intermediate to felsic volcanic rocks with a large portion of volcaniclastic rocks. The five orebodies are from the northwest to the southeast: 1807

Zone, 1806 Zone, Ming North, Ming South and Lower Footwall Zone (Fig. 3.2). They consist of stratabound semi-massive to massive sulfides lenses and underlying discordant sulfide stringers. The orebodies are Cu-rich, precious metal-bearing, and locally enriched in Zn. The sulfide assemblage in the orebodies is complex and is dominated by a pyrite-chalcopyrite assemblage with minor pyrrhotite-sphalerite and traces of galena-arsenopyrite±cubanite±sulfosalts±tellurides±(sulfo-)antimonides±precious metals-oxides (Brueckner et al., 2014, 2016).

Three generations of mafic to intermediate intrusive rocks are present in the deposit. They each have distinctive lithogeochemical signatures and are interpreted to be genetically related to the mafic rocks of the Snooks Arm Group cover sequence (Pilote and Piercey, 2013; Pilote et al., 2014, 2015).

3.3.1. Alteration, deformation, and metamorphism

The Rambler Rhyolite formation, host to the Ming deposit, is overprinted by Cambro-Ordovician moderate to intense hydrothermal alteration (Pilote et al., 2014, 2015). Rocks overlying the massive sulfide orebodies of the Ming deposit post-date mineralization and escaped ore-related hydrothermal alteration. Silurian-Devonian upper greenschist- to lower amphibolite-grade metamorphism affected all rocks of the Rambler Rhyolite formation and Snooks Arm Group (Gale, 1971; Tuach and Kennedy, 1978; Castonguay et al., 2009, 2014), including at least four phases of regional deformation (D_1 to D_4), with D_2 (and M_2) being the most intense (Tuach and Kennedy, 1978; Hibbard, 1983; Castonguay et al., 2009, 2014). Late syn- to post-D_2 biotite, epidote, actinolite, carbonate, and sulfides porphyroblasts overprints structural fabrics defined by various

assemblages predominantly composed of quartz-sericite-chlorite-epidote-sulfides, observed within and outside the deposit (Gale, 1971; Tach and Kennedy, 1978).

3.3.2. Geology of diamond drill hole RMUG13-205

Sulfide clasts described in this study are found in diamond drill hole RMUG13-205, which was drilled in the up-plunge section of the 1807 Zone as part of an underground definition drilling program (Fig. 3.2). The thickness for each unit reported here is core length and a stratigraphic column is shown in Figure 3.3. The hole intersects a 3.5 m thick semi-massive to massive sulfide horizon with significant Cu, Ag, and Au contents (11.7 wt% Cu, 17.6 g/t Ag, and 2.7 g/t Au over 0.45 m; Rambler Metals and Mining Ltd.), and is an ideal drill hole to test the source of Au in the clasts given the elevated Au grades.

Composition and texture of the sulfides within the (semi-)massive sulfide horizon vary from medium-grained equigranular pyrite to coarse-grained, subrounded pyrite supported by a chalcopyrite- and galena-bearing matrix (Fig. 3.4a). The sulfide horizon contains up to 10 vol % intermediate volcanic rock fragments that are quartz altered (Fig. 3.4b). The stratigraphy immediately below the (semi-)massive sulfide horizon is cut by a 6.5 m thick dark green, chlorite-carbonate altered, fine-grained gabbroic dyke separating the intermediate volcanic rocks from the sulfides. Two intervals of sulfide veins are enclosed within the gabbro with contacts at moderate angle to core axis. A similar mafic dike is repeated at depth. The two dikes enclose a 3.5 m thick section of fine-grained actinolite-chlorite altered, intermediate coherent volcanic rock. Both dikes show chilled margins with the volcanic rock and sulfides.

The (semi-)massive sulfide horizon is immediately overlain by a 10 m thick unit of polymictic breccia of mafic to intermediate composition. This unit contains clasts of different compositions including sulfide-bearing clasts and dark purple to medium grey quartz and quartz-sericite hydrothermally altered coherent rhyodacite clasts (Figs. 3.4c and d). The sulfide clasts locally make up to 10 vol.% of the rock, whereas the rhyodacitic clasts make up to 30 vol.%. The majority of the sulfide and silicate clasts are subrounded to subangular, vary in size (≤5 cm), and stretched co-axial to the main stretching lineation related to D_2. The matrix of the breccia is fine to medium grained, foliated, and is composed of an assemblage of recrystallized quartz-plagioclase-epidote-chlorite, with biotite grains forming post-kinematic porphyroblasts, commonly overprinting chlorite (Fig. 3.4e). The biotite porphyroblasts are related to younger Silurian-Devonian (or younger) regional metamorphism. Late quartz-epidote veins with traces of sulfide minerals cut the rock and are transposed into the dominant foliation (Fig. 3.5a). These post-mineralization but pre-deformation veins are also found cross-cutting the underlying massive sulfide orebodies, the felsic footwall rocks, and the mafic dikes and only locally contain traces of pyrite and chalcopyrite (Pilote and Piercey, 2013; Pilote et al., 2014). Gold and Te-bearing minerals have not been found within these veins.

The volcaniclastic unit is overlain by a thin (≤ 1 m), dark purple to black, magnetite-rich siltstone (Fig. 3.4f). This sedimentary horizon represents the base of the Snooks Arm Group and can be traced throughout the deposit (Skulski et al., 2010; Pilote et al., 2015).

3.4. Methodology and sampling

Sulfide clasts (samples 205-2 and 205-3) were extracted from the volcaniclastic unit in RMUG13-205 (Figs. 3.5a and b). The clast samples were collected from drill core, 8.4 m and 9.0 m above the upper part of the (semi-)massive sulfide zone. A chip from sample 205-2 was cut parallel to the elongation of the clast, whereas 205-3 was cut perpendicular to the elongation. The chips were then mounted in 40 mm diameter resin rounds to obtain a maximum surface area for analysis, followed by polishing and the application of a carbon coating. The MLA measurements were made on a FEI MLA 650 field emission gun (FEG) SEM instrument at the CREAIT Centre, Memorial University. Operating conditions included an accelerating voltage of 15 kV and an imaging scan speed of 8 μsec. The use of 15 kV allows for a better resolution during analyses and for imaging on grains of small dimensions (≤5 μm). The mounds were measured in extended backscattered electron (XBSE) mode using a beam current of 10 nA and a spot size of 5.77. X-ray analyses were triggered for a BSE range of 125-255; each X-ray measurement was acquired for 10 msec on a 0.5 x 0.5 mm frame with a resolution of 1000 dpi. Data reduction was performed on MLA Data View (FEI) software version 3.1.4.683.

3.5. Sulfide mineralogy and mineral textures of the sulfide clasts

3.5.1. Sulfide mineralogy

The clasts are composed of a pyrite > chalcopyrite > sphalerite > quartz ≈ biotite assemblage that makes up more than 99.9 wt% of the samples (Fig. 3.6). The remaining percentage consists of an assemblage of tellurides (coloradoite, hessite, and Bi-telluride),

sulfides (arsenopyrite, galena, and pyrrhotite), oxides (cassiterite and hematite), and precious metals (mercurian electrum). The wide range of trace mineral phases identified in both samples with MLA underlines the complex ore mineralogy in the sulfide clasts. Table 3.1 shows results of MLA with values normalized to the abundance of the aforementioned list of trace minerals to emphasize their relative abundances. Gold-bearing minerals were identified with MLA as minerals with > 10 wt.% Au. Brueckner et al. (2014, 2016) showed that Au occurs predominantly as electrum(±Hg) at the Ming deposit orebodies. Although the relative abundances of Ag, Au, and Hg in electrum vary (Brueckner et al., 2016), distinctions between the different Au-bearing alloys in the clasts are difficult to make using MLA due to the semi-quantitative detection and the small size of the analyzed grains. Hence, the term electrum is used in this paper for all Au-bearing phases that have > 10 wt.% Au.

3.5.2. Precious metal textures

Textures of electrum in the sulfide clasts can be divided into: (1) inclusions of electrum and telluride grains within gangue minerals (Fig. 3.7a); (2) inclusions of electrum in association with telluride in pyrrhotite (Fig. 3.7b); and (3) free electrum grains with base metal sulfides and tellurides interstitial between base metal sulphides and along cataclastic fractures in pyrite (Figs. 3.7c and d).

The first texture is characterized by the contact of electrum with gangue phases (quartz, biotite, chlorite, epidote, albite and white micas) where quartz is the predominant gangue mineral in contact with electrum (Fig. 3.7a). The silicified horizon capping and the stringer zone underlying the 1806 Zone also show this type of precious metal texture

(Figs. 3.8a, b; Brueckner et al., 2014, 2016). However, within the sulfide clasts, electrum is also in contact with epidote. Moreover, hessite and Bi-telluride, and fine-grained chalcopyrite are proximal to electrum in the hosting gangue mineral assemblage of the clasts. The origin of this texture is unclear and is either attributed to syngenetic deposition or internal remobilization during Silurian-Devonian deformation and metamorphism (Brueckner et al., 2016). Although uncommon, epidote is also found as a gangue mineral, together with quartz, muscovite, and carbonate minerals in the 1807 massive sulfide orebody (Figs. 3.8c, d)

In the second texture, electrum occurs with hessite in pyrrhotite (Fig. 3.7b). This texture is the most common precious metal texture in the observed sulfide clasts. Electrum occurs either as single grains or is intergown in pyrrhotite. In the 1806 and 1807 zones, electrum inclusions within pyrrhotite are accompanied by arsenopyrite and (sulfo-)antimonides, respectively (Fig. 3.8e; Brueckner et al., 2014, 2016). The origin of these inclusions is unclear and may be the result of late syngenetic decomposition (Dobbe et al., 1991) or (metamorphic) internal replacement (Cook, 1996).

The last precious metal texture observed in the sulfide clasts of the hanging wall of the 1807 Zone is also observed in the underlying orebodies (Fig. 3.8f). The occurrence of precious metals interstitially between (recrystallized) base metal sulfides and/or along cataclastic fractures in pyrite (Fig. 3.7c) is the product of internal remobilization/metamorphic liberation of previously syngenetically deposited precious metal phases during Silurian-Devonian metamorphism (Laroque et al., 1993; Wagner et al., 2007; Brueckner et al., 2014; 2016).

3.6. Discussion

Volcaniclastic rocks locally overlying the Ming VMS deposit are enriched in Au and provide insight into the origin of Au-enrichment in this deposit. Two main models have been invoked for Au-enrichment in VMS deposits: syngenetic (e.g., Hannington et al., 2005) and epigenetic (e.g., Evans, 1999). In the clast-rich unit, mineral assemblages and ore textures involving electrum provide key information required to test the syngenetic versus epigenetic origin of Au-enrichment.

First, the distribution of electrum and closely associated minerals (e.g., tellurides) in the volcaniclastic unit are confined to the sulfide clasts. This is shown in sample 205-2 where an MLA scan was done beyond the extent of the sulfide clast, into the host breccia and a cross-cutting quartz-carbonate vein (Fig. 3.6b). The input of precious metals from an external source such as an epigenetic style of Au-enrichment (e.g., orogenic) would typically result in the deposition of Au within structurally controlled veins and/or fabrics, commonly discordant to and/or associated with carbonate alteration (Dubé and Gosselin, 2007). However, the clasts and their surrounding within the 10 m volcaniclastic unit show no evidence of such features. The presence of electrum exclusively within the clasts and the absence of an overprint of ore forming fluid-related alteration is, therefore, direct evidence for Au-enrichment prior to the deposition of the volcaniclastic unit.

In Table 3.2, precious metal textures observed in sulfide clasts and (semi-)massive sulfides of the Ming deposit are compared. Although there are minor differences, the majority of textures and assemblages found in the clasts are remarkably similar to the (semi-)massive sulfide ores (Fig. 3.8). Furthermore, the hydrothermally altered rhyodacitic clasts exhibit similar alteration as the underlying footwall rhyodacitic host

rocks, together with the sulfide clasts that are spatially restricted and proximal to massive sulfide mineralization, suggest a provenance from the immediately underlying host assemblage and mineralization, respectively. Collectively, the above results support a syngenetic, rather than an epigenetic origin for precious metal-enrichment at Ming.

3.6.1. Au-Te association

The presence of tellurides in VMS deposits is generally uncommon, nevertheless, the presence of Te-bearing minerals in close textural association with Au-bearing minerals has been recorded in some metamorphosed VMS deposits (e.g., Abitibi, Egypt, Urals; see Table A3.1). Telluride co-existence with native gold/electrum, and the possible processes of transport and deposition, have also be documented in modern hydrothermal systems in volcanic arcs and back-arc basins (Watanabe and Kajiruma, 1994; Moss and Scott, 2001; Hannington et al. 2005), and some well-preserved ancient unmetamorphosed VMS deposits (Maslennikova et al., 2008; Maslennikov et al., 2009). Tellurium in VMS deposits is likely to be of magmatic origin as it is commonly mineralogically and chemically associated with other magmatophile volatiles (e.g., Bi, Tl, Sn, Se), and less likely from the hydrothermal leaching of the host rocks (Patten et al., 2015). Tellurium is predominantly transported in the vapor phase (Afifi et al., 1988; Grundler et al., 2013), but the transport as minor aqueous species can also occur, but is rarer (Zhang and Spry, 1994; McPhail, 1995). Transport conditions of Te in VMS deposits occurs in a wide range of temperatures (Maslennikov et al., 2009), and typically in reduced fluids with a high fTe_2/fS_2 (Affifi et al, 1988; Zhang and Spry, 1994). Decrease of the ratio, increase in fO_2, and/or decrease of temperature due to conductive cooling and/or seawater mixing

leads to the precipitation of telluride minerals and/or substitution of S^{2-} by Te^{2-} in other minerals (e.g., galena and arsenopyrite; Afifi et al., 1988; Zhang and Spry, 1994; Brueckner et al., 2016). Syngenetic co-precipitation of Au and Te is suggested in some metamorphosed and unmetamorphosed VMS deposits of the Urals as illustrated by the elevated Au contents (up to 5.2 wt % Au) in telluride minerals (Vikentyev, 2006).

The intimate relationship between Au and Te at the Ming deposit is demonstrated by the close spatial association between electrum and tellurides such as hessite and Bi-telluride. Much like electrum, the tellurides are restricted to the sulfide clasts and the underlying (semi-)massive sulfide orebodies (Brueckner et al., 2014, 2016). Moreover, orogenic Au deposits hosted in the Snooks Arm Group that occur 10 to 20 km north of the Ming deposit have distinct ore mineralogy and associated alteration mineral assemblages (e.g., Fe-carbonate, albite, and leucoxene alteration; Evans, 1999; Ramezani, 2000), which are absent at the Ming deposit (Brueckner et al., 2014; Pilote et al., 2015). In particular, the syn-deformation quartz-carbonate veins hosting native Au in the orogenic Au deposits are devoid of tellurides (Copeland et al., 2015), and formed at higher temperatures (480°C>T>250°C; Ramezani et al., 2000) than the hydrothermal fluids that precipitated electrum (T ≈ 260-300°C) and tellurides (<260°C) in the Ming deposit (Brueckner et al., 2016). Although the Ming deposit was affected by extensive deformation and upper greenschist-lower amphibolite metamorphism, the tellurides and electrum reside in the orebodies and sulfide clasts, are spatially associated with one another, and exhibit no evidence of post-mineralization enrichment (Brueckner et al., 2016). Therefore, a syngenetic Au-Te enrichment of the Ming VMS deposit is proposed.

3.6.2. Genetic implications

The polylithic nature and angularity of the volcaniclastic fragments in the breccia are suggestive of a post-mineralization gravity-controlled debris flow rather than a pyroclastic flow (Fig. 3.9; McPhie et al., 1993). It is difficult to determine the specific cause of this flow but considering: (1) the formation of nearby intermediate to rhyolitic dome(s) and synchronous mafic volcanic rocks based on the current understanding of the regional geologic setting (Castonguay et al., 2009; Skulski et al., 2010), (2) volcanic architectural reconstruction of the deposit (Pilote et al., 2015), and (3) the complex paleoseafloor topography in this type of environment (Ross and Mercier-Langevin, 2014), collapse of at least part of the marginal domal edifice may have triggered mass flow of volcanic debris. During this process, the sulfide clasts were derived from the underlying (semi-)massive sulfides along its flow path and incorporated into the volcaniclastic unit (Fig. 3.9). The sulfide clasts are relatively small (≤5 cm across) compared to sulfide-rich debris flows overlying other VMS deposits (e.g., Bousquet-Laronde; Dubé et al., 2007b, Mercier-Langevin, 2007), and one could argue that with permissive dynamic properties of the host mass flow, small size fragments, including the sulfide clasts, can travel substantial distances (i.e., kilometers) (McPhie et al., 1993). However, the sulfide-rich breccia is restricted to the 1806 and 1807 zones of the deposit; hence, supporting proximal deposition rather than distal. The presence of associated altered volcaniclastic fragments (mostly silicified; Fig. 3.4d) in this unit is also an indication of the proximity of the source. Moreover, owing to textural resemblance of the electrum grains and associated minerals with textures observed in the underlying orebodies, it is extremely likely that the sulfides originated from the 1806 and/or 1807 zones.

Despite the pervasive and multistage deformation that affected rocks in and associated with the Ming deposit (Castonguay et al., 2009; Pilote et al., 2014), and the presence of pre- to post-deformation quartz-epidote-bearing veins cutting the volcaniclastic unit, electrum is restricted to the sulfide clasts. The mineral associations and textural characteristics of electrum are in agreement with the genetic model of Brueckner et al. (2014, 2016) in which precious metals were introduced into the hydrothermal system and deposited syngenetically to form the Ming VMS deposit.

3.6.3. The application of MLA

The application of MLA allowed answering the fundamental questions outlined in this study in a relatively short analytical time frame (~20 hours) and significantly minimized the potential for operator bias and human error (e.g., overlooking the presence or underestimating the amount of micro-scale precious-metal grains due to grain size), and at a much higher resolution compared to common petrographic or exploratory SEM methods (Sylvester, 2012). Although, the application of MLA is often focused in applied mineralogy and metallurgical processes (Fandrich et al., 2007; Ford et al., 2011; Kelvin et al., 2011), heavy mineral provenance in sediments and sedimentary rocks (Lowe et al., 2011; Tsikouras et al., 2011), and till and stream sediment prospecting (Wilton and Winter, 2012), it can be a strategic tool when used with basic geological, stratigraphic, mineralogical, and alteration observations, to solve genetic problems in the study of metallic mineral deposits.

3.7. Conclusions

The use of SEM-MLA on natural samples has shown to be an effective analytical method in detecting a range of submicroscopic minerals, such as electrum. Hence, we were able to identify all the electrum grains (≥ 0.5 μm in size) present on cut surfaces of sulfide-bearing clasts that are part of a volcaniclastic unit, immediately overlying the Cambro-Ordovician Ming VMS deposit. The SEM-MLA results show that electrum is restricted to the sulfide clasts and share similar textural characteristics and mineral associations with the underlying 1806 and 1807 massive sulfide orebodies. The presence of electrum in the sulfide clasts with textural and assemblage features identical to underlying massive sulfide mineralization is evidence for syngenetic and pre-deformation Au-enrichment in the VMS deposit. The results herein also illustrate how SEM-MLA can be a useful tool to provide information to answer genetic questions on how mineral deposits form.

3.8. Acknowledgements

This research has been financially supported by a Natural Sciences and Engineering Research Council of Canada (NSERC) Discovery Grant, by the NSERC-Altius Industrial Research Chair in Mineral Deposits supported by NSERC, Altius Resources Inc., and by the Research and Development Corporation of Newfoundland and Labrador. We sincerely thank Rambler Metals and Mining PLC for drill core access and logistical support during the project. Editorial and scientific review by P. Spry and D. Huston greatly helped improving the manuscript.

3.9. References

Afifi, A. M., Kelly, W. C., and Essene, E. J., 1988, Phase relations among tellurides, sulfides, and oxides: Part II. Applications to telluride-bearing ore deposits: Economic Geology, v. 83, p. 395-404.

Brueckner, S. M., Piercey, S. J., Sylvester, P. J., Maloney, S., and Pilgrim, L., 2014, Evidence for syngenetic precious metal enrichment in an Appalachian volcanogenic massive sulfide system: The 1806 Zone, Ming mine, Newfoundland, Canada: Economic Geology, v. 109, p. 1611-1642.

Brueckner, S., Piercey, S., Pilote, J.-L., Layne, G., and Sylvester, P., 2016, Mineralogy and mineral chemistry of the metamorphosed and precious metal-bearing Ming deposit, Canada. Ore Geology Reviews, v. 72, p. 914-939.

Castonguay, S., Skulski, T., van Staal, C., and Currie, M., 2009, New insights on the structural geology of the Pacquet Harbour group and Point Rousse complex, Baie Verte peninsula, Newfoundland: Current Research Newfoundland and Labrador Department of Natural Resources, Geological Survey, v. Report 09-1, p. 147-158.

Castonguay, S., van Staal, C. R., Joyce, N., Skulski, T., and Hibbard, J. P., 2014, Taconic Metamorphism Preserved in the Baie Verte Peninsula, Newfoundland Appalachians: Geochronological Evidence for Ophiolite Obduction and Subduction and Exhumation of the Leading Edge of the Laurentian (Humber) Margin During Closure of the Taconic Seaway: Geoscience Canada, v. 41, p. 459-482.

Cook, N. L., 1996, Mineralogy of the sulphide deposits at Sulitjelma, northern Norway. Ore Geology Reviews, v. 11, p. 303-338.

Copeland, D., Pitman, C., Evans, D.T.W., McNeill, P., and Slepcev, G., 2015, NI 43-101 Technical report, mineral resource and mineral reserve update on the Pine Cove mine and mineral resource estimate on the Stog'er Tight deposit, Point Rousse project, Baie Verte, Newfoundland and Labrador, Canada. Anaconda Mining Inc.

de Ronde, C.E.J., Massoth, G., Butterfield, D.A., Christenson, B.W., Ishibashi, J., Ditchburn, R.G., Hannington, M.D., Brathwaite, R.L., Lupton, J.E., Kamenetsky, V.S., Graham, I.J., Zellmer, G.F., Dziak, R.P., Embley, R.W., Dekov, V.M.,

Munnik, F., Lahr, J., Evans, L.J., and Takai, K., 2011, Submarine hydrothermal activity and gold-rich mineralization at Brothers Volcano, Kermadec arc, New Zealand: Mineralium Deposita, v. 46, p. 541-584.

Dobbe, R. T. M., 1991, Ullmanite, cobaltian ullmanite and willyamite from Tunaberg, Bergslagen, central Sweden. Canadian Mineralogist, v. 29,199-205.

Dubé, B., and Gosselin, P., 2007, Greenstone-hosted quartz-carbonate vein deposits, *in* Goodfellow, W. D., ed., Mineral deposits of Canada: A synthesis of major deposit-Types, district metallogeny, the evolution of geological provinces, and exploration methods, Special Publication No. 5, Geological Association of Canada, Mineral Deposits Division, p. 49-73.

Dubé, B., Gosselin, P., Mercier-Langevin, P., Hannington, M., and Galley, A., 2007a, Gold-rich volcanogenic massive sulphide deposits, *in* Goodfellow, W. D., ed., Mineral deposits of Canada: A synthesis of major deposit-types, district metallogeny, the evolution of geological provinces, and exploration methods, Special Publication No. 5, Geological Association of Canada, Mineral Deposits Division, p. 75-94.

Dubé, B., Mercier-Langevin, P., Hannington, M., Lafrance, B., Gosselin, G., and Gosselin, P., 2007b, The LaRonde Penna world-class Au-rich volcanogenic massive sulfide deposit, Abitibi, Quebec: mineralogy and geochemistry of alteration and implications for genesis and exploration: Economic Geology, v. 102, p. 633-666.

Evans, D. T. W., 1999, Epigenetic gold mineralization, Baie Verte Peninsula, Newfoundland: Current Research, Newfoundland Department of Mines and Energy, Geological Survey, Report 99-1, p. 163-182.

Fandrich, R., Gu, Y., Burrows, D., and Moeller, K., 2007, Modern SEM-based mineral liberation analysis: International Journal of Mineral Processing, v. 84, p. 310-320.

Ford, F. D., Wercholaz, C. R., and Lee, A., 2011, Predicting process outcomes for Sudbury platinum-group minerals using grade-recovery modeling from mineral liberation analyzer (MLA) data: Canadian Mineralogist, v. 49, p. 1627-1642.

Gale, G.H., 1971, An investigation of some sulphide deposits in the Rambler area, Newfoundland: Unpublished Ph.D. thesis, University of Durham, 137 p.

Grundler, P.V., Brugger, J., Etschmann, B., Helm, L., Liu, W., Spry, P.G., Tian, Y., Testemale, D., and Pring, A., 2013, Speciation of aqueous tellurium (IV) in hydrothermal solutions and vapors and the role of oxidized tellurium species in gold metallogenesis: Geochimica et Cosmochimica Acta, v. 120, p. 298-325.

Hannington, M.D., and Scott, S.D., 1989, Gold mineralization in volcanogenic massive sulfides: implications of data from active hydrothermal vents on the modern sea floor: Economic Geology Monograph 6, p. 491-507.

Hannington, M.D., Peter, J.M., and Scott, S.D., 1986, Gold in sea-floor polymetallic sulfides: Economic Geology, v. 81, p. 1867-1883.

Hannington, M.D., Poulsen, K.H., Thompson, J.F.H., Sillitoe, R.H., 1999, Volcanogenic gold in the massive sulfide environment: Reviews in Economic Geology 8, p. 325-356.

Hannington, M.D., de Ronde, C.E.J., and Petersen, S., 2005, Sea-floor tectonics and submarine hydrothermal systems: Economic Geology 100th anniversary volume, p. 111-141.

Herzig, P.M., and Hannington, M.D., 1995, Polymetallic massive sulfides at the modern seafloor – A review: Ore Geology Reviews, v. 10, p. 95-115.

Hibbard, L. J., 1983, Geology of the Baie Verte Peninsula, Newfoundland: Department of Mines and Energy, Government of Newfoundland and Labrador, Memoir 2, 279 p.

Huston, D.L., 2000, Gold in volcanic-hosted massive sulfide deposits: distribution, genesis and exploration: Reviews in Economic Geology 13, p. 401-426.

Kelvin, M. A., Sylvester, P. J., and Cabri, L. J., 2011, Mineralogy of rare occurrences of precious-metal-enriched massive sulfide in the Voisey's Bay Ni-Cu-Co ovoid deposit, Labrador, Canada: Canadian Mineralogist, v. 49, p. 1505-1522.

Kerr, D. J., and Gibson, H. L., 1993, A comparison of the Horne volcanogenic massive sulfide deposit and intracauldron deposits of the mine sequence; Noranda, Quebec: Economic Geology, v. 88, p. 1419-1442.

Larocque, A. C. L., Hodgson, C. J., and Lafleur, P.-J., 1993, Gold distribution in the Mobrun volcanic-associated massive sulfide deposit, Noranda, Quebec: A

preliminary evaluation of the role of metamorphic remobilization: Economic Geology, v. 88, p. 1443-1459.

Lowe, D. G., Sylvester, P. J., and Enachescu, M. E., 2011, Provenance and paleodrainage patterns of Upper Jurassic and Lower Cretaceous synrift sandstones in the Flemish Pass Basin, offshore Newfoundland, east coast of Canada: AAPG Bulletin, v. 95, p. 1295-1320.

Marquis, P., Hubert, C., Brown, A.C., and Rigg, D.M., 1990, Overprinting of early, redistributed Fe and Pb-Zn mineralization by late-stage Au-Ag-Cu deposition at the Dumagami mine, Bousquet district, Abitibi, Quebec: Canadian Journal of Earth Sciences, v. 27, p. 1651–1671.

Maslennikov, V. V., Maslennikova, S. P., Large, R. R., and Danyushevky, L. V., 2009, Study of trace element zonation in vent chimneys from the Silurian Yaman-Kasy volcanic-hosted massive sulfide deposit (southern Urals, Russia) using laser ablation-inductively coupled plasma mass spectrometry (LA-ICPMS): Economic Geology, v. 104, p. 1111-1141.

Maslennikova, S., Maslennikov, V., and Herrington, R., 2008, Tellurium-bearing mineralization in Paleozoic black smokers: Abstract, 33rd International Geological Congress.

McPhail, D. C., 1995, Thermodynamic properties of aqueous tellurium species between 25 and 350ºC: Geochimica et Cosmochimica Acta, v. 59, p. 851-866

McPhie, J., and Gemmell, J. B., 1992, Mount Read Volcanics: Host sequence to Cambrian massive sulphide deposits in western Tasmania: Bulletin of the Geological Survey of Tasmania, v. 70, p. 161-166.

McPhie, J., Doyle, M., and Allen, R., 1993, Volcanic textures. A guide to the interpretation of textures in volcanic rocks: Hobart, Tasmania, Centre for Ore Deposit Research, University of Tasmania, Hobart, 198 p.

Mercier-Langevin, P., Dubé, B., Hannington, M. D., Davis, D. W., Lafrance, B., and Gosselin, G., 2007, The LaRonde Penna Au-rich volcanogenic massive sulfide deposit, Abitibi greenstone belt, Quebec: Part I. Geology and geochronology: Economic Geology, v. 102, p. 585-609.

Moss, R., and Scott, S. D., 2001, Geochemistry and mineralogy of gold-rich hydrothermal precipitates from the eastern Manus Basin, Papua New Guinea: Canadian Mineralogist, v. 39, p. 957-978.

Patten, C. G. C., Pitcairn, I. K., Teagle, D. A. H., and Harris, M., 2015, Mobility of Au and related elements during the hydrothermal alteration of the oceanic crust: implications for the sources of metals in VMS deposits: Mineralium Deposita, v. 51, p. 179-200.

Piercey, S. J., Jenner, G. A., and Wilton, D. H. C., 1997, The stratigraphy and geochemistry of the southern Pacquet Harbour Group, Baie Verte peninsula, Newfoundland; implications for mineral exploration: Canada, Government of Newfoundland and Labrador. Geological Survey: St. John's, NL, Canada, p. 119-139.

Pilote, J.-L., and Piercey, S.J., 2013, Volcanostratigraphy of the 1807 Zone of the Ming Cu-Au volcanogenic massive-sulphide deposit, Baie Verte Peninsula, northern Newfoundland: Geological Survey of Canada, Current Research 2013-20, 13 p..

Pilote, J.-L., Piercey, S.J., and Mercier-Langevin, P., 2014, Stratigraphy and hydrothermal alteration of the Ming Cu-Au volcanogenic massive-sulphide deposit, Baie Verte Peninsula, Newfoundland: Geological Survey of Canada, Current Research 2014-7, 18 p.

Pilote, J.-L., Piercey, S.J., and Mercier-Langevin, P., 2015, Volcanic architecture and alteration assemblages of the Ming Cu-Au-(Zn-Ag) VMS deposit, Baie Verte, Newfoundland: Implications for Au-enrichment processes and exploration, *in* Peter J.M., and Mercier-Langevin, P. eds., Targeted geoscience initiative 4: Contributions to the understanding of volcanogenic massive sulphide deposit genesis and exploration methods development: Geological Survey of Canada, Open File 7853, p. 197–210.

Ramezani, J., Dunning, G. R., and Wilson, M. R., 2000, Geologic setting, geochemistry of alteration, and U-Pb age of hydrothermal zircon from the Silurian Stog'er Tight gold prospect, Newfoundland Appalachians, Canada: Exploration and Mining Geology, v. 9, p. 171-188.

Ross, P.-S., and Mercier-Langevin, P., 2014, Igneous Rock Associations 14. The Volcanic Setting of VMS and SMS Deposits: A Review: Geoscience Canada, v. 41, p. 13.

Skulski, T., Castonguay, S., McNicoll, V., van Staal, C., Kidd, W., Rogers, N., Morris, W., Ugalde, H., Slavinski, H., Spicer, W., Moussallam, Y., and Kerr, I., 2010, Tectonostratigraphy of the Baie Verte oceanic tract and its ophiolite cover sequence on the Baie Verte Peninsula: Current Research Newfoundland and Labrador Department of Natural Resources, Geological Survey, v. Report 10-1, p. 315-335.

Sylvester, P.J., 2012, Use of the mineral liberation analyzer (MLA) for mineralogical studies of sediments and sedimentary rocks*, in* Sylvester, P., ed., Quantitative mineralogy and microanalysis of sediments and sedimentary rocks: Mineralogical Association of Canada Short Course 42, St. John's, Newfoundland and Labrador, May 2012, p. 1-16.

Tourigny, G., Brown, A.C., Hubert, C., and Crepeau, R., 1989, Synvolcanic and syntectonic gold mineralization at the Bousquet mine, Abitibi greenstone belt: Economic Geology, v. 84, p. 1875–1890.

Tourigny, G., Doucet, D., and Bourget, A., 1993, Geology of the Bousquet 2: An example of a deformed, gold-bearing, polymetallic sulfide deposit: Economic Geology, v. 88, p. 1578–1597.

Tsikouras, B., Pe-Piper, G., Piper, D. J. W., and Schaffer, M., 2011, Varietal heavy mineral analysis of sediment provenance, Lower Cretaceous Scotian Basin, eastern Canada: Sedimentary Geology, v. 237, p. 150-165.

Tuach, J., and Kennedy, M. J., 1978, The geologic setting of the Ming and other sulfide deposits, consolidated Rambler mines, northeast Newfoundland: Economic Geology, v. 73, p. 192-206.

van Staal, C. R., 2007, Pre-Carboniferous tectonic evolution and metallogeny of the Canadian Appalachians, *in* Goodfellow, W. D., ed., Mineral deposits of Canada: A synthesis of major deposit-types, district metallogeny, the evolution of geological provinces, and exploration methods: Geological Association of Canada, Mineral Deposits Division, Special Publication No. 5, p. 793-818.

Vikentyev, I. V., 2006, Precious metal and telluride mineralogy of large volcanic-hosted massive sulfide deposits in the Urals: Mineralogy and Petrology, v. 87, p. 305-326.

Wagner, T., Klemd, R., Wenzel, T., and Mattsson, B., 2007, Direct evidence from laser-ablation–inductively coupled plasma–mass spectrometry analysis of invisible gold: Geology, v. 35, p. 775-778.

Watanabe, K., and Kajimura, T., 1994, The hydrothermal mineralization at Suiyo Seamount, Izu-Ogasawara arc: Resource Geology, v. 44, p. 133-140.

Wilton, D.H.C. and Winter, L., 2012, SEM-MLA (Scanning Electron Microscope – Mineral Liberation Analyser) research on indicator minerals in till and stream sediments – An example from the exploration for awaruite in Newfoundland and Labrador, *in* Sylvester, P., ed., Quantitative mineralogy and microanalysis of sediments and sedimentary rocks: Mineralogical Association of Canada Short Course 42, St. John's, Newfoundland and Labrador, May 2012, p. 265-283.

Yeats, C.J., and Groves, D.I., 1998, The Archean Mount Gibson gold deposits, Yilgarn craton, Western Australia: Products of combined synvolcanic and syntectonic alteration and mineralisation: Ore Geology Reviews, v. 13, p. 103–129.

Zhang, X., and Spry, P. G., 1994, Calculated stability of aqueous tellurium species, calaverite, and hessite at elevated temperatures: Economic Geology, v. 89, p. 1152-1166.

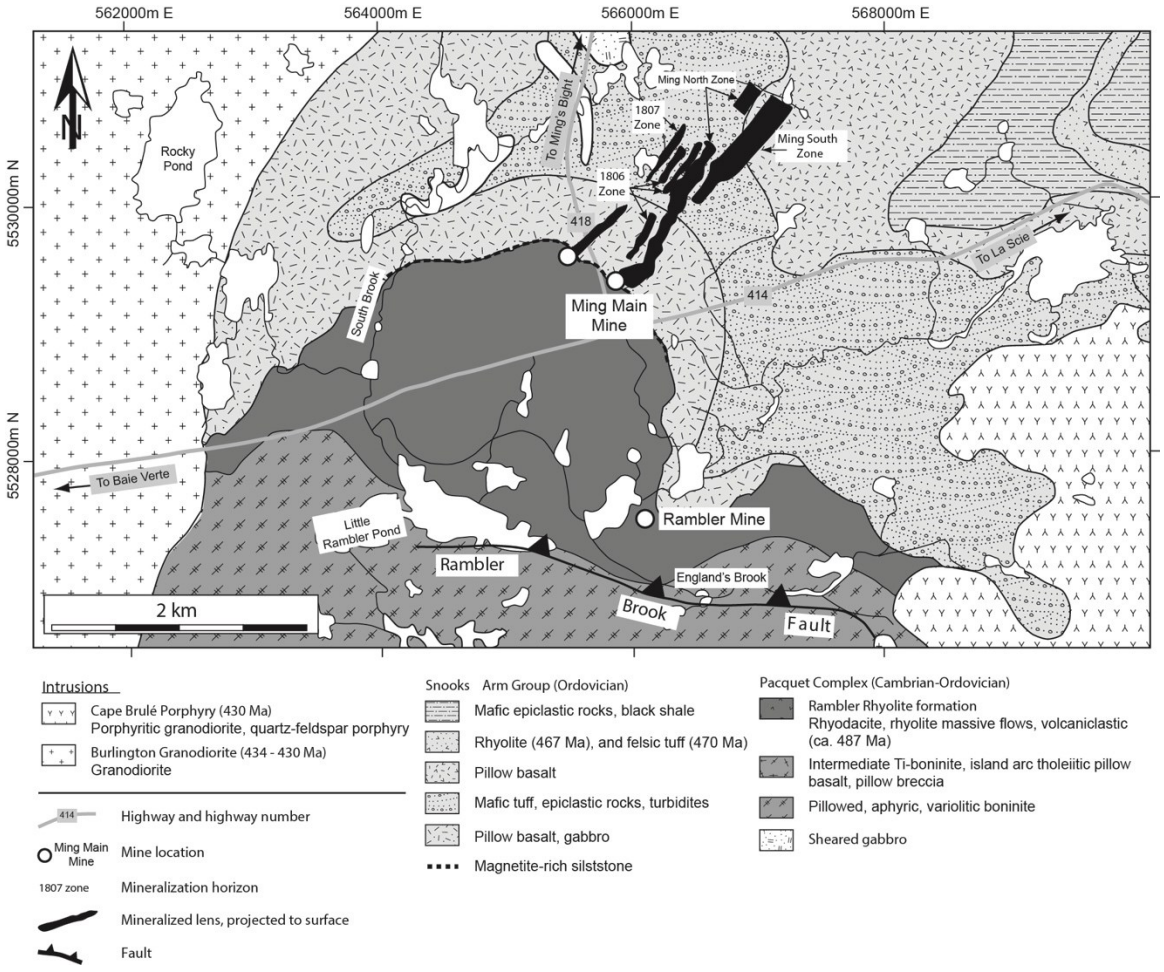

Fig. 3.1. Simplified geological map of the Pacquet Complex with the Ming VMS deposit (modified after Skulski et al., 2010). The different orebodies of the Ming deposit are projected to surface.

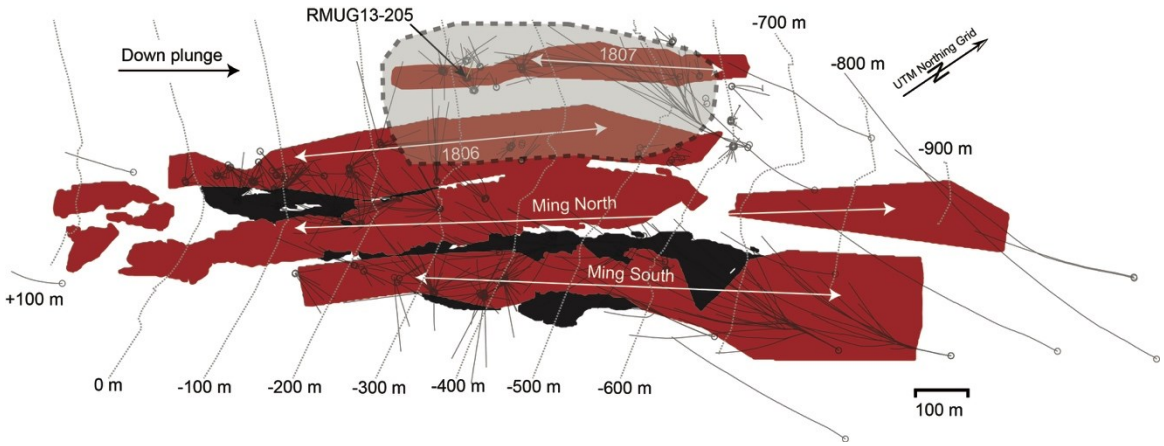

Fig. 3.2. Map outlining all the orebodies (red = massive sulfide; black = Lower Footwall Zone) forming the Ming deposit. Diamond drill hole RMUG13-205 is located in the up-plunge section of the 1807 Zone. The grey shaded area represents the approximate maximum known extension of the sulfide-rich volcaniclastic unit. The grey lines and circles represent drill hole traces and collars, respectively.

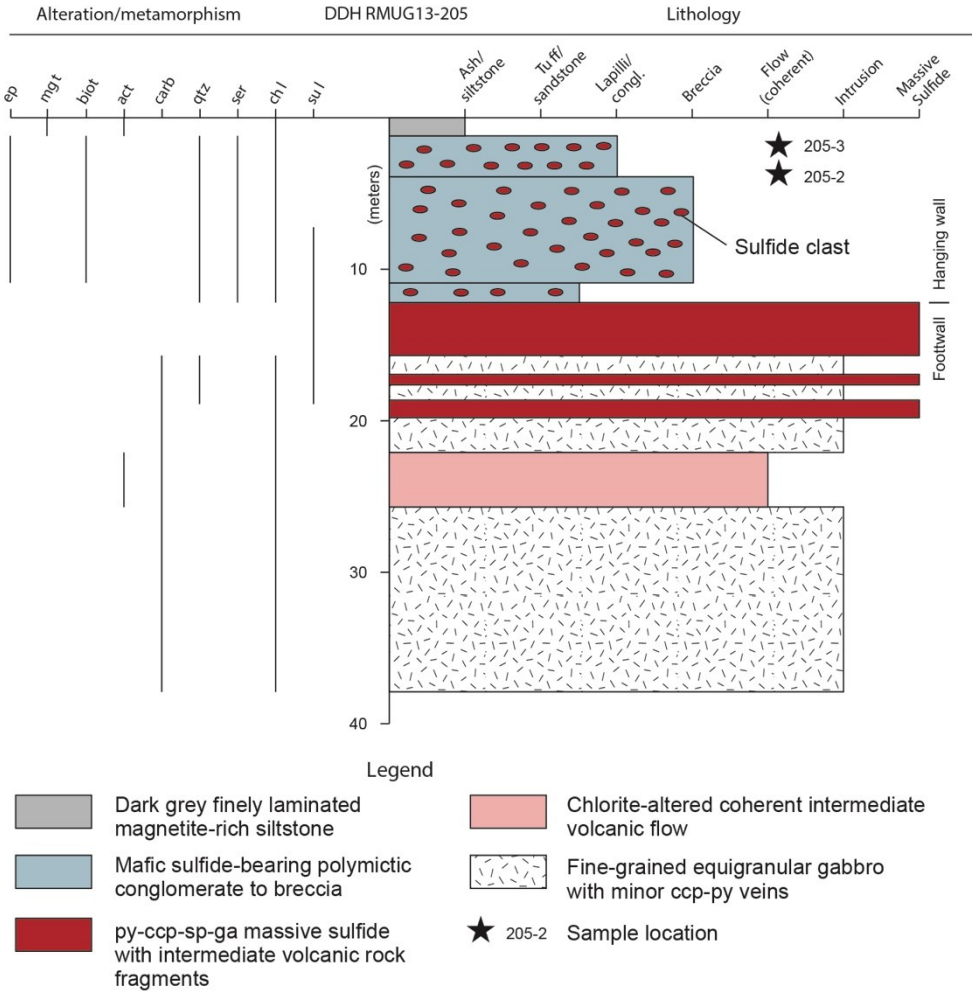

Fig. 3.3. Stratigraphic section of diamond drill hole RMUG13-205, 1807 Zone. Locations of the two samples collected, 205-2 and 205-3, are shown in black stars. Mineral abbreviations: Act = actinolite, biot = biotite, carb = carbonate, ccp = chalcopyrite, chl = chlorite, ep = epidote, ga = galena, mgt = magnetite, py = pyrite, qtz = quartz, ser = sericite, sp = sphalerite, sul = sulfide.

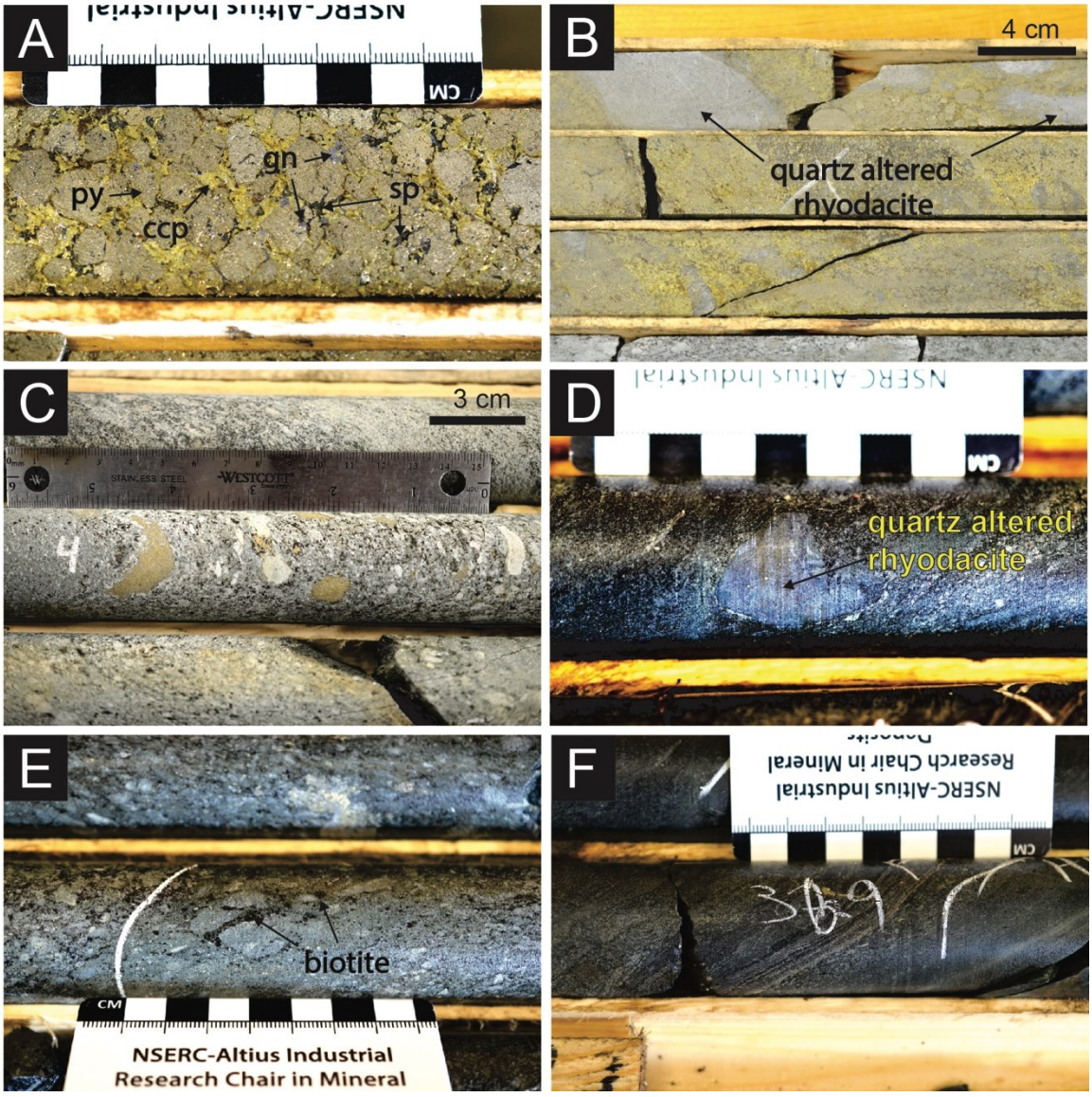

Fig. 3.4. Representative and selected drill core photographs of diamond drill hole RMUG13-205. (A) Massive sulfide consisting of rounded coarse-grained pyrite with interstitial chalcopyrite, galena, and sphalerite. (B) Massive sulfide consisting primarily of fine-grained pyrite-chalcopyrite±sphalerite with quartz altered aphanitic rhyodacite fragments. (C) Polymictic medium- to coarse-grained intermediate breccia with rhyodacite and sulfide clasts. Note the elongation of the clasts due to deformation. (D) Subangular quartz altered rhyodacite in the fine-grained portion of the volcaniclastic unit. (E) Close-up of the fine-grained matrix of the breccia consisting of quartz-plagioclase-sericite-biotite±epidote±chlorite. Note the biotite porphyroblasts. (F) Magnetite-rich siltstone overlying with a sharp contact the volcaniclastic unit. Mineral abbreviations are as in Figure 3.3.

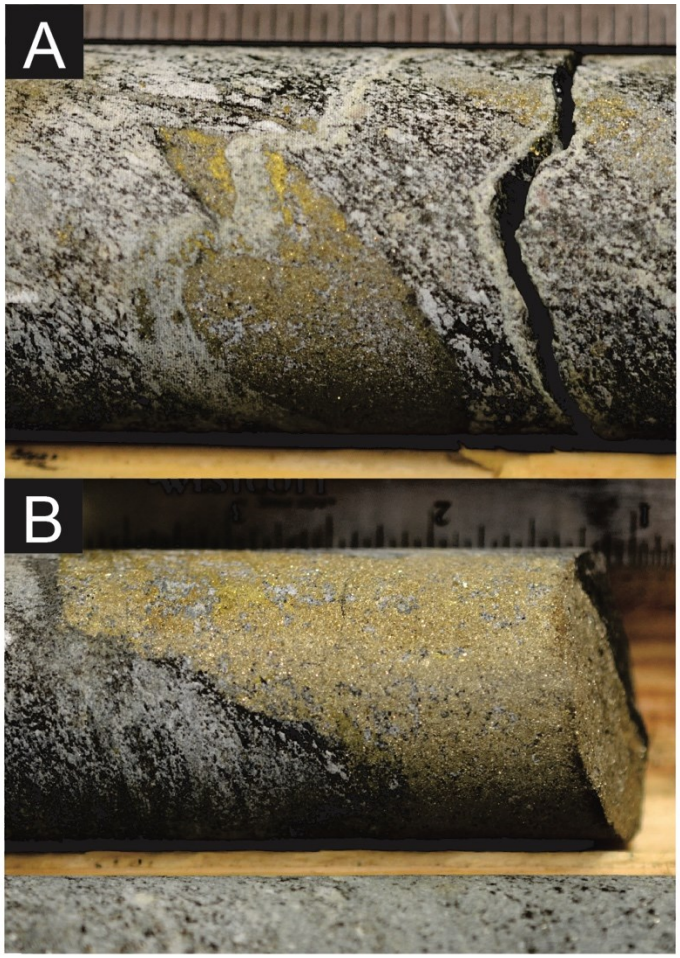

Fig. 3.5. Photographs of samples (A) 205-2 and (B) 205-3 selected for SEM-MLA analyses.

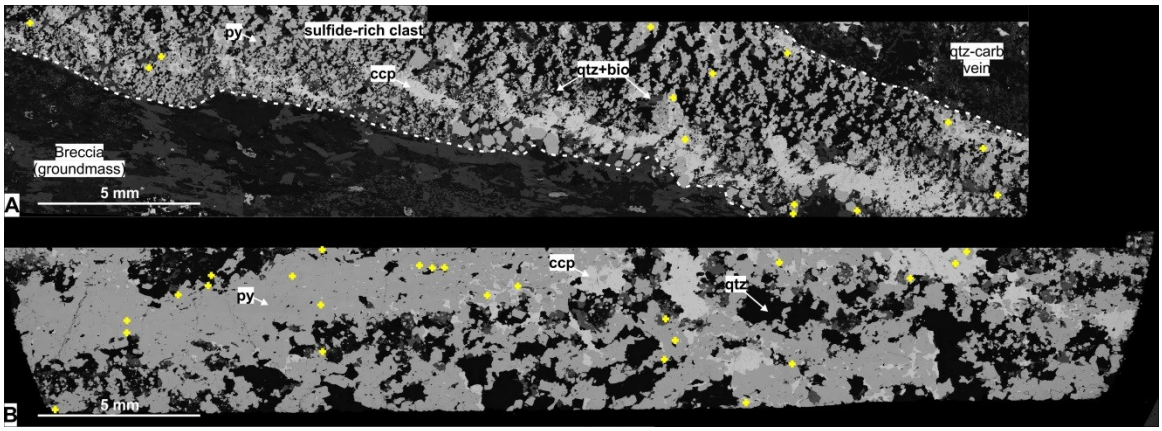

Fig. 3.6. Mosaic of part of the back scattered electron (BSE) images associated with MLA scans. Samples (A) 205-2 and (B) 205-3. The yellow crosses represent locations of electrum grains in the samples. Mineral abbreviations are as in Figure 3.3.

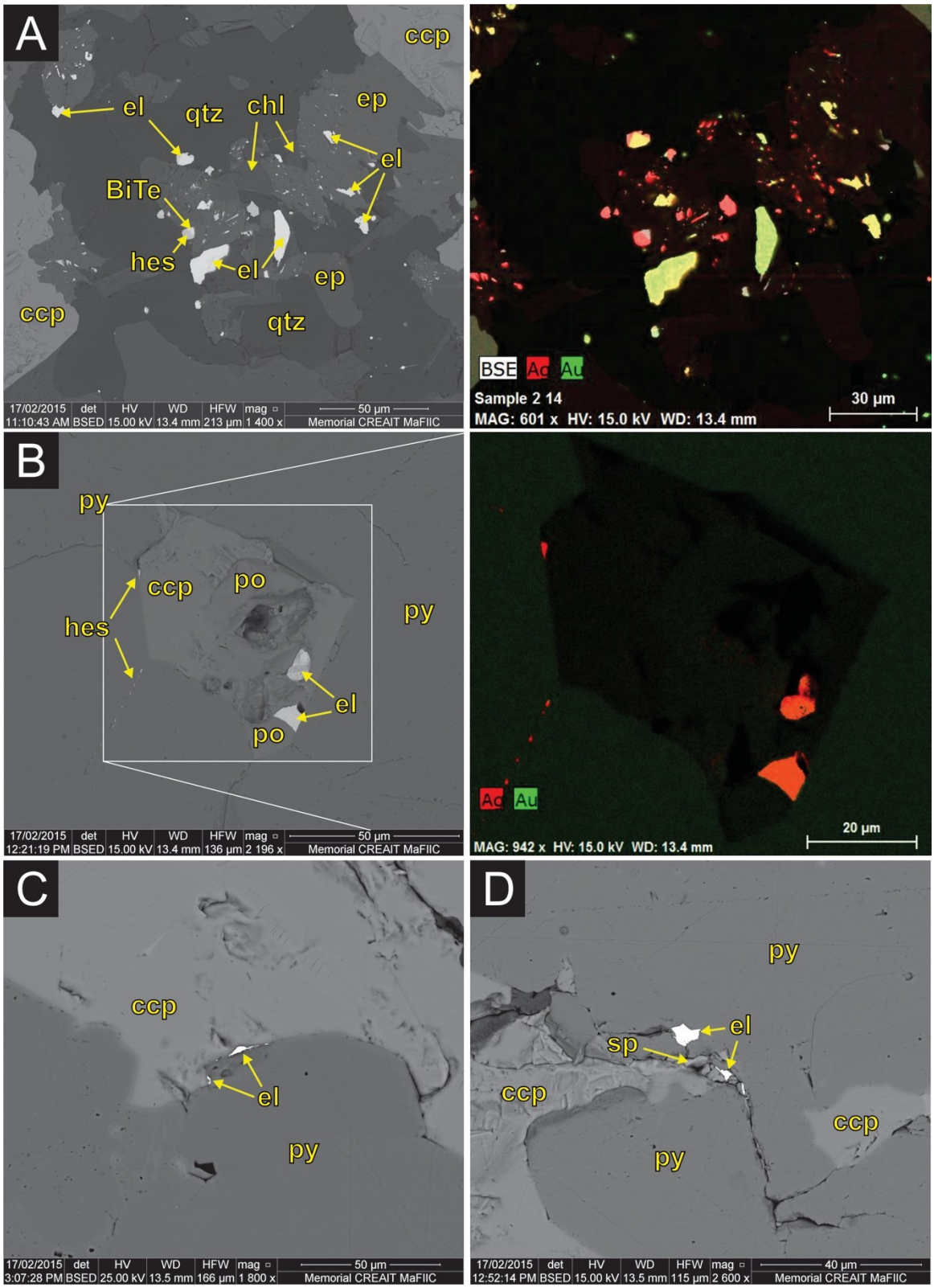
A
ccp
el
qtz
chl
ep
el
BiTe
hes
el
ep
ccp
qtz
17/02/2015 det HV WD HFW mag 50 µm
11:10:43 AM BSED 15.00 kV 13.4 mm 213 µm 1 400 x Memorial CREAIT MaFIIC
BSE Ag Au
Sample 2 14
MAG: 601 x HV: 15.0 kV WD: 13.4 mm
30 µm
B
py
ccp
po
py
hes
el
po
17/02/2015 det HV WD HFW mag 50 µm
12:21:19 PM BSED 15.00 kV 13.4 mm 136 µm 2 196 x Memorial CREAIT MaFIIC
Ag Au
MAG: 942 x HV: 15.0 kV WD: 13.4 mm
20 µm
C
ccp
el
py
17/02/2015 det HV WD HFW mag 50 µm
3:07:28 PM BSED 25.00 kV 13.5 mm 166 µm 1 800 x Memorial CREAIT MaFIIC
D
py
el
sp
ccp
ccp
py
17/02/2015 det HV WD HFW mag 40 µm
12:52:14 PM BSED 15.00 kV 13.5 mm 115 µm 2 600 x Memorial CREAIT MaFIIC

(Previous page) Fig. 3.7. Back scattered electron images and energy dispersive x-ray (EDX) scans by SEM on samples 205-2 and 205-3 for selected elements. Semi-quantitative EDX images show intensities (or relative abundance) of the measured elements. Mineral abbreviations are as in Figure 3 with the addition of: hes – hessite. (A) BSE (left) image showing electrum occurring with Bi-telluride (BiTe), hessite with gangue minerals such as chlorite, quartz, and epidote. EDX (right) scan of Ag and Au highlighting electrum (i.e., Au = lime green) and hessite (i.e., Ag = red). (B) BSE (left) image showing the occurrence of electrum, enclosed in pyrrhotite, with hessite in contact with chalcopyrite and pyrite. Hessite also occurs along a fracture in a recrystallized pyrite grain. Both chalcopyrite and pyrrhotite are enclosed in pyrite. EDX (right) scan of Ag and Au highlighting electrum (Au = green) and hessite (Ag = red). Note the light red colour of electrum indicating a high Ag content. (C) Free grains of electrum coexisting with chalcopyrite and recrystallized pyrite. (D) Brittle fractures in pyrite filled with electrum and sphalerite in close spatial associations with chalcopyrite.

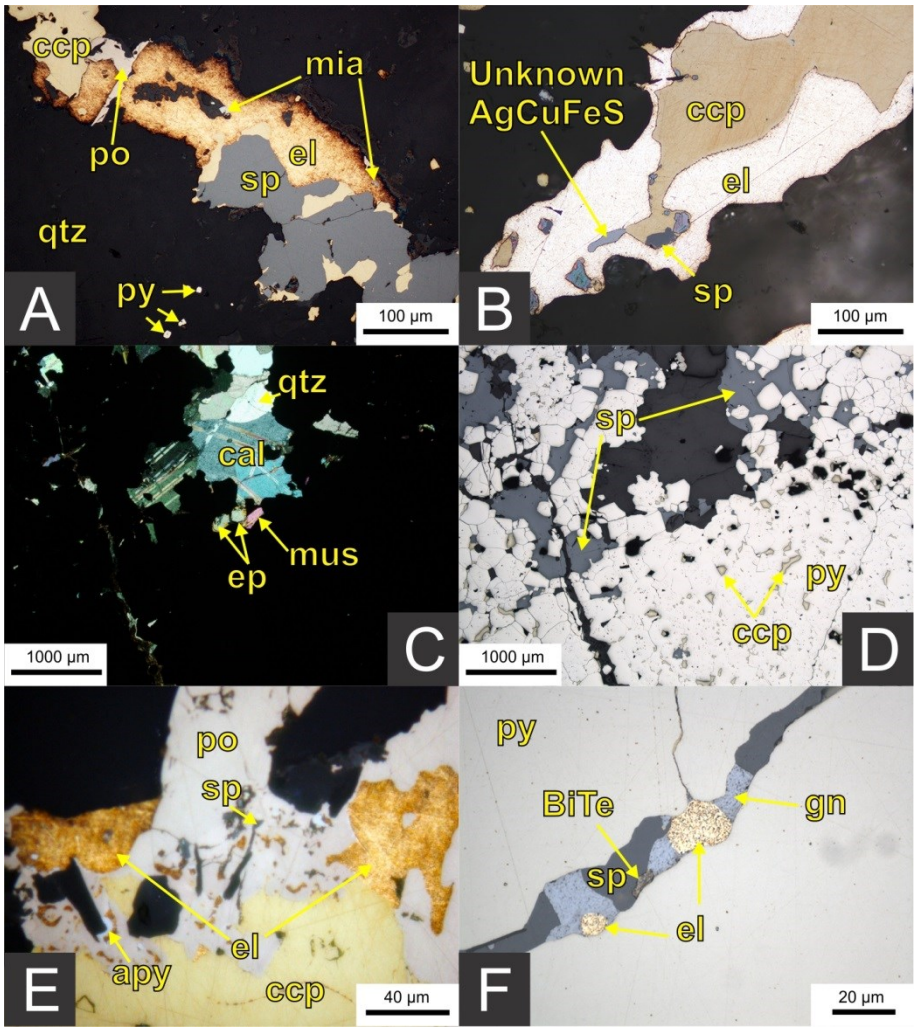

Fig. 3.8. Textural variations of precious metals in Ming massive sulfide orebodies. (A) Electrum with pyrrhotite, sphalerite, and miargyrite ($AgSbS_2$) on chalcopyrite margin with contact to gangue (semi-massive sulfides, 1806 Zone). (B) Electrum marginal on chalcopyrite on contact to (silicic) gangue and adjacent to sphalerite and unknown AgCuFeS phase (silicified horizon in contact with massive sulfides, 1806 Zone). (C) and (D) Gangue minerals in pyrite-sphalerite-chalcopyrite-rich massive sulfide under transmitted (cross-polarized) and reflected light, respectively (1807 zone). (E) Electrum as inclusions in and marginal to pyrrhotite, together with arsenopyrite and sphalerite (silicified horizon in contact with massive sulfides, 1806 Zone). (F) Electrum with galena and spatially close sphalerite and Bi-telluride between recrystallized pyrite (massive sulfides, Ming South Zone). Mineral abbreviations: ars = arsenopyrite, cal = calcite, ccp = chalcopyrite, el = electrum, ep = epidote, gud = gudmundite, mia = miargyrite, mus = muscovite, po = pyrrhotite, py = pyrite, qtz = quartz, sp = sphalerite. Photomicrographs in (A), (B), and (F) are after Bruckner et al. (2016) and (E) from Brueckner et al. (2014).

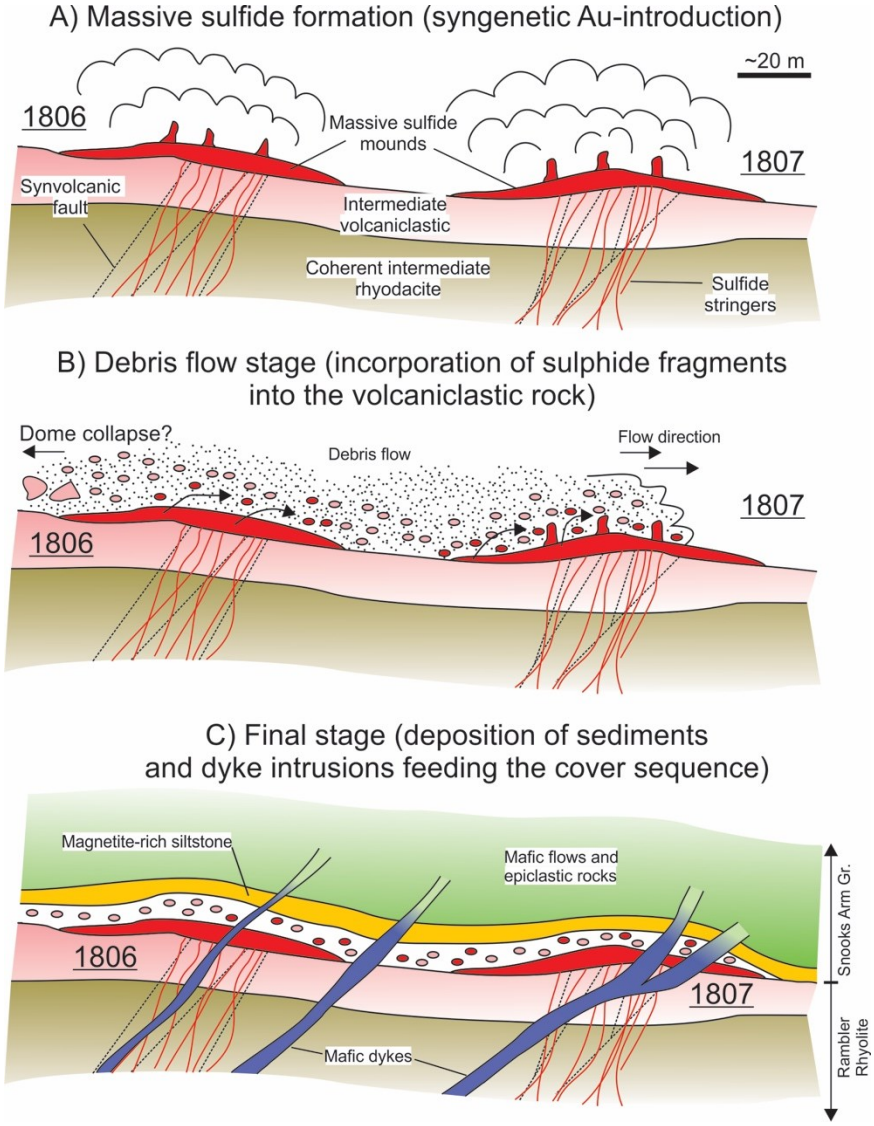

Fig. 3.9. Genetic model for the origin of the massive sulfide clasts in a submarine volcaniclastic mass flow deposit overlying the Ming VMS deposit. See text for explanation.

Table 3.1. Result Data of Trace Minerals from MLA in Samples 205-2 and 205-3[1]

		RMUG13-205-2					RMUG13-205-3				
Sample Mineral	Formula	Wt %	Area (%)	Area (μm²)	Particle count	Grain count	Wt %	Area (%)	Area (μm²)	Particle count	Grain count
Arsenopyrite	FeAsS	0.29	0.29	63.00	23	23	9.29	10.13	1,532.00	60	60
Cassiterite	SnO_2	0.15	0.13	28.25	4	4	0.18	0.17	26.25	9	9
Coloradoite	HgTe	0.93	0.71	154.00	12	12	0.89	0.73	110.50	9	9
Electrum	(Au,Ag)	6.20	3.11	678.50	98	98	14.60	7.93	1,198.50	140	144
Galena	PbS	3.13	2.53	552.50	185	185	6.41	5.61	847.75	128	128
Hematite	Fe_2O_3	0.63	0.73	159.50	25	25	0.02	0.03	4.25	3	3
Hessite	Ag_2Te	29.49	23.73	5,181.75	406	411	54.01	47.07	7,116.50	771	783
Pyrrhotite	$Fe_{1-X}S$	15.82	21.04	4,593.00	1,592	1,597	5.68	8.18	1,237.00	809	811
Bi-telluride	(Bi,Te)	37.32	29.26	6,390.00	218	220	3.81	3.23	488.75	69	70
Unknown[2]		6.04	18.48	4,034.50	1,754	1,770	5.11	16.92	2,557.50	1,272	1,295
Total		100.00	100.00	21,835.00	4,317	4,345	100.00	100.00	15,119.00	3,270	3,312

[1] The list excludes major minerals (pyrite, chalcopyrite, sphalerite, quartz, and biotite) present in the samples and values listed (area (%) and wt %) are normalized to 100% relative to the total area covered by the minerals (in μm²)

[2] Minerals with unknown X-ray spectra

Table 3.2. Comparison of Precious Metal Textures Observed in Sulfide Clasts in the Stratigraphic Hanging Wall and in (Semi-)Massive Sulfide Horizons of the Ming Deposit

Precious metal texture	Sulfide clasts of the hanging wall (this study)	(Semi-)massive sulfide orebodies (Brueckner et al., 2014, 2016)
Free electrum grains in chalcopyrite with contact to other sulfides	x	x
Free electrum grains on sulfide-gangue contact	x	x
Electrum as product of tennantite decomposition	-	x
Precious metals between grain boundaries of recrystallized pyrite/arsenopyrite and/or along cataclastic fractures in pyrite/arsenopyrite	x	x
Electrum with arsenopyrite	-	x
Electrum as inclusion in pyrrhotite partly accompanied by arsenopyrite or (sulfo-)antimonides	x	x

Notes: x = texture observed, - = texture not observed

Table A3.1 Compilation of known telluride occurrences in VMS deposits worldwide.

Deposit	Main commodities	Geologic Age	Geologic Setting	Metamorphic Grade	Telluride Mineralogy	Telluride Mineral Association/Assemblage	Study
Gayskoe deposit	Cu≥Zn (Au, Ag) ("Uralian type")	Middle Devonian	Ural Mts., Russia	unknown	hessite (Ag_2Te), altaite (PbTe), coloradoite (HgTe), calaverite ($AuTe_2$), krennerite (Au_3AgTe_8), tellurobismuthite (Bi_2Te_3)	Tellurides associated with massive pyrite-chalcopyrite sulfides Bornite-bearing ores on flanks of deposit containing gold and sulfosalts but no tellurides other than Ag-sulfotellurides	Novoselov et al. (2006) and references therein
Tash-Tau deposit	Cu-Zn-Pb-Au±barite ("Kuroko type")	Middle Devonian	Ural Mts., Russia	unknown	hessite (Ag_2Te), cervelleite-like mineral	Tellurides occurring in bornite-bearing ore as trace mineral phases together with gold, electrum, jalpaite, germanite, and stromeyerite Cervelleite-like mineral is associated with gold	Novoselov et al. (2006) and references therein
Degtyarsk deposit	Cu≥Zn (Au, Ag) ("Uralian type")	Lower-Middle Devonian	Ural Mts., Russia	unknown, but extensively deformed	altaite (PbTe), coloradoite (HgTe), hessite (Ag_2Te), rucklidgite ($(Bi, Pb)_3Te_4$), stuetzite ($Ag_{5-x}Te_3$), native tellurium (Te), tetradymite (Bi_2Te_2S), tellurobismuthite (Bi_2Te_3), petzite (Ag_3AuTe_2), sylvanite ($(Ag, Au)_2Te_4$),	Tellurides are routinely found in Cu- (but not when bornite is present) and Cu–Zn ores, and are associated with chalcopyrite–tennantite-tetrahedrite–galena Pyrrhotite-bearing ores carry only minor amounts of tellurides Discrete Au-, Ag- and Te-minerals routinely form fine inclusions inside pyrite, chalcopyrite and sphalerite	Vikentyev (2006) and references therein
Gaisk deposit	Cu≥Zn (Au, Ag) ("Uralian type")	Lower-Middle Devonian	Ural Mts., Russia	unknown, but extensively deformed			
Safyanovsk deposit	Cu≥Zn (Au, Ag) ("Uralian type")	Lower-Middle Devonian	Ural Mts., Russia	unknown, but non-deformed			
Uchaly deposit	Zn>Cu (Au, Ag) ("Uralian type")	Lower-Middle Devonian	Ural Mts., Russia	unknown, but extensively deformed			
Uzelginsk	Zn>Cu (Au, Ag)	Lower-	Ural Mts.,	unknown			

deposit	(“Uralian type”)	Middle Devonian	Russia		krennerite (Ag_3AuTe_8), calaverite ($AuTe_2$), montbrayite $(Au,Sb)_2Te_3$), empressite (AgTe), muthmannite ($AuAgTe_2$), volynskite ($AgBiTe_2$) Altaite, hessite and tetradymite are relatively common Native tellurium, Au- and Au–Ag-tellurides are rare	Many tellurides contain solid-solution gold	
Yaman-Kasy deposit	Cu≥Zn (Au, Ag) (“Uralian type”)	Silurian	Ural Mts., Russia	absent; locally zeolite facies	Bi-Pb tellurides, altaite (PbTe), hessite, (Ag_2Te), stuetzite (Ag_7Te_4), sylvanite (AgAuTe4), empressite (AgTe), cervelleite (Ag_4TeS), native tellurium (Te), tellurium oxides, Pb-Ag-Au tellurides	Disseminated tellurides in drusy chalcopyrite within sphalerite-chalcopyrite-pyrite-marcasite chimneys Overgrowth of various tellurim minerals partly observed Pb-Ag-Au tellurides (sylvanite, stuetzite, hessite, empressite, and electrum) partly as micro-inclusions in chalcopyrite Cervelleite in outer part (chalcopyrite zone) of marcasite–chalcopyrite–sphalerite chimneys as	Novoselov et al. (2006) and references therein Maslennikov et al. (2009) and references therein

						separate grains, intergrown with hessite–coloradoite, or thin veinlets in sylvanite–hessite.	
Babaryk deposit	Cu-Zn-Pb-Au±barite (“Kuroko type”)	Paloezoic	Ural Mts., Russia	unknown	cervelleite-like sulfotelluride	Sulfotelluride is in banded pyrite–chalcopyrite–sphalerite–bornite–galena ores with tennantite-tetrahedrite as anhedral to elongated grains within galena At the galena–bornite grain boundary Associated minerals are chalcocite, stromeyerite and electrum	Novoselov et al. (2006)
Severo-Uvaryazhskoe deposit	Cu-Zn-Pb-Au±barite (“Kuroko type”)	Paleozoic	Ural Mts., Russia	unknown	hessite (Ag_2Te), cervelleite (Ag4TeS)	Tellurides occur in poly-metallic ore dominated by sphalerite–galena–tennantite-tetrahedrite with traces of electrum–native silver–argentite Cervelleite is associated with electrum, native silver and acanthite	Novoselov et al. (2006) and references therein
Ming deposit	Cu(-Au)	Cambro-Ordovician	Appalachian Mts., Newfoundland, Canada	upper greenschist/lower amphibolite facies	hessite (Ag_2Te), altaite (PbTe), tsumoite (BiTe), unnamed Bi-telluride (Bi_3Te_2)	Tellurides preferentially with galena ± sphalerite ± pyrrhotite within (semi-)massive sulfides Tellurides never in direct contact with electrum	Brueckner et al. (2016) and this study
Um Samiuki deposit	Zn-Cu-Pb-Ag	Precambrian	Eastern Desert, Egypt	greenschist facies	cervelleite (Ag_4TeS), hessite (Ag_2Te)	Tellurides are associated with sphalerite–pyrite–chalcopyrite–galena–	Helmy (1999)

						bornite–tennantite-tetrahedrite–electrum Cervelleite occurs as small, subhedral grains close to margins of hessite and galena or as inclusions in sphalerite, where it is associated with silver-rich bornite–chalcopyrite–hessite	
Mattagami Lake deposit	Zn-Cu	Archean	Superior Province, Quebec, Canada	greenschist facies	altaite (PbTe), hessite (Ag_2Te), (antimonian and ferroan) mattagamite ($(Co_{0.65}, Fe_{0.37}, Sb_x)_1Te_2$), tellur-antimony ($Sb_{1.9}Te_3$), unknown Ag-Sb telluride ($Ag_{0.9}SbTe_2$)	Tellurides occurring in specific “telluride zone” partly within massive sulfide ore and partly within chloritized porphyritic metarhyolite Tellurides occuring with sphalerite–chalcopyrite–cobaltite–pyrrhotite–pyrite	Thorpe and Harris (1973)

Appendix A3.2 References

Brueckner, S.M, Piercey, S., Pilote, J.-L., Layne, G., and Sylvester, P., 2016, Mineralogy and mineral chemistry of the metamorphosed and precious metal-bearing Ming deposit, Canada. Ore Geology Reviews, v. 72, p. 914-939.

Helmy, H. M., 1999, The Um Samiuki volcanogenic Zn-Cu-Pb-Ag deposit, Eastern Desert, Egypt: A possible new occurrence of cervelleite: Canadian Mineralogist, v. 37, p. 143-154.

Maslennikov, V. V., Maslennikova, S. P., Large, R. R., and Danyushevky, L. V., 2009, Study of trace element zonation in vent chimneys from the Silurian Yaman-Kasy volcanic-hosted massive sulfide deposit (southern Urals, Russia) using laser ablation-inductively coupled plasma mass spectrometry (LA-ICPMS): Economic Geology, v. 104, p. 1111-1141.

Novoselov, K. A., Belogub, E. V., Zaykov, V. V., and Yakovleva, V. A., 2006, Silver sulfotellurides from volcanic-hosted massive sulfide deposits in the Southern Urals: Mineralogy and Petrology, v. 87, p. 327-349.

Thorpe, R. I., and Harris, D. C., 1973, Mattagamite and tellurantimony, two new telluride minerals from Mattagami Lake Mine, Matagami area, Quebec: Canadian Mineralogist, v. 12, p. 55-60.

Vikentyev, I. V., 2006, Precious metal and telluride mineralogy of large volcanic-hosted massive sulfide deposits in the Urals: Mineralogy and Petrology, v. 87, p. 305-326.

Chapter 4
Geochemical evidence for slab melting: Controls on the genesis of the Ming volcanogenic massive sulfide deposit and geodynamic implications for the Taconic seaway, Newfoundland Appalachians, Canada

4.1. Abstract

The Ming Cu-Zn-Ag-Au volcanogenic massive sulfide (VMS) deposit is hosted by the Upper Cambrian-Lower Ordovician Rambler Rhyolite formation, which consists of a folded northeast plunging felsic dome complex, developed in the uppermost segment of the obducted supra-subduction Baie Verte oceanic tract, in the north central Newfoundland Appalachians. The deposit is overlain by interstratified mafic volcanic flows and volcaniclastic rocks of the Snooks Arm Group. The upper 1 km of the Rambler Rhyolite formation consists of a coherent felsic lithofacies at its base, overlain by a quartz-bearing volcaniclastic-dominated lithofacies (units 1.2 and 1.3). Geochemically, these rocks are light rare earth element (LREE)- and large ion lithophile element (LILE)-enriched ($[La/Yb]_{pn}$ = 4-20; Th = 2.58-4.05 ppm), and high field strength element (HFSE)-depleted (Y = 5.64-6.59 ppm) rhyodacite with calk-alkalic affinities (Th/Yb > 2; Zr/Y > 7). The last pulse of felsic volcanism (unit 1.3) is intimately associated with the massive sulfide lenses and has FI- and FII-type rhyolite signatures, commonly attributed to deep (≥ 30 km) crustal melting. The $\varepsilon Nd_{(t)}$ values of the rhyolites range from -2.5 to -1.3, indicating the rocks were influenced by crustal material. A 10% batch partial melt of a garnet-amphibolite metamorphosed normal mid-oceanic ridge basalt (N-MORB) and island arc tholeiite (IAT) crustal material can generate a melt similar to the felsic rocks hosting the Ming deposit; however, the IAT reproduces much better the absolute

abundances of LILE (Th, Sr), HFSE (Nb, Zr, Y) and middle rare earth elements (MREE) of the felsic rocks. It is interpreted that the felsic melt came from melting of a subducted slab with IAT affinity, thus explaining the depth of melt generation and FI-FII signatures of the felsic rocks. Moreover, the slab-derived siliceous melt may also have contributed magmatophile elements (e.g., Ag, Au, Se, Te, Sn, Sb, Hg) into the hydrothermal system once it has reached near-surface depths, and may explain the epithermal suite element-enrichment in the Ming deposit. This study shows that strongly fractionated felsic volcanic rocks associated with boninites, such as those associated with the Ming VMS deposit, can be important hosts for precious metal-enriched VMS and may be as prospective as the tholeiitic felsic (e.g., FIII-FIV-type rhyolite) volcanic sequences.

The base of the Snooks Arm Group is comprised of spatially restricted sulfide-bearing mafic breccia, overlain by a regionally extensive sedimentary sequence ($\varepsilon Nd_{(t)}$ = +3.1 to +5.5), which is in turn overlain by interstratified high-Mg basalt ($\varepsilon Nd_{(t)}$ = +1.6), Th-enriched back-arc basin basalt (BABB), enriched mid-oceanic ridge basalt (E-MORB; $\varepsilon Nd_{(t)}$ = +6.6), and LREE-enriched/low-Ti tholeiitic tuffs ($\varepsilon Nd_{(t)}$ = -0.5). Four generations of mafic to intermediate dikes and sills cross-cut the Rambler Rhyolite formation and share similar geochemical characteristics to the extrusive rocks of the Snooks Arm Group, suggesting comagmatic relationships. The combination of variations in Nb/Yb, Th/Yb, and $\varepsilon Nd_{(t)}$ values within and between units suggest heterogeneous source melts from depleted to enriched mantle material with melts synchronously generated by both slab dehydration and asthenospheric upwelling in the mantle wedge.

4.2. Introduction

The Newfoundland Appalachians host ~45 producing, past producing, and prospective VMS deposits formed during the complex Early Paleozoic evolution of the Iapetus oceanic realm and its subsidiary seaways (Piercey, 2007; van Staal, 2007; Hinchey, 2011). The Ming VMS deposit (combined with the historical Ming West deposit and hereafter referred to as simply the Ming deposit) lies within the obducted Cambro-Ordovician oceanic crustal rocks of the Baie Verte oceanic tract, which is host to six other formerly producing or sub-economic VMS deposits of similar age, including the Rambler, East Rambler, Big Rambler Pond, Terra Nova, Betts Cove, and Tilt Cove deposits (Fig. 4.1). Since commercial production started in November 2012, a total of 809,508 tonnes grading 2.9% Cu, 9.63 g/t Ag, and 1.38 g/t Au were produced with combined measured and indicated resources of almost 28 Mt, averaging 1.48% Cu, 0.06% Zn, 1.99 g/t Ag, and 0.26 g/t Au (as of November 2016, Rambler Metals and Mining Ltd.). The Ming, East Rambler, and Rambler deposits are hosted in the same dome-shaped felsic complex (Rambler Rhyolite formation) that is constructed upon successions of boninitic and island arc tholeiitic rocks (Betts Head and Mount Misery formations, respectively), also host to Cyprus-type VMS mineralization to the south and east of the peninsula (Fig. 4.2; Sangster et al., 2007). These deposits, including the Ming deposit, are stratigraphically overlain by successions of tholeiitic to calc-alkalic mafic to felsic volcanic and volcaniclastic rocks, which collectively forms the ophiolitic cover sequence (Snooks Arm Group; Skulski et al., 2010). In recent years, a number of studies of the Ming deposit have led to the advancement of our understanding of its genesis, including

detailed micro-analytical work on the massive and semi-massive sulfide lenses (Brueckner et al., 2011; 2014; 2015; 2016) and the timing of Au-introduction (Pilote et al., 2016), and a number of preliminary reports on the volcanic architecture, stratigraphy, structure, and alteration of the deposit (Pilote and Piercey, 2013; Pilote et al., 2014; in review). The primary geochemical characteristics and petrogenesis of the felsic rocks and their relationships within their stratigraphic framework, however, have yet to receive any attention.

The composition of host felsic rocks can have direct controls on the metal budget of VMS deposits, either from direct comagmatic degassing (Lydon, 1996; Yang and Scott, 1996; Solomon and Zaw, 1997) and/or hydrothermal leaching of the felsic footwall rocks (Franklin et al., 1981; Lydon, 1988). Not only can a link between the composition of the felsic rocks and associated mineralization be made, tectonic environments they have formed in are interpreted to be a primary controlling factor on magma compositions. Here, an attempt to determine the source of the felsic rocks is made through lithogeochemical modeling of their initial compositions, and additional utilization of immobile compatible (e.g., TiO_2, Al_2O_3) and incompatible (e.g., Zr, REE) elements to characterize their magmatic and tectonic affinities (e.g., Cabanis and Lecolle, 1989; Ross and Bédard, 2009). The base of the overlying Snooks Arm Group is also examined and geochemically characterized in order to reconstruct the magmatic evolution that post-dates the time of formation of the Rambler Rhyolite formation.

The felsic successions that are intimately associated with the Ming massive sulfide lenses are Al-rich and have highly fractionated HREE signatures typical of FI-type

rhyolites, which are conventionally considered infertile for hosting VMS mineralization (Lesher et al., 1986; Hart et al., 2004). Henceforth, the rare association between FI-type felsic rocks and VMS deposits worldwide make the footwall rocks of the Ming deposit an important case study to determine the controlling factors on their genesis, their relationship to mineralization, and how this could impact target generation in other VMS districts, globally. Whereas reconciling the complex tectonic history of the Baie Verte oceanic tract is beyond the scope of this study (e.g., Dewey and Casey, 2015 and references therein), the results presented here will also help refine our current understanding of the Cambrian-Ordovician magmatic and tectonic evolution of the peri-Laurentian seaway during the metallogenic evolution of the Appalachians.

4.3. Geologic Setting

4.3.1. The Baie Verte oceanic tract and adjacent terranes

The Upper Cambrian to Lower Ordovician (489-477 Ma) Baie Verte oceanic tract (BVOT) forms one of the peri-Laurentian tectonic elements assembled during the Cambrian evolution of the Taconic seaway, which developed following the Ediacaran rifting of Dashwoods block from the eastern Laurentia (Waldron and van Staal, 2001; van Staal and Barr, 2012; van Staal et al., 2013). The Baie Verte oceanic tract consists of four ophiolitic slivers of identical age (ca. 490 Ma) that have similar geological assemblages and metallogeny (Hibbard, 1983; Dunning and Krogh, 1985; Cawood et al., 1996; Bédard and Escayola, 2010; Skulski et al., 2010; 2015). The four ophiolitic assemblages are the Betts Cove, Pacquet, Pointe Rousse, and Advocate complexes (Fig. 4.1; Skulski et al.,

2015) and consist of complete to incomplete oceanic crust assemblages that range from variably serpentinized mantle rocks (dunite and harzburgite), overlain by ultramafic cumulate sections, transitioning upward to isotropic gabbros to sheeted dikes, and pillowed boninites of the Betts Head Formation (Fig. 4.2; Bédard et al., 2000). Conformably overlying boninitic rocks are mafic island arc tholeiites and felsic volcanic rocks of variable thicknesses belonging to the Mount Misery and Rambler Rhyolite formations, respectively (Fig. 4.2). Collectively, the extrusive volcanic rocks of the Baie Verte oceanic tract reach a maximum thickness of 5 km in the Pacquet complex, including the Rambler Rhyolite formation, which is host to the Ming deposit.

The Baie Verte oceanic tract is fault bounded to the west by the Baie Verte Line and to the east by the Green Bay Fault, juxtaposing the ophiolitic rocks to the metamorphosed Neoproterozoic to Upper Cambrian sedimentary rocks of the Laurentian paleo-margin (Fleur de Lys Supergroup) in the west, and the Middle to Upper Cambrian (510-501 Ma) Lushs Bight oceanic tract in the east (Fig. 4.1; e.g., van Staal and Barr, 2012). The Lushs Bight oceanic tract comprises a ~505 Ma oceanic assemblage with abundant boninite and primitive oceanic island arc tholeiites (Kean et al., 1995; Swinden, 1996; Swinden et al., 1997). Both the Baie Verte and Lushs Bight oceanic tracts are interpreted to have formed in a supra-subduction zone, probably during their infancy, but the latter is older and was already emplaced onto Dashwoods block by ca. 490 Ma, synchronous with the early development of the Baie Verte oceanic tract (Szybinski, 1995; Swinden et al., 1997; Bédard et al., 1998; van Staal et al., 1998; 2007; 2009).

4.3.2. The upper Pacquet complex, Ming deposit, and cover sequence

In the Pacquet complex, the Rambler Rhyolite formation forms an approximately 3 x 5 km dome-shaped felsic complex, plunging to the northeast due to multiphase deformation (Castonguay et al., 2014). It is overlain and underlain, at least locally, by the mafic-dominated successions of the Mount Misery Formation. Recent detailed work by Pilote et al. (in review) distinguished three lithofacies units forming the upper 1 km of the Rambler Rhyolite formation; 1) at the bottom, a coherent facies that consists of quartz-phyric to aphanitic felsic volcanic rocks (unit 1.1), sharply transitioning to 2) multiple successions of quartz-bearing felsic bedded to massive volcaniclastic rocks of different fragment sizes (unit 1.2), overlain by 3) a thin blue quartz-phyric to quartz-megacrystic felsic coherent flow laterally transitioning to bedded quartz-bearing felsic tuffs (unit 1.3) (Fig. 4.3). Both units 1.2 and 1.3 are fault bounded and/or spatially controlled by synvolcanic faults (Fig. 4.3). The mineralized zones of the Ming deposit occur as massive-sulfide to semi-massive sulfide ruler-shaped lenses, located at the very top of the felsic complex, and they plunge 30-35° to the northeast with significant variations in Cu, Zn, Ag, and Au grades (Fig. 4.2; Brueckner et al., 2014; 2016). The 1806 Zone (Fig. 4.2) represents the most precious metal-rich massive sulfide lens with Ag and Au grades of up to 15.07 g/t and 2.97 g/t, respectively. A Cu-rich stringer zone underlies the sulfide lenses, which represents the stockwork (e.g., Lydon, 1984) of the deposit. Hydrothermal alteration is ubiquitous in the Ming deposit, although it is highly variable in intensity (Pilote et al., 2015). In the context of the potential mobility of some geochemical elements, alteration is addressed in Appendix A4.1.

The stratigraphic successions that immediately overly the Rambler Rhyolite formation are part of the regionally extensive and correlative Lower to Middle Ordovician Snooks Arm Group (also referred to as the cover sequence; Skulski et al., 2010; 2015). At the Ming deposit, the base of the cover sequence is a spatially restricted mafic volcanic breccia with up to 10 vol % sulfide clasts (unit 2; Pilote et al., 2016). This unit is conformably overlain by a thin (≤1 m), dark purple to black, finely laminated shale to siltstone (unit 3), which is considered regionally equivalent to the Nugget Pond horizon (Skulski et al., 2010; 2015). The latter is overlain by multiple successions of mafic tuff, tuff breccia, and massive flows that are compositionally indistinguishable visually. All the rocks above are cross-cut by multiple generations of mafic sills and dikes (Pilote et al., in review); however, these intrusive rocks are geochemically distinctive. Lastly, a major south-directed thrust fault, namely the Rambler Brook Fault, truncates the base of the Rambler Rhyolite formation, structurally juxtaposing the felsic complex with stratigraphically lower parts of the Snooks Arm Group (Fig. 4.2).

4.4. Lithogeochemistry and Whole-Rock Sm-Nd Isotope Compositions of the Pacquet Complex and Cover Sequence

The average major and trace element geochemistry for 92 samples of all units from the Ming deposit, intrusive rocks, and the lower 150 m of the cover sequence are summarized in Table 4.1. Of these samples, 22 were selected for Nd isotopic analyses; the sample descriptions and results are presented in Table 4.2 and 4.3, respectively. Analytical procedures for both whole-rock and isotopic geochemistry are explained in

detail in **Appendix A4.2**. Analytical accuracy and precision values for each element are also presented in **Appendix A4.2**. It is noteworthy that felsic rocks of the Rambler Rhyolite formation have all experienced some degree of hydrothermal alteration, in addition to regional upper greenschist metamorphism (e.g. Castonguay et al., 2014). The list presented here represents a set of least-altered samples that were chosen based on a rigorous set of criteria, which are described in **Appendix A4.1**. The data presented here are supplemented by previously published data from Piercey et al. (1997), Kean et al. (1995), and Bédard (1999) and will be discussed below. The complete geochemical dataset is presented in Appendix 4.

4.4.1. Footwall coherent felsic volcanic and felsic volcaniclastic rocks (units 1.1 and 1.2)

The coherent (unit 1.1) and volcaniclastic (unit 1.2) lithofacies in the footwall of the Ming deposit display similar geochemical compositions (Fig. 4.4; Table 4.1). Both have andesitic compositions (Fig. 4.4A); however, the SiO_2 (= 68.12-71.50 wt %) contents are much higher than normal andesitic rocks and are more akin to dacites or rhyodacites (Fig. 4.4B). The units have calc-alkalic affinities (Ross and Bédard, 2009) (Fig. 4.4C; Table 4.1) and Yb_{cn} values and $[La/Yb]_{cn}$ ratios (cn = chondrite normalized) like FII-type rhyolites (Fig. 4.5A), and Y values and Zr/Y ratios similar to FI- and FII-type rhyolites (Fig. 4.5B) (Lesher et al., 1986; Hart et al., 2004). Some of the key geochemical features are the extremely low Zr (57-63 ppm) and Y (6.51-6.59 ppm) contents in these rocks (Table 4.1). On a primitive mantle-normalized plot they have

moderate to strong negative Nb (Nb/Nb* = ~0.6) and Ti (Ti/Ti* = 0.19) anomalies, positive Zr (Zr/Zr* = 2.3-2.5) anomalies, and weak negative Eu (Eu/Eu* = ~0.95) and Y (Y/Y* = ~0.75) anomalies (Fig. 4.6A; Table 4.1). The ΣREE in units 1.1 and 1.2 is 8 to 19 times chondritic values, and samples exhibit LREE-enrichment ($[La/Sm]_{pn}$ = ~4.0) with depleted HREE that are near primitive mantle values (Fig. 4.6A). Two unaltered samples from unit 1.1 show an $\varepsilon Nd_{(t)}$ of -1.5 and -1.8, whereas altered samples from both unit 1.1 and 1.2 yielded $\varepsilon Nd_{(t)}$ ranging between -2.5 and -1.1 (Table 4.3; Fig. 4.8). The unaltered samples of felsic volcanic rocks located at the same stratigraphic horizon (Skulski et al., 2015) collected (~4 km) south of the Ming deposit by Piercey et al. (1997) share similar geochemical characteristics (Fig. 4.6A) to units 1.1 and 1.2.

4.4.2. Syn-mineralization felsic volcanic rocks (unit 1.3)

The thin (<10 m) blue quartz-bearing coherent and volcaniclastic lithofacies overlying unit 1.2 is intimately associated with the massive sulfide lenses (Fig. 4.3; Pilote et al., in review). Although this unit has previously been mapped and laterally constrained to the Ming South Zone (Pilote et al., in review), quartz-bearing tuff and synvolcanic dikes with similar geochemical characteristics have been locally observed below the 1807 Zone (drill hole RM07-18) and are thus considered as part of the same unit. Three representative samples have andesitic affinities (Fig. 4.4A), but contain higher SiO_2 contents than typical andesite (Fig. 4.4B; Table 4.1). The samples of unit 1.3 have some of the highest Zr/Y ratios in the deposit (average of 14.4; Fig. 4.4C; Table 4.1), but with calc-alkalic affinities (Ross and Bédard, 2009). The samples have FI-type rhyolites

affinities (Figs. 4.5A-B) with higher La/Yb and Z/Yb ratios than units 1.1 and 1.2; this unit also has higher Al_2O_3, TiO_2, Zr, and Th (Table 4.1) and ΣREE (18 to 24 times chondritic values). In addition, rocks of unit 1.3 exhibit enrichment in LREE ($[La/Sm]_{pn}$ = 4.03) with depletion in HREE ($[Gd/Lu]_{pn}$ = 2.37) and Y (5.64 ppm) (Fig. 4.6B; Table 4.1). Moreover, the HREE and Y average values are lower, and MREE are higher than that of units 1.1 and 1.2 (Table 4.1; Fig. 4.6B). On a primitive mantle-normalized diagram, the rocks of unit 1.3 have moderate to strong negative Nb (Nb/Nb* = 0.45) and Ti (Ti/Ti* = 0.24) anomalies, positive Zr (Zr/Zr* = 2.86) anomalies, absent to weak positive Eu (Eu/Eu* = 1.31) anomalies, and weak negative Y (Y/Y* = 0.68) anomalies (Fig. 4.6B; Table 4.1). All units (1.1 to 1.3) show a strong positive Al anomaly on the primitive mantle-normalized extended element plots (Figs. 4.6A-B). A sample of this unit has an $\varepsilon Nd_{(t)}$ of -1.5, and the two altered samples have values of -1.5 and -2.1 (Table 4.3; Fig. 4.8).

4.4.3. Sulfide-bearing mafic volcanic breccia (unit 2)

The sulfide-bearing volcaniclastic lithofacies immediately overlying parts of the massive sulfide in the 1806 and 1807 zones is dominated by basaltic lapilli sized fragments, although is locally polylithic with felsic and basaltic fragments, with locally up to 10 vol % sulfide clasts (Pilote et al., 2016). Representative samples of unit 2 collected from monolithic intersections have basaltic affinities (Figs. 4.4A-B), with calc-alkalic Th/Yb (= 0.95) and Zr/Y (= 7.02) ratios (Fig. 4.4C); however, these latter ratios are accentuated by both strong to weak positive Zr (Zr/Zr* = 2.96) and Y (Y/Y* = 1.17)

anomalies (Figs. 4.6C). In both the Th-Zr-Nb diagram of Wood (1980) and La-Y-Nb diagram of Cabanis and Lecolle (1989), samples of unit 2 show depletion of Nb relative to other HFSE, plotting in the arc fields (Figs. 4.7A-B). Furthermore, on an extended elements-normalized diagram, unit 2 shares geochemical patterns similar to as typical low Ti-tholeiites with a weak LREE enrichment ($[La/Sm]_{pn}$ = 1.47) and positive Th and negative asymmetric Nb (Nb/Nb* = 0.72) anomalies (Fig. 4.6C). Their low Al_2O_3/TiO_2 (= 10.66) ratios and high TiO_2 (= 1.674 ppm) and low V (= 145.7 ppm) contents are, however, inconsistent with low Ti-tholeiitic rocks (Fig. 4.7C; Shervais, 1982) and are more similar to back-arc basin affinities.

4.4.4. Fe-rich shale (unit 3)

The thin (≤1 m) and extensive sedimentary sequence that overlies the Ming massive sulfide lenses, shares similar geochemical characteristics with unit 2 it underlies. The fine-grained sedimentary rocks of unit 3 contain minimal variations in SiO_2 (= 48.01-53.08 wt %), Al_2O_3 (= 15.55-19.49 wt %), and Fe_2O_{3t} (= 6.70-9.40 wt %) and show SiO_2/Al_2O_3 and Fe_2O_{3t}/K_2O ratios that are typical of Fe-rich shale (Fig. 4.7D; Herron, 1988), reflecting the high magnetite content in these rocks. Accordingly, the wide spread of Fe_2O_{3t}/K_2O ratios is due to the variations in K_2O (= 0.20 to 3.08 wt %; Fig. 4.7D Table 4.1). For the sake of simplification, rocks of unit 3 will be hereafter referred to as Fe-rich shale. The latter contains relatively low Th (= 1.44-2.58 ppm), Zr (= 81-125 ppm), and La (= 7.07-11.45 ppm), whereas Ni (= 28.5 to 84.9 ppm) and Sc (= 23-33 ppm) values are high. On a primitive mantle-normalized plot, the samples show weak negative Nb

(Nb/Nb* = 0.89) and weak positive Zr (Zr/Zr* = 2.65) anomalies (Fig. 4.6C) and much like the rocks of unit 2, the Fe-rich shale samples are strongly depleted in V (= 167.7 ppm). On a post-Archean Australian shale (PAAS)-normalized plot, the Fe-rich shale shows depletion in LREE and near flat MREE and HREE patterns, with moderate positive Eu anomalies, and devoid of Ce (Ce/Ce* ≈ 1) anomalies (Fig. 4.6D). Four samples have $\varepsilon Nd_{(t)}$ ranging from +3.1 to +5.5 (Table 4.3; Fig. 4.8). Samples with lower Cr values and Mg# have more evolved $\varepsilon Nd_{(t)}$ values (Tables 4.1, 4.3).

4.4.5. Lower section of the Snooks Arm Group (hanging wall)

The rocks that overly unit 2 and locally intercalated with the Fe-shale were recently combined as part of the Snooks Arm Group (Skulski et al., 2010, 2015) (Fig. 4.1); herein, an emphasis is made on the 200 m section that overlies the Ming deposit. Figure 4.9 illustrates the intersected immediate hanging wall; although, the Fe-shale is absent here. The mafic-dominated volcanic and volcaniclastic successions show distinct geochemical characteristics and are described below.

4.4.5.1. High-Mg basalt

The massive flows to volcaniclastic rocks of the lowermost Snooks Arm Group (Fig. 4.9), which also represent the first pulse of volcanism in the Rambler area that post-dates the deposition of the Fe-shale, are basaltic in composition (SiO_2 = 49.83 wt %; Zr/TiO_2 = 83.15) and characterized by primitive Mg# (= 62.4) and high Cr (= ~200 ppm) and Ni (= ~84 ppm) values (Fig. 4.4A-B; Table 4.1). Their Zr/Y (= 5.61) and La/Yb (=

10.20) ratios suggest a transitional affinity (Barrett and MacLean, 1999); however, the enrichment in Th (= ~2.5 ppm) relative to other HFSE and REE suggests a calk-alkalic affinity (Fig. 4.4C; Ross and Bédard, 2009). The arc-like affinity is mirrored by low Nb/Th (<<5; Swinden et al., 1989) ratios and they plot in the arc-like fields of Wood (1980) and Cabanis and Lecolle (1989) (Figs. 4.7A-B). On a primitive mantle-normalized diagram (Fig. 4.9B), the high-Mg basalt shows enrichment in LREE ($[La/Sm]_{pn}$ = 2.06) with a weak positive Zr (Zr/Zr* = 2.45) anomaly. An $\varepsilon Nd_{(t)}$ value of +1.6 was obtained from this unit (Table 4.3; Fig. 4.8).

4.4.5.2. Th-enriched back-arc basin basalt

This unit consists of massive flows, locally variolitic and/or vesicular, and fragmental rocks of variable thicknesses, intercalated with other units of distinct geochemical affinities (Fig. 4.9). The rocks are basaltic in composition with Zr/TiO_2 = 69.94, Nb/Y = 0.09, and SiO_2 = 47.12 wt % (Fig. 4.4A-B; Winchester and Floyd, 1977; Pearce, 1996). This unit shows fractionated Mg# (= 56.83) with no significant enrichment in Cr, Co, and Ni (Table 4.1). This unit is tholeiitic to transitional based on Zr/Y (= 4.19) and Th/Yb (= 0.17) ratios (Fig. 4.4C; Barrett and MacLean, 1999; Ross and Bédard, 2009) and plots both in the volcanic arc tholeiite and back-arc basin basalt fields on the La-Y-Nb plot (Fig. 4.7B; Cabanis and Lecolle, 1989). This range is due to a systematic drop in Nb (and Eu) and concomitant increase in Th when moving up-stratigraphy. On a primitive mantle-normalized diagram, the rocks of this unit show depletion in LREE and

HREE relative to MREE ($[La/Sm]_{pn}$ = 0.82 and $[Gd/Lu]_{pn}$ = 1.55) with a weak positive Zr (Zr/Zr* = 2.20) anomaly (Fig. 4.9C).

4.4.5.3. Enriched mid-ocean ridge basalt (E-MORB)

This unit consists of <25 m thick massive flows intercalated with pillow lavas of mafic composition (SiO_2 = 46.89 wt %; Zr/TiO_2 = 69.46; Fig. 4.4B-C; Winchester and Floyd, 1977; Pearce, 1996) with fractionated Mg# (= 50.19). The two analyzed samples of this unit share similar geochemical characteristics, except for one sample that shows a moderate negative Nb (Nb/Nb* = 1.98) anomaly (Fig. 4.9D). The rocks have characteristically the lowest Al_2O_3/TiO_2 (= 6.89) ratios (and highest TiO_2) of all rocks analyzed and contain the highest Co and V values of the hanging wall volcanic succession, with averages of 45.7 ppm and 352.4 ppm, respectively (Table 4.1). The basalt shows near-flat LREE to MREE patterns ($[La/Sm]_{pn}$ = 1.12) on primitive mantle-normalized diagrams with a weak depletion in HREE ($[Gd/Lu]_{pn}$ = 1.78) (Fig. 4.9D). The samples straddle the boundary between the arc-basalt and E-MORB fields of Wood (1980) and the back-arc basin basalt (BABB) field of Cabanis and Lecolle (1989) (Figs 4.7A-B). Despite the latter ambiguous magmatic and tectonic affinities, the low Th/Yb and Zr/Y ratios reflect a transitional affinity typical for E-MORB and/or BABB (Fig. 4.4C; Ross and Bédard, 2009), supported by their high Nb/Th ratio (>5), typical for non-arc-like basalts (Swinden et al., 1989). A representative sample of this unit yielded a primitive $\varepsilon Nd_{(t)}$ value of +6.6 (Table 4.3; Fig. 4.8).

4.4.5.4. LREE-enriched/Low-Ti calc-alkalic mafic tuff

The rocks of this unit share similar geochemical characteristics with the high-Mg basalt (Table 4.1), except that the mafic tuff is more enriched in LREE ($[La/Sm]_{pn}$ = 2.95) and shows a relatively strong negative Ti (Ti/Ti* = 0.41) anomaly, which is mirrored in the high Al_2O_3/TiO_2 and Zr/TiO_2 ratios (Table 4.1). Based on the SiO_2 (= 54.64 wt %) content and Zr/TiO_2 (= 136.62) ratio, the rocks have andesitic affinities (Fig. 4.4A-B). The rocks of this unit show variable but overall fractioned Mg# (= 53.15) and are characterized by low V (= 113.6 ppm), Cr (= 135.7 ppm), and Co (= 20.7 ppm). The high Th/Yb (= 2.43) ratios are characteristic of calc-alkalic rocks (Fig. 4.4C; Ross and Bédard, 2009), also reflected by low Nb/Th ratios (= 1.21) (Swinden et al., 1989) and the proportions of Th-Zr-Nb and La-Y-Nb in the rocks (Figs. 4.7A-B). A sample from this unit yielded an $\varepsilon Nd_{(t)}$ value of -0.5, making this unit the most evolved rocks of the immediate cover sequence (Table 4.3; Fig. 4.8).

4.4.6. Post-VMS mineralization intrusions

The multiple generations of sills and dikes cross-cutting the host sequences at the Ming deposit can be divided into four distinct assemblage base on distinct geochemical characteristics, which are as follows: 1) low Nb/Yb and 2) intermediate Nb/Yb tholeiitic gabbros (IN1 of Pilote et al., 2015), 3) transitional diorite (IN2 of Pilote et al., 2015), and 4) calc-alkalic porphyritic quartz monzodiorite (IN3 of Pilote et al., 2015). The contact relationship between the low Nb/Yb gabbro and intermediate Nb/Yb gabbro is unclear;

however, both the latter intrusive units are cross-cut by the transitional diorite followed by the calc-alkalic porphyritic quartz monzodiorite (Pilote et al., 2015).

4.4.6.1. Low Nb/Yb tholeiitic gabbro

The coarse, melanocratic, equigranular gabbro shows a tholeiitic affinity on various discrimination diagrams (Figs. 4.4C, 4.7A-C; Irvine and Baragar, 1971; Barrett and MacLean, 1999; Ross and Bédard, 2009), although its high Zr (= 98 ppm) and low Y contents (= 19.98 ppm) is atypical for such a magmatic affinity (Barrett and MacLean, 1999). The rocks of this unit shows a slight enrichment in LREE ($[La/Yb]_{pn}$ = 1.76) with a strong depletion in Nb on the extended element diagram (Fig. 4.10A). Their high Zr/Y ratios, low Nb, La, and Th are consistent with rocks formed in volcanic arc settings (Figs. 4.7A-B; Wood, 1980; Cabanis and Lecolle, 1989). A sample of low Nb/Yb tholeiitic gabbro yielded a primitive $\varepsilon Nd_{(t)}$ value of +7.1 (Table 4.3; Fig. 4.8).

4.4.6.2. Intermediate Nb/Yb tholeiitic gabbro

This fine-grained porphyritic to coarse equigranular gabbro has a tholeiitic affinity (Figs. 4.4C, 4.7A-C); Irvine and Baragar, 1971; Barrett and MacLean, 1999; Ross and Bédard, 2009) and shares many geochemical similarities with the low Nb/Yb tholeiitic gabbro; however, with significant key major and trace element distinctions; for instance, their respective Mg# and Nb/Yb ratios (Table 4.1; Fig. 4.10C). The highly fractionated intermediate Nb/Yb tholeiitic gabbro generally contains higher V (= 252.6 ppm) and lower Ni (= 69.5 ppm) values than the low Nb/Yb tholeiitic gabbro. The intermediate

Nb/Yb tholeiitic gabbro is slightly more enriched in LREE than its counterpart ($[La/Sm]_{pn}$ = 1.06) and shows no Nb/Nb* anomalies on the extended element diagram (Fig. 4.10C), except for samples with higher Th values. Based on the HFSE contents and the variability of Th (= 0.50 ppm), intermediate Nb/Yb tholeiitic gabbro range from N-MORB to E-MORB to BABB (Figs. 4.7A-B; Wood, 1980; Cabanis and Lecolle, 1989). A representative sample of this unit shows a primitive $\varepsilon Nd_{(t)}$ value of +7.3, similar to that of the low Nb/Yb tholeiitic gabbro (Table 4.3; Fig. 4.8).

4.4.6.3. Transitional diorite

Although most samples of this unit show a tholeiitic trend on a AFM diagram (not shown; Irvine and Baragar, 1971), they straddle the transitional to calc-alkalic fields on a discrimination diagram using immobile trace element systematics (Fig. 4.4C; Barrett and MacLean, 1999; Ross and Bédard, 2009). The transitional diorite shows a wide range in transition elements (i.e., V, Cr, Co, Ni; Table 4.1) and Mg# (Table 4.1). Nonetheless, this unit shows LREE enrichment ($[La/Sm]_{pn}$ = 1.91) with a strong to weak Nb anomaly (Nb/Nb* = 1.22) (Fig. 4.10B). On tectonic setting discrimination diagrams, the rocks of this unit have E-MORB to arc-like signatures (Figs. 4.7A-B; Wood, 1980; Cabanis and Lecolle, 1989). A sample of this unit, although showing weak metamorphic alteration, yielded an $\varepsilon Nd_{(t)}$ value of +2.3 (Table 4.3).

4.4.6.4. Calk-alkalic porphyritic quartz monzodiorite

The dikes and sills of this unit are unequivocally calk-alkalic (Zr/Y > 4.5, Th/Yb > 0.8; Fig. 4.4C; Ross and Bédard, 2009) and intermediate in composition (SiO_2 = 58.24 wt. %; Zr/TiO_2 = 160.30; Figs. 4.4A-B), which is consistent with the high abundance of quartz. They show low TiO_2 (= 0.801 wt %), Y (= 14.06 ppm), and transition elements such as V (= 106.8 ppm), Cr (= 70.0 ppm), Co (= 18.6 ppm). Interestingly, the contents in Ni are found clustering into two groups, one between 31.1 and 51.0 ppm, another one between 91.0 and 117.6 ppm. Samples with high Ni values were collected near (<2 m) the massive sulfide and the high values are possibly due to cross-cutting remobilized sulfide-rich stringers (Pilote et al., in review) containing Ni-rich phases, which have been observed in the massive and semi-massive sulfides (Brueckner et al., 2016). The rocks show LREE enrichment ($[La/Yb]_{pn}$ = 11.80) and strong negative Nb (Nb/Nb* = 0.64) and Ti (Ti/Ti* = 0.44) and positive Zr (Zr/Zr* = 3.02) anomalies on the primitive mantle-normalized diagram (Fig. 4.10D). On a Th-Zr-Nb diagram, this unit plots in the arc field (Fig. 4.7A; Wood, 1980). A sample of this unit yielded an $\varepsilon Nd_{(t)}$ value of +2.4 with a significantly lower $^{147}Sm/^{144}Nd$ ratio (= 0.1116) compared to other rocks of the cover sequence, which range between 0.1389 and 0.1901 (Table 4.3; Fig. 4.8).

4.5. Discussion

4.5.1. Petrogenesis of the FI- and FII-type Rambler Rhyolite formation: Evidence of deep melting and possible link to adakite

The FI- and FII-type geochemical signatures of the Rambler Rhyolite volcanic and volcaniclastic rocks (Lesher et al., 1986; Hart et al., 2004) are part of a four-fold classification of felsic rocks to discriminate potentially prospective vs. less prospective rocks. While originally created for VMS deposits in Archean belts, it has also proven to be applicable to many Proterozoic and Phanerozoic deposits (Lentz, 1998; Piercey, 2011). Briefly, FI- and FII-type rocks are typically moderately to strongly HREE- and Y-depleted with high $[La/Yb]_{cn}$ and Zr/Y ratios and are interpreted to represent products of deep (≥30 km) to intermediate (10-15 km), low temperature (~650 to ~1000°C), low degree partial melts where garnet and amphibole are stable in the residue (Lesher et al., 1986; Hart et al., 2004). In contrast, FIII- and FIV-types generally exhibit flat REE patterns ($[La/Yb]_{cn}$ = 0.2-5), higher Y content, significantly more pronounced negative Eu/Eu* anomalies, and considered to have formed at much shallower (<10 km; ~0.75-0.1 GPa) depths at high solidus temperatures (>1000°C) where plagioclase is stable in the residue. In general, previous workers have suggested that "tholeiitic" rocks of FIII and FIV affinity are more prospective for VMS formation because the melts are generated at higher crustal levels generally reaching the subvolcanic to volcanic environment with their heat intact, and are generally reflective of an environment with an elevated geothermal gradient at shallow levels in the crust (e.g., Lesher et al., 1986; Lentz, 1998; Hart et al., 2004; Piercey, 2011). In contrast, "calc-alkalic" FI and FII felsic rocks are

interpreted to be less prospective because they form at deeper levels in the crust and reflect colder melts that rarely reach the near surface environment with their heat of fusion intact (e.g., Lesher et al., 1986; Lentz, 1998; Hart et al., 2004; Piercey, 2011).

The Rambler Rhyolite formation shows strong depletions in HREE and Y, high $[La/Yb]_{cn}$ and Zr/Y ratios, and lack of negative Eu/Eu* anomalies, suggesting that garnet and/or amphibole were stable in the residue during magma generation (Peacock, 1990) with the melts generated at depths greater than 15-30 km since garnet and amphibole preferentially partition HREE (and Y) and MREE, respectively. Moreover, the Rambler Rhyolite units 1.1 and 1.2 have systematically lower $[La/Yb]_{cn}$ and $[Gd/Lu]_{pn}$ ratios relative to unit 1.3 (Table 1), which suggests that amphibole was present in the residue during melting during formation of unit 1.3, whereas garnet was likely present in the residue during the formation of units 1.1 and 1.2. Although this can be readily observed in Figure 4.6B, the overall geochemical and isotopic variations between units 1.1 to 1.3 are nonetheless minimal on the broader scale. The predominantly FI- to FII-type felsic volcanic rocks hosting the Ming VMS deposits are in stark contrast with conventional wisdom for the prospectivity of VMS-related felsic volcanic rocks, despite having a significant resource of Cu and Au.

Interestingly, many of the geochemical characteristics of FI-type felsic volcanic rocks hosting massive sulfides at Ming are similar to adakite-like rocks that are host to many world-class porphyry Cu-Au(±Mo) deposits (e.g., Defant and Kepezhinskas, 2001; Mungall, 2002). Adakites and adakite-like rocks are generally intermediate to felsic (≥56 wt % SiO_2) arc magmas with high Sr/Y (≥20), La/Yb (≥20), Al_2O_3 (≥15 wt %), Ni (≥20

ppm), Cr (≥30 ppm), and low Y (≤18 ppm) and Yb (≤1.9 ppm) (e.g., Defant and Drummond, 1990; Drummond et al., 1996; Sajona and Maury, 1998; Richards and Kerrich, 2007; Castillo, 2006; 2012). The high LREE/HREE and Sr/Y ratios found in the Rambler Rhyolite and in adakite-like rocks has been interpreted by Defant and Drummond (1990) to reflect partial melts from young (<25 m.y.) hydrated subducted oceanic crust(±sediments) that undergoes amphibolitization and/or eclogitization (garnet-amphibole-pyroxene-oxide-dominated assemblage) leading to Sr enrichments due to the lack of plagioclase in the residue, and Y and HREE depletion due to amphibole and/or garnet in the residue. The proposed link between slab-melts and adakites was re-evaluated by Richards and Kerrich (2007) and Richards (2011) and these authors favor an alternative model where adakite-like compositions can form in mature oceanic arcs or continental arcs due to: 1) fractionation of or equilibration in primitive basaltic arc magmas with mantle or lower crustal garnet that stall at density barriers in the mantle wedge or within the thickened crust; 2) contamination of primitive basaltic arc magmas with deep crustal garnet amphibolites; and/or 3) fractionation of hornblende±titanite±zircon during primitive basaltic arc magma ascent. Richards and Kerrich (2007) and Richards (2011) have argued that the adakitic signatures and processes above occur in evolved arcs with oceanic and/or continental crust that exceed 20-30 km in thickness. In light of the architecture of the of the Baie Verte oceanic tract, it seems highly unlikely that a crustal thickening model would work for the adakite-like signatures present in the Rambler Rhyolite formation. In particular, the ophiolitic host rocks of the Baie Verte Peninsula are relatively thin (Bédard et al, 2000; Skulski et al.,

2015). Even exposed serpentinized ultramafic rocks and the most complete ophiolitic section in the Betts Cove Complex contains no more than 4-5 km of coeval sheeted dikes and associated low-Ti and boninitic flows (Dunning and Krogh, 1985; Bédard et al., 2000; Skulski et al., 2015). Correspondingly, a crustal thickening model for forming the adakitic signatures does not seem to be consistent with observed geological thicknesses of units on the peninsula. In addition, regional tectonics models for the Baie Verte oceanic tract argue that this area underwent Cambrian-Ordovician arc rifting and extension with crustal thickening related to obduction only occurring after VMS formation (e.g., Bédard et al., 1998; van Staal et al., 2007; Pilote et al., in review). Finally, the restricted variation of the incompatible elements within and between units 1.1 to 1.3, the absence of negative Eu/Eu* anomalies, and the lack are of intermediate volcanic rocks in the Pacquet complex and throughout the peninsula suggests that the felsic volcanic rocks are unlikely the product of magmatic differentiation (e.g., crystal fractionation; Shukuno et al., 2006). Correspondingly, the Richards and Kerrich (2007) and Richards (2011) models for the genesis of adakite-like melts, while certainly explaining adakite-like signatures present in porphyry Cu-Au systems, are not consistent with geological and petrological features in the Baie Verte oceanic tract, and cannot explain the garnet and amphibole control on FI-type melt of the Rambler Rhyolite formation. Thus, it appears that a slab melting model might be more appropriate for explaining the origin of these FI- and FII-type rhyodacite with high $[La/Yb]_{cn}$ ratios and low Y values that are host to the Ming deposit.

4.5.2. Petrogenesis of the Rambler Rhyolite formation

Given the spatial and temporal coexistence of boninites, low-Ti tholeiites, and felsic volcanic rocks in the Ming area (Piercey et al., 1997; Skulski et al., 2010; 2015), one could postulate that the depleted HFSE and REE nature of the Rambler Rhyolite are, or in part, are the result of partial melting and/or differentiation of their immediately underlying boninitic/low-Ti tholeiitic crust. The constraints established above on the posited depth (i.e., garnet stability zone) at which melting had to occur to generate high $[La/Yb]_{cn}$ and low Y rhyodacite argue against a possible petrogenetic linkage between the Rambler Rhyolite and its underlying boninitic and low-Ti lower crust since the Baie Verte oceanic tract has insufficient crustal thickness, and shows no evidence of crustal thickening during its evolution that could have otherwise involved intracrustal melting (Bédard et al., 1998). In addition to the arguments provided in the previous section of this paper, a slab melt origin for the FI-FII Rambler Rhyolite felsic rocks is also favoured because of: 1) the presence of arc signatures in the spatially and temporally associated mafic volcanic rocks suggesting subduction zone magmatism to explain the geochemistry of the Baie Verte oceanic tract at the time of its formation (Bédard et al., 1998; Bédard, 1999; Bédard and Escayola, 2010; Piercey et al., 1997; Skulski et al., 2010; 2015); and 2) the required derivation from deep melting where the source would have contained a garnet-bearing residue to account for the HREE-Y depletions, and enrichments in Sr and other LREE.

To further examine the hypothesis of a slab-derived melt at Ming, REE and HFSE of units 1.1 to 1.3 are tested as a function of potential source compositions and depth of

melting (Fig. 4.11), as inferred from minerals present in the residue during melting, using the equilibrium partial melting (modal) equation of Shaw (1970):

$$C^l = C^o/(D_o + F[1 - D_o]) \quad (1)$$

where C^l and C^o are the concentration of an element in the melt and residual solid, respectively, F is the weight fraction of the melt produced, and D_o the bulk partition coefficient of the element in the original solid. Because of the absence of, or the inaccessibility to, samples representative of the subducted crust, assumptions have to be made on the metamorphic mineral assemblages present at depth during crust anatexis. As such, three residual assemblages with different mineral proportions are used in the calculations, together with mineral-melt partition coefficients typical of adakite-like melting assemblages (Martin, 1987; Sajona et al., 2000; Bourdon et al., 2002), including: 1) garnet amphibolite (53% hornblende; 20% plagioclase; 15% garnet; 10% clinopyroxene; 2% ilmenite); 2) amphibolite (68% hornblende; 25.5% plagioclase; 5% clinopyroxene; 1.5% ilmenite); and 3) eclogite (50% garnet; 50% clinopyroxene) (Fig. 4.11). In both hornblende-rich residual assemblages, the high abundances of residual plagioclase could account for the sub-adakitic Sr values (≥400 ppm). However, given the high mobility of Sr during hydrothermal alteration (e.g., Jenner, 1996), it is possible that the Sr abundance is underestimated for units 1.1 to 1.3, even for the least-altered samples, and therefore, Sr cannot be considered as a reliable discriminant. The first inferred source modeled was an N-MORB (Sun and McDonough, 1989), typical of oceanic crust being subducted and often considered the source for slab-derived adakite (e.g., Sajona et al., 2000; Bourdon et al., 2002). On modelled curves, the La/Yb ratios of unit 1.3 are

intermediate between eclogite and garnet amphibolite ranging between 5-30% partial melting, whereas unit 1.1/1.2 produces a horizontal array, at constant La/Yb, intersecting the same modelled curves as unit 1.3 at degrees of melting ranging between 30-40% (Figs. 4.11A and C). In Figure 4.11E, we represent melt models for a broader suite of trace elements, including the residual garnet amphibolite at 3%, 5%, and 10% partial melt. Although the model generally recreates most natural values for Ti and Y at low degrees of partial melts (≤10%), significant differences exist for most trace elements (Fig. 4.11E). With the exception of Th, using an N-MORB source, most elements are overestimated by our model and therefore does not appear to be a suitable source for melting. Given the overestimation using a MORB source, it requires a source with overall lower HFSE, REE, and higher Th abundances. These requirements can be accommodated by instead melting a slightly more depleted source with the composition of an island arc tholeiite. The nearby Mount Misery Formation, which has been geochemically characterized by Bédard (1999), is dominated by island arc tholeiitic flows of Cambrian age and thus, represents a reasonable analogue for our required modelled source composition. We applied the same model above but using the average values of least-altered (i.e., low LOI, Na_2O = 2-5 wt %) islands arc tholeiites of the surrounding Mount Misery Formation (Bédard, 1999). In this case, the trace element signatures from unit 1.3 can be explained by 1-10% partial melts of a garnet amphibolite curves, whereas samples of units 1.1 and 1.2 can be explained by roughly 20-30% partial melting (Figs. 4.11B, D). On an extended-element plot (Fig. 4.11F), with the exception of the modeled MREE that show slightly higher values, melting an island arc tholeiitic source provides a better fit to

the Rambler Rhyolite samples, and lower degrees of partial melting than N-MORB sources.

There are slight variations in the model results. In particular, the listric-shaped trace element patterns and lower LREE contents of units 1.1 and 1.2 relative to the linear slopes of unit 1.3, are suggestive of a greater amphibole control on their melt (Figs. 4.7A, B and 4.11E, F; Table 4.1) since amphibole preferentially partitions MREE and HREE (i.e., $D_{Dy}>D_{Yb}>D_{La}$). Accordingly, the variations in array shown in in Figures 4.11A-D between units 1.1 to 1.3 likely reflects the heterogeneity of the garnet-amphibole-clinopyroxene proportions during melting of an island arc tholeiitic source. The results above have attempted to quantify the specific degree of partial melting involved during slab anatexis, it is often difficult to model in ancient sequences. Nevertheless, the results presented herein and the ≤30% slab partial melt values are similar to models of adakite formation under hornblende eclogitic conditions (Tsuchiya and Kanisawa, 1994), and overlaps the optimum conditions for siliceous melt segregation from a garnet- and hornblende-bearing basaltic protolith (Rapp, 1995).

Rising felsic magmas will likely interact with the mantle wedge and/or overriding crust and often results in Ni-Cr enrichments in the felsic rocks (Frey et al., 1978; Kay, 1978; Sen and Dunn, 1994; Drummond et al., 1996; Martin, 1999; Smithies, 2000). Nickel and Cr typically partition into ferromagnesian minerals (e.g., olivine, orthopyroxene, and hornblende) and Kelemen (1995) suggested that when slab melts interact with the mantle wedge they can dissolve olivine and/or react with the wall rock resulting in Ni-Cr enrichments in the felsic rocks. The high average Ni and Cr (adakitic)

values in units 1.1 to 1.3 at Ming (Table 4.1) relative to normal intermediate to felsic volcanic rocks from island arcs (~9 ppm Ni, ~21 ppm Cr; Drummond et al.,1996) are additional indicators of potential slab melting and melt-mantle interaction; however, further work is needed to test these processes more fully.

An alternative process for the generation of slab-derived melt in juvenile (<10 m.y.) and thin (<15 km) oceanic arc environments was proposed by Macpherson et al. (2006) in which ascending basaltic arc magma derived from slab-dehydration could pond at thermal or rheological boundaries at or below the Moho or within the mantle (≥30 km; i.e., garnet stability field) and undergo fractional crystallization of a garnet-bearing residual assemblage to produce adakite-like magmas. Although we agree with the possibility of thermal and/or rheological boundaries existing beneath some thin arcs (e.g., Stratford and Stern, 2004), it is very difficult to prove their existence in ancient orogenic belts, such as the Appalachians, given the absence of preserved sections of the deeper mantle. Despite the latter, the restricted geochemical variations within the felsic units at Ming and the absence of intermediate rocks do not support crystal fractionation as a viable magmatic process to generate the FI(±FII)-type rhyodacite at Ming and hence, argue against any types of protracted magma ponding below the crust.

The slab melt model also potentially explains rocks that precede the formation of the Rambler Rhyolite and the isotopic systematics of the BVOT. Bédard (1999) estimated that the Betts Cove boninitic rocks, which are similar to those underlying the Rambler Rhyolite, had a small (<0.25%) contribution derived from the subducted slab and was identified as a mixture of hydrous phases, sediments, and/or slab-melts (i.e., adakite).

Moreover, slab derived melting has been advocated for the genesis of boninites, globally (Pearce et al., 1992; Pearce and Parkinson, 1993). It is a difficult problem, however, to discriminate between the relative involvements for each component, if all are contributing in the generation of boninite (e.g., Bédard, 1999). An input of material such as Laurentian-derived sediments, which can be isotopically evolved ($\varepsilon Nd_{(560)}$= -7.7 from a sample of psammite; van Staal et al., 2013), could explain the relatively evolved $\varepsilon Nd_{(t)}$ values in the boninites (+0.7 to +3.9) from Betts Cove, which would have been influenced by slab melts, as opposed to their coeval island arc tholeiites (+5.2 to +8.0), where were likely derived predominantly from the mantle wedge (Fig. 4.8; Swinden et al., 1997; Bédard, 1999). For the Rambler Rhyolite formation, a crustal contribution is unambiguous as it exhibits relatively low $\varepsilon Nd_{(t)}$ values (-2.5 to -1.1). Moreover, Skulski et al. (2015) reported the inheritance of zircons of 1.1Ga and 2.5Ga from a sample collected near the historical Rambler mine (Fig. 4.2). It is, however, difficult to assert with certainty this crustal input to result from a direct bulk sediment influx within the slab-derived melts or by high level contamination within the arc crust. The lack of any field evidence for an underlying old and evolved crust (e.g., Laurentian margin or Dashwoods) beneath the Baie Verte oceanic tract favours derivation of continental material via slab melting. The low $\varepsilon Nd_{(t)}$ values in the Rambler Rhyolite together with the inherited zircon patterns are consistent with Laurentian-derived sediments reported by van Staal et al. (2013).

To summarize, we propose that the units 1.1 to 1.3 hosting the Ming VMS deposit result from low (≤10%; unit 1.3) to moderate (~30%; units 1.2/1.3) degree of partial

melting of a sediment-rich/hydrated subducted oceanic crust composed of island arc tholeiites undergoing amphibolite to eclogite metamorphism at depths exceeding 30 km. Melting with a garnet-amphibole-rich residual solid produced a high $[La/Yb]_{cn}$, Sr/Y, Zr/Y, and low Y, FI- to FII-type rhyodacite with geochemical characteristics that resemble greatly adakites found in many active margins (Defant and Drummond, 1990).

4.5.3. Zircon saturation temperature

Despite the multiple attempts made during the course of this study to extract zircons from a quartz-bearing felsic tuff located immediately below the massive sulfide lens of the 1807 Zone, no grains were yielded. The lack of zircons in the sample collected may be due to: 1) the undersaturation of Zr in the melt (Hanchar and Watson, 2003); and/or 2) rapid cooling inhibiting nucleation of zircons and subsequent growth. Assuming low temperatures (~650-700°C) for melt generation at Ming, only a small concentration (~50 ppm) of Zr is required to reach zircon saturation in the felsic melt, irrespective of the alkalinity of the melt (Watson and Harrison, 1983). Except for rocks of unit 1.3, where concentrations reach up to 90 ppm Zr, all samples of units 1.1 and 1.2 range between 40 and 70 ppm Zr, which are near or above the saturation curve of Watson and Harrison (1983). Skulski et al. (2010; 2015) found a small number of zircons and reported an unpublished U-Pb (SHRIMP) crystallization age of 487±4 Ma with Grenvillian inheritance (1.0-2.4Ga), southwest of the Rambler deposit (sample location in Fig. 4.2). For the sake of the argument, assuming that the sample collected at the Ming deposit was

in fact saturated, but cooling inhibited nucleation of zircon grains, saturation thermometry can be calculated using the following solubility model

$$\ln D_{Zr}^{zircon/melt} = (-3.80 - [0.85(M-1]) + 12900/T \quad (2)$$

of Watson and Harrison (1983) and adapted by Hanchar and Watson (2003), where $D_{Zr}^{zircon/melt}$ is the concentration ratio of Zr in zircon and in the melt, *M* is the cation ratio or alumina saturation factor for the rock (Na+K+2·Ca)/(Al·Si), and *T* is temperature in Kelvin. Results of these calculations are shown in Figure 4.12 with zircon saturation temperature (T_{Zr}) ranging from 615°C to 730°C, which is the same temperature range as has been inferred for the genesis of FI-type felsic magmas, globally (Hart et al., 2004; P-T conditions and source compositions based on experimental work by Spulber and Rutherford, 1983; Beard and Lofgren, 1991; Wyllie and Wolf, 1993; Rapp, 1995). When Nb (also considered as a proxy for HFSE) is plotted against T_{Zr}, a positive covariation exists between the two variables, with minor exceptions (Fig. 4.12A). Samples from units 1.1 and 1.3 are restricted to the higher spectrum of the temperature range, whereas unit 1.2 shows a wide range of temperatures. Except for a few outliers, a positive relationship similar to this is observed at the Wolverine VMS deposit, Yukon, and was interpreted by Piercey et al. (2008) as the result of higher temperature at the melting source accommodating greater amounts of REE and HFSE in the resulting melt. The latter also implies that a smaller degree of partial melting occured for samples with high T_{Zr} and Nb values (Hanchar and Watson, 2003; Piercey et al., 2008 and references therein).

By evaluating the relationship between T_{Zr} and the stratigraphic position at which the samples were collected relative to the massive sulfide horizon (DTMSH; Fig. 4.12B),

an abrupt temperature change exists between unit 1.1 (i.e., the deepest unit of the Ming deposit) and the base of unit 1.2, which shows a systematic increase of temperature with decreasing depth (or DTMSH), reaching a maxima (together with unit 1.3) near or at the contact with the mineralized horizon. This implies that the initial eruption of the volcaniclastic lithofacies (unit 1.2) during or after subsidence of the domal structure (unit 1.1) and development of the nested basin (Pilote et al., in review) was formed by low temperature melts (~620-650°C; low partial melting) and progressively became hotter (~700-730°C; greater partial melting) until onset of the VMS-forming hydrothermal circulation system. Accordingly, this rising temperature of melts (and probably concomitant rising of the geothermal gradient) likely became the driving mechanism for hydrothermal circulation (e.g. Franklin et al., 2005) and the formation of the Ming VMS deposit.

4.5.4. Petrogenesis of the cover sequence and relationships to post-mineralization dikes

The base of the cover sequence (lower 200 m) consists of multiple flows and epiclastic to volcaniclastic accumulations of distinct geochemical and isotopic affinities. Some of the mafic to intermediate sills and dikes that intrude the Ming deposit share geochemical signatures with the extrusive rocks that suggest comagmatic relationships. As such, based on their magmatic and tectonic affinities (Figs. 4.4C and 4.7), incompatible element ratios (Table 4.1), and trace element patterns (Figs. 4.6, 4.9, and 4.10), three intrusive-extrusive assemblages are discriminated, including: 1) low Nb/Yb

tholeiitic gabbro and Th-enriched back-arc basin basalt; 2) intermediate Nb/Yb tholeiitic gabbro and enriched mid-ocean ridge basalt; and 3) transitional diorite and sulfide-rich mafic breccia and high-Mg basalt. Because the transitional diorite shows evidence of differentiation (La = 8.4-15.1 ppm; Mg# ~18 to 53) at near constant La/Sm (~3), it overlaps both the high-Mg basalt (Mg# ~45-53) and sulfide-rich mafic breccia (Mg# ~19-36). In the case of the calc-alkalic porphyritic quartz monzodiorite, its Th- and LREE-enrichment is beyond any other units discussed here and therefore is likely unrelated to rocks from the base of the cover sequence. These calc-alkalic rocks, nonetheless, form only a minor proportion of all the intrusive units at the Ming deposit (Pilote et al., in review).

On an extended element plot, the Fe-shale shares similar patterns with its nearby high-Mg basalt and sulfide-rich mafic breccia (Fig. 4.6C, D), suggesting that the sediments are likely derived from these proximal surrounding units. Inter-element ratios such as Co/Th and La/Sc can be used to determine the bulk composition of the source (Fig. 4.13A) as they are generally immune to secondary processes (e.g., metamorphism; Condie and Wronkiewicz, 1990). The results show congruent ratios to the underlying and overlying units (Table 4.1) and to the average oceanic island-arc tholeiitic basalts of Kelemen et al. (2003). On Th-Zr-Sc and Th-La-Sc discrimination diagrams (Fig. 4.13B-C) of Bhatia and Crook (1986), samples of the shale plot in the oceanic island-arc field, consistent with the juvenile arc signature of the adjacent rocks. The Fe-shale, however, exhibits significantly higher $\varepsilon Nd_{(t)}$ (+3.1 to +5.5) than the other two units (-0.5 to +1.6),

which indicates that the high-Mg basalts and sulfide-rich mafic breccia are not the exclusive sources and therefore, requires a more juvenile input during deposition.

The sulfide-rich mafic breccia, Fe-shale, high-Mg basalt, LREE-enriched/low-Ti tholeiitic tuff, and transitional diorite all show enrichment in Th and depletion in HFSE (Nb, Y) and HREE, signatures typically associated with arc-derived magmas (Tatsumi, 1989), which is supported by their inter-element ratios (Figs. 4.6 and 4.7). In all of these rocks, an evolved crustal contribution at the source and/or during magma ascent is evidenced by their $\varepsilon Nd_{(t)}$ values near the chondritic uniform reservoir ($\varepsilon Nd = 0$) (Table 4.3; Fig. 4.8). On primitive mantle-normalized plots (Figs. 4.6, 4.9, and 4.10), their patterns compare to island-arc tholeiites from other ancient systems (Jenner, 1996; Piercey, 2010). Above the high-Mg basalts and intercalated with the LREE-enriched/low-Ti tholeiitic tuffs are multiple successions of mafic flows from depleted mantle sources ($\varepsilon Nd_{(t)} = +6.6$ to $+7.3$), including Th-enriched back-arc basin basalts and enriched mid-ocean ridge basalt (Fig. 4.9). This transition indicates variability in the sources and processes, and the dynamism in the Cambro-Ordovician subduction complex (e.g., Pearce and Peate, 1995).

Incompatible element ratios such as Th/Yb and Nb/Yb (Fig. 4.14A) are used to assess the mantle composition (e.g., depleted vs fertile), the potential involvement of slab-derived components (e.g., melts, fluids), and/or degree of partial melt controlling the derived melt composition (Pearce et al., 1995; Pearce and Peate, 1995; Peate and Pearce, 1998; Pearce, 2008). For basaltic melts of oceanic realms where the mantle source has not been affected by the addition of subduction-related material, they should plot along the

MORB-OIB array on a Th/Yb vs Nb/Yb plot (Fig. 4.14A), where Nb/Yb reflects the incompatible element enrichment of the mantle source. Dynamic (or continuous) melting (Langmuir et al., 1977) and/or melting of heterogeneous mantle compositions (e.g., E- and N-MORB) will displace the resulting melt parallel to this array since Th and Nb behave similarly during melting (i.e., both are highly incompatible elements; Pearce et al., 1995). Because Th is highly soluble in fluids derived from the dehydration of the subducted slab (as opposed to Yb), a Th-enrichment in the mantle wedge will result in melts with higher Th/Yb ratios. Other types of crustal contribution (slab-derived melt, subducted sediments, overriding crustal contamination) can also influence Th/Yb ratios, thus shifting samples above the MORB-OIB array. With the exception of two samples from the intermediate Nb/Yb tholeiitic gabbro, all units above the massive sulfides at Ming plot above the MORB-OIB array (Fig. 4.14A), indicating a crustal or slab input within a subduction setting. Moreover, most units show a horizontal spread. One possible explanation for this wide range in Nb/Yb at near constant Th/Yb includes the addition of crustal material into a heterogeneous mantle wedge undergoing progressive melting (Pearce et al., 1995; Peate et al., 1997). The two samples from the intermediate Nb/Yb tholeiitic gabbro that plot inside the array show, however, a compositional trend that can be traced from near a primitive mantle value, increase to higher Th/Yb at constant Nb/Yb, and finally vary parallel to and slightly above the MORB-OIB array (Fig. 4.14A). Note that, the extrusive equivalent of the gabbro, the enriched mid-ocean ridge basalt, shows a similar pattern (Fig. 4.14A). Interestingly, the first enriched mid-ocean ridge basalt that reaches surface in the Ming area (Fig. 4.9) plots higher on the slope (Fig. 4.14A), whereas

the stratigraphically higher flow plots with lower ratios (samples from this unit collected beyond the 200 m also show the same systematic decrease in Th and Nb against Yb). This magmatic evolution from high to low Th and Nb against Yb, which is likely mirrored by the comagmatic gabbroic dikes, is best explained by the increase of degree of melting of an enriched mantle source (Pearce and Peate, 1995; Peate and Pearce, 1998; Pearce, 2008), possibly pre-enriched by Th-rich fluids derived from the subducted slab and/or Th-rich melts.

The depth and changes in degree of partial melting can also be evaluated using the TiO_2/Yb vs. Nb/Yb projection of Pearce (2008). This plot is meant as a proxy for melting depth and is typically used for samples unaffected by crustal contamination (Th/Nb < 0.2) and/or oxide fractionation (Ti/Ti* ≈ 1), i.e., samples that plot inside the MORB-OIB array in the Th/Yb vs. Nb/Yb diagram (Fig. 4.14B). Ocean island basalts (OIB) have high TiO_2/Yb and Nb/Yb ratios because of the presence of residual garnets and low degree of partial melting. Any MORB affected by an OIB (e.g., plume-ridge interaction) or OIB-like rocks should display a diagonal or positive trend. Pearce (2008) also demonstrated that variations in partial melting should be reflected by diagonal trends, although less pronounced at pressures ≤2 GPa. Whereas almost all samples of the cover sequence plot outside the MORB-OIB array (Fig. 4.14A), they show systematically high TiO_2/Yb ratios regardless of Nb/Yb (Fig. 4.14B) without positive correlations leading to the OIB field. This argues against the presence of an OIB source in the mantle wedge and deep level melting (low degree of partial melt), which is supported by the lack of alkalic end member magmas in the area, and it is consistent with the conclusions from Bédard (1999)

for the lower stratigraphic successions. One viable explanation for this Ti-enrichment is the metasomatism of the mantle wedge by slab-melt during the building of the Rambler Rhyolite formation. This early hybridization process from siliceous melts is commonly thought to form zones enriched in Ti-hosting minerals, such as amphiboles and/or titanium-bearing oxides in the peridotite, which become unstable during subsequent melting (e.g., Arculus and Powell, 1986; Ryerson and Watson, 1987; Kepezhinskas et al., 1996; Sajona et al., 1996; 2000). The same process of hybridization has been proposed by many workers as a prerequisite for the formation of high-Mg basalts and andesites in adakite-endowed regions (Kay, 1978; Saunders et al., 1987; Tatsumi, 2006) and could be responsible for the high Mg values in the high-Mg basalt at the base of the Snooks Arm Group.

4.5.5. Implications on the evolution of the Baie Verte oceanic tract

The evolution of the Baie Verte oceanic tract (e.g., Bédard et al., 1998; Bédard, 1999; van Staal et al., 2013) is interpreted to reflect sea-floor spreading in a peri-continental supra-subduction zone based on the petrological assemblages present in the Betts Cove ophiolite and regional equivalents, which are commonly restricted to fore-arc environments (Stern and Bloomer, 1992; Bédard et al., 1998; Bédard, 1999; Stern, 2004). Despite remaining uncertainties on the timing of events prior to and during the obduction of the Baie Verte oceanic tract, the most recent tectonic models (van Staal et al., 2013; Castonguay et al., 2014) suggests the following: 1) west-vergent (present coordinates) subduction at ca. 510-505 Ma of oceanic crust (Taconic seaway) that separated Laurentia

from the Dashwoods block, forming the supra-subduction zone-related Lushs Bight oceanic tract; 2) incomplete closure of the Taconic seaway led to the eastward obduction of part of the Lushs Bight oceanic tract onto the Dashwoods block at ca. 495 Ma; 3) subsequent nucleation of an east-vergent subduction of the remnant Lushs Bight oceanic tract, outboard of the Dashwoods block led to the development of the supra-subduction Baie Verte oceanic tract at ca. 495-490 Ma (Fig. 4.15); and 4) a westward obduction of the Baie Verte oceanic tract on the Laurentian margin at ca. 479 Ma and shortly after the establishment of a back-arc spreading system generating tholeiitic and calc-alkalic volcanism in the cover sequence (i.e., Snooks Arm Group) (Bédard et al., 2000; Cousineau and Bédard, 2000; Kessler and Bédard, 2000; Skulski et al., 2010). Petrogenetic modeling of the Rambler Rhyolite, and petrogenetic and stratigraphic relationships in cover sequence rocks, provides critical tests and implications for the model outlined above. Firstly, the modeling of the Rambler Rhyolite suggests that the source region for the rhyolites must have had an island arc tholeiite signature, but also the high $[La/Yb]_{pn}$ ratio requires that the source be present at depth with residual garnet and amphibole. At the time of formation there is ample evidence stratigraphically to suggest that the fore-arc was under extension and the Rambler Rhyolites were forming in volcanic/volcaniclastic basins that were extending with no evidence for crustal thickening (Pilote et al., in review). Correspondingly, this requires a source that maintained the depth of melting where garnet and amphibole were stable and the source requirement for island arc tholeiite. These requirements can be accommodated in light of recent models for closure of the Taconic Seaway. As mentioned above, the nucleation of an east-vergent

subduction may have entrained crust at depth of the Lushs Bight oceanic tract to become the (fluid and melt) source for the Baie Verte oceanic tract. To test this, the average composition of island arc tholeiites from the uppermost section of the Lushs Bight ophiolite (Kean et al., 1995) are plotted in Figure 4.16 and their modelled composition after 10% partial melting from a garnet amphibolite are calculated applying the same method above. The resulted compositions are not only consistent with units 1.1 and 1.1/1.2 but show better fits than the Mount Misery Formation. The implication here is that the subduction of an island arc tholeiite necessitates the pre-existence of a subduction complex in the reverse direction (Fig. 4.15), hence a polarity flip, which corroborates with the tectonic reconstructions of Zagorevski and van Staal (2011), van Staal and Barr (2012), van Staal et al. (2013), and Castonguay et al. (2014).

The association between boninite and adakite, as in the Pacquet complex is not uncommon. Their coexistence has been reported in ancient (Polat and Kerrich, 2001; 2004; Ishiwatari et al., 2006; Niu et al., 2006) and modern day (Falloon et al., 2008; Li et al., 2013) oceanic arc systems. Whereas boninite can form in peri-continental rifting (Piercey et al., 2001), in juvenile oceanic settings such as the Izu-Bonin-Mariana-Tonga trench and the Baie Verte oceanic tract, most boninites (and associated adakites) are generally accepted to form shortly after subduction initiation (Pearce et al., 1992; Stern, 2004; Ishizuka et al., 2006; 2011; Reagan et al., 2010). The resulting extension of the overriding crust from the sinking slab enables ascending asthenospheric mass transfer to undergo significant partial melting (~20-30%), and hence produce N-MORB melts (with lherzolitic residual). Subsequent melting of this refractory mantle would form boninite

(with harzburgitic residual). Unless a pre-depletion event occurred prior to subduction, in which case boninite melts would form first and predominate the base of the newly formed crust. Based on the geology and the nature of the Betts Cove Complex (Bédard et al., 1996, 2000; Skulski et al., 2015), Bédard (1999) has favored the latter for its formation. Shortly after (<5 m.y.), the juxtaposition of hot mantle with hydrated, young, and hot oceanic crust undergoing amphibolite to eclogite metamorphism allows the subducted slab (and its overlying sediments) to partially melt (at ~650-750°C), leaving a garnet-amphibole-rich residua. The melt interacts with the mantle wedge (high Ni, Cr) to finally extrude as a highly fractionated (or adakite/FI-type) felsic rock, with characteristics that are shared with the Rambler Rhyolite formation (Fig. 4.15).

The Snooks Arm Group was interpreted by previous work as an arc (Snooks Arc arc) developed on and during the obduction of the Baie Verte ophiolite (Bédard et al., 2000). The sediment at its base is viewed as the disconformity that marks a change in the geodynamics of the Taconic Seaway, i.e., from fore-arc spreading to a compressional regime leading to the obduction of the ophiolite. Although the time gap between the formation of the Rambler Rhyolite (487 ± 4 Ma)/Mount Misery formations and the first pulse of volcanism overlying the shale is poorly constrained (Skulski et al., 2010), the presence of high-level tholeiitic basalts with primitive $\varepsilon Nd_{(t)}$ (+6.6 to +7.3) values indicates that extension had to continue in order to accommodate upwelling of mantle. However, Skulski et al. (2010) reported a polymictic conglomerate that overlies the Advocate Complex in the western part of the peninsula (Fig. 1) with lithologies and mineralogy suggestive of exhumation from obduction. Nonetheless, it is possible that

localized spreading from transtensional strike-slip movements occurred as some studies suggest a non-orthogonal plate convergence during closure of the Taconic seaway (Cawood and Suhr, 1992; Dewey, 2002). Regardless of the plate dynamics, the interstratification of arc- to non-arc-related rocks with variable Nd isotopic signatures at the base of the Snooks Arm Group reflects the heterogeneity of the mantle, which is a common trait in many evolving arc systems (e.g., Peate and Pearce, 1998). As subduction continued after the volcanic hiatus (deposition of the Fe-shale), slab-dehydration induced partial melting of the HFSE-enriched (TiO_2/Yb > 5) overlying mantle wedge, which led to the formation of the high-Mg basalts (and its intrusive equivalent) and LREE-enriched/low-Ti island arc tholeiite. Thinning of the refractory harzburgitic mantle (due to protracted spreading of the overriding crust) allowed mass transfer of N-MORB to E-MORB mantle material near the base of the crust. More geochronological constraints are needed in order to refine the timing of these pre- to syn-accretionary events.

4.5.6. Implications of high LREE/HREE felsic volcanic rocks on the nature and style of mineralization at the Ming Deposit

The lithogeochemistry of VMS-related felsic volcanic rocks is well documented (e.g., Lesher et al., 1986; Lentz, 1998; Yang and Scott, 2003; Hart et al., 2004; Gaboury and Pearson, 2008; Piercey, 2010, 2011). There has been considerable research into the petrogenetic evolution of magmas and their tectonic settings and how they influence deposit localization and genesis. Moreover, some authors have argued that magmas may directly contribute magmatophile elements (Au, Ag, Te, Se, Bi, Sn) to hydrothermal

fluids that form VMS at or near the seafloor (e.g., Urabe et al., 1983; Urabe, 1987; Lydon, 1996; Sillitoe et al., 1996; Hannington et al., 1999, 2005; Yang and Scott, 2003; Brueckner et al., 2014; 2016). The importance of a direct magmatic input in the Ming deposit has been documented mineralogically (Brueckner et al., 2014, 2016; Pilote et al., 2016). The contribution of magmatic fluids in modern deposits has been established in many cases (e.g., Sillitoe et al., 1996), but in the ancient record, the results are much less concrete and are often by inference (Lydon, 1996). Moreover, linkages between the magmatic evolution of a felsic magma and the precious metal enrichment of VMS deposits is in its infancy (e.g., Urabe, 1987; Urabe et al., 1995; Lydon, 1996; Yang and Scott, 2002; 2003). Recently, workers globally have illustrated that many Au-Ag-bearing deposits are hosted by strongly fractionated FI-type (+/- FII-type) felsic rocks (e.g., Bousquet mining district – Mercier-Langevin et al., 2007; Eagle-Telbel, Géant Dormant, and Duvan deposits – Gauthier et al., 2003; Gaboury and Daigneault, 1999; Tremblay et al., 1996). These authors, however, have not linked the petrogenetic histories of these magmas, nor their tectonic histories to the precious metal endowment present in the associated deposits. The results herein illustrate that it is possible that FI-type (+/- some FII-type) magmas may be associated with slab melting, and while previous studies have considered them less prospective (e.g., Lesher et al., 1986; Hart et al., 2004; Lentz, 1998; Piercey, 2011), these may be attractive targets for Au-Ag-rich VMS mineralization.

The question arises as to why felsic rocks associated with slab melting lead to Au-Ag-rich VMS mineralization. A potential solution to this comes from previous work by Mungall (2002), who presented a geochemical model where partial melting of subducted

ocean crust generates a highly fractionated melt, such as the Rambler Rhyolite (FI-/FII-types), that is highly oxidized. The fO_2 should be significantly greater in slab-derived melts than normal arc melts due to high Fe^{3+} content from sea-floor alteration and their carrying ability for ferric iron should be over 10^4 times more than that of dehydration fluids (Mungall, 2002). This high redox potential of the melts allows them not only to maintain sulfur in oxidized forms (Hamilyn et al., 1985), but to remove chalcophile elements (e.g., Ag, As, Bi, Cu, Se, and Te) from the mantle wedge during hybridization into the sulfide-undersaturated silicate melt. Metals remain in the melt until they are partitioned into the exsolved hydrothermal fluids. Although we agree that most arc magmas (by dehydration of slab melting) are H_2O-rich and represent an essential parameter to magmatic-hydrothermal ore-forming systems (Richards, 2011), in nascent arcs with boninite-adakite (FI/FII-types) associations, the higher fO_2 (redox state) from slab-melting may explain the Au-Ag endowment in ore-deposits, regardless of the magmatic water content. From their work on the LaRonde Penna Au-rich VMS deposit in Abitibi, Mercier-Langevin et al. (2007) recognized the hosting potential of FI-type rhyolite elsewhere and the results presented here provide a possible explanation for their enrichment in precious metals from a petrogenetic perspective. The boninite-adakite(FI-/FII-types) association observed in terranes as old as the Archean may therefore become an important geological assemblage for exploration for precious metal-rich VMS deposits.

4.6. Conclusions

The study of the felsic volcanic and volcaniclastic rocks that host the Ming VMS deposit in Newfoundland, using a variety of major, trace, and isotopic Sm-Nd systematics of least-altered rocks, suggests that their HREE and HFSE depletion (FI- and FII-type) were products of subducted slab-derived partial melts generated at relatively low temperatures (<750°C) where garnet and amphibole were stable in the residue. Although felsic successions have been observed in small amounts elsewhere on the peninsula, the Rambler Rhyolite formation is the result of a combination of optimal conditions (e.g., locally more hydrated crusts and/or higher geothermal gradient) to generate larger amounts of partial melting. Batch melting calculations using island arc tholeiite source suggests ~10% partial melting is sufficient to emulate the immobile trace element compositions of the Rambler Rhyolite formation. Moreover, slab melting was likely critical in generating magmas that are precious metals and other magmatophile element-enriched that exsolved magmatic fluids. Slab melting of island arc tholeiites in a subduction environment is consistent with recent tectonic reconstructions proposed by other workers for the Baie Verte oceanic tract. The magmas derived from these slab melting events have FI to FII affinities, often considered less prospective for VMS mineralization; however, this work has illustrated that FI- and FII-type felsic volcanic rocks may no longer be regarded as non-prospective for hosting VMS, and may be critical in the formation of Au-Ag-rich VMS deposits given the increasing numbers of recent studies reporting their associations with Au-Ag-rich VMS in Archean to Paleozoic successions.

The complex stratigraphic and geochemical relationships of the base of the overlying Snooks Arm Group suggest the extension of the overriding plate (evidenced by the presence of rift-related primitive tholeiitic rocks) while the contribution from the subducted slab continued (presence of evolved transitional to calk-alkalic rocks). The lack of geochronological constraints makes it difficult to determine the time span from the formation of the Ming deposit and the deposition of the volcanic rocks of the Snooks Arm Group. However, the lack of visible unconformity (let alone the presence of the thin Fe-shale sequence reflecting volcanic hiatus) and the interstratification of different volcanic units suggest that the onset of the Snooks Arm volcanism occurred shortly after the formation of the Ming deposit.

4.7. Acknowledgements

The authors would like to thank Larry Pilgrim, Paul Legrow, and staff of Rambler Metals and Mining Canada Ltd. for providing access to the underground workings, drill core, data, and samples; the miners who work or have worked at surface or underground for accommodating so generously despite the busy production schedule; Pam King, Sherry Strong, and Lakmali Hewu (now retired) of CREAIT at Memorial University of Newfoundland (MUN) for their technical support and guidance during the multiple stages of sample preparation and geochemical and isotopic analyses. We appreciate the technical support from and insightful discussions with S.M. Brueckner (Auburn University), J.M. Hanchar (MUN), G. Dunning (MUN), P. Mercier-Langevin (GSC), and T. Skulski (GSC). This research was funded by grants to S.J. Piercey, including an NSERC

Discovery Grant and the NSERC-Altius Industrial Research Chair in Mineral Deposits funded by NSERC, Altius Minerals Inc., and the Research and Development Corporation of Newfoundland and Labrador. This study was also funded in part by the Geological Survey of Canada's Volcanogenic Massive Sulphide Ore System of the Targeted Geoscience Initiative 4 (TGI-4) Program, led by J.M. Peter, whom we thank for support.

4.8. References

Arculus, R.J., and Powell, R., 1986, Source component mixing in the regions of arc magma generation: Journal of Geophysical Research, v. 91, p. 5913-5926.

Barrett, T.J., and MacLean, W.H., 1994, Chemostratigraphy and hydrothermal alteration in exploration for VHMS deposits in greenstones and younger volcanic rocks: Geological Association of Canada, Short Course Notes 11, p. 433-467.

Barrett, T.J., and MacLean, W.H., 1999, Volcanic sequences, lithogeochemistry, and hydrothermal alteration in some bimodal volcanic-associated massive sulfide systems: Reviews in Economic Geology, v. 8, p. 101-131.

Beard, J.S., and Lofgren, G.E., 1991, Dehydration melting and water-saturated melting of basaltic and andesitic greenstones and amphibolites at 1, 3 and 6.9 kb: Journal of Petrology, v. 32, p. 365-401.

Bédard, J.H., 1999, Petrogenesis of boninites from the Betts Cove ophiolite, Newfoundland, Canada: Identification of subducted source components: Journal of Petrology, v. 40, p. 1853-1889.

Bedard, J.H., and Escayola, M., 2010, The Advocate Ophiolite mantle, Baie Verte, Newfoundland; regional correlations and evidence for metasomatism: Canadian Journal of Earth Sciences, v. 47, p. 237-253.

Bédard, J.H., Lauzière, K., Sangster, A., Boisvert, E., Tellier, M., Tremblay, A., and Dec, T., 1996, Geological map of the Betts Cove ophiolitic massif and its cover rocks:

Geological Survey of Canada, Canadian Geoscience Map 3271, scale 1:20 000. doi:10.4095/208188

Bédard, J.H., Lauzière, K., Tremblay, A., and Sangster, A., 1998, Evidence for forearc seafloor-spreading from the Betts Cove ophiolite, Newfoundland: oceanic crust of boninitic affinity: Tectonophysics, v. 284, p. 233-245.

Bhatia, M.R., and Crook, K.A.W., 1986, Trace element characteristics of graywackes and tectonic setting discrimination of sedimentary basins: Contributions to Mineralogy and Petrology, v. 92, p. 181-193.

Bourdon, E., Eissen, J.-P., Gutscher, M.-A., Monzier, M., Samaniego, P., Robin, C., Bollinger, C., and Cotten, J., 2002, Slab melting and slab melt metasomatism in the Northern Andean Volcanic Zone : adakites and high-Mg andesites from Pichincha volcano (Ecuador): Bulletin de la Société Géologique de France, v. 173, p. 195-206.

Brueckner, S.M., Piercey, S.J., Sylvester, P.J., Pilgrim, L., Maloney, S., Hyde, D., and Ogilvie, G., 2011, Stratigraphy, mineralogy, geochemistry, and genesis of an Au-rich volcanogenic massive sulfide (VMS) system from the Baie Verte Peninsula, NW Newfoundland, Canada: The 1806 zone as an example from the Ming mine, Rambler Camp, in Deschenes, G., Dimitrakopoulos, R., and Bouchard, J., eds., World Gold 2011: Montreal, QC, Canada, Canadian Institute of Mining, Metallurgy and Petroleum, p. 899–911.

Brueckner, S.M., Piercey, S.J., Layne, G.D., Piercey, G., and Sylvester, P.J., 2015, Variations of sulphur isotope signatures in sulphides from the metamorphosed Ming Cu(−Au) volcanogenic massive sulphide deposit, Newfoundland Appalachians, Canada: Mineralium Deposita, p. 1-22.

Brueckner, S.M., Piercey, S.J., Pilote, J.-L., Layne, G.D., and Sylvester, P.J., 2016, Mineralogy and mineral chemistry of the metamorphosed and precious metal-bearing Ming deposit, Canada: Ore Geology Reviews, v. 72, p. 914-939.

Brueckner, S.M., Piercey, S.J., Sylvester, P.J., Maloney, S., and Pilgrim, L., 2014, Evidence for syngenetic precious metal enrichment in an Appalachian volcanogenic massive sulfide system: The 1806 Zone, Ming Mine, Newfoundland, Canada: Economic Geology, v. 109, p. 1611-1642.

Cabanis, B., and Lecolle, M., 1989, Le diagramme La/10–Y/15–Nb/8: un outil pour la discrimination des séries volcaniques et la mise en évidence des processus de mélange et/ou de contamination crustal. Comptes Rendus de l'Académie des Sciences, v. 309, p. 2023–2029.

Castillo, P.R., 2006, An overview of adakite petrogenesis: Chinese Science Bulletin, v. 51, p. 258-268.

Castillo, P.R., 2012, Adakite petrogenesis: Lithos, v. 134-135, p. 304-316.

Castonguay, S., Skulski, T., van Staal, C.R., and Currie, M., 2009, New insights on the structural geology of the Pacquet Harbour group and Point Rousse complex, Baie Verte peninsula, Newfoundland: Newfoundland and Labrador Department of Natural Resources, Geological Survey, Current Research, Report 09-1, p. 147-158.

Castonguay, S., van Staal, C.R., Joyce, N., Skulski, T., and Hibbard, J.P., 2014, Taconic metamorphism preserved in the Baie Verte Peninsula, Newfoundland Appalachians: Geochronological evidence for ophiolite obduction and subduction and exhumation of the leading edge of the Laurentian (Humber) margin during closure of the Taconic seaway: Geoscience Canada, v. 14, p. 459-482.

Cawood, P.A., and Suhr, G., 1992, Generation and obduction of ophiolites; constraints for the Bay of Islands Complex, western Newfoundland: Tectonics, v. 11, p. 884-897.

Cawood, P.A., van Gool, J.A.M., and Dunning, G.R., 1996, Geological development of eastern Humber and western Dunnage zones; Corner Brook-Glover Island region, Newfoundland: Canadian Journal of Earth Sciences, v. 33, p. 182-198.

Condie, K.C., and Wronkiewicz, D.J., 1990, The Cr/Th ratio in Precambrian pelites from the Kaapvaal Craton as an index of craton evolution: Earth and Planetary Science Letters, v. 97, p. 256-267.

Cousineau, P.A., and Bédard, J.H., 2000, Sedimentation in a subaqueous arc/back-arc setting; the Bobby Cove Formation, Snooks Arms Group, Newfoundland: Precambrian Research, v. 101, p. 111-134.

Defant, M.J., and Drummond, M.S., 1990, Derivation of some modern arc magmas by melting of young subducted lithosphere: Nature, v. 347, p. 662-665.

Defant, M.J., and Kepezhinskas, P., 2001, Evidence suggests slab melting in arc magmas: Eos, Transactions, American Geophysical Union, v. 82, p. 65.

DePaolo, D.J., 1981, Trace element and isotopic effects of combined wallrock assimilation and fractional crystallization: Earth and Planetary Science Letters, v. 53, p. 189-202.

Dewey, J.F., 2002, Transtension in arcs and orogens: International Geology Review, v. 44, p. 402-439.

Dewey, J.F., and Casey, J.F., 2015, The sole of an ophiolite; the Ordovician Bay of Islands Complex, Newfoundland; reply: Journal of the Geological Society of London, v. 172, p. 521-532.

Drummond, M.S., and Defant, M.J., 1990, A model for trondhjemite-tonalite-dacite genesis and crustal growth via slab melting; Archean to modern comparisons: Journal of Geophysical Research, v. 95, p. 21.

Drummond, M.S., Defant, M.J., and Kepezhinskas, P.K., 1996, Petrogenesis of slab-derived trondhjemite-tonalite-dacite/adakite magmas: Geological Society of America, Special Paper, v. 315, p. 205-215.

Dunning, G.R., and Krogh, T.E., 1985, Geochronology of ophiolites of the Newfoundland Appalachians: Canadian Journal of Earth Sciences, v. 22, p. 1659-1670.

Falloon, T.J., Danyushevsky, L.V., Crawford, A., Meffre, S., Woodhead, J.D., and Bloomer, S.H., 2008, Boninites and adakites from the northern termination of the Tonga Trench; implications for adakite petrogenesis: Journal of Petrology, v. 49, p. 697-715.

Franklin, J.M., Lydon, J.W., and Sangster, D.F., 1981, Volcanic-associated sulfide deposits, in Skinner, B. J., ed., Economic Geology Seventy-Fifth Anniversary Volume, p. 485-627.

Franklin, J.M., Gibson, H.L., Jonasson, I.R., and Galley, A.G., 2005, Volcanogenic massive sulfide deposits, in Hedenquist, J.W., Thompson, J.F.H., Goldfarb, R.J., and Richards, J.P., eds., Economic Geology 100th Anniversary Volume, p. 523-560.

Frey, F.A., Green, D.H., and Roy, S. D., 1978, Integrated models of basalt petrogenesis; a study of quartz tholeiites to olivine melilitites from South eastern Australia utilizing

geochemical and experimental petrological data: Journal of Petrology, v. 19, p. 463-513.

Gaboury, D., and Daigneault, R., 1999, Evolution from sea floor-related to sulfide-rich quartz vein-type gold mineralization during deep submarine volcanic construction; the Géant Dormant gold mine, Archean Abitibi Belt, Canada: Economic Geology, v. 94, p. 3-22.

Gaboury, D., and Pearson, V., 2008, Rhyolite geochemical signatures and association with volcanogenic massive sulfide deposits: Examples from the Abitibi Belt, Canada: Economic Geology, v. 103, p. 1531-1562.

Gauthier, M., Baillargeon, F., and Legault, M., 2003, Étude des faciès sédimentaires et des faciès d'altération primaires du gisement d'or archéen d'Eagle-Telbel, canton de Joutel, Abitibi: Géologie Québec Report MB 2002-06, 33 p.

Hamilyn, P.R., Keays, R.R., Cameron, W.E., Crawford, A.J., and Waldron, H.M., 1985, Precious metals in magnesian low-Ti lavas; implications for metallogenesis and sulfur saturation in primary magmas: Geochimica et Cosmochimica Acta, v. 49, p. 1797-1811.

Hanchar, J.M., and Watson, E.B., 2003, Zircon Saturation Thermometry: Reviews in Mineralogy and Geochemistry, v. 53, p. 89-112.

Hannington, M.D., Poulsen, K.H., Thompson, J.F.H., and Sillitoe, R.H., 1999, Volcanogenic gold in the massive sulfide environment, in Barrie, C.T., Hannington, M.D. , eds., Volcanic-associated massive sulfide deposits: Processes and examples in modern and ancient settings, Reviews in Economic Geology, v. 8, p. 325-351.

Hannington, M. D., C.E.J., D.R., and Petersen, S., 2005, Sea-floor tectonics and submarine hydrothermal systems, in Hedenquist, J.W., Thompson, J.F.H., Goldfarb, R.J., Richards, J.P., eds., Economic Geology 100th Anniversary Volume, p. 111-141.

Hart, T.R., Gibson, H.L., and Lesher, C.M., 2004, Trace element geochemistry and petrogenesis of felsic volcanic rocks associated with volcanogenic massive Cu-Zn-Pb sulfide deposits: Economic Geology, v. 99, p. 1003-1013.

Herron, M.M., 1988, Geochemical classification of terrigenous sands and shales from core or log data: Journal of Sedimentary Research, v. 58, p. 820-829.

Hibbard, L.J., 1983, Geology of the Baie Verte Peninsula, Newfoundland, Department of Mines and Energy, Government of Newfoundland and Labrador, Memoir 2, 279 p.

Hinchey, J.G., 2011, The Tulks Volcanic Belt, Victoria Lake Supergroup, Central Newfoundland – Geology, tectonic setting and volcanogenic massive sulphide mineralization: Government of Newfoundland and Labrador, Department of Natural Resources, Geological Survey, St. John's, Report 2011-02, 167 p.

Irvine, T.N., and Baragar, W.R.A., 1971, A guide to the chemical classification of the common volcanic rocks: Canadian Journal of Earth Sciences, v. 8, p. 523-548.

Ishiwatari, A., Yanagida, Y., Li, Y.-B., Ishii, T., Hiraguchi, S., Koizumi, K., Ichiyama, Y., and Umeka, M., 2006, Dredge petrology of the boninite- and adakite-bearing Hahajima Seamount of the Ogasawara (Bonin) forearc; an ophiolite or a serpentinite seamount?: Island Arc, v. 15, p. 102-118.

Ishizuka, O., Kimura, J.I., Li, Y.B., Stern, R.J., Reagan, M.K., Taylor, R.N., Ohara, Y., Bloomer, S.H., Ishii, T., Hargrove Iii, U.S., and Haraguchi, S., 2006, Early stages in the evolution of Izu-Bonin arc volcanism: New age, chemical, and isotopic constraints: Earth and Planetary Science Letters, v. 250, p. 385-401.

Ishizuka, O., Tani, K., Reagan, M.K., Kanayama, K., Umino, S., Harigane, Y., Sakamoto, I., Miyajima, Y., Yuasa, M., and Dunkley, D.J., 2011, The timescales of subduction initiation and subsequent evolution of an oceanic island arc: Earth and Planetary Science Letters, v. 306, p. 229-240.

Jenner, G.A., 1996, Trace element geochemistry of igneous rocks; geochemical nomenclature and analytical geochemistry: Geological Association of Canada, Short Course Notes 12, p. 51-77.

Jenner, G.A., Longerich, H.P., Jackson, S.E., and Fryer, B.J., 1990, ICP-MS – a powerful tool for high-precision trace element analysis in Earth sciences: Evidence from analysis of selected USGS reference samples: Chemical Geology, v. 83, p. 133–148.

Jweda, J., Bolge, L., Class, C., and Goldstein, S.L., 2016, High precision Sr-Nd-Hf-Pb isotopic compositions of USGS reference material BCR-2: Geostandards and Geoanalytical Research, v. 40, p. 101-115.

Kay, R.W., 1978, Aleutian magnesian andesites; melts from subducted Pacific Ocean crust: Journal of Volcanology and Geothermal Research, v. 4, p. 117-132.

Kean, B.F., Evans, D.T.W., and Jenner, G.A., 1995, Geology and mineralization of the Lushs Bight Group: Canada: Newfoundland and Labrador Department of Natural Resources, Geological Survey, Report 95-2, 223 p.

Kelemen, P.B., 1995, Genesis of high Mg# andesites and the continental crust: Contributions to Mineralogy and Petrology, v. 120, p. 1-19.

Kelemen, P.B., Hanghøj, K., and Greene, A.R., 2003, One view of the geochemistry of subduction-related magmatic arcs, with emphasis on primitive andesite and lower crust, in Holland, H.D., and Turekian, K.K. eds., Treatise on geochemistry, Volume 3: Amsterdam, Elsevier, p. 593–659.

Kepezhinskas, P., Defant, M.J., and Drummond, M.S., 1996, Progressive enrichment of island arc mantle by melt-peridotite interaction inferred from Kamchatka xenoliths: Geochimica et Cosmochimica Acta, v. 60, p. 1217-1229.

Kessler, L.G., and Bedard, J.H., 2000, Epiclastic volcanic debrites; evidence of flow transformations between avalanche and debris flow processes, Middle Ordovician, Baie Verte Peninsula, Newfoundland, Canada: Precambrian Research, v. 101, p. 135-161.

Langmuir, C.H., Bender, J.F., Bence, A.E., and Hanson, G.N., 1977, Petrogenesis of basalts from the FAMOUS area; Mid-Atlantic Ridge: Earth and Planetary Science Letters, v. 36, p. 133-156.

Lentz, D.R., 1998, Petrogenetic evolution of felsic volcanic sequences associated with Phanerozoic volcanic-hosted massive sulphide systems: the role of extensional geodynamics: Ore Geology Reviews, v. 12, p. 289-327.

Lesher, C.M., Goodwin, A.M., Campbell, I.H., and Gorton, M.P., 1986, Trace-element geochemistry of ore-associated and barren, felsic metavolcanic rocks in the Superior Province, Canada: Canadian Journal of Earth Sciences, v. 23, p. 222-237.

Li, Y., Kimura, J.-i., Machida, S., Ishii, T., Ishiwatari, A., Maruyama, S., Qiu, H., Ishikawa, T., Kato, Y., Haraguchi, S., Takahata, N., Hirahara, Y., and Miyazaki, T., 2013, High-Mg adakite and low-Ca boninite from a Bonin fore-arc seamount;

implications for the reaction between slab melts and depleted mantle: Journal of Petrology, v. 54, p. 1149-1175.

Longerich, H.P., Jenner, G.A., Fryer, B.J., and Jackson, S.E., 1990, Inductively coupled plasma-mass spectrometric analysis of geological samples: A critical evaluation based on case studies: Chemical Geology, v. 83, p. 105–118.

Lydon, J.W., 1984, Volcanogenic massive sulphide deposits Part 1: A descriptive model: Geoscience Canada, v. 11, p. 195-202.

Lydon, J.W., 1988, Volcanogenic massive sulphide deposits Part 2: Genetic models: Geoscience Canada, v. 15, p. 43-65.

Lydon, J.W., 1996, Characteristics of volcanogenic massive sulphide deposits; interpretations in terms of hydrothermal convection systems and magmatic hydrothermal systems: Boletin Geologico y Minero, v. 107, p. 215-264.

Macpherson, C.G., Dreher, S.T., and Thirlwall, M.F., 2006, Adakites without slab melting; high pressure differentiation of island arc magma, Mindanao, the Philippines: Earth and Planetary Science Letters, v. 243, p. 581-593.

Martin, H., 1987, Petrogenesis of Archaean trondhjemites, tonalites and granodiorites from eastern Finland; major and trace element geochemistry: Journal of Petrology, v. 28, p. 921-953.

Martin, H., 1999, Adakitic magmas; modern analogues of Archaean granitoids: Lithos, v. 46, p. 411-429.

Mercier-Langevin, P., Dubé, B., Hannington, M.D., Richer-Laflèche, M., and Gosselin, G., 2007, The LaRonde Penna Au-rich volcanogenic massive sulfide deposit, Abitibi Greenstone Belt, Quebec: Part II. Lithogeochemistry and paleotectonic setting: Economic Geology, v. 102, p. 611-631.

Mungall, J.E., 2002, Roasting the mantle; slab melting and the genesis of major Au and Au-rich Cu deposits: Geology, v. 30, p. 915-918.

Nakamura, N., 1974, Determination of REE, Ba, Fe, Mg, Na and K in carbonaceous and ordinary chondrites: Geochimica et Cosmochimica Acta, v. 38, p. 757-775.

Niu, H., Sato, H., Zhang, H., Ito, J. i., Yu, X., Nagao, T., Terada, K., and Zhang, Q., 2006, Juxtaposition of adakite, boninite, high TiO_2 and low TiO_2 basalts in the

Devonian southern Altay, Xinjiang, NW China: Journal of Asian Earth Sciences, v. 28, p. 439-456.

Peacock, S.M., 1990, Fluid processes in subduction zones: Science, v. 248, p. 329-337.

Pearce, J.A., 1996, A user's guide to basalt discrimination diagrams: Geological Association of Canada, Short Course Notes 12, p. 79-113.

Pearce, J.A., 2008, Geochemical fingerprinting of oceanic basalts with applications to ophiolite classification and the search for Archean oceanic crust: Lithos, v. 100, p. 14-48.

Pearce, J.A., and Parkinson, I.J., 1993, Trace element models for mantle melting; application to volcanic arc petrogenesis: Geological Society Special Publications, v. 76, p. 373-403.

Pearce, J.A., and Peate, D.W., 1995, Tectonic implications of the composition of volcanic arc magmas: Annual Review of Earth and Planetary Sciences, v. 23, p. 251-285.

Pearce, J.A., van der Laan, S.R., Arculus, R.J., Murton, B.J., Ishii, T., Peate, D.W., and Parkinson, I.J., 1992, Boninite and harzburgite from Leg 125 (Bonin-Mariana forearc); a case study of magma genesis during the initial stages of subduction: Proceedings of the Ocean Drilling Program, Scientific Results, v. 125, p. 623-659.

Pearce, J.A., Baker, P.E., Harvey, P.K., and Luff, I.W., 1995, Geochemical evidence for subduction fluxes, mantle melting and fractional crystallization beneath the South Sandwich island arc: Journal of Petrology, v. 36, p. 1073-1109.

Peate, D.W., and Pearce, J.A., 1998, Causes of spatial compositional variations in Mariana Arc lavas; trace element evidence: Island Arc, v. 7, p. 479-495.

Peate, D.W., Pearce, J.A., Hawkesworth, C.J., Colley, H., Edwards, C.M.H., and Hirose, K., 1997, Geochemical variations in Vanuatu Arc lavas; the role of subducted material and a variable mantle wedge composition: Journal of Petrology, v. 38, p. 1331-1358.

Piercey, S.J., 2007, Volcanogenic massive sulphide (VMS) deposits of the Newfoundland Appalachians: An overview of their setting, classification, grade-tonnage data and unresolved questions: Newfoundland and Labrador Department of Natural Resources, Geological Survey, Current Research, Report 07-1, p. 169-178.

Piercey, S.J., 2010, An overview of petrochemistry in the regional exploration for volcanogenic massive sulphide (VMS) deposits: Geochemistry: Exploration, Environment, Analysis, v. 10, p. 119-136.

Piercey, S.J., 2011, The setting, style, and role of magmatism in the formation of volcanogenic massive sulfide deposits: Mineralium Deposita, v. 46, p. 449-471.

Piercey, S.J., 2014, A review of quality assurance and quality control (QA/QC) procedures for lithogeochemical data: Geoscience Canada, v. 41, p. 75–88.

Piercey, S.J., Jenner, G.A., and Wilton, D.H.C., 1997, The stratigraphy and geochemistry of the southern Pacquet Harbour Group, Baie Verte Peninsula, Newfoundland; implications for mineral exploration: Newfoundland and Labrador Department of Natural Resources, Geological Survey, Current Research, Report 97-1, p. 119-139.

Piercey, S.J., Murphy, D.C., Mortensen, J.K., and Paradis, S., 2001, Boninitic magmatism in a continental margin setting, Yukon-Tanana terrane, southeastern Yukon, Canada: Geology, v. 29, p. 731-734.

Piercey, S.J., Peter, J.M., Mortensen, J.K., Paradis, S., Murphy, D.C., and Tucker, T.L., 2008, Petrology and U-Pb geochronology of footwall porphyritic rhyolites from the Wolverine volcanogenic massive sulfide deposit, Yukon, Canada: Implications for the genesis of massive sulfide deposits in continental margin environments: Economic Geology, v. 103, p. 5-33.

Pilgrim, L., 2009, Mineral resource estimate for the Ming Mine, Newfoundland, Canada: Rambler Metals and Mining Canada Ltd., Technical Report NI43-101, 114 p.

Pilote, J.-L., and Piercey, S.J., 2013, Volcanostratigraphy of the 1807 zone of the Ming Cu-Au volcanogenic massive-sulphide deposit, Baie Verte Peninsula, northern Newfoundland: Geological Survey of Canada, Current Research, Report 2013-20, 13 p.

Pilote, J.-L., Piercey, S.J., and Mercier-Langevin, P., 2014, Stratigraphy and hydrothermal alteration of the Ming Cu-Au volcanogenic massive-sulphide deposit, Baie Verte Peninsula, Newfoundland: Geological Survey of Canada, Current Research, Report 2014-17, 18 p.

Pilote, J.-L., Piercey, S.J., and Mercier-Langevin, P., 2015, Volcanic architecture and alteration assemblages of the Ming Cu–Au–(Zn–Ag) VMS Deposit, Baie Verte, Newfoundland and Labrador: implications for Au-enrichment processes and exploration methods development, in Peter, J.M., and Mercier-Langevin, P., eds., Targeted Geoscience Initiative 4: Contributions to the Understanding of Volcanogenic Massive Sulfide Deposit Genesis and Exploration: Geological Survey Canada, Open File 7853, p. 1897-210.

Pilote, J.-L., Piercey, S.J., Brueckner, S.M., and Grant, D., 2016, Resolving the relative timing of Au enrichment in volcanogenic massive sulfide deposits using scanning electron microscopy-mineral liberation analyzer: Empirical evidence from the Ming Deposit, Newfoundland, Canada: Economic Geology, v. 111, p. 1495-1508.

Polat, A. and Kerrich, R., 2001. Magnesian andesites, Nb-enriched basalt-andesites, and adakites from late Archean 2.7 Ga Wawa greenstone belts, Superior Province, Canada: Implications for late Archean subduction zone petrogenetic processes: Contribution to Mineralogy and Petrology, v. 141, p. 36-52.

Polat, A. and Kerrich, R., 2004, Precambrian arc associations; boninites, adakites, magnesian andesites, and Nb-enriched basalts: Developments in Precambrian Geology, v. 13, p. 567-597.

Raczek, I., Jochum, P., and Hofmann, A.W., 2003, Neodymium and strontium isotope data for USGS reference materials BCR-1, BCR-2, BHVO-1, BHVO-2, AGV-1, AGV-2, GSP-1, GSP-2 and eight MPI-DING reference glasses: Geostandards Newsletter, 27, p. 173–179.

Rapp, R.P., 1995, Amphibole-out phase boundary in partially melted metabasalt, its control over liquid fraction and composition, and source permeability: Journal of Geophysical Research, v. 100, p. 15.

Reagan, M.K., Ishizuka, O., Stern, R.J., Kelley, K.A., Ohara, Y., Blichert-Toft, J., Bloomer, S. H., Cash, J., Fryer, P., Hanan, B.B., Hickey-Vargas, R., Ishii, T., Kimura, J.-I., Peate, D.W., Rowe, M.C., and Woods, M., 2010, Fore-arc basalts and subduction initiation in the Izu-Bonin-Mariana system: Geochemistry, Geophysics, Geosystems, v. 11, 17 p.

Richards, J.P., 2011, High Sr/Y arc magmas and porphyry Cu ± Mo ± Au deposits; just add water: Economic Geology, v. 106, p. 1075-1081.

Richards, J.P., and Kerrich, R., 2007, Adakite-like rocks: Their diverse origins and questionable role in metallogenesis: Economic Geology, v. 102, p. 537-576.

Ross, P.-S., and Bédard, J.H., 2009, Magmatic affinity of modern and ancient subalkaline volcanic rocks determined from trace-element discriminant diagrams: Canadian Journal of Earth Sciences, v. 46, p. 823-839.

Ryerson, F.J., and Watson, E.B., 1987, Rutile saturation in magmas; implications for Ti-Nb-Ta depletion in island-arc basalts: Earth and Planetary Science Letters, v. 86, p. 225-239.

Sajona, F.G., and Maury, R.C., 1998, Association of adakites with gold and copper mineralization in the Philippines: Comptes Rendus de l'Académie des Sciences, Série II. Sciences de la Terre et des Planètes, v. 326, p. 27-34.

Sajona, F.G., Maury, R.C., Bellon, H., Cotten, J., and Defant, M.J., 1996, High field strength element enrichment of Pliocene-Pleistocene island arc basalts, Zamboanga Peninsula, western Mindanao (Philippines): Journal of Petrology, v. 37, p. 693-726.

Sajona, F.G., Maury, R.C., Prouteau, G., Cotten, J., Schiano, P., Bellon, H., and Fontaine, L., 2000, Slab melt as metasomatic agent in island arc magma mantle sources, Negros and Batan (Philippines): Island Arc, v. 9, p. 472-486.

Sangster, A.L., Douma, S.L., and Lavigne, J., 2007, Base metal and gold deposits of the Betts Cove Complex, Baie Verte Peninsula, Newfoundland, in Goodfellow, W. D., ed., Mineral deposits of Canada: A synthesis of major deposit-types, district metallogeny, the evolution of geological provinces, and exploration methods: Special Publication No. 5, Geological Association of Canada, Mineral Deposits Division, p. 703-722.

Saunders, A.D., Rogers, G., Marriner, G.F., Terrell, D.J., and Verma, S.P., 1987, Geochemistry of Cenozoic volcanic rocks, Baja California, Mexico; implications for the petrogenesis of post-subduction magmas: Journal of Volcanology and Geothermal Research, v. 32, p. 223-245.

Sen, C., and Dunn, T., 1994, Dehydration melting of a basaltic composition amphibolite at 1.5 and 2.0 GPa; implications for the origin of adakites: Contributions to Mineralogy and Petrology, v. 117, p. 394-409.

Shaw, D.M., 1970, Trace element fractionation during anatexis: Geochimica et Cosmochimica Acta, v. 34, p. 237-243.

Shervais, J.W., 1982, Ti-V plots and the petrogenesis of modern and ophiolitic lavas: Earth and Planetary Science Letters, v. 59, p. 101-118.

Sillitoe, R.H., Hannington, M.D., and Thompson, J.F.H., 1996, High sulfidation deposits in the volcanogenic massive sulfide environment: Economic Geology, v. 91, p. 204-212.

Skulski, T., Castonguay, S., McNicoll, V., van Staal, C.R., Kidd, W.S.F., Rogers, N., Morris, W., Ugalde, H., Slavinski, H., Spicer, W., Moussallam, Y., and Kerr, I., 2010, Tectonostratigraphy of the Baie Verte oceanic tract and its ophiolite cover sequence on the Baie Verte Peninsula: Newfoundland and Labrador Department of Natural Resources, Geological Survey, Current Research, Report 10-1, p. 315-335.

Skulski, T., Castonguay, S., Kidd, W.S.F., McNicoll, V., van Staal, C.R., and Hibbard, J., 2015, Geology, Baie Verte and parts of Fleur de Lys, Newfoundland and Labrador, NTS 12-H/16 and part of NTS 12-I/1; Geological Survey of Canada, Canadian Geoscience Map 159, scale 1:50 000. doi:10.4095/295865

Smithies, R.H., 2000, The Archaean tonalite-trondhjemite-granodiorite (TTG) series is not an analogue of Cenozoic adakite: Earth and Planetary Science Letters, v. 182, p. 115-125.

Solomon, M., and Zaw, K., 1997, Formation on the sea floor of the Hellyer volcanogenic massive sulfide deposit: Economic Geology, v. 92, p. 686-695.

Spulber, S.D., and Rutherford, M.J., 1983, The origin of rhyolite and plagiogranite in oceanic crust; an experimental study: Journal of Petrology, v. 24, p. 1-25.

Stern, R.J., 2004, Subduction initiation; spontaneous and induced: Earth and Planetary Science Letters, v. 226, p. 275-292.

Stern, R.J., and Bloomer, S.H., 1992, Subduction zone infancy; examples from the Eocene Izu-Bonin-Mariana and Jurassic California arcs: Geological Society of America Bulletin, v. 104, p. 1621-1636.

Stratford, W.R., and Stern, T.A., 2004, Strong seismic reflections and melts in the mantle of a continental back-arc basin: Geophysical Research Letters, v. 31.

Sun, S.S., and McDonough, W.F., 1989, Chemical and isotopic systematics of oceanic basalts; implications for mantle composition and processes: Geological Society Special Publications, v. 42, p. 313-345.

Swinden, H.S., 1996, The application of volcanic geochemistry to the metallogeny of volcanic-hosted sulphide deposits in central Newfoundland: Geological Association of Canada, Short Course Notes 12, p. 329-358.

Swinden, H.S., Jenner, G.A., Kean, B.F., and Evans, D.T.W., 1989, Volcanic rock geochemistry as a guide for massive sulphide exploration in central Newfoundland: Newfoundland and Labrador Department of Natural Resources, Geological Survey, Report 89-1, p. 201-219.

Swinden, H.S., Jenner, G.A., Fryer, B.J., Hertogen, J., and Roddick, J.C., 1990, Petrogenesis and paleotectonic history of the Wild Bight Group, an Ordovician rifted island arc in central Newfoundland: Contributions to Mineralogy and Petrology, v. 105, p. 219-241.

Swinden, H.S., Jenner, G.A., and Szybinski, Z.A., 1997, Magmatic and tectonic evolution of the Cambrian-Ordovician Laurentian margin of Iapetus; geochemical and isotopic constraints from the Notre Dame Subzone, Newfoundland: Geological Society of America, Memoir 191, p. 337-365.

Szybinski, Z.A., 1995, Paleotectonic and structural setting of the western Notre Dame Bay area, Newfoundland Appalachians: Unpublished Ph.D. thesis, St. John's, Canada, Memorial University of Newfoundland, 690 p.

Tanaka, T., Togashi, S., Kamioka, H., Amakawa, H., Kagami, H., Hamamoto, T., Yuhara, M., Orihashi, Y., Yoneda, S., Shimizu, H., Kunimaru, T., Takahashi, K., Yanagi, T., Nakano, T., Fujimaki, H., Shinjo, R., Asahara, Y., Tanimizu, M., and

Dragusanu, C., 2000, JNdi-1: a neodymium isotopic reference in consistency with LaJolla neodymium: Chemical Geology, v. 168, p. 279-281.

Tatsumi, Y., 1989, Migration of fluid phases and genesis of basalt magmas in subduction zones: Journal of Geophysical Research, v. 94, p. 4697-4707.

Tatsumi, Y., 2006, High-Mg andesites in the Setouchi volcanic belt, southwestern Japan; analogy to Archean magmatism and continental crust formation?: Annual Review of Earth and Planetary Sciences, v. 34, p. 467-499.

Taylor, S.R., and McLennan, S.M., 1985, The continental crust: Its composition and evolution: Oxford, Blackwell Scientific Publications, 312 p.

Tremblay, A., Maisonneuve, S., and Lacroix, S., 1996, Contexte lithologique et structural des gîtes de Duvan et de DuReine, région de La Sarre, Abitibi, Québec: Géologie Québec Report MB 96-36, 66 p.

Tsuchiya, N., and Kanisawa, S., 1994, Early Cretaceous Sr-rich silicic magmatism by slab melting in the Kitakami Mountains, Northeast Japan: Journal of Geophysical Research, v. 99, p. 22.

Tuach, J., and Kennedy, M.J., 1978, The geologic setting of the Ming and other sulfide deposits, consolidated Rambler mines, Northeast Newfoundland: Economic Geology, v. 73, p. 192-206.

Urabe, T., 1987, The effect of pressure on the partitioning ratios of lead and zinc between vapor and rhyolite melts: Economic Geology, v. 82, p. 1049-1052.

Urabe, T., Baker, E.T., Ishibashi, J., Feely, R.A., Marumo, K., Massoth, G.J., Maruyama, A., Shitashima, K., Okamura, K., Lupton, J.E., Sonoda, A., Yamazaki, T., Aoki, M., Gendron, J., Greene, R., Kaiho, Y., Kisimoto, K., Lebon, G., Matsumoto, T., Nakamura, K., Nishizawa, A., Okano, O., Paradis, G., Roe, K., Shibata, T., Tennant, D., Vance, T., Walker, S.L., Yabuki, T., and Ytow, N., 1995, The effect of magmatic activity on hydrothermal venting along the superfast-spreading East Pacific Rise: Science, v. 269, p. 1092-1095.

Urabe, T., Scott, S.D., and Hattori, K., 1983, A comparison of footwall-rock alteration and geothermal systems beneath some Japanese and Canadian volcanogenic massive sulfide deposits: Economic Geology Monograph 5, p. 345-364.

van Staal, C. R., 2007, Pre-Carboniferous tectonic evolution and metallogeny of the Canadian Appalachians, in Goodfellow, W. D., ed., Mineral deposits of Canada: A synthesis of major deposit-types, district metallogeny, the evolution of geological provinces, and exploration methods: Special Publication No. 5, Geological Association of Canada, Mineral Deposits Division, p. 793-818.

van Staal, C.R., and Barr, S.M., 2012, Lithospheric architecture and tectonic evolution of the Canadian Appalachians, in Percival, J.A., Cook, F.A., and Clowes, R.M., eds., Tectonic Styles in Canada Revisited: the LITHOPROBE perspective: Geological Association of Canada Special Paper 49, p. 41-95.

van Staal, C.R., Dewey, J.F., Mac Niocaill, C., and McKerrow, W.S., 1998, The Cambrian-Silurian tectonic evolution of the Northern Appalachians and British Caledonides; history of a complex, west and southwest Pacific-type segment of Iapetus: Geological Society Special Publications, v. 143, p. 199-242.

van Staal, C.R., Whalen, J.B., McNicoll, V.J., Pehrsson, S., Lissenberg, C.J., Zagorevski, A., van Breemen, O., and Jenner, G.A., 2007, The Notre Dame Arc and the Taconic Orogeny in Newfoundland: Geological Society of America Memoir 200, p. 511-552.

van Staal, C.R., Whalen, J.B., Valverde-Vaquero, P., Zagorevski, A., and Rogers, N., 2009, Pre-Carboniferous, episodic accretion-related, orogenesis along the Laurentian margin of the Northern Appalachians: Geological Society Special Publications, v. 327, p. 271-316.

van Staal, C.R., Chew, D.M., Zagorevski, A., McNicoll, V., Hibbard, J., Skulski, T., Escayola, M.P., Castonguay, S., and Sylvester, P.J., 2013, Evidence of Late Ediacaran hyperextension of the Laurentian Iapetan margin in the Birchy Complex, Baie Verte Peninsula, northwest Newfoundland: Implications for the opening of Iapetus, formation of peri-Laurentian microcontinents and Taconic-Grampian orogenesis: Geoscience Canada, v. 40, p. 94-117.

Waldron, J.W.F., and van Staal, C.R., 2001, Taconian Orogeny and the accretion of the Dashwoods Block; a peri-Laurentian microcontinent in the Iapetus Ocean: Geology, v. 29, p. 811-814.

Watson, E.B., and Harrison, T.M., 1983, Zircon saturation revisited; temperature and composition effects in a variety of crustal magma types: Earth and Planetary Science Letters, v. 64, p. 295-304.

Weis, D., Kieffer, B., Maerschalk, C., Pretorius, W., and Barling, J., 2005, High-precision Pb-Sr-Nd-Hf isotopic characterization of USGS BHVO-1 and BHVO-2 reference materials: Geochemistry, Geophysics, Geosystems, v. 6, 10 p.

Winchester, J.A., and Floyd, P.A., 1977, Geochemical discrimination of different magma series and their differentiation products using immobile elements: Chemical Geology, v. 20, p. 325-343.

Wood, D.A., 1980, The application of a Th-Hf-Ta diagram to problems of tectonomagmatic classification and to establishing the nature of crustal contamination of basaltic lavas of the British Tertiary volcanic province: Earth and Planetary Science Letters, v. 50, p. 11-30.

Wyllie, P.J., and Wolf, M.B., 1993, Amphibolite dehydration-melting; sorting out the solidus: Geological Society Special Publications, v. 76, p. 405-416.

Yang, K., and Scott, S.D., 1996, Possible contribution of a metal-rich magmatic fluid to a sea-floor hydrothermal system: Nature, v. 383, p. 420-423.

Yang, K., and Scott, S.D., 2002, Magmatic degassing of volatiles and ore metals into a hydrothermal system on the modern sea floor of the eastern Manus back-arc basin, western Pacific: Economic Geology, v. 97, p. 1079-1100.

Yang, K., and Scott, S.D., 2003, Geochemical relationships of felsic magmas to ore metals in massive sulfide deposits of the Bathurst mining camp, Iberian pyrite belt, Hokuroku District, and the Abitibi Belt: Economic Geology Monograph 11, p. 457-478.

Zagorevski, A., and van Staal, C.R. 2011, The record of Ordovician arc-arc and arc-continent collisions in the Canadian Appalachians during the closure of Iapetus, in Arc-Continent Collision, in Frontiers in Earth Sciences, D. Brown, and P.D. Ryan, eds., Springer, p. 341-371.

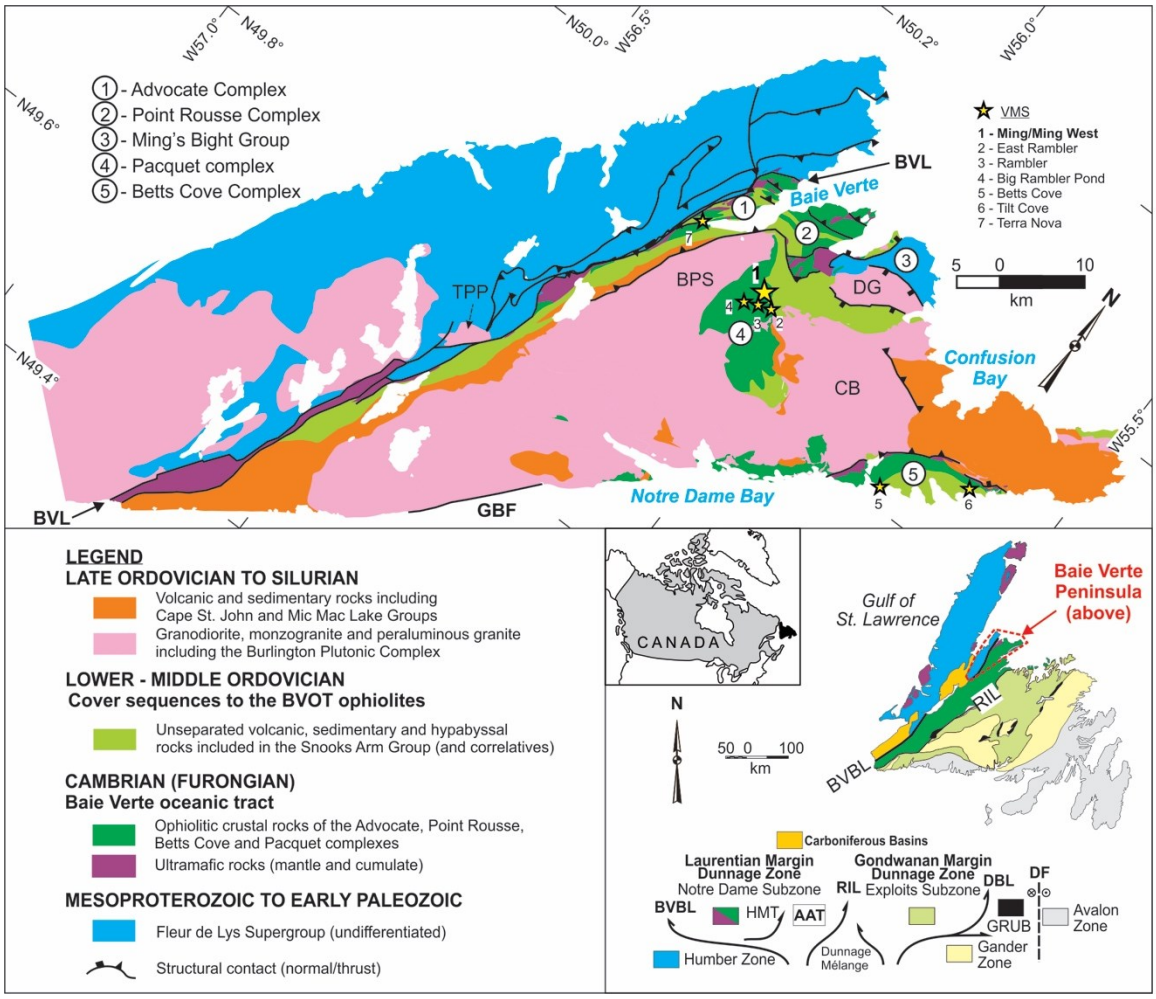

Fig. 4.1. Simplified geology of the Baie Verte Peninsula with major tectonostratigraphic zones that form the Appalachian orogenic belt in Newfoundland (modified from Castonguay et al., 2014 and references therein). Location of major VMS deposits as yellow stars. AAT = Annieopsquotch Accretionary Tract, BPS = Burlington plutonic Suite, BVBL = Baie Verte-Brompton Line, BVL = Baie Verte Line, CB = Cape Brulé, DBL = Dog Bay Line, DF = Dover Fault, DG = Dunamagon Granite, GBF = Green Bay Fault, GRUB = Gander River Ultramafic Belt, TPP = Trap Pond pluton, RIL = Red Indian Line, HMT = Hungry Mountain Thrust.

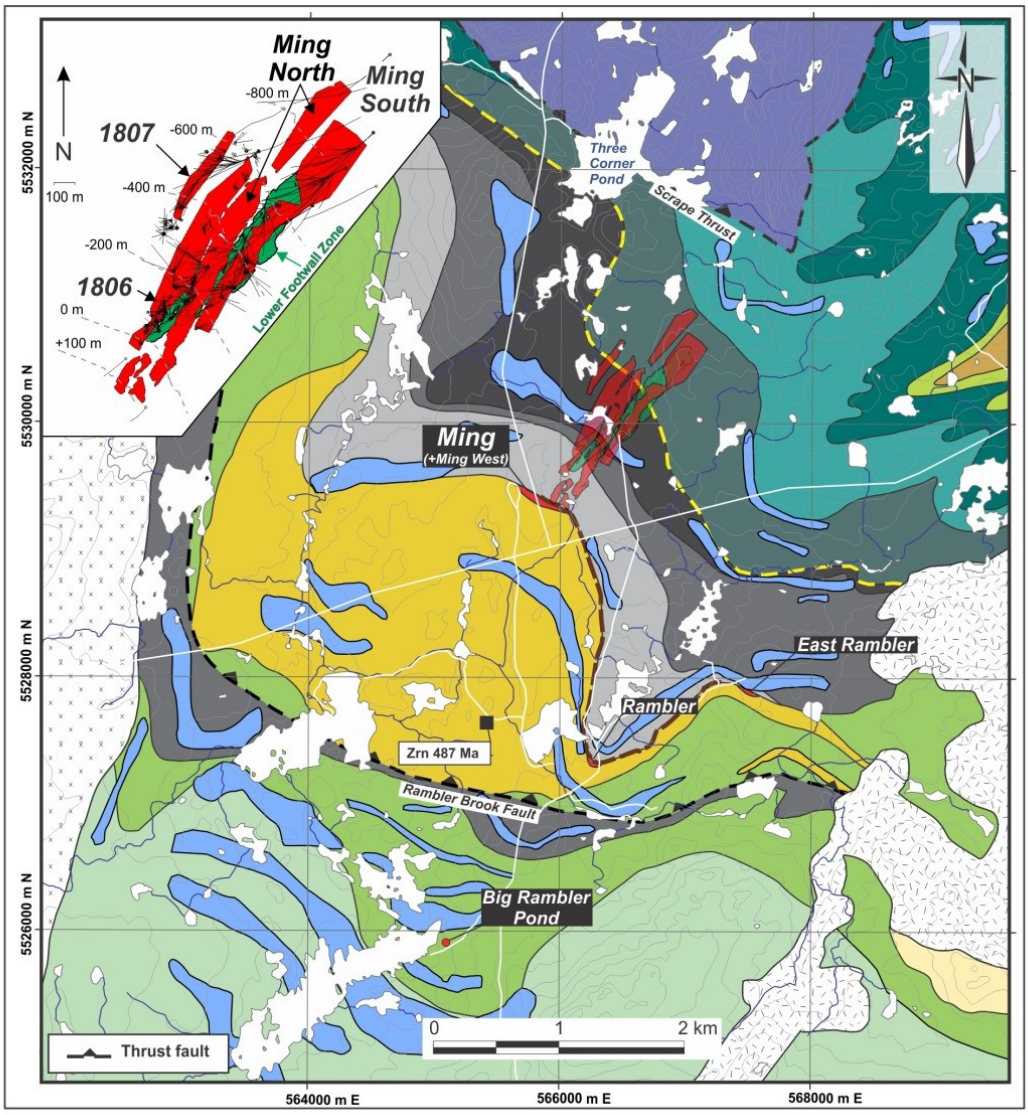

Silurian Cape St. John Group (unseparated)

Clastic, pink-red sedimentary rocks, mafic and/or felsic volcanic rocks.

Burlington Granodiorite (434 - 430 Ma)

Cape Brulé Porphyry (430 Ma)
Porphyritic granodiorite, quartz-feldspar porphyry.

Early-Middle Ordovician Snooks Arm Group (479-467 Ma)

Tholeiitic gabbro sills/dikes, include plagioclase-phyric to fine-grained gabbro. Minor medium-grained equigranular diorite.

Basalm Bud Cove Formation

Volcanogenic turbidite, siltstone, felsic tuffs, basalts.

Calc-alkaline felsic tuff, lapilli tuff.

Venam's Bight Formation
Tholeiitic pillowed basalt, porphyritic and vesicular basalt, siliceous mudstone.

Bobby Cove Formation
Chert, iron formation, volcanogenic sedimentary rocks, minor felsic tuffs.

Mafic tuff, lapilli tuff, epiclastic rocks, interbedded basalt flows.

Clinopyroxene-phyric crystal tuff, lapilli tuff, and tuff breccia (Prairie Hat member).

Calk-alkaline plagioclase-phyric pillow basalt and andesite.

Scrape Point Formation
Mafic volcaniclastic rocks, tuff, lapilli tuff, epiclastic sandstone, shale, interbedded pillow basalt.

Pillowed, massive, amygdaloidal, plgioclase-phyric basalt flows. Tholeiitic affinities.

Magnetite-rich iron formation, chert beds, volcanogenic siltstone (Nugget Pond horizon).

Cambro-Ordovician Pacquet Complex

Rambler Rhyolite formation (487 Ma)
Quartz-phyric rhyolite to rhyodacite flows interbedded with intermediate to felsic tuff, lapilli tuffs, and tuff breccia.

Mt. Misery Formation
Plagioclase- and pyroxene-phyric pillow basalt with tholeiitic affinities, interbedded with boninite.

Betts Head Formation
Spherulitic, amygdaloidal, porphyritic boninitic pillow lavas with aphanitic dark-green groundmass.

Point Rousse ophiolite (490 Ma)
Undifferentiated serpentinized ultramafic rocks with tholeiitic and boninitic affinities.

(Previous page) Fig. 4.2. Geological map of the study area, Baie Verte Peninsula, with Ming VMS orebodies projected to surface (also in the inset) and shown in light red and light green (Lower Footwall Zone = stockwork). Datum is UTM 21N NAD 83. Map compiled and modified from Tuach and Kennedy (1978), Hibbard (1983), Castonguay et al. (2009), Pilgrim (2009), and Skulski et al. (2010). The U-Pb zircon (Zrn) age is from Skulski et al. (2015).

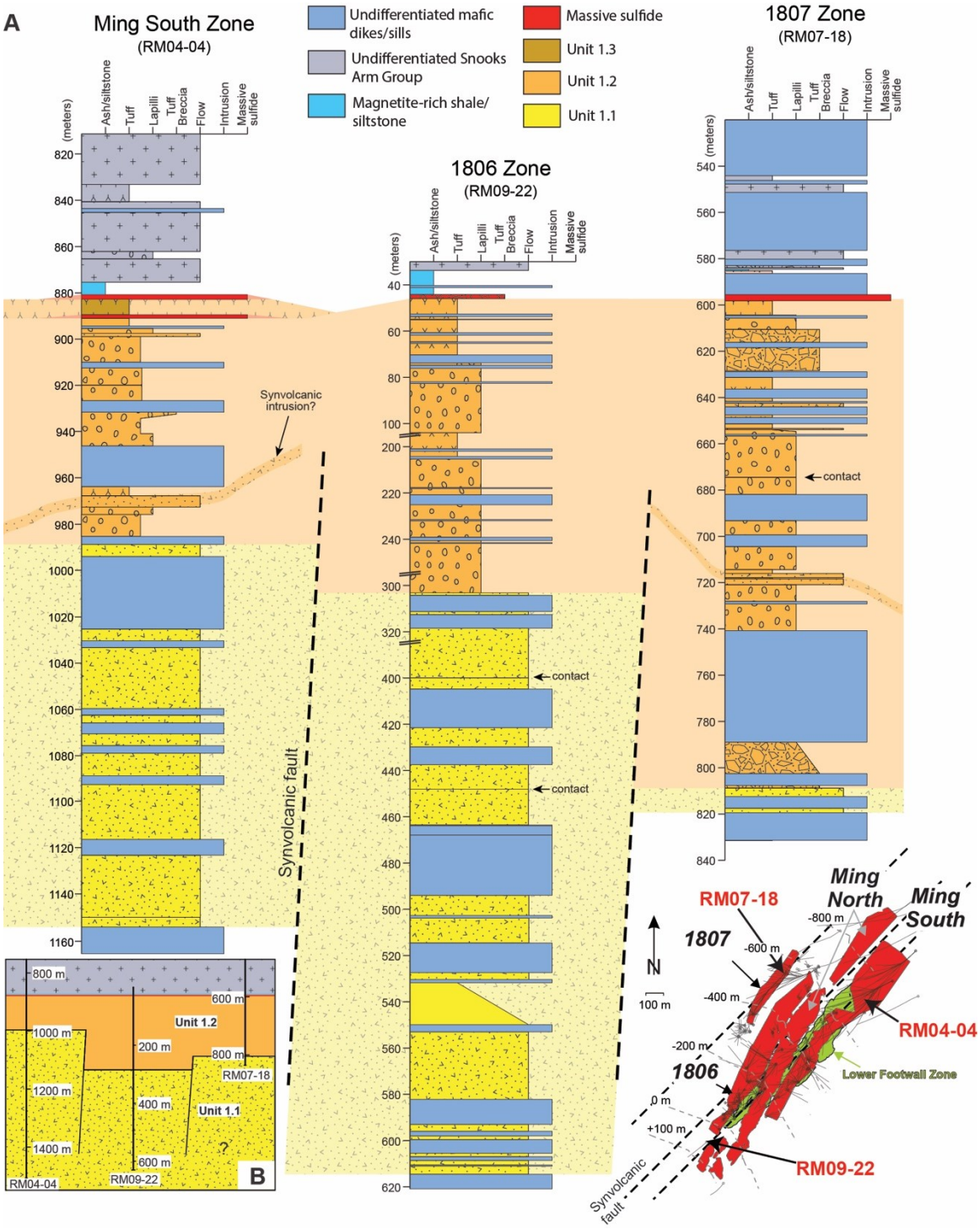
A
Ming South Zone
(RM04-04)
1806 Zone
(RM09-22)
1807 Zone
(RM07-18)
Undifferentiated mafic dikes/sills
Undifferentiated Snooks Arm Group
Magnetite-rich shale/ siltstone
Massive sulfide
Unit 1.3
Unit 1.2
Unit 1.1
Ash/siltstone
Tuff
Lapilli Tuff
Breccia
Flow
Intrusion
Massive sulfide
(meters)
Synvolcanic intrusion?
Synvolcanic fault
contact
800 m
600 m
Unit 1.2
1000 m
200 m
800 m
RM07-18
1200 m
400 m
Unit 1.1
1400 m
600 m
RM04-04
RM09-22
B
Ming North
Ming South
RM07-18
1807
-800 m
-600 m
-400 m
-200 m
1806
0 m
+100 m
N
100 m
RM04-04
Lower Footwall Zone
RM09-22
Synvolcanic fault

(Previous page) Fig. 4.3. Composite stratigraphic columns of the Ming South (DDH RM04-04), 1806 (RM09-22), and 1807 (RM07-18) zones. These illustrate the volcaniclastic lithofacies associated with all zones. Note the downhole breaks of lengths in drill hole RM09-22. The synvolcanic faults are interpreted based on the sharp lateral change in lithofacies and on the distribution of the chlorite-rich alteration spatially and genetically associated with the Lower Footwall Zone (Pilote et al., in review).

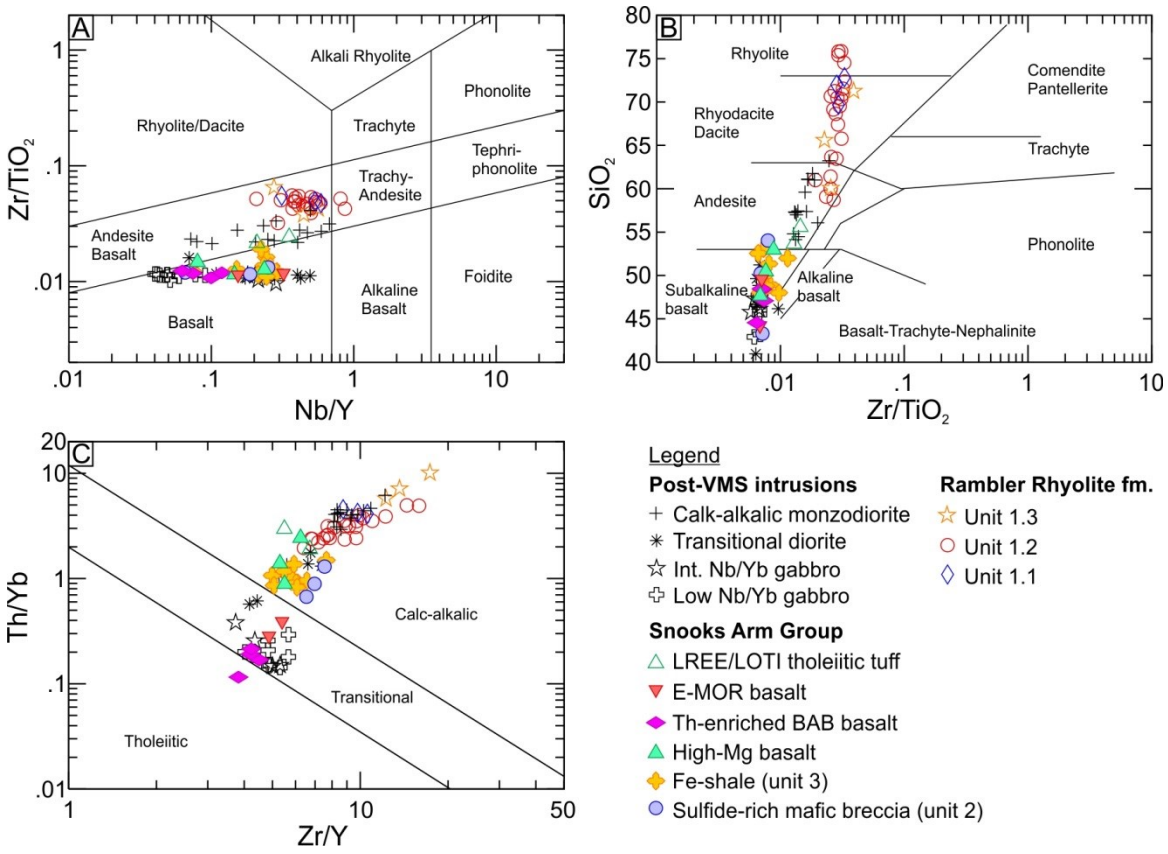

Fig. 4.4. Major and trace element plots of the average composition of the least altered samples of the host units and intrusive rocks of the Ming deposit. A. Zr/TiO_2 vs. Nb/Y discrimination diagram from Winchester and Floyd (1977), revised by Pearce (1996). B. Zr/TiO_2 vs. SiO_2 discrimination diagram from Winchester and Floyd (1977). C. Th/Yb vs. Zr/Y discrimination diagram from Ross and Bédard (2009).

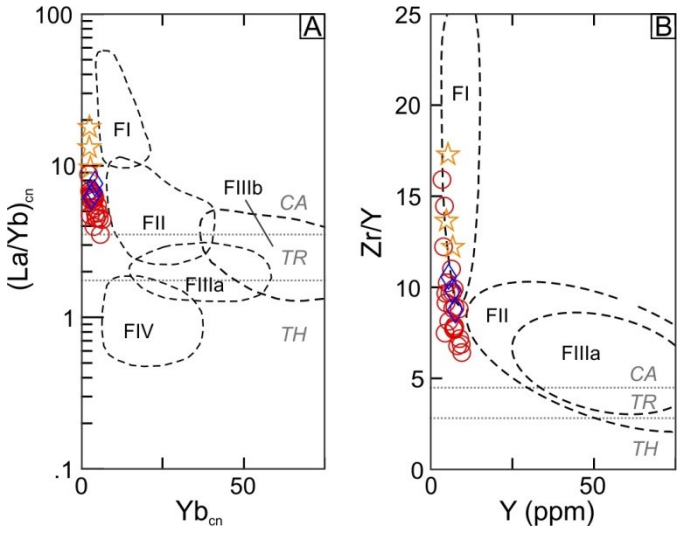

Fig. 4.5. Petrochemical affinity of the least-altered felsic rocks from the Rambler Rhyolite formation. A. Chondrite-normalized $[La/Yb]_{cn}$ vs. Yb_{cn} and B. Zr/Y vs. Y discrimination diagrams from Lesher et al. (1986) and Hart et al. (2004). Symbols are as in Figure 4.4. CA = calc-alkalic, TH = tholeiitic, TR = transitional.

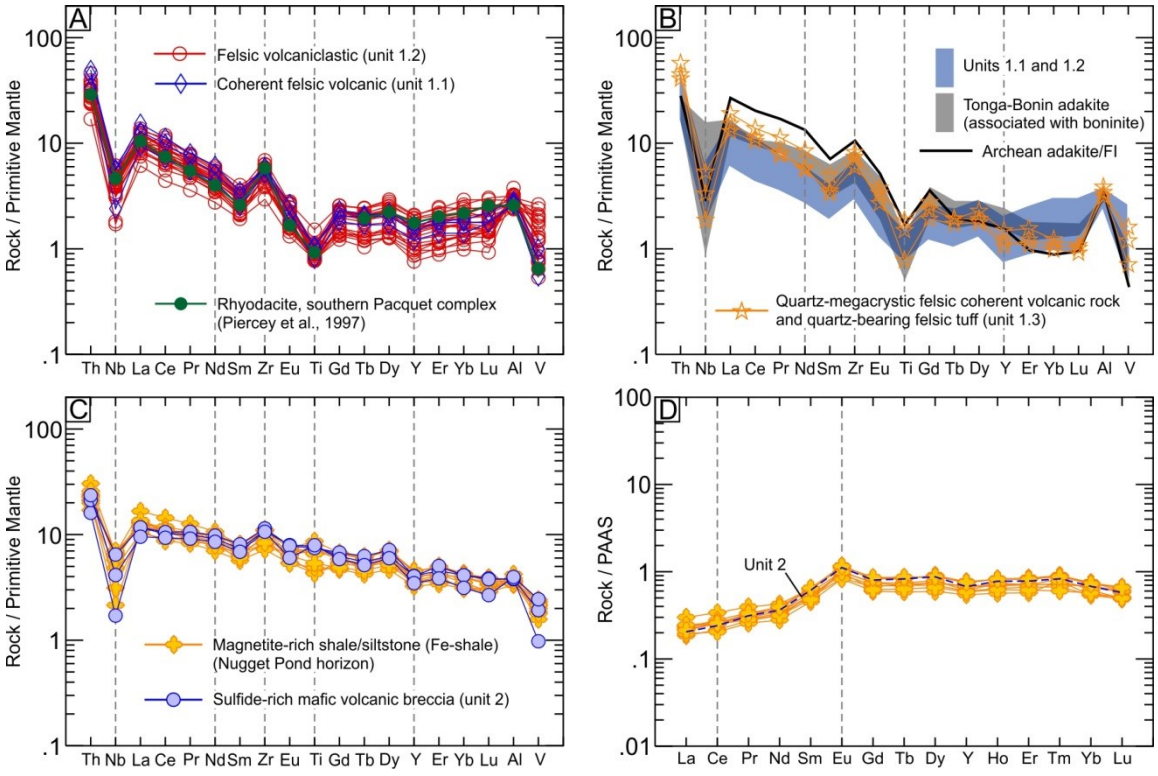

Fig. 4.6. Primitive mantle- and post-Archean Australian shale (PASS)-normalized extended-element plots for least-altered rocks of the Rambler Rhyolite formation and base of the Snooks Arm Group, subdivided based on geochemical criteria (see text for details). Also included is a rhyodacite sample from the southern Pacquet complex (Piercey et al., 1997), adakite associated with boninite in the Tonga (Falloon et al., 2008) and Bonin (Li et al., 2013) fore-arcs, and one adakite/FI-type felsic sample from the Archean Wawa greenstone belt, Superior Province (Polat and Kerrich, 2001). Normalizing values are those of Sun and McDonough (1989) and Taylor and McLennan (1985).

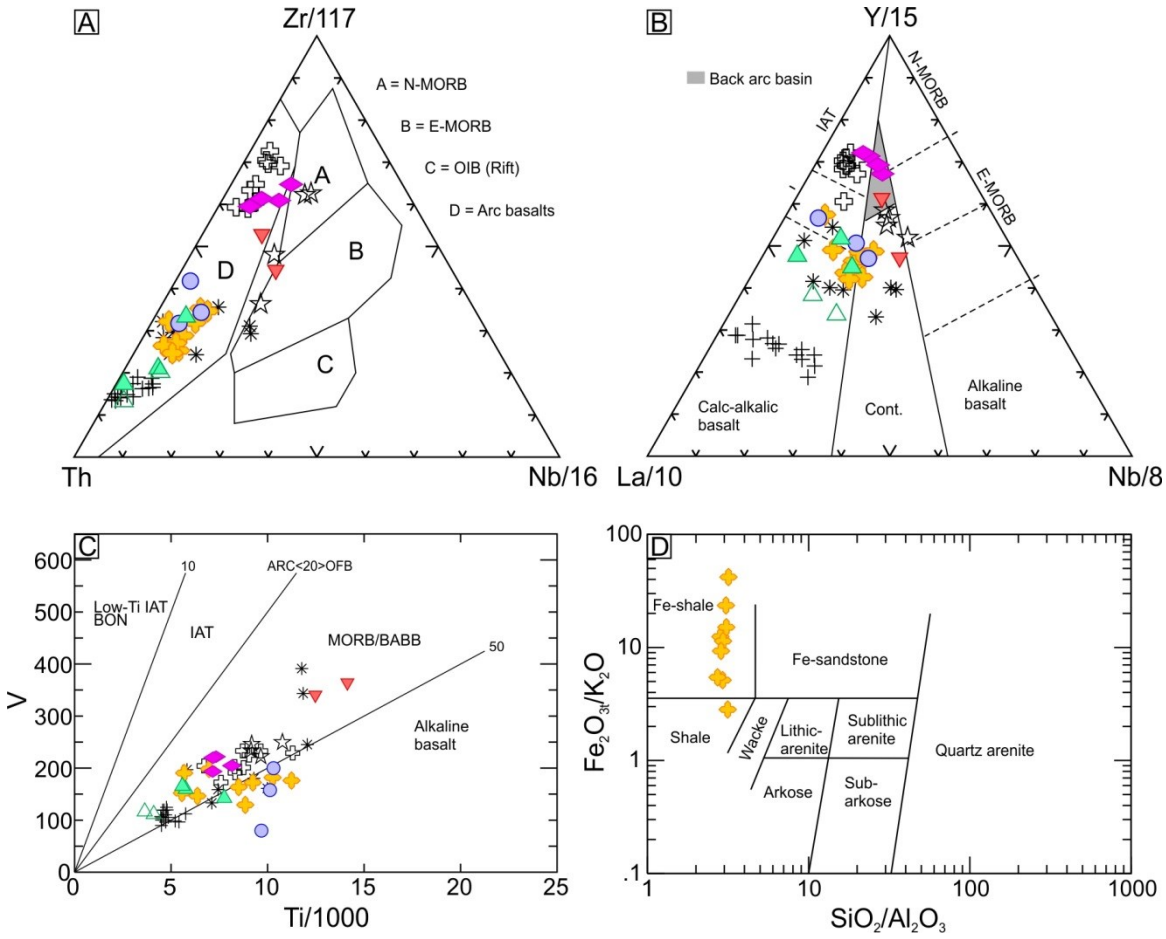

Fig. 4.7. Petrochemical affinity of the Snooks Arm Group. A. Th-Zr-Nb discrimination diagram from Wood (1980). B. Y-La-Nb discrimination diagram from Cabanis and Lecolle (1989). C. V vs. Ti discrimination diagram from Shervais (1982). D. Fe_2O_{3t}/K_2O vs. SiO_2/Al_2O_3 discrimination diagram from Herron (1988). Symbols are as in Figure 4. BON = boninite, IAT = island arc tholeiite, OIB = ocean island basalt.

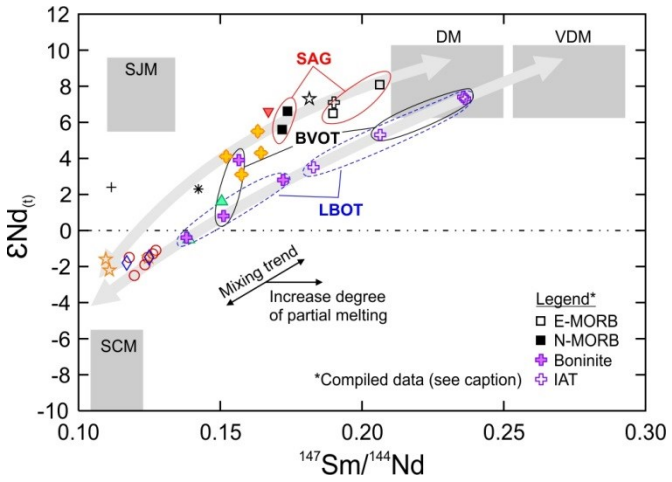

Fig. 4.8. $^{147}Sm/^{144}Nd$ vs. ƐNd(t) diagram for the altered and unaltered samples from the Rambler Rhyolite formation and Snooks Arm Group with various mantle and subduction components interpreted to be involved in its petrogenesis (fields from Swinden et al., 1990). Also shown are compiled values from Swinden et al. (1997) for representative samples from the N- and E-MORB of the Snooks Arm Group, boninites and IAT from the Baie Verte and Lushs Bight oceanic tracts. BVOT = Baie Verte oceanic tract, DM = depleted mantle, IAT = island arc tholeiite, LBOT = Lushs Bight oceanic tract, SAG = Snooks Arm Group, SCM = subducted continental material, SJM = subducted juvenile material, VDM = very depleted mantle. Symbols are as in Figure 4.4.

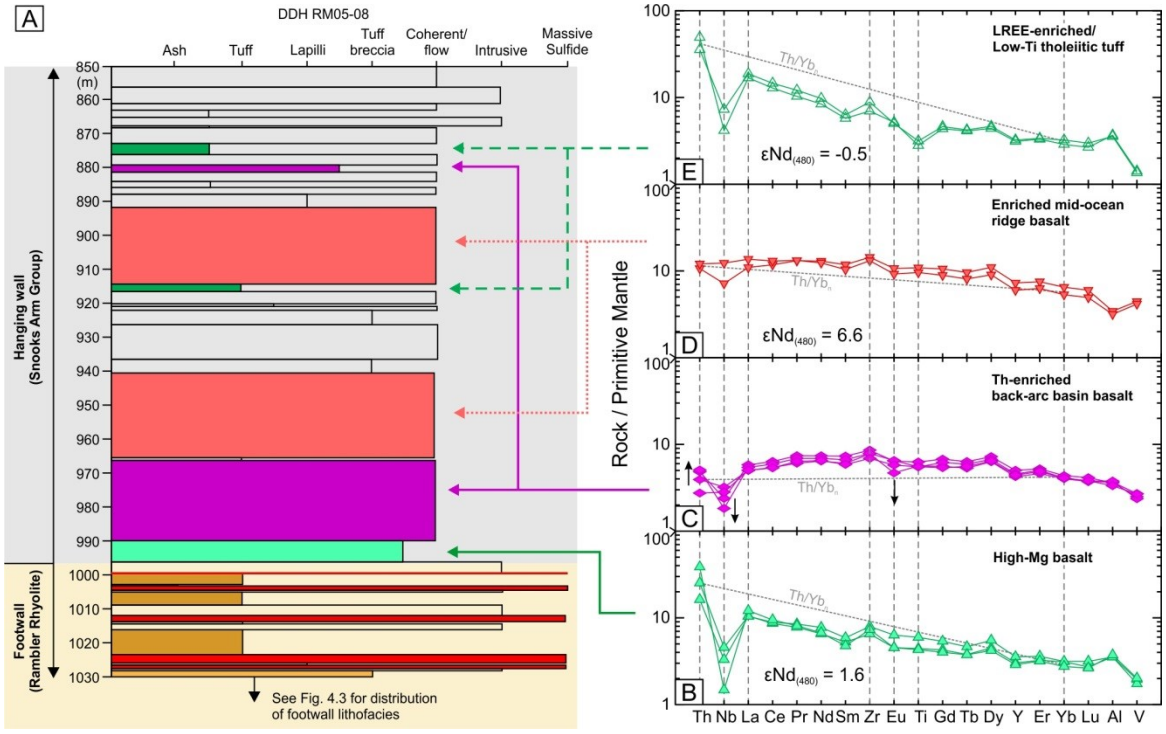

Fig. 4.9. A. Stratigraphic column for part of drill hole RM05-08 (Ming South Zone) and B-E. primitive mantle-normalized extended-element plots, including respective ƐNd(t) values, for representative samples from the base of the Snooks Arm Group, subdivided based on geochemical criteria (see text for details). Normalizing values are those of Sun and McDonough (1989). Symbols are as in Figure 4.4. Note that the Fe-shale does not occur in this drill hole.

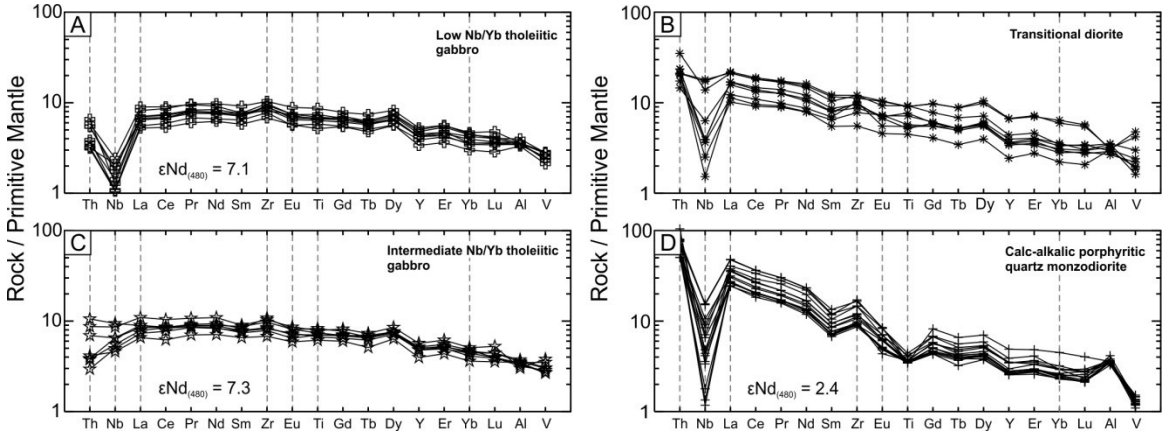

Fig. 4.10. Primitive mantle-normalized extended-element plots, including respective ƐNd(t) values, for the intrusive rocks cross-cutting the Ming deposit, subdivided based on geochemical criteria (see text for details). Normalizing values are those of Sun and McDonough (1989).

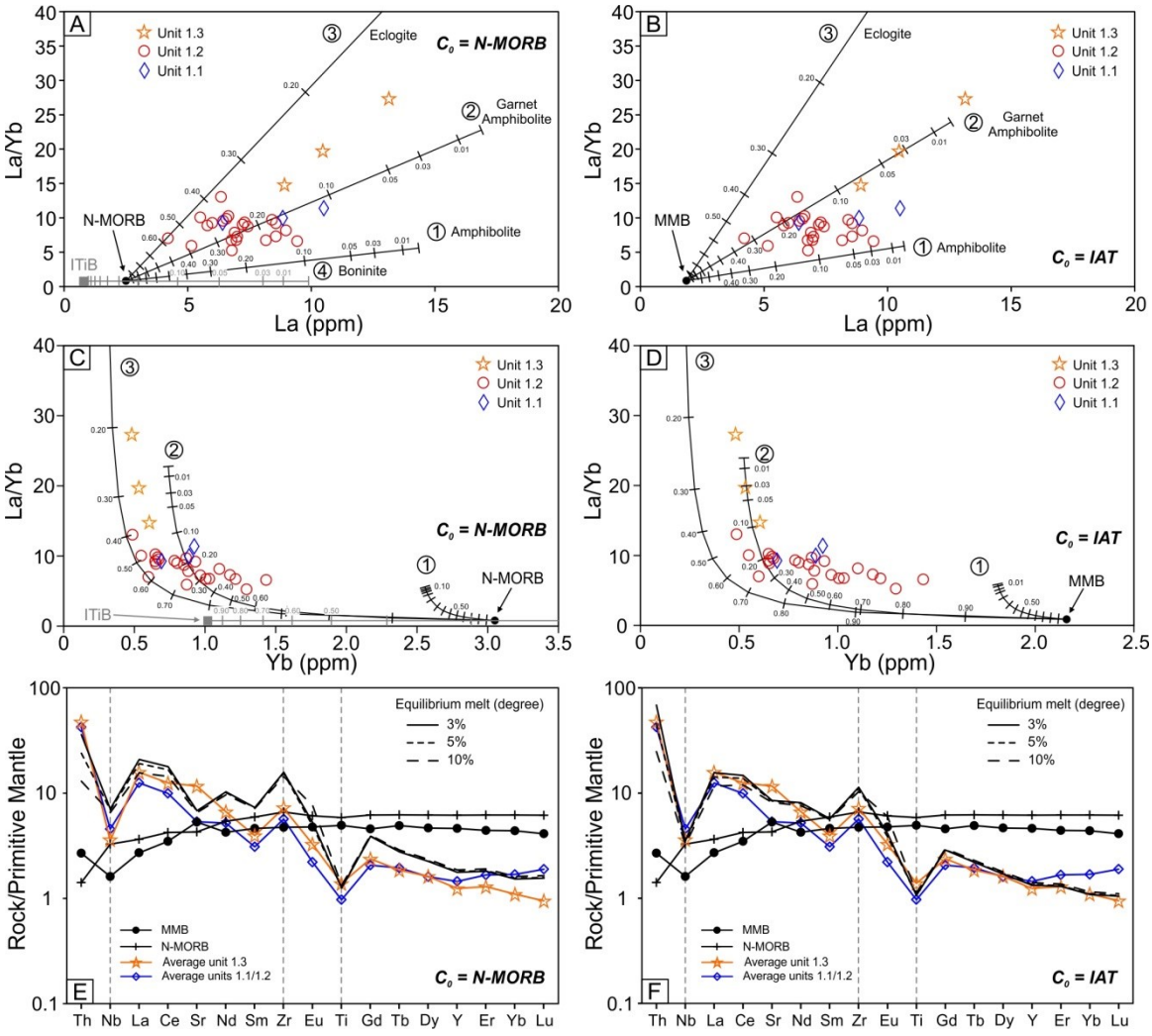

Fig. 4.11. Modelled resulting compositions from simple batch melting. Evolution of A. and B. La/Yb vs. La and C. and D. La/Yb vs. Yb obtained by melting an average N-MORB (values from Sun and McDonough, 1989) and island arc tholeiite (Mount Misery Formation; MMB; values from Bédard, 1999) considering three different melting residues, including: (1) amphibolite (68% hornblende, 25.5% plagioclase, 5% clinopyroxene, 1.5% ilmenite), (2) garnet amphibolite (53% hornblende, 20% plagioclase, 15% garnet, 10% clinopyroxene, 2% ilmenite), and (3) eclogite (50% garnet, 50% clinopyroxene). Residues are adjusted from Martin (1987). Ticks on curves are percentages of partial melting. E. and F. Theoretical primitive mantle-normalized extended-element plots obtained by models of 3%, 5%, and 10% partial melting of an average N-MORB and island arc tholeiite (both shown), using the garnet amphibolite residue (1). Also shows for comparison purposes are average values for units 1.1/1.2 and 1.3. Normalizing values are those of Sun and McDonough (1989).

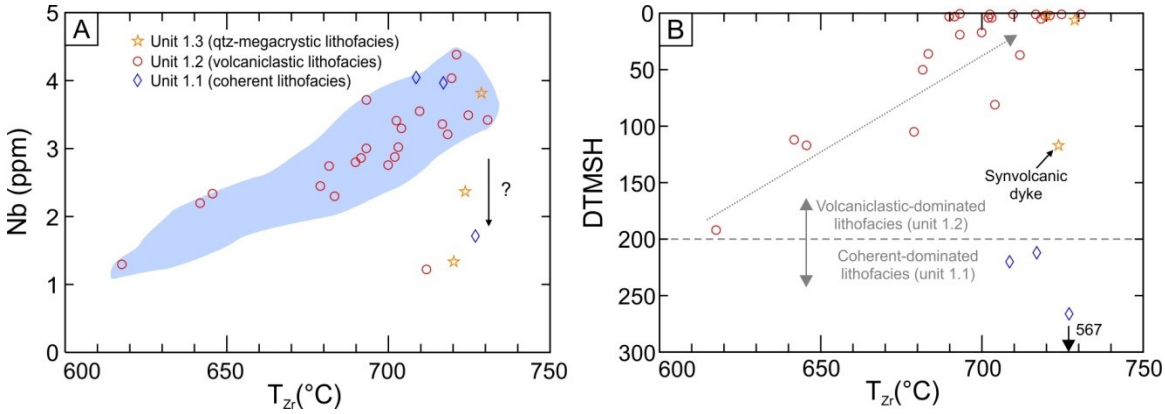

Fig. 4.12. A. Nb vs. zircon saturation temperature (T_{Zr}) and B. relative (depth) to the massive sulfide horizon (DTMSH) vs. T_{Zr} where 0 m represents the ore horizon. Zircon saturation temperature calculations were done exclusively on the least-altered felsic rocks of the Rambler Rhyolite formation. See text for details.

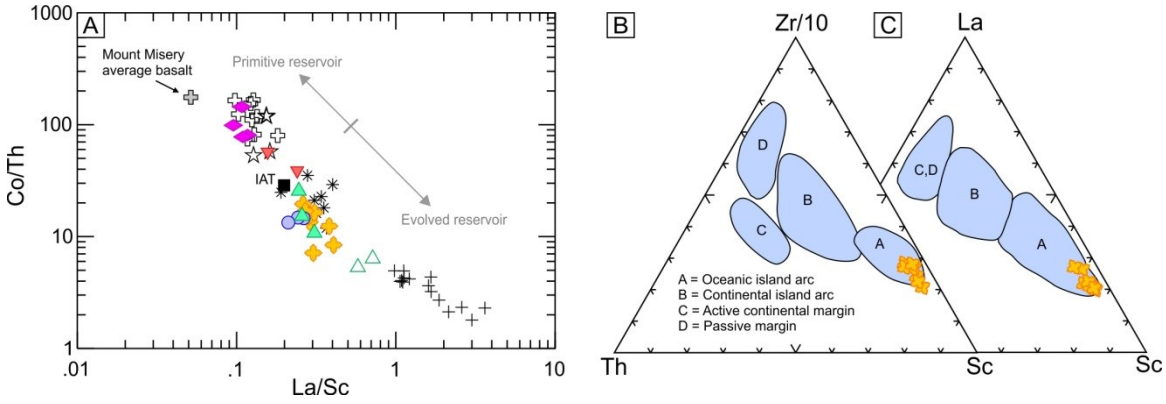

Fig. 4.13. Source plots for the Fe-shale and other rocks of the Snooks Arm Group. A. Co/Th vs. La/Sc plot. The average composition of the basalt from the Mount Misery Formation is also shown. B. and C. Zr (La)-Th-Sc discrimination diagrams of Bathia and Crook (1986). Symbols are as in Figure 4.4.

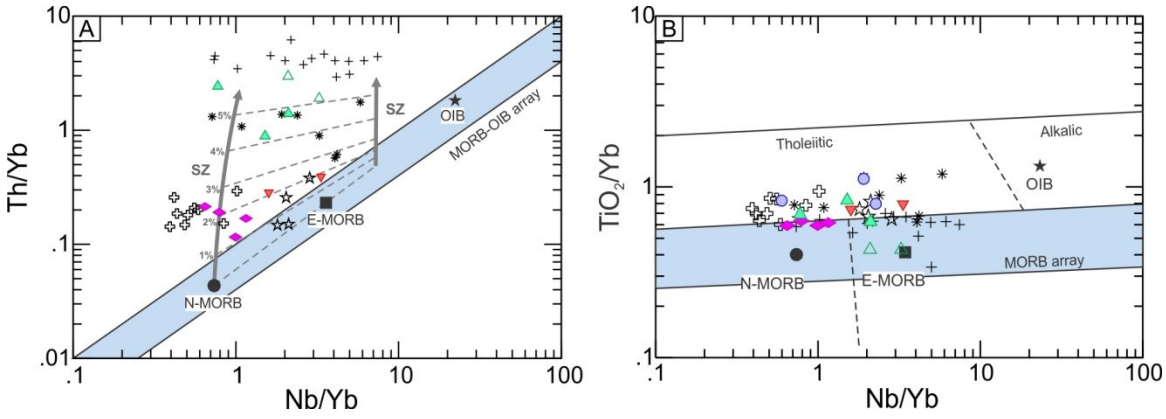

Fig. 4.14. Magmatic differentiation of variably incompatible elements within and between mafic units of the Snooks Arm Group. A. Th/Yb vs. Nb/Yb plot with vectors indicating subduction component (in %) addition and assimilation-fractional crystallization (AFC; Depaolo, 1981) from Pearce (2008). B. TiO_2/Yb vs. Nb/Yb plot. Compositional fields of modern MORB-OIB array and volcanic array are from Pearce and Peate (1995) and Pearce (2008). Average N-MORB, E-MORB, and OIB are from Sun and McDonough (1989). Symbols are as in Figure 4.4.

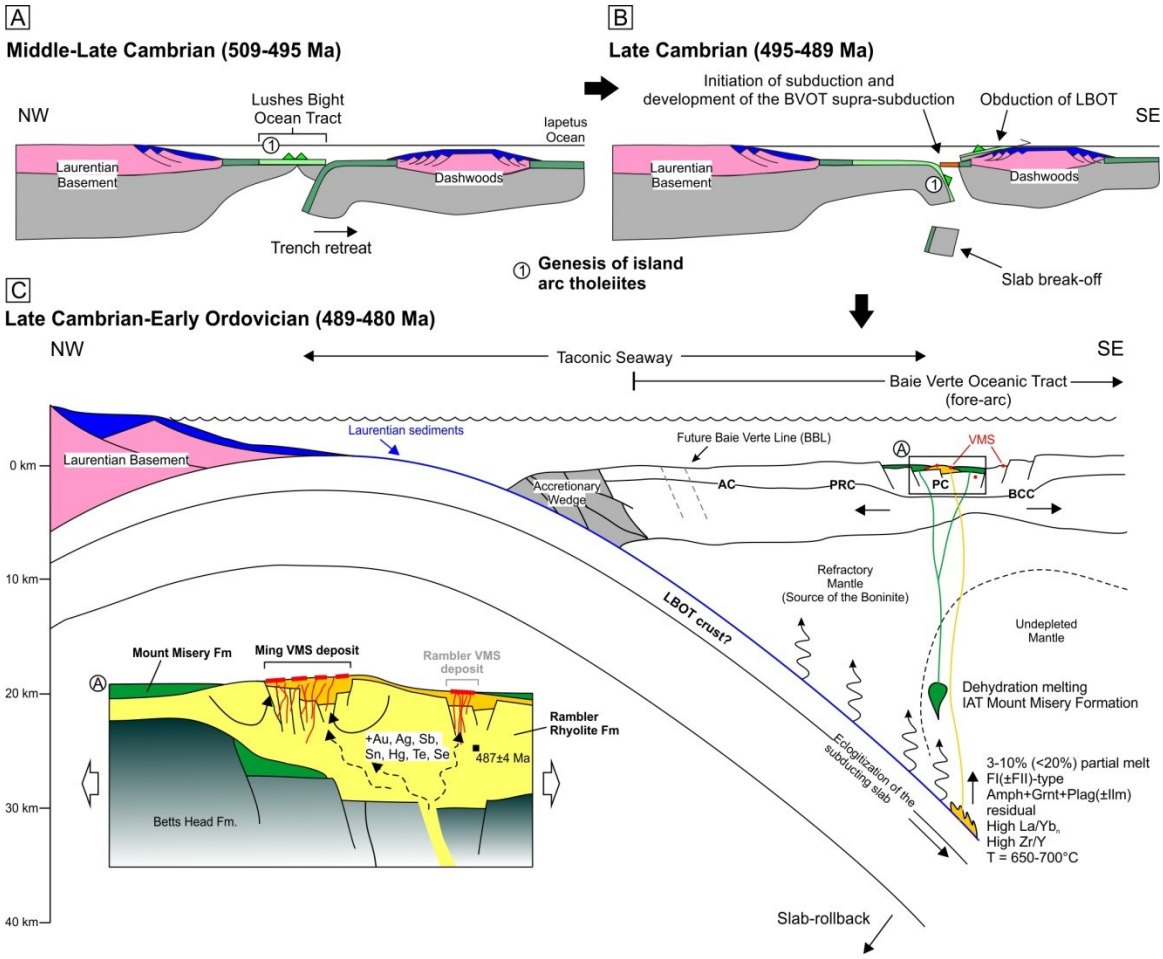

Fig. 4.15. Schematic partial geodynamic and tectonic evolution of the Taconic seaway between the Middle Cambrian and Early Ordovician (ca. 510-480 Ma). These figures are based on the work of Bédard et al. .(2014). They do not take into account the initial opening nor the final closing stages of the seaway (see aforementioned references for more details). The model presented here shows (A) the development of the Lushs Bight supra-subduction crust (LBOT) onto which island arc tholeiites were constructed, (B) then the eastward emplacement of the LBOT onto Dashwoods and nucleation of subduction which led to (C) the development of the extensional Baie Verte supra-subduction zone. The felsic FII- and FI-type host rocks of the Ming deposit result from low-temperature (650-700°C) slab-derived partial melting (~3-10%) accommodating significant amounts of Au and other magmatophile elements. The subduction of remnant arc-like rocks (IAT) from the Lushs Bight oceanic tract that experienced amphibolite facies metamorphism and dehydration could explain the amount of hornblende and garnet required to generate the FI-(±FII-)type felsic magmas. Abbreviations: AC = Advocate Complex, BCC = Betts Cove Complex, PC = Pacquet complex, PRC = Pointe Rousse Complex

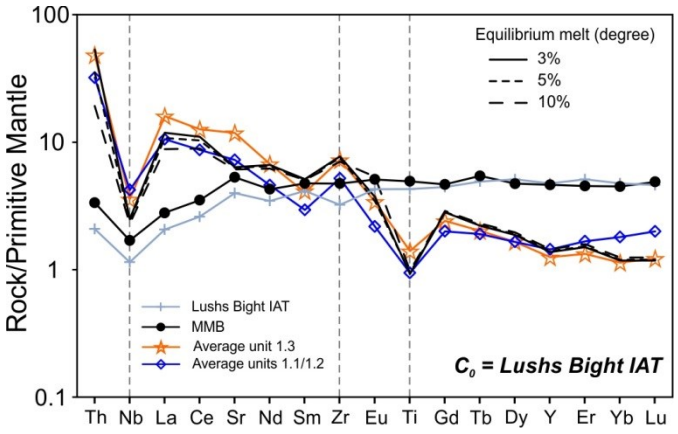

Fig. 4.16. Modelled resulting compositions from simple batch melting of the average Lushs Bight island arc tholeiites from Kean et al. (1995). All units here are recalculated volatile-free at a total of 100 wt % in order to be consistent with Kean et al.'s (1995) data. The modelled compositions use the same parameters as in Fig. 11. Normalizing values are those of Sun and McDonough (1989).

Table 4.1. Average Chemical Composition of Least Altered Host Rocks of the Ming Cu-Zn-Ag-Au VMS Deposit

	Rambler Rhyolite									Snooks Arm Group					
	Coherent facies Unit 1.1			Volcaniclastic facies Unit 1.2			Felsic tuff Unit 1.3			Sulfide-bearing mafic breccia Unit 2			Magnetite-rich shale (Nugget Pond horizon) Unit 3		
	Mean	2σ	n	Mean	2σ	n	Mean	2σ	n	Mean	2σ	n	Mean	2σ	n
SiO_2	71.50	2.68	3	68.12	10.71	23	65.64	9.13	3	49.19	8.88	3	50.30	3.73	9
Al_2O_3	12.58	0.84	3	13.48	2.96	23	16.07	2.74	3	17.83	0.77	3	16.93	2.23	9
$Fe_2O_{3(total)}$	4.48	0.91	3	6.24	4.79	23	4.58	4.89	3	9.75	4.75	3	8.18	1.65	9
MnO	0.052	0.021	3	0.163	0.526	23	0.034	0.020	3	0.120	0.147	3	0.151	0.080	9
MgO	2.94	0.91	3	2.31	3.87	23	1.84	1.83	3	4.07	2.79	3	4.51	3.59	9
CaO	2.20	1.58	3	3.35	2.48	23	3.18	0.90	3	6.79	6.58	3	8.63	3.86	9
Na_2O	4.06	0.08	3	3.46	1.48	23	4.16	1.26	3	3.46	0.72	3	4.05	2.69	9
K_2O	0.37	0.26	3	1.33	1.32	23	1.83	0.63	3	2.40	1.83	3	1.05	1.70	9
TiO_2	0.211	0.049	3	0.203	0.072	23	0.300	0.197	3	1.674	0.087	3	1.347	0.640	9
P_2O_5	0.05	0.00	3	0.05	0.04	23	0.06	0.11	3	0.10	0.05	3	0.13	0.04	9
LOI	1.53	0.31	3	1.05	0.97	23	1.51	0.39	3	3.82	5.46	3	4.74	3.58	9
Total	99.97	1.05	3	99.8	1.6	23	99.21	1.05	3	99.19	1.31	3	100.02	1.51	9
FeO_t[1]	4.03	0.82	3	5.61	4.31	23	4.12	4.40	3	8.77	4.27	3	7.36	1.48	9
Sr	113	71	3	157	93	23	246	229	3	190	127	3	231	127	9
Sc	17	4	3	22	15	23	18	18	3	31	2	3	28	6	9
Zr	63	8	3	57	20	23	80	22	3	123	8	3	106	29	9
Ba	47.6	21.0	3	308.7	574.9	23	463.4	481.3	3	260.5	202.3	3	125.2	357.9	9
Y	6.59	1.71	3	6.51	3.48	23	5.64	1.65	3	17.54	2.51	3	17.88	4.17	9
Nb	3.24	2.16	3	2.94	1.49	23	2.51	2.04	3	2.92	2.77	3	3.81	2.26	9
Cs	0.43	0.59	3	0.76	0.63	23	0.84	0.30	3	1.17	0.54	3	1.02	1.26	9
La	8.59	3.37	3	7.01	2.49	23	10.84	3.49	3	7.50	1.35	3	8.75	2.41	9
Ce	17.61	6.39	3	15.05	6.53	23	22.16	5.40	3	18.79	1.97	3	20.54	5.75	9
Pr	1.91	0.58	3	1.67	0.56	23	2.50	0.89	3	2.73	0.33	3	2.74	0.70	9
Nd	7.03	1.98	3	6.06	2.11	23	9.00	3.54	3	12.35	1.38	3	11.83	2.92	9
Sm	1.37	0.37	3	1.28	0.49	23	1.75	0.64	3	3.31	0.44	3	3.08	0.75	9
Eu	0.37	0.11	3	0.35	0.14	23	0.55	0.15	3	1.22	0.30	3	1.08	0.25	9
Gd	1.23	0.25	3	1.17	0.51	23	1.41	0.41	3	3.75	0.44	3	3.43	0.85	9
Tb	0.21	0.04	3	0.19	0.09	23	0.20	0.02	3	0.61	0.10	3	0.57	0.14	9
Dy	1.18	0.24	3	1.20	0.60	23	1.19	0.26	3	3.85	0.59	3	3.59	0.96	9
Ho	0.26	0.06	3	0.26	0.13	23	0.23	0.07	3	0.78	0.15	3	0.74	0.19	9
Er	0.80	0.19	3	0.78	0.43	23	0.62	0.19	3	2.15	0.47	3	2.05	0.50	9
Tm	0.13	0.03	3	0.14	0.07	23	0.09	0.02	3	0.32	0.05	3	0.31	0.08	9
Yb	0.83	0.20	3	0.88	0.49	23	0.54	0.10	3	1.87	0.46	3	1.83	0.45	9
Lu	0.14	0.03	3	0.14	0.08	23	0.07	0.01	3	0.25	0.08	3	0.25	0.06	9
Ta	bdl			0.23	0.11	15	0.24	0.13	2	0.23	0.25	2	0.29	0.17	9
Tl	0.08	0.06	3	2.08	4.54	23	3.04	6.37	3	3.05	2.88	3	4.72	16.45	9
Pb	4.8	2.9	3	24.0	41.3	23	10.9	3.6	2	55.4	21.9	3	22.6	33.5	9
Bi	0.05	0.05	3	0.26	0.39	23	0.14	0.12	3	0.53	0.08	3	0.61	2.55	9
Th	3.60	1.12	3	2.58	1.04	23	4.05	1.19	3	1.72	0.53	3	1.94	0.61	9
U	1.42	0.51	3	0.84	1.26	23	2.19	3.73	3	1.68	3.37	3	1.22	0.94	9
V	64.2	30.9	3	108.8	98.6	23	95.9	60.2	3	145.7	99.3	3	167.7	41.9	9
Cr	100.5	78.9	3	105.9	305.6	23	80.9	88.1	3	265.5	125.4	3	153.4	134.8	9
Co	10.5	4.1	3	11.9	15.4	23	8.8	3.7	3	24.4	6.4	3	26.0	9.4	9
Ni	22.7	17.2	3	28.6	62.4	21	16.2	9.9	3	64.8	50.6	3	57.1	41.2	9
Cu	48	37	3	92	210	23	13	14	2	416	320	3	106	135	9
Zn	68	51	3	152	239	23	72	25	2	124	80	3	96	39	9
As	1.0	1.0	2	2.6	3.0	19	0.6	0.5	2	2.8	0.6	3	3.9	6.0	9
Ag	0.1	0.1	3	0.1	0.0	2	1.7		1	0.2		1	0.3	0.4	2
Sn	0.7	0.4	3	0.8	0.5	23	0.8	0.3	3	1.2	0.3	3	1.5	2.0	9
Sb	0.2	0.1	2	0.5	0.7	21	2.3	5.7	3	1.0	0.7	3	1.0	1.7	9
Ti[2]	3804	133	3	3430	1212	23	5006	3282	3	27938	1459	3	22476	10677	9
Mg#[3]	56.37	7.60	3	38.46	26.56	23	44.42	9.15	3	44.97	18.16	3	50.30	19.54	9
$[La/Yb]_{cn}$[4]	6.82	1.17	3	5.59	2.30	23	13.75	6.91	3	2.70	0.20	3	3.22	0.76	9
Yb_{cn}	3.79	0.93	3	3.98	2.23	23	2.45	0.46	3	8.49	2.09	3	8.31	2.05	9
$[La/Yb]_{pn}$[5]	7.32	1.26	3	6.00	2.47	23	14.75	7.41	3	2.89	0.22	3	3.45	0.81	9
$[La/Sm]_{pn}$	4.03	0.54	3	3.57	0.58	23	4.03	0.78	3	1.47	0.14	3	1.86	0.53	9
$[Gd/Lu]_{pn}$	1.08	0.12	3	1.11	0.43	23	2.37	0.94	3	1.87	0.47	3	1.74	0.38	9
Nb/Nb*[6]	0.60	0.34	3	0.64	0.24	23	0.45	0.41	3	0.72	0.65	3	0.89	0.50	9
Ti/Ti*[7]	0.19	0.03	3	0.19	0.05	23	0.24	0.13	3	0.93	0.11	3	0.77	0.30	9
Zr/Zr*[8]	2.50	0.11	3	2.33	0.55	23	2.86	0.41	3	2.96	0.05	3	2.65	0.50	9
Eu/Eu*[9]	0.96	0.19	3	0.95	0.25	23	1.31	0.31	3	1.96	0.40	3	1.81	0.25	9
Y/Y*[10]	0.76	0.12	3	0.74	0.22	23	0.68	0.12	3	1.17	0.11	3	1.22	0.15	9

Table 4.1. Average Chemical Composition of Least Altered Host Rocks of the Ming Cu-Zn-Ag-Au VMS Deposit *(Continued)*

	Snooks Arm Group											
	High-Mg basalt			Th-enriched back-arc basin basalt			Enriched mid-ocean ridge basalt			LREE-enriched/Low-Ti tholeiitic mafic tuff		
	Mean	2σ	n	Mean	2σ	n	Mean	2σ	n	Mean	2σ	n
SiO_2	49.83	5.66	3	47.12	3.15	4	46.89	5.36	2	54.61	1.92	2
Al_2O_3	17.17	1.18	3	16.63	1.52	4	15.27	1.27	2	16.72	0.56	2
$Fe_2O_{3(total)}$	7.57	0.27	3	9.16	0.62	4	13.55	1.14	2	8.35	0.78	2
MnO	0.136	0.015	3	0.145	0.014	4	0.174	0.010	2	0.126	0.030	2
MgO	6.73	3.92	3	6.09	0.69	4	6.97	2.16	2	4.89	1.95	2
CaO	7.12	4.08	3	9.74	2.17	4	8.84	0.46	2	5.88	0.79	2
Na_2O	4.26	2.25	3	4.09	0.63	4	3.19	0.45	2	3.93	0.31	2
K_2O	0.37	0.49	3	0.50	0.49	4	0.26	0.19	2	1.24	0.32	2
TiO_2	1.095	0.422	3	1.244	0.136	4	2.220	0.277	2	0.646	0.077	2
P_2O_5	0.10	0.08	3	0.12	0.03	4	0.25	0.02	2	0.17	0.07	2
LOI	5.08	3.61	3	4.44	2.67	4	1.79	2.56	2	2.42	2.20	2
Total	99.47	0.90	3	99.27	1.14	4	99.39	1.82	2	98.97	1.04	2
FeO_t[1]	6.81	0.25	3	8.24	0.56	4	12.19	1.03	2	7.51	0.70	2
Sr	219	99	3	224	47	4	190	81	2	279	128	2
Sc	28	1	3	34	3	4	44	9	2	19	2	2
Zr	91	40	3	87	13	4	154	14	2	89	21	2
Ba	83.1	169.1	3	65.1	48.4	4	27.3	17.9	2	256.4	43.0	2
Y	16.47	8.57	3	20.77	2.61	4	30.16	5.83	2	14.46	0.54	2
Nb	3.04	3.09	3	1.83	0.74	4	6.93	3.67	2	4.08	2.22	2
Cs	0.34	0.28	3	0.73	0.82	4	0.26	0.19	2	2.10	0.45	2
La	8.16	1.41	3	3.65	0.45	4	8.45	1.84	2	12.22	1.33	2
Ce	18.35	4.28	3	10.78	1.50	4	23.18	2.32	2	25.64	3.22	2
Pr	2.46	0.74	3	1.85	0.28	4	3.63	0.02	2	3.09	0.50	2
Nd	10.11	3.28	3	9.18	1.02	4	17.11	0.78	2	12.25	1.83	2
Sm	2.66	1.24	3	2.87	0.51	4	4.92	0.63	2	2.67	0.25	2
Eu	0.92	0.45	3	0.98	0.25	4	1.67	0.25	2	0.86	0.03	2
Gd	2.99	1.48	3	3.56	0.63	4	5.80	0.98	2	2.67	0.16	2
Tb	0.50	0.27	3	0.62	0.08	4	0.95	0.17	2	0.45	0.01	2
Dy	3.13	1.52	3	3.97	0.42	4	5.96	1.17	2	2.69	0.15	2
Ho	0.66	0.33	3	0.83	0.09	4	1.22	0.24	2	0.55	0.04	2
Er	1.88	0.97	3	2.37	0.22	4	3.31	0.59	2	1.60	0.04	2
Tm	0.31	0.09	3	0.37	0.07	4	0.48	0.14	2	0.24	0.03	2
Yb	1.72	0.78	3	2.04	0.13	4	2.91	0.57	2	1.51	0.18	2
Lu	0.25	0.14	3	0.29	0.02	4	0.40	0.08	2	0.21	0.02	2
Ta	0.29	0.09	2	0.13	0.02	4	bdl			0.33		1
Tl	0.28	0.57	3	0.21	0.11	4	0.08	0.10	2	0.43	0.28	2
Pb	7.6	5.8	3	8.4	3.3	4	11.7	1.7	2	12.1	6.4	2
Bi	0.10	0.04	3	0.09	0.02	4	0.18	0.07	2	0.14	0.06	2
Th	2.49	1.13	3	0.35	0.16	4	0.97	0.12	2	3.61	1.17	2
U	1.34	0.33	3	0.24	0.10	4	0.23	0.01	2	1.49	0.15	2
V	163.5	5.7	3	209.9	23.2	4	352.4	23.6	2	113.6	5.1	2
Cr	198.6	180.3	3	199.6	25.8	4	159.8	44.6	2	135.7	22.6	2
Co	28.7	14.9	3	33.3	0.5	4	45.7	12.0	2	20.7	3.1	2
Ni	83.7	94.9	3	50.9	7.2	4	54.2	22.1	2	62.3	14.7	2
Cu	78	72	3	80	23	4	194	294	2	185	85	2
Zn	70	13	3	84	12	4	123	43	2	77	6	2
As	3.0	3.4	2	1.0	0.4	3	bdl			0.5		1
Ag	bdl			0.1		1	0.2		1	0.2		1
Sn	1.5	1.6	3	2.8	7.5	4	1.4	0.2	2	1.1	0.2	2
Sb	1.0	1.7	3	0.5	0.2	4	0.5	0.3	2	0.2	0.1	2
Ti[2]	18271	7042	3	20749	2276	4	37035	4622	2	10771	1285	2
Mg#[3]	62.37	14.65	3	56.83	1.90	4	50.19	5.70	2	53.15	12.34	2
$[La/Yb]_{cn}$[4]	3.30	1.22	3	1.20	0.09	4	1.98	0.81	2	5.43	0.05	2
Yb_{cn}	7.81	3.56	3	9.28	0.59	4	13.23	2.60	2	6.85	0.81	2
$[La/Yb]_{pn}$[5]	3.54	1.31	3	1.28	0.09	4	2.13	0.87	2	5.82	0.06	2
$[La/Sm]_{pn}$	2.06	0.75	3	0.82	0.05	4	1.12	0.39	2	2.95	0.04	2
$[Gd/Lu]_{pn}$	1.51	0.10	3	1.55	0.19	4	1.78	0.04	2	1.60	0.08	2
Nb/Nb*[6]	0.69	0.74	3	0.85	0.42	4	1.98	0.89	2	0.75	0.48	2
Ti/Ti*[7]	0.67	0.10	3	0.72	0.05	4	1.00	0.05	2	0.41	0.03	2
Zr/Zr*[8]	2.45	0.54	3	2.20	0.19	4	3.02	0.05	2	2.43	0.48	2
Eu/Eu*[9]	1.64	0.40	3	1.66	0.34	4	2.18	0.16	2	1.57	0.11	2
Y/Y*[10]	1.19	0.31	3	1.34	0.10	4	1.61	0.16	2	1.13	0.02	2

Table 4.1. Average Chemical Composition of Least Altered Host Rocks of the Ming Cu-Zn-Ag-Au VMS Deposit *(Continued)*

	Post-mineralization dykes and sills (feeders to the Snooks Arm Group and younger successions)											
	Low Nb/Yb tholeiitic gabbro IN1			Intermediate Nb/Yb tholeiitic gabbro IN2			Transitinoal diorite IN3			Calc-alkaline quartz monzodiorite IN4		
	Mean	2σ	n	Mean	2σ	n	Mean	2σ	n	Mean	2σ	n
SiO_2	45.36	5.23	9	46.63	1.81	7	45.62	8.62	9	58.24	5.54	15
Al_2O_3	16.42	1.65	9	15.72	2.01	7	14.34	2.40	9	16.49	1.85	15
$Fe_2O_{3(total)}$	10.11	1.70	9	11.47	2.10	7	11.11	5.75	9	5.73	0.99	15
MnO	0.153	0.023	9	0.255	0.404	7	0.182	0.103	9	0.100	0.125	15
MgO	7.92	1.66	9	6.81	1.06	7	5.98	3.95	9	3.88	1.91	15
CaO	10.14	2.98	9	10.02	2.96	7	9.67	4.83	9	5.16	1.95	15
Na_2O	2.85	1.05	9	2.77	1.07	7	3.00	1.15	9	4.29	1.49	15
K_2O	0.28	0.47	9	0.60	1.65	7	0.83	1.65	9	1.92	0.95	15
TiO_2	1.453	0.405	9	1.566	0.290	7	1.521	0.765	9	0.801	0.121	15
P_2O_5	0.14	0.03	9	0.16	0.05	7	0.21	0.13	9	0.28	0.16	15
LOI	4.72	6.19	9	3.57	2.52	7	6.45	8.41	9	2.77	3.11	15
Total	99.55	1.82	9	99.75	1.69	7	98.90	2.89	9	99.67	1.69	15
FeO_t[1]	9.09	1.53	9	10.32	1.89	7	10.00	5.18	9	5.15	0.89	15
Sr	232	44	9	268	147	7	178	117	9	231	219	15
Sc	37	7	9	40	10	7	35	19	9	14	5	15
Zr	98	23	9	100	30	7	108	45	9	129	62	15
Ba	30.0	55.6	9	86.1	197.6	7	90.1	123.2	9	391.3	414.8	15
Y	19.98	5.02	9	22.24	4.37	7	19.33	12.58	9	14.06	5.69	15
Nb	1.11	0.68	9	4.70	2.40	7	5.61	8.84	9	4.61	6.29	15
Cs	0.40	1.10	9	0.38	1.16	7	0.74	1.56	9	2.28	2.17	15
La	4.71	1.52	9	5.80	1.79	7	11.29	5.81	9	22.42	10.60	15
Ce	13.28	4.12	9	15.56	4.30	7	26.35	13.22	9	46.87	22.50	15
Pr	2.21	0.60	9	2.44	0.56	7	3.64	1.77	9	5.77	2.76	15
Nd	10.66	2.83	9	11.95	2.91	7	15.66	8.15	9	21.78	10.48	15
Sm	3.23	0.78	9	3.53	0.68	7	3.83	1.93	9	3.98	1.80	15
Eu	1.17	0.31	9	1.24	0.30	7	1.28	0.65	9	1.04	0.45	15
Gd	3.86	0.84	9	4.19	0.80	7	4.00	2.22	9	3.21	1.29	15
Tb	0.64	0.16	9	0.70	0.14	7	0.64	0.37	9	0.47	0.18	15
Dy	4.04	0.96	9	4.45	0.71	7	3.99	2.39	9	2.79	1.03	15
Ho	0.82	0.20	9	0.92	0.20	7	0.79	0.51	9	0.55	0.22	15
Er	2.28	0.61	9	2.50	0.50	7	2.15	1.42	9	1.55	0.56	15
Tm	0.33	0.09	9	0.37	0.07	7	0.33	0.19	9	0.24	0.09	15
Yb	1.94	0.52	9	2.19	0.44	7	1.85	1.33	9	1.36	0.53	15
Lu	0.28	0.08	9	0.31	0.08	7	0.26	0.17	9	0.19	0.07	15
Ta	0.09	0.05	7	0.29	0.09	6	0.38	0.51	6	0.42	0.41	8
Tl	0.29	0.76	9	0.65	2.52	6	2.01	5.05	9	3.45	7.78	15
Pb	17.0	23.0	9	7.7	15.2	7	52.8	119.2	9	40.2	81.9	15
Bi	0.19	0.20	9	0.13	0.10	7	1.49	3.97	9	2.94	17.52	15
Th	0.38	0.21	9	0.50	0.46	7	1.86	0.91	9	5.58	2.43	15
U	0.17	0.18	9	0.18	0.12	7	1.09	2.54	9	1.72	0.97	15
V	210.0	39.9	9	252.6	63.3	7	217.9	172.2	9	106.8	20.0	15
Cr	241.1	43.9	9	201.5	126.6	7	231.7	338.0	9	70.0	66.4	15
Co	42.1	8.2	9	40.9	8.4	7	39.9	19.7	9	18.6	5.7	15
Ni	90.6	36.5	9	69.5	46.4	7	77.6	103.1	9	67.6	63.7	15
Cu	145	266	9	95	73	7	497	1188	8	168	604	15
Zn	115	95	9	121	101	7	219	525	9	181	333	15
As	10.5	42.0	9	1.3	1.7	5	23.9	90.2	8	10.1	37.0	12
Ag	bdl			0.3		1	0.3	0.3	4	0.3	0.6	8
Sn	0.8	0.4	9	0.9	0.8	7	1.0	1.0	8	1.0	1.1	15
Sb	1.0	1.6	9	0.5	0.5	7	4.1	13.9	9	2.9	15.9	14
Ti[2]	24239	6759	9	26128	4846	7	25387	12758	9	13387	2082	15
Mg#[3]	60.76	2.97	9	54.07	7.29	7	50.85	23.93	9	56.53	10.36	15
$[La/Yb]_{cn}$[4]	1.64	0.61	9	1.77	0.22	7	4.30	2.00	9	10.99	2.98	15
Yb_{cn}	8.82	2.38	9	9.95	1.98	7	8.39	6.07	9	6.19	2.41	15
$[La/Yb]_{pn}$[5]	1.76	0.65	9	1.89	0.24	7	4.61	2.14	9	11.80	3.20	15
$[La/Sm]_{pn}$	0.94	0.18	9	1.06	0.23	7	1.91	0.33	9	3.64	0.34	15
$[Gd/Lu]_{pn}$	1.72	0.35	9	1.68	0.17	7	1.95	0.44	9	2.13	0.56	15
Nb/Nb*[6]	0.46	0.24	9	1.73	0.46	7	1.22	1.80	9	0.64	0.81	15
Ti/Ti*[7]	0.80	0.14	9	0.83	0.09	7	0.79	0.23	9	0.44	0.07	15
Zr/Zr*[8]	2.35	0.35	9	2.29	0.51	7	2.47	0.63	9	3.02	0.83	15
Eu/Eu*[9]	1.87	0.30	9	1.90	0.31	7	1.93	0.53	9	1.63	0.39	15
Y/Y*[10]	1.29	0.17	9	1.37	0.16	7	1.25	0.42	9	1.09	0.23	15

Table 4.1. Average Chemical Composition of Least Altered Host Rocks of the Ming Cu-Zn-Ag-Au VMS Deposit *(Continued)*

	Rambler Rhyolite									Snooks Arm Group					
	Coherent facies Unit 1.1			Volcaniclastic facies Unit 1.2			Felsic tuff Unit 1.3			Sulfide-bearing mafic breccia Unit 2			Magnetite-rich shale (Nugget Pond horizon) Unit 3		
	Mean	2σ	n	Mean	2σ	n	Mean	2σ	n	Mean	2σ	n	Mean	2σ	n
Zr/Y	9.70	1.51	3	9.23	4.63	23	14.41	4.29	3	7.02	0.83	3	5.96	1.53	9
Zr/TiO_2	302.89	38.60	3	283.46	64.68	23	290.84	142.93	3	73.37	8.55	3	81.37	28.80	9
Th/Yb	4.30	0.37	3	3.10	1.60	23	7.66	3.64	3	0.95	0.52	3	1.08	0.43	9
Al_2O_3/TiO_2	60.64	15.82	3	67.41	15.70	23	59.89	38.65	3	10.66	0.50	3	13.28	6.27	9
La/Yb	10.20	1.76	3	8.36	3.44	23	20.56	10.33	3	4.03	0.30	3	4.81	1.13	9
Nb/Y	0.48	0.24	3	0.47	0.29	23	0.43	0.24	3	0.17	0.15	3	0.21	0.12	9
Nb/Th	0.87	0.40	3	1.13	0.31	23	0.65	0.65	3	1.64	1.38	3	1.98	1.20	9
Nb/Yb	3.77	1.84	3	3.52	2.07	23	4.57	3.13	3	1.59	1.44	3	2.10	1.18	9

	Snooks Arm Group											
	High-Mg basalt			Th-enriched back-arc basin basalt			Enriched mid-ocean ridge basalt			LREE-enriched/Low-Ti tholeiitic mafic tuff		
	Mean	2σ	n	Mean	2σ	n	Mean	2σ	n	Mean	2σ	n
Zr/Y	5.61	0.90	3	4.19	0.48	4	5.13	0.53	2	6.11	1.22	2
Zr/TiO_2	83.15	10.27	3	69.94	6.89	4	69.46	2.36	2	136.62	16.24	2
Th/Yb	1.57	1.27	3	0.17	0.07	4	0.34	0.11	2	2.43	1.06	2
Al_2O_3/TiO_2	16.14	4.88	3	13.41	1.83	4	6.89	0.29	2	26.02	3.97	2
La/Yb	4.93	1.82	3	1.79	0.13	4	2.96	1.22	2	8.12	0.08	2
Nb/Y	0.18	0.14	3	0.09	0.04	4	0.24	0.17	2	0.28	0.14	2
Nb/Th	1.40	1.67	3	5.66	4.41	4	7.08	2.94	2	1.21	1.01	2
Nb/Yb	1.67	1.27	3	0.90	0.39	4	2.47	1.75	2	2.67	1.16	2

	Post-mineralization dykes and sills (feeders to the Snooks Arm Group and younger successions)											
	Low Nb/Yb tholeiitic gabbro IN1			Intermediate Nb/Yb tholeiitic gabbro IN2			Transitinoal diorite IN3			Calc-alkaline quartz monzodiorite IN4		
	Mean	2σ	n	Mean	2σ	n	Mean	2σ	n	Mean	2σ	n
Zr/Y	4.93	1.05	9	4.47	0.98	7	5.83	2.01	9	9.17	2.25	15
Zr/TiO_2	67.60	4.68	9	63.27	8.53	7	72.85	26.62	9	160.30	64.15	15
Th/Yb	0.20	0.10	9	0.22	0.17	7	1.10	0.73	9	4.14	1.46	15
Al_2O_3/TiO_2	11.46	2.53	9	10.12	2.28	7	10.08	5.65	9	20.63	1.86	15
La/Yb	2.45	0.91	9	2.64	0.33	7	6.43	2.99	9	16.44	4.46	15
Nb/Y	0.06	0.03	9	0.21	0.08	7	0.26	0.28	9	0.31	0.36	15
Nb/Th	3.05	2.03	9	10.51	5.42	7	3.03	4.63	9	0.83	1.05	15
Nb/Yb	0.58	0.40	9	2.12	0.74	7	2.78	3.17	9	3.27	3.89	15

[1]Calculated from Fe_2O_{3t}, assuming all iron is present as FeO

[2]Calculated from TiO_2; 10000 x (TiO_2/0.5993)

[3]$Mg\# = Mg^{2+}/(Mg^{2+} + Fe^{2+})$ (molar %)

[4]Normalized to Chondrite (cn) value (Nakamura, 1974)

[5]Normalized to Primitive Mantle (pn) value (Sun and McDonough, 1989)

[6]$Nb/Nb^* = Nb_n/(Th_n + La_n)^{0.5}$ (Normalized to Primitive Mantle)

[7]$Ti/Ti^* = Ti_n/(Gd_n + Sm_n)^{0.5}$ (Normalized to Primitive Mantle)

[8]$Zr/Zr^* = Zr_n/(Gd_n + Sm_n)^{0.5}$ (Normalized to Primitive Mantle)

[9]$Eu/Eu^* = Eu_n/(Gd_n + Sm_n)^{0.5}$ (Normalized to Primitive Mantle)

[10]$Y/Y^* = Y_n/(Dy_n + Er_n)^{0.5}$ (Normalized to Primitive Mantle)

bdl = below detection limit

Table 4.2. Sample Locations and Descriptions for Whole-Rock Nd Isotopic Analyses

Sample	Unit	Sample location (Zone; DDH/Level; Depth (d))	Description
106407	Unit 1.1	1806; RM09-22; 612 m	Dark bluish grey, coherent quartz-phyric (7 vol%), felsic flow with minor chlorite alteration
62521	Unit 1.1	1807; RM07-18; 823 m	Dark purple, coherent quartz-phyric felsic flow with minor silica alteration
62501	Unit 1.3	1807; RM07-18; 607 m	Fine-grained, dark purple, quartz-bearing felsic tuff with silica alteration
60591	Fe-shale (Unit 3)	1807; RM07-20K; 652 m	Fine-grained, laminated shale intercalated with well sorted, immature, siltstone/sandstone overprinted by magnetite-actinolite-chlorite porphyroblasts
60600	Fe-shale (Unit 3)	1807; RM07-18; 589 m	Finely laminated silstone overprinted by magnetite-actinolite-chlorite porphyroblasts
29885	Fe-shale (Unit 3)	1806; RM08-150; 76 m	Dark greenish to pinkish grey, bedded and laminated siltstone with minor shale
29896	Fe-shale (Unit 3)	1807; RM07-20H; 655 m	Dark greenish to pinkish grey, bedded and laminated siltstone with minor shale
62168	LREE/LOTI	Ming South; RM05-08; 915 m	Moderate grey, fine-grained, finely laminated mafic ash tuff/epiclastic, overprinted by biotite porphyroblasts
62175	E-MORB	Ming South; RM05-08; 960 m	Dark grey, fine-grained moderately chloritized mafic flow
62176	High-Mg	Ming South; RM05-08; 990 m	Mafic lapilli tuff with < 1cm bleached angular fragments in a fine-grained moderately chloritized matrix with biotite porphyroblasts
60584	IN1	1807; RM07-20M; 661 m	Dark grey, medium-grained gabbro overprinted by pyrite-actinolite-biotite porphyroblasts
36648	IN2	Ming South; RM04-04; 327 m	Dark grey, medium-grained, equigranular gabbro with minor chlorite alteration
62510	IN4	1807; RM07-18; 701 m	Dark purplish grey, fine-grained, hornblende microporphyritic intermediate intrusive rock

DDH = diamond drill hole; (d) = downhole

Table 4.3. Neodymium Isotopic Data for Representative Samples from the Ming Deposit and Area

Sample	Unit	Nd (ppm)	Sm (ppm)	$^{147}Sm/^{144}Nd_{(0)}$	$^{143}Nd/^{144}Nd_{(0)}$	$^{143}Nd/^{144}Nd_{(t)}$	$\varepsilon Nd_{(t)}$
Unaltered							
106407	Unit 1.1	5.34	1.10	0.1249	0.512336	0.511943	-1.5
62521	Unit 1.1	8.01	1.55	0.1170	0.512296	0.511928	-1.8
62501	Unit 1.3	7.80	1.61	0.1248	0.512334	0.511942	-1.5
60591	Fe-shale (Unit 3)	10.52	2.65	0.1521	0.512710	0.512232	4.1
60600	Fe-shale (Unit 3)	13.94	3.76	0.1632	0.512813	0.512300	5.5
29885	Fe-shale (Unit 3)	14.70	3.83	0.1575	0.512674	0.512179	3.1
29896	Fe-shale (Unit 3)	12.55	3.41	0.1644	0.512759	0.512242	4.3
62168	LREE/LOTI	10.04	2.30	0.1389	0.512433	0.511996	-0.5
62175	E-MORB	16.66	4.60	0.1670	0.512883	0.512358	6.6
62176	High-Mg	8.36	2.08	0.1505	0.512576	0.512103	1.6
60584	IN1	8.94	2.81	0.1901	0.512979	0.512381	7.1
36648	IN2	10.10	3.03	0.1814	0.512962	0.512392	7.3
62510	IN4	19.99	3.69	0.1116	0.512495	0.512144	2.4
Altered							
29952	Unit 1.2	2.61	0.51	0.1179	0.512313	0.511942	-1.5
60551	Unit 1.2	3.91	0.82	0.1273	0.512365	0.511965	-1.1
62506	Unit 1.2	5.05	1.00	0.1197	0.512268	0.511892	-2.5
29883	Unit 1.2	4.52	0.92	0.1234	0.512310	0.511922	-1.9
29827	Unit 1.2	4.84	1.00	0.1244	0.512334	0.511943	-1.5
29832	Unit 1.2	4.06	0.85	0.1262	0.512349	0.511952	-1.3
62525	Unit 1.3	4.83	0.88	0.1109	0.512257	0.511908	-2.2
62177	Unit 1.3	5.42	0.98	0.1096	0.512284	0.511939	-1.6
60587	IN3	21.23	5.00	0.1423	0.512587	0.512140	2.3

Note: $^{143}Nd/^{144}Nd_{(0)}$ and $^{147}Sm/^{144}Nd_{(0)}$ are measured values; analytical uncertainty in $^{143}Nd/^{144}Nd_{(0)}$ is ± 0.000007 or better; $^{143}Nd/^{144}Nd_{(t)}$ is initial ratio at t = 480 Ma; Present-day $^{143}Nd/^{144}Nd_{(CHUR)}$ and $^{147}Sm/^{144}Nd_{(CHUR)}$ values of 0.512638 and 0.1967, respectively, were used to calculate $\varepsilon Nd_{(t)}$.

Appendix A4.1. Selection of Least-Altered Samples

The felsic rocks that host the Ming VMS deposit are in many parts of the deposit, affected by hydrothermal alteration. A regional metamorphic overprint (upper greenschist facies) affects all rocks of the peninsula and therefore, fluids associated with both hydrothermal alteration and metamorphism could have mobilized elements that are most susceptible to these secondary events (large ion lithophile (LILE); Cs, K, Ba, Sr). Petrogenetic signatures and primary geochemical discriminations of a suite of samples can only be achieved using elements that are relatively immune to secondary processes, such as high field strength elements (HFSE; Zr, Nb, Y, Ti, V) and rare earth elements (REE; La-Lu). Although the latter group of elements are generally immobile and resistant to alteration, in order to avoid the exception, only samples that meet the following criteria were used for primary characterization: 1) presence of a primary features in a mineralogical assemblage that shows minimal evidence or absence of hydrothermal alteration in thin sections (e.g., interlocking textures, relic feldspar/amphibole phenocrysts, absence of triple junctions in quartz, absence of foliation or porphyroblasts); 2) loss on ignition (LOI) contents lower than or equal to 2 wt %; 3) Al_2O_3 content higher than 10 wt %; 4) Na_2O between 2 and 5 wt %; and 5) alteration index (AI) between 20 and 60. Aluminum is used here as a proxy for mass change. Samples with less than 10 wt % Al_2O_3 is generally indicative of significant mass gain, hence possible leaching of key diagnostic elements (Lentz, 1998). In Figure A4.1, we compare samples that satisfy the rigorous criteria above with samples that show evidence of alteration (e.g., chlorite-sericite-carbonate-sulfide alteration). Any variation along a slope that intersects the origin

is interpreted as the result of mass changes (see Barrett and MacLean, 1994), whereas differentiation will vary along a shallower slope that intersects the Y-axis.

Because samples of the cover sequence and associated dikes post-date the ore-forming hydrothermal activity, it is reasonable to assume that the use of immobile elements such as HFSE and REE will most likely reflect the original geochemical signatures of these rocks. We have nonetheless applied selection, but less rigorous than the underlying felsic rocks, criteria, i.e. only samples with Na_2O between 2 and 5 wt % and AI between 20 and 60 were used in this study (Appendix 4).

Appendix A4.2. Analytical Methods

A4.2.1. Whole-rock major, trace, and rare earth elements (REE)

A total of 312 samples from the Ming deposit were selected from eight underground workings and 22 drill holes. The sampling methodology during field work was twofold: 1) collect least-altered samples from each unit and facies for a complete primary geochemical characterization (this study) and 2) collect samples throughout the deposit to reconstruct the hydrothermal alteration architecture, which will be published subsequently.

The samples were analyzed for major element oxides (SiO_2, Al_2O_3, Fe_2O_3, MnO, MgO, CaO, Na_2O, K_2O, TiO_2, and P_2O_5) and a selective suite of trace elements (Sr, Sc, and Zr) at Activation Laboratories Ltd. in Ancaster, Ontario, Canada. The samples were crushed and pulverized using mild steel before undergoing lithium metaborate/tetraborate fusion followed by HF-HNO_3 dissolution and subsequent analysis by inductively coupled

plasma emission-mass spectrometry (ICP-ES). A laboratory-independent quality control and assurance using the relative difference (%RD) method of Jenner (1996) and Piercey (2014) on four different reference materials (JR-1, BAMAP-01, PER-1, and CHA-2) of mafic to felsic compositions revealed excellent (<3%RD) accuracy for all major elements, except for P_2O_5 (>10%), which can be explained by the values being below lower limits of detection and/or quantification. For the trace elements, Sr showed very good accuracy (<5%RD), whereas both Sc and Zr showed excellent (<3%RD) to good (~10%RD) recoveries.

An additional suite of trace elements, including LILE, REE, and HFSE, were analyzed by the first author at the Department of Earth Sciences at Memorial University of Newfoundland using the pulps returned from the Activation Laboratory Ltd. The dissolution procedure used here is a modified version of that described by Jenner et al. (1990) and Longerich et al. (1990) and includes the following: 0.1 g of each sample were weighed into a dry teflon screw cap jar with the addition of 2 ml of 8N HNO_3 and 1 ml of HF acids. The covered jars were then placed onto a hot plate at 70°C for ~72 hours. The covers were removed and rinsed with nanopure water and left on the hot plate at 100°C until complete dryness. 2 ml of 8N HNO_3 and 1 ml of HF acids were added, covered for ~24 hours, and dried. 2 ml 8N HNO_3 acid and 1 ml boric acid (0.453M) were added and dried. 2 ml of 8N HNO_3 acid was added then dried. The latter step was repeated. Finally, 2 ml of 8N HNO_3 acid was added, covered, cooled, and transferred into a 120 ml snap seal container with an addition of 1.3 ml oxalic acid (0.22M), 0.665 ml of HF/boric (0.113M HF/0.453M boric) solution, and nanopure water to make up to a final weight of

60 g. Samples were then spiked and analyzed using a Perkin Elmer Elan DRCII Quad© inductively coupled plasma-mass spectrometry (ICP-MS) instrument and followed by offline data reduction. Using the reference materials AGV-2 and JR-1, accuracy tests (relative differences; %RD) on all samples yielded excellent accuracy (<3%RD) for Nb, Ba, Cs, La, Ce, Pr, Nd, Er, Tm, Lu, Pb, Tl and U, very good accuracy (3-7%RD) for Sm, Eu, Gd, Tb, Dy, Ho, Yb, Ta, Bi, V, Sb, Cr, and Ni, and good accuracy (<10%RD) for Y, and Co. Tin (Sn) is at 13%RD and other base metals such as Cu and Zn have poor accuracy (>10%RD) because of their low concentrations (near limit of detection) in JR-1 and AGV-2. Accuracy in Cu and Zn are very good to good when using BAMAP-01 as a reference material since it contains much higher concentrations. Unfortunately, Hf could not be used as it returned very poor accuracy; hence the reason for using Zr from the ICP-ES (Activation Lab) analyses and not from the ICP-MS (MUN), despite, intriguingly, its excellent accuracy from ICP-MS analyses. The least-altered samples are presented in Appendix 4.

Precision was calculated for each analyzed element by using a series of sample duplicates (Jenner, 1996). Table A4.1 shows the calculated precision values as coefficient of variation (CV), which is

$$CV\ (\%) = 100*SD/X$$

where *SD* is the standard deviation and *X* the population mean (Jenner ,1996). Most elements show excellent (≤3%) to good (≤10%) precisions, except for Ta, Tl, Pb, Bi, Ni, Cu, Zn, As, Sn, and Sb, which show imprecise (>10%) values, mainly due to their contents being near the lower limits of detection.

A4.2.2. Whole-rock Sm and Nd isotope determination

Whole-rock powders were dissolved in Savilex© Teflon capsules using an 8 ml (4:1) mixture of 29 M HF – 15 M HNO_3. Prior to acid digestion, a mixed $^{150}Nd/^{149}Sm$ spike is added to each sample. After five days of acid digestion on a hotplate, the solution is then evaporated to dryness, taken back up in 6M HCl for 4-5 days. The sample is finally dried down and then re-dissolved in 2.5 M HCL. The sample is loaded into column containing cation exchange resin AG-50W-X8, H+ form, and 200-400 mesh where a fraction containing REE is isolated. This REE split is then dried and taken up in 0.18 M HCl and loaded on a column containing Eichrom© Ln resin (50-100 mesh) to isolate Sm and Nd separately from the other REE. All reagents are purified in order to ensure a low contamination level. Sm and Nd concentrations and isotopic compositions are determined using a multi-collector Finnigan Mat 262 mass spectrometer at Memorial University of Newfoundland in static mode for concentration determination, and dynamic mode for isotopic composition determination. Instrumental mass fractionation of Sm and Nd isotopes are corrected using a Rayleigh law relative to $^{146}Nd/^{144}Nd = 0.7219$ and $^{152}Sm/^{147}Sm = 1.783$. The reported $^{143}Nd/^{144}Nd$ ratio is corrected for the deviation from repeated duplicates of the JNdi-1 ($^{143}Nd/^{144}Nd = 0.512115$, Tanaka et al., 2000) standard. Replicates of the standard give a 4-month (June-September, 2015) mean value of $^{143}Nd/^{144}Nd = 0.512100 \pm 0.000016$ (2σ, n = 23) and a long-term (2010-2015) mean value of $^{143}Nd/^{144}Nd = 0.512101 \pm 0.000016$ (2σ, n = 185)

The TIMS laboratory periodically analyzes the USGS whole-rock reference material BCR-2 with each analysis comprising a separate dissolution and thus provides

the best estimate of the reproducibility of an individual whole-rock analysis. The results of their BCR-2 analyses over time show an average value of 0.512636 ± 0.000014 (2σ, n = 11), which is in agreement with the results reported by Raczek et al. (2003), Weis et al. (2005), and Jweda et al. (2016).

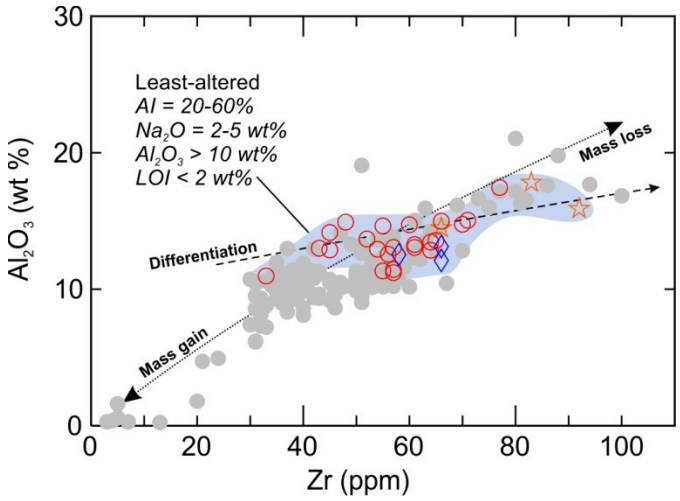

Fig. A4.1. Al_2O_3 vs. Zr diagram. This plot shows the variation in Al_2O_3 and Zr contents due to mass change associated with hydrothermal alteration (grey circles). This highlights the importance for establishing a rigorous set of criteria when determining rocks that are the least altered and subsequently used for petrogenetic assessments. See text for details. Symbols for least-altered samples are as in Figure 4.4.

Table A4.1. Analytical Precision for Each Element

	CV (%)	n		CV (%)	n
SiO_2	0.75	17	Gd	4.28	15
Al_2O_3	1.24	17	Tb	4.64	15
Fe_2O_{3t}	0.80	17	Dy	3.97	15
MnO	0.92	17	Ho	4.86	15
MgO	1.35	17	Er	5.21	15
CaO	1.13	17	Tm	4.95	15
Na_2O	0.97	17	Yb	6.07	15
K_2O	1.46	17	Lu	9.00	15
TiO_2	1.35	17	Ta	15.31	15
P_2O_5	9.65	17	Tl	14.21	15
LOI	1.77	17	Pb	14.76	15
Sr	1.12	17	Bi	15.26	15
Sc	1.67	17	Th	4.36	15
Zr	1.48	17	U	5.67	14
Ba	4.10	15	V	8.26	16
Y	4.66	15	Cr	8.44	16
Nb	5.50	15	Co	8.54	16
Cs	6.13	15	Ni	11.18	16
La	3.17	15	Cu	33.95	16
Ce	2.91	15	Zn	10.93	16
Pr	2.93	15	As	36.80	16
Nd	3.67	15	Sn	21.84	16
Sm	3.68	15	Sb	17.70	16
Eu	3.15	15			

n = number of duplicate sets

Chapter 5
Hydrothermal alteration architecture of the Ming volcanogenic massive sulfide deposit, Baie Verte Peninsula, Newfoundland, Canada

5.1. Abstract

The ~487 Ma Ming volcanogenic massive sulfide (VMS) deposit consists of four subparallel, elongated, semimassive to massive sulfides lenses (the 1807, 1806, Ming North, and Ming South zones) hosted in rhyodacite within the uppermost section of the Rambler Rhyolite formation in the Newfoundland Appalachians. A discordant Cu-rich zone, the Lower Footwall zone, underlies the semimassive to massive sulfide lenses. Alteration assemblages associated with the sulfide mineralization can be divided into nine distinct mappable alteration facies, formed in three paragenetic stages, including: 1) low-temperature weak alteration with quartz-calcite±spessartine, quartz-sericite, and quartz-sericite-chlorite assemblages (stage 1); 2) high-temperature quartz-chlorite, quartz-chlorite-sulfides, and quartz-chlorite-sericite assemblages (stage 2); and 3) low- to intermediate-temperature quartz-sericite-sulfides and localized Mn-Ca-rich assemblages (stage 3). A thin syngenetic silica-rich layer immediately overlies part of the VMS deposit and likely formed during the early stages.

The volcanic facies architecture and synvolcanic fault development controlled the lateral distribution of extrusive rocks and the distribution of hydrothermal alteration. Precipitation of the high temperature, discordant to semi-conformable Cu-rich chloritic assemblages (stockwork) was restricted laterally to one of these synvolcanic faults. It is also stratigraphically controlled by the transition from coherent- to volcaniclastic-dominated lithofacies (i.e., a permeability front). Mass balance calculations illustrate that

the elemental gains in the chloritic assemblages (stage 2) include SiO_2, Fe_2O_3t, MgO, Cr, Ni, and Cu, with losses in Na_2O, MnO, and CaO. Lower temperature, sericitic assemblages (stages 1 and 3) are controlled by the distribution of volcaniclastic rocks and generally form the immediate footwall to the semimassive to sulfide lenses. They show average gains in K_2O, Cr, Ni, Cu, Zn, and Ag and losses in MnO, MgO, CaO, Na_2O, and Y. Assemblages that record Ca- and Mn-enrichment are restricted to the northwest fringe of deposit and likely reflect a low-temperature seawater input, distal to the main hydrothermal discharge zone. These assemblages also show additions in P_2O_5, Y and losses in K_2O. The silica-rich layer that overlies the 1806 zone shows gains in Fe_2O_{3t}, MnO, CaO, P_2O_5, Y, Cr, Ni, Cu, Zn, and Ag and lower MgO, Na_2O, and K_2O contents than least-altered footwall rhyolites. One of the sericitic assemblages, the late quartz-sericite-sulfides assemblage (stage 3), overprints most assemblages and hosts sphalerite-galena-sulfosalt-Ag-Au-rich veins. The chlorite and mica from the late quartz-sericite-sulfides assemblage have significantly lower Fe/Mg ratios than the rest of the alteration assemblages. The stage 3 quartz-sericite-sulfides assemblage is spatially associated with coherent volcanic rocks and the less permeable nature of these rocks is interpreted to have acted as a physical barrier for the ascending metal-rich hydrothermal fluids. Results from the detailed reconstruction of the hydrothermal architecture and paragenetic evolution of the Ming deposit suggests that precious metals were introduced during the waning stage of the hydrothermal system, associated with decrease in temperature and pH of the ore-forming fluids.

5.2. Introduction

The ~487 Ma Ming deposit is a polymetallic Cu-Zn-Ag-Au volcanogenic massive sulfide (VMS) deposit within the Pacquet ophiolite complex located in the northern Newfoundland Appalachians (Fig. 5.1; van Staal and Barr 2012). To date, a total of 0.8 Mt grading 2.9% Cu, 9.63 g/t Ag, and 1.38 g/t Au were processed, with combined measured and indicated resources of almost 28 Mt averaging 1.48% Cu, 0.06% Zn, 1.99 g/t Ag, and 0.26 g/t Au (as of November 2016, Rambler Metals and Mining Ltd.). Much like other well preserved, but metamorphosed VMS deposits (e.g., Flin Flon, LaRonde Penna; DeWolfe 2009; Dubé et al. 2007; Mercier-Langevin et al. 2007), the Ming deposit is a good example of a mound-style VMS deposit associated with a well-developed, extensive and zoned footwall alteration (Pilote et al. 2017). Despite the structural complexity near the massive sulfide horizon and the regional upper greenschist metamorphic overprint (Castonguay et al. 2014), the overall relationship between the mineralization and its altered host rocks is well preserved and relatively intact (Tuach and Kennedy 1978; Pilote et al. 2017). In the Ming deposit the accessibility to the underground workings and drill core from closely-spaced surface and underground drill holes, offers an ideal opportunity to document in detail the mineral assemblages, mineral zonation, whole-rock geochemistry, and hyperspectral reflectance spectrometry (i.e., near infrared-short wave infrared spectrometry (NIR-SWIR)), of hydrothermal alteration in a precious-metal enriched VMS deposit. Further, despite numerous recent studies on the Ming deposit (Brueckner et al. 2011, 2014, 2015, 2016; Pilote et al. 2016, 2017), and historical research (Gale 1971; Tuach and Kennedy 1978; Bailey 2002), very little is

known about the alteration associated with this Appalachian VMS deposit, largely because of the lack of detailed geological and structural information that inhibited the characterization and contextualization of the hydrothermal alteration.

Correspondingly, the aim of this paper is to document the mineralogy, mineral assemblages, paragenesis and distribution of alteration in the Ming VMS deposits, discuss the potential genetic relationships between mineralization and alteration assemblages, and define the physical and chemical processes responsible for the alteration and the nature of fluid/rock interaction. The approach combines field, geochemical, mineralogical, mineral chemical, and infrared spectroscopic data to understand the nature and distribution of alteration, the chemical fluxes associated with alteration, and better understanding of the volcanic and structural control on ore-forming fluids and their evolution in space and time. Because of the well-preserved nature of the Ming VMS deposit and its alteration envelope, this detailed study provides insights into fluid-rock interaction processes associated with precious metal behavior in massive sulfide deposits and the generation of precious metal-bearing deposits in modern and ancient VMS deposits worldwide.

5.3. Geologic Setting

5.3.1. Regional Geology

The Ming deposit is located in the Baie Verte Peninsula, northern Newfoundland, which consists of dissected Upper Cambrian to Lower Ordovician ophiolitic rocks that collectively form the supra-subduction Baie Verte oceanic tract (Waldron and van Staal 2001; van Staal and Barr 2012; van Staal et al. 2013). The Baie Verte oceanic tract is

fault bounded to the west by the Baie Verte Line and to the west by the Green Bay Fault, juxtaposing the ophiolitic rocks against the metamorphosed Neoproterozoic to Upper Cambrian sedimentary rocks of the ancient Laurentian margin (Fleur de Lys Supergroup) in the west, and the Middle to Upper Cambrian (510-501 Ma) Lushs Bight oceanic tract in the east (Fig. 5.1; e.g., van Staal and Barr 2012). Although the ophiolites in the Baie Verte Peninsula have distinct names (i.e., Betts Cove, Pacquet, Pointe Rousse, and Advocate complexes), they consist of four slivers of identical age (ca. 490 Ma) with similar geological assemblages and metallogeny (Hibbard 1983; Dunning and Krogh 1985; Cawood et al. 1996; Bédard and Escayola 2010; Skulski et al. 2010, 2015). They consist of complete to incomplete oceanic crust assemblages that range from variably serpentinized mantle rocks, overlain by ultramafic cumulate sections, transitioning upward to isotropic gabbros to sheeted dikes, and pillowed boninites of the Betts Head Formation (Bédard et al. 1996). Conformably overlying boninitic rocks are mafic island arc tholeiites and felsic volcanic rocks of variable thicknesses belonging to the Mount Misery and Rambler Rhyolite formations, respectively (Fig. 5.2). Collectively, the extrusive volcanic rocks of the Baie Verte oceanic tract reach a maximum thickness of 5 km in the Pacquet complex, including the Rambler Rhyolite formation, which is host to the Ming deposit.

5.3.2. Local and deposit geology

The Rambler Rhyolite formation forms a ~3 x 5 km dome-shaped felsic complex that is located in the central part of an anticlinal fold structure that plunges to the northeast (Fig. 5.2; Castonguay et al. 2014; Pilote et al. 2017). The felsic complex is underlain by mafic-dominated successions of the Mount Misery Formation. Three lithofacies comprise the upper 1000 m of the Rambler Rhyolite formation (Pilote et al. 2017): 1) at the base, a coherent facies that consists of quartz-phyric to aphanitic felsic volcanic rocks (unit 1.1), sharply transitioning to 2) multiple successions of quartz-bearing felsic bedded to massive volcaniclastic rocks of different fragment sizes (unit 1.2); overlain by 3) a thin blue quartz-phyric to quartz-megacrystic felsic coherent flow laterally transitioning to bedded quartz-bearing felsic tuffs (unit 1.3) (Fig. 5.3). Both units 1.2 and 1.3 are fault bounded and/or controlled by synvolcanic faults (Fig. 5.3). The mineralized zones of the Ming deposit occur as ruler-shaped massive-sulfide to semimassive sulfide lenses located at the very top of the felsic complex that plunge 30-35° to the northeast. The lenses have significant variations in Cu, Zn, Ag, and Au grades (Fig. 5.2; Brueckner et al. 2014, 2016; Pilote et al. 2017). The ore zones are divided into different zones including the 1807, 1806, Ming North, Ming South, and the Lower Footwall zones (Fig. 5.2). The 1806 Zone is the most precious metal-rich massive sulfide lens with Ag and Au grading in average 15.07 g/t and 2.97 g/t, respectively. A Cu-rich stringer zone (Lower Footwall Zone) underlies the sulfide lenses, which represents the *feeder zone* (cf. Lydon 1984) of the deposit.

The Rambler Rhyolite formation is overlain by the Lower to Middle Ordovician Snooks Arm Group, which is also referred to as the Snooks Arm cover sequence (Skulski et al. 2010, 2015). At the Ming deposit, the base of the cover sequence is a spatially restricted mafic polymictic volcanic breccia with up to 10 vol % sulfide clasts (Pilote et al. 2016). This unit is conformably overlain by a thin (≤1 m), dark purple to black, finely laminated shale to siltstone, which is considered equivalent to the orogenic Au-associated Nugget Pond "horizon" regionally (Skulski et al. 2010, 2015). These sedimentary sequences show no evidence of hydrothermal alteration and were deposited after the formation of the Ming deposit. The fine-grained sedimentary rocks are overlain by multiple successions of mafic tuff, tuff breccia, and massive flows that are visually similar, and are cut by multiple generations of mafic sills and dikes that are feeders to these units (Pilote and Piercey in review). Lastly, the south-directed Rambler Brook Fault truncates the base of the Rambler Rhyolite formation, structurally juxtaposing the felsic complex with stratigraphically lower parts of the Snooks Arm Group (i.e., thrust sense of movement; Fig. 5.2).

5.3.3. Metamorphism and deformation

The metamorphic grade in the Pacquet complex does not exceed upper greenschist facies, except near the Ordovician-Silurian intrusive bodies where contact metamorphism has locally produced amphibolite facies mineral assemblages (Tuach and Kennedy 1978; Castonguay et al. 2009, 2014). Four major deformation events (D_1 to D_4) are recognized at the Ming deposit, with D_2 being the most intensely developed (Castonguay et al. 2009,

2014; Pilote et al. 2017). The deformation event resulted in penetrative fabrics that dip east at high angles, with sulfides locally transposed and/or remobilized into D_2 structures. Those later structures are commonly accentuated by overprinting D_3 and D_4 structures; however, sulfide remobilization is spatially restricted to the macro-scale (i.e., 10s of meters: Pilote et al. 2017). The synvolcanic hydrothermal alteration assemblages at Ming were metamorphosed to greenschist facies as well, and the different assemblages described below are metamorphic equivalents to alteration assemblages developed as the deposit was formed prior to regional deformation and metamorphism.

5.4. Description of Alteration Assemblages and Distribution

Hydrothermal alteration in the Ming deposit occurs exclusively in the footwall rocks and consists of compositionally diverse mineral assemblages that comprise varying amounts of chlorite, sericite, quartz, and sulfides (±other trace minerals). Field and drill core observations were used to map the distribution and relationships between the major alteration minerals and assemblages, which have been refined and validated via the use of petrography and analytical methods. Microscopic observations helped in establishing the paragenetic sequences reflecting the evolution of the hydrothermal system associated with ore formation. The assemblages are summarized in Table 5.1 and their spatial distribution is shown in Figure 5.4, which also includes a representative section of the volcanic stratigraphy of the host successions (Pilote et al. 2017). The average relative abundance of minerals forming each alteration assemblage is shown in Figure 5.5.

Two main extensive alteration facies are recognized at the Ming deposit, including a chlorite-rich facies that is formed 50 to 300 m below the massive sulfide horizon, and a sericite-rich facies, formed within ~100 m of the massive sulfides and below the chlorite-rich facies (Fig. 5.4). Both are developed sub-parallel to the ore zones. Other less extensive alteration assemblages such as weakly altered rocks and (Mn-rich) garnet-bearing facies are developed in the immediate footwall of the 1807 Zone to the northwest (Fig. 5.4). Lastly, a <3 m-thick stratiform silica-rich layer is developed above the 1806 Zone and parts of the 1807 Zone (Fig. 5.4). These are described in further details below.

5.4.1. Chlorite-rich alteration facies

The chlorite-rich alteration facies can be divided into three distinct assemblages based on its mineral abundances, including: 1) quartz-chlorite, 2) quartz-chlorite-sulfides, and 3) quartz-chlorite-sericite (Figs. 5.4 and 5.5). The first two assemblages are dark bluish grey colored and consist of a pervasive quartz and chlorite alteration with fine- to coarse-grained metamorphic actinolite, epidote, and biotite overgrowths (Fig. 5.6A-D). They affect both the coherent felsic rocks of unit 1.1 and the volcaniclastic-dominated felsic rocks of unit 1.2. Despite the intensity of this alteration, relic quartz phenocrysts and phenoclasts are commonly preserved (Fig. 5.6A). Together they form a >2000 m x ~400 m discordant to semi-conformable alteration zone and are distinguished based on the presence or absence of cm-scale sulfide-rich stringers. Within the chlorite-rich facies, the quartz-chlorite-sulfides assemblage is restricted to most of the Ming South Zone and the up-dip section of the 1806 Zone (Fig. 5.4). It defines the laterally and stratigraphically

restricted ~28 Mt Lower Footwall Zone that represents to footwall stockwork, or *feeder*, of the VMS deposit (Pilote et al. 2017). The quartz-chlorite-sericite assemblage represents the less intense alteration of the chlorite-rich facies. It occurs within units 1.1 and 1.2 of the Ming South and 1807 zones and is commonly found marginal to or within the quartz-chlorite and quartz-chlorite-sulfides assemblages (Fig. 5.4). Although the quartz-chlorite-sericite assemblage occurs at different stratigraphic levels, it is most spatially extensive in the 1806 Zone (Fig. 5.4). In hand sample, the quartz-chlorite-sericite assemblage is characterized by a lighter grey color owing to the abundance of sericite (Fig. 5.6E, F).

5.4.2. Sericite-rich alteration facies

The sericite-rich facies is divided into three main mineral assemblages: a quartz-sericite-chlorite assemblage, a quartz-sericite assemblage, and a quartz-sericite-sulfides assemblage. Except for the quartz-chlorite-sericite assemblage, most of the sericite-rich facies is limited to the upper ~100 m of the host successions; however, all are limited to the Ming South and 1806 zones (Fig. 5.4). Although these sericite-rich assemblages all contain quartz and sericite as predominant constituents, significant differences exist in respect to their composition in trace minerals and sulfides (Fig. 5.5). Moreover, key field relationships are recognized, which helped to discriminate the assemblages. The quartz-sericite-chlorite assemblage is found as thin (<25 m-thick) intersections within coherent and volcaniclastic rocks of units 1.1 and 1.2, commonly at the contact between two different alteration assemblages (Fig. 5.4). The quartz-sericite-chlorite assemblage is light

to intermediate grey with pervasive quartz and sericite (Figs. 5.7A, B). At greater depths, chlorite veins cross-cut this assemblage, likely as a product of the intense nearby chloritic alteration. Both the quartz-sericite and quartz-sericite-sulfides assemblages are light to intermediate grey and contain trace amount of interstitial chlorite (Figs. 5.7C-F) with variable amount of green micas (Fig. 5.4). The green mica is typically found as mm- to cm-scale elongated clots, but also pervasively within sericitic assemblages (Fig. 5.8A). These two assemblages overprints almost exclusively the coherent and tuffaceous facies of units 1.2 and 1.3 (Fig. 5.4); although two samples yielding a quartz-sericite assemblage were found in the deepest section of the examined drill holes (i.e., ~350-450 m below the ore zone). Fine epidote grains are found exclusively in the quartz-sericite assemblage and sulfide are significantly more abundant in the quartz-sericite-sulfides assemblage (Fig. 5.5). In addition, sulfide stringers associated with these alteration facies contain distinct mineralogy, such as galena and pyrrhotite being limited to the quartz-sericite-sulfides assemblage (Figs. 5.5, 5.7E, F). While the field relationships between the quartz-sericite and quartz-sericite-sulfides assemblages are cryptic, a clear overprint of the latter on the quartz-chlorite-sulfides (and validated petrographically) indicates that the quartz-sericite-sulfides assemblage came in late relative to the other assemblages in the system (Fig. 5.8B-D).

5.4.3. Weak alteration facies

A weak alteration is developed throughout the stratigraphic footwall of the 1807 Zone (Fig. 5.4). Most of the primary textures and mineral assemblages are preserved and

contain minor abundances of sericite, chlorite, and other trace minerals, (Fig. 5.5), typically developed in the groundmass of the coherent to volcaniclastic rocks (Fig. 5.9A, B). The weakly altered rocks are purplish grey coloured and relic plagioclase are common in thin sections (Fig. 5.9B). This weak alteration transitions laterally and stratigraphically to a slightly more intense alteration assemblage composed of sericite, garnet, and calcite. The garnet is porphyroblastic and Mn-rich (i.e., spessartine: Pilote et al. 2014) (Fig. 5.9C, D). This sericite-calcite±spessartine assemblage is developed almost entirely in the volcaniclastic rocks of unit 1.2, immediately below the 1807 Zone (≤10 m from the massive sulfides), and to a lesser extent below the 1806 and Ming South zones where it occurs down to a depth of ~30 m below mineralization (Fig. 5.4).

A paragenetically late and spatially restricted discordant assemblage composed of calcite, quartz, and spessartine is developed within 10 m of the 1807 Zone massive sulfide (Fig. 5.4). Previous work also identified significant amounts of Mn in the calcite (Pilote et al. 2014). This assemblage consists of a network of sharp, irregular, salmon pink colored <0.1 to 20 cm discrete veins that cross-cut other alteration assemblages proximal to the massive sulfides (Fig. 5.9E, F). The veins are mainly parallel to the lens and consist of very fine-grained polygonal quartz and coarser calcite accretions, overprinted by very fine-grained idioblastic spessartine and well-developed light colored biotite grains (Fig. 5.9E.

The stratiform silica-rich layer that immediately overlies the 1806 Zone consists of a grey colored, massive and featureless quartz-calcite-rich assemblage (Figs. 5.4, 5.9G, H). It is in sharp contact with the overlying cover sequence and does not cross-cut nor

does it replace surrounding units (no evidence of relic clasts). Thus, it likely represents an accumulation of siliceous fluids on the seafloor. Recrystallized, fine-grained, cubic disseminated pyrite grains are found throughout this assemblage. As well, chalcopyrite, sphalerite, and electrum (Au-Ag alloy) veinlets are developed as D_2-related piercement structures, at high angle to the main S_2 fabric in this assemblage (Pilote et al. 2017).

5.5. Hyperspectral Data and Distribution

Hyperspectral analyses were undertaken on altered samples in the Ming deposit to complement field and petrographic observations and to identify hydrous minerals (e.g., micas, chlorite) and define their compositions. Minerals such as sericite and chlorite (i.e., hydrous minerals) contain mineral bonds with hydroxyl (OH) anions and absorb incident light at specific wavelengths resulting in diagnostic spectra (e.g., Thompson et al. 1999). In micas and chlorites, there are often distinctive absorption hulls for water/OH absorption (i.e., ~1400nm and 1930nm), AlOH absorption (i.e., ~2200nm), FeOH absorption (i.e., ~2250nm), and MgOH absorption (i.e., ~2350nm) (e.g., Thompson et al. 1999; Hermann et al. 2001; Buschette and Piercey 2016). Moreover, there are changes in the spectral positions of the various absorption hulls that vary as a function of mineral composition. For example, the relative position of the AlOH hull can vary from ~2180nm to 2228nm depending on whether a white mica is sodic (<2195nm), potassic (~2200nm), or phengitic (i.e., Fe-Mg-rich; >2216nm), and is related to octahedral Al^{vi} (due to Tschermak substitution, for instance: Post and Noble 1993; Hermann et al. 2001; Jones et al. 2005; Yang et al. 2011). Similarly, the FeOH and MgOH absorption positions and

their depths can change with changing chlorite compositions from Fe- to Fe-Mg to Mg-chlorite (e.g., Herrmann et al. 2001; Jones et al. 2005). In particular, higher Fe contents in chlorite will result in longer MgOH and FeOH absorption wavelengths (Pontual et al. 1997). It is notable that a moderate secondary AlOH absorption can occur near 2340 nm, which overlaps and can partially masks MgOH absorptions (Pontual et al. 1997). Hence, the hyperspectral analyses of chlorite compositions here are based solely on FeOH absorption features. Other features such as H_2O, OH, and CO_3 can also be subjected to interference (Herrmann et al. 2001) and are therefore excluded here.

Specifics about the instrumentation, techniques, and methods of data reduction used in this study are described in detail in Buschette and Piercey (2016) and only summarized here. Detailed logging from 56 drill holes was complemented by hyperspectral analyses within a wide range of alteration assemblages. A total of 1001 systematic or selected measurements were acquired on cleaned, dried, and fresh cut surfaces of underground samples and drill core using a Terraspec^{TM} mineral spectrometer with a spectral range of 350 nm to 2500 nm and a spectral resolution of less than 10 nm. On drill cores with sample numbers starting with the number 3 or 6, measurements were taken at intervals of three meters, excluding the post-mineralization intrusions. The acquisition was done using the RS3 Spectral Acquisition software and optimization and white references were performed every ~25 samples to escape drifts in data. A 4th order polynomial fitting curve was applied over the ranges for the AlOH wavelengths (2180–2230 nm) and for FeOH (2240–2260 nm). Pyrophyllite- and talc-bearing samples were

used as reference materials and measured after each optimization procedure for quality controls.

5.5.1. Results

A total of 1001 analyses were acquired systematically or selectively on 56 drill holes intersecting different parts of the Ming deposit. Maximum AlOH absorption features vary between 2010 and 2012 nm in less intense alteration assemblages (i.e., least-altered, weakly altered, and sericite-calcite±spessartine), whereas the values are lower in the most intense alteration assemblages (Fig. 5.10; Table 5.2), regardless of the unit. Given the spatial distribution of the alteration assemblages, lower absorption values are typically found in the Ming South Zone, whereas higher values are restricted to the 1807 and 1806 zones. Notably higher values in AlOH absorption features are found in the silica-rich layer with an average of ~2228 nm, suggesting micas of phengitic compositions. However, the standard deviation on the latter average is very high (1σ = ~17 nm; Table 5.2), which indicates that the silica-rich layer contain sericite with a broad range of composition. Maximum FeOH absorption wavelengths are relatively constant throughout the alteration facies, i.e., between 2246.4 and 2254.5 nm, although with a slight increase in chloritic assemblages (Fig. 5.10; Table 5.2). Significantly shorter absorption wavelengths (Fe-poor) were yielded in the quartz-sericite-sulfides and silica-rich layer assemblages (Fig. 5.10).

5.6. Mineral Chemistry

The compositions of chlorite, mica, calcite, and biotite in samples representative of each alteration assemblage were obtained by electron probe micro analysis (EPMA). A total of 11 samples representing most of the alteration assemblages were selected for quantitative analyses on chlorite, sericite, calcite, and biotite using a JEOL JXA-8230 EPMA at the Department of Earth Sciences, Memorial University of Newfoundland, St. John's. A total of 14 elements (Si, Ti, Al, Cr, V, Fe, Mg, Mn, Ca, Ba, Na, K, Cl, and F) were analyzed on chlorite and sericite, 12 elements (Si, Ti, Al, Fe, Mg, Mn, Ca, Ba, Na, K, Cl, and F) on biotite, and seven elements (Fe, Mn, Mg, Zn, Ca, Sr, Ba) on calcite. The standard minerals and crystals used for calibration and measured elements are summarized in Table A5.1. Counting times for calibration are 10 seconds on peaks and 5 seconds on backgrounds. Analyses on unknowns were performed using the same crystals as the calibration. The silicates (sericite, chlorite, and biotite) were analyzed using an accelerating voltage of 15 kV, a 20 nA beam current, focused at 3-5 μm, with elemental counting times ranging from 5 to 60 seconds. Calcite grains were analyzed using an accelerating voltage of 20 kV, a 5 nA beam current, defocused at 15 μm, with elemental counts ranging from 5 to 30 seconds. Elemental peaks were carefully selected to avoid overlaps and background (or off-peak) measurements were made at 50% of the counting time on each side of the peak of interest. Average compositions of minerals for each assemblage are given in Tables 5.3 to 5.6. Complete datasets are presented in Appendices 6 to 9.

5.6.1. Chlorite

Chlorite compositions are homogenous within individual samples and are mostly Mg-rich with Fe/(Fe+Mg) ratios ranging between 0.35 and 0.44, plotting within the Mg end-member of the ripidolite field (Fig. 5.11A; Hey 1954). The high-Mg chlorite in the quartz-sericite-sulfides assemblage shows distinctively lower values (~0.17) (Fig. 5.11A).

5.6.2. Sericite and green mica

Herein, we define sericite as foliated aggregates of fine-grained white mica as described by Rieder et al. (1999). Sericite present in assemblages with significant chlorite contains between 2.91 and 4.10 wt. % FeO, whereas sericite in sericite-rich assemblages closer to the massive sulfides have lower FeO contents (1.36 and 1.82 wt. %, respectively; Table 5.4). The samples show a continuous array in Fe/(Fe+Mg)-Al space (Fig. 5.11B), with sericite from the quartz-sericite assemblage having the highest Al values (averaging 36.5 wt. %), whereas in the sericite-calcite±spessartine they have the lowest values (averaging 32.7 wt. %). This range of Al is also consistent with the hyperspectral results where sericite with the highest Al contents have the lowest values in 2200 nm absorption location (Table 5.4).

The Na_2O content in sericite for most assemblages ranges from ~0.5 to 0.7 wt. %, except for the quartz-chlorite assemblage, in which values average 1.29 wt. % Na_2O. The latter also contains the lowest K_2O, BaO, and MgO (Table 5.4). The compositions of muscovite porphyroblasts in sericite-rich layers are identical to the surrounding groundmass, indicating that recrystallization from metamorphic overprinting has not

changed the signature of the white micas and they reflect the original hydrothermal mica compositions.

The distinctive green micas analyzed in the study (n = 3) yielded Cr_2O_3 values up to 0.36 wt. % (Appendix 7) and locally had up to 0.17% V_2O_3 in the Lower Footwall Zone. Besides Cr_2O_3, there are no other geochemical distinctions between green micas and neighbouring sericite.

5.6.3. Calcite

Calcite in the Ming deposit has broadly similar FeO and MgO contents in the Mn-Ca-rich and silica-rich assemblages, and both have trace amounts of Zn, Sr, and Ba (Table 5.5). The MnO content in calcite from the Mn-Ca-rich assemblage (5.32 wt. % MnO) below the 1807 Zone is significantly higher than that in calcite from the silica-rich layer (0.67 wt. % MnO).

5.6.4. Biotite

Biotite in the felsic host rocks is mostly metamorphic in origin, and only a few are of potential primary origin in least-altered rocks. Biotite analyses were predominantly made on porphyroblasts and they have variable color from light yellow-brown to dark green. Some of the light-colored biotite found in the quartz-sericite, quartz-sericite-sulfides, and Mn-Ca-rich assemblages have phlogopitic compositions with high Mg/(Mg+Fe) and Si/Al ratios (Fig. 5.11C), whereas darker biotite generally has lower Mg/(Mg+Fe) and Si/Al ratios. The BaO content in biotite in the Mn-Ca-rich assemblage

is significantly higher than the other assemblages with values averaging 0.64 wt. % BaO (Table 5.6).

5.6.5. Paragenesis

Cross-cutting relationships of the alteration assemblages at various scales, combined with mineral associations and chemistry, revealed a paragenetic evolution of the Ming hydrothermal system (Fig. 5.12). The earliest evidence of alteration includes the quartz-sericite-chlorite assemblage, which generally forms an envelope to the intense chlorite alteration facies (Fig. 5.4). The timing of the quartz-sericite assemblage remains uncertain because of the lack of field relationships with other alteration facies; however, given that it shares similar Fe/(Mg+Fe) ratios in chlorite and sericite with the quartz-sericite-chlorite assemblage (Fig. 5.11A), the quartz-sericite may be paragenetically related to the quartz-sericite-chlorite assemblage and thus, part of stage 1. The overprinting chloritic assemblages (i.e., quartz-chlorite, quartz-chlorite-sulfides, and quartz-chlorite-sericite) are part of the second stage, which are in turn overprinted by the quartz-sericite-sulfides assemblage of the latest stage (stage 3) of alteration (Fig. 5.12). The weak alteration and sericite-calcite±spessartine assemblage are overprinted by the quartz-chlorite assemblage at depth below the 1807 Zone and are therefore attributed to stage 1. In the case of the Mn-Ca-rich assemblage that cross-cuts the footwall of the 1807 Zone, its paragenetic relationship to the chloritic and late quartz-sericite-sulfides is unclear and is considered here as an intermediate stage (stage 2b). In summary, the three stages of alteration show a progressive temporal (and spatial) change from sericite to

chlorite to sericite, reflecting a change in fluid conditions (e.g., pH, temperature). This marks an evolution that is common to the genesis of VMS deposits worldwide (e.g., Large 1992).

5.7. Lithogeochemistry

A suite of 188 samples was selected for lithogeochemistry. The samples were collected throughout the deposit from drill core and underground workings to obtain a complete characterization of the primary and secondary geochemical signatures of the host successions. The analytical and quality assurance and control procedures are described in detail by Pilote and Piercey (in review) and will therefore only be summarized here. A suite of major and trace elements were analyzed at Activation Laboratories Ltd. in Ancaster, Ontario, Canada, where samples were crushed and pulverized using mild steel before undergoing lithium metaborate/tetraborate fusion followed by HF-HNO_3 dissolution and subsequent analysis by inductively coupled plasma emission-mass spectrometry (ICP-ES). An additional suite of trace elements were analyzed at the Department of Earth Sciences at Memorial University of Newfoundland using the pulps returned from the Activation Laboratory Ltd. The dissolution procedure used here is a modified version of that described by Jenner et al. (1990) and Longerich et al. (1990) and was also summarized in Pilote and Piercey (in review). Dissolved samples were spiked and analyzed using a Perkin Elmer Elan DRCII Quad© inductively coupled plasma-mass spectrometry (ICP-MS) instrument and followed by offline data reduction. The complete analytical results are presented in Appendix 5.

5.7.1. Primary signatures

Least-altered samples from the Ming deposit host sequence were carefully selected in Pilote and Piercey (in review) and are presented herein in addition to altered samples, which are used to assess elemental changes related to hydrothermal alteration. The average compositions of the units that are host to the Ming deposit are presented in Table 5.2. Except for the silica-rich layer, regardless of the host units and alteration, most samples plot in the subalkalic fields of andesite-basalt on a Zr/TiO_2 versus Nb/Y plot (Fig. 5.13A; Winchester and Floyd 1977; Pearce 1996); however, their high SiO_2 (~66-69 wt. %) contents make them more akin to dacites or rhyodacites (Fig. 5.13B; Winchester and Floyd 1977; Pilote and Piercey in review). Most samples cluster along a single slope that intersects the origin on an Al_2O_3 versus Zr diagram (Fig. 5.13C), which is diagnostic for mass and/or volume change associated with alteration and suggests the samples are cogenetic and from a similar magma suite (Barrett and MacLean 1994). Their relatively high Th/Yb (~5) and Zr/Y (~10) ratios indicate that the rocks have calk-alkalic affinities (Fig. 5.13D; Ross and Bédard 2009), although unit 1.3 is slightly more enriched than units 1.1 and 1.2. On an extended primitive mantle-normalized plot, the least-altered rocks show light rare earth elements (LREE) enrichment relative to the heavy rare earth elements (HREE) (Fig. 5.13E). The noticeable anomalies in some high field strength elements (HFSE) are typical of subduction zone magmatic rocks influenced by fluids and/or melts from the subducted slab (e.g., Pearce et al. 1995). The samples are generally depleted in trace elements (e.g. Zr < 80 ppm; Table 5.2) and have low Yb_{cn} (cn = chondrite normalized) values and high $(La/Yb)_{cn}$ ratios, which classify as FI- and FII-

types felsic volcanic rocks according to Lesher et al. (1986) and Hart et al. (2004) classifications (Fig. 5.13F). These latter geochemical attributes are products of deep level (>15 km), garnet/amphibole controlled, and low temperature (~700-800°C) partial melting (Lesher et al. 1986; Hart et al. 2004; Pilote and Piercey in review). Because of the limited range in compositions for the least-altered rocks, lack of differentiation, constant incompatible trace element ratios, and general geochemical similarities, the rocks in the Ming deposit can be considered cogenetic. Nevertheless, while units 1.1 and 1.2 are similar geochemically despite their lithofacies differences (Pilote et al. 2017), unit 1.3 is slightly more enriched in trace elements; thus, for simplicity and for alteration and mass balance calculations, units 1.1 and 1.2 are amalgamated hereafter as one single geochemical unit, separate from unit 1.3 (Table 5.2).

5.7.2. Alteration signatures

Alteration geochemical variations of the Ming felsic volcanics are shown in Figures 5.13C and E. The samples have been grouped according to their respective alteration assemblages and their average compositions are presented in Table 5.2.

On the alteration box plot of Large et al. (2001b) (Fig. 5.14), samples from units 1.1/1.2 show similar trends towards the (Fe-rich) chlorite/pyrite node, whereas samples from unit 1.3 show a distinct compositional trend towards the muscovite node (Fig. 5.14A). Alteration assemblages at Ming have chemical signatures that mirror their alteration mineralogy (Fig. 5.14B), including weakly altered rocks overlapping the least-altered field; the samples from the Mn-Ca-rich assemblage and silica-rich layer that plot

near the Ca-rich (epidote/calcite) node; and some samples from the sericite-calcite±spessartine assemblage that show Na-enrichment (i.e., albitization); and the chlorite-sulfide-rich assemblages plot near the pyrite-chlorite node (Fig. 5.14B). In the case of the quartz-sericite and quartz-sericite-sulfides assemblages, although spatially proximal, they record distinct compositional trends (Fig. 5.14B): both form negative linear arrays towards the muscovite (K-rich) node but the quartz-sericite-sulfides assemblage shows systematically higher CCPI values.

Three chemostratigraphic sections constructed from drill holes that intersect the 1807, 1806, and Ming South zones are shown in Figures 5.15 to 5.17 and provide a spatial representation of various geochemical and spectral responses relative to the ore zones. Intersections with greater chlorite abundances show reduction in mobile and immobile elements, with the exception of Cr, whereas the opposite is shown in the sericitic assemblages. Copper and Zn values are the highest in the chlorite-rich and sericite-rich assemblages, respectively. Lower alteration intensities are reflected by lower alteration indices (i.e., AI and CCPI) and Mg#. The Ba/Sr ratios and Eu/Eu* values are generally the highest near the massive sulfide lenses. Moreover, variations in the 2200 nm and 2250 nm absorption ranges are notable with both features increasing near the sulfide lenses.

Some of the spatial trends in Figures 5.15, 5.16, and 5.17 are also replicated when plotted against AI and illustrate key elemental behavior in response to various alteration intensities (Fig. 5.18). Barium is predominantly depleted in the quartz-chlorite-sulfides and quartz-chlorite assemblages, whereas Sr progressively decreases with increasing

intensity of alteration, regardless of the assemblage (Fig. 5.18A, B). The low values in Ba and Sr in the silica-rich layer is likely due to the lack of feldspars (Fig. 5.18A, B). The MnO content is high in the Mn-Ca-rich and sericite-calcite±spessartine assemblages, consistent with the abundance of Mn-rich minerals, is variable in the sericitic assemblages, whereas it virtually remains constant throughout the weakly altered rocks and chloritic assemblages (Fig. 5.18C). Arsenic, Sb, Pb, Zn, and Hg are generally higher in the quartz-sericite and quartz-sericite-sulfides assemblages near the massive sulfide lenses, whereas, as aforementioned, Cu is mostly associated with the chloritic assemblages at depth (Fig. 5.18D-I). In the footwall rocks, the latter metals are hosted in quartz-sulfide-rich stringer veins, in which As, Sb, Pb, Zn, and Hg are found in veins predominantly composed of arsenopyrite, sphalerite, sulfosalts, and tellurides, and Cu in chalcopyrite-rich veins.

5.7.3. HFSE and REE behavior

The normalized "immobile" HFSE and REE (hereafter referred to as trace elements for brevity) in Figure 5.15D were separated into different alteration assemblages in order to examine the influence of alteration on elements that are typically considered immobile (e.g., Jenner 1996) (Fig. 5.19A-E). While they show strong variability in total abundances, the majority of trace element patterns remain generally constant (e.g., LREE/HREE ratios) regardless of alteration type with the exception of their absolute abundances, which can be explained by enrichment and dilution associated with mass changes (e.g., Barrett and MacLean 1994). However, there are some samples that have

signatures that vary from this pattern. In particular, the chlorite-rich assemblages contain lower total trace element abundances than the sericitic ones. Although the quartz-sericite and quartz-sericite-sulfides assemblages show little variations in their trace elements compared to the least-altered rocks, one of the most distinctive features is the high positive Eu/Eu* anomalies (up to 3.14) in some samples (Fig. 5.19C, E). Conversely, chloritic assemblages have the lowest Eu/Eu* values (as low as 0.32; Table 5.2). Enrichment in HREE is noticeable in the sericite-calcite±spessartine assemblage, which can be explained by the abundance of garnet grains. Lastly, as previously described, the silica-rich layer shows strong variability in trace element patterns and abundances, which is explained by some of the elemental values being near detection limits (Fig. 5.19E).

5.7.4. Mass balance and elemental gains and losses

Absolute compositional changes associated with alteration were calculated using Grant's (1986) isocon technique, which involves plotting selected scaled elements in the least-altered sample against altered samples. Immobile elements lie along a straight line, the isocon, whereas elements above and below the line reflect elements gained and lost during the alteration process, respectively (Fig. 5.20). The net mass change (ΔM^A) of an altered rock relative to its protolith can be calculated using $\Delta M^A(\%) = 100(1/m - 1)$, where m represents the slope of the isocon. The slope (m) can be determined by taking the average of ratios C_i^A/C_i^O, where C_i^A and C_i^O represents the concentration of element i in altered and least-altered rocks, respectively. These absolute concentration changes of elements during the alteration process (ΔC_i^A) can be determined by using $\Delta C_i^A =$

$100(C_i^A/(mC_i^O) - 1)$. The calculated relative mass changes are plotted as histograms in Figure 5.21.

Most assemblages show a net gain in mass, except for the quartz-sericite assemblage located below the sulfide lenses (Figs. 5.20A, 5.21A). The relative mass change in SiO_2 mimics the net mass changes in most assemblages, which highlights the role of silica during hydrothermal alteration (Fig. 5.21B). All assemblages exhibit elevated loss-on-ignition (LOI) (Fig. 5.21J), and Na_2O depletions, with the exception of the sericite-calcite±spessartine assemblage in unit 1.3, which has Na_2O addition (albitization) (Fig. 5.21G). Manganese, CaO, P_2O_5, and Y additions mostly occur in the sericite-calcite±spessartine, Mn-Ca-rich assemblages, and the silica-rich layer (Fig. 5.21E, F, I, K). Fine calcite veinlets in the weakly altered rocks can explain the CaO addition (Figs. 5.20A, 21F). The MgO gains are predominant in chloritic assemblages, whereas chlorite-barren assemblages are generally depleted in MgO (Fig. 5.21E). Similar trends occur with Fe_2O_{3t}, although the addition of Fe in the quartz-sericite-sulfides assemblage and silica-rich layer reflect their high sulfides contents (Fig. 5.21C). The quartz-sericite, quartz-sericite-chlorite, and quartz-sericite-sulfides assemblages show significant gains in K_2O, whereas losses are shown in all other assemblages (Fig. 5.21H). Transition metals Ni and Cr are added in most assemblages, except in the Mn-rich and quartz-sericite-chlorite assemblages (Fig. 5.21L, M). Copper, Zn, and Ag are added to various assemblages reflecting the varying abundances chalcopyrite, sphalerite, and Ag-bearing minerals in the alteration assemblages.

5.8. Discussion

5.8.1. Hydrothermal alteration architecture and volcanic controls

The distribution of the various alteration mineral assemblages shown in Figure 5.4 is limited to the footwall rocks of the Ming deposit. Most of the intense chloritic alteration (i.e., quartz-chlorite, quartz-chlorite-sulfides, and quartz-chlorite-sericite) occurs at depth at or near the coherent-volcaniclastic interface of units 1.1 and 1.2, between 300 and 50 m below the massive sulfides. A gap of <100 m separates the chloritic assemblages from the massive sulfide-bearing interval that consists of sericite- and Mn-Ca-rich assemblages. On the scale of the Rambler Rhyolite dome, the deep, laterally restricted, and linear distribution of the alteration reflects controls by synvolcanic structures and focusing of hydrothermal fluid discharge (e.g., Large 1992). Furthermore, recent work has demonstrated that the involvement of synvolcanic faults was critical in the development of the Ming deposit by controlling the extent and geometry of felsic volcaniclastic-dominated units 1.2 and 1.3 and providing permeable, planar, and restricted pathways to hydrothermal fluids (Pilote et al. 2017). The elongated shapes of the ore zones are thus attributed to the controlling effect of these parallel synvolcanic structures and the disposition of the quartz-chlorite-sulfides assemblage (or Lower Footwall Zone) at depth supports this (e.g., see Fig. 5.5 in Pilote et al. 2017).

Although the location of some fluid discharge may have been controlled by synvolcanic faults, the vertical distribution and variation of the alteration assemblages were also controlled by other factors. For example, many of the alteration assemblages are conformable to semi-conformable to stratigraphy and some preferentially associated

with certain types of lithofacies, suggesting a lithological control on fluid circulation (Fig. 5.4). In addition, the chlorite alteration in the Ming deposit is generally restricted to the deeper parts of the Rambler Rhyolite formation, whereas the sericite alteration is located in the upper parts of the formation (Fig. 5.4). In VMS systems, it is widely accepted that chlorite alteration forms due to the reaction of high-temperature (>300°C), slightly acidic (pH ≈ 4-5) fluids with surrounding rocks, whereas sericitic alteration is attributed to cooler (<200°C) and more acidic (pH < 4) fluids (e.g., Walshe and Solomon 1981; Schardt et al. 2001). In the Ming deposit, the alteration distribution suggests that the fluids that altered the upper part of the formation were of lower temperature and pH. It is also possible that this may be partly due to the permeability of units 1.2 and 1.3 at the time of their accumulation, as opposed to coherent felsic volcanic rocks of unit 1.1, which led to greater fluid-rock interaction and intensity of alteration (Large 1992; Gibson 1999), and is partly supported by the presence of chlorite- and Cu-rich mineralization in the Lower Footwall Zone (cf. Lydon 1988, 1996), versus sericite-quartz and Zn-Pb-sulfosalt-rich mineralization in the massive sulfide lenses.

5.8.2. Major element associations and processes

The major and trace element geochemistry in the alteration footprint of VMS deposits reflects the physicochemical nature of the fluids, host rock chemistry and permeability/porosity, and intensity of fluid-rock interaction (e.g., Lydon 1988, 1996). In the Ming deposit, the observed losses in Na_2O, K_2O, Ba, and Sr (Table 5.2; Figs. 5.15, 5.16, 5.17 and5.18A, B) associated with intense chlorite alteration, coupled with the

addition of K, and Mg and Fe reflect the destruction of feldspar and formation of sericite (K) and/or chlorite (Mg-Fe) (Fig. 5.21C, E, H). These elemental changes are common in VMS systems as hydrothermal fluids interact with host rocks during fluid-rock reaction (e.g., ion exchange/substitution and/or hydrolysis: Reed 1997). In particular, hydrolysis or breakdown of feldspars is accompanied by losses in Na^+ (i.e., Na_2O losses), coupled with K^+ fixation in sericite (i.e., K_2O gains) (Fig. 5.22A). At higher temperatures (>300°C), Mg^{2+} and Fe^{2+} in descending seawater are mostly fixed in chlorite and some in micas (Fig. 5.22B). The resulting fluids have low pH (as the product from the reaction releases H^+; Hajash and Chandler 1982) and are capable of carrying significant metal in solution, explaining the association of chlorite +/-sericite alteration with metal enrichment (e.g., Lydon 1988, 1996).

Interestingly, as K_2O continues to decrease towards chlorite-rich zones, Na_2O progressively increases towards the most intense alteration (Fig. 5.22A). This is supported by a number of chlorite analyses in the quartz-chlorite-sulfides assemblage that yielded anomalous Na_2O content (Appendix 6). This relationship is uncommon as most VMS deposits show significant depletion to complete absence in Na_2O at their core (e.g., Spitz and Darling 1978; Gemmell and Large 1992; Large et al. 2001a-c). Whereas it is common for some deposits to undergo a Na-Mg enrichment as the system heats up and/or cools down (flux of Na and Mg from the seawater; Galley 1993), the negative correlation that exists between Na_2O and MgO (Fig. 5.22C) makes this an unlikely process. To explain the increase in Na/K ratio, one could envisage two possible scenarios. The first involves influx of Na-rich fluids from the breakdown of plagioclase in the volcanic successions at

the base of the hydrothermal system or by a late flux of unmodified seawater (e.g., Date et al 1983). The second scenario involves a phase separation in the hydrothermal fluids from adiabatic depressurization (boiling) where NaCl-rich brine with density greater than its vapor phase would begin to separate at depth (Arnòrsson et al. 2007; Monecke et al. 2014). The latter implies that the ascending fluids evolved along the boiling curve in the H_2O-NaCl system and became increasingly saline as the vapor was lost during boiling; hence, increasing the possibility for Na sorption in the chloritic assemblages. Moreover, the presence of Au-Ag-enrichment, sulfosalt-rich mineral assemblages, and epithermal suite element enrichments (e.g., Hg, As, Sb, Bi, Te) in the ores in parts of the Ming deposits (e.g., 1806 Zone) are consistent with magmatic fluid involvement in deposit genesis (e.g., Brueckner et al. 2016) and could partly explain the Na-enrichment present in some of the high temperature alteration zones in the Ming deposit.

Apart from the silica-rich layer, Ca- and Mn-enrichment is limited to the outer edge of the 1807 Zone (Fig. 5.4), within 10 m of the massive sulfide. This enrichment is associated with the pervasive quartz-calcite±spessartine assemblage and the Mn-Ca-rich veining network. Carbonate minerals have a retrograde solubility at fixed pH and partial pressure of CO_2 (Krauskopf and Bird 1995); dissolved Ca, Mn, and CO_2 from the low temperature seawater likely precipitated instantly as Mn-rich calcite at the contact with ascending hot hydrothermal fluids. The restricted distribution at the fringe of the Ming deposit marks the outer limit of the hydrothermal convection cell that formed mineralization, which is consistent with has been seen in other areas (e.g., Herrmann and Hill 2001; Large et al. 2001c; Mercier-Langevin et al. 2014).

5.8.3. Alteration geochemistry in relation to depth: insight on fluid controls

The relationships between depth in the deposit and key geochemical attributes of the hydrothermal alteration are examined in Figure 5.23. This approach provides a more accurate representation of geochemical behavior on the deposit and overcomes local drill hole to drill hole variations (e.g., Figs. 5.15-5.17), while providing insight into fluid-rock interaction.

Aluminum is an effective element for calculating mass change associated with alteration at Ming. In Figure 5.23A, the abundance of Al_2O_3 provides spatial context to these mass changes, with only the upper ~100 m of the host successions demonstrating strong variations in Al_2O_3 content, whereas the lower 400 m shows near constant values, regardless of the alteration assemblages. The wide variation in mass that is restricted to the upper section of the deposit is attributed to the greater permeability of the volcaniclastic units 1.2 and 1.3, thus enabling greater fluid-rock reaction, and by association greater mass changes and Al_2O_3 variability. However, clear divergent patterns are notable near the massive sulfides among the quartz-sericite and quartz-sericite-sulfides assemblages, with an increase and decrease in Al_2O_3 values, respectively (Fig. 5.23A). As demonstrated by the mass change calculations, the bulk Al_2O_3 content is controlled by the addition or loss in SiO_2. Because the early quartz-sericite assemblage shows an increase in Al_2O_3 (i.e., loss in SiO_2), the fluids were evidently more efficient in flushing out Si then the late quartz-sericite-sulfides assemblage. Furthermore, loss in Si may have contributed in the formation of the silica-rich layer above the 1806 Zone.

The marked increase in positive Eu/Eu* anomalies in the sericitic assemblages (Fig. 5.19B, E) is restricted to the uppermost section of the deposit (Fig. 5.23B), implying that the enrichment of divalent Eu (Eu^{2+}) occurred within ~100 m from the massive sulfides. Also, the highest positive anomalies (Eu/Eu* > 1.5) are found exclusively in the 1806 Zone. The solubility of divalent Eu is the greatest in weakly acidic fluids that exceed 250°C (Sverjensky 1984) and the availability for fluids to transport Eu^{2+} likely depends on the destruction of REE-bearing minerals such as phosphates (e.g., apatite) and feldspars. Disequilibrium from the mixing of these Eu^{2+}-enriched fluids with seawater-saturated volcaniclastic rocks could explain the increase in Eu/Eu* values near the massive sulfides. Furthermore, because the enrichment in Eu^{2+} is significantly more important in the 1806 Zone implies that cooling of fluids was more significant in the latter zone than the rest of the deposit (i.e., this part of deposit was directly in contact with seawater).

5.8.4. Lithofacies relationships to mineralization and possible controls on metal distribution

The origin of precious metal enrichment in the Ming deposit has been subject to debate (e.g., syngenetic versus epigenetic); however, recent work has illustrated that the mineralization is associated with syngenetic VMS activity and magmatic fluid involvement (e.g., Brueckner et al. 2014, 2016; Pilote et al. 2016). Zinc, Ag, and Au are co-enriched in the paragenetically late quartz-sericite-sulfides assemblage and reflect elevated sphalerite, electrum, and Ag-bearing sulfosalts associated with this assemblage

(e.g., Brueckner et al. 2014, 2016). Metal grades in the massive sulfides vary within and between lenses and their distribution correlate with the underlying lithofacies, i.e., parts that are elevated in Zn, Au, and Ag grades are immediately underlain by coherent felsic volcanic rocks (Pilote et al. 2017). A similar enrichment is also present at the base of these coherent rocks (Figs. 5.16 and 5.17). The low-permeability of this lithofacies likely acted as a hydrological (and chemical?) cap to the ascending fluids, thus preventing the dissipation of the precious metal-bearing fluids into permeable volcaniclastic rocks; a process akin to many caped VMS deposits worldwide (Doyle and Allen 2003; Hannington et al. 2005) and known to be conducive to their enrichment (Piercey et al. 2015).

5.8.5. Proposed model of formation and possible heat source

The massive sulfides lenses and their stockwork at the Ming deposit are spatially limited to the Rambler Rhyolite dome (Pilote et al. 2017), which was synchronous with Cambro-Ordovician extension within the Baie Verte oceanic tract (Bédard et al. 1998). The three stages of the formation of the Ming deposit are shown in Figure 5.24 with the elemental change during the evolution of the Ming VMS hydrothermal system. Throughout the evolution of the Ming hydrothermal system, fluids are interpreted to have been controlled by the same synvolcanic faults that developed before and during the deposition of units 1.2 and 1.3 (Pilote et al. 2017). The synvolcanic faults controlled the lateral extent of the alteration into the coherent facies (unit 1.1) and fluid discharge near and at the seafloor. Early temperature increases during fluid evolution resulted in feldspar

destruction (hydrolysis) in the felsic host successions, which led to the formation of the quartz-sericite-chlorite and quartz-sericite assemblages, in the southeastern portion of the deposit (i.e., below Ming South and 1806 zones). In contrast, the influx of cold seawater containing Mn, Ca, and Na promoted enrichment in the uppermost part of units 1.2 and 1.3 on the distal edges of the deposit (Fig. 5.24A). Leached silica due to the slightly acidic alteration that formed the quartz-sericite assemblage precipitated on the paleoseafloor to form the silica-rich layer present locally (e.g., above 1806 Zone). Continuation of hydrothermal activity, combined with an increase in temperature (>300°C) produced the chloritic assemblages near the coherent volcanic-volcaniclastic interface due to the fixation and exchange of Mg and Fe from the fluid with pre-existing micas/sericite (Fig. 5.24B). High temperature fluids also enabled the transportation of significant Cu, which precipitated within the chloritic assemblages at the contact with the permeable and cooler volcaniclastic rocks of unit 1.2. The overall waning of the temperature is recorded by the overprinting quartz-sericite-sulfides, which also shows the highest enrichment in precious metals and volatiles. The enrichment of this late epithermal-like (Hannington et al. 1999b; Huston 2000; Brueckner et al. 2016) overprint was likely controlled by the retention efficiency of the coherent facies found in the 1806 Zone (Fig. 5.24C).

The primary heat source for driving hydrothermal circulation at the Ming deposit remains uncertain. Although it is common for VMS deposits to be spatially and potentially genetically related to a subvolcanic intrusion (Galley 2003), such an intrusion has yet to be found in the vicinity of the Ming deposit. Because hydrothermal alteration

and mineralization is restricted to the Rambler Rhyolite formation (Fig. 5.2), it could be argued that cooling of the felsic dome drove hydrothermal circulation; however, given the limited areal extent of this dome and thickness (<200 m where it hosts Rambler and East deposits) it is unlikely that it had the heat energy to drive the hydrothermal system that formed the Ming deposit (e.g., Cathles 1981). Also, the absence of cross-cutting mafic dykes of the Mount Misery Formation in the Rambler Rhyolite formation makes this an unlikely heat source. Therefore, another deeper, structurally restricted type of heat source has to be considered. At Kidd Creek, for example, given the absence of visible subvolcanic intrusions large enough to contribute to the formation of the ~180 Mt deposit (Hannington et al. 2017), workers have proposed structurally controlled upflow driven by the cooling of a ponded ultramafic magmas at ~15 km depth, much deeper than most VMS-associated subvolcanic intrusions (Galley 1993, 2003). In the Baie Verte Peninsula, VMS-style mineralization occurs at different stratigraphic positions, mainly in the upper and lower portions of the Betts Head and Mount Misery formations, respectively (e.g., Betts Cove, Tilt Cove, Big Rambler Pond). These deposits and formations were interpreted to have formed as a result of magmatism associated with forearc extension, resulting in thinning of forearc crust to less than 5 km in places (e.g., Betts Cove Complex; Bédard et al. 1996). This extension would have provided a mechanism to pond magmas at the base of the crust and raise the ambient geothermal gradient. Moreover, forearc extension would have resulted in the formation of extensional faults that could have controlled fluid flow. These two critical ingredients illustrate that the regional

tectonics and magmatism were likely critical for driving the hydrothermal circulation that formed the Ming deposit, common in many VMS districts globally (e.g., Piercey 2011).

5.8.6. Comparisons to other deposits in the Rambler Rhyolite formation

Although studies on VMS deposits in the vicinity are scarce to inexistent, Weick (1993) reported mineral assemblages and textures in and outside the sulfide ore of the historical Rambler deposit (Fig. 5.2) that are very similar to Ming, which some have been validated via field observations by the first author. The Rambler deposit consists of a northeast plunging ≤15 m thick massive sulfide lens that is hosted by a quartz phenoclastic felsic tuff and coherent rhyodacite. Immediately above the massive sulfide is a dark grey ≤1 m thick magnetic shale layer, which is in turn overlain by mafic flows; a geological setting that is similar to Ming. The Rambler footwall hydrothermal alteration is dominated by a quartz-chlorite-sericite assemblage with localized elongated patches of green micas, inferred as Cr-rich micas by Weick (1993). A strong systematic depletion in Na and Ca and an enrichment in K is observed in the footwall towards the outcropping massive sulfide (Weick 1993; J-L Pilote, unpubl. data), attributed to the breakdown of feldspars and development of sericite, respectively. The metamorphosed and deformed Rambler massive sulfide (≥80 vol. % sulfides) consists predominantly of a pyrite-chalcopyrite-sphalerite±galena assemblage, in which gold is found as inclusions in pyrite or interstitial to recrystallized pyrite grains. Moreover, gold in commonly spatially associated with tellurides and arsenopyrite, some in decomposition textures that resemble what Brueckner et al. (2016) have identified as “symplectite” at Ming. Weick (1993) also

pointed out strong color variations in sphalerite, likely owing to differences in their Fe content. The latter has been recorded at Ming and was attributed to a change in fluid conditions (fS_2 and temperature) over the evolution of the VMS formation (Brueckner et al. 2016). Whereas more work is needed at Rambler (and regionally), the broad geological, alteration, mineralogical, and geochemical similarities with Ming, together with its proximity, suffices to suggest that common fluid conditions existed during their formation and that the Rambler Rhyolite formation was fertile to significant Cu(-Au) mineralization (Pilote and Piercey, in review).

5.9. Conclusions

The Pacquet complex of the Baie Verte oceanic tract, part of the Newfoundland Appalachians, is host to the Cu-Zn-Ag-Au Ming VMS deposit. The deposit consists of multiple elongated semimassive to massive sulfide lenses and an underlying subparallel stockwork zone developed in the uppermost section of a nested basin within a rhyodacitic dome. The study of the hydrothermal alteration associated with the formation of the Ming deposit has helped to understand its nature, distribution, and paragenesis and provided insights on the possible controlling factors to the ore-forming fluids. The major outcomes of this study are:

1. The recognition of nine distinct alteration assemblages that formed in three paragenetic stages, including: 1) low temperature weak alteration, quartz-calcite±spessartine, quartz-sericite-chlorite, and quartz-sericite assemblages (stage 1); 2) high temperature quartz-chlorite, quartz-chlorite-sulfides, and quartz-

chlorite-sericite assemblages (stage 2); and low temperature Mn-Ca-rich and quartz-sericite-sulfides assemblages (stage 3). A stratiform silica-rich layer overlaps the 1806 Zone and is related to the Ming hydrothermal system;

2. The Mn- and Ca-rich assemblages that underlie the 1807 Zone are manifestations of low-temperature seawater influx in the footwall rocks and alteration becomes progressively less intense towards the northwest. These are indications that the 1807 Zone represents the northwest fringe of the hydrothermal system;
3. The distribution of the hydrothermal alteration is for the most part restricted to the nested basin developed in the rhyodacitic dome. Fluids discharged were largely controlled by the permeability of the fragmental unit 1.2, where most of the mass changes occured. The development of the Cu-rich stockwork zone was largely controlled by this coherent-volcaniclastic interface, which formed at depth away from the main discharge zone. Moreover, their lateral distribution is strongly controlled by synvolcanic faults recognized by the combination of abrupt lithofacies changes and preferentially oriented alteration assemblages and mineralized zones;
4. The late quartz-sericite-sulfides assemblage is host to Au-Ag-rich veins, suggesting a previous metal introduction in the waning stages of the hydrothermal system;
5. The controlling effects on the precious metal-rich fluids appear to include the coherent volcanic rocks. The physical limitations (or perhaps buffering effects) on the fluids may have induced more focused, hence less diffused, metal transport in

low temperature conditions. We speculate that the combination of higher water/rock ratio at the base of these coherent facies and the impermeable barrier of the latter may also have played a critical role in providing near neutral (higher pH) conditions and a trap to the ascending fluids.

6. The driving mechanism to the hydrothermal circulation was likely the combination of a deep (≥5 km) heat source and from the cooling of the ascending and emplacement of the rhyodacitic Rambler Rhyolite dome. We speculate that the thin nature of the Baie Verte oceanic tract during its formation, hence the high geothermal gradient, could have compensated for the possible absence of subvolcanic intrusions in the area.

5.10. Acknowledgements

The authors would like to thank Rambler Metals and Mining Ltd. and geologists Larry Pilgrim and Paul Legrow for providing access to the underground workings, drill core, data, and samples; Pam King, Lakmali Hewu, and Wanda Aylward of CREAIT at Memorial University of Newfoundland (MUN) for their technical support and guidance during the multiple stages of sample preparation and geochemical and EPMA analyses. We appreciate the technical support from and insightful discussions with J. Cloutier (University of St Andrews) and S.M. Brueckner (Auburn University). This research was funded by grants to S.J. Piercey, including an NSERC Discovery Grant and the NSERC-Altius Industrial Research Chair in Mineral Deposits funded by NSERC, Altius Minerals Inc., and the Research and Development Corporation of Newfoundland and Labrador.

This study was also funded in part by the Geological Survey of Canada's Targeted Geoscience Initiative Program.

5.11. References

Arnórsson S, Stefánsson A, Bjarnarson JÖ (2007) Fluid-fluid interactions in geothermal systems. In: Liebscher A, Heinrich, C.A. (ed) Fluid–fluid interactions, Reviews in Mineralogy and Geochemistry 65, pp 259-312

Bailey DK (1987) Mantle metasomatism—perspective and prospect. Geological Society, Special Publications 30:1-13. https://doi:10.1144/gsl.sp.1987.030.01.02

Barrett TJ, MacLean WH (1994) Chemostratigraphy and hydrothermal alteration in exploration for VHMS deposits in greenstones and younger volcanic rocks. Short Course Notes, Geological Association of Canada 11:433-467

Bédard JH, Escayola M (2010) The Advocate Ophiolite mantle, Baie Verte, Newfoundland; regional correlations and evidence for metasomatism. Canadian Journal of Earth Sciences 47:237-253. https://doi:10.1139/e10-004

Bédard JH, Lauzière K, Tremblay A, Sangster A (1998) Evidence for forearc seafloor-spreading from the Betts Cove ophiolite, Newfoundland: oceanic crust of boninitic affinity. Tectonophysics 284:233-245. https://doi:10.1016/s0040-1951(97)00182-0

Bédard JH, Lauzière K, Sangster A, Boisvert E, Tellier M, Tremblay A, Dec T (1996) Geological map of the Betts Cove ophiolitic massif and its cover rocks. Geological Survey of Canada, Canadian Geoscience Map 3271, scale 1:20 000

Brueckner SM, Piercey SJ, Layne GD, Piercey G, Sylvester PJ (2015) Variations of sulphur isotope signatures in sulphides from the metamorphosed Ming Cu(-Au) volcanogenic massive sulphide deposit, Newfoundland Appalachians, Canada. Mineralium Deposita 50:619-640. https://doi:10.1007/s00126-014-0567-7

Brueckner SM, Piercey SJ, Pilote J-L, Layne GD, Sylvester PJ (2016) Mineralogy and mineral chemistry of the metamorphosed and precious metal-bearing Ming deposit, Canada. Ore Geology Reviews 72:914-939.

Brueckner SM, Piercey SJ, Sylvester PJ, Maloney S, Pilgrim L (2014) Evidence for syngenetic precious metal enrichment in an Appalachian volcanogenic massive sulfide system: The 1806 Zone, Ming mine, Newfoundland, Canada. Economic Geology 109:1611-1642. https://doi:10.2113/econgeo.109.6.1611

Brueckner SM, Piercey SJ, Sylvester PJ, Pilgrim L, Maloney S, Hyde D, Ogilvie G (2011) Stratigraphy, mineralogy, geochemistry, and genesis of an Au-rich volcanogenic massive sulfide (VMS) system from the Baie Verte Peninsula, NW Newfoundland, Canada: The 1806 Zone as an example from the Ming Mine, Rambler Camp. In: Deschênes G, Dimitrakopoulos R, Bouchard J (eds) World Gold 2011, Canadian Institute of Mining, Metallurgy and Petroleum, Montreal, QC, Canada, pp 899-911

Buschette MJ, Piercey SJ (2016) Hydrothermal alteration and lithogeochemistry of the Boundary volcanogenic massive sulphide deposit, central Newfoundland, Canada. Canadian Journal of Earth Sciences 53:506-527. https://doi:10.1139/cjes-2015-0237

Castonguay S, Skulski T, van Staal CR, Currie M (2009) New insights on the structural geology of the Pacquet Harbour group and Point Rousse complex, Baie Verte peninsula, Newfoundland. Newfoundland and Labrador Department of Natural Resources, Geological Survey Report 09-1:147-158

Castonguay S, van Staal CR, Joyce N, Skulski T, Hibbard JP (2014) Taconic metamorphism preserved in the Baie Verte Peninsula, Newfoundland Appalachians: Geochronological evidence for ophiolite obduction and subduction and exhumation of the leading edge of the Laurentian (Humber) margin during closure of the Taconic seaway. Geoscience Canada 14: 459-482. https://doi:10.12789/geocanj.2014.41.055

Cathles LM (1981) Fluid flow and genesis of hydrothermal ore deposits. In: Skinner BJ (ed) Economic Geology Seventy-Fifth Anniversary Volume: 424-457.

Cawood PA, van Gool JAM, Dunning GR (1996) Geological development of eastern Humber and western Dunnage zones; Corner Brook-Glover Island region, Newfoundland. Canadian Journal of Earth Sciences 33:182-198

Date J, Watanabe Y, Saeki Y (1983) Zonal alteration around the Fukazawa Kuroko deposits, Akita Prefecture, northern Japan. Economic Geology Monograph 5:365-386

Deer WA, Howie RA, Zussman J (1966) An introduction to the rock forming minerals. Longman, London, 528 p

DeWolfe YM (2009) Physical volcanology, petrology and tectonic setting of intermediate and mafic volcanic and intrusive rocks in the Flin Flon volcanogenic massive sulphide (VMS) district, Manitoba, Canada. Dissertation, Laurentian University

Doyle MG, Allen RL (2003) Subsea-floor replacement in volcanic-hosted massive sulfide deposits. Ore Geology Reviews 23:183-222. https://doi:10.1016/s0169-1368(03)00035-0

Dubé B, Mercier-Langevin P, Hannington MD, Lafrance B, Gosselin G, Gosselin P (2007) The LaRonde Penna world-class Au-rich volcanogenic massive sulfide deposit, Abitibi, Quebec; mineralogy and geochemistry of alteration and implications for genesis and exploration. Economic Geology 102:633-666. https://doi:10.2113/gsecongeo.102.4.633

Dubé B, Mercier-Langevin P, Kjarsgaard I, Hannington MD, Bécu V, Côté J, Moorhead J, Legault M, Bédard N (2014) The Bousquet 2-Dumagami World-Class Archean Au-Rich Volcanogenic Massive Sulfide Deposit, Abitibi, Quebec: Metamorphosed Submarine Advanced Argillic Alteration Footprint and Genesis. Economic Geology 109:121-166. https://doi:10.2113/econgeo.109.1.121

Dunning GR, Krogh TE (1985) Geochronology of ophiolites of the Newfoundland Appalachians. Canadian Journal of Earth Sciences 22:1659-1670. https://doi:10.1139/e85-174

Gale GH (1971) An investigation of some sulfide deposits of the Rambler Area, Newfoundland. Dissertation, University of Durham

Galley AG (1993) Characteristics of semi-conformable alteration zones associated with volcanogenic massive sulphide districts. Journal of Geochemical Exploration 48:175-200. https://doi:10.1016/0375-6742(93)90004-6

Galley AG (2003) Composite synvolcanic intrusions associated with Precambrian VMS-related hydrothermal systems. Mineralium Deposita 38:443-473. https://doi:10.1007/s00126-002-0300-9

Gemmell JB, Large RR (1992) Stringer system and alteration zones underlying the Hellyer volcanogenic massive sulfide deposit, Tasmania, Australia. Economic Geology 87:620-649. https://doi:10.2113/gsecongeo.87.3.620

Gibson H, Morton RL, Hudak GJ (1999) Submarine volcanic processes, deposits, and environments favorable for the loaction of volcanic-associated massive sulfide deposits. In: Barrie CT, Hannington, M.D. (ed) Volcanic-associated massive sulfide deposits: Processes and examples in modern and ancient settings, Reviews in Economic Geology 8, pp 13-51

Grant JA (1986) The Isocon diagram: A simple solution to Gresens' equation for metasomatic alteration. Economic Geology 81:1976-1982

Hajash A, Chandler GW (1982) An experimental investigation of high-temperature interactions between seawater and rhyolite, andesite, basalt and peridotite. Contributions to Mineralogy and Petrology 78:240-254. https://doi:10.1007/bf00398919

Hannington MD, Barrie CT, Bleeker W (1999a) The giant Kidd Creek volcanogenic massive sulfide deposit, western Abitibi Subprovince, Canada; summary and synthesis. Economic Geology Monograph 10:661-672

Hannington MD, de Ronde CEJ, Petersen S (2005) Sea-floor tectonics and submarine hydrothermal systems. In: Hedenquist JW, Thompson, J.F.H., Goldfarb, R.J., Richards, J.P. (ed) Economic Geology 100th Anniversary Volume, pp 111-141

Hannington, MD, Gemmell T, Monecke T (2018) The Kidd Creek volcanogenic massive sulfide deposit – an update. Reviews in Economic Geology 19:xxx-xxx.

Hannington MD, Kjarsgaard IM, Galley AG, Taylor B (2003) Mineral-chemical studies of metamorphosed hydrothermal alteration in the Kristineberg volcanogenic massive sulfide district, Sweden. Mineralium Deposita 38:423-442. https://doi:10.1007/s00126-002-0299-y

Hannington MD, Poulsen KH, Thompson JFH, Sillitoe RH (1999b) Volcanogenic gold in the massive sulfide environment. In: Barrie CT, Hannington MD (ed) Volcanic-associated massive sulfide deposits: Processes and examples in modern and ancient settings, Reviews in Economic Geology 8, pp 325-351

Hannington MD, Santaguida F, Kjarsgaard IM, Cathles LM (2003) Regional-scale hydrothermal alteration in the Central Blake River Group, western Abitibi subprovince, Canada: implications for VMS prospectivity. Mineralium Deposita 38:393-422. https://doi:10.1007/s00126-002-0298-z

Hart TR, Gibson HL, Lesher CM (2004) Trace element geochemistry and petrogenesis of felsic volcanic rocks associated with volcanogenic massive Cu-Zn-Pb sulfide deposits. Economic Geology 99:1003-1013. https://doi:10.2113/gsecongeo.99.5.1003

Herrmann W, Hill AP (2001) The origin of chlorite-tremolite-carbonate rocks associated with the Thalanga volcanic-hosted massive sulfide deposit, North Queensland, Australia. Economic Geology 96:1149-1173

Herrmann W, Blake MD, Doyle MG, Huston DL, Kamprad J, Merry N, Pontual S (2001) Short wavelength infrared (SWIR) spectral analysis of hydrothermal alteration zones associated with base metal sulfide deposits at Rosebery and Western Tharsis, Tasmania, and Highway-Reward, Queensland. Economic Geology 96:939-955

Hey MH (1954) A new review of the chlorites. Mineralogical Magazine 30:277-292

Hibbard J (1983) Geology of the Baie Verte Peninsula, Newfoundland. Newfoundland Department of Mines and Energy, Geological Survey, Memoir 2, 279 p

Huston DL (1993) The effect of alteration and metamorphism on wall rocks to the Balcooma and Dry River South volcanic-hosted massive sulfide deposits, Queensland, Australia. Journal of Geochemical Exploration 48:277-307. https://doi:10.1016/0375-6742(93)90008-a

Huston DL (2000) Gold in volcanic-hosted massive sulfide deposits: Distribution, genesis, and exploration. In: Hagemann SG, Brown, P.E. (ed) Gold in 2000, Reviews in Economic Geology 13, pp 401-426

Ishikawa Y, Sawaguchi T, Iwaya S, Horiuchi M (1976) Delineation of prospecting targets for Kuroko deposits based on modes of volcanism of underlying dacite and alteration halos. Mining Geology 26:105-117

Jenner GA (1996) Trace element geochemistry of igneous rocks; geochemical nomenclature and analytical geochemistry. Short Course Notes, Geological Association of Canada 12:51-77

Jenner GA, Longerich HP, Jackson SE, Fryer BJ (1990) ICP-MS-a powerful tool for high-precision trace element analysis in Earth sciences: Evidence from analysis of selected USGS reference samples. Chemical Geology 83:133-148

Jones S, Herrmann W, Gemmell JB (2005) Short wavelength infrared spectral characteristics of the HW horizon; implications for exploration in the Myra Falls volcanic-hosted massive sulfide camp, Vancouver Island, British Columbia, Canada. Economic Geology 100:273-294. https://doi:10.2113/100.2.273

Krauskopf KB, Bird DK (1995) Introduction to geochemistry. McGraw-Hill, New York

Large RR (1992) Australian volcanic-hosted massive sulfide deposits: Features, styles, and genetic models. Economic Geology 87:471-510

Large RR, Allen RL, Blake MD, Herrmann W (2001a) Hydrothermal alteration and volatile element halos for the Rosebery K Lens volcanic-hosted massive sulfide deposit, western Tasmania. Economic Geology 96:1055-1072. https://doi:10.2113/gsecongeo.96.5.1055

Large RR, Gemmell JB, Paulick H, Huston DL (2001b) The alteration box plot: A Simple approach to understanding the relationship between alteration mineralogy and lithogeochemistry associated with volcanic-hosted massive sulfide deposits. Economic Geology 96:957-971. https://doi:10.2113/gsecongeo.96.5.957

Large RR, McPhie J, Gemmell JB, Herrmann W, Davidson GJ (2001c) The spectrum of ore deposit types, volcanic environments, alteration halos, and related exploration vectors in submarine volcanic successions: Some examples from Australia. Economic Geology 96:913-938

Lesher CM, Goodwin AM, Campbell IH, Gorton MP (1986) Trace-element geochemistry of ore-associated and barren, felsic metavolcanic rocks in the Superior Province, Canada Canadian Journal of Earth Sciences 23:222-237

Longerich HP, Jenner GA, Fryer BJ, Jackson SE (1990) Inductively coupled plasma-mass spectrometric analysis of geological samples: A critical evaluation based on case studies. Chemical Geology 83:105-118

Lydon JW (1984) Volcanogenic massive sulphide deposits Part 1: A descriptive model. Geoscience Canada 11:195-202

Lydon JW (1988) Volcanogenic massive sulphide deposits Part 2: Genetic models. Geoscience Canada 15:43-65

Lydon JW (1996) Characteristics of volcanogenic massive sulphide deposits; interpretations in terms of hydrothermal convection systems and magmatic hydrothermal systems. Boletin Geologico y Minero 107:215-264

Mercier-Langevin P, Dubé B, Hannington MD, Davis DW, Lafrance B, Gosselin G (2007) The LaRonde Penna Au-rich volcanogenic massive sulfide deposit, Abitibi greenstone belt, Quebec: Part I. Geology and geochronology. Economic Geology 102:585-609

Mercier-Langevin P, Hannington MD, Dubé B, Piercey SJ, Peter JM, Pehrsson SJ (2015) Precious metal enrichment processes in volcanogenic massive sulphide deposits; a summary of key features, with an emphasis on TGI-4 research contributions. Geological Survey of Canada Open File 7853:117-130. https://doi:10.4095/296540

Mercier-Langevin P, Lafrance B, Bécu V, Dubé B, Kjarsgaard I, Guha J (2014) The Lemoine auriferous volcanogenic massive sulfide deposit, Chibougamau Camp, Abitibi Greenstone Belt, Quebec, Canada: Geology and Genesis. Economic Geology 109:231-269. https://doi:10.2113/econgeo.109.1.231

Monecke T, Petersen S, Hannington MD (2014) Constraints on water depth of massive sulfide formation: Evidence from modern seafloor hydrothermal systems in arc-related settings. Economic Geology 109:2079-2101. https://doi:10.2113/econgeo.109.8.2079

Nakamura N (1974) Determination of REE, Ba, Fe, Mg, Na and K in carbonaceous and ordinary chondrites. Geochimica et Cosmochimica Acta 38:757-775. http://dx.doi.org/10.1016/0016-7037(74)90149-5

Pearce JA (1996) A user's guide to basalt discrimination diagrams. Short Course Notes, Geological Association of Canada 12:79-113

Pearce JA, Baker PE, Harvey PK, Luff IW (1995) Geochemical evidence for subduction fluxes, mantle melting and fractional crystallization beneath the South Sandwich island arc. Journal of Petrology 36:1073-1109

Piercey SJ (2011) The setting, style, and role of magmatism in the formation of volcanogenic massive sulfide deposits. Mineralium Deposita 46:449-471 https://doi:10.1007/s00126-011-0341-z

Piercey SJ, Peter JM, Herrington R (2015) Zn-rich volcanogenic massive sulfide (VMS) deposits. In: Archibald SM, Piercey SJ (ed). Current Perspectives on Zinc Deposits. Irish Association for Economic Geology Special Publication on Zinc Deposits, pp 37-57

Pilgrim L (2009) Mineral resource estimate for the Ming Mine, Newfoundland, Canada. Rambler Metals and Mining Canada Ltd., Technical Report NI43-101, 114 p

Pilote J-L, Piercey SJ, Mercier-Langevin P (2014) Stratigraphy and hydrothermal alteration of the Ming Cu-Au volcanogenic massive-sulphide deposit, Baie Verte peninsula, Newfoundland. Geological Survey of Canada, Current Research, Report 2014-7, 18 p. https://doi:10.4095/295145

Pilote J-L, Piercey SJ, Brueckner SM, Grant D (2016) Resolving the relative timing of Au enrichment in volcanogenic massive sulfide deposits using scanning electron microscopy-mineral liberation analyzer: Empirical evidence from the Ming deposit, Newfoundland, Canada. Economic Geology 111:1495-1508. https://doi:10.2113/econgeo.111.6.1495

Pilote J-L, Piercey SJ, Mercier-Langevin P (2017) Volcanic and structural reconstruction of the deformed and metamorphosed Ming volcanogenic massive sulfide deposit, Canada: Implications for ore zone geometry and metal distribution. Economic Geology 112:1305-1332. https://doi:10.5382/econgeo.2017.4511

Pontual S, Merry N, Gamson P (1997) G-Mex Volume 1: Spectral interpretation field manual. Ausspec International Pty. Ltd, Australia

Post JL, Noble PL (1993) The near-infrared combination band frequencies of dioctahedral smectites, micas and illites. Clays and Clay Minerals 41:639-644

Reed MH (1997) Hydrothermal alteration and its relationship to ore fluid composition. In: Barnes HL (ed) Geochemistry of hydrothermal ore deposits, 3rd edn. John Wiley & Sons, New York, pp 303-365

Ross P-S, Bédard JH (2009) Magmatic affinity of modern and ancient subalkaline volcanic rocks determined from trace-element discriminant diagrams. Canadian Journal of Earth Sciences 46:823-839. https://doi:10.1139/e09-054

Schardt C, Cooke DR, Gemmell JB, Large RR (2001) Geochemical modeling of the zoned footwall alteration pipe, Hellyer volcanic-hosted massive sulfide deposit, Western Tasmania, Australia. Economic Geology 96:1037-1054. https://doi:10.2113/gsecongeo.96.5.1037

Skulski T, Castonguay S, Kidd WSF, McNicoll VJ, van Staal CR, Hibbard JP (2015) Geology, Baie Verte and parts of Fleur de Lys, Newfoundland and Labrador, NTS 12-H/16 and part of NTS 12-I/1; Geological Survey of Canada, Canadian Geoscience Map 159, scale 1:50 000. https://doi:10.4095/295865

Skulski T et al. (2010) Tectonostratigraphy of the Baie Verte oceanic tract and its ophiolite cover sequence on the Baie Verte Peninsula. Newfoundland and Labrador Department of Natural Resources, Geological Survey Report 10-1:315-335

Spitz G, Darling R (1978) Major and minor element lithogeochemical anomalies surrounding the Louvem copper deposit, Val d'Or, Quebec. Canadian Journal of Earth Sciences 15:1161-1169. https://doi:10.1139/e78-122

Sun SS, McDonough WF (1989) Chemical and isotopic systematics of oceanic basalts; implications for mantle composition and processes. Geological Society Special Publications 42:313-345

Sverjensky DA (1984) Europium redox equilibria in aqueous solution. Earth and Planetary Science Letters 67:70-78. http://dx.doi.org/10.1016/0012-821X(84)90039-6

Thompson AJB, Hauff PL, Robitaille JA (1999) Alteration mapping in exploration; application of short-wave infrared (SWIR) spectroscopy. SEG Newsletter 39:1-27

Tuach J, Kennedy MJ (1978) The geologic setting of the Ming and other sulfide deposits, Consolidated Rambler Mines, Northeast Newfoundland. Economic Geology 73:192-206. https://doi:10.2113/gsecongeo.73.2.192

van Staal CR, Barr SM (2012) Lithosperic architecture and tectonic evolution of the Canadian Appalachians and associated Atlantic margin. In: Percival JA, Cook FA,

Clowes RM (eds) Tectonic Styles in Canada: The LITHOPROBE perspective. Geological Association of Canada, Special Paper 49, pp 41-95

van Staal CR, Chew DM, Zagorevski A, McNicoll V, Hibbard J, Skulski T, Escayola MP, Castonguay S, Sylvester PJ (2013) Evidence of Late Ediacaran hyperextension of the Laurentian Iapetan margin in the Birchy Complex, Baie Verte Peninsula, northwest Newfoundland: Implications for the opening of Iapetus, formation of peri-Laurentian microcontinents and Taconic-Grampian orogenesis. Geoscience Canada 40:94-117

Waldron JWF, van Staal CR (2001) Taconian Orogeny and the accretion of the Dashwoods Block; a peri-Laurentian microcontinent in the Iapetus Ocean. Geology 29:811-814

Walshe JL, Solomon M (1981) An investigation into the environment of formation of the volcanic-hosted Mt. Lyell copper deposits using geology, mineralogy, stable isotopes, and a six-component chlorite solid-solution model. Economic Geology 76:246-284

Weick RJ (1993) Petrography and stable isotope geochemistry of alteration and mineralization in the Rambler volcanogenic massive sulphide deposit, Baie Verte, Newfoundland. Dissertation, Memorial University of Newfoundland

Winchester JA, Floyd PA (1977) Geochemical discrimination of different magma series and their differentiation products using immobile elements. Chemical Geology 20:325-343

Yang K, Huntington JF, Gemmell JB, Scott KM (2011) Variations in composition and abundance of white mica in the hydrothermal alteration system at Hellyer, Tasmania, as revealed by infrared reflectance spectroscopy. Journal of Geochemical Exploration 108:143-156. http://dx.doi.org/10.1016/j.gexplo.2011.01.001

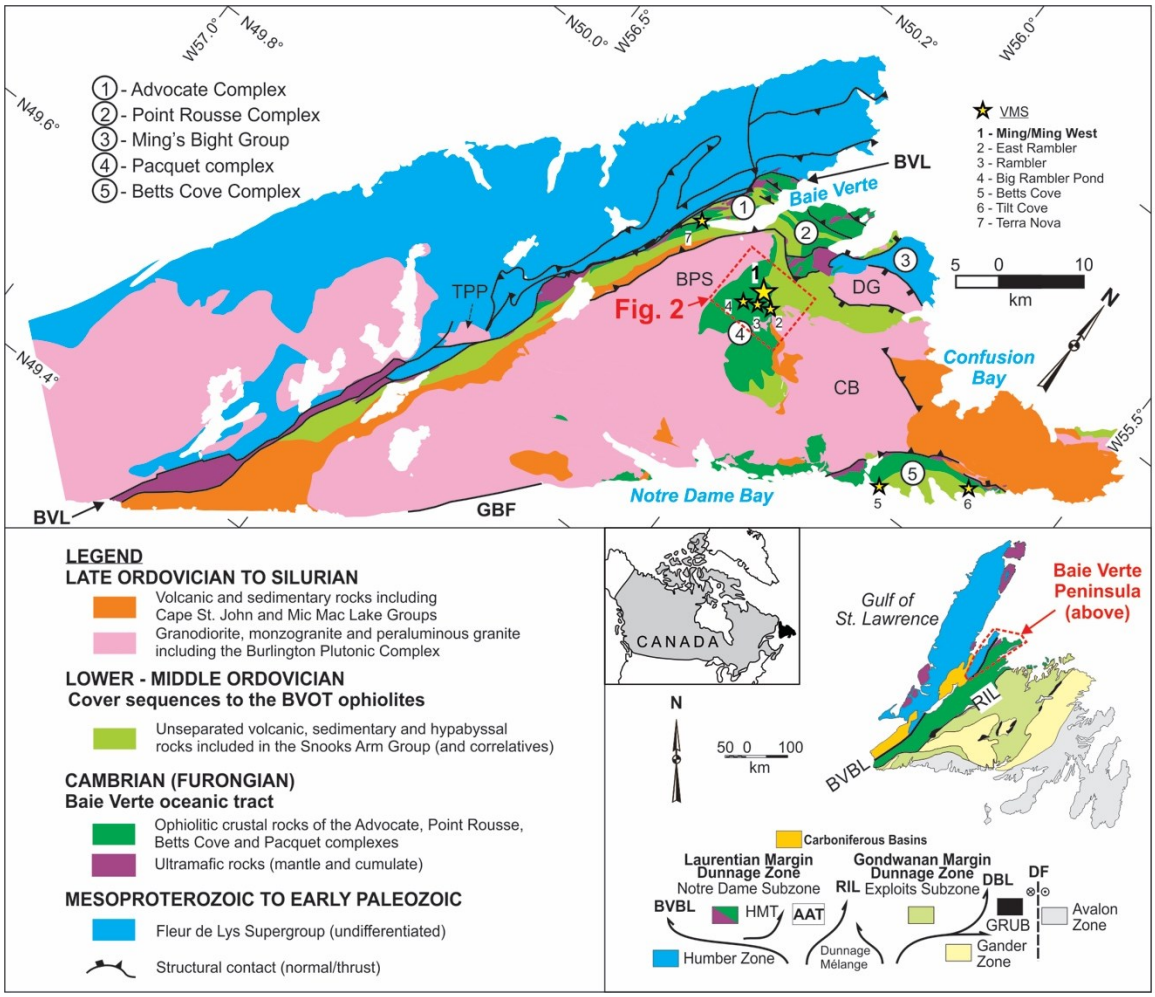

Fig. 5.1. Simplified geology of the Baie Verte Peninsula with major tectonostratigraphic zones that form the Appalachian orogenic belt in Newfoundland (modified from Castonguay et al., 2014 and references therein). Location of major VMS deposits as yellow stars. AAT = Annieopsquotch Accretionary Tract, BPS = Burlington plutonic Suite, BVBL = Baie Verte-Brompton Line, BVL = Baie Verte Line, CB = Cape Brulé, DBL = Dog Bay Line, DF = Dover Fault, DG = Dunamagon Granite, GBF = Green Bay Fault, GRUB = Gander River Ultramafic Belt, TPP = Trap Pond pluton, RIL = Red Indian Line, HMT = Hungry Mountain Thrust.

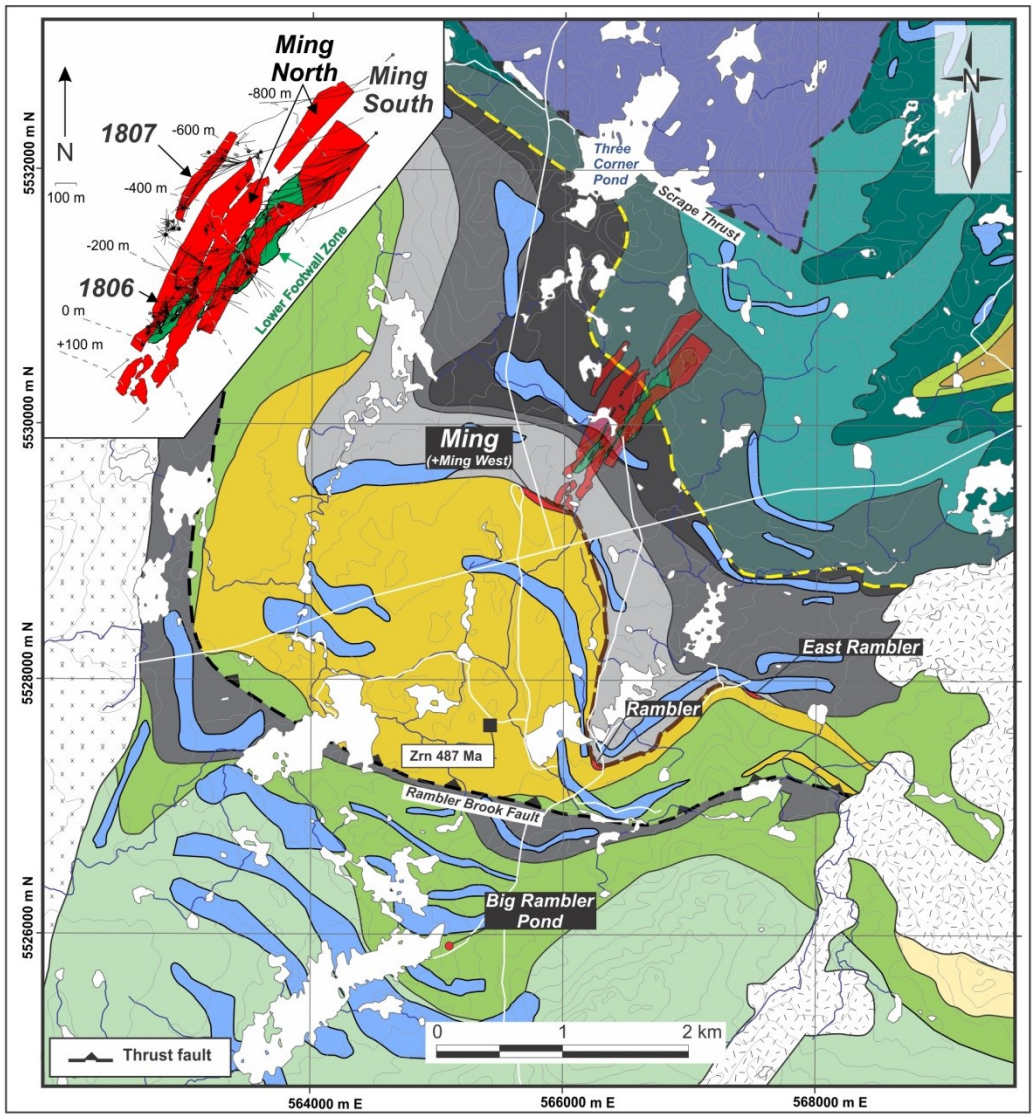

Silurian Cape St. John Group (unseparated)

Clastic, pink-red sedimentary rocks, mafic and/or felsic volcanic rocks.

Burlington Granodiorite (434 - 430 Ma)

Cape Brulé Porphyry (430 Ma)
Porphyritic granodiorite, quartz-feldspar porphyry.

Early-Middle Ordovician Snooks Arm Group (479-467 Ma)

Tholeiitic gabbro sills/dikes, include plagioclase-phyric to fine-grained gabbro. Minor medium-grained equigranular diorite.

Basalm Bud Cove Formation

Volcanogenic turbidite, siltstone, felsic tuffs, basalts.

Calc-alkaline felsic tuff, lapilli tuff.

Venam's Bight Formation
Tholeiitic pillowed basalt, porphyritic and vesicular basalt, siliceous mudstone.

Bobby Cove Formation
Chert, iron formation, volcanogenic sedimentary rocks, minor felsic tuffs.

Mafic tuff, lapilli tuff, epiclastic rocks, interbedded basalt flows.

Clinopyroxene-phyric crystal tuff, lapilli tuff, and tuff breccia (Prairie Hat member).

Calk-alkaline plagioclase-phyric pillow basalt and andesite.

Scrape Point Formation
Mafic volcaniclastic rocks, tuff, lapilli tuff, epiclastic sandstone, shale, interbedded pillow basalt.

Pillowed, massive, amygdaloidal, plgioclase-phyric basalt flows. Tholeiitic affinities.

Magnetite-rich iron formation, chert beds, volcanogenic siltstone (Nugget Pond horizon).

Cambro-Ordovician Pacquet Complex

Rambler Rhyolite formation (487 Ma)
Quartz-phyric rhyolite to rhyodacite flows interbedded with intermediate to felsic tuff, lapilli tuffs, and tuff breccia.

Mt. Misery Formation
Plagioclase- and pyroxene-phyric pillow basalt with tholeiitic affinities, interbedded with boninite.

Betts Head Formation
Spherulitic, amygdaloidal, porphyritic boninitic pillow lavas with aphanitic dark-green groundmass.

Point Rousse ophiolite (490 Ma)

Undifferentiated serpentinized ultramafic rocks with tholeiitic and boninitic affinities.

(Previous page) Fig. 5.2. Geological map of the study area, Baie Verte Peninsula, with Ming VMS orebodies projected to surface (also in the inset) and shown in light red and light green (Lower Footwall Zone = stockwork). Datum is UTM 21N NAD 83. Map compiled and modified from Tuach and Kennedy (1978), Hibbard (1983), Castonguay et al. (2009), Pilgrim (2009), and Skulski et al. (2010). The U-Pb zircon (Zrn) age is from Skulski et al. (2015).

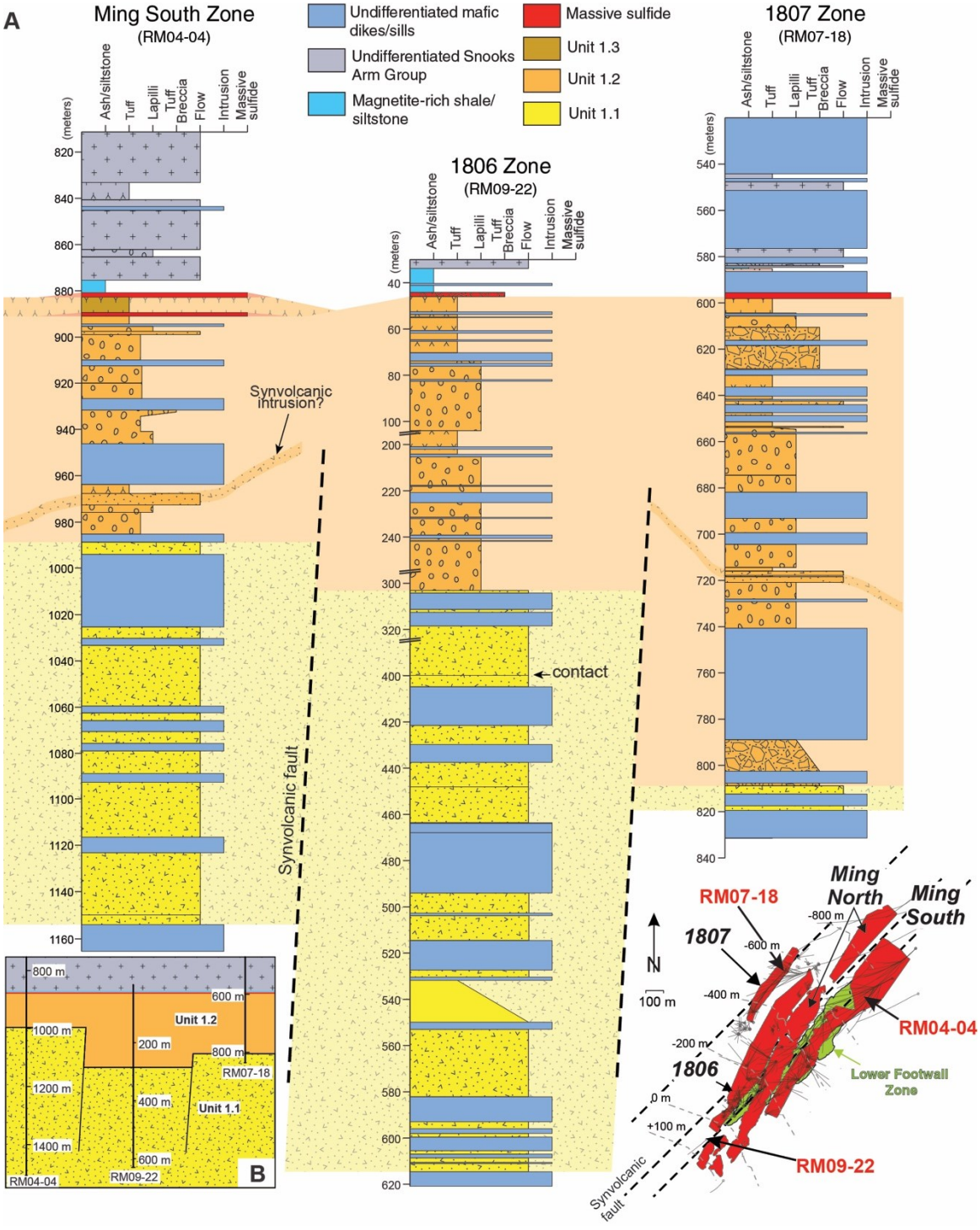
A
Ming South Zone
(RM04-04)
1806 Zone
(RM09-22)
1807 Zone
(RM07-18)
Undifferentiated mafic dikes/sills
Undifferentiated Snooks Arm Group
Magnetite-rich shale/ siltstone
Massive sulfide
Unit 1.3
Unit 1.2
Unit 1.1
Ash/siltstone
Tuff
Lapilli Tuff
Breccia
Flow
Intrusion
Massive sulfide
(meters)
Synvolcanic intrusion?
Synvolcanic fault
contact
B
800 m
600 m
Unit 1.2
1000 m
200 m
800 m
RM07-18
1200 m
400 m
Unit 1.1
1400 m
600 m
RM04-04
RM09-22
Ming North
Ming South
RM07-18
1807
1806
RM04-04
RM09-22
Lower Footwall Zone
N
100 m
-800 m
-600 m
-400 m
-200 m
0 m
+100 m
Synvolcanic fault

(Precious page) Fig. 5.3. Composite stratigraphic columns of the Ming South (DDH RM04-04), 1806 (RM09-22), and 1807 (RM07-18) zones. These illustrate the volcaniclastic lithofacies associated with all zones. Note the downhole breaks of lengths in drill hole RM09-22. The synvolcanic faults are interpreted based on the sharp lateral change in lithofacies and on the distribution of the chlorite-rich alteration assemblages spatially and genetically associated with the Lower Footwall Zone (Pilote et al., 2017).

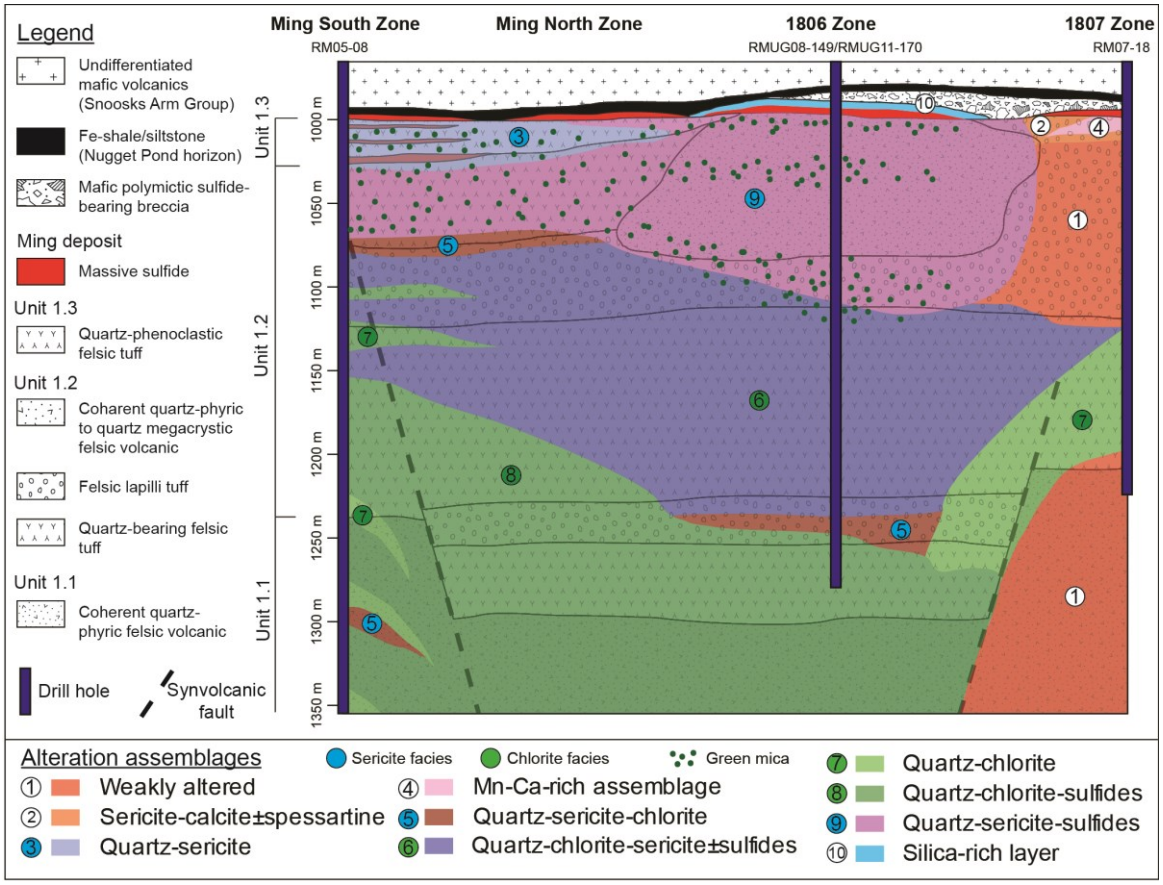

Fig. 5.4. Schematic reconstruction of the volcanic and volcaniclastic host succession, structural, and alteration assemblages associated with the Ming deposit. The dikes were omitted for clarity. This cross-section is constructed based on information collected from representative drill holes, geochemically characterized in detail in Figures 5.14, 5.15, and 5.16. Additional data is integrated to accommodate nearby extensive alteration assemblages.

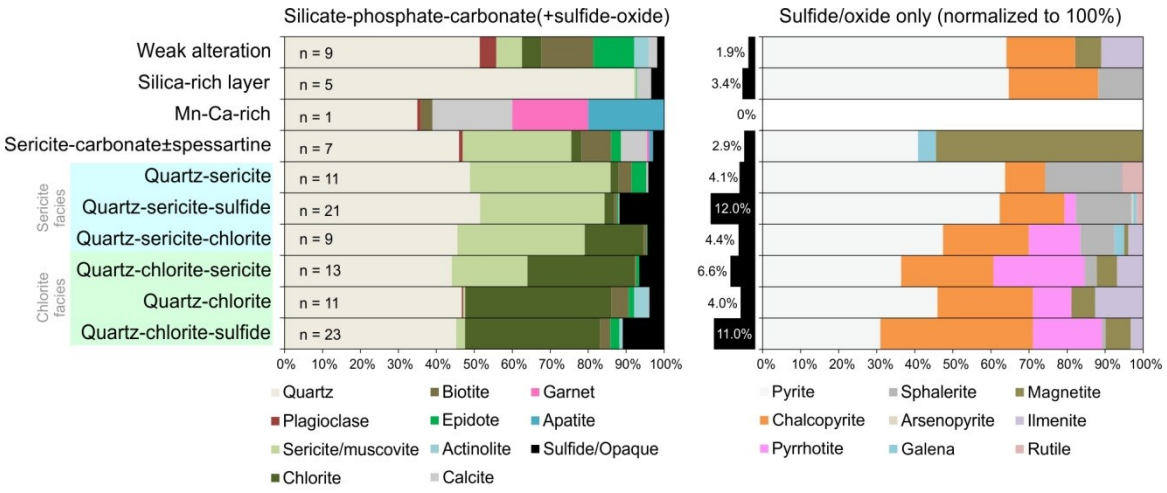

Fig. 5.5. Stacked bar plots of the alteration assemblages with the total mineral proportions (left) and the sulfide and oxide proportions (right). Relative mineral abundances were estimated visually. The proportion of sulfide/oxide minerals is normalized to the relative amount shown as black bars.

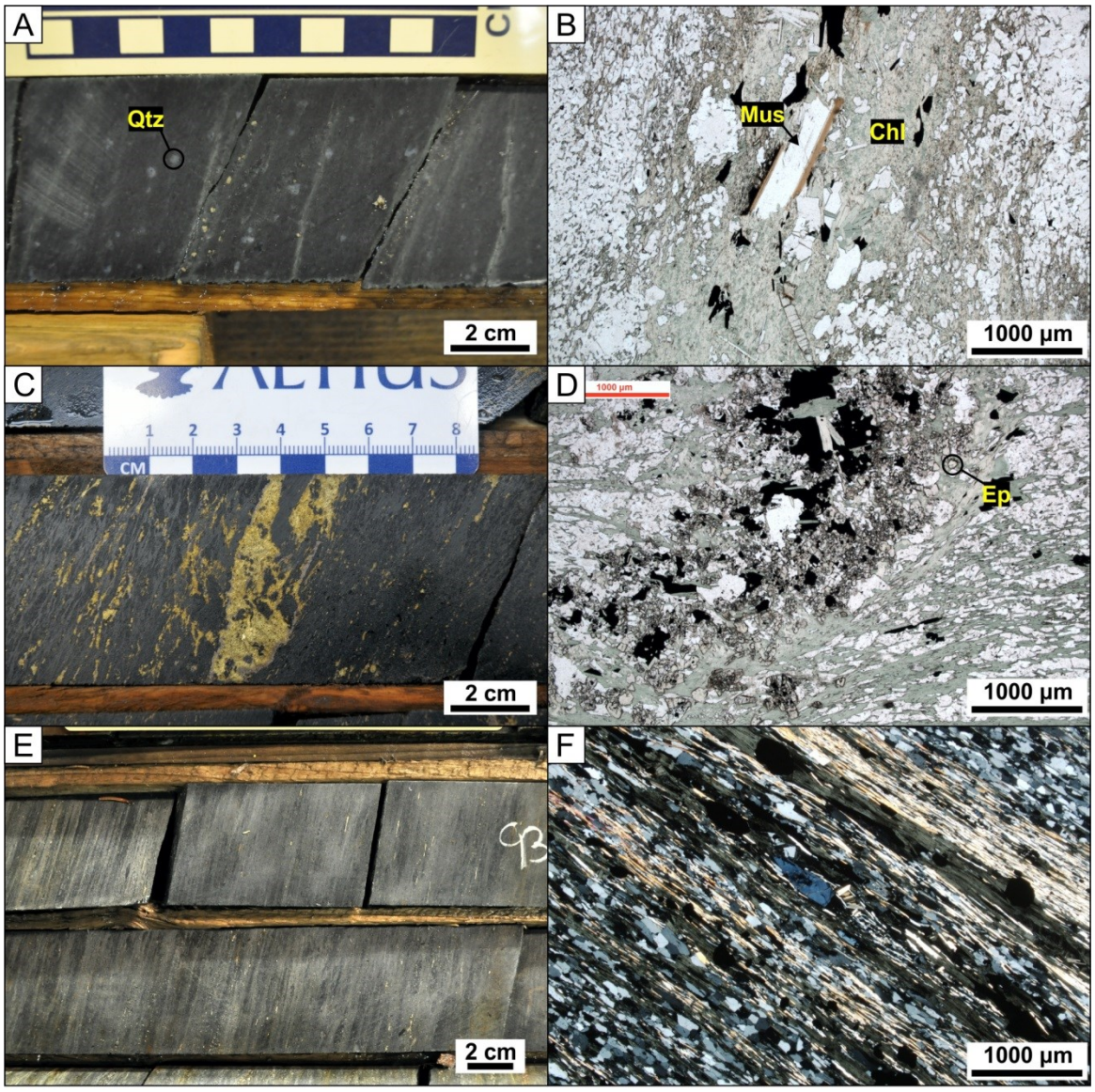

Fig. 5.6. Photographs of representative samples of the different alteration assemblages from the Ming deposit. A. Drill core section representative of the quartz-chlorite assemblage with relic quartz (Qtz) phenocrysts. B. Massive chlorite (Chl) vein, locally overprinted by muscovite (Mus)/biotite, in a fine-grained quartz-rich groundmass (sample 62060; RM04-04; 1040 m; Ming South Zone). C. Drill core section representative of the quartz-chlorite-sulfides alteration assemblage. Note the light reflection onto the surface enhancing the network of anastomosing chlorite veins (RM06-04e; 1120 m; Lower Footwall/Ming South zones). D. Quartz-chlorite-sulfides-epidote vein in a quartz-chlorite groundmass (sample 62085; level 1450; Lower Footwall/Ming South zones). E. Drill core section revealing the pervasive nature of the quartz-chlorite-sericite assemblage (RM04-07; 936 m; Lower Footwall/Ming South zones). F. Pervasive fine-grained quartz-chlorite-sericite alteration assemblage (sample 36636; RMUG11-170; 130 m; Lower Footwall/1806 zones).

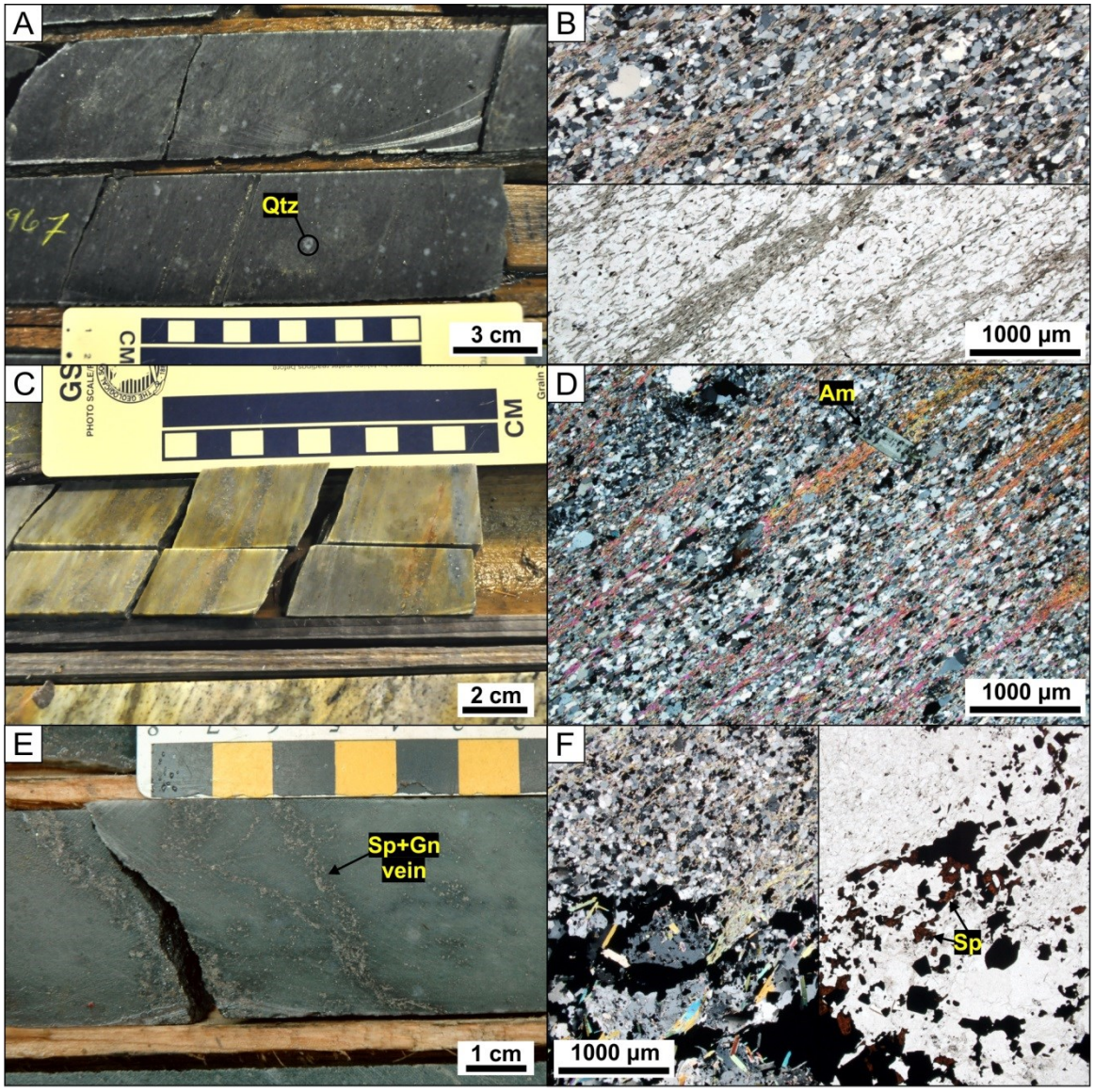
A
Qtz
3 cm
B
1000 µm
C
2 cm
D
Am
1000 µm
E
Sp+Gn
vein
1 cm
F
Sp
1000 µm

(Precious page) Fig. 5.7. Photographs of representative samples of the different alteration assemblages from the Ming deposit. A. Drill core section representative of the quartz-sericite-chlorite assemblage with relic quartz (Qtz) phenocrysts. B. Stitched polarized and transmitted light photomicrographs of the quartz-sericite-chlorite assemblage. Note the coexisting sericite and chlorite developed as layers in a fine-grained quartz-rich matrix (sample 62064; RM04-04; 1087 m; Ming South Zone). C. Representative drill core photo of the quartz-sericite alteration assemblage with sulfide-rich veins transposed onto S_2 fabrics (RM04-04; 893.0 m; Ming South Zone). D. Strong and pervasive quartz-sericite alteration. Amphibole (Am) porphyroblasts developed onto sericitic layers (sample 62057; RM04-04; 893.0 m; Ming South Zone). E. Drill core section representative of the quartz-sericite-sulfides assemblage with associated sphalerite (Sp)-galena (Gn)-rich veins (RMUG08-145; 20 m; 1806 Zone). F. Stitched polarized and transmitted light photomicrographs of red colored sphalerite (Sp)-rich quartz-sulfide vein in a quartz-sericite groundmass (sample 29881; RMUG08-121; 60 m; 1806 Zone).

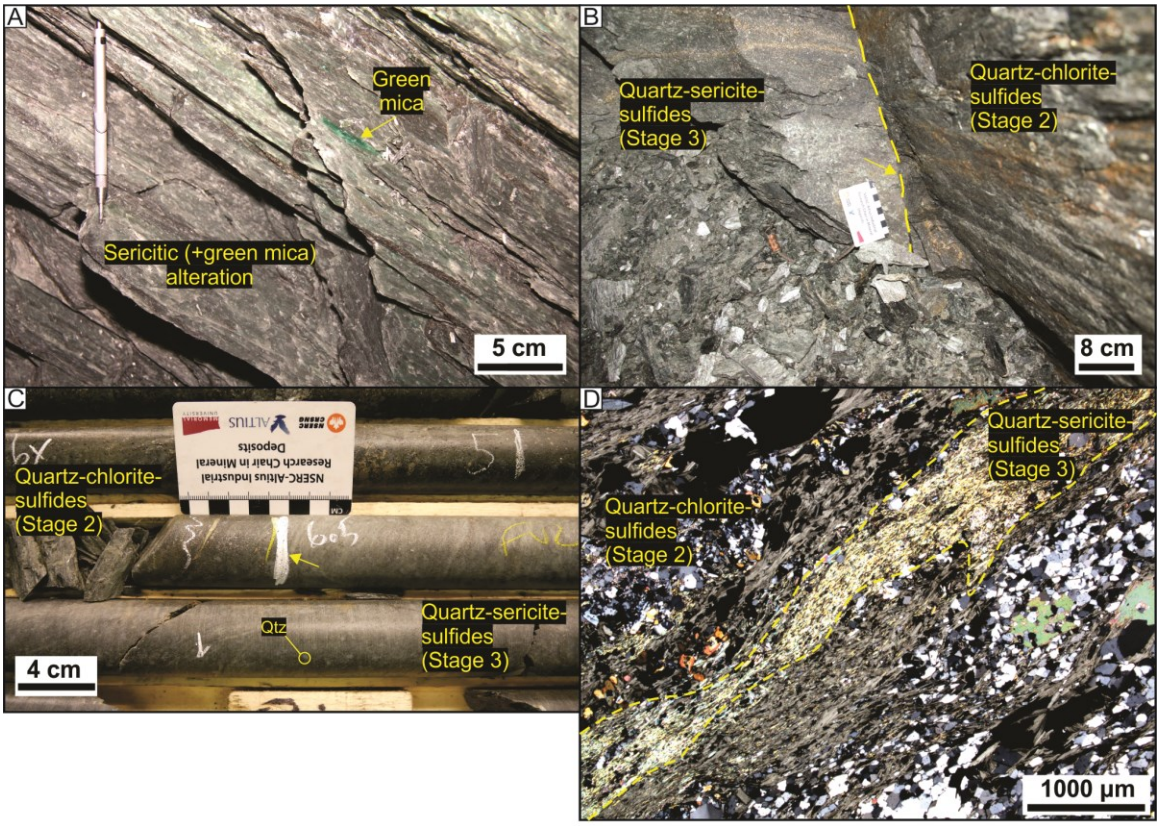

Fig. 5.8. Underground and drill core photos and photomicrographs. A. Distinctive green mica developed within a sericitic assemblage (level 103; 1806 Zone). B. to D. Relationship between the quartz-sericite-sulfides and quartz-chlorite(-sulfides) assemblages; B. Sharp primary contact (yellow arrow) between the two assemblages (level 1450; Lower Footwall Zone). C. Drill core section showing the same contact (white line) as in B (RMUG14-250; 6.5 m; Lower Footwall/1806 zones). D. Photomicrograph showing the chloritic groundmass overprinted by a sericitic vein, belonging to the quartz-sericite-sulfides assemblage. This sample was collected on the right wall in B (sample 103413; level 1450; Lower Footwall/1806 zones).

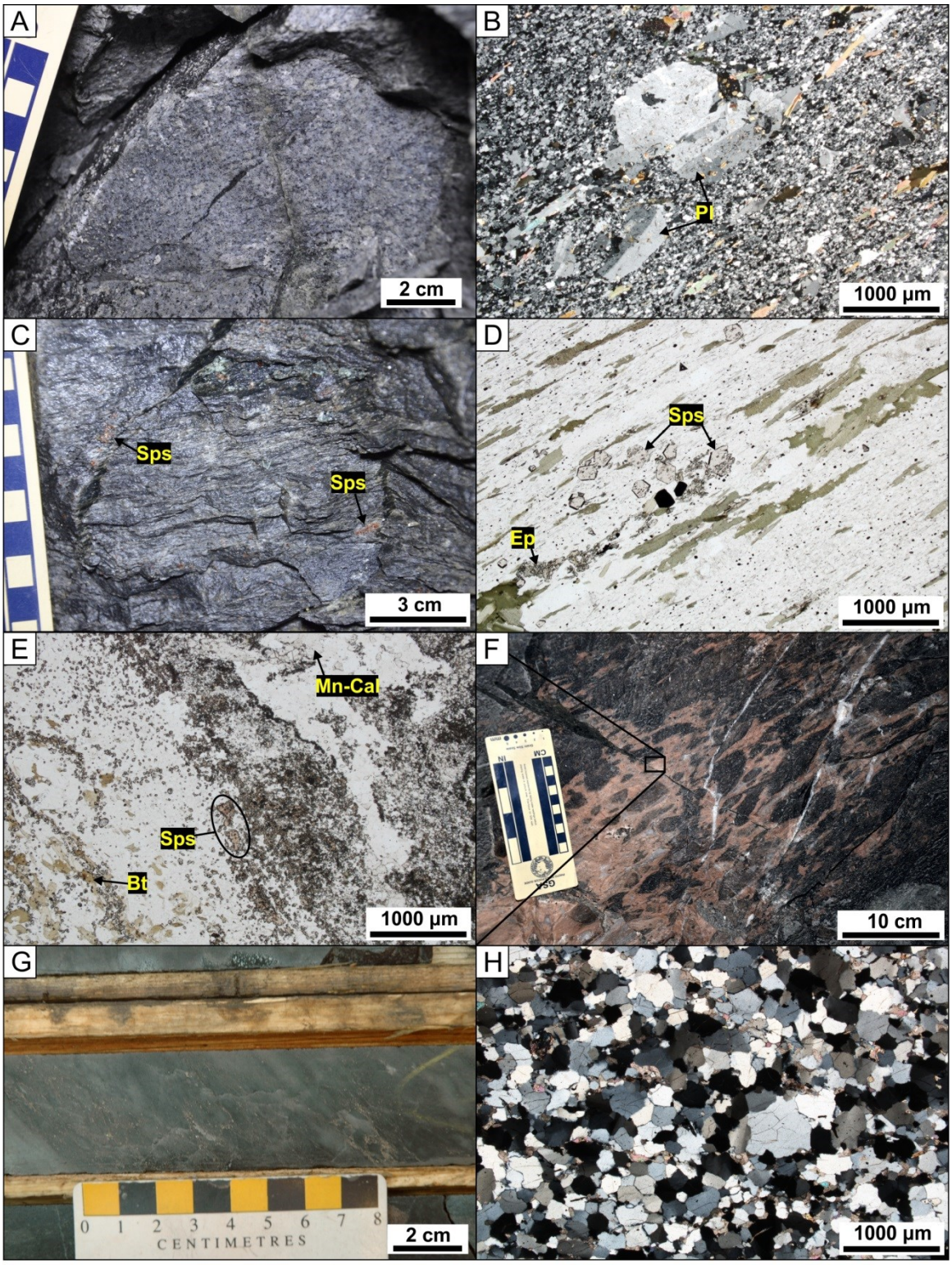
A
2 cm
B
Pl
1000 µm
C
Sps
Sps
3 cm
D
Sps
Ep
1000 µm
E
Mn-Cal
Sps
Bt
1000 µm
F
10 cm
G
0 1 2 3 4 5 6 7 8
CENTIMETRES
2 cm
H
1000 µm

(Precious page) Fig. 5.9. Photographs of representative samples of the different alteration assemblages from the Ming deposit. A. Representative least-altered rhyodacite. Note the pervasive light green epidote alteration and metamorphic fabric defined by biotite (level 469; 1807 Zone). B. Relic plagioclase (Pl) phenocrysts in a fine-grained quartz-plagioclase±sericite groundmass (sample 62081; level 469; 1807 Zone). C. Representative outcrop of the sericite-calcite±spessartine with spessartine (Sps) glomero-porphyroblasts on well-developed foliation (level 329; 1807 Zone). D. Polarized light photomicrograph of the sericite-calcite±spessartine (Sps) assemblage (sample 60507; level 329; 1807 Zone). Some epidote (Ep) also developed in this assemblage. E. A Mn-rich calcite (Mn-Cal), spessartine (Sps), and biotite (Bt) assemblage developed in the 1807 Zone (sample 62199; level 481; 1807 Zone). F. Outcrop-scale example of the Mn-Ca-rich alteration assemblage cross-cutting the weakly- altered assemblage (level 481; 1807 Zone). G. Drill core section representative of the silica-rich layer, immediately overlying the massive sulfides (RMUG08-145; 65 m; 1806 Zone). H. Polygonal quartz assemblage of the silica-rich layer with interstitial calcite (sample 29891; RMUG08-151; 82 m; 1806 Zone).

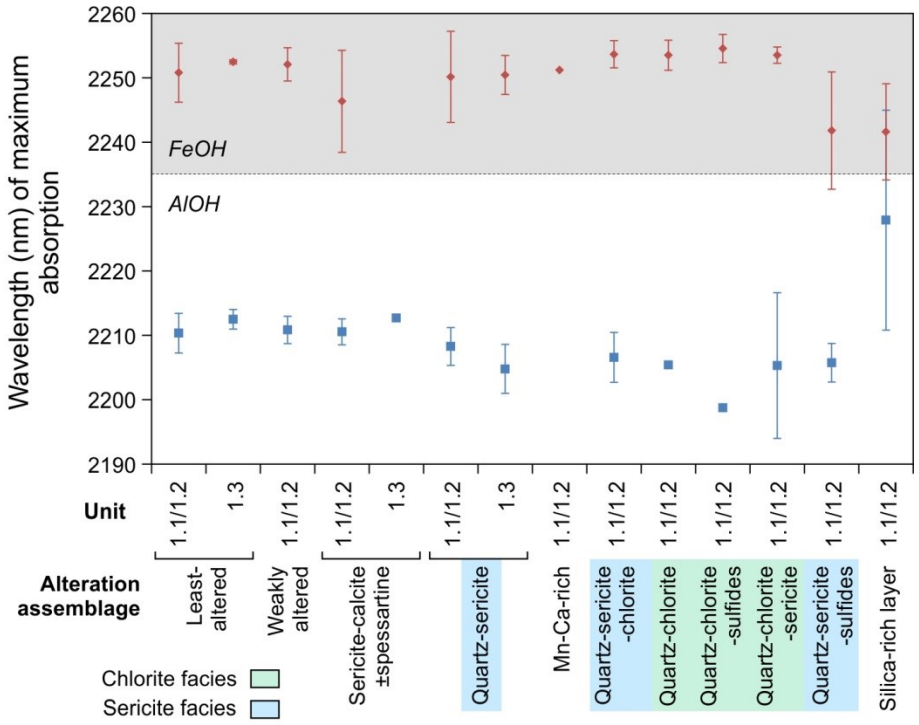

Fig. 5.10. Average maximum absorption features (in nm) of hydrous minerals using hyperspectral reflectance spectrometry for each alteration assemblage and stratigraphic unit. Error bars represent 1 standard deviation (1σ). Features representative of AlOH range in wavelengths <2235 nm, whereas feature representative of FeOH range in longer wavelengths.

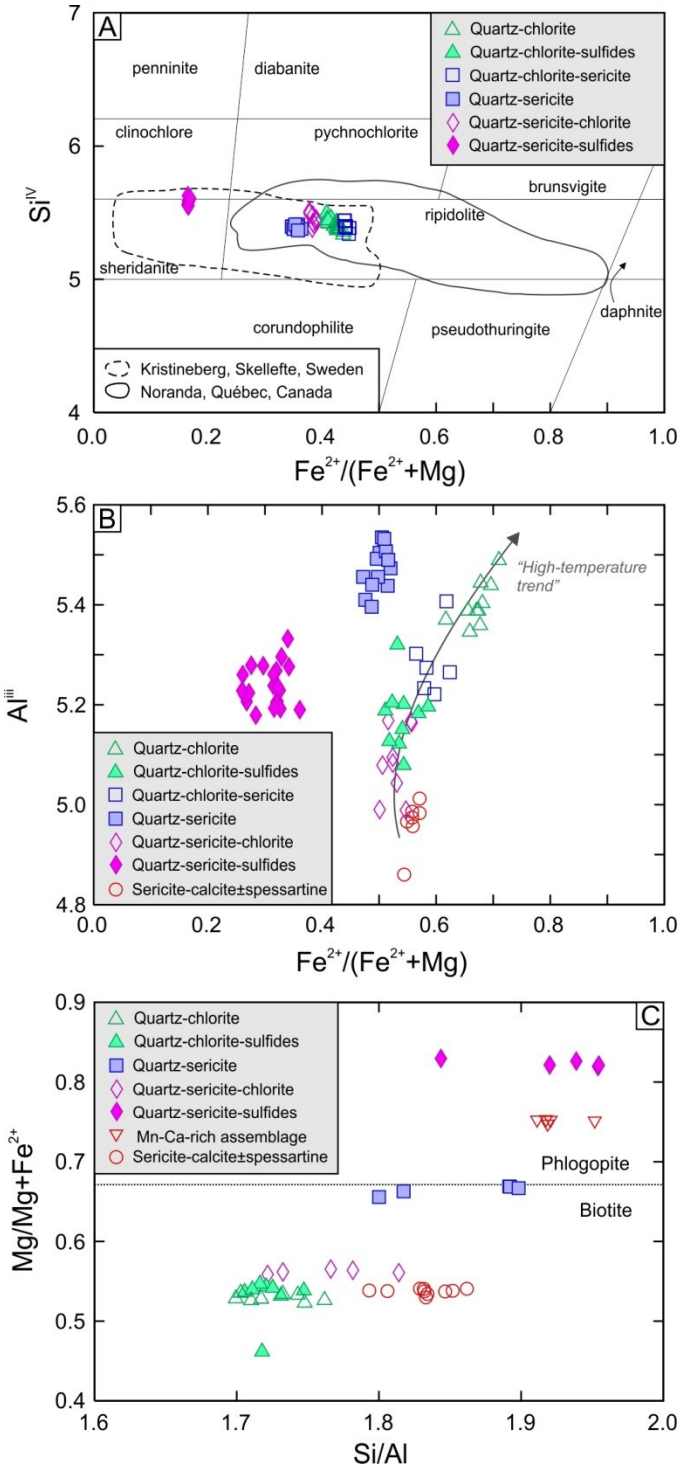
A
penninite
diabanite
clinochlore
pychnochlorite
brunsvigite
ripidolite
sheridanite
daphnite
corundophilite
pseudothuringite
Kristineberg, Skellefte, Sweden
Noranda, Québec, Canada
Quartz-chlorite
Quartz-chlorite-sulfides
Quartz-chlorite-sericite
Quartz-sericite
Quartz-sericite-chlorite
Quartz-sericite-sulfides
Si^IV
Fe2+/(Fe2++Mg)
B
"High-temperature trend"
Sericite-calcite±spessartine
Al^III
C
Mn-Ca-rich assemblage
Phlogopite
Biotite
Mg/Mg+Fe2+
Si/Al

(Precious page) Fig. 5.11. Composition of chlorite in the Ming alteration assemblages. A. Hey diagram showing chlorite compositions of the Ming deposit in the ripidolite, sheridanite, and chlinochlore fields. Also shown are the chlorite compositions from Noranda (Hannington et al., 2003b) and Kristineberg area, Skellefte Group (Hannington et al., 2003a). The chlorite from Ming are generally low in Fe/(Fe+Mg) ratios, comparable to the ones from the Kristineberg area, which likely reflect the low temperature nature of the seawater-saturated volcaniclastic piles of units 1.2 and 1.3. B. Composition of sericite shown on a Al vs. Fe/(Fe+Mg) diagram. The trend in the data is interpreted to reflect chlorite abundance and conditions at higher temperatures than the sericitic assemblages. C. Composition of biotite shown on a Mg/(Mg+Fe) vs. Si/Al diagram. The division between phlogopite and biotite (Mg:Fe = 2:1) is from Deer et al. (1966).

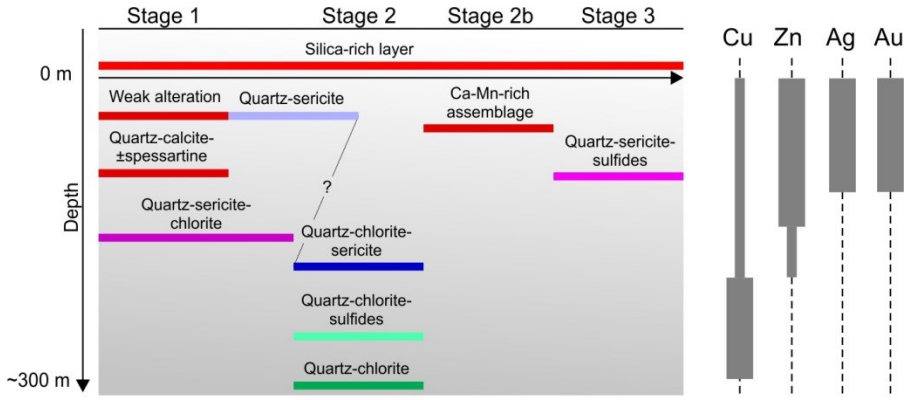

Fig. 5.12. Paragenetic evolution of the alteration assemblages in relation to depth (approximate scale). Three main stages of hydrothermal alteration have been established for the Ming deposit. The paragenetic relationship between some alteration assemblages are not well constrained and require more work. However, this diagram represents with confidence the overall evolution of the hydrothermal system.

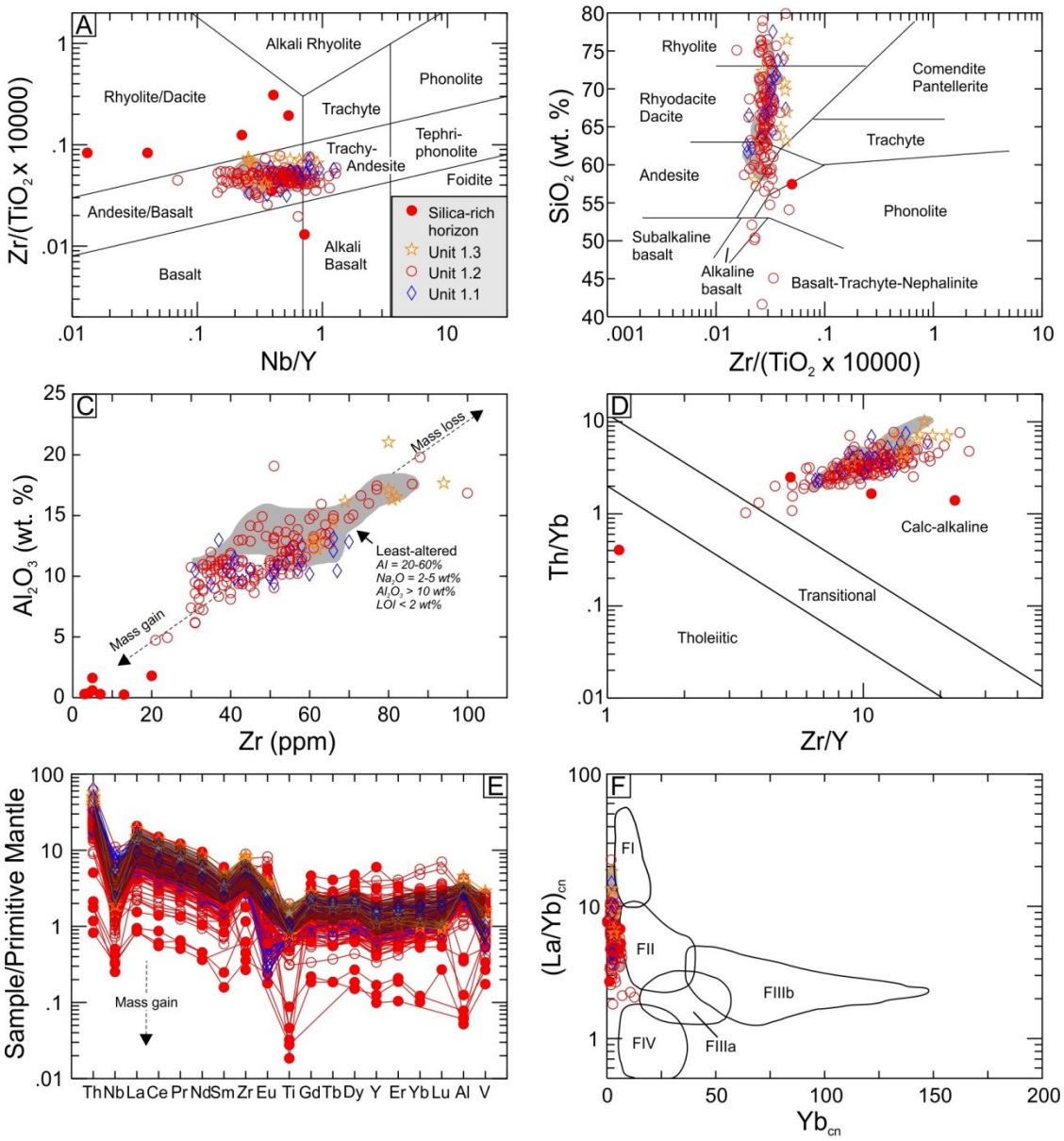

Fig. 5.13. Petrochemical affinity of all analyzed samples from the Rambler Rhyolite formation. A. Zr/TiO_2 vs. Nb/Y discrimination diagram from Winchester and Floyd (1977), revised by Pearce (1996). B. Zr/TiO_2 vs. SiO_2 discrimination diagram from Winchester and Floyd (1977). C. Al_2O_3 vs. Zr. D. Th/Yb vs. Zr/Y discrimination diagram from Ross and Bédard (2009). E. Primitive mantle-normalized extended-elements diagram. F. Chondrite-normalized $[La/Yb]_{cn}$ vs. Yb_{cn} discrimination diagram from Lesher et al. (1986) and Hart et al. (2004). Chondrite and primitive mantle normalizing values are those of Nakamura (1974) and Sun and McDonough (1989), respectively. Fields in grey are least-altered rocks as defined by Pilote and Piercey (in review) with criteria listed in C.

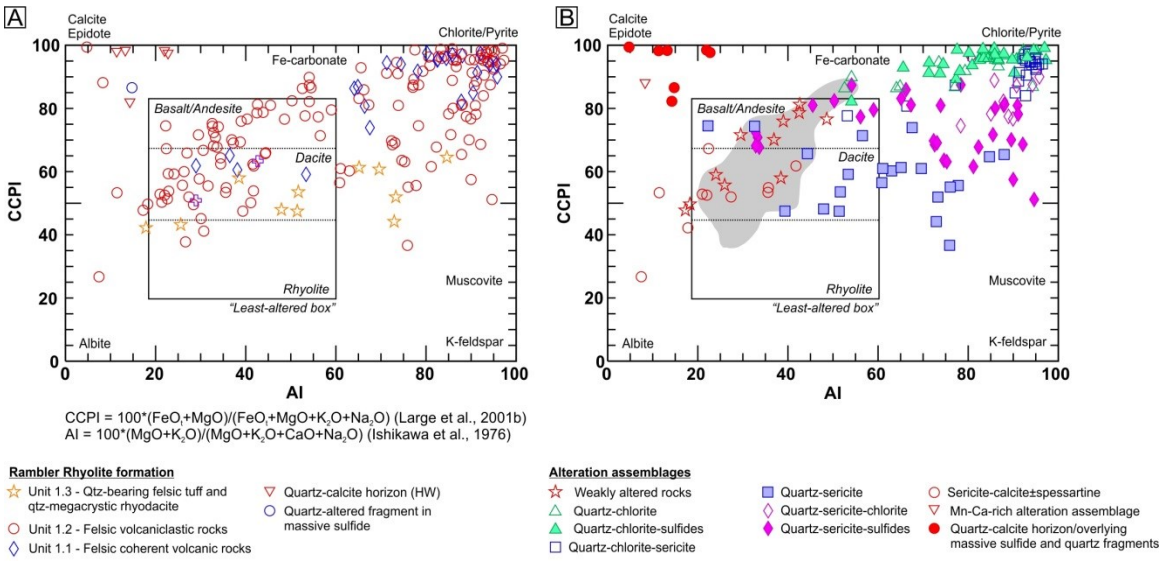

Fig. 5.14. Alteration box plot diagrams of Large et al. (2001b). A. Complete dataset is shown and categorized based on the units rather than alteration assemblages. B. Distribution of the alteration assemblages. In grey is the distribution of least-altered samples, based on the criteria set by Pilote and Piercey (in review). AI = alteration index (Ishikawa et al., 1976), CCPI = chlorite-carbonate-pyrite index (Large et al., 2001b).

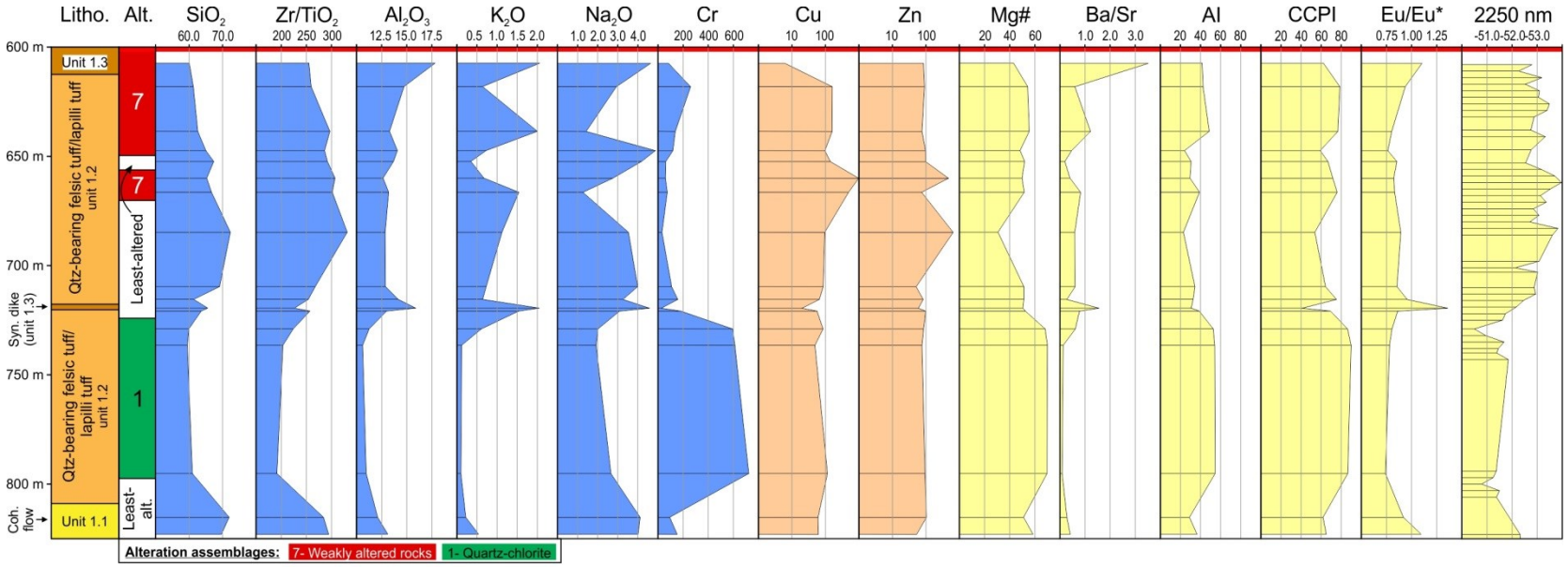

Fig. 5.15. Chemostratigraphic profile of drill hole RM07-18, representative of the 1807 Zone. Horizontal lines represent location of analyzed sample and results. AI = alteration index (Ishikawa et al., 1976), CCPI = chlorite-carbonate-pyrite index (Large et al., 2001b).

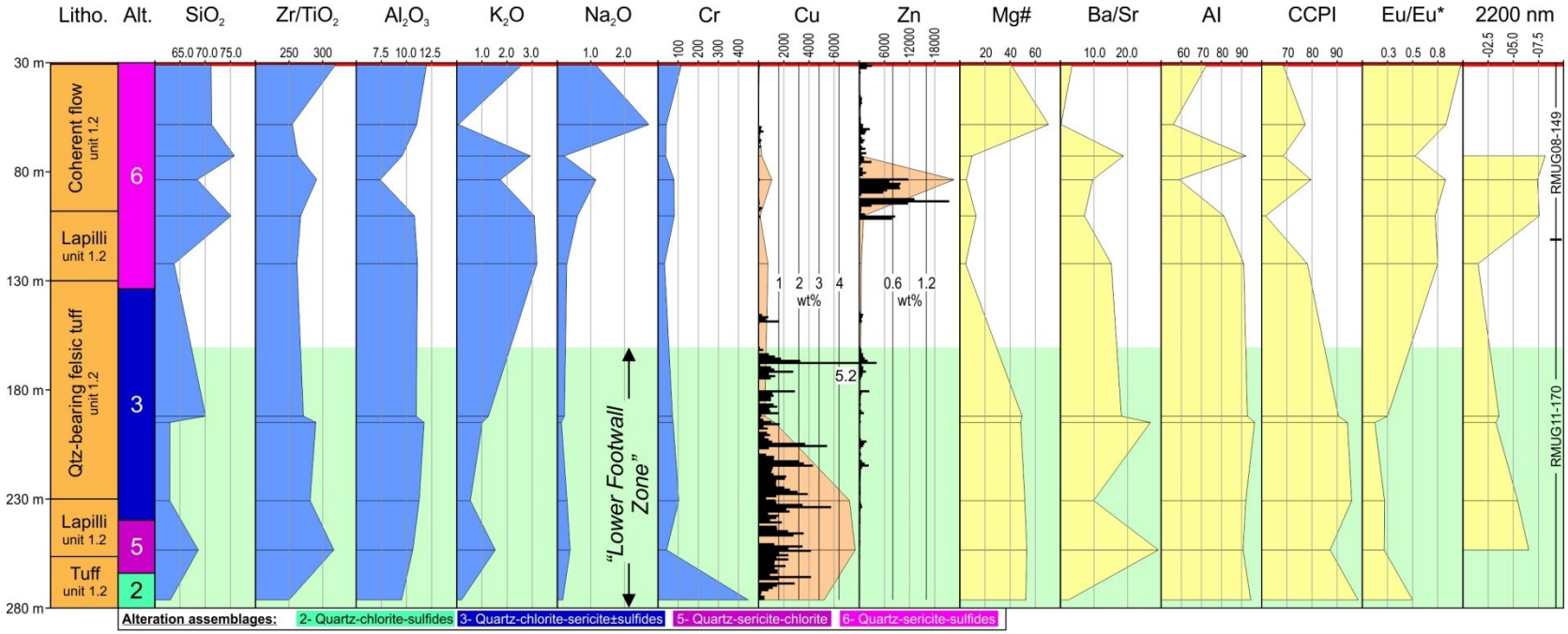

Fig. 5.16. Composite chemostratigraphic profile of drill holes RMUG11-170 and RMUG08-149, representative of the 1806 Zone and part of the Lower Footwall Zone. Horizontal lines represent location of analyzed sample and results. Bar plots for Cu and Zn are on a wt. % scale, which is identified in the central part of the profile. AI = alteration index (Ishikawa et al., 1976), CCPI = chlorite-carbonate-pyrite index (Large et al., 2001b).

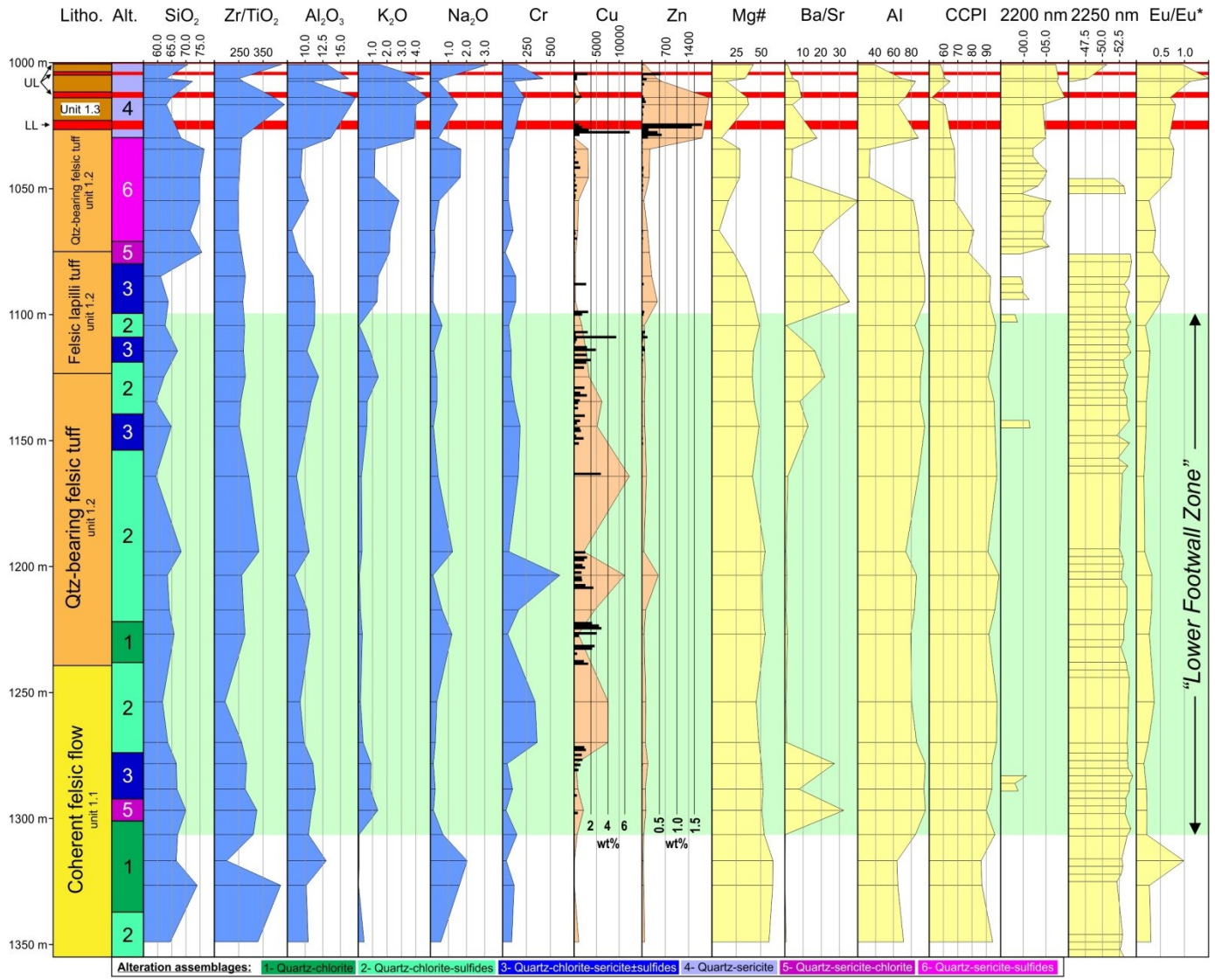
Litho.
Alt.
SiO2
Zr/TiO2
Al2O3
K2O
Na2O
Cr
Cu
Zn
Mg#
Ba/Sr
Al
CCPI
2200 nm
2250 nm
Eu/Eu*
1000 m
1050 m
1100 m
1150 m
1200 m
1250 m
1300 m
1350 m
UL
LL
Unit 1.3
Qtz-bearing felsic tuff unit 1.2
Felsic lapilli tuff unit 1.2
Qtz-bearing felsic tuff unit 1.2
Coherent felsic flow unit 1.1
wt%
wt%
"Lower Footwall Zone"
Alteration assemblages:
1- Quartz-chlorite
2- Quartz-chlorite-sulfides
3- Quartz-chlorite-sericite±sulfides
4- Quartz-sericite
5- Quartz-sericite-chlorite
6- Quartz-sericite-sulfides

(Precious page) Fig. 5.17. Chemostratigraphic profile of drill hole RM05-08, representative of the Ming South Zone. Horizontal lines represent location of analyzed sample and results. Bar plots for Cu and Zn are on a wt. % scale, which is identified in the central part of the profile. AI = alteration index (Ishikawa et al., 1976), CCPI = chlorite-carbonate-pyrite index (Large et al., 2001b), UL = upper lens, LL = lower lens.

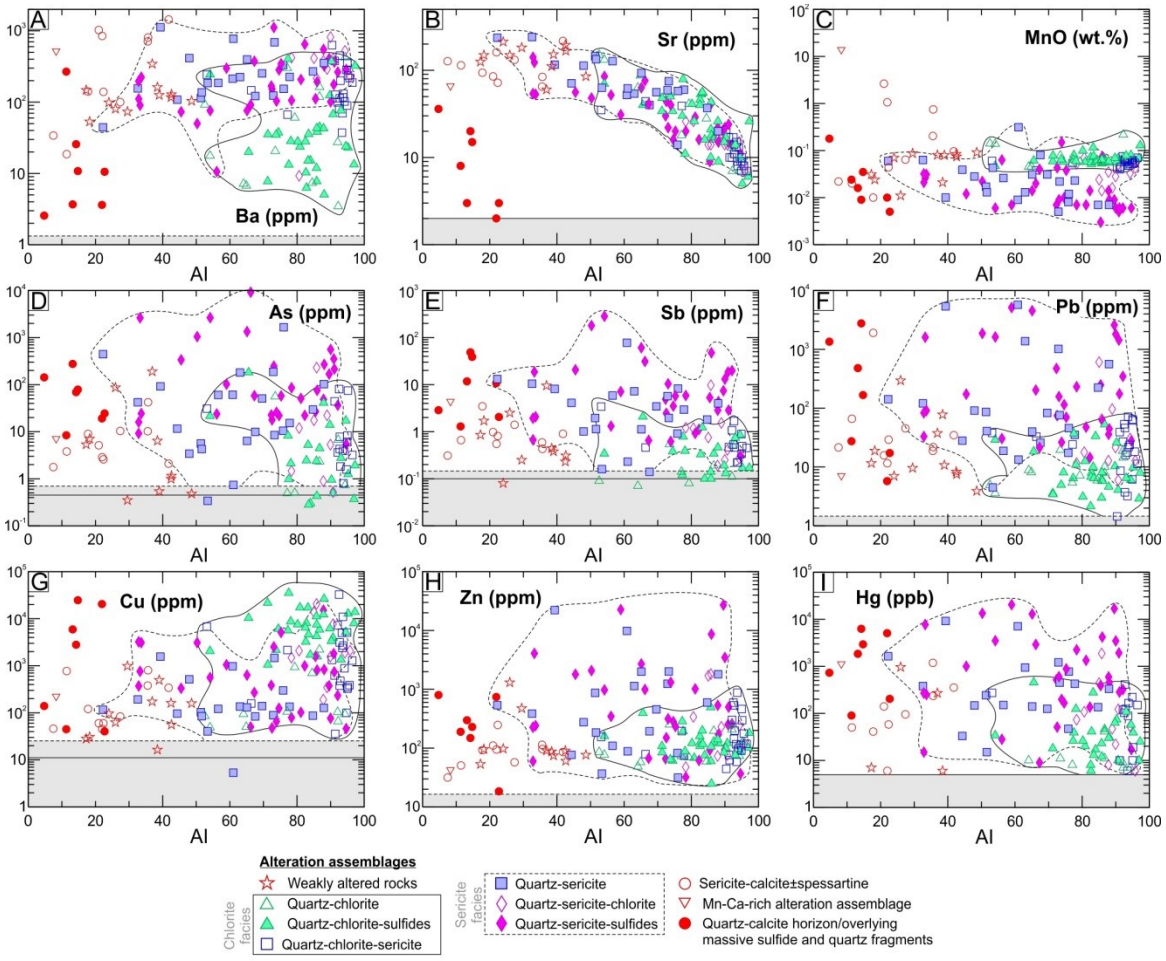

Fig. 5.18. Alteration index (AI; Ishikawa et al., 1976) vs. A. Ba, B. Sr, C. MnO, D. As, E. Sb, F. Pb, G. Cu, H. Zn, and I. Hg for altered felsic rocks from the Ming deposit, showing the variations in trace elements and metals with increasing degree of alteration. The grey fields represent the lower detection limit, with the average values as solid lines, and the upper 2σ as dashed lines.

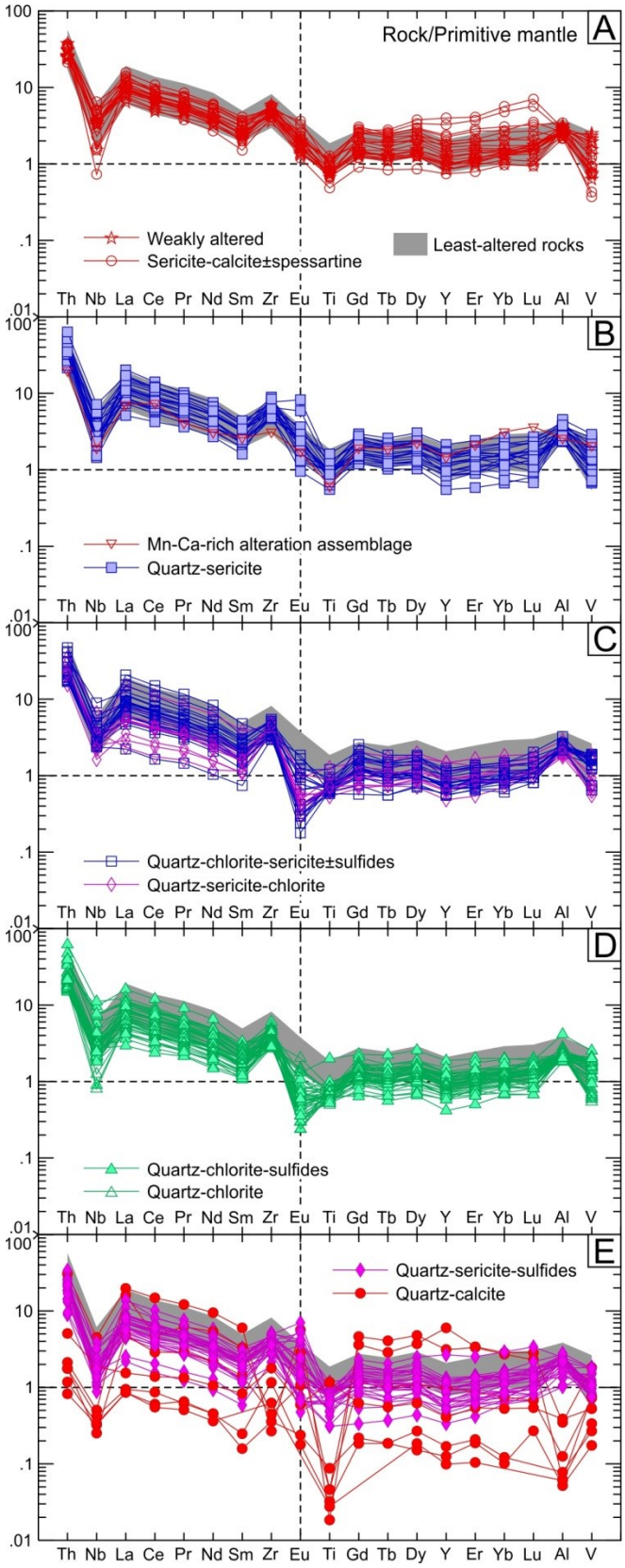
Rock/Primitive mantle
A
Weakly altered
Sericite-calcite±spessartine
Least-altered rocks
B
Mn-Ca-rich alteration assemblage
Quartz-sericite
C
Quartz-chlorite-sericite±sulfides
Quartz-sericite-chlorite
D
Quartz-chlorite-sulfides
Quartz-chlorite
E
Quartz-sericite-sulfides
Quartz-calcite
100
10
1
.1
.01
Th Nb La Ce Pr Nd Sm Zr Eu Ti Gd Tb Dy Y Er Yb Lu Al V

(Precious page) Fig. 5.19. Primitive mantle-normalized extended-element plot for all the alteration assemblages associated with the Ming deposit. A. least-altered rocks (in shaded grey), weakly altered, and sericite-calcite±spessartine assemblage. B. Mn-Ca-rich and quartz-sericite assemblages. C. Quartz-chlorite-sericite(±sulfides) and quartz-sericite-chlorite assemblages. D. Quartz-chlorite-sulfides and quartz-chlorite assemblages. E. Quartz-sericite-sulfides and silica-rich layer assemblages. The least-altered samples (in shaded grey) are shown in all diagrams for comparison purposes. Normalizing values are those of Sun and McDonough (1989).

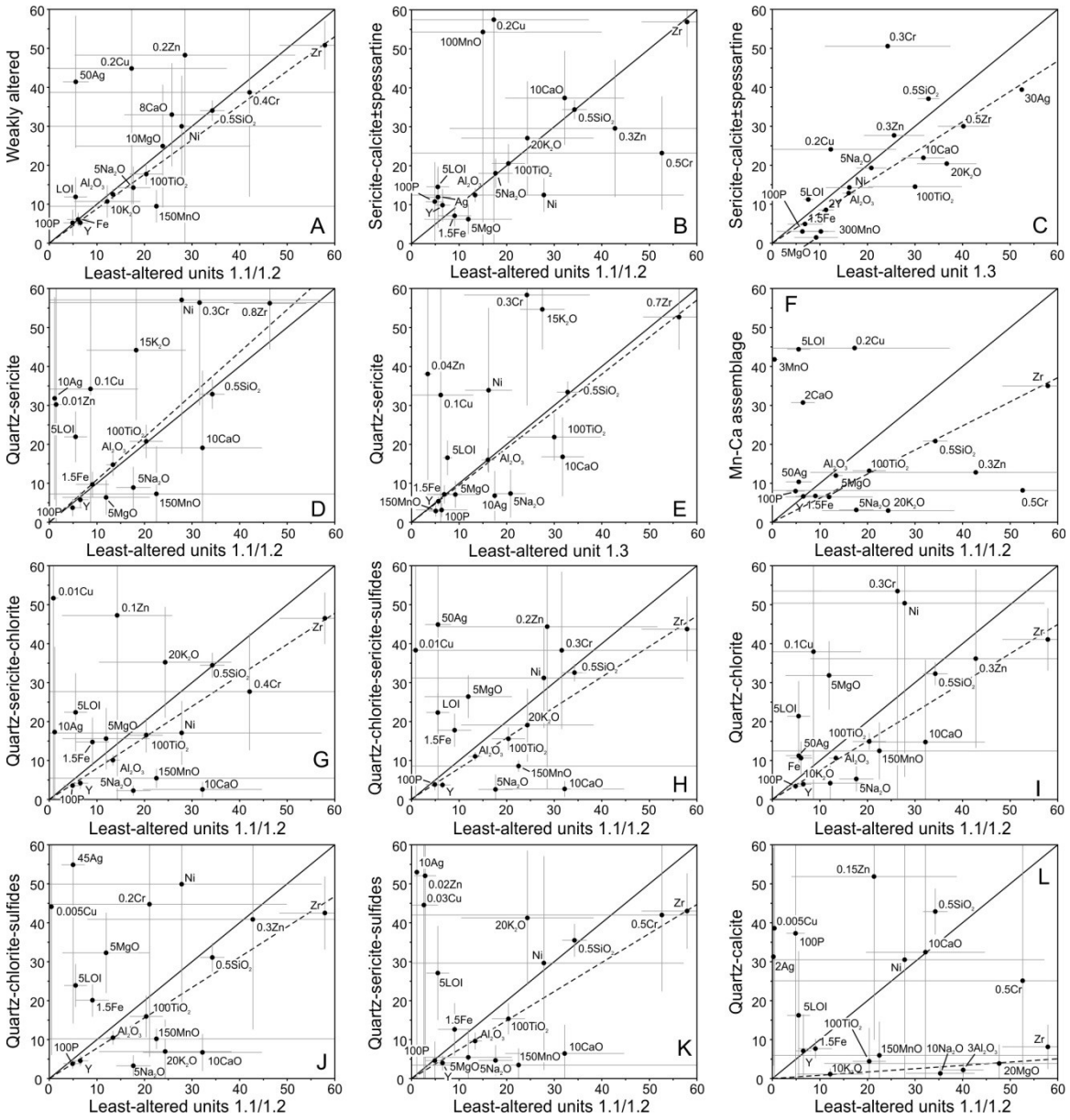

Fig. 5.20. Best-fit isocon diagrams of Grant (1986). Except for C and E, all diagrams are compared to the least-altered rocks of the combined units 1.1 and 1.2. In C and E, the respective alteration assemblages are compared to the least-altered rocks of unit 1.3. Each element is scaled to show changes in components that could otherwise be underestimated. The accompanying horizontal and vertical lines indicate the 1σ error for each element. The propagation of errors follows the method of Huston (1993).

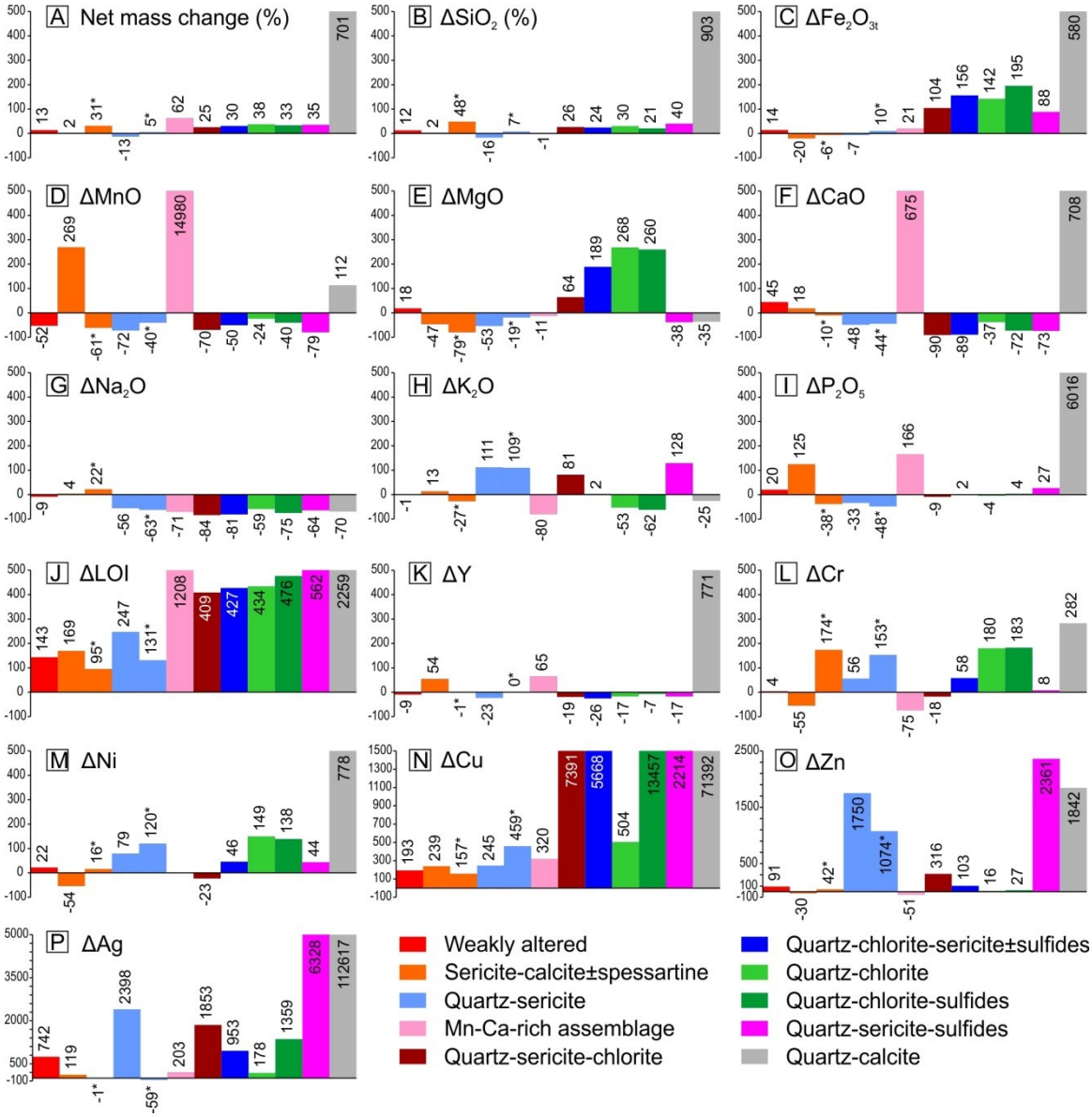

Fig. 5.21. Histogram illustrating relative mass changes (illustrated in Figure 19) for altered rocks at the Ming deposit. These calculations are based on the method proposed by Grant (1986) and assume the immobility of certain elements such as Al_2O_3, TiO_2, and/or Zr. The relative changes (in percent) in each element are indicated on each bar.

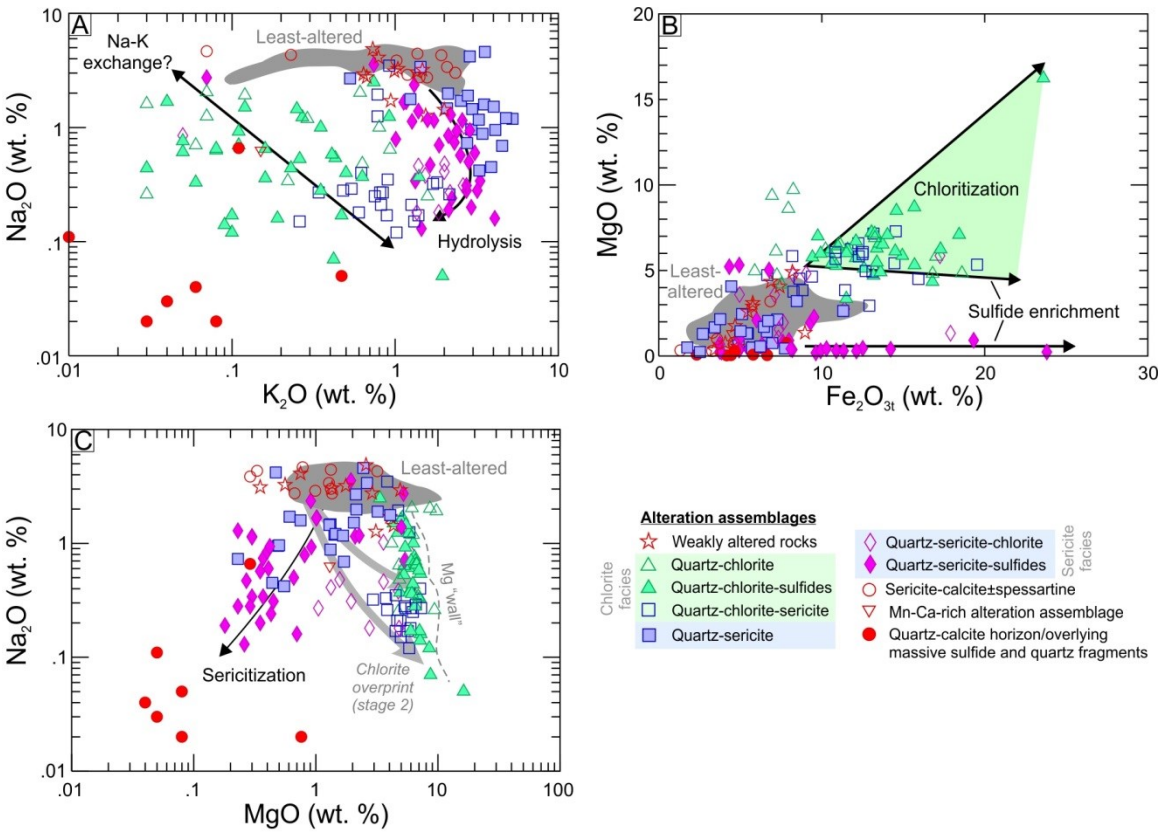

Fig. 5.22. Variation diagrams illustrating geochemical behavior for variably altered rocks from the Ming deposit. A. K_2O vs. Na_2O. B. Fe_2O_{3t} vs. MgO. C. MgO vs. Na_2O.

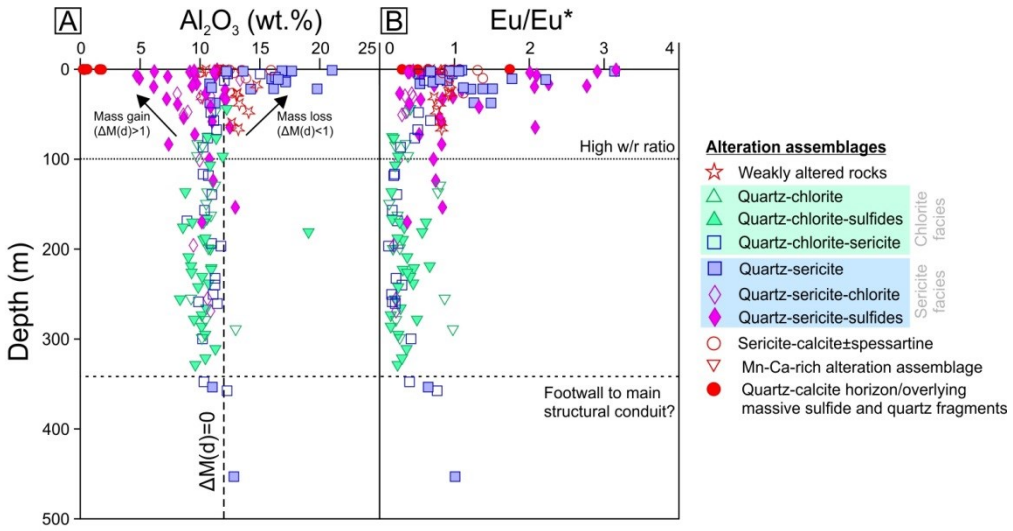

Fig. 5.23. Variation diagrams illustrating the variably altered rocks in relation to depth. A. Al_2O_3. B. Eu/Eu*. Depth here has been normalized to the base of the uppermost massive sulfide lens or the felsic-hanging wall interface. Samples from the overlying silica-rich layer and silica-rich fragments were plotted on the 0 m mark for the sake of simplification.

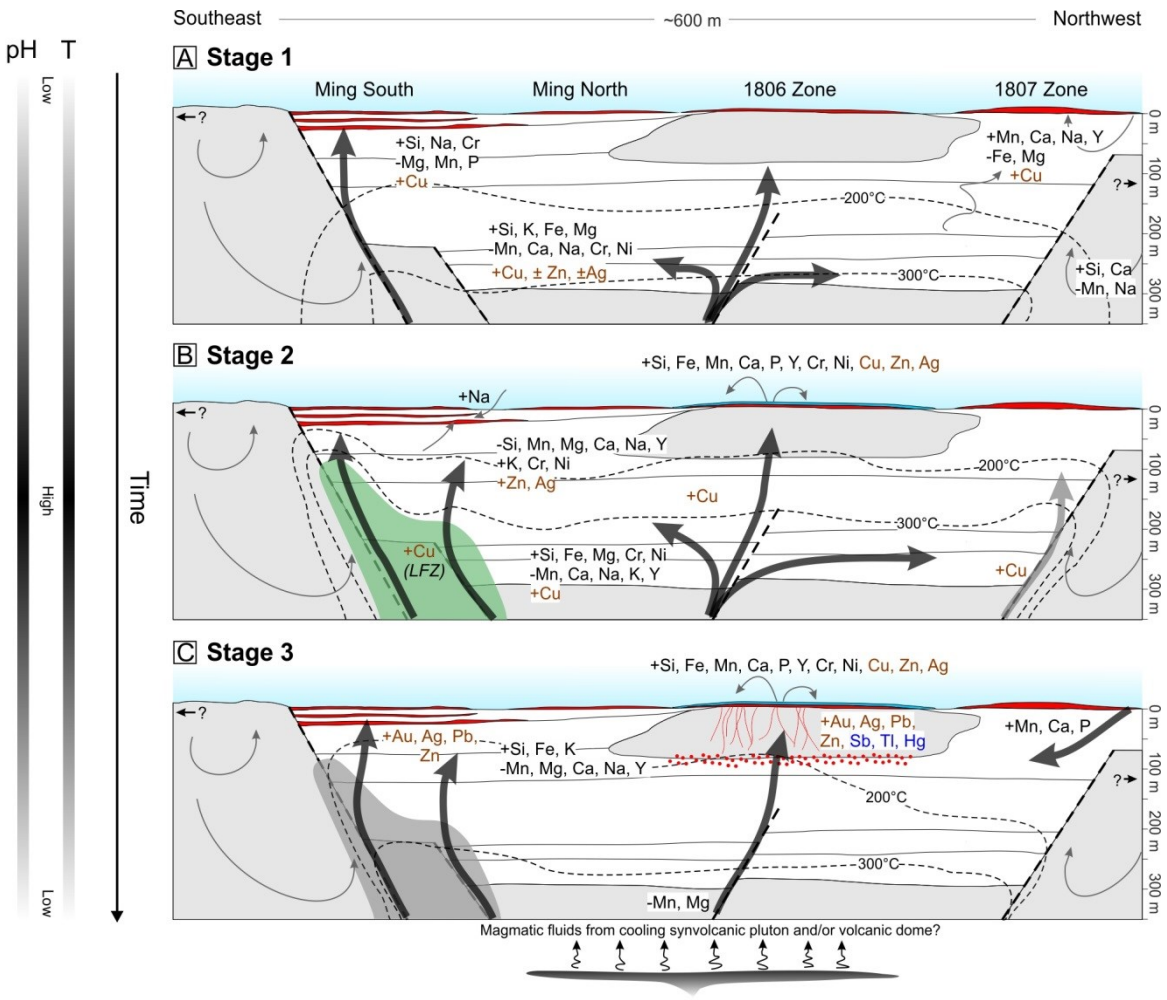

Fig. 5.24. Schematic reconstruction of the hydrothermal system and its evolution and related elemental changes associated with the formation of the Ming deposit. Grey units represent coherent volcanic lithofacies, whereas the white units represent volcaniclastic lithofacies. A. Stage 1: early development of low-temperature alteration assemblages (i.e., quartz-calcite±spessartine, quartz-sericite-chlorite, quartz sericite, and silica-rich layer). B. Stage 2: waxing and high-temperature alteration assemblages (i.e., quartz-chlorite, quartz-chlorite-sulfides, quartz-chlorite-sericite) associated with introduction of base metals. C. Stage 3: waning and low-temperature assemblages (i.e., Ca-Mn-assemblage, quartz-sericite-sulfides) associated with the introduction of base and precious metals. Isocontours represent interpreted ambient temperatures.

Table 5.1. Summary of the Mineralogy and Elemental Changes within the Various Hydrothermal Alteration Assemblages at the Ming Deposit

Alteration assemblage[1]	Zone	Major minerals (vol. %)[2]	Minor and trace minerals (vol. %)[2]	Main elemental changes[3]
1. Weak alteration	1807 Zone (±1806 and Ming South zones)	Quartz (≤76), epidote (≤30), plagioclase (≤20), sericite (≤25), biotite (≤20), actinolite (≤15), chlorite (≤15)	Calcite, pyrite, chalcopyrite, pyrrhotite, magnetite, ilmenite	Losses: MnO, Na_2O, Y Gains: SiO_2, Fe_2O_{3t}, MgO, CaO, P_2O_5
2. Sericite-calcite±spessartine	1807 Zone (±1806 and Ming South zones)	Quartz (≤55), sericite (≤44), calcite (≤25), biotite (≤16), epidote (≤15)	Spessartine, plagioclase, chlorite, apatite, magnetite, pyrite, chalcopyrite, sphalerite, galena, rutile	Losses: Fe_2O_{3t}, MgO, Cr, Ni Gains: MnO, P_2O_5, Y, Cu
3. Quartz-sericite	1806 and Ming South zones (±1807 Zone)	Quartz (≤56), sericite (≤47)	Chlorite, biotite, epidote, pyrite, chaclopyrite, sphalerite, arsenopyrite, galena, sulfosalts, rutile, electrum?	Losses: SiO_2, MnO, MgO, CaO, Na_2O, P_2O_5 Gains: K_2O, Cr, Ni, Cu, Zn, Ag
4. Mn-Ca-rich assemblage	1807 Zone	Quartz (35), Mn-rich calcite (21), spessartine (20)	Apatite, biotite, plagioclase	Losses: Na_2O, K_2O, Cr, Gains: MnO, CaO, P_2O_5, Y, Cu
5. Quartz-sericite-chlorite	1806 and Ming South zones	Quartz (≤55), sericite (≤45), chlorite (≤29)	Pyrite, biotite, chalcopyrite, pyrrhotite, sphalerite, epidote, magnetite, ilmenite, galena	Losses: MnO, CaO, Y, Cr, Ni Gains: SiO_2, Fe_2O_{3t}, MgO, K_2O, Cu, Ag
6. Quartz-chlorite	1807, 1806 and Ming South	Quartz (≤60), chlorite (≤47), biotite (≤30), actinolite (≤30)	Epidote, pyrite, chalcopyrite, pyrrhotite, sphalerite, plagioclase, magnetite, ilmenite, rutile, calcite, sericite	Losses: MnO, CaO, Na_2O, K_2O, Y Gains: SiO_2, Fe_2O_{3t}, MgO, Cr, Ni, Cu
7. Quartz-chlorite-sulfides	1806 and Ming South zones	Quartz (≤65), chlorite (≤79), pyrite (≤20), chalcopyrite (≤20), actinolite (≤15)	Pyrrhotite (≤10), biotite, epidote, sphalerite, magnetite, ilmenite, sericite	Losses: MnO, CaO, Na_2O, K_2O, Y Gains: SiO_2, Fe_2O_{3t}, MgO, Cr, Ni, Cu, Ag
8. Quartz-chlorite-sericite(±sulfides)	1806 and Ming South zones	Quartz (≤55), chlorite (≤37), sericite (≤32)	Pyrite (≤6), chalcopyrite (≤6), pyrrhotite (≤4), epidote, biotite, magnetite, ilmenite, rutile, sphalerite, galena	Losses: MnO, CaO, Na_2O, Y Gains: SiO_2, Fe_2O_{3t}, MgO, Cr, Ni, Cu, Ag
9. Quartz-sericite-sulfides	1806 and Ming South zones	Quartz (≤63), sericite (≤46), pyrite (≤15)	Chalcopyrite, sphalerite, arsenopyrite, galena, sulfosalts, tellurides, Au-Ag alloys (e.g., electrum), chlorite, biotite, calcite, rutile	Losses: MnO, MgO, CaO, Na_2O, Y Gains: SiO_2, Fe_2O_{3t}, K_2O, Cu, Zn, Ag
10. Silica-rich horizon/fragments	1806 Zone (±1807 Zone)	Quartz (≤98), calcite (≤13)	Pyrite (≤4), chalcopyrite, sphalerite, biotite, epidote, electrum	Losses: MgO, Na_2O, K_2O Gains: SiO_2, Fe_2O_{3t}, MnO, CaO, P_2O_5, Y, Cr, Ni, Cu, Zn, Ag

[1]Combining units 1.1 to 1.3

[2]In brackets are the maximum relative amounts. Averages are presented in Figure 9.

[3]Based on mass balance calculations presented in Figure 17

Table 5.2. Average Chemical Composition of Least Altered and Altered Host Rocks of the Ming Deposit

	Least-altered				Weak alteration		Sericite-calcite±spessartine			Quartz-sericite			
	Units 1.1/1.2		Unit 1.3		Units 1.1/1.2		Units 1.1/1.2		Unit 1.3	Units 1.1/1.2		Unit 1.3	
	Avg	1σ	Avg	1σ	Avg	1σ	Avg	1σ		Avg	1σ	Avg	1σ
SiO_2 (wt. %)	68.51	5.17	65.64	4.56	68.07	5.23	68.81	4.89	74.15	65.76	7.58	66.80	5.51
Al_2O_3	13.37	1.43	16.07	1.37	12.53	1.39	12.45	1.77	12.84	14.76	2.88	16.00	2.95
Fe_2O_{3t}	6.04	2.33	4.58	2.44	6.08	1.69	4.76	1.82	3.27	6.46	2.20	4.77	1.58
FeO_t[1]	6.04	2.33	4.58	2.44	5.47	1.52	4.28	1.63	2.94	5.82	1.98	4.30	1.42
MnO	0.150	0.250	0.034	0.010	0.063	0.028	0.543	0.817	0.010	0.049	0.082	0.019	0.010
MgO	2.38	1.84	1.84	0.91	2.49	1.58	1.25	0.76	0.29	1.27	0.90	1.42	0.69
CaO	3.22	1.25	3.18	0.45	4.12	1.66	3.74	1.21	2.19	1.91	1.98	1.68	1.01
Na_2O	3.53	0.72	4.16	0.63	2.85	1.08	3.61	0.76	3.86	1.78	1.07	1.47	1.23
K_2O	1.22	0.70	1.83	0.31	1.07	0.42	1.35	0.73	1.02	2.94	1.19	3.64	0.68
TiO_2	0.204	0.035	0.300	0.098	0.177	0.027	0.206	0.050	0.145	0.208	0.043	0.219	0.061
P_2O_5	0.05	0.02	0.06	0.05	0.05	0.03	0.11	0.10	0.03	0.04	0.02	0.03	0.02
LOI	1.10	0.48	1.51	0.19	2.37	1.01	2.91	0.93	2.24	4.39	1.30	3.31	0.89
Total	99.78	0.78	99.21	0.53	99.88	0.76	99.72	1.01	100.10	99.58	1.61	99.36	0.54
Sr (ppm)	152	48	246	115	148	45	117	46	94	93	72	89	36
Sc	22	7	18	9	24	7	17	5	16	22	6	24	7
Zr	58	10	80	11	51	6	57	6	60	70	15	75	12
Ba	278.6	283.0	463.4	240.7	126.9	76.8	569.0	484.7	140.6	324.2	298.5	299.8	183.9
Y	6.52	1.66	5.64	0.82	5.23	1.14	9.86	4.16	4.27	5.76	2.04	5.36	1.17
Nb	2.98	0.80	2.51	1.02	2.45	0.60	2.57	1.23	1.09	2.25	0.86	2.46	0.92
Cs	0.72	0.33	0.84	0.15	0.61	0.21	0.56	0.26	0.37	0.98	0.47	1.42	0.72
La	7.19	1.40	10.84	1.75	6.00	0.71	8.28	1.55	6.57	7.65	2.95	8.16	1.46
Ce	15.35	3.36	22.16	2.70	12.03	1.44	15.62	2.82	12.94	15.26	5.40	16.63	3.37
Pr	1.69	0.29	2.50	0.45	1.41	0.14	1.86	0.36	1.38	1.76	0.58	1.91	0.37
Nd	6.17	1.09	9.00	1.77	5.13	0.51	6.75	1.31	4.78	6.36	2.06	6.66	1.23
Sm	1.29	0.24	1.75	0.32	1.07	0.10	1.43	0.30	0.89	1.26	0.37	1.32	0.28
Eu	0.35	0.07	0.55	0.08	0.28	0.04	0.41	0.11	0.25	0.52	0.33	0.38	0.11
Gd	1.17	0.25	1.41	0.20	0.93	0.14	1.42	0.35	0.72	1.16	0.36	1.15	0.24
Tb	0.19	0.04	0.20	0.01	0.15	0.03	0.23	0.06	0.12	0.18	0.05	0.18	0.04
Dy	1.20	0.29	1.19	0.13	0.93	0.17	1.55	0.47	0.76	1.13	0.36	1.11	0.20
Ho	0.26	0.06	0.23	0.04	0.20	0.04	0.35	0.13	0.16	0.23	0.09	0.22	0.04
Er	0.79	0.21	0.62	0.10	0.62	0.14	1.15	0.47	0.57	0.70	0.25	0.64	0.12
Tm	0.14	0.03	0.09	0.01	0.11	0.02	0.21	0.09	0.13	0.14	0.05	0.11	0.03
Yb	0.87	0.23	0.54	0.05	0.70	0.12	1.38	0.71	0.70	0.78	0.28	0.68	0.15
Lu	0.14	0.04	0.07	0.00	0.11	0.02	0.24	0.14	0.13	0.13	0.04	0.11	0.04
Ta	0.23	0.05	0.24	0.07	0.22	0.02	0.16	0.05	-	0.15	0.09	0.17	0.00
Tl	1.85	2.23	3.04	3.19	1.05	1.83	2.08	1.49	4.81	7.13	6.10	7.58	3.91
Pb	21.8	20.4	854.1	1192.5	40.9	85.1	29.4	16.2	1900.6	1120.2	2014.0	207.1	310.6
Bi	0.23	0.19	0.14	0.06	0.20	0.11	0.35	0.36	0.12	0.24	0.15	0.35	0.47
Th	2.70	0.62	4.05	0.60	2.24	0.20	2.69	0.44	2.71	2.74	0.58	3.61	0.52
U	0.91	0.63	2.19	1.87	1.26	0.51	0.87	0.45	3.81	6.25	7.04	2.62	1.25
V	103.6	48.8	95.9	30.1	129.0	53.7	71.1	31.3	119.6	115.9	40.2	133.7	57.6
Cr	105.3	144.3	80.9	44.0	96.7	67.0	46.5	29.1	168.5	187.9	87.8	194.5	94.6
Co	11.7	7.3	8.8	1.8	13.8	5.8	23.9	23.2	7.1	16.3	4.7	9.2	4.6
Ni	27.8	29.4	16.2	4.9	30.0	13.0	12.5	4.3	14.3	57.1	39.5	33.9	21.2
Cu	87	100	61	69	224	284	287	293	120	342	459	326	451
Zn	143	116	85	21	241	373	99	59	92	3021	6328	952	679
As	2.5	1.5	1.8	1.8	32.5	61.6	9.0	12.1	8.9	223.0	447.8	37.0	58.9
Ag	0.1	0.1	1.7	-	0.8	0.3	0.2	0.2	1.3	3.2	2.6	0.7	0.6
Sn	0.8	0.3	0.8	0.1	0.9	0.3	0.7	0.2	0.6	1.1	0.6	3.1	3.6
Sb	0.4	0.4	2.3	2.9	1.8	2.8	0.7	0.3	3.5	11.9	20.1	2.3	1.5
Hg (ppb)	33	50	33	-	412	402	265	362	41	1906	2999	308	361
AI[2]	33.62	7.82	32.61	6.71	32.46	10.41	24.96	10.73	17.80	58.14	19.23	64.58	12.23
CCPI[3]	61.58	11.09	48.90	9.55	66.62	11.83	52.74	10.42	42.18	60.31	10.66	54.02	7.02
Mg#[4]	38.21	13.53	41.85	4.52	39.69	15.29	33.59	9.30	14.94	26.47	10.31	35.61	13.09
Ba/Sr	2.13	2.59	1.97	1.14	1.21	1.53	5.29	4.49	1.50	6.83	7.19	4.11	2.76
Eu/Eu*[5]	0.95	0.12	1.31	0.16	0.84	0.09	1.03	0.20	0.84	1.38	0.70	1.02	0.23
2200 nm	2210.34	3.08	2212.50	1.53	2210.84	2.12	2210.55	2.03	2212.70	2208.27	2.93	2204.79	3.81
2250 nm	2250.79	4.58	2252.49	0.32	2252.09	2.58	2246.36	7.93		2250.15	7.09	2250.45	3.03

[1]Calculated from Fe_2O_{3t}, assuming all iron is present as FeO

[2]Alteration Index: $AI = 100 \times (K_2O+MgO)/(K_2O+MgO+Na_2O+CaO)$

[3]Chlorite-carbonate-pyrite index: $CCPI = 100 \times (MgO + FeO_t)/(MgO+FeO_t+Na_2O+K_2O)$

[4]$Mg\# = Mg^{2+}/(Mg^{2+} + Fe^{2+})$ (molar %)

[5]$Eu/Eu^* = Eu_n/(Gd_n + Sm_n)^{0.5}$ (n = Normalized to Primitive Mantle; Sun and McDonough, 1989)

Below detection limit (-)

Table 5.2. Average Chemical Composition of Least Altered and Altered Host Rocks of the Ming Deposit *(Continued)*

	Mn-Ca-rich Units 1.1/1.2	Quartz-sericite-chlorite Units 1.1/1.2		Quartz-chlorite Units 1.1/1.2		Quartz-chlorite-sulfides Units 1.1/1.2		Quartz-chlorite-sericite Units 1.1/1.2		Quartz-sericite-sulfides Units 1.1/1.2		Silica-rich horizon Units 1.1/1.2	
		Avg	1σ	Avg	1σ	Avg	1σ	Avg	1σ	Avg	1σ	Avg	1σ
SiO_2 (wt. %)	41.63	68.90	6.43	64.54	5.82	62.18	7.39	65.08	4.48	70.95	8.40	85.75	11.82
Al_2O_3	11.97	10.09	1.41	10.61	0.88	10.49	1.78	11.05	1.13	9.63	2.18	0.74	0.62
Fe_2O_{3t}	4.50	9.83	4.17	10.62	4.22	13.41	2.83	11.85	2.84	8.42	4.50	5.13	1.67
FeO_t[1]	4.05	8.84	3.75	9.55	3.80	12.07	2.55	10.67	2.55	7.57	4.05	4.61	1.50
MnO	13.930	0.036	0.017	0.083	0.049	0.068	0.017	0.057	0.010	0.023	0.029	0.040	0.058
MgO	1.30	3.12	1.58	6.37	1.76	6.45	2.06	5.28	1.10	1.09	1.44	0.19	0.25
CaO	15.36	0.26	0.20	1.47	2.11	0.67	0.48	0.27	0.20	0.64	0.74	3.24	5.23
Na_2O	0.63	0.45	0.26	1.05	0.65	0.66	0.54	0.51	0.76	0.93	0.79	0.13	0.22
K_2O	0.15	1.76	0.71	0.42	0.45	0.35	0.41	0.95	0.47	2.06	0.86	0.11	0.15
TiO_2	0.132	0.165	0.044	0.149	0.022	0.160	0.054	0.156	0.029	0.153	0.040	0.044	0.086
P_2O_5	0.08	0.04	0.01	0.03	0.01	0.04	0.01	0.04	0.01	0.05	0.05	0.37	0.82
LOI	8.88	4.47	2.01	4.28	1.80	4.78	1.10	4.46	1.00	5.42	2.42	3.25	3.29
Total	98.58	99.11	1.36	99.63	0.83	99.25	1.47	99.72	1.49	99.35	1.27	99.00	2.34
Sr (ppm)	66	17	6	49	46	31	19	15	10	40	31	12	11
Sc	9	17	4	24	7	23	6	23	4	15	5	2	2
Zr	35	47	7	41	8	43	9	44	8	43	10	8	6
Ba	520.1	370.3	202.3	95.9	125.0	68.8	105.6	198.2	142.8	244.3	215.5	46.3	90.6
Y	6.64	4.19	1.51	3.92	0.65	4.56	1.35	3.73	0.90	4.00	1.92	7.09	9.40
Nb	1.37	2.33	0.91	1.89	0.68	2.74	1.72	2.55	1.07	1.28	0.49	0.84	1.04
Cs	0.23	0.48	0.15	0.34	0.31	0.51	0.55	0.41	0.23	0.56	0.24	0.86	1.57
La	4.90	4.05	2.29	5.15	1.27	5.18	2.08	6.36	2.89	4.92	1.77	4.39	5.11
Ce	13.82	8.53	4.66	10.45	2.50	10.78	4.23	12.83	5.62	9.86	3.31	6.92	8.91
Pr	1.13	1.02	0.50	1.20	0.25	1.22	0.45	1.46	0.60	1.16	0.36	0.96	1.11
Nd	4.16	3.68	1.89	4.32	0.91	4.44	1.61	5.14	2.10	4.23	1.35	3.74	4.31
Sm	1.16	0.78	0.34	0.85	0.15	0.87	0.27	0.98	0.37	0.87	0.28	0.89	0.92
Eu	0.29	0.09	0.04	0.14	0.09	0.10	0.05	0.11	0.08	0.35	0.27	0.30	0.33
Gd	1.15	0.67	0.24	0.75	0.12	0.77	0.22	0.80	0.26	0.78	0.25	1.03	1.03
Tb	0.20	0.11	0.04	0.11	0.01	0.13	0.04	0.12	0.03	0.12	0.04	0.16	0.16
Dy	1.33	0.72	0.23	0.71	0.11	0.80	0.24	0.70	0.19	0.75	0.27	0.92	1.05
Ho	0.30	0.15	0.05	0.15	0.02	0.17	0.05	0.14	0.04	0.16	0.06	0.20	0.23
Er	1.02	0.49	0.15	0.46	0.07	0.54	0.15	0.45	0.11	0.48	0.19	0.59	0.66
Tm	0.20	0.10	0.02	0.09	0.02	0.10	0.02	0.08	0.02	0.09	0.03	0.14	0.10
Yb	1.55	0.58	0.16	0.54	0.09	0.60	0.15	0.49	0.12	0.56	0.22	0.58	0.57
Lu	0.27	0.09	0.02	0.09	0.02	0.09	0.03	0.09	0.02	0.10	0.04	0.10	0.08
Ta	-	0.19	0.10	0.17	0.06	0.22	0.10	0.20	0.06	0.08	0.05	0.12	0.11
Tl	0.20	0.90	0.56	0.17	0.13	0.24	0.18	0.43	0.36	5.62	5.30	1.90	2.39
Pb	7.1	88.0	174.8	9.5	5.1	11.5	11.6	28.1	20.7	753.7	1277.2	686.5	956.1
Bi	1.11	1.18	0.71	0.57	0.87	1.67	1.39	0.93	1.04	0.55	0.50	5.55	6.85
Th	1.68	1.98	0.45	1.82	0.49	2.15	0.88	2.18	0.75	1.75	0.47	0.53	0.86
U	0.26	1.10	0.25	0.93	0.27	0.98	0.28	1.02	0.31	3.56	5.60	2.81	5.75
V	169.9	85.8	36.6	115.8	41.8	113.5	40.9	120.1	33.9	90.1	29.2	54.0	42.3
Cr	16.4	69.2	37.6	213.9	212.9	223.7	196.0	127.6	67.4	84.0	39.2	50.2	82.2
Co	114.0	30.5	24.4	26.1	7.6	55.2	40.6	38.8	34.1	17.9	16.4	12.8	17.0
Ni	-	17.1	8.2	50.4	44.6	49.9	32.5	31.2	12.9	29.6	27.4	30.5	35.4
Cu	224	5168	6501	379	613	8821	7622	3829	6862	1485	2818	7719	9647
Zn	43	473	646	121	76	136	94	222	208	2603	6116	346	279
As	7.1	32.6	69.9	11.1	20.2	14.7	38.5	19.4	26.6	636.6	1701.8	88.1	87.3
Ag	0.2	1.7	2.2	0.2	0.0	1.2	0.9	0.9	1.1	5.3	9.4	15.6	14.0
Sn	3.4	1.6	0.7	1.0	0.9	1.7	0.9	1.2	0.6	3.2	2.6	1.8	2.1
Sb	4.4	1.7	2.9	0.2	0.2	0.5	0.5	0.8	0.8	24.7	57.6	16.6	17.8
Hg (ppb)	1120	275	545	13	11	60	94	131	114	3127	5282	2444	2253
AI[2]	8.31	87.74	5.22	77.09	13.75	83.04	9.20	89.69	10.35	70.19	19.15	14.71	5.73
CCPI[3]	88.15	83.88	6.74	91.47	4.39	95.03	3.41	91.62	5.40	73.83	8.93	94.42	6.45
Mg#[4]	36.40	38.40	14.14	54.99	11.99	48.44	5.83	47.10	6.83	19.04	18.15	5.95	5.21
Ba/Sr	7.88	25.51	14.72	7.68	15.96	3.09	4.69	16.23	10.68	11.11	11.96	6.01	11.24
Eu/Eu*[5]	0.82	0.33	0.11	0.45	0.28	0.32	0.14	0.35	0.18	1.14	0.81	0.78	0.50
2200 nm		2206.58	3.86	2205.39	0.00	2198.75	0.00	2205.31	11.32	2205.75	3.00	2227.89	17.09
2250 nm	2251.20	2253.66	2.11	2253.52	2.33	2254.55	2.18	2253.52	1.26	2241.81	9.11	2241.61	7.47

Table 5.3. Average Chlorite Compositions from Microprobe Analyses from the Ming Deposit

	Quartz-sericite *n = 8*		Quartz-sericite-chlorite *n = 8*		Quartz-chlorite *n = 10*		Quartz-chlorite-sulfides *n = 8*		Quartz-chlorite-sericite *n = 9*		Quartz-sericite-sulfides *n = 6*	
	Avg	1σ	Avg	1σ	Avg	1σ	Avg	1σ	Avg	1σ	Avg	1σ
SiO_2	26.57	0.18	26.73	0.21	26.13	0.19	26.53	0.22	26.00	0.18	28.87	0.16
TiO_2	0.06	0.01	0.08	0.02	0.05	0.02	0.08	0.01	0.06	0.01	0.05	0.01
Al_2O_3	23.40	0.22	22.77	0.22	22.88	0.18	22.65	0.20	22.68	0.15	23.18	0.18
Cr_2O_3	0.02	0.01	0.09	0.01	0.09	0.03	0.08	0.02	0.05	0.04	0.03	0.01
V_2O_3	0.01	0.00	0.01	0.01	0.04	0.01	0.04	0.00	0.04	0.00	0.02	0.01
FeO[1]	18.30	0.27	19.87	0.36	21.91	0.27	21.25	0.43	22.45	0.20	9.04	0.09
MgO	18.71	0.21	17.87	0.12	16.38	0.20	16.91	0.20	15.83	0.14	25.47	0.12
MnO	0.11	0.01	0.23	0.01	0.17	0.01	0.28	0.01	0.26	0.01	0.38	0.01
CaO	0.01	0.01	0.01	0.00	0.01	0.00	0.02	0.01	0.01	0.00	0.02	0.00
BaO	0.03	0.01	0.01	0.00	0.01	0.00	0.02	0.01	0.02	0.01	0.02	0.01
Na_2O	0.02	0.01	0.02	0.01	0.02	0.00	0.07	0.08	0.01	0.00	0.02	0.01
K_2O	0.01	0.01	0.03	0.06	0.01	0.01	0.02	0.01	0.01	0.01	0.01	0.00
F	-	-	-	-	-	-	-	-	-	-	-	-
Cl	0.01	0.01	0.01	0.01	0.01	0.01	0.02	0.01	0.01	0.01	0.01	0.00
Total	87.15	0.46	87.47	0.43	87.49	0.24	87.75	0.67	87.23	0.35	87.04	0.37
Number of ions calculated on the basis of 28 (O):												
Si	5.39	0.02	5.45	0.04	5.39	0.03	5.43	0.03	5.40	0.03	5.59	0.03
Ti	0.01	0.00	0.01	0.00	0.01	0.00	0.01	0.00	0.01	0.00	0.01	0.00
Al	5.60	0.03	5.47	0.06	5.56	0.04	5.47	0.05	5.55	0.04	5.29	0.03
Cr	0.00	0.00	0.01	0.00	0.02	0.00	0.01	0.00	0.01	0.01	0.01	0.00
V	0.00	0.00	0.00	0.00	0.01	0.00	0.01	0.00	0.01	0.00	0.00	0.00
Fe^{2+}	3.11	0.04	3.39	0.05	3.78	0.05	3.64	0.06	3.90	0.03	1.46	0.01
Mg	5.66	0.07	5.43	0.02	5.03	0.05	5.16	0.05	4.90	0.03	7.34	0.02
Mn	0.02	0.00	0.04	0.00	0.03	0.00	0.05	0.00	0.05	0.00	0.06	0.00
Ca	0.00	0.00	0.00	0.00	0.00	0.00	0.00	0.00	0.00	0.00	0.00	0.00
Ba	0.00	0.00	0.00	0.00	0.00	0.00	0.00	0.00	0.00	0.00	0.00	0.00
Na	0.01	0.00	0.01	0.00	0.01	0.00	0.03	0.03	0.01	0.00	0.01	0.00
K	0.00	0.00	0.01	0.02	0.00	0.00	0.00	0.00	0.00	0.00	0.00	0.00
Total cations	19.80	0.17	19.82	0.20	19.82	0.19	19.83	0.24	19.82	0.15	19.77	0.10
Cl	0.00	0.00	0.00	0.00	0.00	0.00	0.01	0.00	0.00	0.00	0.00	0.00
F	-	-	-	-	-	-	-	-	-	-	-	-
Fe/(Fe+Mg)	0.35	0.01	0.38	0.00	0.43	0.01	0.41	0.01	0.44	0.00	0.17	0.00

[1]Assuming all Fe is Fe^{2+}
Below detection limit (-)

Table 5.4. Average Sericite Compositions from Microprobe Analyses from the Ming Deposit

	Sericite-calcite ±spessartine *n = 7*		Quartz-sericite -chlorite *n = 9*		Quartz-sericite *n = 13*		Quartz-chlorite *n = 10*		Quartz-chlorite -sulfides *n = 10*		Quartz-chlorite -sericite *n = 6*		Quartz-sericite -sulfides *n = 21*	
	Avg	1σ	Avg	1σ	Avg	1σ	Avg	1σ	Avg	1σ	Avg	1σ	Avg	1σ
SiO_2	49.67	0.39	49.31	0.40	48.93	0.71	48.89	0.44	49.59	0.49	48.82	0.28	49.90	0.49
TiO_2	0.40	0.04	0.43	0.12	0.32	0.04	0.32	0.02	0.40	0.14	0.41	0.04	0.36	0.11
Al_2O_3	32.71	0.23	33.38	0.59	36.48	0.81	35.99	0.32	34.33	0.59	34.87	0.60	34.94	0.46
Cr_2O_3	0.02	0.01	0.04	0.07	0.06	0.03	0.12	0.03	0.10	0.04	0.03	0.01	0.11	0.09
V_2O_3	0.06	0.01	0.04	0.01	0.03	0.01	0.11	0.02	0.14	0.01	0.10	0.01	0.07	0.02
FeO[1]	4.10	0.07	3.07	0.19	1.82	0.08	2.91	0.18	2.91	0.30	3.06	0.36	1.36	0.12
MgO	1.82	0.07	1.53	0.11	1.03	0.06	0.80	0.10	1.39	0.08	1.17	0.09	1.74	0.17
MnO	0.04	0.01	0.01	0.00	0.01	0.01	0.01	0.01	0.02	0.01	0.02	0.00	0.01	0.01
CaO	0.02	0.02	0.01	0.00	0.02	0.02	0.01	0.00	0.01	0.01	0.01	0.00	0.02	0.02
BaO	0.37	0.02	0.26	0.08	0.04	0.01	0.09	0.03	0.20	0.03	0.17	0.01	0.09	0.02
Na_2O	0.54	0.45	0.63	0.09	0.67	0.07	1.29	0.18	0.61	0.11	0.59	0.11	0.57	0.06
K_2O	9.69	0.19	9.76	0.25	9.70	0.29	8.93	0.24	9.41	0.47	9.56	0.49	9.88	0.30
F	-	-	-	-	0.05	0.03	-	-	-	-	-	-	0.03	0.01
Cl	0.01	0.00	0.01	0.01	0.02	0.01	0.01	0.00	0.02	0.01	0.03	0.02	0.01	0.00
Total	99.34	0.60	98.38	0.53	99.13	1.45	99.37	0.77	99.02	0.79	98.75	0.40	99.03	0.65
Number of ions calculated on the basis of 22 (O):														
Si	6.39	0.01	6.38	0.03	6.23	0.02	6.23	0.03	6.34	0.03	6.28	0.03	6.35	0.03
Ti	0.04	0.00	0.04	0.01	0.03	0.00	0.03	0.00	0.04	0.01	0.04	0.00	0.03	0.01
Al	4.96	0.04	5.09	0.07	5.47	0.04	5.40	0.04	5.18	0.06	5.28	0.06	5.24	0.04
Cr	0.00	0.00	0.00	0.01	0.01	0.00	0.01	0.00	0.01	0.00	0.00	0.00	0.01	0.01
V	0.01	0.00	0.00	0.00	0.00	0.00	0.01	0.00	0.01	0.00	0.01	0.00	0.01	0.00
Fe^{2+}	0.44	0.01	0.33	0.02	0.19	0.01	0.31	0.02	0.31	0.03	0.33	0.04	0.15	0.01
Mg	0.35	0.01	0.30	0.02	0.19	0.01	0.15	0.02	0.26	0.02	0.22	0.02	0.33	0.03
Mn	0.00	0.00	0.00	0.00	0.00	0.00	0.00	0.00	0.00	0.00	0.00	0.00	0.00	0.00
Ca	0.00	0.00	0.00	0.00	0.00	0.00	0.00	0.00	0.00	0.00	0.00	0.00	0.00	0.00
Ba	0.02	0.00	0.01	0.00	0.00	0.00	0.00	0.00	0.01	0.00	0.01	0.00	0.00	0.00
Na	0.13	0.11	0.16	0.02	0.16	0.02	0.32	0.04	0.15	0.03	0.15	0.03	0.14	0.02
K	1.59	0.04	1.61	0.05	1.58	0.06	1.45	0.04	1.54	0.07	1.57	0.09	1.60	0.06
Total cations														
Cl	0.00	0.00	0.00	0.00	0.00	0.00	0.00	0.00	0.00	0.00	0.01	0.00	0.00	0.00
F	-	-	-	-	0.02	0.01	-	-	-	-	-	-	0.01	0.00
Fe/(Fe+Mg)	0.56	0.01	0.53	0.02	0.50	0.01	0.67	0.02	0.54	0.02	0.59	0.02	0.31	0.03

[1]Assuming all Fe is Fe^{2+}

Below detection limit (-)

Table 5.5. Average Calcite Compositions from Microprobe Analyses from the Ming Deposit

	Mn-Ca-rich assemblage		Silica-rich horizon	
	n = 19		*n = 12*	
	Avg	1σ	Avg	1σ
FeO[1]	1.05	0.10	0.65	0.36
MnO	5.32	0.50	0.67	0.27
ZnO	0.02	0.01	0.01	0.00
MgO	1.78	0.08	1.15	0.54
CaO	45.54	0.38	50.58	1.48
SrO	0.05	0.03	0.03	0.01
BaO	0.02	0.01	0.03	0.01
Total[2]	53.72	0.29	52.97	0.41
Number of ions calculated on the basis of 6 (O):				
Fe^{2+}	0.09	0.01	0.06	0.03
Mn	0.48	0.04	0.06	0.02
Zn	0.00	0.00	0.00	0.00
Mg	0.28	0.01	0.18	0.09
Ca	5.15	0.05	5.72	0.15
Sr	0.00	0.00	0.00	0.00
Ba	0.00	0.00	0.00	0.00
Total cations	6.00	0.12	6.02	0.29

[1]Assuming all Fe is Fe^{2+}

[2]CO_2 was not analyzed

Below detection limit (-)

Table 5.6. Average Biotite Compositions from Microprobe Analyses from the Ming Deposit

	Sericite-calcite ±spessartine		Quartz-sericite -chlorite		Quartz-sericite		Quartz-chlorite		Quartz-chlorite -sulfides		Quartz-sericite -sulfides		Mn-Ca-rich assemblage	
	n = 10		*n = 5*		*n = 5*		*n = 8*		*n = 8*		*n = 5*		*n = 5*	
	Avg	1σ	Avg	1σ	Avg	1σ	Avg	1σ	Avg	1σ	Avg	1σ	Avg	1σ
SiO_2	38.12	0.24	37.98	0.50	39.84	0.41	37.22	0.24	37.56	0.81	41.38	0.22	40.03	0.19
TiO_2	1.57	0.16	1.96	0.16	1.02	0.02	1.48	0.06	1.87	0.23	1.00	0.12	1.32	0.13
Al_2O_3	17.65	0.17	18.28	0.20	18.18	0.24	18.29	0.32	18.50	0.39	18.27	0.38	17.65	0.15
FeO[1]	17.31	0.22	16.32	0.20	13.02	0.13	17.88	0.16	17.53	1.38	7.06	0.12	9.60	0.14
MgO	11.28	0.13	11.75	0.21	14.47	0.21	11.27	0.14	11.06	0.36	18.48	0.19	16.28	0.12
MnO	0.66	0.03	0.13	0.01	0.05	0.01	0.11	0.01	0.16	0.02	0.23	0.01	0.85	0.03
CaO	0.00	0.00	0.01	0.01	0.01	0.01	0.01	0.01	0.01	0.02	0.02	0.01	0.03	0.02
BaO	0.10	0.03	0.07	0.02	0.02	0.00	0.07	0.02	0.04	0.02	0.04	0.00	0.64	0.12
Na_2O	0.10	0.01	0.10	0.01	0.21	0.04	0.16	0.03	0.12	0.02	0.18	0.01	0.13	0.02
K_2O	9.40	0.10	9.58	0.20	9.14	0.12	9.48	0.08	9.41	0.53	9.54	0.13	9.04	0.10
F	0.06	0.00	-	-	1.17	0.08	0.06	0.00	-	-	0.98	0.08	0.33	0.03
Cl	0.01	0.01	0.02	0.00	0.01	0.01	0.03	0.01	0.01	0.00	0.02	0.01	0.01	0.00
Total	96.17	0.34	96.16	0.74	96.63	0.45	95.99	0.48	96.24	0.72	96.75	0.32	95.77	0.35
Number of ions calculated on the basis of 22 (O):														
Si	5.67	0.02	5.62	0.03	5.77	0.03	5.57	0.01	5.58	0.06	5.82	0.03	5.78	0.01
Ti	0.18	0.02	0.22	0.02	0.11	0.00	0.17	0.01	0.21	0.03	0.11	0.01	0.14	0.01
Al	3.10	0.03	3.19	0.05	3.10	0.05	3.22	0.04	3.24	0.03	3.03	0.05	3.00	0.02
Fe^{2+}	2.15	0.03	2.02	0.02	1.58	0.02	2.24	0.03	2.18	0.20	0.83	0.02	1.16	0.02
Mg	2.50	0.03	2.59	0.04	3.12	0.03	2.51	0.03	2.45	0.05	3.87	0.04	3.50	0.02
Mn	0.08	0.00	0.02	0.00	0.01	0.00	0.01	0.00	0.02	0.00	0.03	0.00	0.10	0.00
Ca	0.00	0.00	0.00	0.00	0.00	0.00	0.00	0.00	0.00	0.00	0.00	0.00	0.00	0.00
Ba	0.01	0.00	0.00	0.00	0.00	0.00	0.00	0.00	0.00	0.00	0.00	0.00	0.04	0.01
Na	0.03	0.00	0.03	0.00	0.06	0.01	0.05	0.01	0.04	0.01	0.05	0.00	0.04	0.01
K	1.79	0.02	1.81	0.04	1.69	0.02	1.81	0.02	1.78	0.08	1.71	0.03	1.67	0.02
Total cations	15.51	0.15	15.49	0.20	15.44	0.17	15.58	0.15	15.50	0.47	15.45	0.19	15.43	0.13
Cl	0.03	0.00	-	-	0.52	0.03	0.03	0.00	-	-	0.43	0.03	0.15	0.01
F	0.00	0.00	0.00	0.00	0.00	0.00	0.01	0.00	0.00	0.00	0.00	0.00	0.00	0.00
Mg/Mg+Fe	0.54	0.00	0.56	0.00	0.66	0.00	0.53	0.00	0.53	0.03	0.82	0.00	0.75	0.00
Si/Al	1.83	0.02	1.76	0.03	1.86	0.04	1.73	0.02	1.72	0.01	1.92	0.04	1.92	0.01

[1]Assuming all Fe is Fe^{2+}

Below detection limit (-)

Table A5.1. Calibration parameters for EPMA

Element	Standard	X-ray	Crystal
F	Fluorotopaz	Kα	LDE1
Ti	Benitoite	Kα	LIFL
Mn	Rhodenite	Kα	LIFL
Cr	Chromium oxide	Kα	LIFL
Cl	Tugtupite	Kα	PETL
K	Orthoclase	Kα	PETL
Ca	Plagioclase	Kα	PETL
Na	Albite	Kα	TAP
Si	Albite	Kα	TAP
Al	Albite	Kα	TAP
Mg	Periclase	Kα	TAP
Fe	Almandine	Kα	LIFH
Ba	BaSO4	Lα	LIFH
V	V	Kα	LIFH

Chapter 6
Conclusions and Implications for Future Research

6.1. Conclusions

The Ming volcanogenic massive sulfide (VMS) deposit consists of elongated stratiform lenses of massive to semimassive sulfides (from northwest to southeast: 1807, 1806, Ming North, and Ming South zones), which are variably endowed in Cu, Zn, Ag, and Au, developed subparallel to each another and underlain by a discordant Cu-chlorite-rich stockwork zone (Lower Footwall Zone). The deposit is hosted in a 3x5 km felsic dome (i.e., Rambler Rhyolite formation), which was emplaced during the late stages of the evolution of the peri-Laurentian Taconic seaway. The Ming deposit records volcanic, hydrothermal alteration, and deformation that were poorly constrained prior to this study, mainly due to the lack of sufficient data from and accessibility to the study site. From field relationships and whole-rock and mineralogical geochemistry, the results from this multi-method study provide significant insights into the genesis and evolution of the Ming VMS deposit and its host rocks. Additionally, a number of the results presented here helps to substantiate ideas or concepts that were put forward by previous workers. Some of the key findings include:

1) The geometry and the overall disposition of the sulfide lenses and the Cu-rich Lower Footwall Zone are interpreted to be predominantly expressions of primary processes, and overprinting deformation and metamorphism only have accentuated this elongation. This is largely supported by the volcanic (Chapter 3), structural (Chapter 3), and hydrothermal alteration (Chapter 5) reconstruction. Evidences for this primary control include: 1) abrupt lateral changes in volcanic lithofacies that are expressions of

synvolcanic faults in the footwall rocks are recognized throughout the deposit. These are oriented more or less parallel to the sulfides lenses and acted as the main conduits to ascending ore-forming fluids; 2) the most intense chloritic alteration and its paragenetically associated Cu-rich stringers (stockwork) are restricted to the Ming South and up-dip section of the 1806 Zone (Chapter 2). The distribution of the stockwork overlaps areas of abrupt lateral lithofacies changes. These synvolcanic structures also appear to have controlled the location and distribution of the hydrothermal fluids responsible for the late quartz-sericite-sulfides alteration assemblage (Chapter 5); and 3) Although the main stretching elongation is locally parallel to the sulfide lenses (i.e., ~045°N), the Lower Footwall Zone is 10-15° east of the main lineation. If deformation (mainly D_2) was responsible for the stretching of the ore zones, a parallel arrangement of all the ore zones would be expected throughout the deposit, which is not the case.

2) Metamorphic/deformation-induced remobilization of sulfides is limited to a maximum of 20 m from the source. An external body of massive sulfides formed by deformation was mapped in the northwestern extremity of the 1807 Zone and shows significant enrichment in Au and Cu due to the selective remobilization of least competent minerals, such as chalcopyrite and electrum. Sphalerite-rich layers and bands, piercement structures, and localized enrichments within the massive sulfides are recognized throughout the deposit but have not affected the overall distribution of metals on the deposit-scale.

3) The timing of the introduction of precious metals is synchronous with the formation of the deposit, which is in agreement with the conclusions from recent studies.

In this project, the syngenetic relationship is supported by a combination of field relationships and petrographic observations, which include: 1) Au-rich phases (AgAu alloys; electrum) and telluride minerals enclosed in sulfide clasts within a polymictic volcanic breccia immediately above parts of the 1807 and 1806 zones (Chapter 3); and 2) the close spatial relationship between precious metals and the quartz-sericite-sulfides alteration assemblage, which is cross-cut by pre-deformation mafic dykes (Chapter 5).

4) The coherent lithofacies of units 1.1 and 1.2 developed near the paleoseafloor played a fundamental role in controlling Zn, Au, and Ag (among other volatiles) precipitation (Chapter 5). This controlled distribution is interpreted to be the result of the impermeable nature of the coherent facies, as opposed to the surrounding volcaniclastic and permeable rocks of unit 1.2. This 'cap' likely impeded fluid dispersion and promoted sulfide accumulation at their base, which became an important precious metal reservoir to the overlying sulfide lenses.

5) The felsic host successions (units 1.1 to 1.3) have arc-like geochemical signatures (e.g., high Th, negative Nb-Ti anomalies) and are interpreted to be products of direct partial melting of a subducted slab (Chapter 4). A garnet-controlled source is evidenced by the elevated whole-rock $[La/Yb]_n$ ratios in the Rambler Rhyolite formation and its overall depleted trace element contents (e.g., Zr < 80 ppm, low HREE). The combination of restricted differentiation of the felsic rocks, the required depths for garnet stability (> 15-30 km), and the thin (< 10 km) crust of the Baie Verte oceanic tract at the time of its formation are consistent with the partial melting a an eclogitized subducted slab. Furthermore, geochemical modelling results suggest that not only the source was an

eclogitized tholeiitic rock, but that an island arc tholeiite was the most likely source to the FI-/FII-type Rambler Rhyolite formation, which is consistent with recent tectonic reconstructions of the Taconic seaway.

6) The Ming deposit records the evolution from low- to high- to low-temperatures of the hydrothermal system with three paragenetically distinct episodes of metal enrichment, including early and late sericite-rich assemblages (stages 1 and 3) and intermediate chlorite-rich assemblages (stage 2) (Chapter 5). The latter reflect the highest temperatures (300-350°C) of the hydrothermal fluids and are closely associated with precipitation of chalcopyrite-pyrrhotite-pyrite forming the Cu-rich stockwork of the deposit (i.e., Lower Footwall Zone), whereas the early and late sericitic assemblages reflect cooler (≤ 250°C) and acidic (pH ≈ 4) fluids. The sericitic assemblages are constrained in the upper section of the Rambler Rhyolite formation, controlled by the distribution of the volcaniclastic units 1.2 and 1.3 in which permeability was likely greater than the coherent rocks of unit 1.1. Precious metals are mainly enriched within the late quartz-sericite-sulfides assemblage, suggesting that their introduction was late, during the waning of the temperature of the hydrothermal system. The overall hydrothermal alteration architecture of the Ming deposit shows a strong spatial affinity with the hosting volcanic architecture; i.e., the extent of the alteration is restricted to the nested basin that was developed during the extension of the Rambler Rhyolite dome, which was filled with volcaniclastic rocks (units 1.2 and 1.3). The synvolcanic faults controlled the distribution of both the volcanic rocks and the hydrothermal overprint. Because other surrounding VMS deposits (East and Rambler) have similar geometry to the Ming deposit, it is

plausible that major synvolcanic faults were developed parallel to each another, hence becoming important conduits to hydrothermal and magmatic fluids.

6.2. Recommendations for future research

This study has provided new insights on the stratigraphic, structural, magmatic, and alteration history of the Ming deposit but numerous questions remain unanswered. In this section, unresolved questions are presented with the objective of providing future research directions that are specific to the Ming deposit and its surroundings.

6.2.1. Complete characterization of the Rambler Rhyolite formation and its relationships to the VMS deposits

Although bedrock exposures are relatively poor in the area, a number of outcrops are readily accessible in the region and historical drill holes are available at the government core storage facility in Baie Verte for one to confidently reassess the lithologies and facies of the entire Rambler Rhyolite formation. Previous workers commonly overlooked the primary volcanic structures and textures of the footwall rocks and used instead metamorphic terminology (e.g., chlorite/sericite schist), which provide very limited information about the physical volcanology, obscuring the overall understanding of the primary volcanic architecture of the deposit or region. This study has shown that even in highly altered and deformed rocks, primary volcanic structures are often preserved. Considering that the volcanic architecture (including synvolcanic structures) played a fundamental role in the genesis of the massive sulphides at Ming, it is

reasonable to hypothesize that the nearby Rambler and East deposits were subjected to similar controlling factors. In the context of mineral exploration, these questions are fundamentally important as they may provide key vectors in the search of new VMS-style mineralization and/or extend with higher confidence currently know orebodies that are "open at depth". Moreover, if sites of mineralization are controlled by major synvolcanic structures, as suggested in Chapters 2 and 5, they should thus become first order vectors.

6.2.2. Geochronology and relationships with surrounding units

The relative timing between the emplacement of the Rambler Rhyolite formation and its overlying sedimentary and volcanic sequences and cross-cutting dykes is well constrained; however, their absolute timing is very poorly controlled. Except for an unpublished U-Pb age obtained from a rhyodacite south of the Ming property (reported in Skulski et al., 2015), no other ages have been obtained in the immediate surroundings. Although numerous attempts were made over the course of this project to date the felsic volcanic rocks immediately stratigraphically below the massive sulphide, other attempts should be made elsewhere in the deposit. Particularly, the higher Zr contents of unit 1.3 make the latter a good candidate for finding zircon grains.

6.2.3. Lithogeochemistry and petrogenesis of the Rambler Rhyolite formation

One of the most provocative ideas proposed in this thesis is the FI-/FII-type felsic volcanic rocks of the Rambler Rhyolite formation being derived primarily from the partial

melting of an eclogitized subducted slab. This could also have important implications in the Au-endowment of the VMS deposit (e.g., Mungall, 2002). Despite the convincing evidences put forward to support this, a number of uncertainties remain to be constrained in order to "fine-tune" the magmatic evolution of the Rambler Rhyolite formation. Robust isotopic systems such as whole-rock Lu-Hf can be utilized in order to identify the relative roles of primitive and evolved components.

In addition, intermediate to felsic intrusions and volcanic rocks have been identified elsewhere in the BVOT (e.g., Skulski et al., 2010). Very minor work has been undertaken to understand their petrogenesis and are often assumed (off record) to be results of residual melts from the crystallizing boninitic and low-Ti melts.

To substantiate the role of subduction in the genesis of the felsic rocks in the area, assuming that the relative disposition of the ophiolitic complexes were maintained after obduction (i.e., from Betts Cove to Pointe Rousse would represent a cross-section of the supra-subduction zone), one could assess the trace element and isotopic signatures (Nd, Hf, and Pb where appropriate) across the peninsula such that any variations could shed light onto the evolution and architecture of the subduction (e.g., see Peate and Pearce, 1998; Li et al., 2013)

6.2.4. Sphalerite chemistry

The Fe content in sphalerite is dependant of the oxidation and sulfidation states and temperature of the co-existing hydrothermal fluids (Barton and Toulmin, 1966; Brueckner et al., 2016) but can also be strongly influenced by secondary processes such

as metamorphism (Marshall et al., 2000). Considering the numerous evidences of internal and external sulfide remobilization and recrystallization throughout the Ming deposit, a thorough re-examination of the Fe contents in sphalerite is recommended by contextualizing sphalerite chemistry in relation to degree of strain and deformation fabrics.

6.3. References

Barton Jr., P.B., and Toulmin, P., 1966, Phase relations involving sphalerite in the Fe-Zn-S system: Economic Geology, v. 61, p. 815-849.

Brueckner, S.M., Piercey, S.J., Pilote, J.-L., Layne, G.D., and Sylvester, P.J., 2016, Mineralogy and mineral chemistry of the metamorphosed and precious metal-bearing Ming deposit, Canada: Ore Geology Reviews, v. 72, p. 914-939.

Li, Y., Kimura, J.-i., Machida, S., Ishii, T., Ishiwatari, A., Maruyama, S., Qiu, H., Ishikawa, T., Kato, Y., Haraguchi, S., Takahata, N., Hirahara, Y., and Miyazaki, T., 2013, High-Mg adakite and low-Ca boninite from a Bonin fore-arc seamount; implications for the reaction between slab melts and depleted mantle: Journal of Petrology, v. 54, p. 1149-1175.

Marshall, B., and Spry, P.G., 2000, Discriminating between regional metamorphic remobilization and syntectonic emplacement in the genesis of massive sulfide ores: Reviews in Economic Geology, v. 11, p. 39-79.

Mungall, J.E., 2002, Roasting the mantle; slab melting and the genesis of major Au and Au-rich Cu deposits: Geology, v. 30, p. 915-918.

Peate, D.W., and Pearce, J.A., 1998, Causes of spatial compositional variations in Mariana Arc lavas; trace element evidence: Island Arc, v. 7, p. 479-495.

Skulski, T., Castonguay, S., McNicoll, V., van Staal, C.R., Kidd, W.S.F., Rogers, N., Morris, W., Ugalde, H., Slavinski, H., Spicer, W., Moussallam, Y., and Kerr, I., 2010, Tectonostratigraphy of the Baie Verte oceanic tract and its ophiolite cover

sequence on the Baie Verte Peninsula: Newfoundland and Labrador Department of Natural Resources, Geological Survey, Current Research, Report 10-1, p. 315-335.

Appendix 1
Volcano-stratigraphy of the 1807 zone of the Ming Cu-Au volcanogenic massive sulfide (VMS) deposit, Baie Verte Peninsula, northern Newfoundland

Abstract

The Ming Cu-Au Ming volcanogenic massive sulfide deposit (10.67 Mt grading 1.77% Cu, 0.61 g/t Au, 3.88 g/t Ag, and 0.15 % Zn) is located in the Rambler mining camp which comprises the upper ophiolitic sequence of the Baie Verte Oceanic Tract in the northern Notre Dame subzone. The deposit is hosted by intermediate to felsic volcanic and volcaniclastic rocks of the early Ordovician (ca. 487 Ma) Pacquet Harbour Group, which is part of a regional mafic-dominated rock assemblage of boninitic to tholeiitic affinity. The volcano-stratigraphy and petrography of the 1807 zone have been documented using systematic detailed underground mapping, diamond drill-core description, and polished thin section microscopy.

The deposit consists of four parallel elongated shallowly plunging lenses, of which the 1807 zone is currently being mined and was the focus of our 2012 fieldwork. The 1807 zone consists of a Cu-Zn-Au-rich massive sulfide horizon hosted by a sequence of intermediate to aphanitic to quartz-phyric dacitic tuff, lapilli tuff, and tuff breccia. It is structurally to disconformably overlain by a mafic-dominated subaqueous volcanic sequence comprised of mafic to intermediate volcaniclastic to epiclastic rocks with thin intercalated magnetite-rich horizons. The immediate footwall rocks are hydrothermally altered to chlorite + quartz + sericite ± biotite ± calcite ± epidote, with zones of quartz + sericite ± green mica, whereas the deeper (~100 m below the massive sulfide) footwall rocks are altered to chlorite + quartz ± biotite.

The massive sulfide horizon in the 1807 zone shows evidence of deformation and possible remobilization during a regional compressional deformation. Structural modifications include regional-scale anticlinal and micro- to meso-scale synclinal folds with a NE-SW trending axial plane with a shallow plunging 030°N trending mineral lineation. In addition, three generations of mafic to intermediate dykes are recognized solely based on cross-cutting relationships, textures and petrographic characteristics: 1) an early melanocratic gabbro (IN1) with magmatic to structural contact with the felsic volcanic footwall rocks; 2) a boudinaged mesocratic hornblende-rich intermediate dyke (IN2) that displays clear contact relationships with IN1; and 3) a latest syn-kinematic gabbroic dyke (IN3) with structural features indicative of a close temporal relationship with the remobilization of the sulfide horizons.

Ongoing research will refine knowledge of the stratigraphic relationships and test the hypothesis that there exists a close structural relationship between emplacement of the dykes and massive sulfide remobilization.

Introduction

The producing Ming mine is located in the northern central part of the Baie Verte Belt of Newfoundland (Fig. 1). It is one of a number of deposits, some of which are past producers, in the Rambler mining camp. The Ming mine is a bimodal-mafic volcanogenic massive sulfide (VMS) deposit that contains four ore zones are hosted within a felsic volcanic/volcaniclastic package, near the contact with the overlying mafic volcanic hangingwall. Combined measured and indicated resource for all four zones is 3.65 Mt at

2.26 wt% Cu, 1.13 g/t Au, 6.78 g/t Ag, and 0.32 wt% Zn, and the 1807 zone is most Cu- and Au-rich of these with combined measured and indicated resources of 432 000 t grading 3.68 wt% Cu, 1.76 g/t Au, 7.03 g/t Ag, and 0.75 wt% Zn (Pilgrim, 2009).

Detailed mapping was undertaken northwest of the Ming mine in different underground levels along the 1807 zone (i.e., 375, 381, 469, and 481 meter levels). This work is part of a larger study evaluating the stratigraphy, alteration mineralogy and structure of the entire deposit. Because the 1807 zone was actively mined during the time field work was conducted, it was critical to take advantage of the extensive and fresh exposures. The stratigraphy of the Rambler camp is well established at a regional scale, but not so at the deposit scale, mainly because of the lack of outcrop exposures (Tuach and Kennedy, 1978; Hibbard, 1983). Herein we provide detailed stratigraphic, petrographic, and alteration mineralogical information and preliminary structural data for the 1807 zone. Work by others indicates a syngenetic origin for base and precious metal mineralization within the 1807 zone with later structural and metamorphic remobilization without significant changes in metal content (e.g., Brueckner et al., 2011).

Geologic Setting

The Baie Verte Peninsula (Fig. 1) is comprised of tectonized slivers of ophiolitic sequences ranging in age from 490 to 484 Ma (Dunning and Krogh, 1985; Cawood et al., 1996); these are mainly closely spatially associated with the Baie Verte-Brompton Line (BVBL) (Fig. 1; Skulski et al., 2009, 2010; Zagorevski and van Staal, 2011). These ophiolitic slivers are characterized by harzburgite, ultramafic cumulates, isotropic gabbro,

sheeted dykes, pillow basalt, and locally felsic domes (Rambler camp) of boninitic to island arc tholeiitic affinities (Bédard et al., 1998; Skulski et al., 2009, 2010 and references therein). The slivers are disconformably overlain by a cover sequence comprising the ca. 476-647 Ma Snooks Arm Group and its equivalent in the Pacquet Harbour Group (PHG), Pointe Rousse Complex, and Flatwater Pond Group (Fig. 1; Skulski et al., 2010), ranging from enriched mid-ocean ridge basalt (E-MORB) (or tholeiitic back-arc basin basalt) to calc-alkaline volcanic rocks (Bédard et al., 1998).

The Ming mine is underlain by the PHG (Hibbard 1983), a northeast dipping sequence dominated by mafic and felsic volcanic rocks. It has been divided into two sequences based on their geochemical affinities and geochronology: the lower and upper PHG (Fig. 3; Skulski et al., 2009, 2010). The upper and lower PHG are in disconformable contact (Skulski et al. 2009, 2010). The lower PHG represents an incomplete ophiolitic sequence and is located south of the Ming mine. Metamorphism in the lower and upper PHG does not exceed upper greenschist facies, except near the intrusive bodies (Fig. 2) (e.g. Cape Brulé porphyry and Dunamagon granite) where contact metamorphism locally reaching amphibolite facies (Tuach and Kennedy, 1978). The lower PHG is divided by the Rambler Brook Fault (Fig. 2), a south-directed, east-west structural feature that contains low-Ti boninites with minor felsic tuff and rhyodacite at its base (Hibbard 1983; Piercey et al., 1997). The hangingwall of the Rambler Brook Fault contains rocks that host the deposits of the Rambler camp, including the Ming mine. These structural hanging wall (not deposit hanging wall) rocks comprise boninitic basalt overlain by a 2.5 km-thick sequence of quartz-phyric, rhyodacite, felsic tuff and tuff breccia (Rambler

Rhyolite formation; Skulski et al., 2010). A felsic volcanic rock sample collected ca. 1 km along strike and south of the Ming mine yielded a U/Pb zircon age of ca. 487 Ma (Hibbard 1983; V. McNicoll, unpublished data, 2008 in Castonguay et al., 2009 and Skulski et al., 2009). The age indicates that the lower PHG is coeval with other ophiolites in the peninsula (i.e., Advocate, Pointe Rousse, and Betts Cove ophiolite complexes; Fig. 1). The upper PHG (Fig. 2) is located northeast of the Ming mine and its base is locally comprised of iron formation and black chert that are overlain by a sequence of epiclastic wacke, siltstone, volcaniclastic rocks, and basalts of tholeiitic to calk-alkaline affinities (Skulski et al., 2009).

The mineralized lenses of the Ming mine are characterized by semi-massive to massive sulfide (< 50 vol.% sulfides) or narrow (< 1 m wide) transposed sulfide veins and veinlets macroscopically composed of pyrite, chalcopyrite, sphalerite, and pyrrhotite minerals. The lenses are spatially associated with several metamorphosed hydrothermal alteration mineral assemblages developed mainly in the footwall. These lenses are located in the upper sequence of the Rambler Rhyolite formation felsic volcanic rocks. There are four regional deformation events, with the most intense being a D2 L > S fabric and north- to northeast-dipping folds (Castonguay et al., 2009, and references therein) characterized by a shallowly plunging 030°N-trending mineral lineation (Tuach and Kennedy, 1978; Hibbard, 1983).

Stratigraphy and Petrography of the 1807 Zone

Intermediate to felsic rocks – Upper Rambler Rhyolite formation

Previous workers at the Ming mine separated rock types based on the proportion and abundance of secondary minerals (i.e., chlorite, actinolite, and sericite; Gale, 1971; Tuach, 1976; Tuach and Kennedy, 1978; Bailey, 2002). Although primary minerals and some textures have been obliterated, in many low strain zones the primary textures and rock types can be discerned. In the 1807 zone the footwall underlying the massive sulphide zone is comprised of coherent aphanitic to porphyritic felsic volcanic and associated irregularly distributed and less abundant felsic volcaniclastic rocks. This latter package is five to ten meters thick, and has sharp to gradational contacts with underlying and overlying rocks. The sulfide horizons of the 1807 zone are up to six meters thick and are locally crosscut by mafic dykes (Fig. 4).

The contact between the felsic rocks and the overlying massive sulfides is sharp and irregular in most levels (Figs. 4 and 5a). Some relict islands of highly silicified rhyolite occur in the massive sulfide, but only at its base. Fragments can be up to one meter in size. The rhyolite contains abundant disseminated secondary pyrite porphyroblasts and an increase in quartz alteration occurs near the contact with the massive sulfide (Fig. 4). The ubiquitous biotite grains in the rhyolite are interpreted to be metamorphic in origin. On level 481 the footwall contains monolithic volcaniclastic rocks that are in gradational contact with the overlying rhyolite flows (Fig. 5b). The clasts are subrounded within a dark grey actinolite-rich matrix (Fig. 5b).

Down-plunge of the 1807 zone (i.e., on the 469 and 481 levels), the magmatic contact between the felsic volcanic rocks and mafic dykes of unknown thickness have been modified by shearing (Fig. 4). The dyke emplacement is interpreted to be coincident with deformation, as evidenced by the presence of sharp, undeformed intrusive contacts with host rocks away from zones of high strain, but folded proximal to zones of high strain and mineralization (Fig. 4). The contacts of the dyke with volcanic rocks proximal to mineralization are typically sheared with a crenulated chlorite-rich matrix.

Overlying the massive sulphide are highly quartz-altered (silicified) intermediate to felsic volcaniclastic rocks, generally less than three meters in thickness, that are comprised of variably altered quartz eye porphyritic rhyolite (Fig. 5c). Along the base of the hangingwall rocks on the 375 and 381 levels, there is a foliation demarcated by elongated silica- and epidote-rich clasts up to 10 cm long that occur with, and are imbricated by elongated sugary pyrite lenses up to 50 cm long. These lenses have an average aspect ratio of 20:1 (Fig. 5c). The sulfides are in irregular contact with the host felsic volcaniclastic rocks suggesting they have a replacement origin, and are not a chemical sedimentary product (Fig. 5c).

The rocks underlying and overlying the ore are light grey to dark purple porphyritic to aphanitic felsic tuff, lapilli tuff, and flows. Petrographic analyses of representative samples reveal a predominance of fine-grained heterogranular quartz grains occur together with biotite (Fig. 5d). Two varieties of biotite have been identified; 1) commonly anhedral containing pleochroic haloes, possibly surrounding zircon inclusions, and 2) devoid of zircon inclusions and displaying glomero-porphyroblastic textures to

homogenously distributed throughout the rock. The latter has been interpreted to result from the metamorphism of previously K-Fe-Mg-altered rocks. Both varieties, however, are aligned parallel to foliations. In addition, very fine- to fine-grained interstitial muscovite (<30 vol. %) and epidote (<2 vol. %) occur throughout the rock. Some samples show relict fine-grained anhedral plagioclase grains with albite and Carlsbad twinning (Fig. 5e). These latter grains have been variably altered to epidote, zoicite, sericite and albite.

Near (<5 m) the massive sulfides of the 1807 zone, the felsic rocks are silicified with biotite that appears to be of two generations, along with muscovite (sericite), epidote and sulfide minerals. Up-plunge of the 1807 zone, minor green mica (possibly fuchsite) is also present. The entire mineral assemblage in the felsic volcanic rocks is consistent with the upper greenschist metamorphism of a sericitic alteration type (Bernier et al., 1987; Barrett and MacLean, 1994; Bonnet and Corriveau, 2007). Moreover, in the lower footwall (> 50 m below sulfide horizons), the predominant hydrothermal alteration products include chlorite associated with two textural varieties of biotite porphyroblasts and pyrite and chalcopyrite as the main sulfide phases (Fig. 5f). Based on the presence of chalcopyrite, this latter assemblage represents the high temperature core of the upflow zone of a VMS system because copper is only transported at temperatures >300°C (e.g., Franklin et al., 2005). Considering the regional-scale thrusting in the Baie Verte peninsula (Castonguay et al., 2009) and the presence of shearing and faulting within the deposit, at present, it is hypothesized that the distance separating the massive sulfide horizons from

the chloritic zone is due to faulting. More structural and stratigraphic analyses will help to define this hypothesis.

Two main fabrics are evident in thin section, based on the orientations of biotite, with a 30° angle between them. Rotated σ-type mantled quartz porphyroclasts suggest a southwest-directed compressional regime (Fig. 5d). At present, it is not known if both fabrics are kinematically related. Thin sections cut perpendicular to the predominant lineation (trending 030 ±005°N) show one fabric revealed by aligned biotites. Based on this, the two biotite varieties are most likely syn- to post-kinematic, and aligned parallel to foliation.

Mafic rocks – Lower Scrape Point Formation

The mafic rocks are minor to absent near the massive sulfide horizon in underground exposures. Stratigraphic interpretations and descriptions are made based on drill core observations from the nearby 1806 zone. The mafic volcanic and volcaniclastic rocks overlying the felsic volcanic, and locally the massive sulfide horizon, are mainly comprised of distal volcanic turbidites and ash to lapilli tuff of mixed composition (Fig. 6a).

Very fine-grained mafic tuff with felsic fragments (up to 3 cm in length) occurs near (<5 m) the basal contact with the footwall felsic lapilli tuff (Fig. 6b). The contact between the hangingwall and footwall is commonly sheared, truncated by mafic dykes, or contains quartz veins with disseminated chalcopyrite, pyrite, and pyrrhotite. The mafic

volcaniclastic rocks are dark grey to light grey with subrounded elongate fragments (up to 3 cm in length) and range from thin beds of mafic tuff to lapilli-tuff rich units.

The mafic volcanic package is relatively underformed and metamorphosed to upper greenschist facies (Tuach and Kennedy, 1978). Both flows and volcaniclastic rocks are dominated by very fine-grained matrix composed of (in decreasing order) porphyroblastic actinolite, quartz, chlorite, biotite, relict plagioclase, leucoxene (fine-grained mixture of rutile and anatase) and minor opaque phases such as magnetite and Fe-oxides (Figs. 6c-f). In hand specimens the rocks are dark green to dark blue in colour. The rocks show a well-developed foliation, and have rotated porphyroclasts of feldspar. The actinolites are light to olive green, euhedral, and commonly glomero-porphyroblastic, ranging from 0.5 to 2 mm in length and concordant to discordant to foliation. Quartz is very fine grained, anhedral and ubiquitously present. It also occurs in pressure shadows of feldspar porphyroclasts. Fine grained chlorite is interstitial to foliae, and occurs together with quartz. Moreover, the biotite and chlorite grains occur together and are aligned in the plane of the foliation. Later calcite veins crosscut the main foliation in the rocks.

Intrusive Rocks

Three generations of dykes have been recognized in the field, based on crosscutting relationships. Their absolute ages are not yet known and the relationships with the rocks they crosscut have long been unclear. Samples of all three phases of dykes were collected for petrographic and lithogeochemical analysis. The most abundant phase are medium-grained, equigranular hypidiomorphic gabbroic dykes (IN1) that vary from

10-20 m in thickness, have an east-west orientation, dip 45-50° to the north, and their magmatic contact with felsic volcanic rocks have been offset by faulting locally (Fig. 7a). The structural contact indicates that deformation post-dated dyke solidification. Furthermore, the contacts of the dykes with felsic volcanic rocks contain slickensides indicative of shearing and strike-slip motion parallel to the regional dominant stretching lineation (Castonguay et al., 2009). Despite IN1 having a structural relationship with the felsic volcanic rocks in some areas, clear intrusive contacts have been identified (e.g., in level 481 of the Ming mine; Fig. 7b).

The second most abundant intrusive phase is medium-grained granodioritic dykes (IN2) composed of (in decreasing order of abundance) quartz, biotite, and actinolite with minor calcite, chlorite, epidote and magnetite. These dykes are east-northeast trending, and dip at a 50° ± 5° angle to the northwest-north. Their contacts with the felsic volcanic rocks are sharp and irregular, with cuspate-lobate and flame-like morphologies (Fig. 7c).On the 469 level an IN2 dyke cross-cuts an IN1 dyke, suggesting that the former postdate IN1 dykes (Fig. 7d). The IN2 dyke has been boudinaged (seen on the 469 and 481 levels) and dismembered during extension along the axis of the dyke, indicating that the dyke is syn-deformation; this may explain the nature of the contact with the host felsic volcanic rocks. This dyke has been subsequently truncated attendant with the remobilization of the sulfide minerals (Fig. 4).

The third phase of dykes (IN3) are diorite that area composed of (in decreasing order) quartz, biotite, actinolite, calcite, zircon, Fe-oxide, and chlorite. These dykes vary from 2 to 3 m in thickness and have clear intrusive contacts with the felsic volcanic rocks (Figs 4

and 7e). On the 469 and 481 levels, the dyke cuts the massive sulfides and have been tightly folded, displaying axial planes oriented 030°N, and parallel to the main foliation and lineation in the felsic volcanic rocks (Fig. 7f).

Preliminary Interpretations and Economic Implications

The stratigraphy of the Rambler Rhyolite formation has long been recognized to be complex, and correlations across the Baie Verte Peninsula have been difficult (Tuach, 1976; Tuach and Kennedy, 1978; Hibbard, 1983). Rocks in the area have been subjected to at least four deformation events (D1 to D4: Skulski et al., 2009, 2010; Castonguay et al., 2010) and metamorphism has obliterated many primary textures, making interpretations difficult. Preliminary detailed mapping of the 1807 zone allow some further constraints to be placed on the nature and origin of the felsic to mafic volcanic and intrusive rocks.

Based on stratigraphic relationships determined from underground mapping, the up-plunge section (levels 375 and 389) of the 1807 zone has felsic volcanic rocks overlying the massive sulfide that have been silicified and these area assumed to have acted as a cap (physical barrier) to the metal-rich hydrothermal fluids. Such a cap, comprised of quartz-phyric tuff and coherent flow, is also documented in the 1806 zone (Brueckner et al., 2011). However, in the down-plunge section of the 1807 zone (levels 469 and 481), the massive sulfide is truncated by mafic intrusive dykes that have commonly been structurally displaced to form the structural hanging wall to the mineralization. Overall,

the 1807 zone is structurally more complex than the other zones of the deposit, including the extensively described 1806 zone (Brueckner et al., 2011; unpubl. Data).

The relatively thin sulfide-bearing felsic volcaniclastic sequence overlying the massive sulfide in the up-plunge section of the 1807 zone may have served as a semi-permeable cap that allowed hydrothermal fluids to percolate into the mound and promote subseafloor replacement and the accumulation (and preservation) of sulfides (Gibson et al., 1999). Such a semi-permeable cap has also been recognized in drill core in other zones; its absence in the lower part 1807 zone could be a result of removal by structural displacement or dyke emplacement after sulfide deposition.

Based on the presence of intrusive contacts, both the IN1 and IN2 dykes intruded along the primary contact between the felsic volcanic footwall host rocks and mineralization of the 1807 zone. Preliminary structural analyses of the tightly folded IN3 dyke cutting the massive sulfides indicate that the latter has been remobilized during dyke emplacement. On this basis, IN1 and IN2 dykes are older than IN3 dykes. The cross-cutting relationships between dykes IN1 and IN2 has been determined on the 469 level, and this, together with the observation that emplacement of IN1 dykes has thermally metamorphosed sulfides in the 1806 zone (Brueckner et al., 2011), suggests that all mafic dykes were emplaced after VMS formation. The orientations of the fold axes in the IN3 dyke on the 469 and 481 levels are parallel to the predominant lineation found everywhere in the mine, (i.e., shallowly plunging 030°N). However, additional structural measurements are needed in order to differentiate deformation events more accurately. Nonetheless, our preliminary data suggest that IN3 dykes were emplaced syn-

kinematically, whereas dykes IN1 and IN2 were emplaced subsequent to VMS formation but prior to the main phases of deformation (e.g., D2 of Castonguay et al., 2010). The IN1 mafic dykes did not play a role in the genesis of the sulfide, but they may have controlled the distribution of the sulfides during deformation due to the differences in competency with the felsic volcanic rocks.

Previous work in the lower Pacquet Harbour Group south of the Rambler Brook Fault suggested that there is a comagmatic relationship between the mafic dykes cutting the lower Pacquet Harbour Group and mafic volcanic rocks of the ophiolite cover Sequence (Piercey et al., 1997). Although the absolute ages of these dykes have not yet been determined, a correlation (if possible) of the overlying mafic volcanic cover sequence with the feeder dykes will place constraints on the timing of deformation. The disconformity is poorly exposed but gabbro of the equivalent Pointe Rousse Cover sequence which hosts mineralization at Sto'ger Tight has yielded an age of 481 Ma (Ramezani, 2000), and this constrains the timing of volcanism in the suprasubduction zone. Regional reconstruction of the Baie Verte peninsula area indicates obduction occurred at ca. 479 Ma, based on ages of granitoid clasts in the Flat Water Pond Group (Fig. 1) basal conglomerate that giving a maximum age of deposition (V. McNicoll, unpublished data, 2009; in Skulski et al., 2010). The evolution from a suprasubduction ophiolitic complex (at ca. 489 Ma) to juvenile island arc in which the Rambler Rhyolite formed (at ca. 487 Ma) must have occurred in a very short period of time, and within an extensional to neutral regime. The presence of iron formation and pillow basalt at the

base of the cover sequence suggests that the environment was still subaqueous during obduction (at 479 Ma).

Acknowledgements

This study was funded by the Targeted Geoscience Initiative (TGI-4) program of the Geological Survey of Canada. The authors wish to express their sincere appreciation to Rambler Metals and Mining PLC for granting access underground and providing valuable data of the Ming mine, particularly L. Pilgrim and P. Legrow. J.-L. Pilote would especially like to thank S. Brueckner for field assistance and for sharing ideas during mapping. This research has also been financially supported by a Natural Sciences and Engineering Research Council of Canada (NSERC) Discovery Grant and the NSERC-Altius Industrial Research Chair in Mineral Deposits supported by NSERC, Altius Resources Inc. and the Research and Development Corporation of Newfoundland and Labrador. Thanks to J. Peter for his careful reviews of this manuscript.

References

Bailey, J., 2002. Chemostratigraphy surrounding the Ming Mine VMS mineralization in the northern Pacquet Harbour Group (PHG) and correlations with the southern PHG, Baie Verte Peninsula, Newfoundland; B.Sc. thesis, Memorial University of Newfoundland and Labrador, 125 p.

Barrett, T. J., and MacLean, W. H., 1994. hemostratigraphy and hydrothermal alteration in exploration for VHMS deposits in greenstones and younger volcanic rocks: Short Course Notes - Geological Association of Canada, v. 11, p. 433-467.

Bédard, J. H., 1999. Petrogenesis of Boninites from the Betts Cove Ophiolite, Newfoundland, Canada: Identification of Subducted Source Components: Journal of Petrology, v. 40, p. 1853-1889.

Bédard, J. H., Lauzière, K., Tremblay, A., and Sangster, A., 1998. Evidence for forearc seafloor-spreading from the Betts Cove ophiolite, Newfoundland: oceanic crust of boninitic affinity: Tectonophysics, v. 284, p. 233-245.

Bernier, L. R., Pouliot, G., and MacLean, W. H., 1987. Geology and metamorphism of the Montauban north gold zone; a metamorphosed polymetallic exhalative deposit, Grenville Province, Quebec: Economic Geology, v. 82, p. 2076-2090.

Bonnet, A.-L., and Corriveau, L., 2007, Alteration vectors to metamorphosed hydrothermal systems in gneissic terranes, in Goodfellow, W.D., ed., Mineral deposits of Canada—A synthesis of major deposit-types, district metallogeny, the evolution of geological provinces, and exploration methods: Geological Association of Canada, Mineral Deposits Division, Special Publication No. 5, p. 1035–1049.

Brueckner, S. M., Piercey, S. J., Sylvester, P. J., Pilgrim, L., Maloney, S., Hyde, D., and Ogilvie, G., 2011. Stratigraphy, mineralogy, geochemistry, and genesis of an Au-rich volcanogenic massive sulfide (VMS system from the Baie Verte Peninsula, NW Newfoundland, Canada: The 1806 Zone as an example from the Ming Mine, Rambler Camp, in Deschênes, G., Dimitrakopoulos, R., and Bouchard, J., eds., World Gold 2011: Montreal, QC, Canada, Canadian Institute of Mining, Metallurgy and Petroleum, p. 899-911.

Castonguay, S., Skulski, T., van Staal, C., and Currie, M., 2009. New insights on the structural geology of the Pacquet Harbour group and Point Rousse complex, Baie Verte peninsula, Newfoundland: Current Research Newfoundland and Labrador Department of Natural Resources, Geological Survey, v. Report 09-1, p. 147-158.

Cawood, P. A., van Gool, J. A. M., and Dunning, G. R., 1993. Silurian age for movement on theBaie Verte Line: Implications for accretionary tectonics in the Northern Appalachians: Geological Society of America, Abstract with Programs, v. 25, p. A422.

Cawood, P. A., van Gool, J. A. M., and Dunning, G. R., 1996. Geological development of eastern Humber and western Dunnage zones; Corner Brook-Glover Island region, Newfoundland: Canadian Journal of Earth Sciences, v. 33, p. 182-198.

Dunning, G. R., and Krogh, T. E., 1985. Geochronology of ophiolites of the NewfoundlandAppalachians: Canadian Journal of Earth Sciences, v. 22, p. 1659-1670.

Franklin, J. M., Gibson, H. L., Jonasson, I. R., and Galley, A. G., 2005. Volcanogenic massive sulfide deposits, in Hedenquist, J. W., Thompson, J. F. H., Goldfarb, R. J., and Richards, J. P., eds., Economic Geology 100th Anniversary Volume, 1905-2005, Society of Economic Geologists, p. 523-560.

Gale, G. H., 1971. An investigation of some sulfide deposits of the Rambler Area, Newfoundland: Unpub. Ph.D. thesis, University of Durham (United Kingdom), 137 p.

Gibson, H., Morton, R. L., and Hudak, G. J., 1999. Submarine volcanic processes, deposits, and environments favorable for the loaction of volcanic-associated massive sulfide deposits, in Barrie, C. T., Hannington, M.D. , ed., Volcanic-associated massive sulfide deposits: Processes and examples in modern and ancient settings, 8. Reviews in Economic Geology: Boulder, CO, Society of Economic Geologists, p. 13-51.

Hibbard, L. J., 1983. Geology of the Baie Verte Peninsula, Newfoundland, Department of Mines and Energy, Government of Newfoundland and Labrador, Memoir 2, 279 p.

Piercey, S. J., Jenner, G. A., and Wilton, D. H. C., 1997. The stratigraphy and geochemistry of the southern Pacquet Harbour Group, Baie Verte Peninsula, Newfoundland; implications for mineral exploration: Canada, Government of Newfoundland and Labrador. Geological Survey : St. John's, NL, Canada, p. 119-139.

Pilgrim, L., 2009. Mineral resource estimate for the Ming Mine, Newfoundland, Canada, Rambler Metals and Mining Canada Ltd, p. 114.

Ramezani, J., Dunning, G. R., and Wilson, M. R., 2000. Geologic setting, geochemistry of alteration, and U-Pb age of hydrothermal zircon from the Silurian Stog'er Tight

gold prospect, Newfoundland Appalachians, Canada: Exploration and Mining Geology, v. 9, p. 171-188.

Skulski, T., Castonguay, S., McNicoll, V., van Staal, C., Kidd, W., Rogers, N., Morris, W., Ugalde, H., Slavinski, H., Spicer, W., Moussallam, Y., and Kerr, I., 2010. Tectonostratigraphy of the Baie Verte oceanic tract and its ophiolite cover sequence on the Baie Verte Peninsula: Current Research Newfoundland and Labrador Department of Natural Resources, Geological Survey, v. Report 10-1, p. 315-335.

Skulski, T., Castonguay, S., van Staal, C., Rogers, N., McNicoll, V., Kerr, A., and Escayola, M., 2009. Baie Verte Peninsula: An evolving geological story, in Rogers, N., and Kerr, A., eds., Annual Field Trip, October 2-5, 2009, Geological Association of Canada, Newfoundland and Labrador Section, p. 76.

Tuach, J., 1976. Structural and stratigraphic setting of the Ming and other sulfide deposits in the Rambler area, Newfoundland; M.Sc. thesis, Memorial University of Newfoundland, 183 p.

Tuach, J., and Kennedy, M. J., 1978. The geologic setting of the Ming and other sulfide deposits, consolidated Rambler mines, Northeast Newfoundland: Economic Geology, v. 73, p. 192-206.

Zagorevski, A., and van Staal, C.R. 2011. The record of Ordovician arc-arc and arc-continent collisions in the Canadian Appalachians during the closure of Iapetus, in Arc-Continent Collision. Edited by D. Brown and P.D. Ryan. Frontiers in Earth Sciences, Springer, p. 341-371.

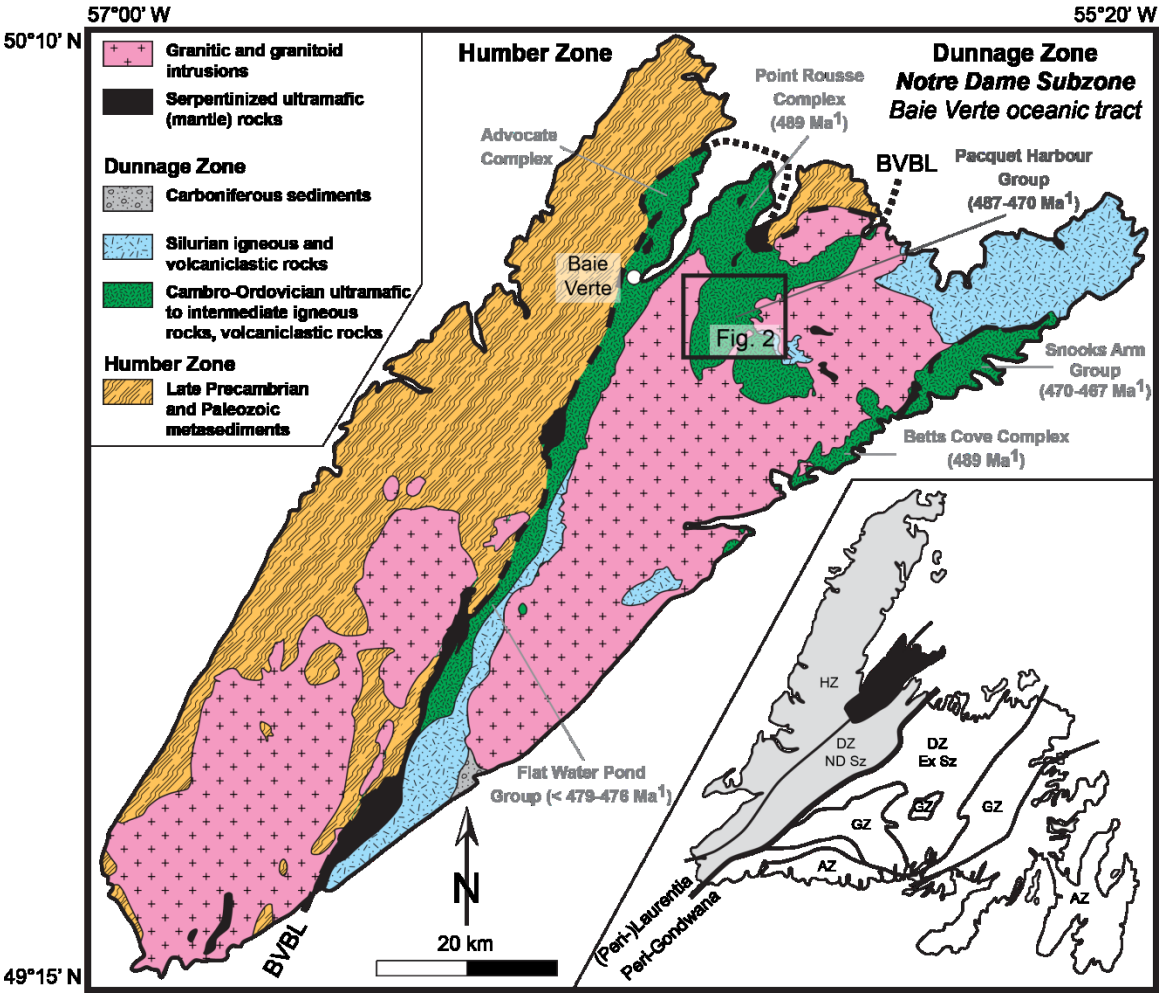

Fig. 1. Simplified geologic map of the Baie Verte Penninsula (modified after Castonguay et al., 2009 and reference therein). Abbreviations; HZ = Humber zone, DZ = Dunnage zone, ND SZ = Notre-Dame Subzone, Ex SZ = Exploits Subzone, GZ = Gander zone, AZ = Avalon zone, BVBL = Baie Verte-Brompton Line.

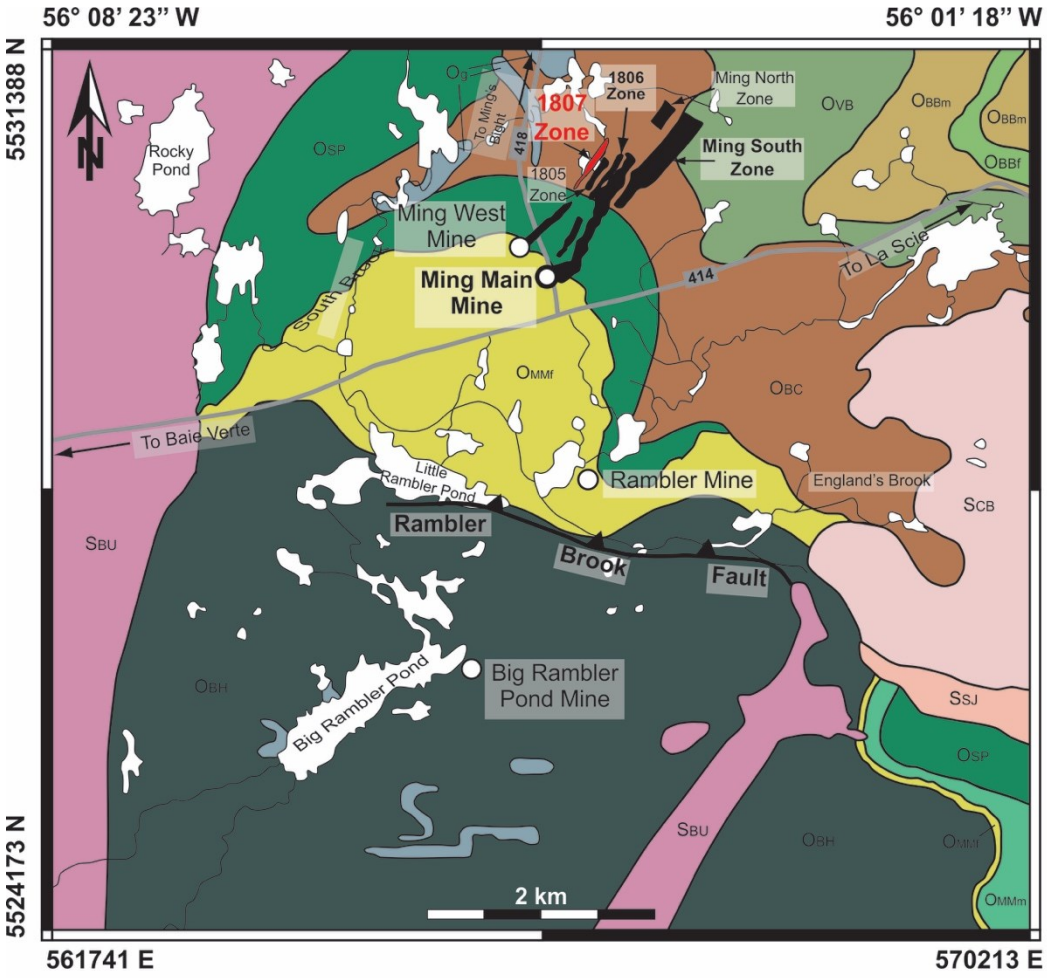

Silurian Intrusions and effusive rocks

- SCB — **Cape Brulé Porphyry (430 Ma)** Porphyritic granodiorite, quartz-feldspar porphyry
- SBU — **Burlington Granodiorite (434 - 430 Ma)** Granodiorite
- SSJ — **Cape St. John Group (early Silurian)** Rhyolitic and trachytic flows and tuffs, intrusives, locally mafic and intermediate tuffs and flows

414 — **Highway and highway number**

Ming Main Mine — **Mine location**

1807 zone — **Mineralization horizon**

Underground shaft

Fault

Ordovician rocks - Pacquet Harbour Group (PHG)

Upper PHG (Mid- to Early Ordovician)

- OBBm — **Balsam Bud Cove Formation** Mafic epiclastic rocks, black shale
- OBBf — **Balsam Bud Cove Formation** Rhyolite (467 Ma), and felsic tuff (470 Ma)
- OVB — **Venam's Bight Formation** Pillow basalt
- OBC — **Bobby Cove Formation** Mafic tuff, epiclastic rocks, turbidites
- OSP — **Scrape Point Formation** Pillow basalt, gabbro (483 Ma)

Lower PHG (Early Ordovician)

- OMMf — **Mt. Misery Formation** Rhyodacite, rhyolite massive flows, tuff breccia ('Rambler rhyolite'; 487 Ma)
- OMMm — **Mt. Misery Formation** Intermediate Ti-boninite, island arc tholeiitic pillow basalt, pillow breccia
- OBH — **Betts Head Formation** Pillowed, aphyric, variolitic boninite
- Og — **Sheared gabbro**

(Previous page) Fig. 2. Regional geology map of the study area, Baie Verte Peninsula. Both datums are shown in WGS 84 (top and right) and UTM 21N NAD 83 (bottom and left). Map modified after Pilgrim (2009), Tuach and Kennedy (1978), Castonguay et al. (2009), and Hibbard (1983). Ages are from Castonguay et al. (2009) and Cawood et al. (1993).

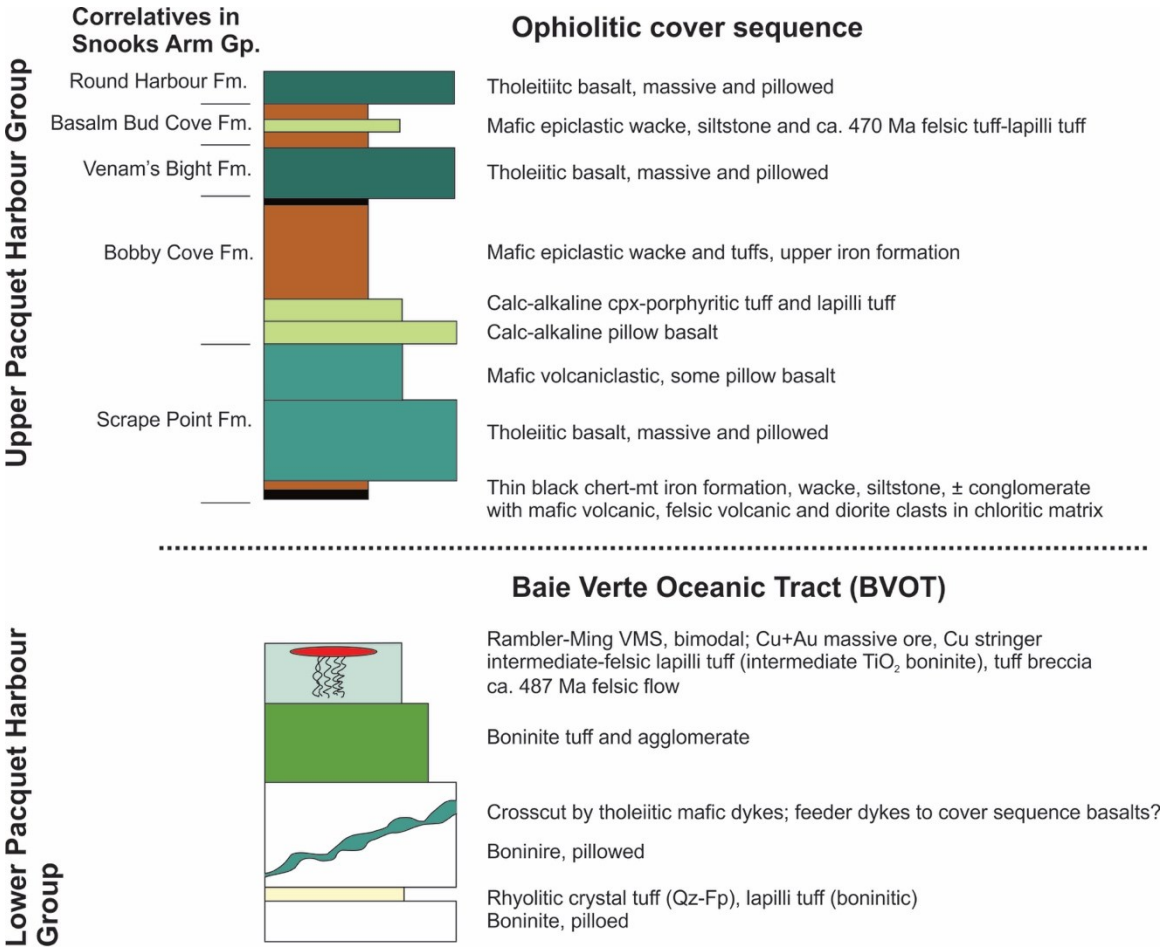

Fig. 3. Simplified stratigraphic section of the Pacquet Harbour Group. Correlative formations from the Snooks Arm Group are based on the stratigraphy of Bédard (1999). The U-Pb zircon ages are from G. Dunning (pers. comm.). Abbreviations: cpx, clinopyroxene; mt, magnetite; Qz-Fp, quartz-feldspar; Fm, formation. Diagram modified after Skulski et al. (2009).

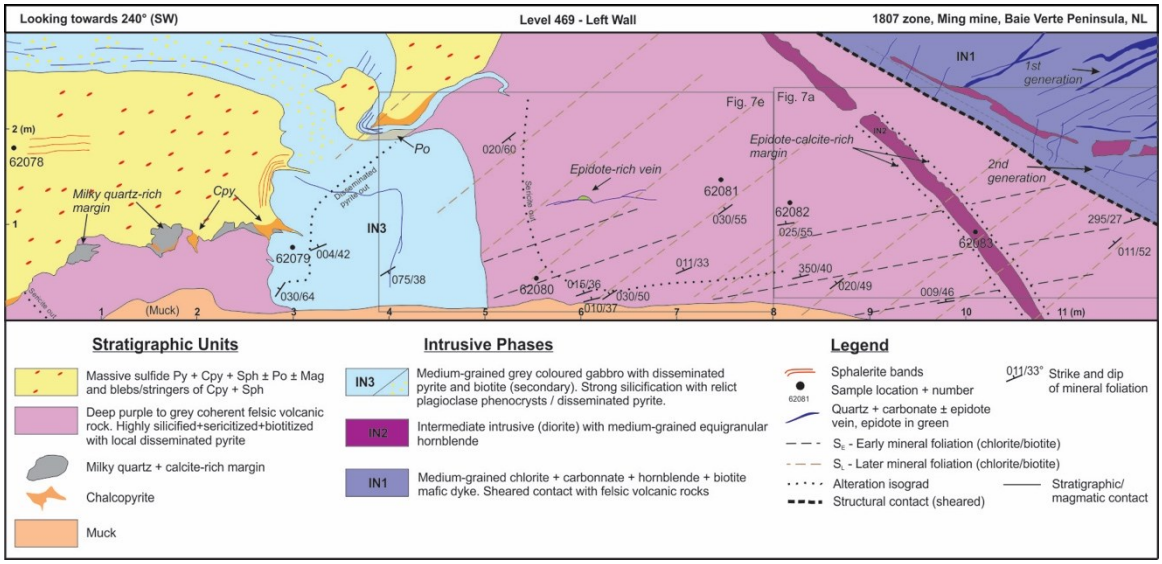

Fig. 4. Schematic cross-section of the back wall in level 469, 1807 zone showing the relationship between the different lithological units, including the massive sulfide horizon where it is intruded by IN3. Also shown is the close spatial relationship between the pyrite porphyroblasts in the dyke IN3 and the massive sulfide.

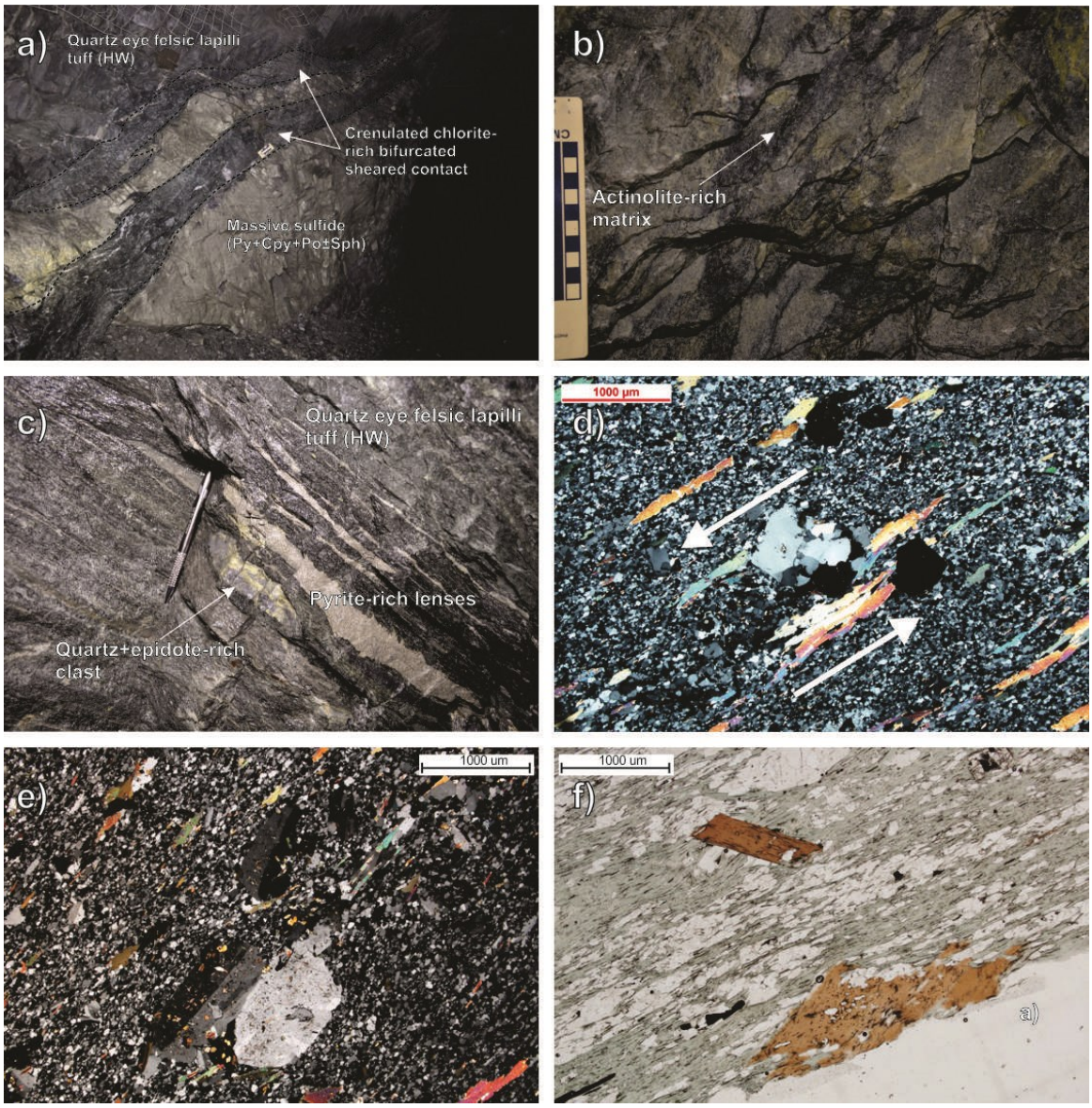
a)
Quartz eye felsic lapilli tuff (HW)
Crenulated chlorite-rich bifurcated sheared contact
Massive sulfide (Py+Cpy+Po±Sph)
b)
Actinolite-rich matrix
c)
Quartz eye felsic lapilli tuff (HW)
Pyrite-rich lenses
Quartz+epidote-rich clast
d)
1000 µm
e)
1000 um
f)
1000 um

Fig. 5. Photographs of underground exposures and photomicrographs of felsic volcanic and volcaniclastic rocks of the 1807 zone, Ming mine. a) View looking southwest in level 375 of the sheared contact between the coherent quartz eye felsic lapilli tuff (HW = hanging wall) and massive sulfide. The scale in the center is 15 cm long. b) View looking southwest in level 481 of the actinolite-rich matrix felsic volcaniclastic rock with epidotized fragments in the footwall zone. c) View looking northwest in level 375 of the quartz eye felsic lapilli tuff with imbricated replacement sulfide lenses and quartz-epidote-rich fragments along the predominant foliation. d) Sheared polycrystalline quartz porphyroclasts with biotite along the predominant foliation with shear sense indicated by arrows (cross-polarized; sample 62080a, level 469). e) Relict plagioclase phenocrysts showing Carlsbad twinning with internal replacement by epidote and sericite (cross polarized; sample 62081a, level 469). f) Chlorite-quartz-biotite-rich showing two phases of biotite grains (sample 62086, lower footwall zone, 100 m below the 1807 zone). Abbreviations: Cpy, chalcopyrite; Po, Pyrrhotite; Py, pyrite; Sph, sphalerite.

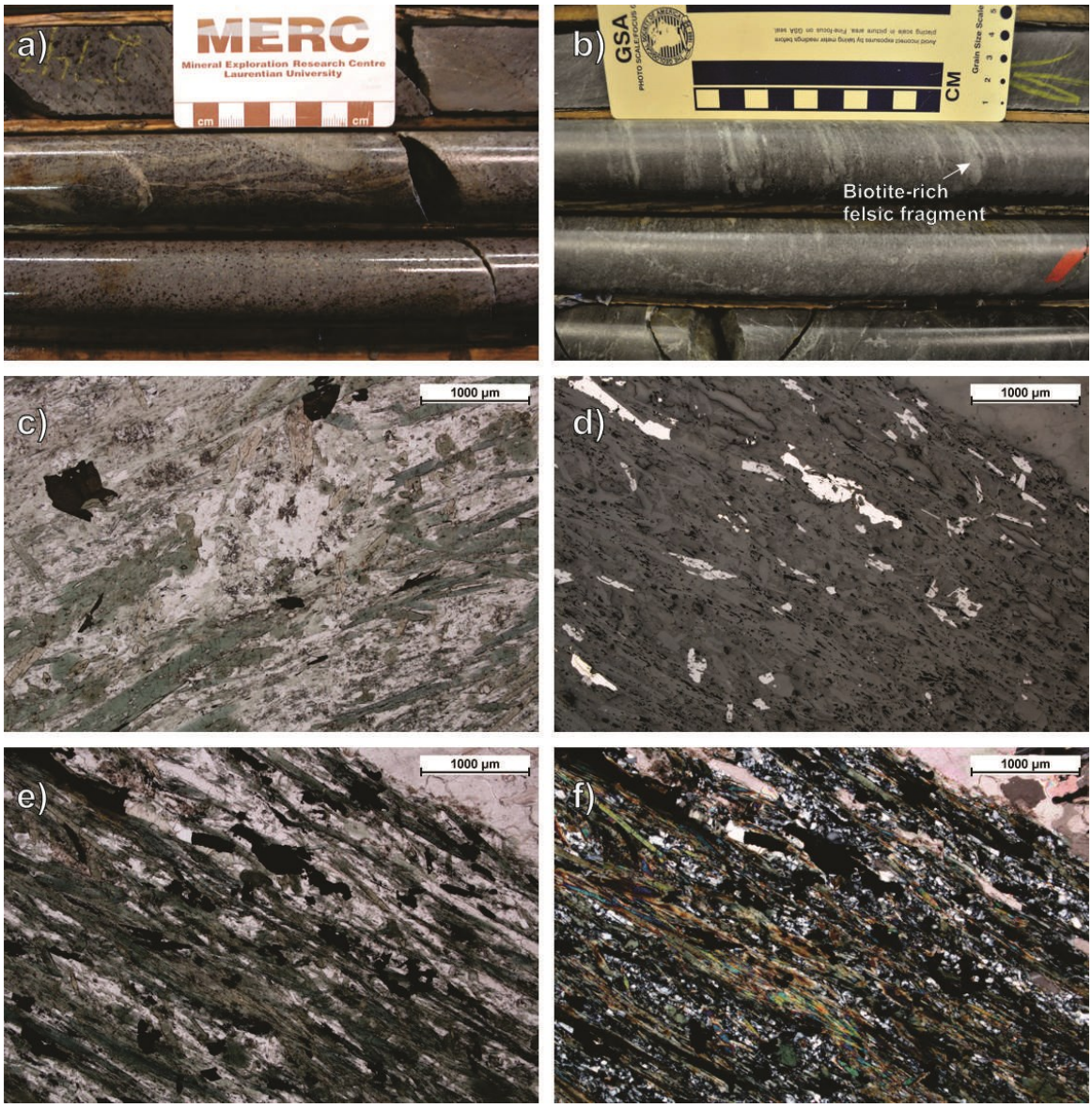

Fig. 6. Representative drill core photographs and photomicrographs of the mafic volcanic and volcaniclastic rocks most immediately (<30 m) overlying the deposit. a) Mixed lapilli tuff with fragments of felsic composition, one meter above the felsic volcanic flow hosting the massive sulfide (DDH RMUG08-123; 67 m downhole). b) Biotite-rich felsic lapilli fragments in a mafic tuffaceous matrix, five meters above mineralization (DDH RMUG08-136; 52 m downhole). c) Actinolite-chlorite-leucoxene-quartz-calcite-rich basalt with relict plagioclase porphyroclasts in the center of the photograph, 10 m above mineralization (sample 62176; DDH RM05-08; 990 m downhole). d) Disseminated chalcopyrite and pyrite grains within a chlorite-actinolite-quartz-rich rock, 104 m above mineralization (cross-polarized; sample 62167; DDH RM05-08; 896 m downhole). e) and f) same sample as d) but in plane-polarized and cross-polarized, respectively. The sample is cut by later concordant calcite vein (upper right corner).

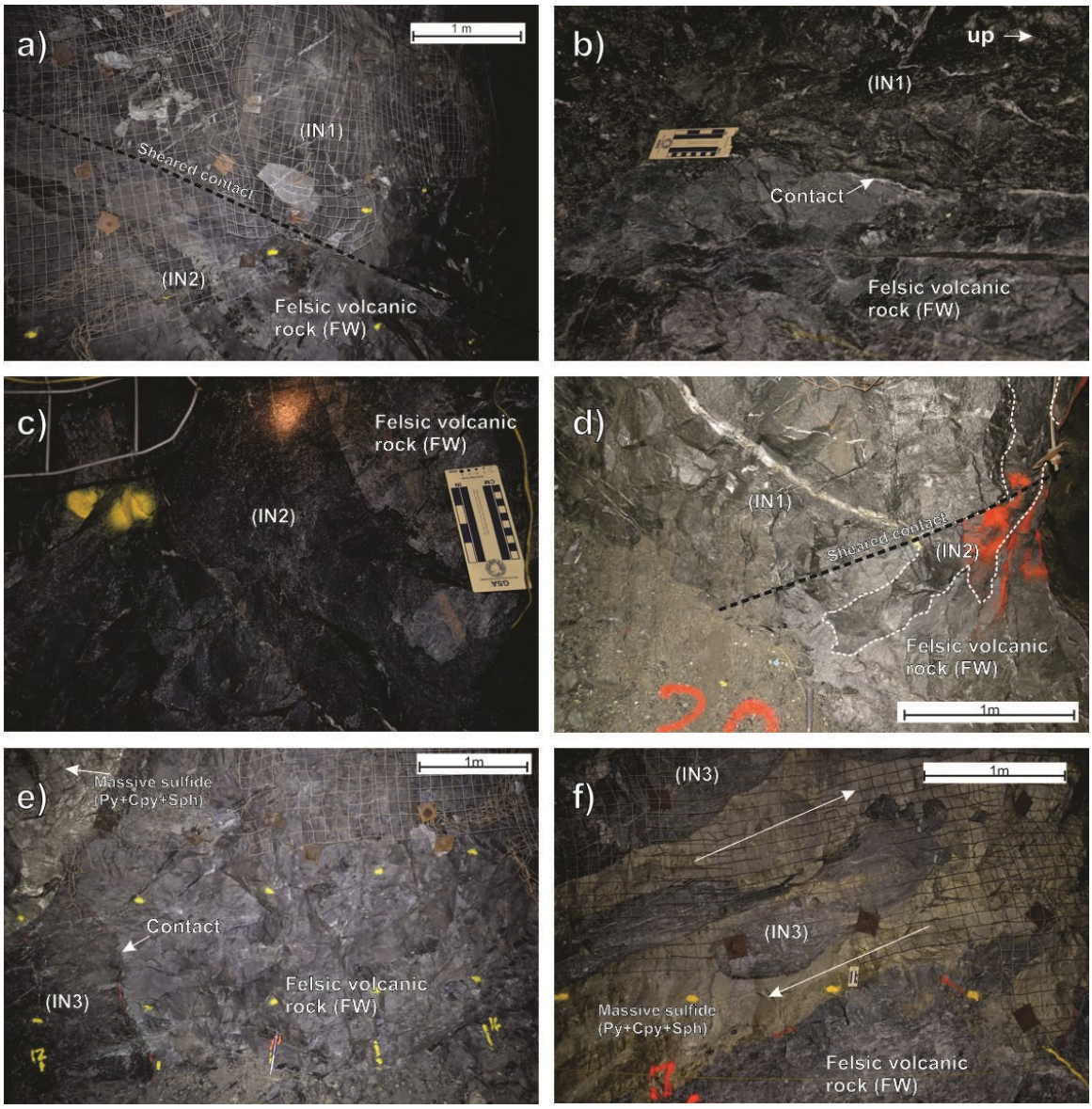
a)
1 m
(IN1)
Sheared contact
(IN2)
Felsic volcanic
rock (FW)
b)
up
(IN1)
Contact
Felsic volcanic
rock (FW)
c)
Felsic volcanic
rock (FW)
(IN2)
d)
(IN1)
Sheared contact
(IN2)
Felsic volcanic
rock (FW)
1m
e)
Massive sulfide
(Py+Cpy+Sph)
1m
Contact
(IN3)
Felsic volcanic
rock (FW)
f)
(IN3)
1m
(IN3)
Massive sulfide
(Py+Cpy+Sph)
Felsic volcanic
rock (FW)

Fig. 7. Photographs of underground exposures of relationships of the intrusive phases in the 1807 zone, Ming mine. a) View looking southwest on the 469level of the structural contact between the massive melanocratic gabbroic dyke (IN1) and the coherent felsic volcanic footwall rocks. The mesocratic hornblende-rich intermediate dyke (IN2) is emplaced near the contact. b) View looking northeast on the 481level of the magmatic contact between IN1 and the felsic volcanic footwall rocks. c) View looking southwest on the 481 level of the irregular contact between IN2 and the felsic volcanic footwall rocks. d) View looking northeast on the 469 level showing the relationship between dykes IN1 and IN2 that have been displaced by the structural contact between IN1 and the felsic volcanic footwall rocks. e) View looking southwest on the 469 level showing the nature of the magmatic contact between IN3 and the felsic volcanic and volcaniclastic footwall rocks. f) View looking southwest on the 481 level of the folded IN3 within the massive sulfide with northeast-directed movement. Abbreviations are as in Fig. 5.

Appendix 2
The Ming Cu-Au Volcanogenic Massive Sulphide Deposit, Baie Verte Peninsula, Newfoundland: Stratigraphy and Hydrothermal Alteration

Abstract

The Cambro-Ordovician bimodal-mafic Ming Cu-Au-(Zn-Ag) volcanogenic massive sulphide (VMS) deposit is a type example of an Appalachian precious metal-enriched VMS deposit. The deposit's footwall comprises at least three distinct felsic volcanic and volcaniclastic units. The immediate hanging wall is lithologically heterogeneous, comprising a highly silicified volcaniclastic rock and a magnetite-rich volcanogenic siltstone. Three generations of mafic to intermediate sills and dykes intrude the deposit and have distinctive lithogeochemical signatures; they are interpreted to be genetically related to the mafic rocks in the ophiolitic cover sequence that overlies the deposit.

The Ming deposit has distinct hydrothermal alteration mineral assemblages including: 1) chlorite-quartz-epidote; 2) sericite-quartz-green mica; 3) quartz-pyrite; and 4) Mn-garnet-calcite. Other minor secondary phases include biotite, tremolite, and magnetite. A Cu-rich zone consisting primarily of chalcopyrite, pyrrhotite, and pyrite with minor Bi-Te sulfosalts and sphalerite in a strongly chlorite-quartz-epidote altered felsic volcanic rock occurs 50 to 100 metres below the main sulphide lens, and represents the high-temperature discharge zone of the Ming hydrothermal system. An overprint of metamorphic biotite is ubiquitous throughout the felsic footwall rocks and represents metamorphosed K-Fe-(Mg) alteration to upper greenschist facies.

Despite local remobilization of the sulphides due to deformation and metamorphism, the relationship between the host rocks, the alteration assemblages and their spatial distribution, and the ore strongly favor a syngenetic origin for the sulphide zones and their base and precious metals, suggesting intrinsically precious metal-enriched VMS ore-forming fluids at Ming.

Introduction

Volcanic-associated hydrothermal events in ancient and modern submarine environments result in the formation of stratabound to stratiform accumulations of sulphide minerals referred to as volcanogenic massive sulphide (VMS) and seafloor volcanogenic sulfides (SMS). They are formed at or near the ocean floor in various tectonic settings (e.g., mid ocean rift, arc, back arc) and consequently occur in a wide variety of host-rock lithologies (e.g., Franklin et al., 1981, 2005; Hannington et al., 1999). Some VMS deposits are enriched in precious metals, with Au contents (in g/t) that typically exceed the associated Cu+Pb+Zn grades (in wt %) (e.g., Poulsen and Hannington, 1996; Mercier-Langevin et al., 2011). The origin of the Au enrichment in these anomalous VMS deposits is commonly debated (e.g., syngenetic vs. metamorphic overprint). Where Au-rich or auriferous VMS deposits occur in deformed and metamorphosed volcanic settings, they may be characterized by features that are epigenetic (e.g., overprinting Au-bearing syntectonic veins and fractures, structurally discordant ore zones, etc.), giving the impression that gold was introduced late in those deposits, leading to a post-VMS gold enrichment interpretation (e.g., Tourigny et al.,

1989; Yeats and Groves, 1998). In other cases, workers argue that the enrichment is due to syngenetic processes and/or magmatic contributions (e.g., Hannington et al., 1999; Huston, 2000; Dubé et al., 2007a; Mercier-Langevin et al., 2007; 2013; 2014). Although they can both occur within the same district, the setting of Au-rich VMS systems and associated hydrothermal alteration assemblages differ somewhat from "Au-poor" VMS deposits (e.g., Sillitoe et al., 1996; Dubé et al., 2007a). Therefore, in districts where the origin of gold enrichment in the deposits is debated, it is important to constrain factors that possibly control the variation in metal content and the origin of precious metal enrichment (e.g., volcano-stratigraphy, lithology, deformation, and geodynamic setting; Mercier-Langevin et al., 2011).

The host-rock commonly associated with Au-rich VMS deposits are felsic volcanic and volcaniclastic rocks that are near, or at the interface with, mafic-intermediate volcanic or clastic sedimentary rocks (Dubé et al., 2007a). In the general VMS classification scheme, Au-VMS are commonly thought to be hybrid systems between VMS and epithermal Au deposits in bimodal felsic (or bimodal mafic in the case of Ming) settings (Galley et al., 2007). Furthermore, the lithological characteristics may control or influence the fluid flow pathways, and hence the morphology, deposit growth process, and proximal discordant and regional semiconformable alteration assemblages and extents (Gibson et al., 1999). Therefore, stratigraphic reconstructions of a well-preserved VMS deposit such as Ming may provide insight on the magmatic evolution of the host volcanic complex and the relative timing of hydrothermal events.

The Ming deposit in northern central Newfoundland contains high Au and Cu contents, and with locally high Ag and Zn. The Ming deposit is currently being mined and has reserves (diluted and recovered) of 1.50 Mt grading 1.71 wt% Cu, 0.36 wt% Zn, 9.15 g/t Ag, and 2.06 g/t Au, and combined measured and indicated resources of 2.47 Mt grading 2.27 wt% Cu, 0.44 wt% Zn, 9.08 g/t Ag, and 2.15 g/t Au. The deposit is comprised of four discrete, elongated Cu-Au-(Zn-Ag) massive to semi-massive (< 50 vol.%) sulphide lenses, all plunging 30-35° to the north-northeast and spaced 30 to 50 metres apart from each other at a similar stratigraphic position. Herein we provide preliminary observations on stratigraphic and alteration features and discuss possible genetic relationships between the host rocks and the genesis of synvolcanic, precious metal-rich sulphide lenses at Ming.

Geological Setting

The Ming Mine is located in the Baie Verte Peninsula (Fig. 1) in north central Newfoundland. These rocks straddle the boundary between the Humber Zone to the west and a series of ophiolitic slivers and enclaves to the east in a narrow fault-bounded belt, situated between the Baie Verte Brompton Line and the Green Bay Fault (Hibbard, 1983). The ophiolites comprise mainly suprasubduction-zone rocks of mafic to ultramafic composition, including boninites (van Staal and Barr, 2012). These include the ca. 490 Ma (Dunning and Krogh, 1985; Cawood et al., 1996; Skulski et al., 2010) Advocate Complex (Burnshall, 1975), the Pointe Rousse Complex (Norman and Strong, 1975), the Betts Cove Complex (Bédard et al., 1998; Bédard, 1999), and rocks within the southern

Pacquet Harbour Group (PHG) (Hibbard, 1983; Piercey et al., 1997). Collectively, the ophiolites form the Baie Verte Oceanic Tract (BVOT; van Staal, 2007) and basement to the disconformably overlying volcano-sedimentary cover sequences of the Snooks Arm Group (cover to the Betts Cove Complex) (Upadhyay, 1973; Jenner and Fryer, 1980; Hibbard, 1983), its equivalent upper PHG (Skulski et al., 2010), Flat Water Pond Group, and Pointe Rousse cover sequence. Several large Late Ordovician to Early Silurian granitoid plutons intrude the BVOT including the ca. 446-432 Ma Burlington granodiorite, the ca. 436 Ma Cape Brulé porphyry, and the ca. 429 Ma Dunamagon granite (Fig. 2; Hibbard, 1983; Cawood et al., 1993; V. McNicoll, unpublished data, 2009).

The Ming deposit host sequence is part of the lower PHG. The base of the PHG consists of low-Ti boninite with minor felsic tuff and rhyodacitic flows (Fig. 2; Hibbard, 1983; Piercey et al., 1997) that are intruded by multiple generations of tholeiitic gabbro dykes that may possibly be the co-genetic tholeiitic feeders to units higher in the lower PHG (Piercey et al., 1997). This is overlain by a 2.5 km wide (Skulski et al., 2010) sequence of quartz-pyric, rhyodacite, felsic tuff, and tuff breccia herein referred to as the Rambler Rhyolite formation. The Ming deposit is hosted in the Rambler Rhyolite formation, in the uppermost part of the lower PHG (Fig. 2)

The ore consists of chalcopyrite, pyrite, sphalerite, pyrrhotite, minor galena and trace electrum (Au-Ag alloy). The sulphide lenses are spatially associated with several zones of metamorphosed hydrothermally altered footwall rocks.

Metamorphism in the lower PHG does not exceed upper greenschist facies, except near the Ordovician-Silurian intrusive bodies where contact metamorphism locally reaches the amphibolite facies (Tuach and Kennedy, 1978). The regional structural evolution of the peninsula has recently been examined by Castonguay et al. (2009 and references therein), and re-evaluated by Skulski et al. (2010). The Ming area was affected by at least three phases of regional deformation. D_1 results from the obduction of the BVOT and is poorly developed east of the BVBL (Skulski et al., 2010). D_2 is defined by an east-west striking cleavage to a penetrative schistosity (S_2) that is axial-planar to megascopic east-trending open to tight F_2 folds. The S2 fabric is locally associated with a strong L > S fabric. The north-dipping south-directed Rambler Brook Fault, south of the Rambler Rhyolite formation is interpreted as a D_2 structure. D_3 is characterized by open, upright cross folds with axial planes trending north-northeast (Fig. 2). The elongated-shape of the orebodies (Fig. 2) is in large part due to the S_2 stretching and superimposed effect of D_3 deformation (Castonguay et al., 2009). The extent to which the deformation has affected the architecture and metal distribution of the Ming deposit remains unconstrained and currently under study (Brueckner et al., 2014).

Ore lenses and Host Units

Detailed mapping was undertaken northwest of the deposit in different underground levels (329, 434, and 444) along the 1807 zone. The mapping is complementary to the work by Pilote and Piercey (2013). Moreover, a total of 23 surface and underground drill holes (16 from the Ming South down plunge or hereafter referred to

as MSDP) were logged in an attempt to establish a stratigraphic correlation and identify the different units hosting and overlying the deposit. Rocks underlying the massive sulphides are hydrothermally altered and regionally metamorphosed; thus, in most case obliterating the primary mineralogy of the rocks. Rock types are therefore identified based on the texture, presence of relict phenocrysts, secondary mineralogy, and geochemistry. Nomenclature used for volcanic and volcaniclastic rocks classification is as White and Houghton (2006). Least altered volcanic and volcaniclastic rocks (i.e., SiO_2 > 66 wt. % and Na_2O = 2-5 wt. %), although deemed felsic, have intermediate compositions based on immobile trace element ratios (e.g., $Zr/TiO_2 < 0.07$) (Pilote, unpublished data).

1807 zone

Based on underground mapping on several levels in the 1807 zone of the deposit, the stratigraphic footwall unit to the massive sulphides on level 329 (Fig. 4) is a dark purple to olive green coloured felsic lapilli-tuff (Fig. 5a) with quartz porphyroclasts making up to 15 vol. % of the rock. The lapilli-sized fragments, which make up 30 vol. % of the rock, are lighter in colour and are subangular and elongated parallel to the main lineation. This fragmental unit is in sharp contact with a lower unit composed predominantly of a dark purple, coherent, equigranular to quartz-phyric rhyodacite that contains up to 15 vol. % quartz. Down plunge of the 1807 zone, rocks on levels 434 and 444 are similar to those present on level 329; however, there are significant differences in the distribution and size of fragments, indicating lateral volcanic facies changes. On levels 434 and 444, stratigraphically underlying the massive sulphide is a 3 meter-thick

unit of dark purple-grey, biotite-rich felsic lapilli-tuff with bombs comprising 10% of the rock. The bombs are dark pink-purple coloured, quartz-phyric (≈5-10 vol. %), and vary from 2 to 30 cm in length (length to width ratio of 3:1). This unit has a minimum thickness of approximately three meters. This unit is in gradational contact with the lower coherent felsic volcanic unit and the transition from a lapilli tuff to coherent felsic volcanic rocks occurs over a stratigraphic interval of 10 meters from the underlying massive sulphides.

The massive sulphide body is stratiform to locally discordant to the host volcanic rocks and has a maximum thickness of ≈4 meters. The massive sulphides are composed of pyrite and chalcopyrite with trace amounts of sphalerite that forms clots that are less than two cm in diameter. Quartz dominates (<20 vol. %) the gangue mineralogy, is interstitial to the sulphides, and occurs throughout the lens. In the southeast part of the lens, on levels 434 and 434, cm-scale layers of chalcopyrite are gradually replaced by cm-scale layers of sphalerite towards the northwest. The massive sulphide contains up to 20 vol. % of strongly quartz- to sericite-altered felsic volcanic clasts as shown on level 329 (Fig. 4). The clasts are elongated and folded due to deformation and cut by a foliated porphyritic hornblende-rich granodiorite (IN3; Fig. 4) setting a maximum age (pre-main deformation) relationship for their incorporation into the lens.

Stratigraphically overlying the massive sulphide lens is an up to 12 meter-thick unit of light white-grey coloured to dark grey polymictic felsic quartz-phyric crystal lithic lapilli tuff that fines upwards. This hanging-wall fragmental unit contains irregularly-shaped pyrite-rich pods that are elongate parallel to S_2, a feature also present on level 375

(Pilote and Piercey, 2013). This unit is overlain by a dark grey to reddish grey magnetite-rich siltstone (Fig. 5b). The siltstone comprises numerous ≤3 cm-thick syn-sedimentary layers of magnetite. This sedimentary unit has a sharp upper contact in which it contains coarse-grained rosette-shaped porphyroblasts of hornblende along a preferred structural plane (*garbenschiefer* texture). This unit occurs throughout the deposit and constitutes a marker horizon at the base of the upper PHG, indicating a hiatus in volcanism.

Ming South down plunge (MSDP)

The MSDP is the deepest and easternmost known orebody of the Ming deposit and contains combined measured and indicated resources of 1.11 Mt grading 1.64 wt% Cu, 0.57 wt% Zn, 9.94 g/t Ag, and 2.24 g/t Au (Pilgrim, 2009). The zone is not currently being mined and there is no underground access; however, information was obtained from diamond drill cores. The footwall of the MSDP is characterized by three main units (Fig. 6) to a maximum available drill core depth of approximately 270 meters below the ore horizon. It also intersects the Cu-rich Lower Footwall Zone (*see below*).

The lowermost unit has a minimum thickness of 175 m and is a medium to dark grey, fine-grained coherent felsic quartz-phyric tuff (or flow?) with quartz porphyroclasts up to 1-3 mm in diameter. It is overlain by a felsic volcaniclastic succession consisting predominantly of crystal tuff to crystal lithic lapilli tuff. The rock contains up to 10 vol. %, 2-5 mm-wide white to bluish coloured quartz phenocrysts. It is cut by chalcopyrite, pyrite, and pyrrhotite stringer veins that constitute 10-15 vol. % of the rock. This unit is overlain by two stratabound and stratiform massive sulphide lenses. The lower lens is

comprised mainly of massive chalcopyrite, pyrite, and minor sphalerite with elongated quartz-phyric rhyodacite clasts, whereas the upper lens is comprised of granular pyrite, chalcopyrite with minor sphalerite and interstitial quartz. It also contains silicified felsic volcanic clasts (< 10 cm in diameter) with green mica of possibly fuchsitic composition; the green mica constitute less than 1 vol. % of the rock. A clear mineralogical distinction exists between the two lenses, and this is also reflected in their different metal abundances (Fig. 7), with significantly higher Cu and Au grades in the lower lens.

The two MSDP lenses are separated by three discrete beds (of a total maximum thickness of 10 m) of felsic tuff (Fig. 8). The lowermost bed is a medium to dark grey medium-grained quartz-phyric crystal tuff (Fig. 8a); quartz grains are a white to bluish in colour. The middle bed is a light grey to white quartz-phyric crystal tuff (Fig. 8b). The quartz crystals in that bed vary in size (2 to 5 mm in diameter) and are elongated parallel to S_2 that is cut by chalcopyrite-pyrite-quartz stringer veins. The uppermost bed is enclosed within the upper massive sulphide lens and is a medium reddish grey coloured felsic quartz-phyric crystal tuff (Fig. 8c). This bed contains pyrite-quartz stringer veins (< 5 mm in thickness) that constitute less than 2 vol.% of the rock. A correlation is possible among the different drill holes (Fig. 8) intersecting the upper part of the MSDP, which reaches a maximum thickness of about 11 m in its central part (RM06-04e). Although the massive sulphides and/or host tuffaceous facies are cut by, or intercalated with mafic intrusions in some areas, the ~100 m along-strike stratigraphic continuity of the MSDP suggests a syn-genetic style of mineralization.

Intrusive rocks

Pilote and Piercey (2013) documented the presence of three distinct generations of dykes and sills in the Ming deposit host succession; further information about those intrusive rocks is given here. The first generation (IN1) is a coarse-grained equigranular clinopyroxene gabbro. The clinopyroxene is often replaced (pseudomorphed) by chlorite. The contact with the host felsic volcanic rocks is irregular and is locally truncated by sulphides due to deformation, with no evidence of intruding the latter. The coarse-grained gabbro is intruded by a fine-grained diorite (IN2) that intrudes massive sulphide where it is boudinaged, dismembered, and folded. The last generation of dykes (IN3) is a porphyritic hornblende-rich granodiorite that intrudes both IN2 and the massive sulphides (see Fig. 7d in Pilote and Piercey, 2013), and is similarly deformed when cutting the latter. Preliminary lithogeochemical data indicates significant geochemical differences between each generation of dykes (Fig. 9) with the first generation (IN1) having a flat rare-earth element (REE) pattern, whereas IN2 and IN3 are progressively more evolved with slight to moderate light-REE enrichment, respectively.

Hydrothermal Alteration

The different hydrothermal alteration assemblages present at Ming were characterized by core logging, underground mapping, petrographic microscopy, and scanning electron microscopy-energy dispersion X-ray imaging (SEM-EDX) at Memorial University. Whole-rock lithogeochemical analysis and visible to near infrared-shortwave infrared spectrometry (VNIR-SWIR) have also been done, but results and data analysis

are pending and will therefore be discussed in a later publication. Alteration mineral assemblages vary among the deposit and with depth and will be discussed in terms of their mineralogical assemblages.

A sericite (muscovite)-green mica-quartz±chlorite±epidote± magnetite±sulphides (herein referred to as sericitic) alteration assemblage is ubiquitous in the deposit host succession, interpreted as resulting from rock interaction with a low-temperature hydrothermal fluid (e.g., Franklin et al., 2005). This sericitic alteration, responsible for a greyish coloration in felsic rocks, underlies the 1807 and 1806 (Brueckner et al., 2014), and MSDP zones. The relative proportions of the various key minerals in this assemblage vary throughout the deposit. Chlorite and epidote are progressively more abundant at depth starting from the immediate footwall. There are no chemical analyses of the green mica available yet, but its bright green colour is distinct from all other micaceous phases in the deposit. In the 1807 and MSDP zones, the green mica forms foliation-parallel elongated pods that are <2 cm-long closely associated with the massive sulphides. The green mica is widespread and abundant (>5 vol. %) up to ~50 m stratigraphically below the 1806 zone (Fig. 10a) where it correlates with high Au content (Brueckner et al., in press). Epidote, magnetite, and garnet are minor phases in this alteration assemblage. Epidote is fine- to very fine-grained, and occurs as anhedral to lath-shaped grains together with quartz. Magnetite occurs as small (<2 mm diameter) euhedral grains and less than 2 mm in size. Garnet is restricted to the footwall of the 1807 zone. The grains are hypidioblastic, less than 3 mm in size, and commonly occur together with narrow (<5 mm) quartz veinlets that crosscut the foliation in the host rocks and the massive sulphides

(Fig. 10b). Stringer veins of pyrite-chalcopyrite-pyrrhotite comprise up to 50 vol. % of the host rock in the sericite altered footwall units. The semi-massive sulphides consist of anastomosed stringer veins and veinlets that crosscut the host rocks (Fig. 10c).

Fifty to 100 m stratigraphically below the Ming South and Ming North zones, the footwall consists of a coherent dark bluish coloured quartz-phyric volcanic rock that that is overprinted by a hydrothermal alteration assemblage of chlorite-quartz-epidote-chalcopyrite-pyrrhotite-pyrite±apatite±sphalerite±Bi-tellurides. This rock only occurs below the Ming South and Ming North zones. A sample collected from below the Ming North orebody at the 1450 level (~440 m below surface), shows an intergrowth relationship between quartz, chalcopyrite, pyrrhotite, and epidote forming stringer veins (Fig. 10d). The stringer veins are partly transposed into the dominant foliation and range from a few mm to up to 10 cm in thickness. The dark bluish coloration of the rock results from the high abundance of Fe-rich chlorite; this mineral typically occurs in the stockwork or high temperature hydrothermal fluid upflow zone to VMS deposits (e.g., Lydon, 1984; Goodfellow et al., 2003). Moreover, the chlorite altered rocks contain Bi-tellurides, which are also present in the 1806 zone (Brueckner et al., 2014); this mineral generally occurs in Au-rich VMS, epithermal, porphyry Au (±Cu), and Au skarn deposits (Cook et al., 2009 and references therein) and is considered to reflect input of magmatic fluids/volatiles to the hydrothermal system (e.g., Huston, 2000; Dubé et al., 2007a, 2007b).

The 1807 zone is characterized by a greyish to salmon-pink coloured alteration, also within the sericitic zone described above, that consists of veins and veinlets (5 mm

up to 20 cm in thickness) that crosscut (and have brecciated, in some areas) the volcanic rocks. This alteration seems to be restricted to the 1807 zone and its proximal footwall (extends ≈10 m below the sulphides).The veins and veinlets are composed of quartz-garnet-carbonate minerals that are transposed and folded in the foliation (Fig. 10e). Scanning electron microscope (SEM)-energy-dispersive X-ray (EDX) spectroscopy illustrates that the material consists of fine-grained quartz with a dusty matrix of very fine-grained Mn-Ca-Fe spessartine-almandine and Mn-rich calcite (Fig. 10f). Element distribution maps of this alteration show Mn-rich minerals disseminated throughout the volcanic rocks fragments (Fig. 10g) that could suggest a Mn diffusive exchange with the hydrothermal alteration fluids (Ganguly, 2002). Despite the latter, fragments have retained most of their sericitic mineral assemblages. All generations of mafic dykes cross-cut this Mn alteration and the presence of a Mn-altered felsic tuff xenolith within a dyke of granodiorite belonging to the latest generation (IN3) provides some temporal constraints for Mn introduction in the Ming system.

Quartz-pyrite alteration is locally present in the deposit and is stratigraphically immediately below and above the massive sulphides throughout the Ming deposit. The intensely quartz-altered zone extends 20-30 cm within the immediate footwall and hanging-wall rocks and also contains cubic pyrite porphyroblasts up to 1 meter below and above massive sulphides. The pyrite grains are stretched into the dominant lineation (~030°N). Both quartz and pyrite overprint IN3 dykes (Fig. 10h), and this indicates that this alteration assemblage postdates the intrusive phase and may be syn-deformation. Samples from immediately above the massive sulphides in the MSDP and 1806 zones

have SiO_2 > 88 wt. % with Na_2O < 0.11 wt. % (n=4; Pilote, unpublished data), reflecting the intense silicification (and/or leaching of other elements) of the rock.

Discussion and Summary

The footwall succession at Ming consists predominantly of a coherent volcanic rock of intermediate to felsic composition. The relative abundance of fragmental facies gradually increases up-stratigraphy (Fig. 6). The massive to volcaniclastic transition may reflect the evolution from a subaqueous intermediate to felsic flow-dome complex to an eruptive volcaniclastic succession. It has been suggested by Gibson et al. (1999) that the morphology of massive sulphide deposits is controlled primarily by the facies architecture of the host volcanic rocks (i.e., flows/dome complex versus volcaniclastic rocks). A flow-dominated succession, such as the Rambler rhyolite at Ming, may have inhibited diffusion and mixing of ascending hydrothermal fluids as opposed to volcaniclastic rocks that are much more permeable. The localization of mineralization in volcaniclastic rocks (but proximal to the flow/domes), suggests that the fluids were likely focused along permeability contrasts boundaries between the coherent and volcaniclastic rocks. It is possible that these boundaries are synvolcanic structures that focused the circulating hydrothermal fluids, resulting in the development of a lens-shaped massive sulphide deposit above a stringer vein or stockwork zone. Based on the spatial distributions of the LFZ (i.e., sub-parallel to the MSDP and Ming North lenses; Fig. 3) and the intense chlorite alteration and chalcopyrite-pyrrhotite-rich sulphide assemblages, it is likely that this zone represents high temperature hydrothermal fluid discharge along a synvolcanic

structure. The elongated shape of the massive sulphide zones at Ming is the result of multi-phase deformation (interference between D_1 and D_2: Tuach and Kennedy, 1978; Hibbard, 1983; Brueckner et al., 2014). However, the current *en-echelon* distribution of the lenses is likely due to the development of a set of synvolcanic faults and related secondary splays in an extensional setting. The primary architecture of the volcanic complex hosting the Ming ore lenses and its effects on the distribution and style of alteration and associated ore zones will be determined through detailed stratigraphic reconstruction as part of the current project.

The results herein suggest that the chloritic alteration in the MSDP and Ming North ore bodies represent high temperature hydrothermal alteration (>300°C; e.g., Lydon, 1988; Ohmoto, 1996). In contrast, the sericite-dominated alteration in the 1806 and 1807 zones is more consistent with these zones forming from lower temperature hydrothermal fluids (e.g., Lydon, 1988; Brueckner et al., 2014). In both the chloritic and sericitic alteration zones at Ming there are also ubiquitous biotite porphyroblasts that overprint the chloritic and sericitic alteration assemblages and formed as an upper greenschist metamorphic overprint of the hydrothermally altered rocks (Barrett and Maclean, 1994).

Manganese enrichment is locally important at Ming, as evidenced by the enrichment of Mn in garnet and calcite below the 1807 zone. Although it has not yet been determined, the origin of the Mn enrichment at Ming may be similar to that observed in other VMS deposits, notably at LaRonde Penna and Bousquet 2-Dumagami in the Abitibi greenstone belt. Dubé et al. (2007b; 2014) documented a Mn-alteration characterized by

transposed mm-wide bands of Mn-rich Fe-Ca spessartine or almandine-epidote-clinozoïsite-muscovite-pyrite ± pyrrhotite in the footwall rocks. Dubé et al. (2007b) propose that the Mn- enrichment of the garnets results from the replacement and leaching of manganiferous Fe carbonate from the surrounding rocks, which is locally present as disseminations below one of the auriferous orebody (i.e. 20 North lens), followed by metamorphism of Mn-enriched chloritic zones and concentration of Mn within garnet and other aluminous phases. Although preliminary at his point, further mineralogical and geochemical investigations will shed light on the source(s) and process(es) causing this Mn-enrichment at Ming. Moreover, this assemblage of alteration has economic implications at LaRonde where Mn-rich zones are commonly spatially associated with auriferous massive sulphides (Dubé et al., 2007b).

Quartz alteration (silicification) is important in some zones of the Ming deposit. In the 1806, 1807, and MSDP zones, the intensely silicified (± pyrite) horizon immediately overlying and underlying the massive sulphides was previously thought to have formed as a result of hydrothermal leaching, and this semi-permeable siliceous cap then permitted sulphide deposition below the seafloor (Pilote and Piercey, 2013). This interpretation was based on the presence of elongated, cm-scale sulphide lenses in the hanging wall and which indicated prolonged hydrothermal circulation and replacement of the felsic volcaniclastic rocks. However, Brueckner et al. (2014) argued that the silicification occurred during the waxing and peak of the hydrothermal activity together with the deposition of precious metal-bearing phases. The recent discovery of the silica-pyrite alteration assemblage overprinting IN2, however, indicates that it formed long after VMS

deposition and may be the result of silica mobilization from the massive sulphides into the immediately adjacent wall rocks during metamorphism and/or deformation.

In addition to synvolcanic faulting, the geometry of the various lenses in the Ming deposit is largely controlled by deformation, which is especially true for the 1807 zone that exhibits evidence of cm- to orebody-scale mechanical remobilization of the massive sulphides (e.g. massive sulphides piercing in the host rocks). A mafic dyke (IN2) intruding the massive sulphides on level 434 records multiple generations of chalcopyrite veinlets oriented parallel with the structural fabrics (Fig. 11). The massive sulphides in the northern part of the 1807 lens show distinct characteristics from it southern counterpart (Fig. 12). The former has higher Cu-Au contents coexisting with thin layers of sphalerite and also contains less silicified volcanic host rock fragments in the massive sulphides than the latter. Preliminary structural analyses show a structural relationship between a late NE fabric (S_3 of Castonguay et al., 2009) and the orientation of the massive sulphide lens. These features provide evidence for local remobilization of metals attendant with deformation and metamorphism, and this is the focus of ongoing work at Ming as part of this research project.

Despite local mechanical remobilization of the massive sulphides in the northwesternmost part of the 1807 zone due to post-mineralization deformation events (Taconic 3, Salinic, and Acadian orogenies; e.g., van Staal and Barr, 2012), evidence for a synvolcanic origin for the massive sulphide lenses and their precious metal enrichment include: 1) the spatial distribution of the massive sulphides and their relationship with the host rocks (i.e., stratabound and stratiform in the southern part of the 1807, 1806, and

MSDP zones); 2) the presence of cross-cutting high temperature (chloritic) and lower temperature proximal (sericitic) hydrothermal alteration assemblages underlying the massive sulphides; 3) the presence of synvolcanic dykes that cut the ore; 4) the intense deformation of all ore and alteration assemblages; 4) the presence of atypical mineralogy with abundant sulfosalts associated with an enrichment in the epithermal suite of elements (Au, Ag, As, Hg, Sb, Bi) that suggest a magmatic contribution to the mineralizing fluids (Brueckner et al., 2014); and 5) the extent of the main structural features (i.e., faults, shear zones, foliation, and folds) that are present beyond the ore bodies and deposit (Pilote, unpublished data). None of the locally (cm-scale) remobilized gold extends outside the deposit, which implies that any structurally controlled gold must have been remobilized from the deposit.

Acknowledgements

This study was funded by the Targeted Geoscience Initiative (TGI-4) program of the Geological Survey of Canada. We express our sincere appreciation to Rambler Metals and Mining PLC (particularly L. Pilgrim and P. Legrow) for granting underground access and providing data. J.-L. Pilote especially thanks S. Brueckner for field assistance and for sharing ideas during mapping. This research has also been financially supported by a Natural Sciences and Engineering Research Council of Canada (NSERC) Discovery Grant and the NSERC-Altius Industrial Research Chair in Mineral Deposits supported by NSERC, Altius Resources Inc. and the Research and Development Corporation of

Newfoundland and Labrador. Thanks to J. Peter for his careful reviews of this manuscript.

References

Barrett, T. J., and MacLean, W. H., 1994. Chemostratigraphy and hydrothermal alteration in exploration for VHMS deposits in greenstones and younger volcanic rocks: Short Course Notes, Geological Association of Canada, v. 11, p. 433-467.

Bédard, J. H., 1999. Petrogenesis of boninites from the Betts Cove Ophiolite, Newfoundland, Canada: Identification of Subducted Source Components: Journal of Petrology, v. 40, p. 1853-1889.

Bédard, J. H., Lauzière, K., Tremblay, A., and Sangster, A., 1998. Evidence for forearc seafloor-spreading from the Betts Cove ophiolite, Newfoundland: oceanic crust of boninitic affinity: Tectonophysics, v. 284, p. 233-245.

Brueckner, S., Piercey, S.J., Sylvester, P.J., Maloney, S., and Pilgrim, L., 2014. Evidence for syngenetic precious metal enrichment in an Appalachian volcanogenic massive sulfide system: The 1806 zone, Ming Mine, Newfoundland. Economic Geology, v. 109, p. 1611-1642.

Burnshall, J.T., 1975. Stratigraphy, structure and metamorphism west of Baie Verte, Burlington Peninsula, Newfoundland. Unpub. Ph.D. thesis, Cambridge University, 337 p.

Castonguay, S., Skulski, T., van Staal, C., and Currie, M., 2009. New insights on the structural geology of the Pacquet Harbour group and Point Rousse complex, Baie Verte peninsula, Newfoundland: Current Research Newfoundland and Labrador Department of Natural Resources, Geological Survey, v. Report 09-1, p. 147-158.

Cawood, P. A., van Gool, J. A. M., and Dunning, G. R., 1993. Silurian age for movement on the Baie Verte Line: Implications for accretionary tectonics in the Northern Appalachians: Geological Society of America, Abstract with Programs, v. 25, p. A422.

Cawood, P. A., van Gool, J. A. M., and Dunning, G. R., 1996. Geological development of eastern Humber and western Dunnage zones; Corner Brook-Glover Island region, Newfoundland: Canadian Journal of Earth Sciences, v. 33, p. 182-198.

Cook, N. J., Ciobanu, C. L., Spry, P. G., and Voudouris, P., 2009. Understanding gold-(silver)-telluride-(selenide) mineral deposits: Episodes, v. 32, p. 249-263.

Dubé, B., Gosselin, P., Mercier-Langevin, P., Hannington, M., and Galley, A., 2007a. Gold-rich volcanogenic massive sulphide deposits, in Goodfellow, W. D., ed., Mineral deposits of Canada: A synthesis of major deposit-types, district metallogeny, the evolution of geological provinces, and exploration methods, Special Publication No. 5, Geological Association of Canada, Mineral Deposits Division, p. 75-94.

Dube, B., Mercier-Langevin, P., Hannington, M. D., Lafrance, B., Gosselin, G., and Gosselin, P., 2007b. The LaRonde Penna world-class Au-rich volcanogenic massive sulfide deposit, Abitibi, Quebec; mineralogy and geochemistry of alteration and implications for genesis and exploration: Economic Geology, v. 102, p. 633-666.

Dunning, G. R., and Krogh, T. E., 1985. Geochronology of ophiolites of the Newfoundland Appalachians: Canadian Journal of Earth Sciences, v. 22, p. 1659-1670.

Franklin, J. M., Gibson, H. L., Jonasson, I. R., and Galley, A. G., 2005. Volcanogenic massive sulphide deposits, in Hedenquist, J. W., Thompson, J. F. H., Goldfarb, R. J., and Richards, J. P., eds., Economic Geology 100th Anniversary Volume, 1905-2005, Society of Economic Geologists, p. 523-560.

Franklin, J. M., Lydon, J. W., and Sangster, D. F., 1981. Volcanic-associated sulfide deposits, in Skinner, B. J., ed., Economic Geology Seventy-Fifth Anniversary Volume, Society of Economic Geologists, p. 485-627.

Galley, A., Hannington, M., and Jonasson, I., 2007. Volcanogenic massive sulphide deposits, in Goodfellow, W. D., ed., Mineral Deposits of Canada: A synthesis of major deposit-types, district metallogeny, the evolution of geological provinces, and exploration methods, Special Publication No. 5, Geological Association of Canada, Mineral Deposits Division, p. 141-161.

Ganguly, J., 2002. Diffusion kinetics in minerals: Principles and applications to tectono-metamorphic processes, in Energy Modelling in Minerals. EMU Notes in Mineralogy. Gramaccioli, C.M. (eds) Eötvös University Press, Budapest, vol. 4, p. 271-309.

Gibson, H. L., 2005. Volcano-hosted ore deposits: United States, Cambridge University Press: New York, New York, United States, p. 333-386.

Gibson, H., Morton, R. L., and Hudak, G. J., 1999. Submarine volcanic processes, deposits, and environments favorable for the location of volcanic-associated massive sulphide deposits, in Barrie, C. T., Hannington, M.D., eds., Volcanic-associated massive sulphide deposits: Processes and examples in modern and ancient settings. Reviews in Economic Geology, v. 8: Boulder, CO, Society of Economic Geologists, p. 13-51.

Goodfellow, W. D., McCutcheon, S. R., and Peter, J. M., 2003. Massive sulfide deposits of the Bathurst mining camp, New Brunswick, and northern Maine; introduction and summary of findings: Economic Geology Monographs 11, p. 1-16.

Hannington, M. D., Poulsen, K. H., Thompson, J. F. H., and Sillitoe, R. H., 1999. Volcanogenic gold in the massive sulphide environment, in Barrie, C. T., Hannington, M.D., eds., Volcanic-associated massive sulphide deposits: Processes and examples in modern and ancient settings, Reviews in Economic Geology, v. 8: Boulder, CO, Society of Economic Geologists, p. 325-351.

Hibbard, L. J., 1983. Geology of the Baie Verte Peninsula, Newfoundland, Department of Mines and Energy, Government of Newfoundland and Labrador, Memoir 2, 279 p.

Huston, D. L., 2000. Gold in volcanic-hosted massive sulfide deposits: Distribution, genesis, and exploration, in Hagemann, S. G., Brown, P.E., eds., Gold in 2000, Reviews in Economic Geology v. 13: Boulder, CO, Society of Economic Geologists, p. 401-426.

Jenner, G. A., and Fryer, B. J., 1980. Geochemistry of the upper Snooks Arm Group basalts, Burlington Peninsula, Newfoundland; evidence against formation in an island arc: Canadian Journal of Earth Sciences, v. 17, p. 888-900.

Lydon, J. W., 1984. Volcanogenic massive sulphide deposits Part 1: A descriptive model: Geoscience Canada, v. 11, p. 195-202.

Lydon, J. W., 1988. Volcanogenic massive sulphide deposits Part 2: Genetic models: Geoscience Canada, v. 15, p. 43-65.

Mercier-Langevin, P., McNicoll, V., Allen, R., Blight, J. S., and Dubé, B., 2013. The Boliden gold-rich volcanogenic massive sulfide deposit, Skellefte district, Sweden: new U–Pb age constraints and implications at deposit and district scale: Mineralium Deposita, v. 48, p. 485-504.

Mercier-Langevin, P., Hannington, M. D., Dubé, B., and Bécu, V., 2011. The gold content of volcanogenic massive sulphide deposits: Mineralium Deposita, v. 46, p. 509-539.

Norman, R. E., and Strong, D. F., 1975. The geology and geochemistry of ophiolitic rocks exposed at Ming's Bight, Newfoundland: Canadian Journal of Earth Sciences, v. 12, p. 777-797.

Ohmoto, H., 1996. Formation of volcanogenic massive sulfide deposits: The Kuroko perspective: Ore Geology Reviews, v. 10, p. 135-177.

Piercey, S. J., Jenner, G. A., and Wilton, D. H. C., 1997. The stratigraphy and geochemistry of the southern Pacquet Harbour Group, Baie Verte Peninsula, Newfoundland: Implications for mineral exploration: in Current Research Newfoundland and Labrador Department of Natural Resources, Geological Survey, Report 97-1, p. 119-139.

Pilgrim, L., 2009. Mineral resource estimate for the Ming Mine, Newfoundland, Canada: Baie Verte, Newfoundland and Labrador, Rambler Metals and Mining Canada Ltd, 114 p.

Pilote, J.-L. and Piercey, S.J., 2013. Volcanostratigraphy of the 1807 zone of the Ming Cu-Au volcanogenic massive sulphide deposit, Baie Verte Peninsula, northern Newfoundland; Geological Survey of Canada, Current Research 2013-20, 13 p., doi:10.4095/293128.

Poulsen, K. H., and Hannington, M. D., 1996. Volcanic-associated massive sulphide gold, in Eckstrand, O. R., Sinclair, W.D., Thorpe, R.I., ed., Geology of Canadian Mineral Deposit Types, 8, Geological Survey of Canada, p. 183-196.

Sillitoe, R. H., Hannington, M. D., and Thompson, J. F. H., 1996. High sulfidation deposits in the volcanogenic massive sulfide environment: Economic Geology, v. 91, p. 204-212.

Skulski, T., Castonguay, S., McNicoll, V., van Staal, C., Kidd, W., Rogers, N., Morris, W., Ugalde, H., Slavinski, H., Spicer, W., Moussallam, Y., and Kerr, I., 2010. Tectonostratigraphy of the Baie Verte oceanic tract and its ophiolite cover sequence on the Baie Verte Peninsula: in Current Research Newfoundland and Labrador Department of Natural Resources, Geological Survey, Report 10-1, p. 315-335.

Sun, S. S., and McDonough, W. F., 1989. Chemical and isotopic systematics of oceanic basalts; implications for mantle composition and processes: Geological Society Special Publication, v. 42, p. 313-345.

Tourigny, G., Brown, A. C., Hubert, C., and Crepeau, R., 1989. Synvolcanic and syntectonic gold mineralization at the Bousquet Mine, Abitibi greenstone belt, Quebec: Economic Geology, v. 84, p. 1875-1890.

Tuach, J., and Kennedy, M. J., 1978. The geologic setting of the Ming and other sulphide deposits, Consolidated Rambler Mines, Northeast Newfoundland, Economic Geology, v. 73, p. 192-206.

Upadhyay, H. D., 1973. The Betts Cove ophiolite and related rocks of the Snooks Arm Group, Newfoundland, Unpublished Ph.D thesis, Memorial University of Newfoundland, St. John's, Newfoundland and Labrador 224 p.

van Staal, C. R., 2007. Pre-Carboniferous tectonic evolution and metallogeny of the Canadian Appalachians, in Goodfellow, W. D., ed., Mineral deposits of Canada: A synthesis of major deposit-types, district metallogeny, the evolution of geological provinces, and exploration methods, Special Publication No. 5, Geological Association of Canada, Mineral Deposits Division, p. 793-818.

van Staal, C. R., and Barr, S. M., 2012. Lithosperic architecture and tectonic evolution of the Canadian Appalachians and associated Atlantic margin, in Percival, J. A., Cook,

F. A., and Clowes, R. M., eds., Tectonic Styles in Canada: The LITHOPROBE perspective, Geological Association of Canada, Special Paper 49, p. 41-96.

White, J. D. L., and Houghton, B. F., 2006. Primary volcaniclastic rocks: Geology, v. 34, p. 677-680.

Williams, H., 1979. Appalachian orogen in Canada: Canadian Journal of Earth Sciences, v. 16, p. 792-807.

Yeats, C. J., and Groves, D. I., 1998. The Archaean Mount Gibson gold deposits, Yilgarn Craton, Western Australia: Products of combined synvolcanic and syntectonic alteration and mineralisation: Ore Geology Reviews, v. 13, p. 103-129.

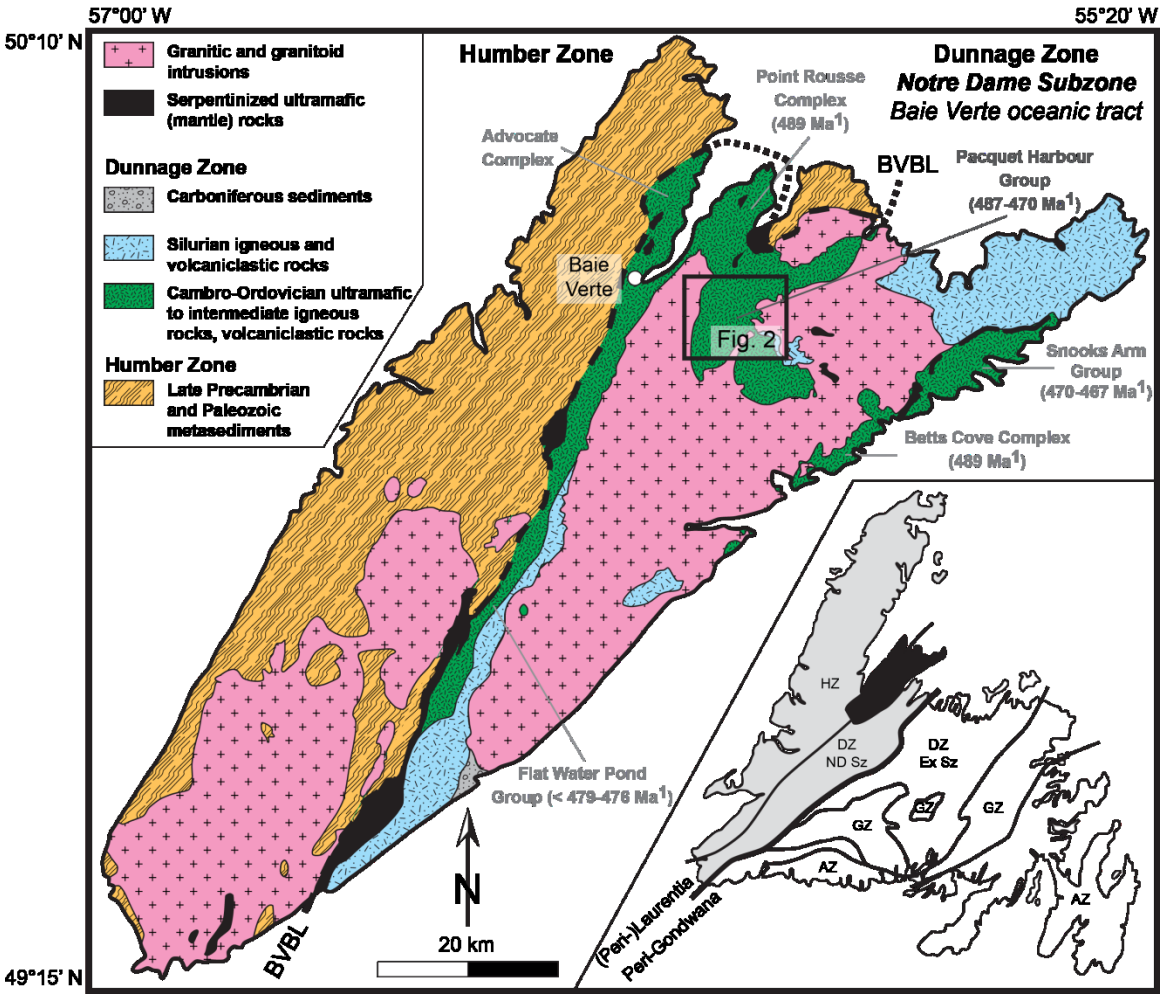

Fig. 1. Simplified geological map of the Baie Verte Peninsula (modified from Skulski et al., 2010, and references therein) with the (peri-)Laurentian (inset: in grey) and (peri-)Gondwanan tectonostratigraphic zones forming the Appalachian orogenic belt in Newfoundland (Williams, 1979). BVBL - Baie Verte-Brompton Line.

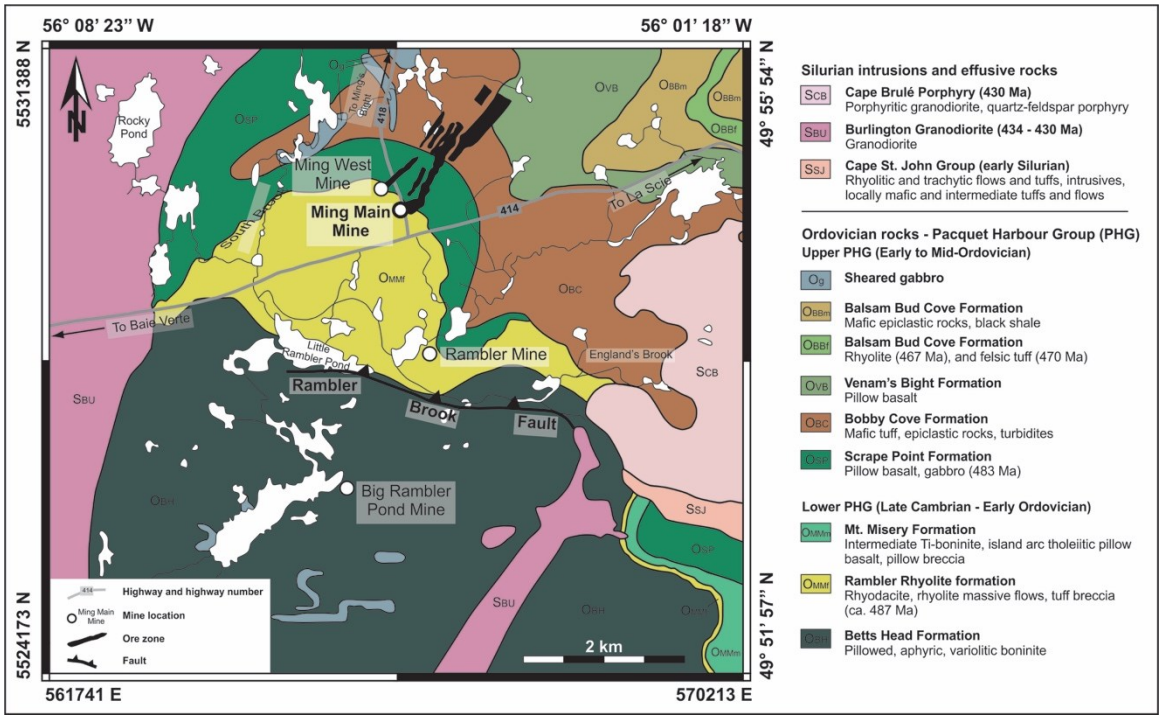

Fig. 2. Regional geology map of the study area, Baie Verte Peninsula with Ming VMS orebodies projected to surface and shown in black. Both datums are shown in WGS 84 (top and right) and UTM 21N NAD 83 (bottom and left). Map modified from Pilgrim (2009), Tuach and Kennedy (1978), Castonguay et al. (2009), and Hibbard (1983). Ages are from Castonguay et al. (2009) and Cawood et al. (1993).

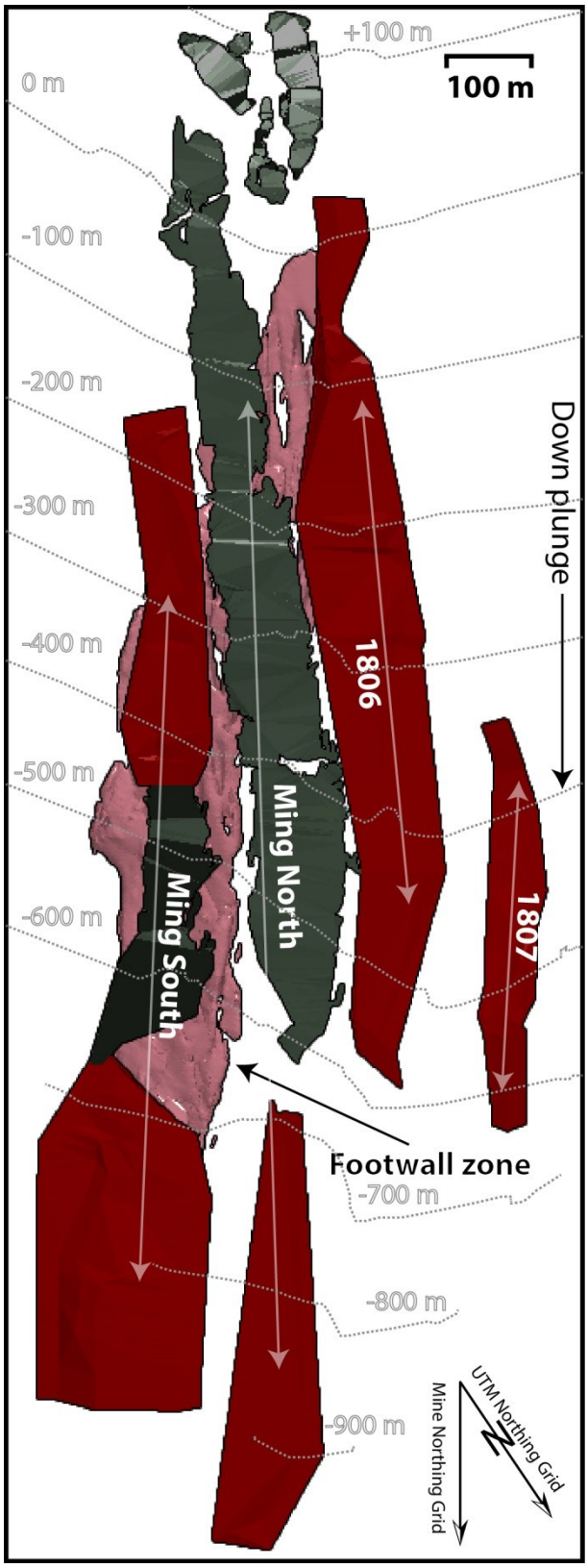
+100 m
0 m
100 m
-100 m
-200 m
-300 m
-400 m
-500 m
-600 m
-700 m
-800 m
-900 m
Down plunge
1806
1807
Ming North
Ming South
Footwall zone
UTM Northing Grid
Mine Northing Grid

Fig. 3. Plan view of 3D model of Ming orebodies projected to surface (0m). The surface of wireframes in red represent orebodies currently in production or those that will be mined, whereas those in grey have been previously mined orebodies. Mine north is 34° east of UTM north. Model modified from Pilgrim (2009).

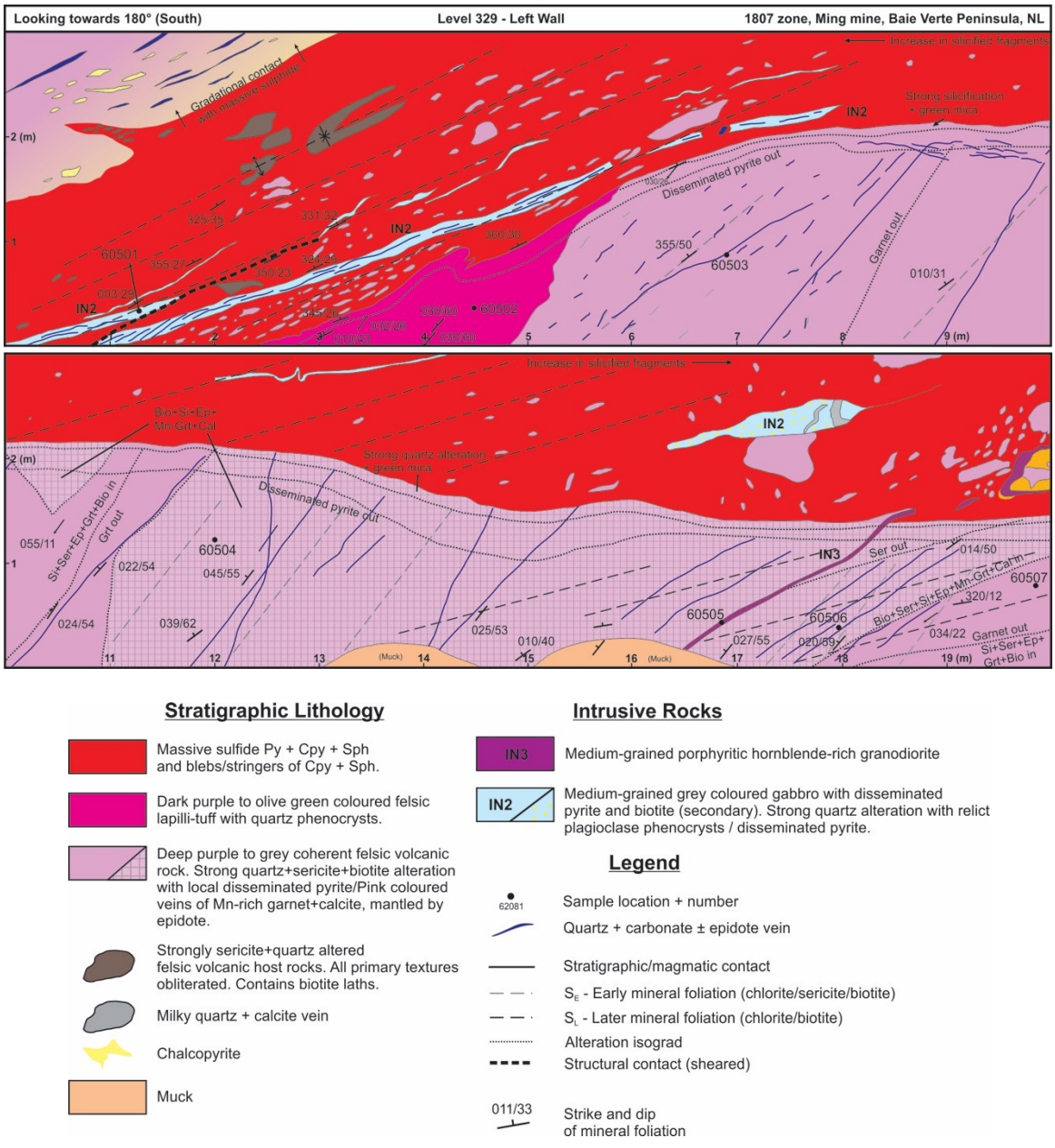

Fig. 4. a) Schematic cross-section of the back wall in level 329, 1807 zone showing the relationship between the different lithological units, including the massive sulphide horizon where it is intruded by IN2 and IN3; b) Legend. Abbreviations: Bio – biotite, Cal – calcite, Cpy – chalcopyrite, Ep – epidote, Grt – garnet, Py – pyrite, Ser – sericite, Si – Silica, Sph – sphalerite.

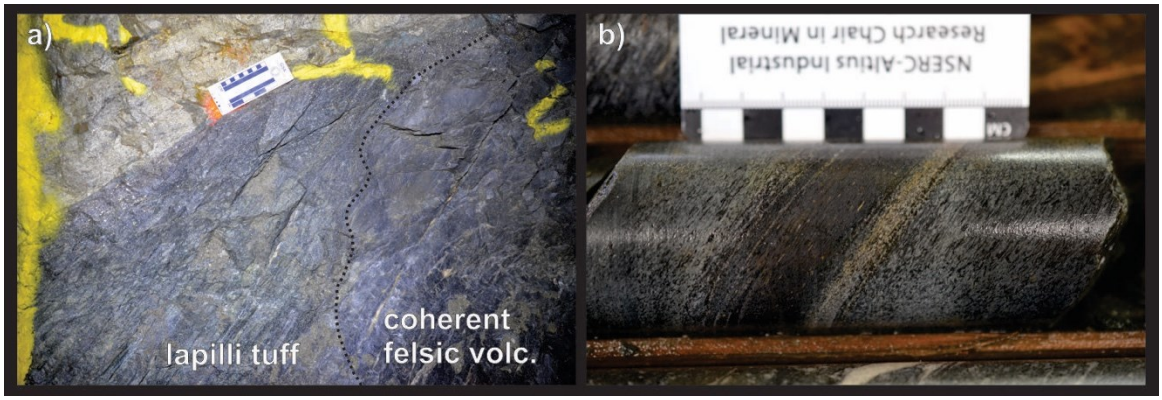

Fig. 5. Photographs of an underground exposure and a drill core section. a) View looking south in level 329 of the contact between the medium-grained, light green, quartz-phyric crystal lithic lapilli tuff and the deep purple coherent felsic volcanic units underlying the massive sulphide. b) Representative sample of the magnetite-pyrite-rich layer intercalated with a fine- to medium-grained volcanogenic sedimentary rock (predominantly siltstone) (DDH RM07-20m; 635 m downhole).

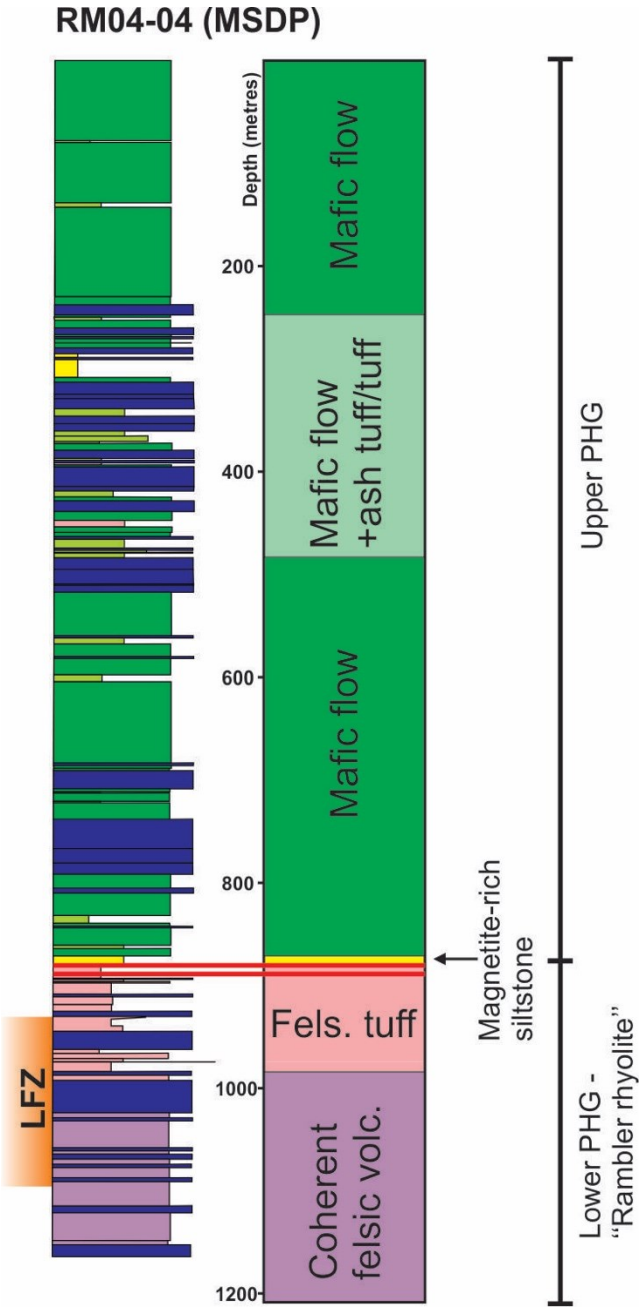

Fig. 6. Representative stratigraphic section of the Ming South Down Plunge (MSDP). The red lines represent the two massive sulphide lenses, underlain by two units of felsic tuff and coherent felsic volcanic rocks (Rambler rhyolite). The massive sulphide is overlain by a magnetite-rich siltstone, which in turn is overlain by mafic flows and ash tuff rocks (upper Pacquet Harbour Group). Blue units represent undifferentiated mafic dykes. The LFZ (Lower Footwall Zone) represents the Cu-rich stockwork underlying part of the Ming deposit.

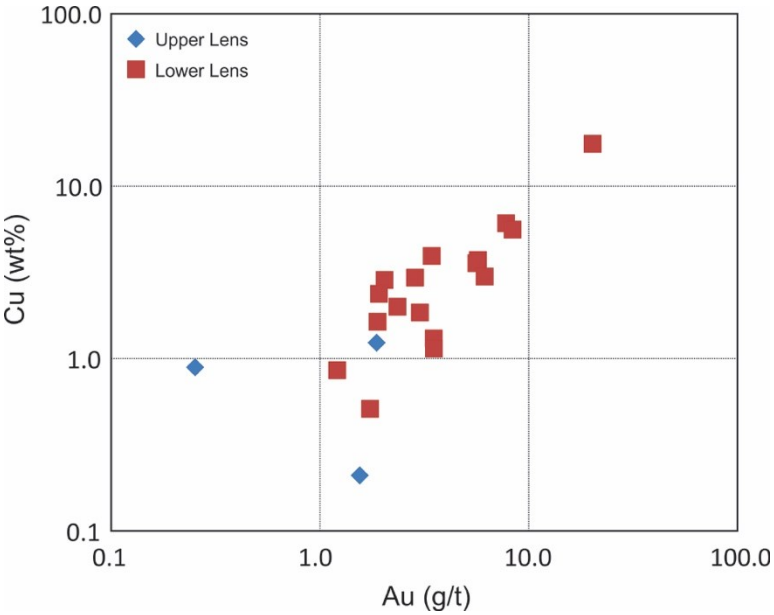

Fig. 7. Historical Cu (wt%) and Au (g/t) grades from diamond drill holes intersecting the two massive sulphide lenses in the MSDP. Grades are for meter-long assay intervals.

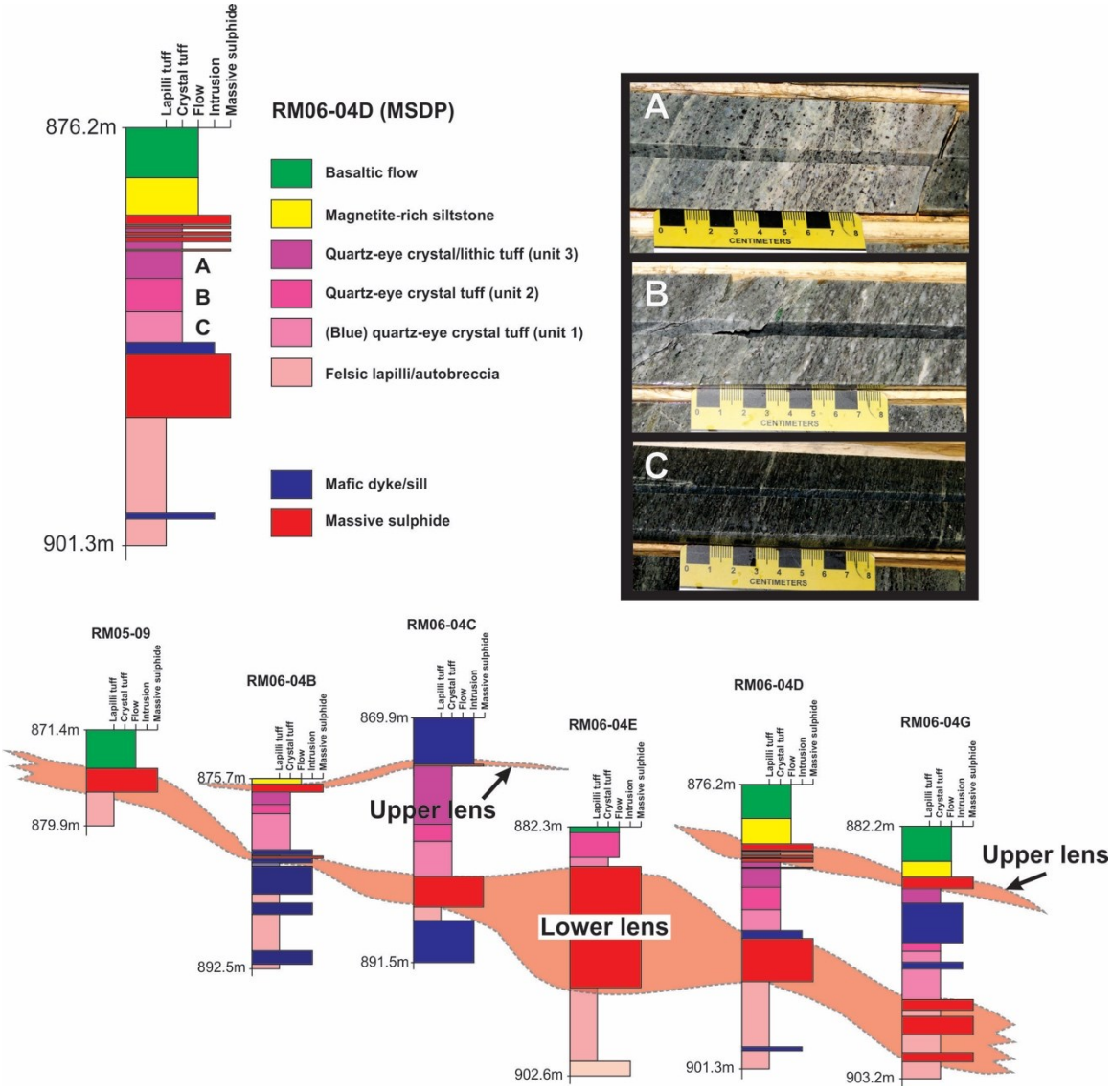

Fig. 8. Graphic logs for representative diamond drill holes intersecting the MSDP massive sulphide lenses arranged in a schematic cross-section, with representative drill core photographs of the different tuffaceous facies separating the massive sulphide lenses: A) quartz-phyric crystal/lithic tuff; B) quartz-phyric crystal tuff; C) melanocratic blue quartz-phyric crystal tuff. The relative horizontal positions of the drill holes are not to scale.

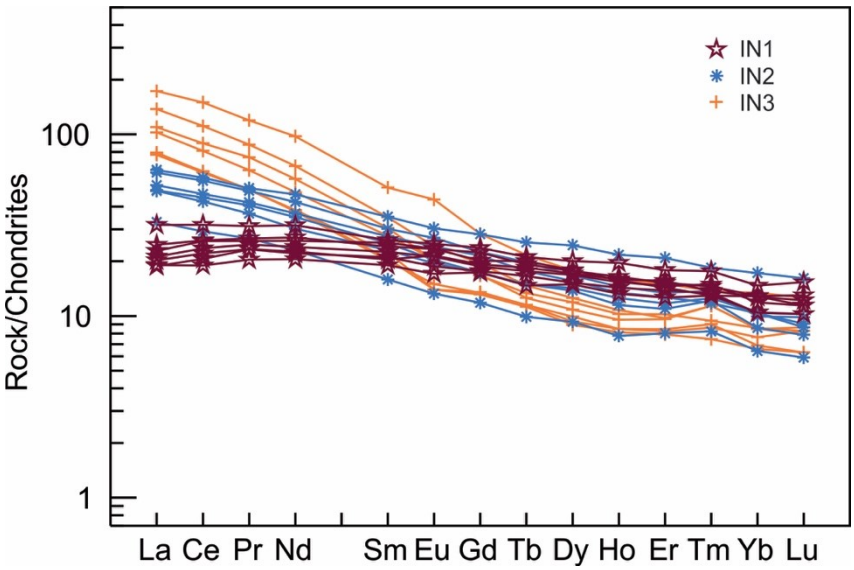

Fig. 9. Chondrite normalized rare-earth element plots for samples from mafic to intermediate dykes (IN1, IN2, and IN3) in this study. Chondrite-normalizing values are from Sun and McDonough (1989).

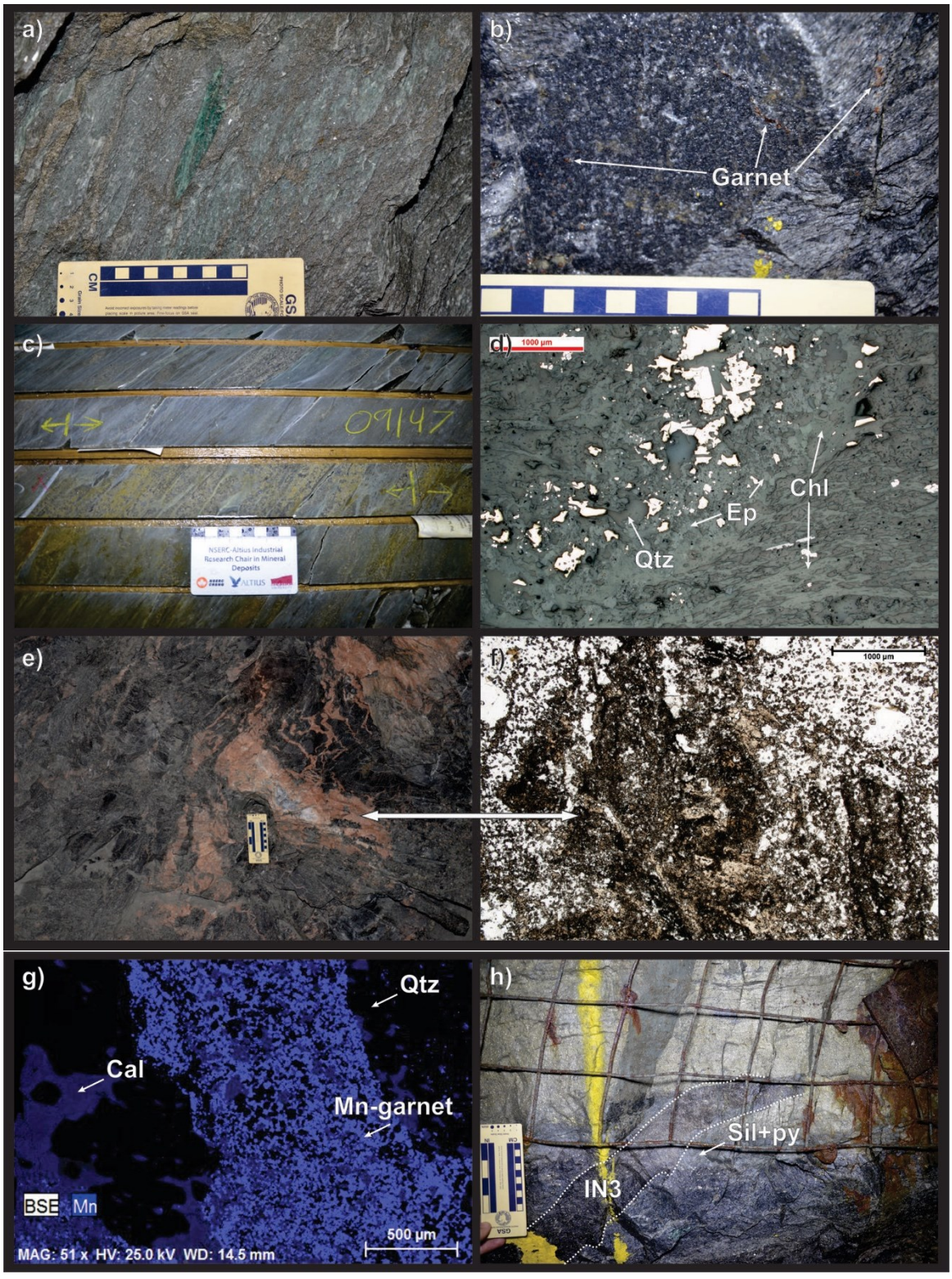
a)
b)
Garnet
c)
09147
NSERC-Altius Industrial Research Chair in Mineral Deposits
d)
1000 µm
Chl
Ep
Qtz
e)
f)
1000 µm
g)
Qtz
Cal
Mn-garnet
BSE Mn
500 µm
MAG: 51 x HV: 25.0 kV WD: 14.5 mm
h)
Sil+py
IN3

Fig. 10. Representative and selected underground and drill photographs and photomicrographs of the different alteration styles characterizing the Ming footwall rocks. a) A coherent felsic volcanic rock is altered to sericite (with green mica) and sulphide mineralization oriented parallel to foliation (level 107, 1806 zone). Scale is in cm. b) A deep purple sericite altered coherent felsic volcanic overprinted by garnet-biotite (level 329, 1807 zone). Scale is in cm. c) A representative drill core section underlying the massive sulphide with strong sericite+sulphide alteration (RM04-04; 219 m downhole). Scale is in cm. d) Photomicrograph in reflected light of a strongly chlorite altered felsic folcanic rock with coexisting chlorite, quartz, epidote, chalcopyrite, and pyrrhotite (sample 62085; level 1450). e) View looking southwest of a Mn-altered quartz-phyric coherent felsic volcanic rock underlying the massive sulphide. The pink, light grey, white, and dark green-black rocks are Mn-garnet, quartz, calcite, and quartz-phyric felsic volcanic rock, respectively. (level 481, 1807 zone). Scale is in cm. f) Photomicrograph in transmitted light of sample 62199 (level, 481, 1807 zone) showing very fine- to fine-grained quartz (clear) with dusty Mn-garnet (light to dark pink) and calcite (clear). g) SEM-EDX image of sample 62199 (level 481, 1807 zone) showing the distribution of Mn (blue) and the relationship between calcite, quartz and Mn-rich garnet. Note the abundant Mn-rich inclusions in quartz in the right part of the image. h) View looking south in level 329 of the silica+pyrite alteration overprinting IN3 and the felsic volcanic footwall rocks. Abbreviations: Cal – calcite, py – pyrite, Qtz – quartz, Sil – silica. Scale is in cm.

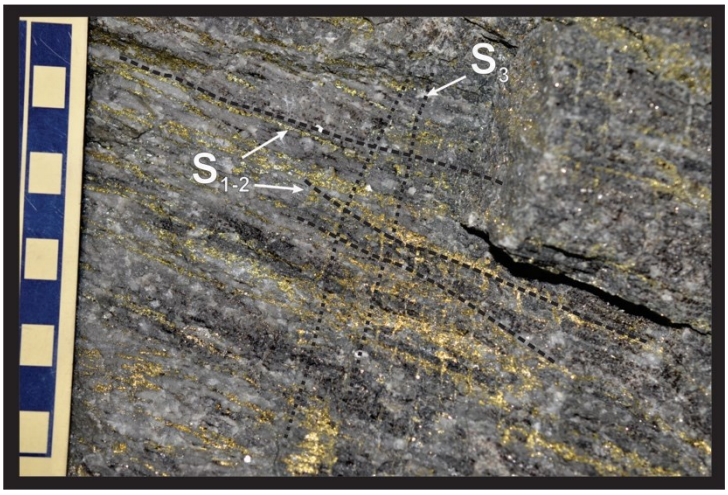

Fig. 11. Chalcopyrite veinlets oriented parallel to structural foliations S_{1-2} and overprinted at high-angle by chalcopyrite veinlets oriented in the plane of the S_3 fabric, hosted in a IN2 diorite intruding the massive sulphide in level 434 (1807 zone). View looking northwest, perpendicular to the longitudinal orientation of the massive sulphide. Scale is in cm.

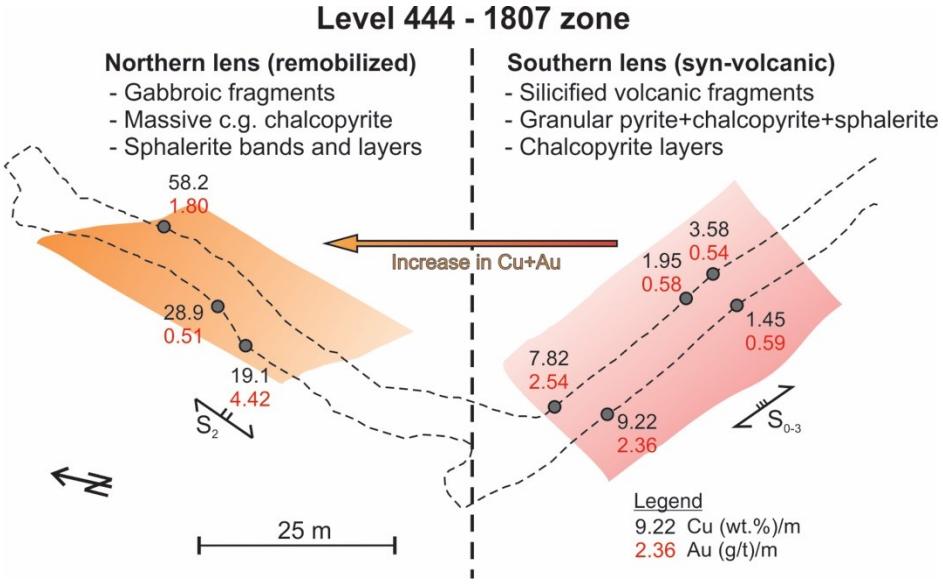

Fig. 12. Plan view of level 444 in the 1807 zone. The northern and southern lenses (in orange) show mineralogical, geochemical, structural, and textural distinctions. A general trend is observed with Cu and Au contents increasing towards the north.

Appendix 3
Volcanic Architecture and Alteration Assemblages of the Ming Cu-Au-(Zn-Ag) VMS Deposit, Baie Verte, Newfoundland: Implications for Gold-enrichment Processes and Exploration

Abstract

The Ming deposit is hosted in Cambro-Ordovician intermediate to felsic rocks underlain by ca. 490 Ma ophiolite slivers of boninitic composition. The deposit consists of five elongated semimassive to massive sulphide lenses that gently plunge 30° to the northeast and occur in the uppermost part of a calc-alkalic intermediate to felsic volcanic succession. The immediate hanging wall varies from mafic volcanic breccia to magnetite-rich volcanogenic siltstone. Three generations of mafic to intermediate intrusive rocks are present in the deposit; they each have distinctive lithogeochemical signatures and are interpreted to be genetically related to the mafic rocks of the cover sequence.

The Ming deposit has seven distinct alteration mineral assemblages (from proximal to distal from mineralization): quartz-pyrite, quartz-calcite-garnet, sericite-green mica-sulphide, sericite-quartz-pyrite, chlorite-amphibole-quartz, chlorite-sericite-quartz-sulphide, and chlorite-stringer zone assemblages. A chalcopyrite-pyrrhotite-pyrite stringer zone associated with the chlorite-stringer zone assemblage occurs 50-100 m stratigraphically below the Ming North and Ming South lenses, and this was the site of high-temperature fluid discharge of the hydrothermal system. The spatial and temporal geological relationships between the stratigraphic package, alteration styles, mineralization, and deformation strongly support a syngenetic origin for mineralization and Au-enrichment.

Introduction

The Ming deposit is a Au-Ag-bearing volcanogenic massive sulphide (VMS) deposit located in the Baie Verte Peninsula in northern Newfoundland, which is part of the Notre-Dame subzone of the Canadian Appalachian orogen (Fig. 1). The deposit is part of a group of four past and currently producing precious metal-rich VMS deposits that collectively are known as the consolidated Rambler and Ming mining camp (herein referred to as the Rambler camp). The Rambler camp deposits are hosted by the ~489-487 Ma upper Pacquet Complex, part of the Baie Verte Oceanic Tract (Fig. 2; van Staal and Barr, 2012; van Staal et al., 2013). The Ming deposit consists of five Cu-Au-Zn-Ag-rich, semi-massive to massive pyrite-rich lenses, veins, and stringer zones located within variously sericite-chlorite-quartz-altered intermediate to felsic volcanic rocks with a large proportion of volcaniclastic rocks. These zones are, from the northwest to the southeast, the 1807, 1806, Ming North, Ming South, and Lower Footwall zones (Fig. 3). The current combined measured and indicated resources at Ming are estimated at 12.5 Mt grading 1.52 wt. % Cu, 0.45 wt. % Zn, 8.11 g/t Ag, and 1.69 g/t Au (Pilgrim, 2009). The base and precious metal contents vary among these zones (Fig. 4) with the highest Au grades in the 1806 zone (measured resources of 267,000 tonnes at 0.56 wt% Cu, 1.31 wt% Zn, 32.15 g/t Ag, and 4.31 g/t Au), which puts it into the subclass of "auriferous" VMS deposits (Poulsen and Hannington, 1996; Poulsen et al., 2000; Mercier-Langevin et al., 2011a; Brueckner et al., 2014a).

The timing and mode of Au-Ag introduction in ancient VMS deposits in general, including Ming, is debated due to modifications to the primary features through

superimposed deformation and metamorphism (e.g., Mercier-Langevin et al., this volume); this lack of agreement has hampered the development of improved exploration models. In this study, we describe the geology of the Ming deposit and recently discovered precious metal-rich zones, the hydrothermal alteration, and the geochemical composition of the host rocks in order to constrain the timing and processes of precious metal-enrichment so as to develop improved genetic and exploration models.

Regional Geology

The Ming deposit is hosted by intermediate to felsic rocks of the informally named Rambler Rhyolite formation (Skulski et al., 2010), which consists of a 6 km wide and 2.5 km thick folded dome-shaped sequence of quartz-phyric rhyodacite, felsic tuff and tuff breccia, roughly striking northwest and dipping 30° (Fig. 3; Hibbard, 1983; Castonguay et al., 2009). Rhyolite immediately stratigraphically below the nearby Rambler Main deposit yielded a U-Pb zircon age of 487±4 Ma (Fig. 2; Skulski et al., 2010). Stratigraphically below the Rambler Rhyolite formation are low-Ti boninites intercalated with thin (<50 m) beds of felsic tuffs and rhyodacite flows (Hibbard, 1983; Piercey et al., 1997; Skulski et al., 2010) of the Betts Head Formation (Skulski et al., 2010), which host the Big Rambler Pond (Fig. 2) and the Tilt Cove and Betts Cove VMS deposits (Fig. 1). Stratigraphically overlying the Betts Head Formation are rocks of intermediate Ti boninite, island arc tholeiitic pillow basalt, breccia, and minor felsic tuff, which are part of the Mount Misery Formation (Skulski et al., 2010). The upper part of this sequence is structurally repeated in the hanging wall of the Rambler Brook Fault

(Fig. 2; Castonguay et al., 2009) where it hosts the Rambler Rhyolite formation and the massive sulphide lenses of the Ming deposit in the upper part of the formation. The Rambler Rhyolite formation is locally overlain by thin lenses of basalt of island-arc affinity that are chemically similar to those of the Mount Misery Formation (Skulski et al., 2010). The latter are overlain by the ca. 479-467 Ma Snooks Arm Group, which is the cover sequence to the Pacquet Complex. The base of the Snooks Arm Group consists of a thin (<1 m) sequence of chert, magnetite-rich mudstone to siltstone, and sandstone (Nugget Pond horizon). This sequence is laterally extensive and is present throughout the Baie Verte Peninsula (Skulski et al., 2010). Overlying this unit are thin (<1 m) to thick (>100 m) alternating sequences of volcaniclastic monomictic to polymictic conglomerate, epiclastic wacke, iron formations, high-Ti tholeiitic to calc-alkaline basalt, and mafic to felsic volcaniclastic rocks (Hibbard, 1983; Skulski et al., 2010).

Deposit Geology

The stratigraphic footwall of the deposit is composed of three main volcanic and volcaniclastic units (classified following the nomenclature of White and Houghton, 2006).

The lower part of the stratigraphic footwall at Ming (Fig. 5) is dominated by quartz-phyric rhyodacite (Fig. 6a), with minor intercalated beds of fine rhyodacitic tuff to coarse lapilli tuff (unit 1.1). This unit has a minimum thickness of 150 m and has transitional to sharp contacts with the flows. The rhyodacite is massive with up to 15 vol % quartz phenocrysts (≤5 mm in size). Overlying unit 1.1 is a sequence predominantly

composed of volcaniclastic rocks (unit 1.2) ranging from a dominantly fine tuff in the southeast (Ming South zone) to a tuff breccia in the northwest (1807 zone) (Fig. 6b and c). Unit 1.2 is ~100 m thick and consists of several volcaniclastic sequences with subrounded and intermediate tuffaceous fragments that are elongated due to deformation. Quartz porphyroclasts occur both in the matrix and the latter fragments with similar abundance to rocks of unit 1.1. Units 1.1 and 1.2 contain discordant sulphide stringer veins, such as the Lower Footwall zone (Fig. 6d), and stratiform to discordant semi-massive to massive sulphide. The semi-massive to massive sulphide lenses have a maximum thickness of 11 m (average ~4 m), with >30 metal-bearing minerals (Brueckner et al., 2014b), with pyrite, chalcopyrite, pyrrhotite, and sphalerite most common with quartz gangue.

The Ming South zone contains two stratabound and stratiform massive sulphide lenses separated by three ≤10 m thick discrete beds of rhyodacitic tuff (unit 1.3; Fig. 6e). The tuff beds are quartz-bearing (Fig. 6f), light to dark grey, and cut by chalcopyrite-pyrite-quartz stringer veins (<2 vol. % of the rock). The upper and lower sulphide lenses in the Ming South zone have different mineral assemblages; the lower lens has chalcopyrite, sphalerite, and galena, whereas the upper lens has pyrite and chalcopyrite. The grades in the lower lens average 3.58 wt. % Cu and 4.8 g/t Au, and the upper lens averages 0.78 wt. % Cu and 1.2 g/t Au (averaged sulphide assays from five diamond drill holes; RM06-04c, d, e, g, and RM05-09, L. Pilgrim, unpublished data, 2015), in agreement with the dominant sulphides mineralogy.

The massive sulphides in the 1806 and 1807 zones are immediately stratigraphically overlain by a dark grey mafic tuff breccia with sulphide clasts (unit 2; Fig. 6g). The matrix is fine-grained and biotite-rich and the fragments are medium-grained pyrite-quartz clasts, quartz-altered aphanitic felsic volcanic clasts, and epidote-altered mafic volcanic clasts. The fragments are subrounded, elongated, and up to 5 cm in length. Unit 2 is overlain by the regionally extensive magnetite-rich siltstone (unit 3; Fig. 6h).

Three generations of mafic to intermediate sills and dykes have intrudes the deposit, and they cross-cut all styles of mineralization each dyke generation has a distinctive lithogeochemical signature (Pilote et al., 2014). The dykes have similar geochemical affinities to the rocks of the Snooks Arm Group (Pilote, unpublished data, 2014) and are cogenetic with them.

The Baie Verte Peninsula was affected by three phases of regional deformation, but only the last two are recognized at Ming. In the deposit, the D_2 deformation is defined by an east-west-striking cleavage to a penetrative schistosity (S_2) that is axial-planar to megascopic east-trending open to tight F_2 folds, with strong L > S fabrics. The north-dipping, south-directed Rambler Brook Fault and Scrape Thrust (Fig. 2), are interpreted to be D_2 structures (Castonguay et al., 2009). The D_3 deformation is characterized by open, upright cross folds with axial planes trending north-northeast. The elongated-shape of the orebodies (Fig. 2 and 3) is in large part due to the S_2 stretching (L_2) and superimposed effect of D_3 deformation (Castonguay et al., 2009).

Hydrothermal Alteration Assemblages

The Ming stratigraphic footwall rocks contain seven alteration assemblages that have distinctive mineralogy and relative abundances of key minerals (Table 1), with a strong lateral and vertical alteration zonation. Immediately above and below the 1806 and 1807 zone massive sulphide lenses, the rocks have grey-coloured quartz-pyrite alteration (Fig. 7a) with samples containing up to 92 wt. % SiO_2 (Pilote, unpublished data, 2014).

The footwall of the 1807 zone contains a distinct salmon pink-coloured quartz-calcite-Mn-rich garnet alteration assemblage that extends up to 10 m stratigraphically below the massive sulphides (Fig. 7b and 8). This mineral assemblage is comprised of fine-grained (≤100 μm) polygonal quartz and idioblastic garnet. This alteration overprints a sericite-quartz-altered, quartz-bearing, medium-grained felsic tuff (unit 1.2).

A sericite-green mica-sulphide assemblage occurs in all zones within 30 m of the massive sulphide lenses (Fig. 7c). This alteration assemblage is cut by discordant stringers of pyrite-chalcopyrite-sphalerite-galena with trace electrum, sulphosalts, and tellurides (up to 10 vol. %). This assemblage also contains trace euhedral magnetite and syn-D_2 garnet and biotite porphyroblasts. Green mica is more abundant in the Au-rich 1806 zone (≤30 vol. %) than in the other zones (≤5 vol. %). Preliminary lithogeochemical analyses indicate that green mica-bearing rocks have a higher Cr content (~1600 ppm) than the surrounding sericite-rich rock (~100 ppm) (Pilote, unpublished data, 2014).

Sericite-quartz-pyrite alteration is present in the 1806, Ming North, and Ming South zones up to ~50 m stratigraphically below the massive sulphide lenses (Fig. 7d). The assemblage is dominated by sericite, quartz, and disseminated anhedral pyrite with

minor sphalerite, biotite, epidote, ilmenite, rutile, and chlorite. Sphalerite, pyrite, and ilmenite form thin (≤1 mm), discontinuous bands within this assemblage, whereas epidote, rutile, and biotite form hypidiomorphic porphyroblasts.

A chlorite-amphibole-quartz assemblage occurs in places throughout the footwall in all zones within 50 m stratigraphically below the massive sulphides (Fig. 7e). This assemblage predominantly occurs in volcaniclastic rocks and is composed of chlorite, actinolite, and quartz with subordinate epidote, and biotite. The biotite and actinolite grains are porphyroblastic and actinolite is paragenetically later than biotite.

Below the Ming North and Ming South zones, a chlorite-sericite-quartz-sulphide alteration assemblage occurs mostly in the volcaniclastic rocks and is proximal to the chlorite-stringer zone assemblage (see below). This assemblage also contains minor biotite, epidote and apatite. This assemblage also includes ≤5 mm wide bands of fine-grained sericite and quartz veins that cut the chlorite-quartz-sulphide assemblage (Fig. 7f and g), and these bands themselves are cut by discordant <1 cm-wide pyrite, chalcopyrite, and pyrrhotite stringer veins.

Lastly, a pervasive chlorite-stringer zone alteration assemblage occurs 50 to 100 m stratigraphically below the Ming South and Ming North zones. This assemblage hosts the Lower Footwall stringer zone and is composed predominantly of chalcopyrite, pyrrhotite, pyrite, Bi-tellurides, chlorite, quartz, minor biotite, epidote, actinolite, titanite, apatite, and zircon (Fig. 7h). The sulphide minerals and Bi-tellurides form discordant and transposed to S_2 cm-scale stringer veins.

Discussion

Deposit Architecture and Preliminary Genetic Model

The nature and style of the ore and alteration of VMS deposits are partly controlled by the volcanic architecture of the host succession (Gibson et al., 1999). The Ming deposit is hosted by massive rhyodacitic and intercalated volcaniclastic rocks that grade upward into predominantly rhyodacitic volcaniclastic rocks where semi-massive to massive sulphide lenses occur. The vertical transition from unit 1.1 to 1.2 may reflect the evolution from a subaqueous flow-dome complex to an eruptive volcaniclastic succession, common for shallow marine environments and the setting of numerous VMS deposits (e.g., Allen et al., 1996; Franklin et al., 2005; Gibson, 2005; Ross and Mercier-Langevin, 2014). The lack of sedimentary rocks and/or laminated tuff in the footwall rocks (units 1.1 and 1.2) may be due to rapid emplacement and formation of the flow-dome complex.

The mineralization in the 1807, 1806, Ming North and Ming South (lower lens) zones are immediately stratigraphically underlain by a distinctive rhyodacitic fine tuff to lapilli tuff unit, suggesting that all sulphide zones formed contemporaneously. In the southeastern part of the deposit, a younger succession of intermediate tuff beds and pyrite-rich massive sulphides (upper lens) were deposited above underlying sulphide lenses (Ming South and possibly Ming North), whereas in the northwestern part of the deposit, a sulphide-rich volcanic breccia succession was formed instead, possibly coeval with the deposition of unit 1.3. The occurrence of a sulphide-rich volcanic breccia succession could indicate that flow-breccia or talus-breccia deposits formed on top, or at

the margin, of the flow-dome complex, or it could indicate the presence of a depression controlled by synvolcanic faulting.

Mineralization at Ming is hosted predominantly in volcaniclastic rocks, close to a flow-dome complex. This volcanic architecture is likely due to permeability contrasts between the coherent and volcaniclastic rocks (Pilote et al., 2014). The spatial distribution of the alteration assemblages (Fig. 8) reflects these lithofacies changes. The lithofacies changes together with the hydrothermal fluid conditions (i.e, T, P, pH, fO_2, and fS_2) were likely controlled by emplacement into relatively shallow water. The pervasive chlorite-stringer zone alteration assemblage that occurs adjacent to, and sub-parallel with the Ming North and Ming South zones, and the discordant chalcopyrite-pyrite stringer veins indicate high temperature fluid-rock interaction and ore deposition (>300°C; e.g., Lydon, 1988; Ohmoto, 1996) in the Lower Footwall zone. No such alteration occurs stratigraphically below the 1806 and 1807 zones, and this indicates that these zones were formed from lower temperature fluids and potentially distal parts of the hydrothermal system (Fig. 8; Brueckner et al., 2014a). Within 50 m of massive sulphide the alteration mineral assemblage is dominated by sericite and quartz, and this is consistent with lower temperature alteration (Fig. 8; e.g., Lydon, 1988).

Timing for mineralization and gold-enrichment

Determination of the timing of Au introduction to Au-enriched VMS (and modern seafloor massive sulphide) deposits is key to formulating and refining exploration models for such deposits and understanding their genesis. At Ming, multiple lines of evidence

suggest Au-enrichment was synvolcanic: 1) the multiple stratabound massive sulphide lenses occur at the same stratigraphic position (i.e. at the top of units 1.2 and 1.3) which reflects a stratigraphic control, favouring a syngenetic model of mineralization; 2) mafic to intermediate feeder dykes to the hanging-wall Snooks Arm Group cross-cut the massive sulphides (Pilote and Piercey, 2013; Pilote et al., 2014). These dykes and rocks of the Snooks Arm Group postdate mineralization, are deformed, and are unmineralized, indicating that Au-enrichment was likely not due to a later structural and metamorphic overprint, as these post-mineralization rocks should display Au-enrichment as well if this were the case; 3) despite deposit-scale variations in Au and Ag contents, Au and Ag are almost exclusively confined to the massive sulphides, and only locally is Au remobilization into hosting volcanic rocks documented (e.g. 1807 zone; Pilote et al., 2014). The massive sulphide and rocks above and below it are deformed with cross-cutting structures extending outside the deposit. These structures are Au-barren which, together with the evidence presented in 2), suggests that the precious metals originated in the primary ore and were not introduced by a later orogenic overprint; and 4) the Au-enriched 1806 zone and parts of the 1807 and Ming South zones are enveloped by the synvolcanic sericite-green mica-sulphide alteration assemblage. Green mica is present in some VMS systems (e.g., Que River and Hellyer: Gemmell and Fulton, 2001; LaRonde-Penna: Dubé et al., 2007). Although the evidence is circumstantial, the close association between Au-enriched ore and green mica alteration in the 1806 zone at Ming may represent a key indicator to Au-rich mineralization. The relationship of this green mica alteration with the Au-enrichment process(es) at Ming is currently under investigation.

The Au-enrichment at Ming may originate from direct magmatic-hydrothermal fluids containing Ag and Au. Based on the presence of abundant sulphosalts including Ag-bearing tennantite-tetrahedrite, stannite, boulangerite, and loellingite, and precious metal-rich phases (tellurides, miargyrite, pyrargyrite, mercurian stephanite, unnamed AgCuFeS phase, Ag-Hg ± Au alloys), Brueckner et al. (2014a) concluded the mineralization is of an intermediate-sulfidation type in which magmatic-hydrothermal fluids containing volatiles and Au were introduced by magmatic degassing of a large rhyodacitic flow-dome complex in the immediate footwall to the deposit; this model is similar to that proposed at the LaRonde Penna deposit, Quebec (Mercier-Langevin et al., 2007b).

Implications for Exploration

Numerous geological field criteria from the Ming deposit can be used to determine proximity to mineralization, and these may be useful in exploring for precious metal-rich VMS deposits elsewhere. Key criteria include: the presence of altered rhyodacitic rocks; proximal to ore, alteration assemblages are typified by sericite-green mica-pyrite and sericite-quartz-pyrite, and peripheral to mineralization, alteration is quartz-calcite-garnet; intense chlorite-stringer zone alteration occurs stratigraphically below and distal to some of the massive sulphide lenses; these lenses are commonly Cu-rich and Au-Ag-poor (e.g., Ming and East Mine deposits). It is also notable that there is a spatial "gap" between the chlorite-stringer zone alteration assemblage and the massive sulphide lenses. The Au-rich 1806 zone and parts of the Ming South and 1807 zones do

not have associated advanced argillic alteration typical of other Au-rich VMS deposits (e.g., Bousquet 2-Dumagami; Dubé et al., 2014) They do, however, contain alteration assemblages similar to those in intermediate sulphidation VMS deposits (e.g., Eskay Creek: Roth et al., 1999).-Characteristic ore minerals such as tellurides, sulphosalts, and Ag-bearing phases (e.g., occurring with gold/electrum can also be used as pathfinders for Au-enriched mineralization.

No major structural breaks have been identified southeast of the Ming deposit and there has been limited surface or subsurface outside of the immediate deposit area; therefore, the prospectivity of the area outside of the immediate deposits remains high. It is now recognized that the Ming, Rambler Main, and East deposits are located at the top of the Rambler rhyolite at the contact with the overlying rocks of the Snooks Arm Group (Castonguay et al., 2009; Skulski et al., 2010). At or near (≤5 m from massive sulphide mineralization) this contact is an iron-rich sedimentary rock (Nugget Pond horizon) that serves as a regional "favourable" horizon that is a focus of exploration in the Rambler camp.

Future Work

Our ongoing research on the Ming deposit will focus on the characterization of the petrogenesis and geochronology of the host rocks. The element mobility due to hydrothermal alteration will be characterized using lithogeochemical and optical reflectance spectroscopy on altered and unaltered host rock samples. The structural relationships will be established from detailed underground mapping to determine the

deformation history of the deposit and controls on the geometry and distribution of the ore.

Acknowledgements

This study was funded by the Targeted Geoscience Initiative (TGI-4) program of Natural Resources Canada. We sincerely thank Rambler Metals and Mining PLC (particularly L. Pilgrim and P. Legrow) for underground access and providing data. This research has also been financially supported by a Natural Sciences and Engineering Research Council of Canada (NSERC) Discovery Grant, by the NSERC-Altius Industrial Research Chair in Mineral Deposits supported by NSERC, Altius Resources Inc., and by the Research and Development Corporation of Newfoundland and Labrador. Thanks to P.-S. Ross and J.M. Peter for their careful reviews of this manuscript.

References

Allen, R.L., Weihed, P., and Svenson, S.-A., 1996, Setting of Zn-Cu-Au-Ag massive sulfide deposits in the evolution and facies architecture of a 1.9 Ga marine volcanic arc, Skellefte District, Sweden: Economic Geology, v. 91, p. 1022-1053.

Brueckner, S.M., Piercey, S.J., Sylvester, P.J., Maloney, S., and Pilgrim, L., 2014a, Evidence for Syngenetic Precious Metal Enrichment in an Appalachian Volcanogenic Massive Sulfide System: The 1806 Zone, Ming Mine, Newfoundland, Canada: Economic Geology, v. 109, p. 1611-1642.

Brueckner, S., Piercey, S., Layne, G., Piercey, G., and Sylvester, P., 2014b, Variations of sulphur isotope signatures in sulphides from the metamorphosed Ming Cu(−Au) volcanogenic massive sulphide deposit, Newfoundland Appalachians, Canada: Mineralium Deposita. doi: 10.1007/s00126-014-0567-7.

Castonguay, S., Skulski, T., van Staal, C., and Currie, M., 2009. New insights on the structural geology of the Pacquet Harbour group and Point Rousse complex, Baie Verte peninsula, Newfoundland: Current Research Newfoundland and Labrador Department of Natural Resources, Geological Survey, Report 09-1, p. 147-158.

Cawood, P. A., van Gool, J. A. M., and Dunning, G. R., 1993, Silurian age for movement on the Baie Verte Line: Implications for accretionary tectonics in the Northern Appalachians: Geological Society of America, Abstract with Programs, v. 25, p. A422.

Dubé, B., Mercier-Langevin, P., Hannington, M.D., Lafrance, B., Gosselin, G., and Gosselin, P., 2007, The LaRonde Penna world-class Au-rich volcanogenic massive sulfide deposit, Abitibi, Quebec; mineralogy and geochemistry of alteration and implications for genesis and exploration: Economic Geology, v. 102, p. 633-666.

Dubé, B., Mercier-Langevin, P., Kjarsgaard, I., Hannington, M., Bécu, V., Côté, J., Moorhead, J., Legault, M., and Bédard, N., 2014, The Bousquet 2-Dumagami World-Class Archean Au-Rich Volcanogenic Massive Sulfide Deposit, Abitibi, Quebec: Metamorphosed Submarine Advanced Argillic Alteration Footprint and Genesis: Economic Geology, v. 109, p. 121-166.

Franklin, J.M., Gibson, H.L., Jonasson, I.R., and Galley, A.G., 2005. Volcanogenic massive sulfide deposits: Economic Geology 100th Anniversary Volume, p. 523-560.

Gemmell, J.B., and Fulton, R., 2001, Geology, genesis, and exploration implications of the footwall and hanging-wall alteration associated with the Hellyer volcanic-hosted massive sulfide deposit, Tasmania, Australia: Economic Geology, v. 96, p. 1003-1035.

Gibson, H., Morton, R.L., and Hudak, G.J., 1999, Submarine volcanic processes, deposits, and environments favorable for the loaction of volcanic-associated massive sulfide deposits: Reviews in Economic Geology, v. 8, p. 13-51.

Gibson, H.L., 2005. Volcano-hosted ore deposits: United States, Cambridge University Press: New York, NY, United States, p. 333-386.

Hibbard, L.J., 1983, Geology of the Baie Verte Peninsula, Newfoundland, Department of Mines and Energy, Government of Newfoundland and Labrador, Memoir 2, 279 p.

Lydon, J.W., 1988. Volcanogenic massive sulphide deposits Part 2: Genetic models: Geoscience Canada, v. 15, p. 43-65.

Mercier-Langevin, P., Dubé, B., Hannington, M.D., Richer-Laflèche, M., and Gosselin, G., 2007b, The LaRonde Penna Au-Rich volcanogenic massive sulfide deposit, Abitibi greenstone belt, Quebec: Part II. Lithogeochemistry and paleotectonic setting: Economic Geology, v. 102, p. 611-631.

Mercier-Langevin, P., Hannington, M.D., Dubé, B., and Bécu, V., 2011a, The gold content of volcanogenic massive sulfide deposits: Mineralium Deposita, v. 46, p. 509-539.

Mercier-Langevin, P., Hannington, M.D., Dube, B., Piercey, S.J., Peter, J.M., and Pehrsson, S.J., 2015. Precious metal enrichment processes in volcanogenic massive sulphide deposits — A summary of key features, with an emphasis on TIGI-4 research contributions, in Peter, J.M., and Mercier-Langevin, P., eds., Targeted Geoscience Initiative 4: Contributions to the Understanding of Volcanogenic Massive Sulphide Deposit Genesis and Exploration Methods Development: Geological Survey of Canada, Open File 7853, p. 117–130.

Ohmoto, H., 1996, Formation of volcanogenic massive sulfide deposits: The Kuroko perspective: Ore Geology Reviews, v. 10, p. 135-177.

Piercey, S.J., Jenner, G.A., and Wilton, D.H.C., 1997, The stratigraphy and geochemistry of the southern Pacquet Harbour Group, Baie Verte Peninsula, Newfoundland; implications for mineral exploration, *in* Current Research, (eds.) C.P.G. Pereira, and D.G. Walsh; Newfoundland and Labrador Department of Mines and Energy, p. 119-139.

Pilgrim, L., 2009, Mineral resource estimate for the Ming Mine, Newfoundland, Canada, Rambler Metals and Mining Canada Ltd., unpublished Technical Report, p. 114.

Pilote, J.-L., and Piercey, S.J., 2013, Volcanostratigraphy of the 1807 zone of the Ming Cu-Au volcanogenic massive-sulphide deposit, Baie Verte Peninsula, northern Newfoundland; Geological Survey of Canada, Current Research 2013-20, 13 p. DOI 10.4095/293128.

Pilote, J.-L., Piercey, S.J., and Mercier-Langevin, P., 2014, Stratigraphy and hydrothermal alteration of the Ming Cu-Au volcanogenic massive-sulphide deposit, Baie Verte Peninsula, Newfoundland; Geological Survey of Canada, Current Research 2014-7, 18 p., DOI 10.4095/295145.

Poulsen, K.H., and Hannington, M.D., 1996, Volcanic-associated massive sulphide gold: Geology of Canadian Mineral Deposit Types, 8, Geological Survey of Canada, p. 183-196.

Poulsen, K.H., Robert, F., and Dubé, B., 2000, Geological classification of Canadian gold deposits, Geological Survey of Canada, Bulletin 540, 113 p.

Ross, P.-S., and Mercier-Langevin, P., 2014, Igneous Rock Associations 14. The volcanic setting of VMS and SMS deposits: a review: Geoscience Canada, v. 41, p. 365-377.

Roth, T., Thompson, J.F.H., and Sillitoe, R.H., 1999, The precious metal-rich Eskay Creek deposit, northwestern British Columbia: Reviews in Economic Geology, v. 8, p. 357-373.

Skulski, T., Castonguay, S., McNicoll, V., van Staal, C., Kidd, W., Rogers, N., Morris, W., Ugalde, H., Slavinski, H., Spicer, W., Moussallam, Y., and Kerr, I., 2010, Tectonostratigraphy of the Baie Verte oceanic tract and its ophiolite cover sequence on the Baie Verte Peninsula: Current Research Newfoundland and Labrador Department of Natural Resources, Geological Survey, Report 10-1, p. 315-335.

Tuach, J., and Kennedy, M.J., 1978, The geologic setting of the Ming and other sulfide deposits, consolidated Rambler mines, Northeast Newfoundland: Economic Geology, v. 73, p. 192-206.

van Staal, C.R., and Barr, S.M., 2012, Lithospheric architecture and tectonic evolution of the Canadian Appalachians and associated Atlantic margin: *in* Tectonic Styles in Canada: The LITHOPROBE Perspective, (eds.) J.A. Percival, F.A. Cook, and R.M. Clowes; Geological Association of Canada, Special Paper 49, p. 41-96.

van Staal, C.R., Chew, D.M., Zagorevski, A., McNicoll, V., Hibbard, J., Skulski, T., Escayola, M.P., Castonguay, S., and Sylvester, P.J., 2013, Evidence of Late Ediacaran hyperextension of the Laurentian Iapetan margin in the Birchy Complex, Baie Verte Peninsula, Northwest Newfoundland: implications for the opening of

Iapetus, formation of Peri-Laurentian micro-continents and Taconic – Grampian orogenesis: Geoscience Canada, v. 40, p. 94-117.

White, J.D.L., and Houghton, B.F., 2006, Primary volcaniclastic rocks: Geology, v. 34, p. 677-680.

Williams, H., 1979, Appalachian orogen in Canada: Canadian Journal of Earth Sciences, v. 16, p. 792-807.

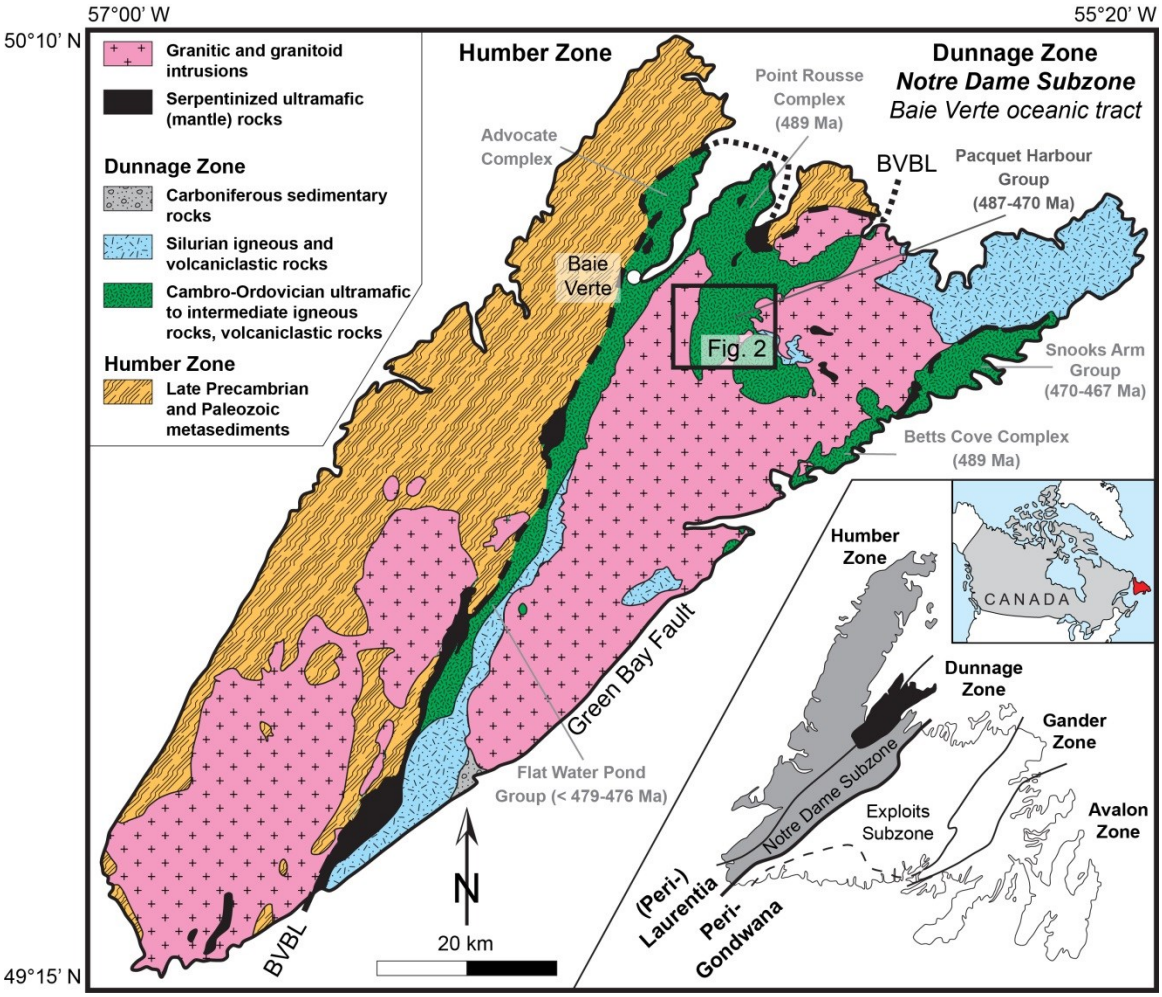

Fig. 1. Simplified geological map of the Baie Verte Peninsula (modified from Skulski et al., 2010) with the (peri-) Laurentian (inset: in grey) and (peri-) Gondwanan tectonostratigraphic zones forming the Appalachian orogenic belt in Newfoundland (Williams, 1979). BVBL = Baie Verte-Brompton Line.

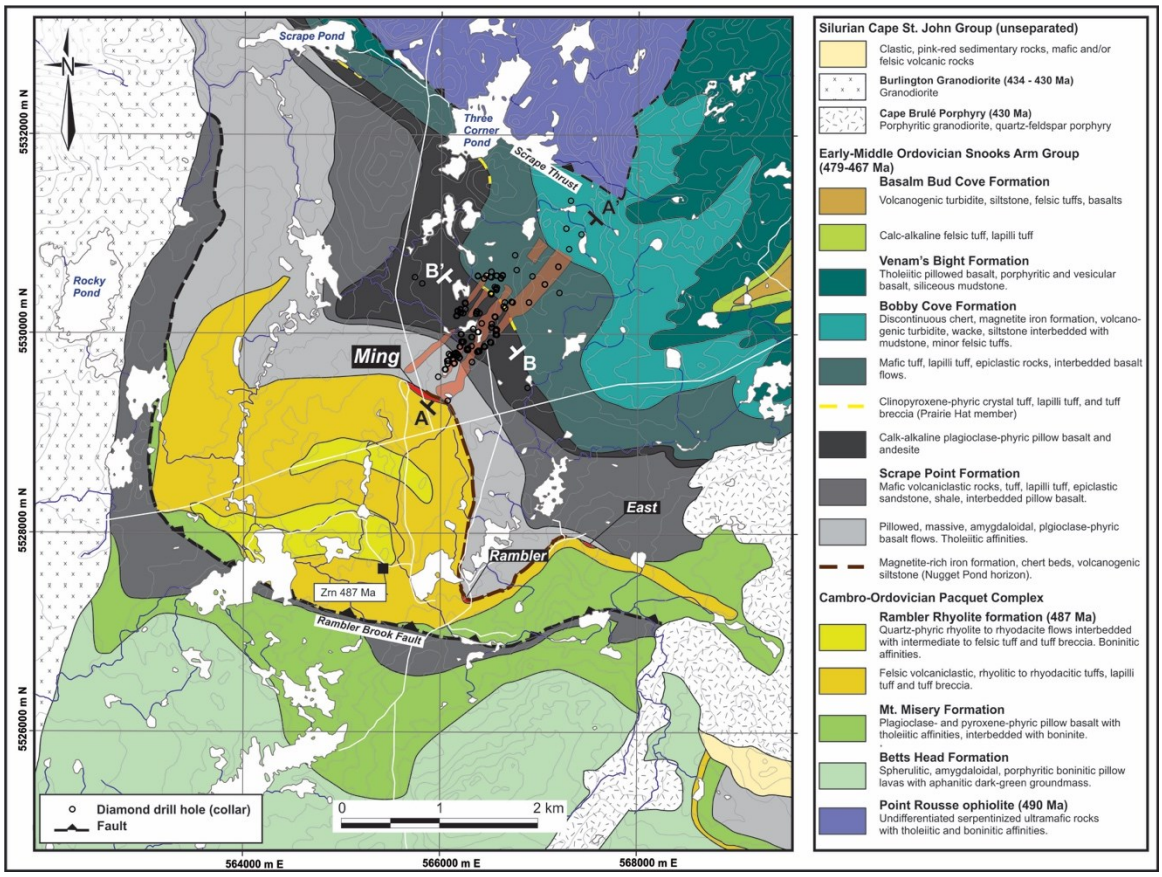

Fig. 2. Geological map of the study area, Baie Verte Peninsula, with Ming VMS orebodies projected to surface and shown in light red. Datum is UTM 21N NAD 83. Map compiled and modified from Tuach and Kennedy (1978), Hibbard (1983), Castonguay et al. (2009), Pilgrim (2009), and Skulski et al. (2010). Ages are from Cawood et al. (1993), Castonguay et al. (2009), and Skulski et al. (2010).

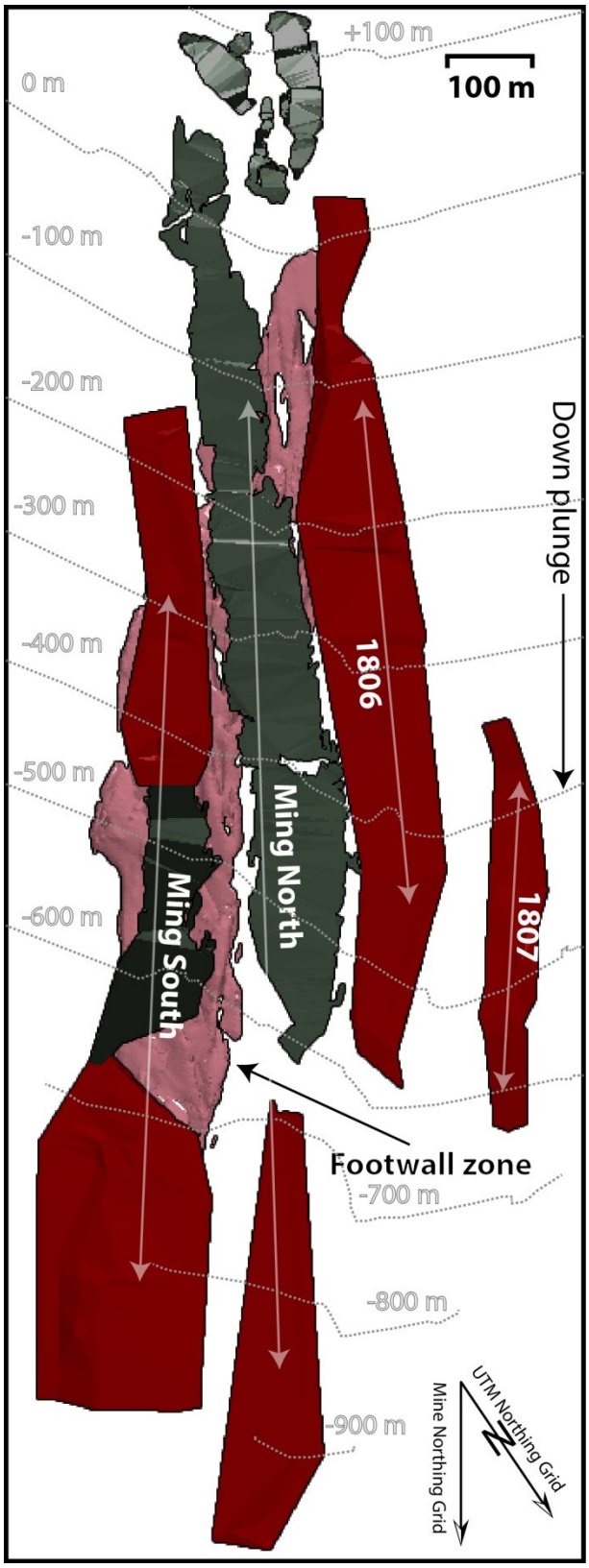
+100 m
0 m
100 m
-100 m
-200 m
-300 m
-400 m
-500 m
-600 m
-700 m
-800 m
-900 m
Down plunge
1806
1807
Ming North
Ming South
Footwall zone
UTM Northing Grid
Mine Northing Grid

Fig. 3. Plan view of 3D model of Ming orebodies projected to surface (0 m). The surface of wireframes in red represent orebodies currently in production or those that will be mined, whereas those in grey were mined in the past. Mine north is 34° east of UTM north. Model modified from Pilgrim (2009).

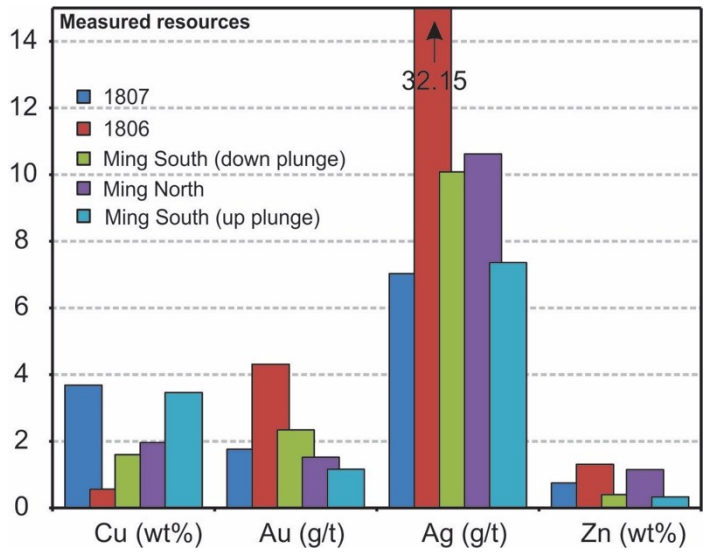

Fig. 4. Measured resources of Cu (wt%), Au (g/t), Ag (g/t), an Zn (wt%) for the 1807, 1806, Ming South (down and up plunge), and Ming North zones. Data from Pilgrim (2009).

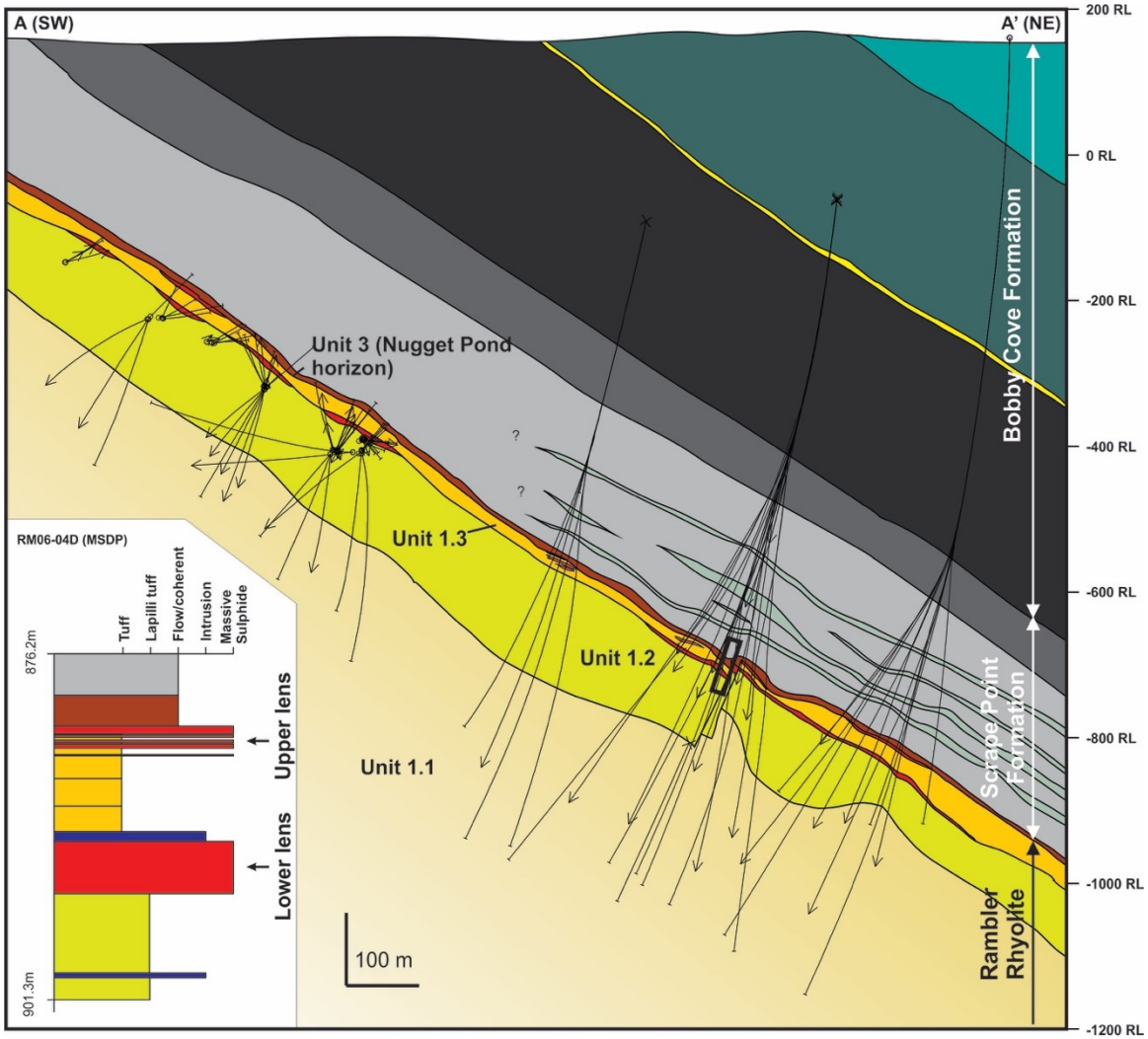

Legend

Bobby Cove Formation
Discontinuous chert, magnetite iron formation, volcanogenic turbidite, wacke, siltstone interbedded with mudstone, minor felsic tuffs.

Mafic tuff, lapilli tuff, epiclastic rocks, interbedded basalt flows.

Clinopyroxene-phyric crystal tuff, lapilli tuff, and tuff breccia (Prairie Hat member)

Calk-alkaline plagioclase-phyric pillow basalt and andesite

Scrape Point Formation
Mafic volcaniclastic rocks, tuff, lapilli tuff, epiclastic sandstone, shale, interbedded pillow basalt.

Pillowed, massive, amygdaloidal, plgioclase-phyric basalt flows. Tholeiitic affinities/intercalated epiclastic sandstone

3 — Magnetite-rich iron formation, chert beds, volcanogenic siltstone (Nugget Pond horizon).

Ming South massive sulphide lenses

Ming footwall (Rambler Rhyolite formation)

1.3 — Quartz-phyric rhyodacitic medium tuff with sulphide stringers (three distinct sequences)

1.2 — Quartz-phyric, fine to lapilli tuff with localized coherent rhyodacite with sulphide stringers

1.1 — Quartz-phyric to aphanitic rhyodacite intercalated with rhyodacitic volcaniclastics

Fig. 5. Simplified geological cross-section of the Ming South zone (looking southwest). The black lines represent drill hole traces from which the geology was interpreted. The dykes were omitted to simplify the map. Units 1.1, 1.2, 1.3, and 2 are described in the text. The inset shows the stratigraphy close to the mineralization from a representative drill hole (location indicated by the black box). Unit names are from Skulski et al. (2010). The Ming North, 1806, and 1807 lenses are not depicted here as they occur northwest of this cross-section.

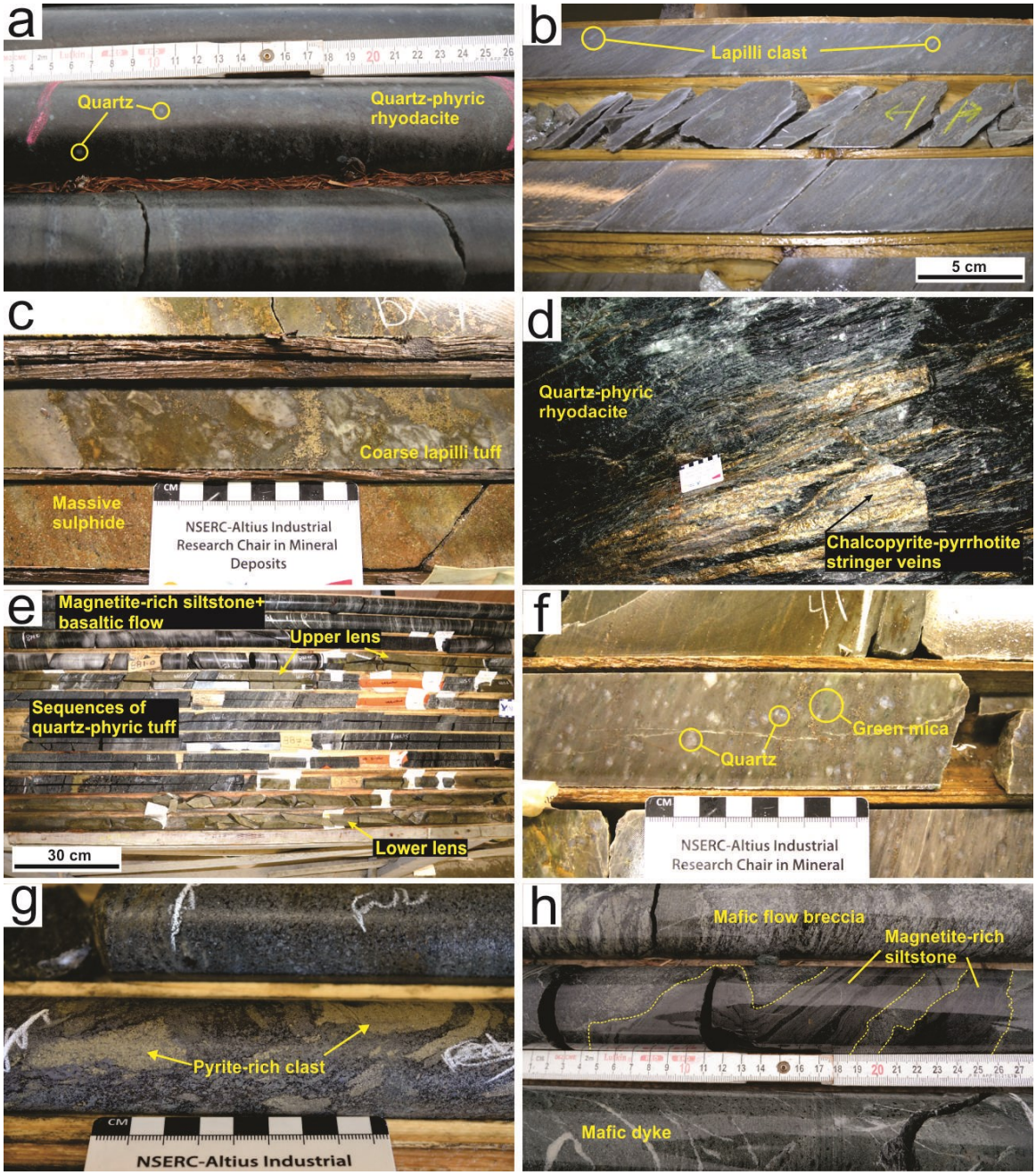
a
Quartz
Quartz-phyric rhyodacite
b
Lapilli clast
5 cm
c
Coarse lapilli tuff
Massive sulphide
NSERC-Altius Industrial Research Chair in Mineral Deposits
d
Quartz-phyric rhyodacite
Chalcopyrite-pyrrhotite stringer veins
e
Magnetite-rich siltstone+ basaltic flow
Upper lens
Sequences of quartz-phyric tuff
30 cm
Lower lens
f
Green mica
Quartz
NSERC-Altius Industrial Research Chair in Mineral
g
Pyrite-rich clast
NSERC-Altius Industrial
h
Mafic flow breccia
Magnetite-rich siltstone
Mafic dyke

Fig. 6. Representative and selected underground and drill core photographs of the different units in the Ming footwall. a) Coherent quartz-phyric rhyodacite from the Ming North footwall (unit 1.1; DDH RM09-22, 612.5 m depth). Scale is in cm. b) Rhyodacitic tuff to lapilli tuff typical of the Ming South zone footwall (unit 1.2; RM04-04, 1036.5m depth). c) Coarse lapilli tuff with the matrix replaced by sulphides immediately below the 1806 massive sulphide lens (unit 1.2; RMUG08-140; 40.5 m depth). Scale is in cm. d) Transposed sulphide (chalcopyrite+pyrrhotite) stringer veins cutting a quartz-phyric rhyodacite in the Lower Footwall zone (1450 Level). Scale is in cm. e) Drill core intersection showing the upper and lower sulphide lenses of the Ming South zone, separated by quartz-phyric tuff beds. The upper lens is overlain by magnetite-rich siltstone and basalt (unit 1.3; RM06-04D, starting at 876.2 m depth). f) Quartz-bearing rhyodacitic tuff with minor green mica, representative of unit 1.3, between the lower and upper sulphide lenses of the Ming South zone (RMUG08-25, 42.5 m depth). g) Polymictic mafic tuff breccia with up to 20 vol. % pyrite-rich clasts. This unit occurs above the 1806 and 1807 zones (Unit 2; RMUG13-205, 34 m depth). Scale is in cm. h) Folded magnetite-rich siltstone bed part of the Nugget Pond horizon (unit 3), overlain by a mafic flow breccia. This unit is extensive and occurs at or near the contact with the Ming deposit (RM09-22, 40 m depth). Scale is in cm.

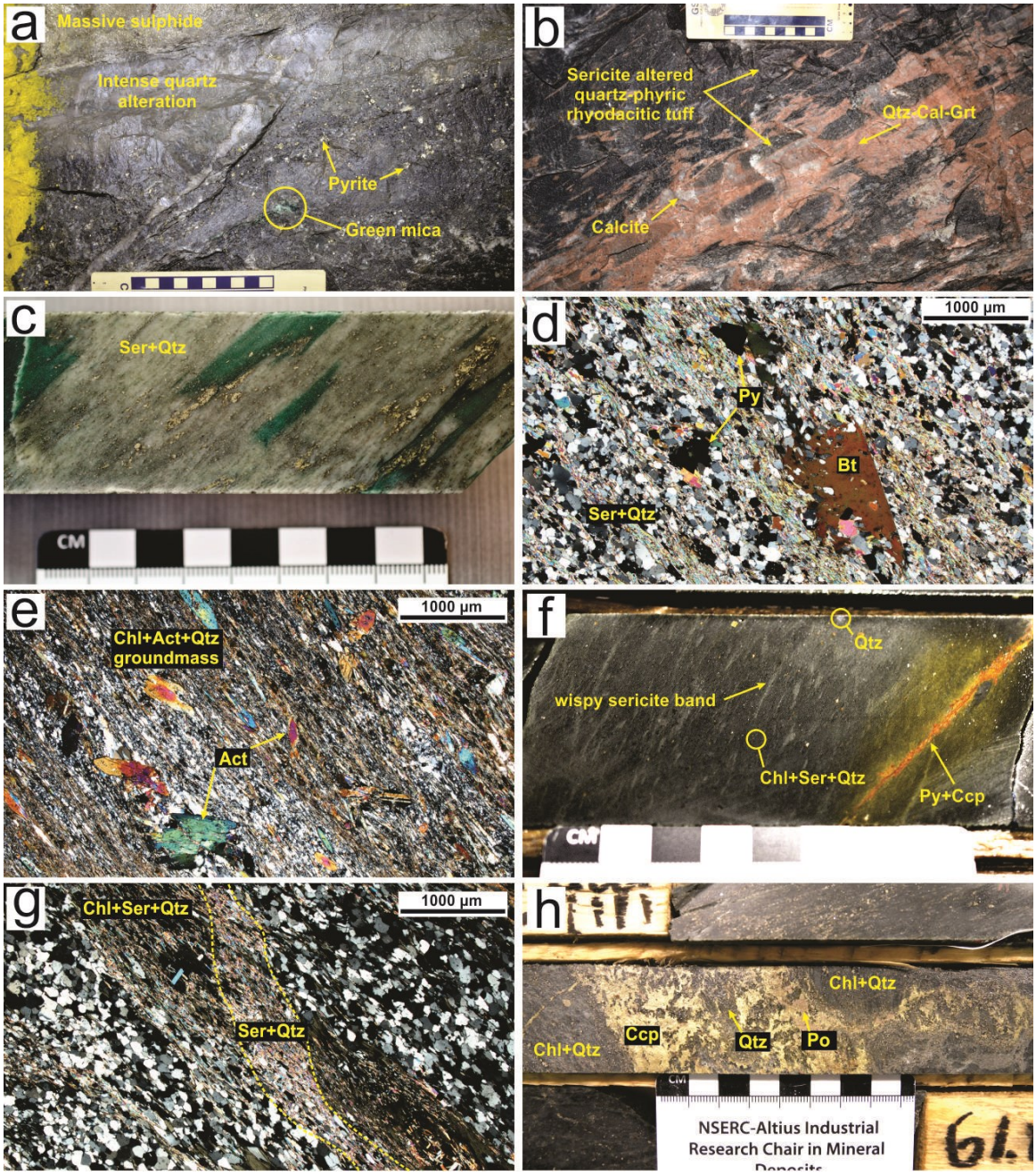
a
Massive sulphide
Intense quartz alteration
Pyrite
Green mica
b
Sericite altered quartz-phyric rhyodacitic tuff
Qtz-Cal-Grt
Calcite
c
Ser+Qtz
CM
d
1000 µm
Py
Bt
Ser+Qtz
e
1000 µm
Chl+Act+Qtz groundmass
Act
f
Qtz
wispy sericite band
Chl+Ser+Qtz
Py+Ccp
CM
g
Chl+Ser+Qtz
1000 µm
Ser+Qtz
h
Chl+Qtz
Ccp
Qtz
Po
Chl+Qtz
NSERC-Altius Industrial Research Chair in Mineral

Fig. 7. Representative and selected underground and drill core photographs and photomicrographs of the different alteration styles characterizing the Ming footwall rocks. a) View looking south in level 329 (1807 zone) of the silica-pyrite alteration overprinting the weakly sericitized ±green mica rhyodacitic tuff. b) View looking southwest of a Mn-altered (Mn-garnet, quartz and calcite) quartz-phyric rhyodacitic tuff underlying the massive sulphide (level 481, 1807 zone). c) Drill core showing intense sericite-green mica-pyrite alteration in the 1806 zone (RMUG14-261, 28.6 m depth). d) Photomicrograph illustrating the close relationship between quartz, sericite, disseminated pyrite and biotite porphyroblasts in the sericite-quartz-pyrite alteration assemblage (sample 60553; RM05-08, 1054 m depth). e) A fine-grained groundmass composed of chlorite-actinolite-quartz with randomly oriented actinolite porphyroblasts (sample 62515; RM07-18, 729 m depth). f) Wispy sericite bands cutting an intense chlorite-sericite-quartz altered quartz-phyric rhyodacite. These are in turn cut by a pyrite-chalcopyrite stringer vein (RM05-08, 1275 m depth). g) A photomicrograph of f) showing the relationship between the chlorite-sericite-quartz alteration assemblage cut by a later vein of sericite-quartz. h) Intense chlorite alteration cut by discordant chalcopyrite-pyrrhotite-quartz-rich veins representative of the chlorite-stringer zone alteration assemblage (RMUG14-250, 59.5 m depth).

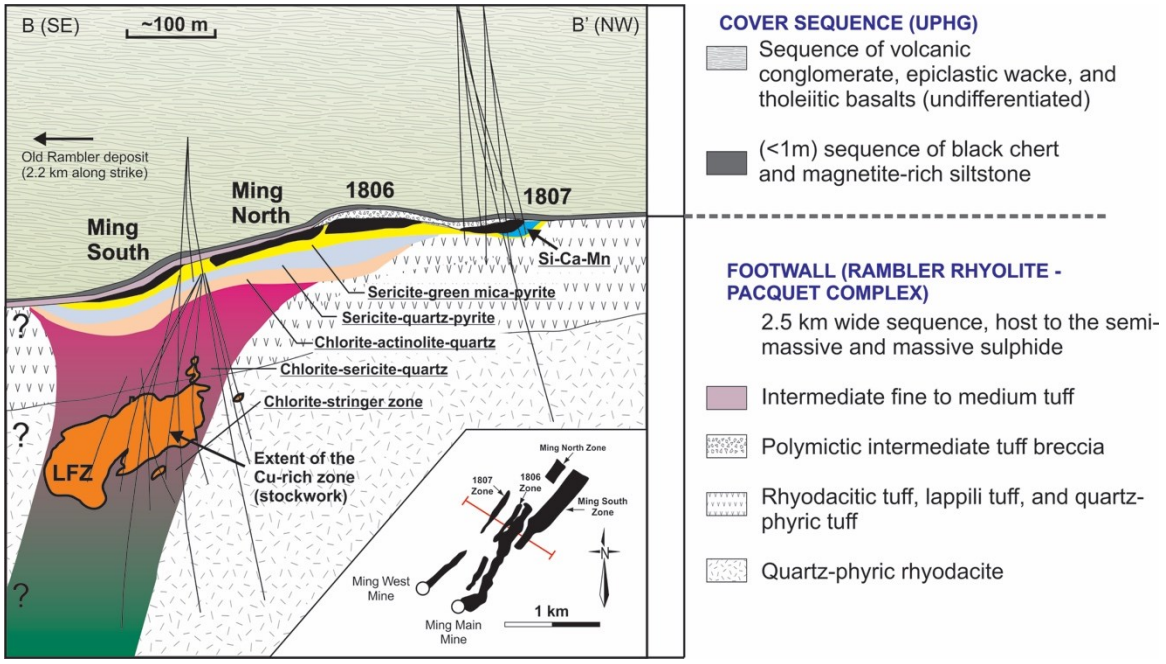

Fig. 8. Simplified geological cross-section (looking southwest) of the Ming deposit. The distribution of the alteration assemblages, described in more detail in the text, was defined using petrographic, hyperspectral and geochemical analyses (Pilote, unbublished data, 2014) from numerous diamond drill holes (black lines) and undeground mapping.

Table 1. Charateristics of the Alteration Assemblages of the Ming Deposit.

Mineralogical assemblage	Main minerals (vol %)	Associated minerals (minor and traces)	Distribution
1. Quartz-pyrite	Quartz (≤90%), pyrite (≤10%)	Green mica	Immediately above and below the massive sulphide of the 1806 and 1807 zones
2. Quartz-calcite-garnet	Quartz (≤40%), Calcite (≤20%), garnet (≤40%)	Epidote (≤10%)	1807 zone to a maximum depth of 10 m
3. Sericite-green mica-pyrite	Sericite (≤40%), green mica (≤30%), pyrite (≤20%), quartz (≤10%)	Biotite, garnet, magnetite, chalcopyrite, sphalerite, galena, electrum, sulfosalts, tellurides	In all zones to a depth of 30 m
4. Sericite-quartz-pyrite	Sericite (≤45%), quartz (≤40%), pyrite (≤5%)	Sphalerite, biotite, epidote, ilmenite, rutile, and chlorite	1806, Ming North, Ming South to a maximum depth of 50 m
5. Chlorite-actinolite-quartz	Chlorite (≤40%), actinolite (≤20%), quartz (≤20%)	Epidote (≤10%), biotite (≤10%)	Sporadically throughout all zones but mainly 1806, Ming North and Ming South
6. Chlorite-sericite-quartz-sulphide	Chlorite (≤45%), sericite (≤45%), quartz (≤10%)	Biotite, epidote, apatite, pyrite, chalcopyrite, pyrrhotite	Below Ming South and Ming North at a minimum depth of 50 m
7. Chlorite-stringer zone	Chlorite (≤45%), quartz (≤45%)	Biotite, epidote, actinolite, titanite, apatite, zircon, epidote, chalcopyrite, pyrrhotite, pyrite, Bi-telluride	Below Ming South and Ming North at a minimum depth of 50 m

Appendix 4.
Complete Dataset of Least-Altered Samples from the Rambler Rhyolite Formation and Surrounding Units

Table A4. Complete Dataset of Least-Altered Samples from the Rambler Rhyolite Formation and Surrounding Units

Sample ID	62520	62521	106407	29888	29897	60502	60503	60504	60510	60511	60516
Hole ID	RM07-18	RM07-18	RM09-22	RM08-151	RM07-20H	-	-	-	-	-	-
Level	-	-	-	-	-	329	329	329	444	444	434
Depth (m)	815.20	823.00	611.8	46.61	668.27	329	329	329	444	444	434

Unit	Unit 1.1	Unit 1.1	Unit 1.1	Unit 1.2	Unit 1.2	Unit 1.2	Unit 1.2	Unit 1.2	Unit 1.2	Unit 1.2	Unit 1.2
SiO_2 (wt %)	71.98	69.67	72.85	75.85	74.51	58.71	70.66	65.76	70.86	68.62	59.08
Al_2O_3	12.10	13.12	12.53	13.06	11.22	14.72	13.27	13.06	11.34	14.98	17.45
$Fe_2O_{3(total)}$	4.60	4.96	3.87	2.05	4.90	12.39	7.43	8.15	5.60	5.30	7.30
$FeO_{(total)}$[1]	4.14	4.46	3.48	1.84	4.41	11.15	6.69	7.33	5.04	4.77	6.57
MnO	0.054	0.064	0.038	0.024	0.185	0.289	0.121	1.283	0.498	0.187	0.047
MgO	2.42	3.53	2.88	1.45	0.75	2.96	0.71	1.95	1.03	1.25	3.34
CaO	2.36	3.08	1.16	1.45	2.99	4.47	2.04	3.27	3.21	1.55	3.79
Na_2O	4.11	4.01	4.06	4.91	2.55	2.03	4.39	2.85	3.17	3.93	3.22
K_2O	0.22	0.54	0.34	0.86	1.59	2.12	1.19	1.68	1.25	2.58	2.27
TiO_2	0.232	0.224	0.176	0.184	0.174	0.223	0.239	0.196	0.174	0.236	0.329
P_2O_5	0.05	0.05	0.05	0.06	0.05	0.03	0.07	0.11	0.06	0.06	0.01
LOI	1.39	1.45	1.74	0.87	1.74	1.55	0.43	0.64	1.50	1.16	1.89
Total	99.52	100.70	99.68	100.80	100.70	99.48	100.60	98.95	98.68	99.83	98.72
Sr (ppm)	126	148	64	84	100	176	123	152	157	102	221
Sc	17	20	15	18	14	25	20	16	14	20	28
Zr	66	66	58	57	57	60	61	61	55	66	77
Ba	35.4	61.0	46.3	97.0	808.6	322.6	164.2	693.8	863.8	1044.4	166.5
Y	6.74	7.55	5.48	5.88	7.33	6.79	9.52	4.22	7.17	7.41	8.74
Nb	3.97	4.04	1.71	1.22	3.02	3.72	3.55	3.41	2.80	3.49	4.38
Cs	0.18	0.84	0.26	0.74	0.62	0.74	0.27	0.71	0.54	0.88	1.10
La	8.85	10.51	6.41	5.15	6.90	6.79	9.43	6.43	6.97	8.57	8.98
Ce	18.42	21.06	13.37	10.39	13.61	17.48	19.84	22.19	12.80	17.43	21.14
Pr	1.98	2.22	1.52	1.30	1.69	1.71	2.19	1.69	1.61	2.08	2.13
Nd	6.99	8.26	5.83	4.64	6.17	6.29	8.11	5.86	5.86	7.43	7.79
Sm	1.42	1.56	1.12	0.94	1.39	1.42	1.78	1.29	1.27	1.57	1.58
Eu	0.35	0.44	0.31	0.24	0.30	0.35	0.41	0.41	0.38	0.44	0.46
Gd	1.22	1.38	1.08	0.85	1.18	1.35	1.53	1.03	1.41	1.34	1.53
Tb	0.22	0.22	0.18	0.14	0.19	0.23	0.26	0.18	0.21	0.21	0.26
Dy	1.22	1.30	1.01	0.95	1.35	1.41	1.74	1.06	1.36	1.32	1.59
Ho	0.27	0.29	0.22	0.23	0.27	0.32	0.38	0.22	0.29	0.28	0.34
Er	0.84	0.89	0.67	0.73	0.84	1.01	1.15	0.56	0.87	0.93	1.00
Tm	0.15	0.13	0.12	0.17	0.17	0.20	0.19	0.11	0.15	0.15	0.18
Yb	0.89	0.92	0.69	0.87	0.88	1.29	1.43	0.67	1.03	0.93	1.10
Lu	0.13	0.16	0.13	0.13	0.13	0.22	0.22	0.11	0.19	0.16	0.15
Ta	bdl	bdl	bdl	0.10	0.23	bdl	bdl	bdl	bdl	bdl	bdl
Tl	0.08	0.12	0.05	1.88	0.84	6.07	2.67	3.69	1.09	3.07	6.12
Pb	6.8	4.4	3.3	48.7	29.0	56.3	21.2	14.8	11.3	20.0	36.8
Bi	0.08	0.06	0.02	0.08	0.18	0.67	0.33	0.30	0.13	0.77	0.26
Th	3.74	4.20	2.86	2.11	2.29	3.04	2.79	3.34	2.63	2.95	3.89
U	1.50	1.69	1.08	3.15	0.92	0.25	0.72	0.12	0.34	0.20	0.38
V	44.8	82.5	65.4	105.7	75.8	97.1	135.6	60.5	52.8	76.6	113.9
Cr	92.3	152.4	56.8	234.9	19.0	304.7	48.0	20.0	26.2	14.4	82.3
Co	10.8	12.8	7.8	3.2	9.2	16.4	9.6	12.3	10.8	7.7	12.5
Ni	22.2	33.5	12.4	28.7	6.3	55.8	15.0	18.4	10.0	10.4	30.2
Cu	61	62	22	10	21	289	192	91	23	457	42
Zn	104	53	48	174	65	164	100	152	83	220	196
As	1.5	bdl	0.5	2.1	4.7	4.0	4.4	4.1	2.7	2.3	2.4
Sn	0.8	0.8	0.4	0.5	0.6	0.7	0.8	0.7	0.7	1.0	1.0
Sb	0.2	0.1	bdl	0.4	0.4	1.7	0.9	0.4	0.5	0.6	0.8
Ti[2]	3871	3738	2937	3070	2903	3721	3988	3270	2903	3938	5490

Table A4. Complete Dataset of Least-Altered Samples from the Rambler Rhyolite Formation and Surrounding Units *(continued)*

Sample ID	60585	60588	60594	60595	62080	62082	62193	62194	62198	62505	62508
Hole ID	RM07-20M	RM07-20M	RM07-20K	RM07-20K	-	-	-	-	-	RM07-18	RM07-18
Level	-	-	-	-	469	469	481	481	481	-	-
Depth (m)	670.80	686.00	681.15	698.60	469	469	481	481	481	652	685
Unit	Unit 1.2	Unit 1.2	Unit 1.2	Unit 1.2	Unit 1.2	Unit 1.2	Unit 1.2	Unit 1.2	Unit 1.2	Unit 1.2	Unit 1.2
SiO_2 (wt %)	71.53	75.39	59.99	63.46	70.48	71.24	70.34	69.52	75.81	67.40	72.35
Al_2O_3	13.57	11.44	14.64	14.91	15.05	12.93	14.76	13.45	12.56	13.68	12.85
$Fe_2O_{3(total)}$	5.82	4.17	11.77	8.02	4.43	4.31	4.21	5.64	3.50	5.88	4.42
$FeO_{(total)}$[1]	5.24	3.75	10.59	7.22	3.99	3.88	3.79	5.08	3.15	5.29	3.98
MnO	0.023	0.037	0.250	0.078	0.027	0.028	0.027	0.031	0.070	0.089	0.042
MgO	0.76	0.98	2.92	4.43	1.37	0.87	1.37	1.88	0.63	3.20	0.99
CaO	2.65	2.40	2.70	4.24	2.72	3.13	3.11	4.07	1.63	3.88	3.57
Na_2O	3.29	3.99	4.39	3.20	4.44	4.04	2.28	2.80	3.46	4.18	3.53
K_2O	1.99	0.89	0.72	0.60	1.47	1.08	2.49	1.73	1.56	0.35	1.12
TiO_2	0.203	0.194	0.216	0.169	0.246	0.197	0.226	0.212	0.190	0.178	0.193
P_2O_5	0.07	0.07	0.02	0.03	0.04	0.05	0.05	0.03	0.05	0.04	0.06
LOI	0.96	0.73	0.90	1.78	0.50	0.51	0.94	0.66	0.76	0.79	0.25
Total	100.90	100.30	98.51	100.90	100.80	98.39	99.81	100.00	100.20	99.67	99.38
Sr (ppm)	102	136	149	182	207	170	202	178	95	202	182
Sc	17	15	33	34	21	16	18	17	16	27	16
Zr	65	57	55	48	71	54	70	64	56	52	64
Ba	172.3	299.4	319.8	99.8	438.8	148.2	249.1	116.1	615.5	39.9	108.2
Y	6.68	7.25	3.46	3.93	7.16	6.98	6.37	9.33	8.25	5.08	8.92
Nb	3.36	2.76	3.00	2.30	4.03	2.86	3.42	2.87	3.21	2.74	3.30
Cs	0.62	0.99	1.03	0.58	0.68	0.72	0.88	0.91	0.48	0.34	0.71
La	7.30	7.00	6.35	5.51	7.22	8.41	7.43	8.57	6.77	6.64	8.17
Ce	15.09	13.93	15.82	12.25	15.08	16.39	16.47	16.85	14.20	13.66	16.73
Pr	1.73	1.64	1.47	1.31	1.75	1.92	1.79	1.92	1.66	1.57	1.90
Nd	6.31	5.91	5.15	4.75	6.60	7.04	6.60	7.28	5.85	5.77	6.84
Sm	1.35	1.25	0.96	0.93	1.42	1.44	1.42	1.49	1.32	1.13	1.47
Eu	0.36	0.38	0.27	0.26	0.38	0.47	0.41	0.45	0.35	0.29	0.36
Gd	1.24	1.26	0.79	0.88	1.30	1.33	1.31	1.52	1.33	0.93	1.37
Tb	0.21	0.20	0.13	0.13	0.22	0.21	0.22	0.26	0.22	0.15	0.23
Dy	1.29	1.21	0.75	0.76	1.36	1.41	1.34	1.67	1.35	0.86	1.52
Ho	0.27	0.27	0.14	0.16	0.28	0.29	0.27	0.37	0.29	0.19	0.33
Er	0.79	0.84	0.42	0.49	0.81	0.85	0.78	1.19	0.94	0.58	1.05
Tm	0.12	0.13	0.08	0.09	0.15	0.17	0.14	0.20	0.16	0.11	0.18
Yb	0.78	0.97	0.49	0.55	0.80	0.87	0.85	1.18	1.01	0.65	1.22
Lu	0.11	0.15	0.07	0.09	0.11	0.12	0.11	0.18	0.16	0.11	0.17
Ta	0.28	0.25	0.24	0.21	bdl	bdl	0.30	0.30	0.25	0.25	0.28
Tl	8.25	0.38	0.19	0.10	2.45	2.48	4.45	2.65	0.57	0.08	0.12
Pb	30.8	9.4	11.5	6.7	23.4	18.4	36.3	50.7	88.6	5.6	7.4
Bi	0.43	0.11	0.11	0.07	0.25	0.20	0.33	0.65	0.23	0.06	0.13
Th	2.74	2.35	2.39	2.13	3.19	2.72	3.00	2.79	2.40	2.43	2.68
U	0.56	1.00	0.20	0.62	0.48	0.74	1.57	0.49	1.14	1.20	1.22
V	104.7	65.3	162.2	146.7	69.5	43.7	62.5	99.0	61.3	173.3	62.3
Cr	20.8	25.3	155.6	107.9	24.2	17.0	20.6	36.6	16.0	60.8	31.1
Co	4.0	4.2	23.2	16.9	6.3	4.6	6.0	11.0	4.6	13.9	6.8
Ni	7.5	5.3	31.0	28.9	bdl	bdl	14.6	22.9	5.5	24.3	11.0
Cu	22	28	16	8	46	20	14	201	66	141	96
Zn	185	99	89	102	110	110	157	285	136	98	652
As	2.6	0.7	0.3	0.5	4.1	4.8	2.2	3.1	3.8	bdl	0.6
Sn	0.9	0.7	0.9	0.8	0.8	0.5	1.7	1.2	0.8	0.7	1.4
Sb	0.7	0.2	0.1	0.2	0.4	0.8	0.5	0.6	0.6	bdl	0.4
Ti[2]	3387	3237	3604	2820	4105	3287	3771	3537	3170	2970	3220

Table A4. Complete Dataset of Least-Altered Samples from the Rambler Rhyolite Formation and Surrounding Units *(continued)*

Sample ID	62511	62512	62514	62518	62501	62513	62526	60596	60598	62051	29842
Hole ID	RM07-18	RM07-18	RM07-18	RM07-18	RM07-18	RM07-18	RM06-04C	RMUG13-205	RMUG13-205	-	RM06-4E
Level	-	-	-	-	-	-	-	-	-	375	-
Depth (m)	710	716	721	795	607	720	879	27	37	375	865
Unit	Unit 1.2	Unit 1.2	Unit 1.2	Unit 1.2	Unit 1.3	Unit 1.3	Unit 1.3	Sulfide-rich mafic breccia (Unit 2)	Sulfide-rich mafic breccia (Unit 2)	Sulfide-rich mafic breccia (Unit 2)	Fe-shale (Unit 3)
SiO_2 (wt %)	69.12	61.40	63.65	60.99	60.07	65.60	71.25	43.30	54.03	50.23	48.01
Al_2O_3	12.88	14.16	13.00	10.97	17.82	15.90	14.48	17.46	17.68	18.36	16.90
$Fe_2O_{3(total)}$	5.56	7.73	6.73	8.19	8.03	3.06	2.66	6.43	10.95	11.86	8.59
$FeO_{(total)}$[1]	5.00	6.96	6.06	7.37	7.23	2.75	2.39	5.79	9.85	10.67	7.73
MnO	0.056	0.102	0.103	0.148	0.040	0.042	0.020	0.224	0.062	0.074	0.167
MgO	2.95	4.11	3.75	9.52	3.07	1.58	0.88	3.63	2.63	5.96	7.08
CaO	3.02	6.57	5.26	5.37	2.56	3.61	3.36	11.40	5.04	3.94	8.17
Na_2O	3.99	3.26	3.09	2.66	4.64	4.58	3.27	3.20	3.97	3.21	4.01
K_2O	0.73	0.64	1.54	0.10	2.06	2.05	1.39	3.55	2.34	1.31	0.69
TiO_2	0.168	0.177	0.167	0.172	0.325	0.406	0.169	1.689	1.615	1.719	0.948
P_2O_5	0.05	0.04	0.04	0.03	0.02	0.14	0.03	0.13	0.09	0.07	0.15
LOI	1.04	1.20	1.34	1.96	1.24	1.60	1.69	7.39	0.77	3.30	5.54
Total	99.56	99.39	98.67	100.10	99.87	98.58	99.19	98.40	99.18	100.00	100.30
Sr (ppm)	169	257	191	84	180	407	150	130	278	162	183
Sc	29	33	32	36	29	7	19	30	33	31	33
Zr	45	45	43	33	83	92	66	121	128	119	92
Ba	103.1	72.2	148.8	7.5	633.9	633.2	123.0	347.4	315.5	118.7	87.4
Y	5.53	4.66	4.70	4.41	6.77	5.31	4.84	18.50	18.35	15.76	18.45
Nb	2.45	2.20	2.34	1.30	3.82	2.37	1.33	1.22	4.60	2.95	4.48
Cs	1.21	1.06	1.54	0.11	0.99	0.89	0.64	0.96	1.55	1.00	1.21
La	6.56	5.99	5.80	4.20	8.92	13.14	10.47	7.93	8.03	6.55	9.28
Ce	12.97	12.05	11.62	8.24	19.47	25.85	21.16	19.19	19.74	17.43	21.06
Pr	1.46	1.44	1.37	0.99	2.12	3.12	2.24	2.74	2.93	2.52	2.64
Nd	5.31	5.13	5.03	3.71	7.63	11.50	7.88	12.30	13.21	11.53	11.87
Sm	1.03	1.07	0.97	0.85	1.57	2.20	1.48	3.28	3.59	3.05	2.92
Eu	0.28	0.32	0.27	0.22	0.45	0.63	0.57	1.34	1.31	1.01	1.00
Gd	0.94	0.87	0.81	0.73	1.43	1.64	1.14	3.73	4.03	3.49	3.25
Tb	0.14	0.14	0.14	0.11	0.21	0.21	0.19	0.59	0.67	0.55	0.53
Dy	0.92	0.84	0.85	0.78	1.36	1.14	1.06	3.74	4.25	3.56	3.52
Ho	0.20	0.18	0.19	0.17	0.28	0.22	0.20	0.80	0.85	0.68	0.74
Er	0.64	0.57	0.55	0.47	0.75	0.52	0.58	2.18	2.42	1.84	2.03
Tm	0.10	0.13	0.11	0.12	0.11	0.07	0.09	0.33	0.34	0.28	0.29
Yb	0.67	0.65	0.65	0.60	0.61	0.48	0.53	2.03	2.03	1.54	1.91
Lu	0.11	0.09	0.11	0.11	0.08	0.07	0.08	0.28	0.28	0.20	0.26
Ta	0.21	0.20	0.22	0.14	0.30	0.17	bdl	0.10	0.35	bdl	0.29
Tl	0.16	0.13	0.24	0.05	1.34	0.28	7.51	4.81	3.06	1.29	0.38
Pb	4.2	7.1	11.0	2.3	12.7	9.1	2540.5	70.5	50.7	45.0	12.6
Bi	0.17	0.19	0.14	0.10	0.07	0.14	0.22	0.49	0.53	0.58	0.09
Th	2.03	2.01	2.06	1.44	3.47	4.87	3.80	1.36	1.80	2.00	2.05
U	0.99	1.21	1.12	0.81	0.19	1.70	4.68	4.06	0.38	0.60	1.03
V	152.3	215.8	197.4	167.6	97.8	58.1	131.7	157.6	79.9	199.8	190.5
Cr	108.2	157.1	182.1	722.5	83.7	25.6	133.3	284.8	180.9	330.8	258.5
Co	13.9	19.5	20.9	36.6	11.4	7.6	7.5	19.9	26.6	26.7	33.4
Ni	27.3	42.5	51.1	152.9	23.2	12.1	13.4	53.9	40.7	99.7	80.8
Cu	86	66	56	115	6	20	158	636	353	260	118
Zn	51	83	98	94	85	60	111	139	70	164	119
As	bdl	0.5	bdl	bdl	0.8	0.4	4.3	3.2	2.5	2.6	0.7
Sn	0.9	0.5	0.9	0.4	0.9	0.6	0.9	1.0	1.3	1.3	0.9
Sb	bdl	0.2	0.2	0.1	0.3	0.3	6.3	1.6	0.7	0.9	0.4
Ti[2]	2803	2953	2787	2870	5423	6775	2820	28183	26948	28683	15818

Table A4. Complete Dataset of Least-Altered Samples from the Rambler Rhyolite Formation and Surrounding Units *(continued)*

Sample ID	29843	29877	29885	29893	29895	29896	60591	60600	36640	60590	62176
Hole ID	RM06-4E	RM08-123	RM08-150	RM08-151	RM07-20H	RM07-20H	RM07-20K	RM07-18	RMUG08-136	RM07-20K	RM05-08
Level	-	-	-	-	-	-	-	-	-	-	-
Depth (m)	873	74	76	99	653	655	652	589	52	649	990
Unit	Fe-shale (Unit 3)	Fe-shale (Unit 3)	Fe-shale (Unit 3)	Fe-shale (Unit 3)	Fe-shale (Unit 3)	Fe-shale (Unit 3)	Fe-shale (Unit 3)	Fe-shale (Unit 3)	High-Mg basalt	High-Mg basalt	High-Mg basalt
SiO_2 (wt %)	51.98	48.92	53.08	48.03	48.82	49.99	51.34	52.54	50.45	46.10	52.95
Al_2O_3	16.31	16.68	19.49	15.55	16.55	15.87	17.92	17.09	16.40	17.83	17.29
$Fe_2O_{3(total)}$	8.39	8.26	8.48	8.29	6.82	8.70	6.70	9.40	7.70	7.38	7.63
$FeO_{(total)}$[1]	7.55	7.43	7.63	7.46	6.14	7.83	6.03	8.46	6.93	6.64	6.87
MnO	0.143	0.172	0.075	0.143	0.184	0.224	0.116	0.139	0.147	0.132	0.130
MgO	7.29	2.21	2.52	3.83	4.86	3.68	3.11	6.01	8.73	4.07	7.38
CaO	6.47	12.01	7.65	9.01	10.40	10.30	8.16	5.46	4.84	9.79	6.74
Na_2O	3.81	1.80	3.87	5.56	5.18	2.09	5.96	4.21	3.57	5.84	3.36
K_2O	0.20	1.61	1.56	0.55	0.60	3.08	0.72	0.40	0.30	0.70	0.11
TiO_2	0.928	1.476	1.712	1.541	1.062	1.418	1.163	1.875	0.960	1.393	0.932
P_2O_5	0.12	0.11	0.10	0.13	0.12	0.17	0.12	0.15	0.09	0.16	0.06
LOI	4.96	5.66	2.08	8.01	5.80	5.09	3.34	2.21	5.95	6.73	2.57
Total	100.60	98.90	100.60	100.70	100.40	100.60	98.65	99.47	99.14	100.10	99.16
Sr (ppm)	181	291	361	154	228	172	270	241	149	256	252
Sc	31	30	29	27	26	27	23	30	28	28	27
Zr	106	121	125	106	81	105	94	124	73	119	82
Ba	35.3	69.7	86.3	27.3	56.9	628.5	68.0	67.9	32.2	202.3	15.0
Y	18.18	20.06	16.33	16.15	14.74	20.73	15.85	20.42	13.76	22.52	13.13
Nb	4.06	4.69	4.72	3.46	2.22	1.53	4.13	5.00	3.24	4.82	1.05
Cs	0.35	0.87	0.72	0.76	0.82	2.65	1.18	0.58	0.41	0.46	0.14
La	8.93	11.45	8.80	7.07	7.45	8.33	9.35	8.11	7.23	8.93	8.33
Ce	20.47	26.95	22.14	17.19	16.24	20.66	19.79	20.33	16.11	21.23	17.72
Pr	2.57	3.49	2.98	2.43	2.27	2.85	2.50	2.94	2.15	2.98	2.24
Nd	11.19	14.40	11.75	10.64	9.46	13.08	10.69	13.34	8.83	12.43	9.08
Sm	2.83	3.55	3.22	2.91	2.51	3.46	2.67	3.60	2.33	3.53	2.11
Eu	0.91	1.26	1.08	1.07	0.89	1.20	1.06	1.25	0.76	1.24	0.76
Gd	3.12	3.94	3.49	3.48	2.78	3.87	2.90	4.00	2.55	4.03	2.39
Tb	0.56	0.66	0.58	0.54	0.46	0.64	0.49	0.67	0.41	0.70	0.41
Dy	3.47	4.16	3.70	3.28	2.78	4.25	3.09	4.09	2.68	4.20	2.51
Ho	0.71	0.86	0.77	0.67	0.59	0.85	0.65	0.85	0.57	0.89	0.53
Er	2.02	2.41	2.02	1.90	1.64	2.32	1.75	2.33	1.55	2.57	1.52
Tm	0.29	0.37	0.33	0.27	0.31	0.36	0.24	0.36	0.30	0.37	0.27
Yb	1.92	2.12	1.73	1.52	1.52	2.09	1.61	2.04	1.54	2.26	1.36
Lu	0.25	0.26	0.21	0.21	0.22	0.29	0.22	0.28	0.20	0.35	0.20
Ta	0.24	0.32	0.41	0.30	0.22	0.13	0.34	0.41	0.25	0.34	bdl
Tl	0.14	6.07	2.47	0.81	2.66	27.49	1.75	0.75	0.68	0.08	0.07
Pb	8.4	25.7	32.2	9.3	14.7	64.5	24.7	11.4	10.7	3.7	8.3
Bi	0.10	0.16	0.11	0.05	0.15	0.44	4.21	0.20	0.12	0.07	0.10
Th	1.98	1.92	2.58	1.45	1.79	1.79	2.20	1.69	2.14	2.04	3.28
U	0.98	1.12	1.30	0.82	1.13	1.30	2.48	0.86	1.15	1.55	1.32
V	152.0	129.2	181.8	172.3	146.3	163.3	198.3	176.0	159.4	165.8	165.1
Cr	175.1	232.3	48.4	171.7	202.2	99.0	97.0	96.4	295.6	78.4	221.8
Co	26.8	23.7	18.4	28.3	27.3	29.4	18.4	28.5	32.6	18.3	35.3
Ni	69.2	68.7	28.5	84.9	69.0	44.5	31.5	36.7	131.4	19.0	100.7
Cu	62	83	26	202	108	236	85	31	74	35	124
Zn	125	115	69	77	78	102	81	102	76	61	74
As	1.0	5.0	5.1	2.6	3.8	11.1	3.7	1.7	4.6	bdl	1.3
Sn	4.3	1.3	1.3	1.0	0.9	1.1	2.0	1.0	0.8	2.6	1.0
Sb	0.3	3.0	1.1	0.3	0.6	1.6	1.3	0.2	2.1	0.1	0.7
Ti[2]	15485	24629	28567	25713	17721	23661	19406	31287	16019	23244	15551

Table A4. Complete Dataset of Least-Altered Samples from the Rambler Rhyolite Formation and Surrounding Units *(continued)*

Sample ID	29841	36316	36318	62165	62167	62175	62163	62168	62517	62196
Hole ID	RM06-4E	RM04-04	RM04-04	RM05-08	RM05-08	RM05-08	RM05-08	RM05-08	RM07-18	-
Level	-	-	-	-	-	-	-	-	-	481
Depth (m)	844	850	851	881	896	960	873	915	767	481
Unit	Th-enriched back arc basin basalt	Th-enriched back arc basin basalt	Th-enriched back arc basin basalt	Th-enriched back arc basin basalt	E-MORB	E-MORB	LREE-enriched/Low-Ti tholeiitic mafic tuff	LREE-enriched/Low-Ti tholeiitic mafic tuff	Low Nb/Yb tholeiitic gabbro (IN1)	Low Nb/Yb tholeiitic gabbro (IN1)
SiO_2 (wt %)	48.37	48.47	47.08	44.56	44.21	49.57	55.57	53.65	47.72	47.28
Al_2O_3	17.02	16.65	17.44	15.41	15.90	14.63	16.44	17.00	16.67	16.68
$Fe_2O_{3(total)}$	9.28	9.61	8.83	8.91	14.12	12.98	8.74	7.96	9.64	10.20
$FeO_{(total)}$[1]	8.35	8.65	7.95	8.02	12.71	11.68	7.86	7.16	8.67	9.18
MnO	0.144	0.144	0.135	0.155	0.169	0.179	0.141	0.111	0.154	0.156
MgO	6.40	6.39	6.02	5.56	8.05	5.89	3.91	5.86	7.37	7.85
CaO	8.93	9.41	9.01	11.59	8.61	9.07	6.27	5.48	10.32	11.15
Na_2O	4.53	4.05	4.13	3.64	3.41	2.96	4.08	3.77	3.25	2.76
K_2O	0.35	0.46	0.28	0.91	0.16	0.35	1.08	1.40	0.15	0.13
TiO_2	1.223	1.360	1.194	1.197	2.358	2.081	0.684	0.607	1.388	1.453
P_2O_5	0.12	0.14	0.12	0.10	0.24	0.26	0.20	0.13	0.14	0.14
LOI	3.56	3.05	4.62	6.54	3.07	0.51	1.32	3.52	1.74	2.87
Total	99.93	99.73	98.84	98.59	100.30	98.48	98.45	99.49	98.54	100.70
Sr (ppm)	190	226	256	223	149	230	343	215	266	233
Sc	36	34	34	32	48	39	18	20	36	36
Zr	87	96	88	77	161	147	99	78	92	101
Ba	42.2	69.1	46.0	103.1	18.4	36.2	234.9	277.9	14.4	12.6
Y	19.32	22.84	20.79	20.13	33.08	27.25	14.73	14.19	22.85	19.03
Nb	2.29	1.70	1.30	2.01	5.10	8.77	5.19	2.97	1.35	0.77
Cs	0.46	0.69	0.37	1.42	0.16	0.35	1.87	2.32	0.09	0.10
La	3.44	3.99	3.73	3.45	7.53	9.38	12.88	11.56	4.65	4.42
Ce	10.14	11.86	11.08	10.02	22.02	24.35	27.25	24.03	12.80	12.63
Pr	1.67	2.04	1.91	1.76	3.62	3.65	3.34	2.84	2.20	2.11
Nd	8.67	9.95	9.31	8.78	17.50	16.72	13.16	11.34	10.60	10.23
Sm	2.68	3.25	2.96	2.60	5.24	4.60	2.80	2.55	3.34	3.14
Eu	0.79	1.08	1.10	0.97	1.80	1.55	0.84	0.87	1.23	1.13
Gd	3.34	4.02	3.68	3.21	6.29	5.31	2.75	2.60	4.22	3.81
Tb	0.57	0.68	0.64	0.60	1.04	0.87	0.46	0.44	0.67	0.63
Dy	3.76	4.30	4.00	3.83	6.54	5.37	2.77	2.62	4.47	3.80
Ho	0.78	0.91	0.83	0.81	1.34	1.10	0.57	0.53	0.94	0.80
Er	2.21	2.51	2.41	2.34	3.61	3.02	1.62	1.59	2.69	2.18
Tm	0.31	0.41	0.36	0.40	0.55	0.41	0.23	0.26	0.40	0.32
Yb	1.98	2.15	2.01	2.02	3.20	2.63	1.60	1.42	2.31	1.95
Lu	0.28	0.31	0.28	0.28	0.44	0.37	0.22	0.20	0.36	0.27
Ta	0.13	0.15	0.12	0.14	bdl	bdl	0.33	bdl	0.10	0.06
Tl	0.14	0.27	0.18	0.26	0.03	0.13	0.29	0.57	0.05	0.03
Pb	6.3	7.5	10.7	9.0	12.5	10.8	15.3	8.9	2.2	30.1
Bi	0.08	0.10	0.09	0.09	0.22	0.14	0.17	0.11	0.07	0.11
Th	0.33	0.41	0.43	0.23	0.91	1.03	3.03	4.20	0.46	0.28
U	0.23	0.31	0.27	0.17	0.22	0.23	1.42	1.57	0.23	0.09
V	221.9	204.6	193.5	219.8	364.2	340.6	111.1	116.1	191.0	233.0
Cr	213.9	184.1	210.7	189.7	182.1	137.6	124.4	147.0	213.1	259.5
Co	33.0	33.1	33.4	33.6	51.7	39.8	19.2	22.3	37.7	42.9
Ni	53.5	49.7	54.8	45.6	65.3	43.1	55.0	69.6	90.4	105.2
Cu	62	95	81	82	341	48	227	142	111	98
Zn	94	82	78	83	101	144	80	74	91	90
As	1.0	1.3	0.8	bdl	bdl	bdl	0.5	bdl	0.5	2.7
Sn	9.3	0.7	0.6	0.7	1.5	1.3	1.0	1.2	1.0	0.6
Sb	0.4	0.6	0.5	0.3	0.4	0.7	0.2	0.3	0.2	1.5
Ti[2]	20407	22693	19923	19973	39346	34724	11413	10128	23160	24245

Table A4. Complete Dataset of Least-Altered Samples from the Rambler Rhyolite Formation and Surrounding Units *(continued)*

Sample ID	62197	60584	60589	60580	36633	29853	106416	29840	29866	36647	36648
Hole ID	-	RM07-20M	RM07-20K	RM05-08	RMUG11-170	RM06-4E	-	RMUG08-140	RM06-4E	RM04-04	RM04-04
Level	481	-	-	-	-	-	1450	-	-	-	-
Depth (m)	481	661	645	1335	39	1052	300	58	1216	322	327
Unit	Low Nb/Yb tholeiitic gabbro (IN1)	Low Nb/Yb tholeiitic gabbro (IN1)	Low Nb/Yb tholeiitic gabbro (IN1)	Low Nb/Yb tholeiitic gabbro (IN1)	Low Nb/Yb tholeiitic gabbro (IN1)	Low Nb/Yb tholeiitic gabbro (IN1)	Low Nb/Yb tholeiitic gabbro (IN1)	Intermediate Nb/Yb tholeiitic gabbro (IN2)	Intermediate Nb/Yb tholeiitic gabbro (IN2)	Intermediate Nb/Yb tholeiitic gabbro (IN2)	Intermediate Nb/Yb tholeiitic gabbro (IN2)
SiO_2 (wt %)	42.92	39.95	46.07	47.58	43.21	47.99	45.50	46.98	46.12	45.22	46.90
Al_2O_3	18.44	15.33	16.07	16.03	15.83	16.56	16.14	15.91	17.21	16.12	15.57
$Fe_2O_{3(total)}$	12.37	9.71	9.71	9.79	9.90	10.33	9.31	10.19	11.65	11.65	9.86
$FeO_{(total)}$[1]	11.13	8.74	8.74	8.81	8.91	9.30	8.38	9.17	10.48	10.48	8.87
MnO	0.178	0.145	0.144	0.159	0.152	0.158	0.133	0.151	0.173	0.191	0.145
MgO	9.72	7.85	8.88	7.69	7.38	7.77	6.76	6.84	7.48	7.52	6.99
CaO	7.18	8.20	10.01	11.88	10.12	11.94	10.43	10.45	7.44	10.93	10.04
Na_2O	2.09	4.01	2.70	2.47	2.62	2.59	3.15	2.87	3.60	2.84	3.38
K_2O	0.58	0.79	0.12	0.14	0.38	0.14	0.13	0.16	0.22	0.27	0.35
TiO_2	1.885	1.266	1.120	1.461	1.383	1.509	1.609	1.610	1.797	1.333	1.451
P_2O_5	0.18	0.12	0.12	0.15	0.14	0.14	0.15	0.16	0.18	0.13	0.14
LOI	5.28	11.04	4.25	1.57	8.28	1.64	5.85	4.24	4.80	3.15	3.74
Total	100.80	98.41	99.20	98.91	99.38	100.80	99.17	100.90	100.70	99.36	98.56
Sr (ppm)	246	199	224	248	217	254	201	283	234	430	249
Sc	45	39	35	36	35	41	34	35	38	44	35
Zr	116	87	76	100	95	105	109	109	121	76	92
Ba	49.9	96.9	17.4	11.9	46.6	12.3	8.2	17.5	35.3	41.3	71.3
Y	24.00	15.33	17.69	20.60	19.34	21.77	19.20	21.79	22.78	18.00	21.87
Nb	1.23	0.75	0.77	1.02	1.50	0.91	1.74	3.93	4.63	3.27	3.55
Cs	0.26	1.58	0.11	0.10	1.25	0.04	0.07	0.10	0.24	0.08	0.09
La	5.62	3.81	3.59	4.85	4.46	4.80	6.17	5.41	5.84	4.52	5.03
Ce	16.14	11.06	9.99	13.89	12.63	13.53	16.85	15.80	15.97	11.61	14.42
Pr	2.67	1.88	1.66	2.28	2.21	2.22	2.63	2.46	2.54	1.94	2.35
Nd	13.18	8.96	8.41	11.34	10.32	10.56	12.36	12.11	12.63	9.59	11.21
Sm	4.07	2.86	2.57	3.34	3.22	3.13	3.41	3.87	3.69	2.91	3.45
Eu	1.49	0.94	0.96	1.18	1.09	1.25	1.24	1.36	1.36	0.99	1.23
Gd	4.65	3.27	3.24	3.99	3.63	3.95	4.01	4.14	4.59	3.57	3.85
Tb	0.80	0.55	0.51	0.66	0.62	0.69	0.64	0.75	0.72	0.55	0.66
Dy	4.92	3.39	3.35	4.23	3.87	4.35	3.97	4.53	4.49	3.79	4.27
Ho	0.98	0.65	0.70	0.82	0.81	0.90	0.78	0.89	0.93	0.75	0.87
Er	2.70	1.74	2.01	2.25	2.29	2.58	2.08	2.37	2.52	2.09	2.42
Tm	0.38	0.25	0.28	0.34	0.34	0.35	0.29	0.33	0.37	0.33	0.38
Yb	2.22	1.48	1.76	2.09	1.77	2.17	1.71	2.18	2.19	1.78	2.02
Lu	0.30	0.21	0.27	0.30	0.26	0.31	0.25	0.29	0.33	0.26	0.29
Ta	0.10	0.07	0.06	0.08	0.13	bdl	bdl	0.26	0.32	0.22	0.26
Tl	0.80	1.12	0.03	0.05	0.37	0.04	0.08	0.13	0.08	0.07	0.11
Pb	38.9	25.6	5.5	8.9	17.5	10.8	13.9	10.6	7.6	2.9	3.0
Bi	0.30	0.26	0.08	0.37	0.22	0.22	0.11	0.10	0.19	0.11	0.12
Th	0.46	0.27	0.33	0.31	0.27	0.56	0.50	0.32	0.33	0.35	0.25
U	0.15	0.39	0.13	0.10	0.15	0.11	0.13	0.11	0.12	0.12	0.14
V	228.9	172.4	203.9	200.9	202.6	224.9	232.7	222.4	249.5	286.3	218.7
Cr	274.4	245.0	260.6	216.6	214.4	257.1	229.0	219.0	235.1	275.8	229.2
Co	51.1	43.8	40.6	36.6	44.7	41.6	39.9	38.0	39.4	44.6	41.2
Ni	105.1	62.6	125.5	83.7	92.1	69.8	81.3	59.0	69.8	119.6	78.8
Cu	85	515	69	142	96	126	64	103	47	72	166
Zn	153	232	87	77	128	91	82	91	134	93	86
As	8.2	5.6	0.6	0.3	2.3	69.5	5.1	1.8	bdl	0.5	bdl
Sn	1.2	0.5	0.7	0.8	0.7	0.8	1.0	1.0	1.9	0.5	0.6
Sb	2.4	0.6	0.6	0.3	0.4	0.7	2.1	0.9	0.2	0.4	0.4
Ti[2]	31453	21125	18688	24378	23077	25179	26848	26865	29985	22243	24212

Table A4. Complete Dataset of Least-Altered Samples from the Rambler Rhyolite Formation and Surrounding Units *(continued)*

Sample ID	60505	62095	62509	29865	29871	36315	60517	60583	62052	62055	62094
Hole ID	-	RM05-08	RM07-18	RM06-4E	RM07-8F	RM04-04	-	RM07-20M	-	-	RM05-08
Level	329	-	-	-	-	-	434	-	375	375	-
Depth (m)	329	656	694	1213	996	749	434	649	375	375	650
Unit	Intermediate Nb/Yb tholeiitic gabbro (IN2)	Intermediate Nb/Yb tholeiitic gabbro (IN2)	Intermediate Nb/Yb tholeiitic gabbro (IN2)	Transitional diorite (IN3)	Transitional diorite (IN3)	Transitional diorite (IN3)	Transitional diorite (IN3)	Transitional diorite (IN3)	Transitional diorite (IN3)	Transitional diorite (IN3)	Transitional diorite (IN3)
SiO_2 (wt %)	45.77	48.08	47.32	51.22	46.17	46.62	39.24	49.63	48.84	39.47	48.41
Al_2O_3	14.70	14.00	16.51	14.44	14.90	14.00	13.57	14.11	16.33	13.40	16.04
$Fe_2O_{3(total)}$	12.60	12.94	11.38	13.25	7.83	7.66	15.92	14.11	13.20	10.29	8.88
$FeO_{(total)}$[1]	11.34	11.64	10.24	11.92	7.05	6.89	14.33	12.70	11.88	9.26	7.99
MnO	0.748	0.198	0.176	0.212	0.084	0.138	0.140	0.231	0.243	0.225	0.152
MgO	6.17	6.10	6.57	5.85	3.12	8.49	3.50	5.26	7.03	4.22	8.44
CaO	8.26	11.17	11.82	8.15	11.15	12.35	7.99	9.07	5.29	12.99	8.13
Na_2O	2.10	2.38	2.21	3.75	3.17	3.13	3.13	3.17	2.01	3.23	3.44
K_2O	2.61	0.44	0.17	0.36	2.28	0.12	2.24	0.61	1.18	0.23	0.27
TiO_2	1.525	1.714	1.531	1.976	1.186	0.972	1.241	1.964	2.012	1.667	1.125
P_2O_5	0.15	0.21	0.16	0.25	0.11	0.14	0.12	0.27	0.29	0.22	0.24
LOI	5.28	1.48	2.27	1.53	9.53	4.79	11.64	1.25	4.38	10.28	2.39
Total	99.91	98.73	100.10	101.00	99.53	98.41	98.73	99.67	100.80	96.21	97.52
Sr (ppm)	169	257	256	178	152	214	76	241	162	163	287
Sc	48	45	38	49	23	41	25	43	46	33	24
Zr	88	116	95	135	114	62	87	126	135	107	111
Ba	319.8	95.8	21.6	35.6	181.2	18.4	190.4	110.7	126.5	36.8	74.0
Y	23.54	25.85	21.83	30.47	15.47	11.07	16.50	30.21	19.97	16.17	18.00
Nb	6.70	6.14	4.66	12.27	1.08	2.60	1.78	12.83	9.86	2.79	2.78
Cs	1.78	0.22	0.11	0.11	2.70	0.15	1.25	0.84	0.63	0.28	0.14
La	6.14	7.52	6.16	15.09	8.44	7.80	6.98	14.67	14.59	11.67	11.57
Ce	15.62	19.43	16.06	35.31	20.45	17.90	17.12	34.06	33.99	27.45	26.11
Pr	2.38	2.97	2.45	4.80	2.73	2.54	2.46	4.74	4.64	3.86	3.48
Nd	11.41	14.76	11.91	21.81	11.73	10.74	10.64	20.77	19.81	16.37	14.12
Sm	3.30	4.00	3.49	5.38	3.09	2.43	2.88	5.17	4.62	3.85	3.52
Eu	1.09	1.45	1.19	1.76	0.93	0.77	1.23	1.73	1.56	1.18	1.13
Gd	4.21	4.87	4.09	5.79	3.28	2.43	3.28	5.85	4.63	3.56	3.54
Tb	0.72	0.79	0.70	0.95	0.53	0.37	0.57	0.95	0.74	0.56	0.56
Dy	4.54	5.09	4.42	6.22	3.28	2.36	3.42	5.87	4.24	3.50	3.62
Ho	0.95	1.11	0.92	1.23	0.65	0.44	0.72	1.24	0.82	0.65	0.71
Er	2.66	2.96	2.50	3.45	1.71	1.33	1.91	3.36	2.22	1.81	1.94
Tm	0.39	0.45	0.37	0.47	0.27	0.21	0.27	0.50	0.35	0.31	0.32
Yb	2.36	2.50	2.29	2.93	1.52	1.09	1.64	3.16	1.69	1.46	1.76
Lu	0.29	0.39	0.33	0.41	0.22	0.15	0.25	0.42	0.25	0.20	0.22
Ta	bdl	0.34	0.32	0.66	0.08	0.21	bdl	0.78	bdl	bdl	0.20
Tl	3.47	0.06	bdl	0.18	3.36	0.06	5.74	0.25	6.92	0.45	0.07
Pb	24.9	2.3	2.7	7.8	38.8	5.0	200.4	5.9	76.1	67.4	3.5
Bi	0.22	0.07	0.08	0.18	0.63	0.10	3.62	0.08	1.32	1.16	0.10
Th	0.90	0.74	0.59	1.79	1.99	1.48	1.77	1.80	2.98	2.01	1.72
U	0.27	0.23	0.24	0.57	0.66	0.48	4.66	0.59	0.74	0.80	0.83
V	233.8	311.0	246.2	343.5	133.1	197.0	158.8	391.2	245.0	160.8	151.5
Cr	236.1	80.2	134.9	39.4	104.9	576.3	265.4	32.2	254.0	132.5	268.5
Co	47.7	41.3	33.8	37.8	23.7	36.7	62.1	41.0	47.9	36.1	37.8
Ni	50.6	43.4	65.2	23.3	38.5	91.9	64.5	22.1	72.9	55.2	156.4
Cu	74	123	78	158	bdl	126	1710	104	1260	470	31
Zn	240	103	101	107	82	59	229	132	215	117	85
As	2.7	0.7	0.7	1.8	3.8	0.5	142.3	2.0	14.9	14.8	bdl
Sn	0.9	0.8	0.7	bdl	1.5	0.3	2.1	0.7	1.1	0.6	0.9
Sb	0.7	0.4	0.3	0.3	1.0	0.3	5.5	0.4	2.5	23.2	0.2
Ti[2]	25446	28600	25546	32972	19790	16219	20707	32772	33573	27816	18772

Table A4. Complete Dataset of Least-Altered Samples from the Rambler Rhyolite Formation and Surrounding Units *(continued)*

Sample ID	62190	29954	36319	60509	60518	60565	60569	60592	62074	62076
Hole ID	-	RM08-91	RM04-04	-	-	RM05-08	RM05-08	RM07-20K	-	-
Level	481	-	-	444	434	-	-	-	469	469
Depth (m)	481	67	864	444	434	1175	1220	663	469	469
Unit	Transitional diorite (IN3)	Calk-alkaline quartz monzodiorite (IN4)	Calk-alkaline quartz monzodiorite (IN4)	Calk-alkaline quartz monzodiorite (IN4)	Calk-alkaline quartz monzodiorite (IN4)	Calk-alkaline quartz monzodiorite (IN4)	Calk-alkaline quartz monzodiorite (IN4)	Calk-alkaline quartz monzodiorite (IN4)	Calk-alkaline quartz monzodiorite (IN4)	Calk-alkaline quartz monzodiorite (IN4)
SiO_2 (wt %)	40.95	61.00	56.06	57.32	57.24	59.60	63.23	57.44	54.13	54.47
Al_2O_3	12.31	16.63	19.21	15.09	15.76	16.33	16.59	16.11	15.57	16.17
$Fe_2O_{3(total)}$	8.86	5.14	5.30	5.77	5.96	5.91	5.19	6.24	5.13	5.84
$FeO_{(total)}$[1]	7.97	4.63	4.77	5.19	5.36	5.32	4.67	5.62	4.62	5.26
MnO	0.212	0.087	0.065	0.322	0.097	0.084	0.058	0.083	0.125	0.117
MgO	7.91	2.38	2.96	4.30	4.79	3.70	2.48	4.93	5.33	4.53
CaO	11.90	4.89	5.42	5.53	5.95	5.13	4.16	5.37	5.88	6.65
Na_2O	1.96	4.57	5.26	3.58	3.93	4.36	5.20	3.91	3.63	4.99
K_2O	0.15	1.94	2.12	2.03	2.18	1.73	1.51	1.20	2.13	0.96
TiO_2	1.550	0.871	0.960	0.745	0.774	0.753	0.751	0.795	0.762	0.752
P_2O_5	0.22	0.41	0.48	0.21	0.23	0.23	0.32	0.23	0.21	0.25
LOI	12.23	2.00	1.34	4.60	3.24	2.32	1.11	2.91	5.40	6.27
Total	98.25	99.91	99.16	99.50	100.10	100.20	100.60	99.22	98.31	101.00
Sr (ppm)	131	223	339	133	218	240	502	117	297	200
Sc	27	9	13	15	17	13	11	16	17	15
Zr	98	164	192	97	102	119	185	110	101	105
Ba	36.8	510.7	355.1	822.6	292.1	361.1	293.8	192.0	263.1	184.5
Y	16.13	15.98	17.66	11.57	12.46	12.72	22.25	11.86	12.09	11.67
Nb	4.50	10.80	5.03	4.68	2.55	6.01	11.06	2.96	0.96	0.84
Cs	0.55	2.19	3.53	1.33	3.10	4.51	2.98	0.99	1.35	0.44
La	10.83	32.64	27.90	16.89	18.09	20.86	33.03	17.94	18.79	18.27
Ce	24.80	67.96	62.82	34.29	38.51	42.60	68.23	38.80	38.08	37.74
Pr	3.49	8.33	7.73	4.36	4.71	5.28	8.34	4.66	4.73	4.69
Nd	14.91	31.26	29.69	15.98	18.30	19.78	31.49	17.63	17.58	17.73
Sm	3.57	5.34	5.21	2.99	3.42	3.78	5.96	3.20	3.10	3.17
Eu	1.20	1.40	1.39	0.84	1.02	1.03	1.43	0.73	0.87	0.81
Gd	3.65	4.00	4.05	2.58	2.98	3.03	4.89	2.64	2.75	2.70
Tb	0.56	0.55	0.60	0.35	0.45	0.43	0.71	0.41	0.43	0.42
Dy	3.38	3.19	3.51	2.23	2.58	2.49	4.18	2.41	2.37	2.27
Ho	0.66	0.61	0.70	0.46	0.51	0.50	0.87	0.46	0.48	0.46
Er	1.64	1.61	1.97	1.24	1.42	1.40	2.32	1.33	1.36	1.31
Tm	0.25	0.29	0.27	0.21	0.21	0.22	0.34	0.19	0.22	0.19
Yb	1.38	1.45	1.44	1.15	1.27	1.22	2.21	1.14	1.30	1.12
Lu	0.21	0.20	0.17	0.16	0.18	0.16	0.30	0.16	0.21	0.16
Ta	0.32	0.70	0.40	bdl	bdl	0.42	0.72	0.21	bdl	bdl
Tl	1.04	0.33	0.96	1.31	10.34	1.75	0.51	2.22	13.81	5.57
Pb	70.2	9.5	15.6	9.6	55.0	8.6	40.2	19.3	139.4	101.6
Bi	6.23	0.11	0.17	0.16	0.51	0.11	0.56	0.11	35.35	5.38
Th	1.24	6.40	6.70	4.68	5.16	4.88	6.84	4.27	5.41	5.03
U	0.44	2.41	2.45	1.37	1.42	1.70	2.76	1.35	1.48	1.34
V	180.2	98.1	112.0	106.7	119.4	104.3	89.6	124.5	119.1	100.2
Cr	412.4	30.1	32.6	93.9	98.2	62.2	46.5	111.9	113.1	97.1
Co	36.0	14.7	14.2	20.0	20.5	17.7	12.3	21.1	21.2	21.0
Ni	173.8	31.1	32.7	91.0	97.3	51.0	31.5	117.6	101.6	95.4
Cu	117	30	25	105	130	90	60	12	1264	324
Zn	945	91	89	171	104	71	52	134	683	431
As	11.3	1.5	2.2	2.4	4.2	1.0	1.6	3.7	69.4	19.9
Sn	0.9	1.1	0.9	0.6	0.7	0.8	1.1	0.6	2.9	0.7
Sb	3.7	0.3	0.4	0.5	0.7	0.1	0.1	0.3	31.1	5.8
Ti[2]	25864	14534	16019	12431	12915	12565	12531	13265	12715	12548

Table A4. Complete Dataset of Least-Altered Samples from the Rambler Rhyolite Formation and Surrounding Units *(continued)*

Sample ID	62083	62164	62166	62180	62191	62510
Hole ID	-	RM05-08	RM05-08	RM05-08	-	RM07-18
Level	469	-	-	-	481	-
Depth (m)	469	875	884	1011	481	701
Unit	Calk-alkaline quartz monzodiorite (IN4)	Calk-alkaline quartz monzodiorite (IN4)	Calk-alkaline quartz monzodiorite (IN4)	Calk-alkaline quartz monzodiorite (IN4)	Calk-alkaline quartz monzodiorite (IN4)	Calk-alkaline quartz monzodiorite (IN4)
SiO_2 (wt %)	56.99	61.05	61.10	61.74	54.79	57.37
Al_2O_3	16.83	17.61	16.28	16.90	16.16	16.14
$Fe_2O_{3(total)}$	6.87	5.99	5.78	5.01	6.21	5.58
$FeO_{(total)}$[1]	6.18	5.39	5.20	4.51	5.59	5.02
MnO	0.099	0.060	0.076	0.056	0.088	0.088
MgO	5.11	3.24	3.53	2.87	4.67	3.40
CaO	5.02	2.86	4.98	3.60	6.45	5.57
Na_2O	4.47	5.49	2.84	3.76	3.53	4.84
K_2O	2.28	1.86	2.76	2.57	2.09	1.38
TiO_2	0.787	0.810	0.788	0.903	0.800	0.769
P_2O_5	0.23	0.27	0.26	0.40	0.24	0.25
LOI	2.10	1.22	1.25	1.32	3.51	3.00
Total	100.80	100.50	99.64	99.13	98.55	98.38
Sr (ppm)	92	176	149	202	168	413
Sc	17	15	13	10	17	13
Zr	106	135	131	164	102	125
Ba	227.2	406.5	929.3	372.3	332.8	327.1
Y	12.42	15.70	15.73	13.49	12.56	12.73
Nb	3.44	6.55	2.39	3.13	1.27	7.54
Cs	1.38	3.36	2.41	2.86	2.34	1.36
La	18.49	24.91	24.28	25.97	16.66	21.68
Ce	38.31	50.52	49.64	54.60	36.30	44.65
Pr	4.70	6.02	6.03	7.10	4.48	5.44
Nd	17.88	22.67	22.41	26.52	16.85	20.85
Sm	3.43	4.19	4.22	4.66	3.20	3.81
Eu	0.81	1.05	1.19	1.17	0.84	1.07
Gd	2.78	3.33	3.43	3.46	2.56	3.00
Tb	0.43	0.52	0.50	0.47	0.40	0.45
Dy	2.52	3.13	3.02	2.75	2.52	2.61
Ho	0.48	0.63	0.58	0.54	0.50	0.53
Er	1.40	1.76	1.69	1.59	1.38	1.42
Tm	0.23	0.30	0.24	0.29	0.21	0.20
Yb	1.17	1.58	1.46	1.44	1.24	1.23
Lu	0.16	0.20	0.21	0.22	0.16	0.19
Ta	bdl	0.37	bdl	bdl	0.09	0.47
Tl	3.61	0.50	0.55	4.13	5.93	0.21
Pb	14.7	9.0	8.8	73.2	91.1	7.4
Bi	0.20	0.08	0.06	0.12	1.08	0.10
Th	4.99	4.61	6.59	8.87	4.29	5.00
U	1.28	1.45	1.41	2.37	1.36	1.71
V	96.3	105.2	110.0	96.4	119.6	100.4
Cr	117.4	33.0	34.1	28.7	91.7	59.2
Co	20.2	20.0	17.8	20.7	21.2	16.1
Ni	104.3	38.9	36.3	39.3	98.1	48.2
Cu	126	121	34	104	69	30
Zn	285	78	80	127	236	83
As	5.0	bdl	bdl	5.4	4.9	bdl
Sn	0.6	0.6	1.1	1.1	1.2	0.9
Sb	0.3	0.2	bdl	0.7	0.5	0.1
Ti[2]	13132	13516	13149	15068	13349	12832

Table A4. Complete Dataset of Least-Altered Samples from the Rambler Rhyolite Formation and Surrounding Units *(continued)*

Sample ID	62520	62521	106407	29888	29897	60502	60503	60504	60510	60511	60516
Hole ID	RM07-18	RM07-18	RM09-22	RM08-151	RM07-20H	-	-	-	-	-	-
Level	-	-	-	-	-	329	329	329	444	444	434
Depth (m)	815.20	823.00	611.8	46.61	668.27	329	329	329	444	444	434

Unit	Unit 1.1	Unit 1.1	Unit 1.1	Unit 1.2	Unit 1.2	Unit 1.2	Unit 1.2	Unit 1.2	Unit 1.2	Unit 1.2	Unit 1.2
AI[3]	28.98	36.47	38.15	26.64	29.70	43.87	22.81	37.23	26.33	41.14	44.45
CCPI[4]	61.85	65.11	60.54	37.76	57.71	78.72	59.33	69.04	60.00	50.15	65.96
Mg#[5]	51.03	58.50	59.58	58.35	23.27	32.12	15.92	32.16	26.71	31.84	47.54
$[La/Yb]_{cn}$[6]	6.66	7.61	6.19	3.96	5.24	3.51	4.40	6.39	4.52	6.15	5.45
Yb_{cn}[6]	4.04	4.20	3.15	3.96	4.01	5.88	6.51	3.06	4.68	4.24	5.01
$[La/Yb]_{pn}$[7]	7.15	8.16	6.65	4.25	5.62	3.76	4.73	6.86	4.85	6.60	5.85
$[La/Sm]_{pn}$[7]	4.03	4.36	3.70	3.53	3.22	3.09	3.42	3.22	3.55	3.52	3.66
$[Gd/Lu]_{pn}$[7]	1.16	1.04	1.03	0.79	1.12	0.75	0.88	1.21	0.92	1.04	1.28
Nb/Nb*[8]	0.74	0.70	0.37	0.30	0.70	0.77	0.73	0.69	0.61	0.71	0.80
Ti/Ti*[9]	0.21	0.19	0.17	0.20	0.16	0.20	0.19	0.19	0.16	0.20	0.27
Zr/Zr*[10]	2.57	2.44	2.49	2.70	2.25	2.29	2.12	2.53	2.15	2.45	2.78
Eu/Eu*[11]	0.92	1.10	0.88	0.77	0.79	0.89	0.96	1.14	0.98	1.09	1.10
Y/Y*[12]	0.76	0.83	0.68	0.73	0.80	0.71	0.91	0.54	0.78	0.80	0.88
Zr/Y	9.79	8.74	10.58	9.69	7.77	8.84	6.41	14.45	7.67	8.91	8.81
Zr/TiO_2	284.48	294.64	329.55	309.78	327.59	269.06	255.23	311.22	316.09	279.66	234.04
Th/Yb	4.21	4.55	4.13	2.42	2.60	2.35	1.95	4.95	2.56	3.16	3.53
Al_2O_3/TiO_2	52.16	58.57	71.19	70.98	64.48	66.01	55.52	66.63	65.17	63.47	53.04
La/Yb	9.96	11.37	9.26	5.92	7.83	5.25	6.58	9.55	6.76	9.19	8.15
Nb/Y	0.59	0.54	0.31	0.21	0.41	0.55	0.37	0.81	0.39	0.47	0.50
Nb/Th	1.06	0.96	0.60	0.58	1.32	1.22	1.27	1.02	1.06	1.18	1.13
Nb/Yb	4.47	4.38	2.47	1.40	3.43	2.87	2.48	5.06	2.71	3.75	3.98

[1]Calculated from $Fe_2O_{3(total)}$, assuming all iron is present as Fe^{2+}

[2]Calculated from TiO_2; 10000 x (TiO_2/0.5993)

[3]AI = Hashimoto alteration index = 100*[(MgO+K_2O)/(MgO+K_2O+Na_2O+CaO)] (Ishikawa et al., 1976)

[4]CCPI = Chlorite-carbonate-pyrite alteration index = 100*[(MgO+FeO)/(MgO+FeO+K_2O+Na_2O)] (Large et al., 2001)

[5]Mg# = $Mg^{2+}/(Mg^{2+} + Fe^{2+})$ (molar %)

[6]Normalized to Chondrite (cn) value (Nakamura, 1974)

[7]Normalized to Primitive Mantle (pn) value (Sun and McDonough, 1989)

[8]$Nb/Nb^* = Nb_n/(Th_n + La_n)^{0.5}$ (Normalized to Primitive Mantle)

[9]$Ti/Ti^* = Ti_n/(Gd_n + Sm_n)^{0.5}$ (Normalized to Primitive Mantle)

[10]$Zr/Zr^* = Zr_n/(Gd_n + Sm_n)^{0.5}$ (Normalized to Primitive Mantle)

[11]$Eu/Eu^* = Eu_n/(Gd_n + Sm_n)^{0.5}$ (Normalized to Primitive Mantle)

[12]$Y/Y^* = Y_n/(Dy_n + Er_n)^{0.5}$ (Normalized to Primitive Mantle)

bdl = below detection limit

Table A4. Complete Dataset of Least-Altered Samples from the Rambler Rhyolite Formation and Surrounding Units *(continued)*

Sample ID	60585	60588	60594	60595	62080	62082	62193	62194	62198	62505	62508
Hole ID	RM07-20M	RM07-20M	RM07-20K	RM07-20K	-	-	-	-	-	RM07-18	RM07-18
Level	-	-	-	-	469	469	481	481	481	-	-
Depth (m)	670.80	686.00	681.15	698.60	469	469	481	481	481	652	685

Unit	Unit 1.2	Unit 1.2	Unit 1.2	Unit 1.2	Unit 1.2	Unit 1.2	Unit 1.2	Unit 1.2	Unit 1.2	Unit 1.2	Unit 1.2
AI[3]	31.65	22.64	33.92	40.34	28.40	21.38	41.73	34.45	30.08	30.58	22.91
CCPI[4]	55.48	51.35	74.19	76.62	49.53	50.29	53.91	62.41	45.14	66.72	53.78
Mg#[5]	20.55	31.77	32.95	52.25	37.99	28.57	39.20	39.77	26.29	51.88	30.73
$[La/Yb]_{cn}$[6]	6.23	4.84	8.71	6.72	6.02	6.48	5.83	4.87	4.50	6.85	4.49
Yb_{cn}[6]	3.56	4.40	2.21	2.49	3.65	3.94	3.87	5.35	4.57	2.95	5.53
$[La/Yb]_{pn}$[7]	6.68	5.19	9.35	7.21	6.46	6.96	6.26	5.23	4.83	7.35	4.82
$[La/Sm]_{pn}$[7]	3.51	3.61	4.29	3.85	3.28	3.77	3.38	3.72	3.32	3.79	3.58
$[Gd/Lu]_{pn}$[7]	1.43	1.04	1.44	1.25	1.46	1.39	1.48	1.03	1.04	1.07	0.98
Nb/Nb*[8]	0.72	0.63	0.69	0.56	0.82	0.60	0.71	0.60	0.73	0.62	0.70
Ti/Ti*[9]	0.18	0.18	0.24	0.18	0.22	0.17	0.20	0.18	0.17	0.18	0.17
Zr/Zr*[10]	2.57	2.29	2.63	2.27	2.73	2.06	2.69	2.35	2.19	2.29	2.41
Eu/Eu*[11]	0.95	1.02	0.85	0.82	0.97	1.20	1.06	1.11	0.92	0.85	0.89
Y/Y*[12]	0.75	0.82	0.52	0.57	0.79	0.75	0.71	0.89	0.88	0.68	0.90
Zr/Y	9.73	7.86	15.90	12.22	9.91	7.73	10.99	6.86	6.78	10.24	7.18
Zr/TiO_2	320.20	293.81	254.63	284.02	288.62	274.11	309.73	301.89	294.74	292.13	331.61
Th/Yb	3.50	2.43	4.91	3.89	3.98	3.14	3.52	2.37	2.38	3.74	2.20
Al_2O_3/TiO_2	66.85	58.97	67.78	88.22	61.18	65.63	65.31	63.44	66.11	76.85	66.58
La/Yb	9.32	7.24	13.03	10.05	9.00	9.70	8.72	7.28	6.73	10.24	6.72
Nb/Y	0.50	0.38	0.87	0.58	0.56	0.41	0.54	0.31	0.39	0.54	0.37
Nb/Th	1.22	1.17	1.25	1.08	1.26	1.05	1.14	1.03	1.34	1.13	1.23
Nb/Yb	4.29	2.85	6.16	4.19	5.02	3.30	4.01	2.44	3.19	4.23	2.71

[1]Calculated from $Fe_2O_{3(total)}$, assuming all iron is present as Fe^{2+}

[2]Calculated from TiO_2; 10000 x (TiO_2/0.5993)

[3]AI = Hashimoto alteration index = 100*[(MgO+K_2O)/(MgO+K_2O+Na_2O+CaO)] (Ishikawa et al., 1976)

[4]CCPI = Chlorite-carbonate-pyrite alteration index = 100*[(MgO+FeO)/(MgO+FeO+K_2O+Na_2O)] (Large et al., 2001)

[5]Mg# = $Mg^{2+}/(Mg^{2+} + Fe^{2+})$ (molar %)

[6]Normalized to Chondrite (cn) value (Nakamura, 1974)

[7]Normalized to Primitive Mantle (pn) value (Sun and McDonough, 1989)

[8]Nb/Nb* = $Nb_n/(Th_n + La_n)^{0.5}$ (Normalized to Primitive Mantle)

[9]Ti/Ti* = $Ti_n/(Gd_n + Sm_n)^{0.5}$ (Normalized to Primitive Mantle)

[10]Zr/Zr* = $Zr_n/(Gd_n + Sm_n)^{0.5}$ (Normalized to Primitive Mantle)

[11]Eu/Eu* = $Eu_n/(Gd_n + Sm_n)^{0.5}$ (Normalized to Primitive Mantle)

[12]Y/Y* = $Y_n/(Dy_n + Er_n)^{0.5}$ (Normalized to Primitive Mantle)

bdl = below detection limit

Table A4. Complete Dataset of Least-Altered Samples from the Rambler Rhyolite Formation and Surrounding Units *(continued)*

Sample ID	62511	62512	62514	62518	62501	62513	62526	60596	60598	62051	29842
Hole ID	RM07-18	RM07-18	RM07-18	RM07-18	RM07-18	RM07-18	RM06-04C	RMUG13-205	RMUG13-205	-	RM06-4E
Level	-	-	-	-	-	-	-	-	-	375	-
Depth (m)	710	716	721	795	607	720	879	27	37	375	865
Unit	Unit 1.2	Unit 1.2	Unit 1.2	Unit 1.2	Unit 1.3	Unit 1.3	Unit 1.3	Sulfide-rich mafic breccia (Unit 2)	Sulfide-rich mafic breccia (Unit 2)	Sulfide-rich mafic breccia (Unit 2)	Fe-shale (Unit 3)
AI[3]	34.42	32.58	38.78	54.50	41.61	30.71	25.51	32.97	35.55	50.42	38.95
CCPI[4]	64.32	75.22	69.36	86.52	62.36	41.17	43.17	59.85	68.28	79.77	76.93
Mg#[5]	51.24	51.30	52.47	69.72	43.10	50.57	39.59	52.79	32.24	49.89	62.02
$[La/Yb]_{cn}$[6]	6.58	6.19	5.94	4.69	9.85	18.24	13.16	2.61	2.65	2.84	3.24
Yb_{cn}[6]	3.03	2.94	2.97	2.72	2.75	2.19	2.42	9.24	9.22	7.02	8.70
$[La/Yb]_{pn}$[7]	7.07	6.64	6.37	5.03	10.57	19.58	14.12	2.80	2.84	3.05	3.48
$[La/Sm]_{pn}$[7]	4.14	3.60	3.87	3.19	3.66	3.87	4.57	1.56	1.45	1.39	2.05
$[Gd/Lu]_{pn}$[7]	1.03	1.14	0.95	0.83	2.23	3.01	1.89	1.63	1.79	2.19	1.54
Nb/Nb*[8]	0.59	0.54	0.57	0.38	0.73	0.38	0.24	0.32	1.13	0.72	1.03
Ti/Ti*[9]	0.17	0.18	0.18	0.20	0.27	0.30	0.15	0.94	0.86	0.99	0.56
Zr/Zr*[10]	2.04	2.04	2.04	1.66	3.04	2.96	2.57	2.93	2.97	2.98	2.37
Eu/Eu*[11]	0.85	0.96	0.86	0.74	1.10	1.36	1.47	2.15	2.03	1.69	1.72
Y/Y*[12]	0.72	0.64	0.64	0.64	0.76	0.67	0.61	1.24	1.16	1.11	1.27
Zr/Y	8.14	9.66	9.15	7.49	12.26	17.34	13.64	6.54	6.98	7.55	4.99
Zr/TiO_2	267.86	254.24	257.49	191.86	255.38	226.60	390.53	71.64	79.26	69.23	97.05
Th/Yb	3.05	3.10	3.16	2.41	5.73	10.10	7.15	0.67	0.89	1.30	1.07
Al_2O_3/TiO_2	76.67	80.00	77.84	63.78	54.83	39.16	85.68	10.34	10.95	10.68	17.83
La/Yb	9.85	9.26	8.88	7.01	14.73	27.28	19.68	3.90	3.96	4.24	4.85
Nb/Y	0.44	0.47	0.50	0.29	0.56	0.45	0.28	0.07	0.25	0.19	0.24
Nb/Th	1.20	1.10	1.13	0.90	1.10	0.49	0.35	0.89	2.55	1.47	2.19
Nb/Yb	3.67	3.39	3.58	2.16	6.30	4.91	2.51	0.60	2.27	1.91	2.34

[1]Calculated from $Fe_2O_{3(total)}$, assuming all iron is present as Fe^{2+}

[2]Calculated from TiO_2; 10000 x (TiO_2/0.5993)

[3]AI = Hashimoto alteration index = 100*[(MgO+K_2O)/(MgO+K_2O+Na_2O+CaO)] (Ishikawa et al., 1976)

[4]CCPI = Chlorite-carbonate-pyrite alteration index = 100*[(MgO+FeO)/(MgO+FeO+K_2O+Na_2O)] (Large et al., 2001)

[5]Mg# = $Mg^{2+}/(Mg^{2+} + Fe^{2+})$ (molar %)

[6]Normalized to Chondrite (cn) value (Nakamura, 1974)

[7]Normalized to Primitive Mantle (pn) value (Sun and McDonough, 1989)

[8]Nb/Nb* = $Nb_n/(Th_n + La_n)^{0.5}$ (Normalized to Primitive Mantle)

[9]Ti/Ti* = $Ti_n/(Gd_n + Sm_n)^{0.5}$ (Normalized to Primitive Mantle)

[10]Zr/Zr* = $Zr_n/(Gd_n + Sm_n)^{0.5}$ (Normalized to Primitive Mantle)

[11]Eu/Eu* = $Eu_n/(Gd_n + Sm_n)^{0.5}$ (Normalized to Primitive Mantle)

[12]Y/Y* = $Y_n/(Dy_n + Er_n)^{0.5}$ (Normalized to Primitive Mantle)

bdl = below detection limit

Table A4. Complete Dataset of Least-Altered Samples from the Rambler Rhyolite Formation and Surrounding Units *(continued)*

Sample ID	29843	29877	29885	29893	29895	29896	60591	60600	36640	60590	62176
Hole ID	RM06-4E	RM08-123	RM08-150	RM08-151	RM07-20H	RM07-20H	RM07-20K	RM07-18	RMUG08-136	RM07-20K	RM05-08
Level	-	-	-	-	-	-	-	-	-	-	-
Depth (m)	873	74	76	99	653	655	652	589	52	649	990

Unit	Fe-shale (Unit 3)	Fe-shale (Unit 3)	Fe-shale (Unit 3)	Fe-shale (Unit 3)	Fe-shale (Unit 3)	Fe-shale (Unit 3)	Fe-shale (Unit 3)	Fe-shale (Unit 3)	High-Mg basalt	High-Mg basalt	High-Mg basalt
AI[3]	42.15	21.67	26.15	23.11	25.95	35.30	21.34	39.86	51.78	23.38	42.58
CCPI[4]	79.63	75.43	66.95	66.48	66.90	70.54	59.49	76.97	80.94	63.65	81.22
Mg#[5]	63.25	34.64	37.06	47.79	58.54	45.59	47.90	55.88	69.19	52.21	65.71
$[La/Yb]_{cn}$[6]	3.10	3.62	3.40	3.11	3.27	2.67	3.89	2.65	3.14	2.64	4.11
Yb_{cn}[6]	8.75	9.61	7.85	6.90	6.92	9.49	7.31	9.29	6.99	10.29	6.16
$[La/Yb]_{pn}$[7]	3.33	3.88	3.65	3.34	3.51	2.86	4.17	2.85	3.37	2.83	4.41
$[La/Sm]_{pn}$[7]	2.04	2.08	1.76	1.57	1.92	1.56	2.26	1.45	2.00	1.64	2.55
$[Gd/Lu]_{pn}$[7]	1.55	1.86	2.02	2.06	1.55	1.66	1.67	1.75	1.57	1.45	1.52
Nb/Nb*[8]	0.95	1.05	1.01	0.93	0.55	0.37	0.92	1.25	0.76	1.11	0.21
Ti/Ti*[9]	0.56	0.79	0.97	0.90	0.68	0.77	0.72	1.00	0.64	0.74	0.64
Zr/Zr*[10]	2.78	2.83	3.08	2.69	2.25	2.48	2.54	2.88	2.11	2.77	2.47
Eu/Eu*[11]	1.59	1.96	1.78	1.81	1.66	1.88	1.92	1.93	1.47	1.92	1.53
Y/Y*[12]	1.26	1.27	1.11	1.15	1.14	1.32	1.17	1.31	1.09	1.41	1.06
Zr/Y	5.83	6.03	7.65	6.56	5.50	5.07	5.93	6.07	5.30	5.28	6.25
Zr/TiO_2	114.22	81.98	73.01	68.79	76.27	74.05	80.83	66.13	76.04	85.43	87.98
Th/Yb	1.03	0.91	1.50	0.95	1.18	0.86	1.37	0.83	1.39	0.90	2.42
Al_2O_3/TiO_2	17.58	11.30	11.38	10.09	15.58	11.19	15.41	9.11	17.08	12.80	18.55
La/Yb	4.64	5.41	5.09	4.65	4.89	3.99	5.81	3.97	4.70	3.95	6.14
Nb/Y	0.22	0.23	0.29	0.21	0.15	0.07	0.26	0.24	0.24	0.21	0.08
Nb/Th	2.05	2.45	1.83	2.39	1.24	0.85	1.88	2.96	1.51	2.36	0.32
Nb/Yb	2.11	2.22	2.73	2.28	1.46	0.73	2.57	2.45	2.11	2.13	0.78

[1]Calculated from $Fe_2O_{3(total)}$, assuming all iron is present as Fe^{2+}

[2]Calculated from TiO_2; 10000 x (TiO_2/0.5993)

[3]AI = Hashimoto alteration index = 100*[(MgO+K_2O)/(MgO+K_2O+Na_2O+CaO)] (Ishikawa et al., 1976)

[4]CCPI = Chlorite-carbonate-pyrite alteration index = 100*[(MgO+FeO)/(MgO+FeO+K_2O+Na_2O)] (Large et al., 2001)

[5]Mg# = $Mg^{2+}/(Mg^{2+} + Fe^{2+})$ (molar %)

[6]Normalized to Chondrite (cn) value (Nakamura, 1974)

[7]Normalized to Primitive Mantle (pn) value (Sun and McDonough, 1989)

[8]$Nb/Nb^* = Nb_n/(Th_n + La_n)^{0.5}$ (Normalized to Primitive Mantle)

[9]$Ti/Ti^* = Ti_n/(Gd_n + Sm_n)^{0.5}$ (Normalized to Primitive Mantle)

[10]$Zr/Zr^* = Zr_n/(Gd_n + Sm_n)^{0.5}$ (Normalized to Primitive Mantle)

[11]$Eu/Eu^* = Eu_n/(Gd_n + Sm_n)^{0.5}$ (Normalized to Primitive Mantle)

[12]$Y/Y^* = Y_n/(Dy_n + Er_n)^{0.5}$ (Normalized to Primitive Mantle)

bdl = below detection limit

Table A4. Complete Dataset of Least-Altered Samples from the Rambler Rhyolite Formation and Surrounding Units *(continued)*

Sample ID	29841	36316	36318	62165	62167	62175	62163	62168	62517	62196
Hole ID	RM06-4E	RM04-04	RM04-04	RM05-08	RM05-08	RM05-08	RM05-08	RM05-08	RM07-18	-
Level	-	-	-	-	-	-	-	-	-	481
Depth (m)	844	850	851	881	896	960	873	915	767	481
Unit	Th-enriched back arc basin basalt	Th-enriched back arc basin basalt	Th-enriched back arc basin basalt	Th-enriched back arc basin basalt	E-MORB	E-MORB	LREE-enriched/Low-Ti tholeiitic mafic tuff	LREE-enriched/Low-Ti tholeiitic mafic tuff	Low Nb/Yb tholeiitic gabbro (IN1)	Low Nb/Yb tholeiitic gabbro (IN1)
AI[3]	33.40	33.73	32.41	29.82	40.58	34.15	32.53	43.97	35.66	36.46
CCPI[4]	76.26	78.01	77.10	76.08	86.13	85.08	71.03	72.78	83.34	86.20
Mg#[5]	57.74	56.85	57.46	55.28	53.04	47.34	46.98	59.32	60.23	60.39
$[La/Yb]_{cn}$[6]	1.16	1.24	1.24	1.14	1.57	2.39	5.40	5.45	1.35	1.52
Yb_{cn}[6]	9.01	9.78	9.15	9.17	14.54	11.93	7.25	6.44	10.48	8.85
$[La/Yb]_{pn}$[7]	1.24	1.33	1.33	1.23	1.69	2.56	5.80	5.85	1.45	1.63
$[La/Sm]_{pn}$[7]	0.83	0.79	0.82	0.86	0.93	1.32	2.97	2.93	0.90	0.91
$[Gd/Lu]_{pn}$[7]	1.51	1.64	1.63	1.42	1.76	1.80	1.56	1.64	1.47	1.73
Nb/Nb*[8]	1.08	0.73	0.56	1.01	1.54	2.43	0.99	0.51	0.54	0.34
Ti/Ti*[9]	0.73	0.74	0.68	0.73	1.02	0.97	0.42	0.39	0.74	0.81
Zr/Zr*[10]	2.28	2.29	2.19	2.05	3.04	2.99	2.67	2.19	2.15	2.46
Eu/Eu*[11]	1.37	1.71	1.82	1.72	2.26	2.10	1.52	1.63	1.91	1.83
Y/Y*[12]	1.29	1.42	1.33	1.32	1.69	1.53	1.14	1.12	1.39	1.27
Zr/Y	4.50	4.20	4.23	3.83	4.87	5.39	6.72	5.50	4.03	5.31
Zr/TiO_2	71.14	70.59	73.70	64.33	68.28	70.64	144.74	128.50	66.28	69.51
Th/Yb	0.17	0.19	0.21	0.12	0.28	0.39	1.90	2.96	0.20	0.14
Al_2O_3/TiO_2	13.92	12.24	14.61	12.87	6.74	7.03	24.04	28.01	12.01	11.48
La/Yb	1.73	1.85	1.85	1.71	2.35	3.57	8.08	8.16	2.02	2.27
Nb/Y	0.12	0.07	0.06	0.10	0.15	0.32	0.35	0.21	0.06	0.04
Nb/Th	6.87	4.15	3.02	8.62	5.62	8.55	1.71	0.71	2.93	2.76
Nb/Yb	1.16	0.79	0.65	1.00	1.59	3.34	3.25	2.09	0.59	0.39

[1]Calculated from $Fe_2O_{3(total)}$, assuming all iron is present as Fe^{2+}

[2]Calculated from TiO_2; 10000 x (TiO_2/0.5993)

[3]AI = Hashimoto alteration index = 100*[(MgO+K_2O)/(MgO+K_2O+Na_2O+CaO)] (Ishikawa et al., 1976)

[4]CCPI = Chlorite-carbonate-pyrite alteration index = 100*[(MgO+FeO)/(MgO+FeO+K_2O+Na_2O)] (Large et al., 2001)

[5]Mg# = $Mg^{2+}/(Mg^{2+} + Fe^{2+})$ (molar %)

[6]Normalized to Chondrite (cn) value (Nakamura, 1974)

[7]Normalized to Primitive Mantle (pn) value (Sun and McDonough, 1989)

[8]$Nb/Nb^* = Nb_n/(Th_n + La_n)^{0.5}$ (Normalized to Primitive Mantle)

[9]$Ti/Ti^* = Ti_n/(Gd_n + Sm_n)^{0.5}$ (Normalized to Primitive Mantle)

[10]$Zr/Zr^* = Zr_n/(Gd_n + Sm_n)^{0.5}$ (Normalized to Primitive Mantle)

[11]$Eu/Eu^* = Eu_n/(Gd_n + Sm_n)^{0.5}$ (Normalized to Primitive Mantle)

[12]$Y/Y^* = Y_n/(Dy_n + Er_n)^{0.5}$ (Normalized to Primitive Mantle)

bdl = below detection limit

Table A4. Complete Dataset of Least-Altered Samples from the Rambler Rhyolite Formation and Surrounding Units *(continued)*

Sample ID	62197	60584	60589	60580	36633	29853	106416	29840	29866	36647	36648
Hole ID	-	RM07-20M	RM07-20K	RM05-08	RMUG11-170	RM06-4E	-	RMUG08-140	RM06-4E	RM04-04	RM04-04
Level	481	-	-	-	-	-	1450	-	-	-	-
Depth (m)	481	661	645	1335	39	1052	300	58	1216	322	327
Unit	Low Nb/Yb tholeiitic gabbro (IN1)	Low Nb/Yb tholeiitic gabbro (IN1)	Low Nb/Yb tholeiitic gabbro (IN1)	Low Nb/Yb tholeiitic gabbro (IN1)	Low Nb/Yb tholeiitic gabbro (IN1)	Low Nb/Yb tholeiitic gabbro (IN1)	Low Nb/Yb tholeiitic gabbro (IN1)	Intermediate Nb/Yb tholeiitic gabbro (IN2)	Intermediate Nb/Yb tholeiitic gabbro (IN2)	Intermediate Nb/Yb tholeiitic gabbro (IN2)	Intermediate Nb/Yb tholeiitic gabbro (IN2)
AI[3]	52.63	41.44	41.46	35.30	37.85	35.25	33.66	34.45	41.09	36.13	35.36
CCPI[4]	89.22	78.53	86.83	87.01	85.21	86.89	83.05	84.90	83.36	86.04	81.88
Mg#[5]	60.89	61.56	64.43	60.88	59.62	59.84	58.99	57.08	55.98	56.12	58.41
$[La/Yb]_{cn}$[6]	1.69	1.72	1.36	1.55	1.68	1.48	2.42	1.66	1.78	1.70	1.67
Yb_{cn}[6]	10.10	6.72	8.02	9.51	8.07	9.88	7.76	9.90	9.97	8.09	9.19
$[La/Yb]_{pn}$[7]	1.82	1.85	1.46	1.66	1.80	1.58	2.59	1.78	1.91	1.82	1.79
$[La/Sm]_{pn}$[7]	0.89	0.86	0.91	0.94	0.89	0.99	1.17	0.90	1.02	1.00	0.94
$[Gd/Lu]_{pn}$[7]	1.93	1.92	1.51	1.67	1.73	1.58	1.97	1.75	1.74	1.69	1.66
Nb/Nb*[8]	0.47	0.36	0.36	0.44	0.67	0.35	0.63	1.61	1.85	1.40	1.55
Ti/Ti*[9]	0.94	0.75	0.68	0.79	0.77	0.84	0.87	0.83	0.92	0.77	0.79
Zr/Zr*[10]	2.51	2.25	2.03	2.37	2.32	2.54	2.56	2.46	2.70	1.92	2.18
Eu/Eu*[11]	2.16	1.62	1.70	1.86	1.78	2.01	1.95	2.05	2.02	1.66	1.94
Y/Y*[12]	1.42	1.10	1.24	1.32	1.27	1.34	1.27	1.35	1.40	1.21	1.38
Zr/Y	4.83	5.67	4.30	4.85	4.91	4.82	5.68	5.00	5.31	4.22	4.21
Zr/TiO_2	61.54	68.72	67.86	68.45	68.69	69.58	67.74	67.70	67.33	57.01	63.40
Th/Yb	0.21	0.18	0.19	0.15	0.15	0.26	0.29	0.15	0.15	0.20	0.12
Al_2O_3/TiO_2	9.78	12.11	14.35	10.97	11.45	10.97	10.03	9.88	9.58	12.09	10.73
La/Yb	2.53	2.58	2.04	2.32	2.51	2.21	3.61	2.48	2.66	2.54	2.49
Nb/Y	0.05	0.05	0.04	0.05	0.08	0.04	0.09	0.18	0.20	0.18	0.16
Nb/Th	2.66	2.82	2.34	3.28	5.55	1.62	3.48	12.28	14.08	9.33	14.16
Nb/Yb	0.56	0.51	0.44	0.49	0.84	0.42	1.02	1.80	2.11	1.84	1.75

[1]Calculated from $Fe_2O_{3(total)}$, assuming all iron is present as Fe^{2+}

[2]Calculated from TiO_2; 10000 x (TiO_2/0.5993)

[3]AI = Hashimoto alteration index = 100*[(MgO+K_2O)/(MgO+K_2O+Na_2O+CaO)] (Ishikawa et al., 1976)

[4]CCPI = Chlorite-carbonate-pyrite alteration index = 100*[(MgO+FeO)/(MgO+FeO+K_2O+Na_2O)] (Large et al., 2001)

[5]Mg# = $Mg^{2+}/(Mg^{2+} + Fe^{2+})$ (molar %)

[6]Normalized to Chondrite (cn) value (Nakamura, 1974)

[7]Normalized to Primitive Mantle (pn) value (Sun and McDonough, 1989)

[8]$Nb/Nb^* = Nb_n/(Th_n + La_n)^{0.5}$ (Normalized to Primitive Mantle)

[9]$Ti/Ti^* = Ti_n/(Gd_n + Sm_n)^{0.5}$ (Normalized to Primitive Mantle)

[10]$Zr/Zr^* = Zr_n/(Gd_n + Sm_n)^{0.5}$ (Normalized to Primitive Mantle)

[11]$Eu/Eu^* = Eu_n/(Gd_n + Sm_n)^{0.5}$ (Normalized to Primitive Mantle)

[12]$Y/Y^* = Y_n/(Dy_n + Er_n)^{0.5}$ (Normalized to Primitive Mantle)

bdl = below detection limit

Table A4. Complete Dataset of Least-Altered Samples from the Rambler Rhyolite Formation and Surrounding Units *(continued)*

Sample ID	60505	62095	62509	29865	29871	36315	60517	60583	62052	62055	62094
Hole ID	-	RM05-08	RM07-18	RM06-4E	RM07-8F	RM04-04	-	RM07-20M	-	-	RM05-08
Level	329	-	-	-	-	-	434	-	375	375	-
Depth (m)	329	656	694	1213	996	749	434	649	375	375	650
Unit	Intermediate Nb/Yb tholeiitic gabbro (IN2)	Intermediate Nb/Yb tholeiitic gabbro (IN2)	Intermediate Nb/Yb tholeiitic gabbro (IN2)	Transitional diorite (IN3)	Transitional diorite (IN3)	Transitional diorite (IN3)	Transitional diorite (IN3)	Transitional diorite (IN3)	Transitional diorite (IN3)	Transitional diorite (IN3)	Transitional diorite (IN3)
AI[3]	45.87	32.55	32.45	34.29	27.38	35.74	34.05	32.41	52.93	21.53	42.95
CCPI[4]	79.94	87.10	88.29	82.29	66.77	83.25	78.34	83.67	86.38	80.75	82.36
Mg#[5]	49.24	48.29	53.35	46.66	44.11	68.71	30.34	42.48	51.34	44.83	65.31
$[La/Yb]_{cn}$[6]	1.74	2.01	1.80	3.45	3.73	4.79	2.84	3.11	5.76	5.35	4.40
Yb_{cn}[6]	10.72	11.38	10.39	13.31	6.89	4.96	7.46	14.34	7.70	6.63	7.99
$[La/Yb]_{pn}$[7]	1.87	2.16	1.93	3.70	4.00	5.14	3.05	3.34	6.18	5.74	4.72
$[La/Sm]_{pn}$[7]	1.20	1.22	1.14	1.81	1.77	2.08	1.57	1.83	2.04	1.96	2.12
$[Gd/Lu]_{pn}$[7]	1.79	1.56	1.56	1.78	1.85	1.97	1.60	1.72	2.33	2.18	1.97
Nb/Nb*[8]	2.13	1.94	1.64	2.62	0.25	0.68	0.45	2.76	1.84	0.62	0.64
Ti/Ti*[9]	0.82	0.85	0.82	0.87	0.69	0.64	0.73	0.87	0.97	0.89	0.62
Zr/Zr*[10]	2.06	2.50	2.21	2.58	2.88	1.79	2.24	2.43	2.83	2.50	2.66
Eu/Eu*[11]	1.70	2.08	1.84	2.24	1.56	1.48	2.11	2.23	2.18	1.83	1.81
Y/Y*[12]	1.43	1.48	1.35	1.59	1.13	0.94	1.16	1.62	1.28	1.14	1.24
Zr/Y	3.74	4.49	4.35	4.43	7.37	5.60	5.27	4.17	6.76	6.62	6.17
Zr/TiO_2	57.70	67.68	62.05	68.32	96.12	63.79	70.10	64.15	67.10	64.19	98.67
Th/Yb	0.38	0.30	0.26	0.61	1.31	1.35	1.08	0.57	1.76	1.38	0.98
Al_2O_3/TiO_2	9.64	8.17	10.78	7.31	12.56	14.40	10.93	7.18	8.12	8.04	14.26
La/Yb	2.60	3.01	2.69	5.15	5.57	7.16	4.25	4.65	8.62	8.00	6.58
Nb/Y	0.28	0.24	0.21	0.40	0.07	0.24	0.11	0.42	0.49	0.17	0.15
Nb/Th	7.46	8.31	7.94	6.85	0.55	1.76	1.01	7.12	3.31	1.39	1.61
Nb/Yb	2.84	2.45	2.04	4.19	0.72	2.39	1.09	4.07	5.82	1.92	1.58

[1]Calculated from $Fe_2O_{3(total)}$, assuming all iron is present as Fe^{2+}

[2]Calculated from TiO_2; 10000 x (TiO_2/0.5993)

[3]AI = Hashimoto alteration index = 100*[(MgO+K_2O)/(MgO+K_2O+Na_2O+CaO)] (Ishikawa et al., 1976)

[4]CCPI = Chlorite-carbonate-pyrite alteration index = 100*[(MgO+FeO)/(MgO+FeO+K_2O+Na_2O)] (Large et al., 2001)

[5]Mg# = $Mg^{2+}/(Mg^{2+} + Fe^{2+})$ (molar %)

[6]Normalized to Chondrite (cn) value (Nakamura, 1974)

[7]Normalized to Primitive Mantle (pn) value (Sun and McDonough, 1989)

[8]$Nb/Nb^* = Nb_n/(Th_n + La_n)^{0.5}$ (Normalized to Primitive Mantle)

[9]$Ti/Ti^* = Ti_n/(Gd_n + Sm_n)^{0.5}$ (Normalized to Primitive Mantle)

[10]$Zr/Zr^* = Zr_n/(Gd_n + Sm_n)^{0.5}$ (Normalized to Primitive Mantle)

[11]$Eu/Eu^* = Eu_n/(Gd_n + Sm_n)^{0.5}$ (Normalized to Primitive Mantle)

[12]$Y/Y^* = Y_n/(Dy_n + Er_n)^{0.5}$ (Normalized to Primitive Mantle)

bdl = below detection limit

Table A4. Complete Dataset of Least-Altered Samples from the Rambler Rhyolite Formation and Surrounding Units *(continued)*

Sample ID	62190	29954	36319	60509	60518	60565	60569	60592	62074	62076
Hole ID	-	RM08-91	RM04-04	-	-	RM05-08	RM05-08	RM07-20K	-	-
Level	481	-	-	444	434	-	-	-	469	469
Depth (m)	481	67	864	444	434	1175	1220	663	469	469
Unit	Transitional diorite (IN3)	Calk-alkaline quartz monzodiorite (IN4)	Calk-alkaline quartz monzodiorite (IN4)	Calk-alkaline quartz monzodiorite (IN4)	Calk-alkaline quartz monzodiorite (IN4)	Calk-alkaline quartz monzodiorite (IN4)	Calk-alkaline quartz monzodiorite (IN4)	Calk-alkaline quartz monzodiorite (IN4)	Calk-alkaline quartz monzodiorite (IN4)	Calk-alkaline quartz monzodiorite (IN4)
AI[3]	36.77	31.35	32.23	41.00	41.36	36.39	29.89	39.78	43.96	32.05
CCPI[4]	88.82	53.60	52.81	64.22	63.76	61.21	53.34	68.61	64.49	63.54
Mg#[5]	63.88	47.84	52.52	59.62	61.42	55.36	48.63	61.02	67.30	60.58
$[La/Yb]_{cn}$[6]	5.25	15.04	12.93	9.83	9.53	11.47	9.98	10.53	9.64	10.87
Yb_{cn}[6]	6.28	6.60	6.56	5.22	5.77	5.53	10.06	5.18	5.92	5.11
$[La/Yb]_{pn}$[7]	5.63	16.14	13.87	10.55	10.23	12.31	10.71	11.30	10.35	11.67
$[La/Sm]_{pn}$[7]	1.96	3.95	3.46	3.65	3.42	3.57	3.58	3.63	3.92	3.73
$[Gd/Lu]_{pn}$[7]	2.14	2.45	2.95	2.00	2.07	2.37	2.04	2.08	1.67	2.08
Nb/Nb*[8]	1.15	1.37	0.65	0.73	0.38	0.90	1.37	0.48	0.14	0.13
Ti/Ti*[9]	0.84	0.41	0.46	0.46	0.44	0.42	0.33	0.48	0.46	0.45
Zr/Zr*[10]	2.33	3.38	3.98	2.60	2.56	2.88	3.55	2.88	2.65	2.74
Eu/Eu*[11]	1.90	1.92	1.93	1.51	1.70	1.67	1.83	1.28	1.51	1.41
Y/Y*[12]	1.18	1.19	1.23	1.01	1.01	1.05	1.42	1.00	1.02	1.00
Zr/Y	6.07	10.26	10.87	8.38	8.18	9.36	8.31	9.27	8.36	9.00
Zr/TiO_2	63.23	188.29	200.00	130.20	131.78	158.03	246.34	138.36	132.55	139.63
Th/Yb	0.90	4.41	4.64	4.07	4.07	4.01	3.09	3.75	4.15	4.47
Al_2O_3/TiO_2	7.94	19.09	20.01	20.26	20.36	21.69	22.09	20.26	20.43	21.50
La/Yb	7.84	22.49	19.33	14.70	14.25	17.16	14.93	15.75	14.42	16.26
Nb/Y	0.28	0.68	0.28	0.40	0.20	0.47	0.50	0.25	0.08	0.07
Nb/Th	3.64	1.69	0.75	1.00	0.49	1.23	1.62	0.69	0.18	0.17
Nb/Yb	3.26	7.44	3.48	4.07	2.01	4.95	5.00	2.60	0.73	0.74

[1]Calculated from $Fe_2O_{3(total)}$, assuming all iron is present as Fe^{2+}

[2]Calculated from TiO_2; 10000 x (TiO_2/0.5993)

[3]AI = Hashimoto alteration index = 100*[(MgO+K_2O)/(MgO+K_2O+Na_2O+CaO)] (Ishikawa et al., 1976)

[4]CCPI = Chlorite-carbonate-pyrite alteration index = 100*[(MgO+FeO)/(MgO+FeO+K_2O+Na_2O)] (Large et al., 2001)

[5]Mg# = $Mg^{2+}/(Mg^{2+} + Fe^{2+})$ (molar %)

[6]Normalized to Chondrite (cn) value (Nakamura, 1974)

[7]Normalized to Primitive Mantle (pn) value (Sun and McDonough, 1989)

[8]Nb/Nb* = $Nb_n/(Th_n + La_n)^{0.5}$ (Normalized to Primitive Mantle)

[9]Ti/Ti* = $Ti_n/(Gd_n + Sm_n)^{0.5}$ (Normalized to Primitive Mantle)

[10]Zr/Zr* = $Zr_n/(Gd_n + Sm_n)^{0.5}$ (Normalized to Primitive Mantle)

[11]Eu/Eu* = $Eu_n/(Gd_n + Sm_n)^{0.5}$ (Normalized to Primitive Mantle)

[12]Y/Y* = $Y_n/(Dy_n + Er_n)^{0.5}$ (Normalized to Primitive Mantle)

bdl = below detection limit

Table A4. Complete Dataset of Least-Altered Samples from the Rambler Rhyolite Formation and Surrounding Units *(continued)*

Sample ID	62083	62164	62166	62180	62191	62510
Hole ID	-	RM05-08	RM05-08	RM05-08	-	RM07-18
Level	469	-	-	-	481	-
Depth (m)	469	875	884	1011	481	701
Unit	Calk-alkaline quartz monzodiorite (IN4)	Calk-alkaline quartz monzodiorite (IN4)	Calk-alkaline quartz monzodiorite (IN4)	Calk-alkaline quartz monzodiorite (IN4)	Calk-alkaline quartz monzodiorite (IN4)	Calk-alkaline quartz monzodiorite (IN4)
AI[3]	43.78	37.92	44.58	42.50	40.38	31.47
CCPI[4]	63.96	55.67	62.44	55.45	65.94	59.08
Mg#[5]	59.57	51.73	54.75	53.16	59.84	54.69
$[La/Yb]_{cn}$[6]	10.52	10.58	11.09	12.09	8.96	11.81
Yb_{cn}[6]	5.34	7.16	6.65	6.53	5.65	5.58
$[La/Yb]_{pn}$[7]	11.29	11.35	11.90	12.98	9.62	12.67
$[La/Sm]_{pn}$[7]	3.48	3.85	3.72	3.60	3.37	3.68
$[Gd/Lu]_{pn}$[7]	2.22	2.04	2.07	1.98	1.93	1.96
Nb/Nb*[8]	0.52	0.96	0.32	0.37	0.21	1.11
Ti/Ti*[9]	0.46	0.43	0.41	0.46	0.48	0.43
Zr/Zr*[10]	2.69	3.11	2.99	3.63	2.69	3.02
Eu/Eu*[11]	1.36	1.61	1.81	1.73	1.47	1.72
Y/Y*[12]	1.02	1.16	1.18	1.05	1.04	1.03
Zr/Y	8.54	8.60	8.33	12.16	8.12	9.82
Zr/TiO_2	134.69	166.67	166.24	181.62	127.50	162.55
Th/Yb	4.25	2.93	4.50	6.18	3.45	4.07
Al_2O_3/TiO_2	21.39	21.74	20.66	18.72	20.20	20.99
La/Yb	15.73	15.82	16.58	18.08	13.40	17.66
Nb/Y	0.28	0.42	0.15	0.23	0.10	0.59
Nb/Th	0.69	1.42	0.36	0.35	0.30	1.51
Nb/Yb	2.93	4.16	1.64	2.18	1.02	6.14

[1]Calculated from $Fe_2O_{3(total)}$, assuming all iron is present as Fe^{2+}

[2]Calculated from TiO_2; 10000 x (TiO_2/0.5993)

[3]AI = Hashimoto alteration index = 100*[($MgO+K_2O$)/($MgO+K_2O+Na_2O+CaO$)] (Ishikawa et al., 1976)

[4]CCPI = Chlorite-carbonate-pyrite alteration index = 100*[(MgO+FeO)/($MgO+FeO+K_2O+Na_2O$)] (Larg

[5]Mg# = $Mg^{2+}/(Mg^{2+} + Fe^{2+})$ (molar %)

[6]Normalized to Chondrite (cn) value (Nakamura, 1974)

[7]Normalized to Primitive Mantle (pn) value (Sun and McDonough, 1989)

[8]$Nb/Nb^* = Nb_n/(Th_n + La_n)^{0.5}$ (Normalized to Primitive Mantle)

[9]$Ti/Ti^* = Ti_n/(Gd_n + Sm_n)^{0.5}$ (Normalized to Primitive Mantle)

[10]$Zr/Zr^* = Zr_n/(Gd_n + Sm_n)^{0.5}$ (Normalized to Primitive Mantle)

[11]$Eu/Eu^* = Eu_n/(Gd_n + Sm_n)^{0.5}$ (Normalized to Primitive Mantle)

[12]$Y/Y^* = Y_n/(Dy_n + Er_n)^{0.5}$ (Normalized to Primitive Mantle)

bdl = below detection limit

Appendix 5.
Complete Dataset of Altered Samples from the Rambler Rhyolite Formation

Table A5. Complete Dataset of Altered Samples from the Rambler Rhyolite Formation

Sample ID	29801	29849	29850	29874	60570	60577	60578	60579
Alteration	Quartz-chlorite	Quartz-chlorite	Quartz-chlorite	Quartz-chlorite	Quartz-chlorite	Quartz-chlorite	Quartz-chlorite	Quartz-chlorite
DDH-Level	RM07-8F	RM06-4E	RM06-4E	RM07-8F	RM05-08	RM05-08	RM05-08	RM05-08
Zone	Ming South	Ming South	Ming South	Ming South	Ming South	Ming South	Ming South	Ming South
Depth	1152.37	950.57	986.34	1086.28	1226.8	1306.4	1316.8	1326.5
Unit	Unit 1.2	Unit 1.2	Unit 1.2	Unit 1.2	Unit 1.2	Unit 1.1	Unit 1.1	Unit 1.1
SiO_2 (wt. %)	72.25	54.74	61.05	57.20	65.81	67.07	66.57	73.97
Al_2O_3	10.92	11.28	9.79	9.76	10.70	10.48	12.98	10.17
Fe_2O_{3t}	7.25	17.02	16.80	18.60	10.23	11.10	7.19	5.89
FeO_t[1]	6.52	15.32	15.12	16.74	9.21	9.99	6.47	5.30
MnO	0.046	0.078	0.067	0.060	0.057	0.062	0.045	0.045
MgO	4.72	5.81	4.81	4.84	6.23	6.54	6.12	4.96
CaO	0.13	0.87	0.24	0.36	0.51	0.51	1.43	1.09
Na_2O	0.25	1.25	0.64	0.48	1.19	0.70	2.04	1.61
K_2O	1.58	0.07	0.93	0.63	0.29	0.06	0.07	0.03
TiO_2	0.160	0.134	0.107	0.115	0.141	0.145	0.184	0.142
P_2O_5	0.03	0.04	0.02	bdl	0.04	0.03	0.05	0.03
LOI	3.52	7.67	5.17	8.01	3.82	4.03	3.46	2.76
Total	100.90	98.96	99.62	100.10	99.02	100.70	100.10	100.70
Sr (ppm)	7	54	16	17	41	28	63	87
Sc	13	25	24	22	23	24	30	15
Zr	53	42	36	35	39	45	37	60
Ba	422.4	20.5	162.6	118.6	60.5	7.4	7.1	6.7
Y	4.27	4.01	3.32	2.87	3.45	3.66	5.69	4.44
Nb	2.40	1.93	2.11	1.40	2.11	2.32	1.48	3.39
Cs	0.36	0.13	0.92	0.22	0.64	0.28	0.08	0.05
La	6.59	6.27	7.02	4.23	4.48	4.60	5.82	7.29
Ce	13.30	11.95	14.03	8.16	9.16	9.73	11.60	15.11
Pr	1.43	1.34	1.54	1.00	1.07	1.10	1.31	1.71
Nd	5.47	4.73	5.70	3.56	3.88	3.51	4.87	5.76
Sm	1.06	0.92	1.01	0.66	0.74	0.68	1.08	1.03
Eu	0.08	0.11	0.11	0.10	0.08	0.06	0.34	0.09
Gd	0.91	0.75	0.79	0.59	0.66	0.60	1.00	0.86
Tb	0.13	0.10	0.12	0.08	0.10	0.11	0.15	0.12
Dy	0.85	0.75	0.58	0.48	0.66	0.64	0.95	0.77
Ho	0.16	0.14	0.12	0.10	0.13	0.14	0.20	0.16
Er	0.47	0.47	0.38	0.32	0.42	0.41	0.61	0.58
Tm	0.08	0.09	0.06	0.06	0.08	0.09	0.10	0.10
Yb	0.56	0.56	0.45	0.35	0.50	0.58	0.67	0.70
Lu	0.11	0.07	0.07	0.06	0.08	0.10	0.10	0.13
Ta	0.17	0.15	0.17	0.13	0.19	0.20	0.14	0.32
Tl	0.35	0.05	0.44	0.16	0.11	bdl	bdl	bdl
Pb	bdl	19.5	7.9	10.0	7.1	5.9	8.8	8.1
Bi	0.31	0.75	1.75	3.16	0.26	0.23	0.14	0.10
Th	1.90	1.87	1.73	1.32	1.78	2.05	1.57	3.37
U	1.03	1.31	0.78	0.62	0.82	0.97	1.13	1.56
V	52.0	148.8	132.1	bdl	147.5	100.7	123.5	44.5
Cr	24.6	80.3	91.1	bdl	55.4	150.7	39.1	121.8
Co	19.5	34.6	33.2	bdl	37.2	25.1	18.1	17.9
Ni	8.8	24.7	33.4	bdl	21.6	35.3	21.8	25.6
Cu	94	83	2198	bdl	932	694	94	50
Zn	73	251	196	bdl	69	59	48	57
As	0.7	55.9	2.3	bdl	0.5	bdl	bdl	bdl
Ag	0.3	0.2	0.2	bdl	0.3	0.2	bdl	bdl
Sn	1.9	0.6	3.4	bdl	0.7	0.2	0.3	bdl
Sb	bdl	0.5	0.2	bdl	0.1	bdl	0.1	bdl
Hg (ppb)	7	11	11	41	bdl	bdl	10	bdl
AI[2]	94.31	73.50	86.71	86.69	79.32	84.51	64.08	64.89
CCPI[3]	86.74	94.53	93.23	95.48	91.75	95.87	86.32	86.87
Mg#[4]	56.33	40.34	36.19	34.01	54.68	53.86	62.77	62.52
Ba/Sr	60.35	0.38	10.17	6.97	1.47	0.26	0.11	0.08
Eu/Eu*[5]	0.24	0.37	0.35	0.38	0.27	0.22	0.98	0.27
2200W								
2250W	2253.52	2257.67	2253.33	2259.38	2253.19	2253.64	2252.86	2252.16

[1]Calculated from Fe_2O_{3t}, assuming all iron is present as FeO

[2]Alteration Index: AI = 100 x (K_2O+MgO)/(K_2O+MgO+Na_2O+CaO)

[3]Chlorite-carbonate-pyrite index: CCPI = 100 x (MgO + FeO_t)/(MgO+FeO_t+Na_2O+K_2O)

[4]Mg# = $Mg^{2+}/(Mg^{2+} + Fe^{2+})$ (molar %)

[5]$Eu/Eu^* = Eu_n/(Gd_n + Sm_n)^{0.5}$ (n = Normalized to Primitive Mantle; Sun and McDonough, 1989)

bdl = Below detection limit

Table A5. Complete Dataset of Altered Samples from the Rambler Rhyolite Formation *(continued)*

Sample ID	62059	62060	62515	62516	106404	29802	29803	29804	29805	29806
Alteration	Quartz-chlorite	Quartz-chlorite	Quartz-chlorite	Quartz-chlorite	Quartz-chlorite	Quartz-chlorite -sulfides	Quartz-chlorite -sulfides	Quartz-chlorite -sulfides	Quartz-chlorite -sulfides	Quartz-chlorite -sulfides
DDH-Level	RM04-04	RM04-04	RM07-18	RM07-18	RM09-22	RM07-8F	RM07-8F	RM07-8F	RM07-8F	RM07-8F
Zone	Ming South	Ming South	1807	1807	1806	Ming South	Ming South	Ming South	Ming South	Ming South
Depth	975.7	1040.4	729	736.5	300.7	1189.46	1208.71	1227.81	1245.48	1276
Unit	Unit 1.2	Unit 1.1	Unit 1.2	Unit 1.2	Unit 1.2	Unit 1.2	Unit 1.2	Unit 1.2	Unit 1.2	Unit 1.2
SiO_2 (wt. %)	72.50	62.22	59.95	59.47	66.26	63.23	66.16	58.67	59.33	67.19
Al_2O_3	10.22	10.52	11.26	10.61	9.26	10.87	9.26	10.73	8.33	10.14
Fe_2O_{3t}	7.52	13.26	7.95	8.25	6.95	13.04	12.09	15.68	15.69	11.59
FeO_t[1]	6.77	11.93	7.15	7.42	6.25	11.73	10.88	14.11	14.12	10.43
MnO	0.054	0.072	0.140	0.138	0.216	0.068	0.051	0.064	0.055	0.053
MgO	4.18	6.90	8.61	9.72	9.37	7.20	5.73	8.70	5.31	6.22
CaO	0.48	0.27	6.30	6.43	0.53	0.24	0.59	0.39	0.10	0.59
Na_2O	1.00	0.34	2.02	1.92	0.26	0.54	0.61	0.07	0.63	0.44
K_2O	0.80	0.22	0.61	0.12	0.03	0.43	0.05	0.42	0.08	0.03
TiO_2	0.147	0.182	0.156	0.162	0.160	0.164	0.144	0.165	0.126	0.161
P_2O_5	0.03	0.04	0.03	0.04	0.03	0.03	0.04	0.02	bdl	0.04
LOI	3.03	4.09	2.00	2.38	5.64	4.40	5.18	5.51	5.00	4.22
Total	99.96	98.10	99.03	99.24	98.70	100.20	99.90	100.40	94.66	100.70
Sr (ppm)	18	13	150	132	7	15	53	5	9	21
Sc	13	28	36	35	30	27	23	33	21	16
Zr	48	39	35	33	32	34	38	30	37	53
Ba	299.9	27.4	92.3	17.7	3.4	67.4	6.3	22.9	5.0	7.8
Y	3.86	3.87	4.12	3.94	3.47	3.70	4.57	4.83	1.89	5.82
Nb	2.30	1.78	1.92	0.57	0.89	1.59	1.73	1.49	1.75	2.36
Cs	0.21	0.20	1.02	0.18	0.09	1.07	0.14	0.82	0.20	0.31
La	5.04	3.51	4.88	3.81	3.40	2.80	3.82	5.49	3.23	7.63
Ce	10.67	7.17	9.77	7.65	7.54	5.80	7.82	12.42	7.22	16.37
Pr	1.30	0.90	1.16	0.89	0.86	0.68	0.93	1.34	0.77	1.68
Nd	4.74	3.13	4.15	3.26	3.40	2.47	3.66	4.98	2.85	5.92
Sm	0.89	0.67	0.83	0.73	0.76	0.55	0.69	0.92	0.56	1.22
Eu	0.06	0.04	0.24	0.22	0.25	0.05	0.18	0.14	0.05	0.05
Gd	0.73	0.71	0.79	0.69	0.69	0.60	0.60	0.84	0.42	0.96
Tb	0.12	0.11	0.12	0.11	0.10	0.09	0.10	0.15	0.06	0.18
Dy	0.74	0.71	0.76	0.70	0.66	0.61	0.71	0.90	0.39	1.06
Ho	0.15	0.16	0.16	0.16	0.14	0.14	0.15	0.19	0.07	0.22
Er	0.47	0.44	0.52	0.46	0.42	0.44	0.53	0.52	0.24	0.67
Tm	0.11	0.13	0.09	0.07	0.07	0.09	0.10	0.09	0.07	0.11
Yb	0.56	0.54	0.58	0.52	0.50	0.51	0.64	0.52	0.33	0.58
Lu	0.10	0.06	0.09	0.10	0.08	0.07	0.09	0.08	0.05	0.08
Ta	0.18	0.15	0.18	0.06	bdl	0.13	0.15	0.09	0.12	0.20
Tl	0.21	0.13	0.07	bdl	0.04	0.27	bdl	0.25	0.05	0.05
Pb	5.4	18.7	4.9	3.6	14.4	4.1	8.0	9.8	bdl	6.2
Bi	0.29	0.13	0.11	0.09	0.04	0.78	1.24	1.76	2.90	0.94
Th	1.75	1.48	1.75	1.41	1.65	1.41	1.81	1.26	1.51	2.82
U	1.00	0.65	0.88	0.60	0.74	0.66	0.85	0.63	0.63	1.36
V	51.4	170.8	149.8	144.1	124.3	143.3	94.8	153.8	90.7	64.7
Cr	63.5	237.0	594.2	611.9	497.7	95.8	277.7	636.5	265.8	162.7
Co	11.4	25.0	31.2	30.2	30.1	59.4	62.6	85.0	52.6	43.6
Ni	14.9	46.3	144.0	130.5	97.8	43.2	47.0	162.3	51.7	38.3
Cu	105	104	85	49	66	3925	8035	12760	26336	4225
Zn	73	207	85	77	250	121	129	126	119	60
As	0.5	bdl	bdl	bdl	6.7	0.5	2.4	1.2	bdl	bdl
Ag	bdl	bdl	bdl	bdl	0.2	0.6	0.8	1.6	3.0	0.6
Sn	1.7	0.6	0.9	0.5	0.3	2.0	1.3	2.5	2.5	1.0
Sb	0.1	0.1	0.1	bdl	0.5	bdl	0.3	0.2	bdl	bdl
Hg (ppb)	8	9	bdl	bdl	7	10	41	39	31	bdl
AI[2]	77.09	92.11	52.57	54.10	92.25	90.73	82.81	95.20	88.07	85.85
CCPI[3]	86.67	97.30	86.29	89.81	98.25	95.43	96.43	98.03	96.73	97.43
Mg#[4]	52.41	50.76	68.21	70.01	72.76	52.24	48.42	52.36	40.14	51.53
Ba/Sr	16.66	2.10	0.62	0.13	0.49	4.50	0.12	4.58	0.56	0.37
Eu/Eu*[5]	0.21	0.13	0.81	0.78	0.87	0.18	0.67	0.45	0.21	0.15
2200W	2205.39									
2250W	2253.33	2252.99	2250.50	2251.68	2251.51	2259.44	2255.09	2253.29	2255.56	2253.48

[1]Calculated from Fe_2O_{3t}, assuming all iron is present as FeO

[2]Alteration Index: $AI = 100 \times (K_2O+MgO)/(K_2O+MgO+Na_2O+CaO)$

[3]Chlorite-carbonate-pyrite index: $CCPI = 100 \times (MgO + FeO_t)/(MgO+FeO_t+Na_2O+K_2O)$

[4]$Mg\# = Mg^{2+}/(Mg^{2+} + Fe^{2+})$ (molar %)

[5]$Eu/Eu^* = Eu_n/(Gd_n + Sm_n)^{0.5}$ (n = Normalized to Primitive Mantle; Sun and McDonough, 1989)

bdl = Below detection limit

Table A5. Complete Dataset of Altered Samples from the Rambler Rhyolite Formation *(continued)*

Sample ID	29808	29809	29846	29857	29858	29859	29860	29861	29863
Alteration	Quartz-chlorite -sulfides	Quartz-chlorite -sulfides	Quartz-chlorite -sulfides	Quartz-chlorite -sulfides	Quartz-chlorite -sulfides	Quartz-chlorite -sulfides	Quartz-chlorite -sulfides	Quartz-chlorite -sulfides	Quartz-chlorite -sulfides
DDH-Level	RM07-8F	RM07-8F	RM06-4E	RM06-4E	RM06-4E	RM06-4E	RM06-4E	RM06-4E	RM06-4E
Zone	Ming South	Ming South	Ming South	Ming South	Ming South	Ming South	Ming South	Ming South	Ming South
Depth	1300.84	1263.27	907.22	1084.39	1112.3	1124.3	1126.21	1134.09	1169.18
Unit	Unit 1.2	Unit 1.2	Unit 1.2	Unit 1.2	Unit 1.2	Unit 1.2	Unit 1.2	Unit 1.2	Unit 1.1
SiO_2 (wt. %)	59.68	68.74	56.52	27.84	67.91	50.11	62.02	63.87	68.39
Al_2O_3	11.29	10.16	9.59	19.07	9.04	10.95	10.93	10.18	10.53
Fe_2O_{3t}	14.58	10.89	16.79	23.60	11.51	18.43	13.38	12.59	10.61
FeO_t[1]	13.12	9.80	15.11	21.24	10.36	16.58	12.04	11.33	9.55
MnO	0.069	0.055	0.061	0.128	0.058	0.080	0.057	0.059	0.057
MgO	8.49	5.27	4.34	16.24	6.02	7.09	6.29	5.12	5.40
CaO	0.15	0.37	0.84	0.46	0.60	1.74	0.57	0.40	0.97
Na_2O	0.12	0.53	1.50	0.05	0.40	0.33	1.00	1.68	0.92
K_2O	0.10	0.26	0.12	1.95	0.50	0.06	0.35	0.04	0.11
TiO_2	0.170	0.152	0.151	0.431	0.149	0.164	0.202	0.154	0.164
P_2O_5	0.04	0.02	0.03	0.06	0.06	0.05	0.07	0.03	0.05
LOI	5.42	3.76	7.38	8.18	4.25	6.21	4.31	4.30	3.59
Total	100.10	100.20	97.32	98.00	100.50	95.21	99.17	98.43	100.80
Sr (ppm)	6	18	40	26	16	79	26	34	34
Sc	29	13	16	41	17	29	21	13	15
Zr	43	51	42	51	51	37	51	55	57
Ba	13.4	38.2	20.0	322.0	44.6	13.3	23.7	7.7	37.4
Y	4.53	4.23	4.32	8.51	4.82	6.01	5.33	6.21	5.53
Nb	2.49	2.35	2.03	5.41	4.10	6.82	5.06	7.90	5.22
Cs	0.32	0.17	0.12	3.05	0.65	0.21	0.58	0.23	0.20
La	4.42	3.70	2.47	7.05	6.01	10.99	7.75	8.53	7.40
Ce	9.10	7.79	5.11	14.54	12.03	22.31	15.74	17.29	15.21
Pr	1.01	0.87	0.61	1.76	1.38	2.49	1.71	1.87	1.65
Nd	3.92	3.34	2.12	6.64	4.82	8.79	6.29	6.70	5.97
Sm	0.84	0.69	0.52	1.39	0.87	1.47	1.10	1.28	1.12
Eu	0.11	0.04	0.13	0.22	0.11	0.18	0.10	0.15	0.09
Gd	0.74	0.64	0.64	1.35	0.78	1.22	0.88	1.07	0.94
Tb	0.12	0.10	0.11	0.24	0.11	0.18	0.15	0.16	0.16
Dy	0.79	0.71	0.82	1.52	0.82	1.13	0.93	1.06	0.97
Ho	0.17	0.16	0.17	0.33	0.16	0.22	0.20	0.22	0.21
Er	0.55	0.52	0.50	0.96	0.55	0.63	0.57	0.71	0.69
Tm	0.11	0.09	0.09	0.19	0.11	0.10	0.10	0.12	0.10
Yb	0.62	0.63	0.54	0.99	0.60	0.72	0.68	0.74	0.71
Lu	0.11	0.11	0.09	0.14	0.11	0.10	0.10	0.14	0.11
Ta	0.21	0.19	0.16	bdl	bdl	0.46	0.36	0.49	0.34
Tl	0.10	0.07	0.44	0.85	0.22	bdl	0.20	bdl	0.04
Pb	2.9	5.7	18.3	8.0	52.6	37.0	12.5	3.6	8.0
Bi	0.96	1.31	2.45	1.70	0.85	5.98	1.61	3.08	1.24
Th	2.02	1.90	1.59	3.08	3.46	2.29	2.98	5.24	2.83
U	0.96	0.91	1.19	0.81	1.25	1.01	1.18	1.35	1.21
V	124.9	48.1	90.0	206.8	77.4	135.2	101.1	48.5	55.7
Cr	208.3	47.3	69.3	953.0	221.3	167.1	154.7	53.5	132.3
Co	41.5	24.5	68.8	80.9	81.6	68.4	42.9	38.4	30.2
Ni	50.5	38.1	17.7	114.6	35.8	68.6	47.3	40.8	33.7
Cu	7956	1570	10323	13839	5847	35164	17303	21682	6070
Zn	101	25	394	180	128	193	68	108	61
As	0.4	bdl	181.4	1.9	4.4	1.0	bdl	bdl	bdl
Ag	0.8	0.2	2.8	1.7	0.6	3.6	1.8	2.6	0.5
Sn	0.9	bdl	1.9	2.0	1.2	4.9	2.0	1.8	0.7
Sb	bdl	bdl	2.1	0.2	0.3	0.8	bdl	bdl	0.4
Hg (ppb)	10	bdl	453	25	46	39	20	18	bdl
AI[2]	96.95	86.00	65.59	97.27	86.70	77.55	80.88	71.27	74.46
CCPI[3]	99.06	95.34	92.88	95.22	95.12	98.49	93.58	91.15	93.96
Mg#[4]	53.56	48.94	33.87	57.68	50.89	43.25	48.22	44.62	50.21
Ba/Sr	2.23	2.12	0.50	12.39	2.79	0.17	0.91	0.23	1.10
Eu/Eu*[5]	0.36	0.15	0.50	0.57	0.37	0.46	0.31	0.41	0.28
2200W									
2250W	2251.53	2259.65	2255.24	2253.65	2254.14	2254.98	2257.51	2253.49	2260.80

[1]Calculated from Fe_2O_{3t}, assuming all iron is present as FeO

[2]Alteration Index: AI = 100 x (K_2O+MgO)/(K_2O+MgO+Na_2O+CaO)

[3]Chlorite-carbonate-pyrite index: CCPI = 100 x (MgO + FeO_t)/(MgO+FeO_t+Na_2O+K_2O)

[4]Mg# = $Mg^{2+}/(Mg^{2+} + Fe^{2+})$ (molar %)

[5]Eu/Eu* = $Eu_n/(Gd_n + Sm_n)^{0.5}$ (n = Normalized to Primitive Mantle; Sun and McDonough, 1989)

bdl = Below detection limit

Table A5. Complete Dataset of Altered Samples from the Rambler Rhyolite Formation *(continued)*

Sample ID	29864	29867	29899	36322	36638	60558	60561	60562	60564
Alteration	Quartz-chlorite -sulfides	Quartz-chlorite -sulfides	Quartz-chlorite -sulfides	Quartz-chlorite -sulfides	Quartz-chlorite -sulfides	Quartz-chlorite -sulfides	Quartz-chlorite -sulfides	Quartz-chlorite -sulfides	Quartz-chlorite -sulfides
DDH-Level	RM06-4E	RM06-4E	RM08-91	RM04-04	RMUG11-170	RM05-08	RM05-08	RM05-08	RM05-08
Zone	Ming South	Ming South	Ming South	Ming South	Ming South	Ming South	Ming South	Ming South	Ming South
Depth	1198.5	1232.1	11.27	966.1	176.3	1104.35	1124.7	1134.5	1164.15
Unit	Unit 1.1	Unit 1.1	Unit 1.2	Unit 1.2	Unit 1.2	Unit 1.2	Unit 1.2	Unit 1.2	Unit 1.2
SiO_2 (wt. %)	67.35	69.14	63.32	65.01	63.08	62.67	62.27	59.44	59.36
Al_2O_3	10.44	9.61	12.23	10.64	9.50	11.35	11.90	10.84	8.78
Fe_2O_{3t}	10.98	10.44	11.51	13.18	13.06	13.53	13.61	14.94	17.29
FeO_t[1]	9.88	9.39	10.36	11.86	11.75	12.17	12.25	13.44	15.56
MnO	0.056	0.072	0.047	0.064	0.080	0.058	0.057	0.069	0.059
MgO	6.42	6.03	3.35	4.70	7.23	6.58	4.90	5.86	6.24
CaO	0.60	0.60	0.98	0.41	0.27	0.62	0.31	0.37	0.45
Na_2O	0.76	0.70	2.49	1.24	0.16	0.65	0.37	0.37	0.44
K_2O	0.05	0.11	0.74	0.92	0.19	0.08	1.40	0.63	0.23
TiO_2	0.153	0.138	0.215	0.125	0.124	0.142	0.144	0.139	0.113
P_2O_5	0.03	0.03	0.06	0.03	0.02	0.04	0.04	0.03	0.02
LOI	3.92	4.02	5.22	4.17	5.48	4.26	3.94	5.58	6.85
Total	100.80	100.90	100.20	100.50	99.19	99.98	98.95	98.27	99.82
Sr (ppm)	46	40	70	30	10	16	17	15	26
Sc	19	14	20	24	32	23	27	24	22
Zr	67	43	55	37	31	39	40	36	33
Ba	10.3	28.1	243.6	402.4	23.9	15.2	373.3	124.5	42.7
Y	6.85	5.22	4.86	2.89	3.16	2.62	4.19	3.02	4.45
Nb	5.46	2.47	2.64	1.84	1.29	1.92	2.05	1.74	1.56
Cs	0.17	0.19	0.21	1.04	0.18	0.12	0.42	0.28	0.65
La	7.77	4.28	5.89	4.72	2.95	2.02	6.08	3.48	7.65
Ce	16.16	9.06	12.11	9.82	6.09	4.41	12.37	7.32	16.01
Pr	1.76	1.02	1.39	1.22	0.69	0.59	1.42	0.83	1.85
Nd	6.49	3.80	5.01	4.07	2.53	1.99	4.94	2.85	6.51
Sm	1.23	0.86	0.91	0.76	0.47	0.49	0.90	0.59	1.16
Eu	0.09	0.07	0.13	0.05	0.12	0.04	0.08	0.05	0.06
Gd	0.98	0.80	0.78	0.69	0.57	0.38	0.81	0.53	1.01
Tb	0.18	0.13	0.13	0.09	0.10	0.07	0.13	0.08	0.14
Dy	1.12	0.86	0.91	0.59	0.51	0.43	0.79	0.56	0.84
Ho	0.25	0.19	0.20	0.12	0.11	0.10	0.16	0.12	0.16
Er	0.84	0.56	0.61	0.36	0.39	0.38	0.47	0.37	0.54
Tm	0.14	0.10	0.11	0.10	0.06	0.11	0.08	0.07	0.09
Yb	0.96	0.64	0.78	0.34	0.47	0.44	0.56	0.44	0.53
Lu	0.15	0.14	0.12	0.05	0.08	0.06	0.09	0.07	0.09
Ta	0.43	0.18	0.20	0.17	0.11	0.18	0.18	0.17	0.15
Tl	0.05	0.10	0.28	0.40	0.25	0.06	0.58	0.23	0.41
Pb	6.8	2.1	28.9	6.4	6.0	33.3	26.0	10.2	4.6
Bi	0.49	0.65	0.59	1.28	1.44	0.48	1.03	1.97	6.16
Th	4.03	1.76	2.21	1.50	1.36	1.77	1.77	1.47	1.38
U	2.00	1.09	1.28	0.89	0.80	0.73	0.89	0.64	0.90
V	64.7	59.0	95.9	150.6	148.2	131.5	153.1	157.2	124.3
Cr	131.1	95.6	67.9	80.6	449.2	66.7	89.3	125.5	165.5
Co	37.2	37.6	31.7	33.2	34.4	40.8	40.6	39.6	255.6
Ni	34.7	31.0	17.2	25.6	87.0	23.1	30.6	35.3	41.0
Cu	3223	6448	2054	5608	5200	1705	3341	6179	12233
Zn	108	159	160	285	86	75	101	84	140
As	bdl	bdl	21.5	8.2	17.2	0.3	1.0	14.0	41.0
Ag	0.4	1.1	1.1	1.3	0.6	0.2	0.3	0.5	1.7
Sn	bdl	bdl	1.4	2.6	1.2	0.7	2.0	2.2	2.5
Sb	bdl	bdl	0.3	0.1	0.8	0.1	0.1	0.2	0.5
Hg (ppb)	6	8	34	26	57	17	74	63	30
AI[2]	82.63	82.53	54.10	77.30	94.52	83.98	90.26	89.76	87.91
CCPI[3]	95.55	95.31	82.14	89.22	98.30	96.50	91.27	95.41	97.23
Mg#[4]	53.67	53.36	36.57	41.40	52.31	49.07	41.63	43.73	41.69
Ba/Sr	0.22	0.70	3.48	13.41	2.39	0.95	21.96	8.30	1.64
Eu/Eu*[5]	0.25	0.24	0.41	0.17	0.50	0.19	0.25	0.21	0.16
2200W						2198.75			
2250W	2256.85	2255.35	2255.09	2254.07	2253.14	2254.20	2253.73	2253.62	2252.93

[1]Calculated from Fe_2O_{3t}, assuming all iron is present as FeO

[2]Alteration Index: AI = 100 x (K_2O+MgO)/(K_2O+MgO+Na_2O+CaO)

[3]Chlorite-carbonate-pyrite index: CCPI = 100 x (MgO + FeO_t)/(MgO+FeO_t+Na_2O+K_2O)

[4]Mg# = $Mg^{2+}/(Mg^{2+} + Fe^{2+})$ (molar %)

[5]Eu/Eu* = $Eu_n/(Gd_n + Sm_n)^{0.5}$ (n = Normalized to Primitive Mantle; Sun and McDonough, 1989)

bdl = Below detection limit

Table A5. Complete Dataset of Altered Samples from the Rambler Rhyolite Formation *(continued)*

Sample ID	60566	60567	60568	60572	60573	60581	62063	62087	106413
Alteration	Quartz-chlorite -sulfides	Quartz-chlorite -sulfides	Quartz-chlorite -sulfides	Quartz-chlorite -sulfides	Quartz-chlorite -sulfides	Quartz-chlorite -sulfides	Quartz-chlorite -sulfides	Quartz-chlorite -sulfides	Quartz-chlorite -sulfides
DDH-Level	RM05-08	RM05-08	RM05-08	RM05-08	RM05-08	RM05-08	RM04-04	1450	1450
Zone	Ming South	Ming South	Ming South	Ming South	Ming South	Ming South	Ming South	Ming South	Ming South
Depth	1194.05	1203.45	1217.2	1253.6	1269.8	1349	1078.9	300	300
Unit	Unit 1.2	Unit 1.2	Unit 1.2	Unit 1.1	Unit 1.1	Unit 1.1	Unit 1.1	Unit 1.2	Unit 1.2
SiO_2 (wt. %)	68.32	63.44	64.13	61.70	63.57	64.45	62.58	60.93	69.38
Al_2O_3	10.57	8.58	10.29	9.30	9.85	10.45	10.46	10.32	9.35
Fe_2O_{3t}	9.43	13.25	12.10	14.51	13.74	9.76	13.38	14.03	9.93
FeO_t[1]	8.49	11.92	10.89	13.06	12.36	8.78	12.04	12.62	8.94
MnO	0.064	0.064	0.076	0.099	0.064	0.078	0.060	0.116	0.078
MgO	5.77	7.15	6.70	6.12	6.52	7.00	5.47	7.07	5.99
CaO	0.92	1.06	0.71	1.19	0.85	2.40	0.15	1.27	0.31
Na_2O	1.23	0.14	0.65	0.36	0.28	0.58	1.45	0.17	0.17
K_2O	0.27	0.09	0.16	0.16	0.35	0.41	0.25	0.10	0.47
TiO_2	0.159	0.118	0.148	0.180	0.156	0.155	0.162	0.125	0.113
P_2O_5	0.05	0.03	0.04	0.05	0.04	0.04	0.03	0.03	0.03
LOI	3.26	4.59	4.48	4.24	4.35	3.55	4.03	5.05	4.28
Total	100.00	98.50	99.48	97.91	99.79	98.85	98.03	99.21	100.10
Sr (ppm)	50	10	55	41	43	48	11	56	14
Sc	13	27	23	26	26	18	24	31	22
Zr	53	31	40	35	41	51	31	35	32
Ba	34.7	11.9	35.5	27.9	43.0	35.3	28.4	15.1	76.1
Y	5.19	3.33	4.08	5.20	5.06	5.59	2.97	4.37	2.65
Nb	2.41	1.74	0.64	1.87	2.17	3.09	1.53	1.29	1.74
Cs	0.55	0.36	0.58	0.66	1.02	1.30	0.20	0.23	0.27
La	3.88	3.01	3.73	5.26	5.45	6.56	4.78	4.23	2.87
Ce	8.26	6.17	7.80	10.77	11.87	13.71	9.75	8.52	6.16
Pr	0.96	0.72	0.94	1.24	1.41	1.50	1.12	1.01	0.67
Nd	3.64	2.76	3.29	4.57	5.20	5.38	4.17	3.66	2.65
Sm	0.72	0.62	0.75	0.87	1.07	0.97	0.85	0.76	0.53
Eu	0.05	0.08	0.09	0.12	0.08	0.10	0.07	0.18	0.06
Gd	0.78	0.53	0.63	0.94	0.90	0.87	0.68	0.67	0.46
Tb	0.12	0.09	0.10	0.14	0.15	0.15	0.11	0.13	0.07
Dy	0.83	0.58	0.68	0.90	0.99	0.89	0.60	0.77	0.41
Ho	0.19	0.12	0.15	0.20	0.19	0.21	0.13	0.17	0.10
Er	0.64	0.41	0.50	0.57	0.61	0.68	0.35	0.49	0.31
Tm	0.10	0.09	0.10	0.10	0.10	0.12	0.06	0.11	0.05
Yb	0.72	0.46	0.55	0.66	0.63	0.82	0.43	0.62	0.41
Lu	0.12	0.08	0.09	0.10	0.10	0.12	0.06	0.09	0.06
Ta	0.21	0.17	0.18	0.16	0.19	0.33	0.14	bdl	bdl
Tl	0.23	0.13	0.14	0.17	0.22	0.19	0.10	0.35	0.44
Pb	5.0	3.0	6.4	3.1	8.1	3.4	10.9	10.0	6.5
Bi	0.63	2.67	0.68	1.02	3.12	0.57	0.55	2.75	0.73
Th	1.95	1.58	1.84	1.53	1.94	3.33	1.48	1.92	1.82
U	0.93	0.74	0.81	0.71	0.99	1.12	0.85	0.85	1.17
V	55.1	136.5	148.3	113.1	116.3	77.3	129.8	169.8	165.0
Cr	65.7	600.3	168.8	340.8	361.9	96.1	275.3	281.8	251.9
Co	45.6	104.3	46.6	58.4	50.9	30.3	38.7	33.1	25.8
Ni	16.2	129.5	39.8	75.1	71.2	25.9	50.4	44.4	29.2
Cu	2163	11156	4596	7537	7513	1053	8688	17183	1357
Zn	64	493	117	121	106	84	88	198	76
As	bdl	2.4	0.3	bdl	0.4	bdl	2.1	5.2	2.8
Ag	0.3	1.2	0.9	2.5	1.9	bdl	0.6	1.5	0.3
Sn	0.6	1.4	0.9	1.2	1.5	0.6	0.7	2.7	0.8
Sb	bdl	0.1	bdl	bdl	0.1	bdl	0.4	1.2	0.7
Hg (ppb)	bdl	23	13	26	12	bdl	124	277	108
AI[2]	73.75	85.78	83.45	80.20	85.88	71.32	78.14	83.28	93.08
CCPI[3]	91.02	98.89	95.87	97.54	96.98	94.42	91.73	98.74	96.14
Mg#[4]	54.79	51.67	52.31	45.52	48.45	58.69	44.75	49.96	54.44
Ba/Sr	0.69	1.19	0.65	0.68	1.00	0.73	2.58	0.27	5.44
Eu/Eu*[5]	0.17	0.33	0.31	0.37	0.25	0.30	0.24	0.62	0.27
2200W									
2250W	2252.52	2252.86	2253.63	2253.80	2253.67	2252.84	2252.57	2252.34	

[1]Calculated from Fe_2O_{3t}, assuming all iron is present as FeO

[2]Alteration Index: AI = 100 x (K_2O+MgO)/(K_2O+MgO+Na_2O+CaO)

[3]Chlorite-carbonate-pyrite index: CCPI = 100 x (MgO + FeO_t)/(MgO+FeO_t+Na_2O+K_2O)

[4]Mg# = $Mg^{2+}/(Mg^{2+} + Fe^{2+})$ (molar %)

[5]$Eu/Eu^* = Eu_n/(Gd_n + Sm_n)^{0.5}$ (n = Normalized to Primitive Mantle; Sun and McDonough, 1989)

bdl = Below detection limit

Table A5. Complete Dataset of Altered Samples from the Rambler Rhyolite Formation *(continued)*

Sample ID	29807	29852	29855	29856	29862	29868	29869	29873	29875
Alteration	Quartz-chlorite -sericite	Quartz-chlorite -sericite	Quartz-chlorite -sericite	Quartz-chlorite -sericite	Quartz-chlorite -sericite	Quartz-chlorite -sericite	Quartz-chlorite -sericite	Quartz-chlorite -sericite	Quartz-chlorite -sericite
DDH-Level	RM07-8F	RM06-4E	RM06-4E	RM06-4E	RM06-4E	RM06-4E	RM06-4E	RM07-8F	RM07-8F
Zone	Ming South	Ming South	Ming South	Ming South	Ming South	Ming South	Ming South	Ming South	Ming South
Depth	1289.77	1021.72	1060.33	1072.17	1143.6	1251.15	1261.1	1066.42	1129.22
Unit	Unit 1.2	Unit 1.2	Unit 1.2	Unit 1.2	Unit 1.1	Unit 1.2	Unit 1.1	Unit 1.2	Unit 1.2
SiO_2 (wt. %)	66.89	65.86	62.83	52.08	71.55	70.20	69.48	64.73	63.43
Al_2O_3	10.21	10.71	10.38	8.92	11.25	10.33	12.27	10.64	10.99
Fe_2O_{3t}	12.52	11.79	14.54	19.53	8.27	8.19	6.66	12.92	13.17
FeO_t[1]	11.27	10.61	13.08	17.57	7.44	7.37	5.99	11.63	11.85
MnO	0.059	0.064	0.070	0.057	0.042	0.054	0.038	0.040	0.064
MgO	6.08	6.25	7.29	5.34	3.76	5.84	4.73	2.94	7.16
CaO	0.30	0.14	0.26	0.19	0.26	0.71	0.85	0.13	0.21
Na_2O	0.15	0.25	0.27	0.28	0.33	1.25	1.94	0.32	0.40
K_2O	0.26	0.75	0.34	0.48	1.81	0.78	0.78	1.71	0.62
TiO_2	0.147	0.143	0.178	0.154	0.169	0.158	0.175	0.131	0.144
P_2O_5	0.04	0.03	0.03	0.01	0.06	0.05	0.05	0.04	0.03
LOI	4.27	4.80	4.60	7.21	3.16	3.23	3.08	5.55	4.67
Total	100.90	100.80	100.80	94.26	100.70	100.80	100.00	99.13	100.90
Sr (ppm)	13	9	15	17	21	39	44	17	11
Sc	19	23	28	23	14	15	22	25	31
Zr	57	45	38	33	58	51	55	36	39
Ba	37.3	283.4	69.8	81.3	630.2	66.6	146.3	377.9	113.1
Y	5.04	3.42	3.25	3.02	5.21	4.66	3.75	2.50	3.16
Nb	3.46	4.33	2.87	2.19	6.36	2.33	3.18	1.98	1.97
Cs	0.16	0.39	0.63	0.31	0.81	0.96	0.25	0.43	0.98
La	12.22	6.25	4.23	6.08	8.54	4.27	10.45	5.08	5.91
Ce	24.56	12.90	8.65	12.52	17.50	8.36	20.21	9.70	11.59
Pr	2.63	1.43	1.04	1.43	1.94	0.95	2.11	1.10	1.30
Nd	9.26	5.01	3.74	5.35	6.85	3.56	7.21	4.07	4.48
Sm	1.50	0.88	0.67	0.98	1.27	0.75	1.36	0.70	0.83
Eu	0.16	0.06	0.04	0.07	0.11	0.11	0.28	0.13	0.07
Gd	1.04	0.75	0.61	0.69	0.98	0.73	1.08	0.59	0.69
Tb	0.16	0.10	0.10	0.11	0.15	0.11	0.15	0.08	0.12
Dy	0.90	0.60	0.56	0.65	0.95	0.72	0.82	0.47	0.65
Ho	0.20	0.13	0.11	0.12	0.19	0.18	0.16	0.10	0.12
Er	0.61	0.37	0.41	0.33	0.64	0.60	0.41	0.32	0.34
Tm	0.09	0.06	0.08	0.07	0.11	0.10	0.07	0.06	0.05
Yb	0.68	0.52	0.46	0.38	0.73	0.63	0.46	0.33	0.43
Lu	0.10	0.08	0.07	0.07	0.13	0.11	0.09	0.08	0.07
Ta	0.22	0.31	bdl	bdl	0.39	0.18	0.32	0.16	0.17
Tl	0.05	0.25	0.33	0.16	0.39	0.31	0.17	0.43	0.34
Pb	17.5	bdl	3.2	53.3	1.4	24.1	32.7	39.1	3.7
Bi	0.86	0.70	0.59	5.39	0.49	0.50	0.24	1.19	0.85
Th	3.55	4.00	2.62	1.98	2.96	1.66	3.44	1.45	1.76
U	1.38	1.05	0.72	0.74	1.13	0.93	1.75	1.01	0.71
V	60.1	138.6	146.9	114.7	52.7	53.4	103.5	135.9	156.6
Cr	209.0	54.4	252.5	204.5	36.1	50.1	176.9	121.3	279.9
Co	38.2	28.1	80.7	182.0	20.7	27.0	24.3	51.7	22.0
Ni	45.0	17.8	57.9	48.1	11.5	28.0	36.6	32.0	57.1
Cu	5012	100	2398	32508	1329	2153	158	622	376
Zn	116	112	58	592	44	194	79	77	144
As	bdl	1.6	bdl	80.4	bdl	bdl	bdl	44.0	4.3
Ag	0.4	0.2	0.2	4.2	0.4	0.4	bdl	bdl	bdl
Sn	0.5	1.2	0.9	2.8	1.3	bdl	bdl	1.1	1.1
Sb	bdl	bdl	bdl	0.5	bdl	bdl	0.5	0.5	bdl
Hg (ppb)	bdl	bdl	6	103	bdl	bdl	bdl	10	bdl
AI[2]	93.37	94.72	93.50	92.53	90.42	77.16	66.39	91.18	92.73
CCPI[3]	97.84	94.75	97.28	97.03	84.90	87.36	80.72	88.65	95.22
Mg#[4]	49.03	51.22	49.83	35.13	47.39	58.55	58.45	31.07	51.85
Ba/Sr	2.87	31.49	4.65	4.78	30.01	1.71	3.33	22.23	10.28
Eu/Eu*[5]	0.42	0.19	0.17	0.24	0.30	0.40	0.77	0.47	0.23
2200W	2243.89								
2250W	2253.24	2251.50	2251.67	2251.85	2253.84	2251.32	2253.59	2254.14	2257.35

[1]Calculated from Fe_2O_{3t}, assuming all iron is present as FeO

[2]Alteration Index: AI = 100 x (K_2O+MgO)/(K_2O+MgO+Na_2O+CaO)

[3]Chlorite-carbonate-pyrite index: CCPI = 100 x (MgO + FeO_t)/(MgO+FeO_t+Na_2O+K_2O)

[4]Mg# = $Mg^{2+}/(Mg^{2+} + Fe^{2+})$ (molar %)

[5]$Eu/Eu^* = Eu_n/(Gd_n + Sm_n)^{0.5}$ (n = Normalized to Primitive Mantle; Sun and McDonough, 1989)

bdl = Below detection limit

Table A5. Complete Dataset of Altered Samples from the Rambler Rhyolite Formation *(continued)*

Sample ID	36321	36634	36635	36636	60556	60557	60559	60563	60574
Alteration	Quartz-chlorite -sericite	Quartz-chlorite -sericite	Quartz-chlorite -sericite	Quartz-chlorite -sericite	Quartz-chlorite -sericite	Quartz-chlorite -sericite	Quartz-chlorite -sericite	Quartz-chlorite -sericite	Quartz-chlorite -sericite
DDH-Level	RM04-04	RMUG11-170	RMUG11-170	RMUG11-170	RM05-08	RM05-08	RM05-08	RM05-08	RM05-08
Zone	Ming South	Ming South	Ming South	Ming South	Ming South	Ming South	Ming South	Ming South	Ming South
Depth	939.1	91.9	94.8	130.65	1084.8	1094.9	1114.4	1144.4	1278.18
Unit	Unit 1.2	Unit 1.2	Unit 1.2	Unit 1.2	Unit 1.2	Unit 1.2	Unit 1.2	Unit 1.2	Unit 1.1
SiO_2 (wt. %)	62.41	70.07	62.97	62.95	61.03	63.75	67.05	64.81	66.63
Al_2O_3	10.91	10.97	11.75	11.26	11.15	11.39	10.27	10.26	11.10
Fe_2O_{3t}	14.46	9.40	12.27	12.24	15.93	12.69	13.11	12.50	10.85
FeO_t[1]	13.01	8.46	11.04	11.01	14.33	11.42	11.80	11.25	9.76
MnO	0.067	0.062	0.070	0.075	0.052	0.062	0.048	0.058	0.055
MgO	5.42	4.64	5.82	6.59	4.50	4.97	4.93	5.95	5.67
CaO	0.15	0.24	0.13	0.32	0.13	0.18	0.17	0.17	0.13
Na_2O	0.27	0.21	0.12	0.29	0.17	0.15	0.21	0.18	0.17
K_2O	0.81	1.26	1.02	0.54	1.39	1.31	0.82	0.60	0.89
TiO_2	0.140	0.140	0.138	0.135	0.133	0.142	0.126	0.150	0.145
P_2O_5	0.03	0.02	0.03	0.04	0.03	0.04	0.02	0.04	0.04
LOI	4.93	3.62	4.72	4.61	6.43	5.00	3.98	4.55	3.92
Total	99.60	100.60	99.04	99.04	101.00	99.69	100.80	99.27	99.61
Sr (ppm)	9	11	7	10	9	10	8	7	8
Sc	26	23	23	20	28	26	23	23	23
Zr	41	38	40	38	37	38	34	38	41
Ba	116.8	199.8	187.7	99.0	236.8	355.2	131.3	89.3	217.7
Y	3.19	3.36	3.49	2.57	4.12	4.40	2.64	3.19	3.58
Nb	1.87	1.86	1.78	1.74	1.79	2.18	1.69	2.11	2.34
Cs	0.24	0.39	0.27	0.21	0.38	0.40	0.24	0.29	0.30
La	6.31	5.33	4.01	3.23	14.26	7.85	1.53	4.87	3.46
Ce	12.54	10.87	8.55	6.79	28.02	15.37	3.06	10.22	7.42
Pr	1.45	1.25	1.01	0.83	3.21	1.75	0.40	1.17	0.88
Nd	4.88	4.54	3.48	2.81	11.23	6.18	1.40	4.16	3.22
Sm	0.95	0.84	0.70	0.54	2.12	1.21	0.33	0.85	0.67
Eu	0.16	0.07	0.03	0.05	0.31	0.18	0.05	0.06	0.04
Gd	0.81	0.69	0.55	0.45	1.52	0.93	0.34	0.76	0.59
Tb	0.12	0.10	0.09	0.06	0.20	0.14	0.06	0.11	0.11
Dy	0.63	0.55	0.59	0.44	1.10	0.83	0.42	0.65	0.62
Ho	0.12	0.11	0.12	0.10	0.17	0.17	0.10	0.13	0.14
Er	0.43	0.39	0.45	0.31	0.41	0.53	0.38	0.38	0.45
Tm	0.11	0.11	0.06	0.09	0.08	0.08	0.08	0.06	0.08
Yb	0.43	0.47	0.48	0.30	0.42	0.57	0.40	0.42	0.52
Lu	0.07	0.06	0.07	0.06	0.07	0.09	0.06	0.07	0.09
Ta	0.19	0.14	0.16	0.17	0.15	0.18	0.15	0.19	0.19
Tl	0.28	0.68	0.58	0.51	0.37	0.42	0.52	0.36	0.17
Pb	71.4	16.0	11.3	26.8	61.7	64.4	21.9	6.1	18.2
Bi	0.74	0.36	0.48	1.82	0.80	0.42	1.07	1.30	0.53
Th	1.53	1.52	1.67	1.44	1.63	1.96	1.49	1.88	1.92
U	0.94	0.70	0.77	0.67	0.95	0.96	0.96	0.95	0.99
V	154.4	152.8	153.5	143.4	128.0	141.8	131.5	147.9	114.3
Cr	127.5	71.9	75.1	103.5	138.8	138.5	91.5	185.9	48.5
Co	22.2	25.9	45.7	38.1	35.7	33.9	38.3	24.5	25.1
Ni	25.2	24.6	19.4	25.4	28.1	31.7	29.8	44.6	16.5
Cu	10941	477	1289	7231	351	326	2675	5103	385
Zn	875	199	118	303	297	463	93	91	177
As	3.9	1.8	3.2	3.6	74.6	8.3	0.8	6.1	bdl
Ag	2.0	bdl	bdl	0.4	0.2	0.2	0.6	0.6	bdl
Sn	1.5	1.7	1.1	1.1	1.3	1.1	1.6	1.8	0.4
Sb	0.2	0.5	0.4	1.1	0.5	0.3	0.2	0.9	bdl
Hg (ppb)	88	124	150	119	19	10	165	221	bdl
AI[2]	93.68	92.91	96.47	92.12	95.15	95.01	93.80	94.93	95.63
CCPI[3]	94.85	90.52	94.07	95.78	92.91	92.36	94.60	95.94	93.97
Mg#[4]	42.61	49.44	48.44	51.61	35.88	43.69	42.69	48.53	50.87
Ba/Sr	12.98	18.16	26.81	9.90	26.31	35.52	16.41	12.75	27.22
Eu/Eu*[5]	0.52	0.25	0.12	0.22	0.68	0.51	0.28	0.20	0.16
2200W	2204.82	2203.59	2203.27	2205.43	2199.46	2201.30	2198.92	2201.50	
2250W	2254.17	2254.58	2253.87	2253.67	2253.96	2253.69	2254.22	2253.03	2253.69

[1]Calculated from Fe_2O_{3t}, assuming all iron is present as FeO

[2]Alteration Index: AI = 100 x (K_2O+MgO)/(K_2O+MgO+Na_2O+CaO)

[3]Chlorite-carbonate-pyrite index: CCPI = 100 x (MgO + FeO_t)/(MgO+FeO_t+Na_2O+K_2O)

[4]Mg# = $Mg^{2+}/(Mg^{2+} + Fe^{2+})$ (molar %)

[5]$Eu/Eu^* = Eu_n/(Gd_n + Sm_n)^{0.5}$ (n = Normalized to Primitive Mantle; Sun and McDonough, 1989)

bdl = Below detection limit

Table A5. Complete Dataset of Altered Samples from the Rambler Rhyolite Formation *(continued)*

Sample ID	60575	62058	62065	62522	36317	62178	62179	62181	62182
Alteration	Quartz-chlorite -sericite	Quartz-chlorite -sericite	Quartz-chlorite -sericite	Quartz-chlorite -sericite	Quartz-sericite	Quartz-sericite	Quartz-sericite	Quartz-sericite	Quartz-sericite
DDH-Level	RM05-08	RM04-04	RM04-04	RM06-04C	RM04-04	RM05-08	RM05-08	RM05-08	RM05-08
Zone	Ming South	Ming South	Ming South	Ming South	Ming South	Ming South	Ming South	Ming South	Ming South
Depth	1288.35	903.5	1149.7	889	882.6	1006.3	1007.4	1013.8	1016.7
Unit	Unit 1.1	Unit 1.2	Unit 1.1	Unit 1.2	Unit 1.3	Unit 1.3	Unit 1.3	Unit 1.3	Unit 1.3
SiO_2 (wt. %)	66.79	68.10	70.91	57.19	69.78	62.88	72.31	64.86	63.13
Al_2O_3	11.45	12.03	9.88	15.03	16.30	16.15	10.97	17.15	16.54
Fe_2O_{3t}	10.83	8.82	8.63	11.43	2.70	6.45	6.23	5.02	6.71
FeO_t[1]	9.75	7.94	7.77	10.29	2.43	5.80	5.61	4.52	6.04
MnO	0.053	0.063	0.045	0.060	0.017	0.031	0.007	0.022	0.031
MgO	6.07	3.85	4.52	3.85	1.29	1.70	0.55	1.45	2.05
CaO	0.16	0.21	0.16	0.72	2.58	2.03	0.27	1.06	1.73
Na_2O	0.27	0.26	0.35	3.48	1.45	0.69	0.42	1.21	1.52
K_2O	0.84	2.15	0.90	0.92	2.97	4.53	3.28	4.78	4.02
TiO_2	0.148	0.206	0.160	0.262	0.187	0.273	0.202	0.202	0.187
P_2O_5	0.05	0.04	0.04	0.08	bdl	0.05	0.06	0.03	0.01
LOI	4.06	4.17	3.08	4.52	2.37	4.86	4.40	3.83	2.87
Total	100.70	99.91	98.66	97.54	99.64	99.65	98.68	99.61	98.81
Sr (ppm)	13	14	10	35	145	56	37	75	93
Sc	26	20	15	28	20	31	19	25	23
Zr	41	53	50	61	81	69	54	80	82
Ba	101.9	449.8	126.7	242.0	113.8	253.0	269.7	690.8	396.0
Y	3.05	5.23	3.57	5.61	3.82	7.64	5.65	4.29	4.93
Nb	1.98	1.93	2.65	3.52	2.10	2.65	1.48	3.90	4.01
Cs	0.20	0.57	0.24	0.38	1.47	2.31	0.93	2.17	2.37
La	5.53	7.62	6.51	6.30	9.22	8.43	5.91	6.76	7.77
Ce	11.94	14.94	13.08	13.48	19.20	17.12	11.44	13.86	15.52
Pr	1.32	1.62	1.50	1.72	2.16	2.00	1.36	1.64	1.81
Nd	4.93	5.51	4.90	6.23	7.40	7.07	4.94	5.66	5.96
Sm	0.90	1.15	1.03	1.31	1.37	1.48	1.12	1.13	1.09
Eu	0.06	0.21	0.05	0.20	0.34	0.61	0.39	0.24	0.28
Gd	0.75	1.01	0.71	1.25	1.11	1.42	1.07	0.94	1.00
Tb	0.11	0.16	0.10	0.16	0.17	0.23	0.18	0.15	0.15
Dy	0.65	1.04	0.62	1.05	1.06	1.35	1.08	0.90	1.00
Ho	0.11	0.22	0.13	0.21	0.20	0.31	0.23	0.20	0.21
Er	0.34	0.61	0.44	0.66	0.50	0.86	0.64	0.56	0.67
Tm	0.05	0.11	0.11	0.13	0.07	0.16	0.13	0.08	0.13
Yb	0.42	0.67	0.43	0.72	0.45	0.99	0.68	0.57	0.58
Lu	0.07	0.11	0.08	0.15	0.06	0.17	0.12	0.09	0.07
Ta	0.16	0.19	0.22	bdl	0.17	bdl	bdl	bdl	bdl
Tl	0.11	1.77	0.20	1.08	8.59	6.74	3.14	5.50	4.32
Pb	23.7	46.0	8.6	37.9	86.1	82.9	223.6	76.0	40.0
Bi	0.56	0.60	0.09	0.82	0.07	0.11	0.39	0.19	0.25
Th	1.81	2.06	2.57	2.98	3.18	3.54	2.73	4.06	4.20
U	0.82	1.54	1.09	1.71	2.01	1.56	3.25	5.40	1.15
V	138.7	100.2	60.9	111.7	139.7	128.6	91.6	215.3	91.7
Cr	105.7	64.7	181.0	89.3	114.1	423.4	117.2	229.0	194.9
Co	28.7	18.0	23.8	20.1	2.3	19.7	11.2	7.4	8.5
Ni	28.4	15.7	43.0	19.6	10.4	82.8	27.8	bdl	32.5
Cu	881	3113	36	6775	103	139	87	1465	131
Zn	101	531	62	155	870	456	595	2005	1988
As	bdl	7.8	bdl	31.0	5.6	50.7	29.5	8.5	6.4
Ag	0.2	1.3	bdl	2.2	bdl	0.2	0.6	1.1	0.3
Sn	0.4	1.1	0.5	2.3	1.6	1.3	1.6	12.5	1.1
Sb	bdl	1.7	bdl	3.4	2.0	3.4	1.8	2.0	1.1
Hg (ppb)	bdl	411	bdl	272	243	125	135	449	140
AI[2]	94.14	92.74	91.40	53.18	51.39	69.61	84.73	73.29	65.13
CCPI[3]	93.84	84.02	91.32	77.64	47.44	60.96	64.69	51.93	61.26
Mg#[4]	52.61	46.37	50.92	40.02	48.63	34.30	14.89	36.39	37.70
Ba/Sr	7.84	32.13	12.67	6.91	0.79	4.52	7.29	9.21	4.26
Eu/Eu*[5]	0.21	0.60	0.17	0.53	0.91	1.51	1.12	0.71	0.81
2200W	2198.87	2202.30	2201.97	2203.74	2201.26	2207.82	2207.49	2209.21	2204.31
2250W	2253.96	2253.17	2253.41		2254.23	2247.86	2245.61		2251.49

[1]Calculated from Fe_2O_{3t}, assuming all iron is present as FeO

[2]Alteration Index: AI = 100 x $(K_2O+MgO)/(K_2O+MgO+Na_2O+CaO)$

[3]Chlorite-carbonate-pyrite index: CCPI = 100 x $(MgO + FeO_t)/(MgO+FeO_t+Na_2O+K_2O)$

[4]Mg# = $Mg^{2+}/(Mg^{2+} + Fe^{2+})$ (molar %)

[5]Eu/Eu* = $Eu_n/(Gd_n + Sm_n)^{0.5}$ (n = Normalized to Primitive Mantle; Sun and McDonough, 1989)

bdl = Below detection limit

Table A5. Complete Dataset of Altered Samples from the Rambler Rhyolite Formation *(continued)*

Sample ID	62192	62524	106401	29816	29819	29827	29828	29829	29882
Alteration	Quartz-sericite	Quartz-sericite	Quartz-sericite	Quartz-sericite	Quartz-sericite	Quartz-sericite	Quartz-sericite	Quartz-sericite	Quartz-sericite
DDH-Level	481	RM06-04C	RMUG08-25	RM08-145	RM08-145	RMUG08-142	RMUG08-142	RMUG08-142	RM08-121
Zone	1807	Ming South	Ming South	1806	1806	1806	1806	1806	1806
Depth	481	882	42.5	21.37	56.63	20.52	36	47.1	66.72
Unit	Unit 1.3	Unit 1.3	Unit 1.3	Unit 1.2	Unit 1.2	Unit 1.2	Unit 1.2	Unit 1.2	Unit 1.2
SiO_2 (wt. %)	58.01	66.92	76.47	73.25	58.13	71.21	59.35	67.07	58.88
Al_2O_3	21.04	17.67	12.20	11.27	17.59	10.82	19.79	15.99	16.64
Fe_2O_{3t}	5.11	3.44	2.53	4.89	5.91	5.47	6.63	5.72	7.27
FeO_t[1]	4.60	3.10	2.28	4.40	5.32	4.92	5.97	5.15	6.54
MnO	0.028	0.013	0.005	0.009	0.010	0.039	0.023	0.012	0.060
MgO	2.45	1.67	0.23	0.61	0.47	1.32	1.42	0.49	2.13
CaO	1.93	3.45	0.38	0.31	0.96	2.80	0.71	0.50	6.60
Na_2O	4.59	1.17	0.73	1.71	4.19	1.47	1.19	0.95	2.69
K_2O	3.55	3.26	2.76	2.53	2.87	2.08	5.24	4.11	0.53
TiO_2	0.350	0.210	0.138	0.162	0.261	0.160	0.280	0.226	0.230
P_2O_5	0.01	0.02	0.04	0.03	0.01	0.05	0.02	bdl	0.01
LOI	2.75	2.29	3.10	3.82	4.72	5.41	5.62	4.68	5.36
Total	99.82	100.10	98.58	98.60	95.12	100.80	100.30	99.74	100.40
Sr (ppm)	113	134	59	52	116	71	60	58	236
Sc	36	20	14	17	29	15	31	21	26
Zr	80	94	62	52	86	58	88	75	73
Ba	414.2	137.0	123.6	213.6	1118.9	108.2	225.9	153.2	44.3
Y	5.53	6.52	4.55	2.51	7.10	5.61	7.03	5.28	9.73
Nb	1.96	1.66	1.96	1.03	1.09	1.66	1.93	2.11	3.48
Cs	0.93	0.90	0.33	0.42	0.56	0.92	0.94	0.75	1.02
La	10.28	9.85	7.04	5.05	13.93	5.82	7.84	5.50	11.19
Ce	21.72	20.40	13.79	10.19	26.34	11.75	16.59	11.53	21.37
Pr	2.57	2.18	1.53	1.13	2.81	1.37	1.88	1.32	2.52
Nd	8.99	7.47	5.76	4.23	10.21	4.96	7.09	5.03	8.85
Sm	1.94	1.44	1.02	0.88	1.84	0.98	1.38	1.01	1.77
Eu	0.49	0.36	0.35	0.45	1.38	0.42	0.54	0.58	0.99
Gd	1.64	1.18	0.89	0.73	1.60	1.01	1.32	0.95	1.76
Tb	0.24	0.21	0.14	0.11	0.25	0.16	0.20	0.15	0.28
Dy	1.42	1.22	0.83	0.61	1.43	0.99	1.39	1.06	1.81
Ho	0.26	0.24	0.16	0.10	0.28	0.21	0.30	0.21	0.40
Er	0.68	0.75	0.48	0.28	0.83	0.68	0.91	0.63	1.16
Tm	0.12	0.14	0.09	0.05	0.14	0.11	0.14	0.11	0.22
Yb	0.77	0.73	0.70	0.33	0.92	0.74	1.08	0.81	1.30
Lu	0.13	0.08	0.15	0.06	0.17	0.13	0.18	0.13	0.20
Ta	0.17	bdl	bdl	0.04	0.06	0.10	0.08	0.13	0.29
Tl	7.65	16.83	7.92	3.68	16.40	1.75	14.79	19.65	2.94
Pb	90.9	40.7	1016.5	5718.3	5364.8	28.0	35.2	45.8	141.8
Bi	1.57	0.16	0.10	0.21	0.43	0.61	0.08	0.08	0.16
Th	3.51	4.34	3.27	1.82	3.14	1.97	3.13	2.83	2.77
U	2.59	1.95	3.07	2.72	13.63	1.98	4.09	16.43	22.45
V	238.4	83.1	80.8	94.6	169.9	54.8	137.9	154.3	190.0
Cr	193.3	137.6	146.3	101.3	345.5	73.8	221.4	145.1	342.7
Co	8.8	7.2	8.2	10.3	20.2	9.6	15.0	21.2	25.4
Ni	33.4	25.0	25.4	28.5	67.1	20.9	39.8	99.5	166.1
Cu	514	84	89	976	1559	96	135	bdl	116
Zn	275	184	1239	9839	22096	77	74	31	536
As	3.4	4.3	187.3	61.0	91.6	11.6	15.2	1657.1	442.5
Ag	0.4	0.1	2.1	5.9	8.2	0.7	1.0	0.6	3.0
Sn	3.3	1.0	2.1	0.4	0.6	1.2	1.2	0.7	1.4
Sb	1.0	1.1	5.7	77.6	8.1	4.1	2.9	8.3	13.1
Hg (ppb)	147	15	1210	7100	9160	33	424	771	1630
AI[2]	47.92	51.62	72.93	60.85	39.34	44.33	77.80	76.03	22.26
CCPI[3]	48.15	53.56	44.16	56.47	47.47	65.67	55.59	55.10	74.48
Mg#[4]	48.71	49.02	15.26	19.82	13.61	32.34	29.79	14.51	36.72
Ba/Sr	3.67	1.02	2.09	4.11	9.65	1.52	3.77	2.64	0.19
Eu/Eu*[5]	1.10	0.94	1.06	1.49	3.14	1.26	1.38	1.77	2.22
2200W	2207.69	2203.21	2197.29	2209.61	2213.36	2209.66	2210.74	2207.42	2203.57
2250W	2250.04	2253.49			2236.06			2252.63	2255.05

[1]Calculated from Fe_2O_{3t}, assuming all iron is present as FeO

[2]Alteration Index: $AI = 100 \times (K_2O+MgO)/(K_2O+MgO+Na_2O+CaO)$

[3]Chlorite-carbonate-pyrite index: $CCPI = 100 \times (MgO + FeO_t)/(MgO+FeO_t+Na_2O+K_2O)$

[4]$Mg\# = Mg^{2+}/(Mg^{2+} + Fe^{2+})$ (molar %)

[5]$Eu/Eu^* = Eu_n/(Gd_n + Sm_n)^{0.5}$ (n = Normalized to Primitive Mantle; Sun and McDonough, 1989)

bdl = Below detection limit

Table A5. Complete Dataset of Altered Samples from the Rambler Rhyolite Formation *(continued)*

Sample ID	29889	29951	29953	36639	60521	62184	29847	29848	29851
Alteration	Quartz-sericite	Quartz-sericite	Quartz-sericite	Quartz-sericite	Quartz-sericite	Quartz-sericite	Quartz-sericite -chlorite	Quartz-sericite -chlorite	Quartz-sericite -chlorite
DDH-Level	RM08-151	RM08-91	RM08-91	RMUG08-136	434	RM05-08	RM06-4E	RM06-4E	RM06-4E
Zone	1806	Ming South	Ming South	1806	1807	Ming South	Ming South	Ming South	Ming South
Depth	61.13	39.02	53.46	34.65	434	1029.95	915.08	934.2	1004.64
Unit	Unit 1.2	Unit 1.2	Unit 1.2	Unit 1.2	Unit 1.2	Unit 1.2	Unit 1.2	Unit 1.2	Unit 1.2
SiO_2 (wt. %)	67.48	81.53	54.09	59.51	70.38	68.26	68.67	67.89	59.02
Al_2O_3	14.24	10.80	16.84	17.15	12.32	13.61	13.35	10.05	9.97
Fe_2O_{3t}	6.97	1.75	11.32	8.47	5.41	7.74	7.11	11.40	17.25
FeO_t[1]	6.27	1.57	10.19	7.62	4.87	6.96	6.40	10.26	15.52
MnO	0.013	0.008	0.063	0.026	0.312	0.007	0.052	0.033	0.070
MgO	0.75	0.50	2.63	3.21	1.32	0.44	3.58	2.75	5.86
CaO	0.91	0.13	5.00	2.71	2.15	0.14	0.70	0.10	0.57
Na_2O	1.59	0.96	3.39	1.90	0.88	0.45	1.02	0.18	0.85
K_2O	3.51	2.93	1.43	2.79	3.43	3.88	2.64	1.85	0.05
TiO_2	0.202	0.120	0.213	0.237	0.194	0.205	0.276	0.186	0.132
P_2O_5	0.08	0.05	0.03	0.02	0.07	0.04	0.04	0.04	0.03
LOI	5.02	2.09	4.93	4.28	1.33	5.38	3.41	4.94	6.35
Total	100.80	100.90	99.95	100.30	97.80	100.20	100.80	99.42	100.20
Sr (ppm)	54	14	241	127	62	20	26	15	26
Sc	23	12	27	28	16	24	24	16	23
Zr	64	55	100	77	61	54	56	50	39
Ba	224.7	330.6	155.7	186.3	775.3	354.0	420.0	523.4	9.3
Y	7.94	3.88	6.16	3.23	6.90	3.79	6.68	6.83	4.23
Nb	1.68	3.03	2.81	2.32	3.89	1.94	1.95	2.55	4.73
Cs	0.75	0.82	1.92	0.86	2.02	0.80	0.50	0.44	0.30
La	8.17	5.49	11.19	3.52	8.18	5.95	3.59	10.13	5.52
Ce	16.07	11.02	22.68	7.92	15.46	12.23	7.74	20.75	11.53
Pr	2.00	1.28	2.55	1.00	1.94	1.39	0.90	2.33	1.25
Nd	6.85	4.40	8.94	3.65	7.24	4.87	3.76	8.61	4.77
Sm	1.42	0.86	1.68	0.71	1.50	1.01	0.79	1.70	0.85
Eu	0.48	0.16	0.38	0.25	0.40	0.22	0.16	0.18	0.07
Gd	1.39	0.75	1.37	0.71	1.54	0.83	0.90	1.22	0.68
Tb	0.21	0.13	0.22	0.12	0.21	0.13	0.16	0.19	0.10
Dy	1.40	0.73	1.31	0.70	1.39	0.75	1.18	1.02	0.68
Ho	0.31	0.14	0.26	0.13	0.30	0.16	0.26	0.24	0.15
Er	0.98	0.44	0.78	0.44	0.82	0.43	0.80	0.64	0.45
Tm	0.22	0.13	0.17	0.12	0.16	0.08	0.13	0.10	0.08
Yb	1.09	0.63	0.80	0.36	0.77	0.57	0.90	0.75	0.56
Lu	0.16	0.13	0.10	0.05	0.10	0.10	0.14	0.12	0.08
Ta	0.08	0.21	0.30	0.20	bdl	bdl	0.15	0.18	0.45
Tl	5.68	1.49	4.34	8.03	0.55	6.30	1.54	0.62	0.11
Pb	1377.8	17.4	120.4	18.7	13.3	561.4	11.6	30.4	17.8
Bi	0.34	0.17	0.28	0.16	0.16	0.25	0.30	0.83	2.27
Th	2.29	2.26	4.02	2.75	3.14	2.77	1.89	1.91	2.98
U	8.30	1.59	1.72	0.43	0.47	1.22	0.90	1.12	1.03
V	113.4	57.6	121.5	111.7	80.8	104.2	135.2	86.3	129.6
Cr	204.3	117.9	249.0	220.8	119.4	113.5	56.1	106.4	63.0
Co	19.7	11.7	19.6	16.1	11.9	15.3	19.8	24.0	37.9
Ni	75.2	33.0	39.7	50.6	32.1	32.1	16.7	14.8	29.2
Cu	136	299	192	121	5	127	1488	1889	2083
Zn	1135	82	385	109	88	1803	48	241	340
As	180.2	10.5	42.1	60.3	0.7	102.6	1.5	4.3	11.9
Ag	4.4	bdl	bdl	bdl	bdl	1.6	0.6	0.5	0.4
Sn	1.8	0.5	2.4	0.6	0.8	1.6	1.8	1.9	0.6
Sb	7.2	0.9	10.5	5.8	0.2	4.0	1.2	0.3	1.2
Hg (ppb)	940	47	380	150	bdl	332	73	53	108
AI[2]	63.02	75.88	32.61	56.55	61.05	87.98	78.34	94.26	80.63
CCPI[3]	60.22	36.64	74.32	71.35	60.96	65.39	74.49	87.45	96.25
Mg#[4]	17.57	36.14	31.52	42.88	32.58	10.12	49.94	32.34	40.23
Ba/Sr	4.16	23.61	0.65	1.47	12.51	17.70	16.15	34.90	0.36
Eu/Eu*[5]	1.22	0.54	0.93	0.90	0.97	0.68	0.54	0.45	0.25
2200W	2206.04	2210.99		2206.31		2204.98	2207.99	2207.62	
2250W			2253.34	2253.68			2255.21	2249.83	2257.21

[1]Calculated from Fe_2O_{3t}, assuming all iron is present as FeO

[2]Alteration Index: AI = 100 x $(K_2O+MgO)/(K_2O+MgO+Na_2O+CaO)$

[3]Chlorite-carbonate-pyrite index: CCPI = 100 x $(MgO + FeO_t)/(MgO+FeO_t+Na_2O+K_2O)$

[4]Mg# = $Mg^{2+}/(Mg^{2+} + Fe^{2+})$ (molar %)

[5]Eu/Eu* = $Eu_n/(Gd_n + Sm_n)^{0.5}$ (n = Normalized to Primitive Mantle; Sun and McDonough, 1989)

bdl = Below detection limit

Table A5. Complete Dataset of Altered Samples from the Rambler Rhyolite Formation *(continued)*

Sample ID	29898	29900	36320	36637	60555	60576	62064	29810	29811
Alteration	Quartz-sericite -chlorite	Quartz-sericite -chlorite	Quartz-sericite -chlorite	Quartz-sericite -chlorite	Quartz-sericite -chlorite	Quartz-sericite -chlorite	Quartz-sericite -chlorite	Quartz-sericite -sulfides	Quartz-sericite -sulfides
DDH-Level	RM08-91	RM08-91	RM04-04	RMUG11-170	RM05-08	RM05-08	RM04-04	RM08-149	RM08-149
Zone	Ming South	Ming South	Ming South	Ming South	Ming South	Ming South	Ming South	1806	1806
Depth	4.42	27.96	920.5	153.3	1075.25	1296.8	1086.9	1.8	18.4
Unit	Unit 1.2	Unit 1.2	Unit 1.2	Unit 1.2	Unit 1.2	Unit 1.1	Unit 1.1	Unit 1.2	Unit 1.2
SiO_2 (wt. %)	74.33	56.27	71.08	68.62	75.60	69.96	77.53	75.14	68.42
Al_2O_3	8.62	8.10	10.88	10.63	8.98	10.88	9.45	10.79	7.39
Fe_2O_{3t}	7.38	17.90	7.65	8.26	7.34	9.04	4.96	5.49	10.89
FeO_t[1]	6.64	16.11	6.88	7.43	6.60	8.13	4.46	4.94	9.80
MnO	0.024	0.014	0.028	0.050	0.016	0.042	0.035	0.007	0.007
MgO	1.57	1.33	1.95	4.74	1.05	4.81	3.59	0.41	0.30
CaO	0.15	0.14	0.20	0.26	0.13	0.09	0.23	0.21	0.26
Na_2O	0.48	0.41	0.31	0.38	0.27	0.18	0.46	0.60	1.15
K_2O	2.01	2.00	2.61	1.53	2.17	1.36	1.39	3.08	1.73
TiO_2	0.131	0.115	0.199	0.161	0.137	0.160	0.153	0.157	0.103
P_2O_5	0.03	bdl	0.03	0.03	0.05	0.03	0.04	bdl	0.02
LOI	3.50	9.73	3.54	3.48	3.60	3.56	2.62	4.26	6.79
Total	98.22	96.01	98.47	98.14	99.34	100.10	100.40	100.10	97.07
Sr (ppm)	14	14	14	14	19	7	16	29	31
Sc	14	13	16	13	17	13	16	22	14
Zr	40	40	50	51	36	52	51	42	30
Ba	413.0	216.8	816.3	408.8	291.3	226.3	377.4	207.4	298.5
Y	2.95	2.19	4.20	5.08	2.92	3.96	2.86	2.43	2.94
Nb	1.76	1.16	2.63	2.29	2.16	2.49	1.59	1.62	1.11
Cs	0.45	0.46	0.78	0.66	0.52	0.39	0.27	0.58	0.39
La	2.00	2.47	1.61	4.25	3.53	3.69	3.68	4.84	4.15
Ce	4.47	5.05	3.30	9.10	7.73	8.07	7.54	10.11	8.50
Pr	0.57	0.63	0.44	1.16	0.99	0.93	0.96	1.16	1.00
Nd	2.10	2.13	1.60	3.99	3.64	3.29	2.95	4.28	3.74
Sm	0.48	0.48	0.51	0.90	0.72	0.69	0.70	0.89	0.80
Eu	0.07	0.10	0.08	0.07	0.09	0.06	0.05	0.22	0.24
Gd	0.44	0.41	0.55	0.77	0.59	0.64	0.45	0.73	0.76
Tb	0.08	0.08	0.11	0.13	0.09	0.12	0.08	0.10	0.12
Dy	0.54	0.42	0.75	0.91	0.56	0.66	0.51	0.56	0.66
Ho	0.10	0.08	0.16	0.18	0.12	0.15	0.10	0.11	0.11
Er	0.37	0.26	0.47	0.61	0.37	0.50	0.42	0.33	0.32
Tm	0.11	0.09	0.08	0.15	0.07	0.09	0.12	0.07	0.07
Yb	0.47	0.35	0.59	0.68	0.41	0.65	0.41	0.43	0.36
Lu	0.08	0.07	0.08	0.11	0.07	0.11	0.08	0.08	0.08
Ta	0.15	0.06	0.21	0.18	0.18	0.21	0.12	0.09	0.05
Tl	0.85	1.91	1.27	1.07	1.14	0.17	0.35	1.82	1.25
Pb	606.0	64.9	21.4	6.0	96.3	12.8	12.8	47.5	5129.8
Bi	1.76	2.24	1.16	0.84	0.83	1.44	0.09	0.76	1.18
Th	1.59	1.31	2.02	1.91	1.73	1.93	2.54	1.77	1.22
U	1.09	0.87	0.87	1.08	1.78	1.16	1.09	0.91	2.51
V	62.1	51.1	76.0	58.8	151.0	44.9	62.8	85.1	89.0
Cr	54.7	67.0	69.9	42.8	29.8	37.7	164.4	80.9	79.8
Co	21.4	101.4	16.3	27.2	18.4	23.1	15.6	8.8	20.0
Ni	15.1	19.5	7.7	15.7	7.5	10.6	34.0	21.3	32.7
Cu	13770	20593	1554	7678	346	2084	191	102	1049
Zn	1695	1808	95	76	230	120	73	1015	22647
As	17.4	229.1	5.3	0.5	22.3	bdl	0.9	50.9	102.1
Ag	6.4	5.1	0.5	0.7	0.4	1.0	bdl	0.3	7.8
Sn	2.0	2.8	1.7	1.8	2.4	0.6	0.9	1.2	2.5
Sb	0.7	9.7	0.3	0.4	1.5	bdl	0.2	0.9	7.1
Hg (ppb)	438	1870	22	122	47	6	8	1340	20400
AI[2]	85.04	85.82	89.94	90.74	88.95	95.81	87.83	81.16	59.01
CCPI[3]	78.23	88.86	76.68	87.19	77.47	89.99	82.21	61.59	79.53
Mg#[4]	29.65	12.83	33.55	53.20	22.08	51.32	58.91	12.89	5.17
Ba/Sr	29.50	15.48	58.31	29.20	15.33	32.33	23.59	7.15	9.63
Eu/Eu*[5]	0.30	0.43	0.34	0.22	0.35	0.22	0.19	0.72	0.83
2200W	2211.69	2211.39	2204.54	2206.53	2199.20		2203.66	2207.59	2207.41
2250W	2251.35		2255.61	2252.72	2254.14	2253.50	2253.40	2232.27	2232.06

[1]Calculated from Fe_2O_{3t}, assuming all iron is present as FeO

[2]Alteration Index: $AI = 100 \times (K_2O+MgO)/(K_2O+MgO+Na_2O+CaO)$

[3]Chlorite-carbonate-pyrite index: $CCPI = 100 \times (MgO + FeO_t)/(MgO+FeO_t+Na_2O+K_2O)$

[4]$Mg\# = Mg^{2+}/(Mg^{2+} + Fe^{2+})$ (molar %)

[5]$Eu/Eu^* = Eu_n/(Gd_n + Sm_n)^{0.5}$ (n = Normalized to Primitive Mantle; Sun and McDonough, 1989)

bdl = Below detection limit

Table A5. Complete Dataset of Altered Samples from the Rambler Rhyolite Formation *(continued)*

Sample ID	29812	29813	29814	29817	29822	29823	29824	29826	29830
Alteration	Quartz-sericite -sulfides	Quartz-sericite -sulfides	Quartz-sericite -sulfides	Quartz-sericite -sulfides	Quartz-sericite -sulfides	Quartz-sericite -sulfides	Quartz-sericite -sulfides	Quartz-sericite -sulfides	Quartz-sericite -sulfides
DDH-Level	RM08-149	RM08-149	RM08-149	RM08-145	RM08-123	RM08-123	RM08-123	RMUG08-142	RMUG08-142
Zone	1806	1806	1806	1806	1806	1806	1806	1806	1806
Depth	43.72	29.3	70.95	35.9	39.05	48.25	55.94	3.9	51.08
Unit	Unit 1.2	Unit 1.2	Unit 1.2	Unit 1.2	Unit 1.2	Unit 1.2	Unit 1.2	Unit 1.2	Unit 1.2
SiO_2 (wt. %)	71.27	75.82	71.20	68.25	84.04	75.65	75.09	78.05	45.08
Al_2O_3	11.02	9.57	11.99	12.10	6.14	4.94	6.19	8.64	11.30
Fe_2O_{3t}	4.33	6.49	6.01	4.94	4.59	11.34	7.62	4.95	23.81
FeO_t[1]	3.90	5.84	5.41	4.45	4.13	10.20	6.86	4.45	21.43
MnO	0.063	0.006	0.043	0.074	0.007	0.007	0.022	0.010	0.006
MgO	5.22	0.35	2.10	5.32	0.27	0.30	0.81	0.37	0.23
CaO	1.41	0.08	0.62	0.47	0.26	0.11	1.01	0.17	0.76
Na_2O	2.73	0.20	1.15	0.70	0.47	0.34	0.79	0.74	1.29
K_2O	0.07	2.93	2.58	1.86	1.64	1.33	1.01	2.31	2.19
TiO_2	0.204	0.175	0.169	0.174	0.091	0.067	0.200	0.172	0.148
P_2O_5	0.07	0.06	0.04	0.04	0.02	0.02	0.05	0.02	bdl
LOI	4.00	4.72	4.61	5.09	3.36	6.54	5.57	3.51	13.40
Total	100.40	100.40	100.50	99.02	100.90	100.60	98.36	98.93	98.23
Sr (ppm)	52	14	44	42	30	20	48	16	85
Sc	16	15	18	17	9	7	11	13	9
Zr	52	46	54	55	31	24	31	46	50
Ba	10.6	264.0	152.0	192.5	167.9	105.9	50.0	283.1	76.1
Y	4.31	2.97	4.45	5.01	4.27	1.53	4.68	2.54	1.93
Nb	1.08	1.41	1.23	0.73	1.00	0.76	1.69	1.23	1.18
Cs	0.33	0.50	0.48	0.33	0.37	0.37	0.28	0.55	0.34
La	9.35	4.87	6.12	6.08	4.13	1.50	4.14	4.74	1.74
Ce	18.96	10.39	11.86	12.68	7.45	2.91	8.26	9.41	3.83
Pr	2.09	1.22	1.46	1.43	0.90	0.34	1.03	1.19	0.44
Nd	7.77	4.48	5.02	5.10	3.66	1.26	4.48	3.98	1.73
Sm	1.46	1.02	1.10	1.12	0.71	0.26	0.98	0.91	0.32
Eu	0.32	0.17	0.34	0.38	0.59	0.12	0.94	0.24	0.40
Gd	1.19	0.83	1.05	0.97	0.76	0.20	0.87	0.74	0.32
Tb	0.18	0.12	0.18	0.17	0.11	0.04	0.13	0.10	0.06
Dy	0.92	0.64	0.96	1.05	0.67	0.26	0.76	0.57	0.40
Ho	0.17	0.13	0.19	0.21	0.16	0.06	0.17	0.10	0.09
Er	0.46	0.37	0.52	0.58	0.46	0.20	0.50	0.36	0.25
Tm	0.07	0.09	0.11	0.12	0.09	0.05	0.08	0.15	0.06
Yb	0.59	0.53	0.64	0.73	0.53	0.30	0.57	0.36	0.33
Lu	0.10	0.09	0.10	0.12	0.10	0.06	0.10	0.08	0.06
Ta	0.03	0.06	0.05	0.03	0.06	0.04	0.11	0.05	0.07
Tl	0.08	2.09	1.12	3.64	5.52	8.95	10.39	1.32	15.60
Pb	30.4	346.3	74.6	61.8	471.5	230.9	1863.0	114.7	1622.1
Bi	0.17	0.49	0.15	0.32	0.25	0.29	0.16	0.33	0.18
Th	2.43	1.86	1.97	1.98	1.11	0.76	1.23	1.52	1.58
U	1.09	1.83	0.94	3.24	3.42	1.11	2.99	1.12	4.61
V	58.4	68.0	71.1	80.0	103.9	88.7	125.3	62.3	68.0
Cr	41.5	38.5	115.8	103.2	118.0	79.6	210.6	33.9	142.4
Co	6.0	6.9	6.2	8.4	5.2	1.1	12.0	5.9	20.7
Ni	8.4	11.6	22.1	18.5	16.8	7.4	52.8	10.9	45.6
Cu	bdl	233	48	813	383	79	3097	124	561
Zn	346	260	150	8649	66	32	2075	282	975
As	23.8	36.4	17.8	75.7	22.6	85.8	1045.1	22.0	2642.8
Ag	0.3	1.0	0.7	1.8	4.8	1.9	31.3	0.7	26.3
Sn	bdl	1.3	0.5	0.4	4.8	6.2	11.9	1.7	6.5
Sb	1.3	19.9	2.5	47.5	4.9	5.8	180.1	3.5	283.5
Hg (ppb)	28	321	51	4180	517	2240	13400	166	3500
AI[2]	56.10	92.13	72.56	85.99	72.35	78.37	50.28	74.65	54.14
CCPI[3]	77.33	68.61	68.50	80.03	69.73	87.45	82.40	63.56	87.35
Mg#[4]	70.49	9.65	40.91	68.09	10.44	4.98	17.39	12.90	1.88
Ba/Sr	0.20	18.86	3.46	4.58	5.60	5.29	1.04	17.69	0.89
Eu/Eu*[5]	0.83	0.53	0.98	1.10	2.07	0.76	2.91	0.80	2.10
2200W		2208.17	2205.86		2207.47	2205.61	2205.19	2211.58	2199.18
2250W	2249.62			2255.25	2232.35	2245.20	2247.57		

[1]Calculated from Fe_2O_{3t}, assuming all iron is present as FeO

[2]Alteration Index: $AI = 100 \times (K_2O+MgO)/(K_2O+MgO+Na_2O+CaO)$

[3]Chlorite-carbonate-pyrite index: $CCPI = 100 \times (MgO + FeO_t)/(MgO+FeO_t+Na_2O+K_2O)$

[4]$Mg\# = Mg^{2+}/(Mg^{2+} + Fe^{2+})$ (molar %)

[5]$Eu/Eu^* = Eu_n/(Gd_n + Sm_n)^{0.5}$ (n = Normalized to Primitive Mantle; Sun and McDonough, 1989)

bdl = Below detection limit

Table A5. Complete Dataset of Altered Samples from the Rambler Rhyolite Formation *(continued)*

Sample ID	29831	29834	29836	29845	29872	29879	29880	29881	29887
Alteration	Quartz-sericite -sulfides	Quartz-sericite -sulfides	Quartz-sericite -sulfides	Quartz-sericite -sulfides	Quartz-sericite -sulfides	Quartz-sericite -sulfides	Quartz-sericite -sulfides	Quartz-sericite -sulfides	Quartz-sericite -sulfides
DDH-Level	RMUG08-142	RMUG08-140	RMUG08-140	RM06-4E	RM07-8F	RM08-121	RM08-121	RM08-121	RM08-151
Zone	1806	1806	1806	Ming South	Ming South	1806	1806	1806	1806
Depth	57.16	17.76	30.03	900.6	1023.68	36.28	45.07	59.5	18.46
Unit	Unit 1.2	Unit 1.2	Unit 1.2	Unit 1.2	Unit 1.2	Unit 1.2	Unit 1.2	Unit 1.2	Unit 1.2
SiO_2 (wt. %)	67.50	80.54	50.40	64.57	66.14	66.51	73.62	61.36	73.73
Al_2O_3	11.43	9.73	11.42	9.16	12.16	10.89	7.22	9.34	12.50
Fe_2O_{3t}	7.99	3.85	19.32	12.52	9.31	8.19	9.64	14.23	3.74
FeO_t[1]	7.19	3.46	17.39	11.27	8.38	7.37	8.67	12.80	3.37
MnO	0.026	0.006	0.020	0.014	0.021	0.009	0.005	0.014	0.006
MgO	0.91	0.23	0.92	0.45	1.94	0.37	0.18	0.40	0.70
CaO	2.09	0.05	0.76	0.13	1.91	0.09	0.04	0.50	0.11
Na_2O	2.36	0.28	0.93	0.31	3.56	0.34	0.19	0.85	0.16
K_2O	1.31	2.74	2.39	2.74	0.74	3.32	2.13	2.12	4.08
TiO_2	0.167	0.141	0.254	0.134	0.201	0.167	0.107	0.136	0.178
P_2O_5	0.27	bdl	0.02	0.02	0.05	0.01	bdl	bdl	0.07
LOI	5.03	3.11	11.61	6.95	4.53	6.22	6.57	9.27	3.12
Total	99.09	100.70	98.04	96.99	100.60	96.11	99.70	98.21	98.39
Sr (ppm)	123	22	76	22	141	20	15	63	11
Sc	16	11	21	17	9	17	11	13	18
Zr	55	46	58	45	56	51	33	43	56
Ba	90.2	101.1	91.6	548.8	110.8	406.6	176.6	76.1	286.9
Y	12.16	6.04	4.00	3.68	5.63	4.36	2.12	4.40	5.26
Nb	2.21	1.01	0.63	1.27	1.18	2.20	1.08	0.84	2.74
Cs	1.04	0.38	0.45	0.70	1.15	0.57	0.29	0.66	0.98
La	9.64	7.69	4.09	3.06	6.14	4.66	3.10	3.50	5.41
Ce	15.29	14.96	7.92	6.86	12.49	10.15	5.99	7.05	11.57
Pr	1.76	1.78	1.05	0.76	1.46	1.23	0.75	0.83	1.34
Nd	6.52	6.41	3.79	2.98	5.81	4.38	2.46	2.83	4.85
Sm	1.18	1.36	0.90	0.57	1.10	0.91	0.51	0.59	1.06
Eu	1.18	0.86	0.62	0.10	0.19	0.41	0.20	0.69	0.71
Gd	1.37	1.20	0.81	0.59	1.08	0.78	0.51	0.52	0.99
Tb	0.22	0.18	0.12	0.11	0.18	0.13	0.08	0.10	0.16
Dy	1.48	1.26	0.78	0.65	1.16	0.83	0.42	0.64	1.01
Ho	0.36	0.25	0.17	0.14	0.22	0.19	0.08	0.15	0.20
Er	1.21	0.67	0.56	0.44	0.67	0.56	0.29	0.55	0.69
Tm	0.20	0.09	0.12	0.08	0.10	0.12	0.08	0.12	0.11
Yb	1.44	0.69	0.66	0.57	0.65	0.73	0.33	0.82	0.80
Lu	0.25	0.11	0.12	0.10	0.13	0.13	0.05	0.13	0.16
Ta	bdl	bdl	bdl	0.07	0.13	0.16	0.07	0.05	0.22
Tl	12.01	9.50	21.05	5.04	1.78	7.92	9.60	17.49	2.85
Pb	1605.4	1811.7	202.6	35.9	33.0	2586.9	1437.0	4528.6	27.8
Bi	0.59	0.06	0.26	1.73	0.34	0.25	0.19	0.21	0.08
Th	2.88	2.26	2.10	1.58	2.18	1.90	1.21	1.73	2.22
U	23.98	4.91	24.53	1.09	2.31	2.52	5.50	5.58	2.06
V	88.5	46.3	147.4	95.1	60.1	61.4	121.0	61.1	79.0
Cr	90.8	31.2	132.2	83.5	71.2	117.7	79.4	70.1	115.5
Co	34.4	7.5	62.8	38.9	57.1	12.4	10.7	10.6	9.9
Ni	58.7	bdl	144.0	19.8	29.8	32.8	58.5	81.2	21.8
Cu	760	76	50	15185	371	374	1812	633	46
Zn	4068	3468	992	533	60	27065	251	2695	37
As	2622.4	558.5	9208.6	48.8	16.0	168.0	351.3	1339.7	5.4
Ag	8.6	3.0	2.6	4.0	0.3	6.8	7.3	39.8	0.4
Sn	5.2	1.5	0.8	4.2	bdl	7.0	7.0	4.2	1.1
Sb	18.6	13.1	31.0	2.9	0.7	7.4	18.5	60.7	0.3
Hg (ppb)	7700	3460	2910	593	15	16800	1920	12900	17
AI[2]	33.28	90.00	66.20	87.88	32.88	89.56	90.94	65.12	94.65
CCPI[3]	70.80	57.46	85.91	80.96	72.35	70.05	80.89	83.13	51.15
Mg#[4]	18.41	10.58	8.62	6.65	29.22	8.21	3.57	5.27	27.05
Ba/Sr	0.73	4.59	1.20	24.94	0.79	20.33	11.77	1.21	26.08
Eu/Eu*[5]	3.16	2.26	2.01	0.40	0.55	1.33	0.84	2.77	2.08
2200W	2201.26	2207.32	2209.06	2201.49		2203.76	2207.38	2205.65	2211.42
2250W	2236.27		2232.44	2232.19	2253.91	2232.38	2234.25	2249.18	

[1] Calculated from Fe_2O_{3t}, assuming all iron is present as FeO

[2] Alteration Index: $AI = 100 \times (K_2O+MgO)/(K_2O+MgO+Na_2O+CaO)$

[3] Chlorite-carbonate-pyrite index: $CCPI = 100 \times (MgO + FeO_t)/(MgO+FeO_t+Na_2O+K_2O)$

[4] $Mg\# = Mg^{2+}/(Mg^{2+} + Fe^{2+})$ (molar %)

[5] $Eu/Eu^* = Eu_n/(Gd_n + Sm_n)^{0.5}$ (n = Normalized to Primitive Mantle; Sun and McDonough, 1989)

bdl = Below detection limit

Table A5. Complete Dataset of Altered Samples from the Rambler Rhyolite Formation *(continued)*

Sample ID	29890	29952	36632	60551	60552	60553	60554	62057	62523
Alteration	Quartz-sericite -sulfides	Quartz-sericite -sulfides	Quartz-sericite -sulfides	Quartz-sericite -sulfides	Quartz-sericite -sulfides	Quartz-sericite -sulfides	Quartz-sericite -sulfides	Quartz-sericite -sulfides	Quartz-sericite -sulfides
DDH-Level	RM08-151	RM08-91	RMUG11-170	RM05-08	RM05-08	RM05-08	RM05-08	RM04-04	RM06-04C
Zone	1806	Ming South	Ming South	Ming South	Ming South	Ming South	Ming South	Ming South	Ming South
Depth	76.2	46.98	22	1034.3	1045.5	1054.7	1066.65	893	887
Unit	Unit 1.2	Unit 1.2	Unit 1.2	Unit 1.2	Unit 1.2	Unit 1.2	Unit 1.2	Unit 1.2	Unit 1.2
SiO_2 (wt. %)	87.50	74.00	63.82	76.43	74.80	74.93	71.47	78.97	69.01
Al_2O_3	4.72	7.31	11.10	9.61	9.38	10.50	8.14	9.52	11.17
Fe_2O_{3t}	3.74	9.93	12.13	4.95	4.96	6.34	10.29	4.92	8.10
FeO_t[1]	3.37	8.94	10.92	4.45	4.46	5.71	9.26	4.43	7.29
MnO	0.003	0.012	0.006	0.031	0.032	0.014	0.009	0.038	0.009
MgO	0.26	0.30	0.29	1.02	1.01	0.66	0.43	0.35	0.42
CaO	0.16	0.75	0.06	2.64	2.71	0.25	0.12	0.37	0.27
Na_2O	0.13	1.13	0.28	1.68	1.66	0.50	0.24	0.57	0.94
K_2O	1.45	1.27	3.19	1.17	1.13	2.83	2.23	2.51	2.87
TiO_2	0.069	0.107	0.191	0.166	0.166	0.182	0.128	0.145	0.169
P_2O_5	0.05	0.02	0.03	0.05	0.05	0.06	0.03	0.01	bdl
LOI	2.54	5.69	7.47	2.97	2.99	3.69	5.98	3.37	5.34
Total	100.60	100.50	98.57	100.70	98.89	99.96	99.06	100.80	98.30
Sr (ppm)	9	56	24	53	54	16	15	20	22
Sc	7	13	17	16	15	16	15	18	22
Zr	21	32	50	43	42	45	32	39	43
Ba	111.5	73.1	363.9	223.2	196.4	648.6	321.6	345.2	1114.7
Y	2.46	3.08	4.88	5.63	5.28	2.99	2.33	2.92	2.41
Nb	1.22	0.81	0.83	1.09	0.93	2.29	1.66	0.96	1.41
Cs	0.25	0.43	0.47	0.91	0.84	0.95	0.55	0.68	0.77
La	3.70	3.27	6.17	5.17	4.69	5.10	4.22	3.82	5.91
Ce	6.87	6.60	12.38	10.47	9.71	10.60	8.97	7.56	12.86
Pr	0.87	0.75	1.40	1.25	1.16	1.24	1.03	0.98	1.33
Nd	2.92	2.72	5.07	4.54	4.33	4.53	3.77	3.26	4.76
Sm	0.52	0.56	1.10	0.97	1.05	0.88	0.77	0.53	0.90
Eu	0.13	0.21	0.25	0.26	0.24	0.08	0.11	0.11	0.12
Gd	0.47	0.51	0.92	0.97	0.88	0.74	0.59	0.58	0.72
Tb	0.07	0.07	0.15	0.15	0.14	0.10	0.10	0.08	0.12
Dy	0.41	0.53	0.92	1.02	0.91	0.65	0.55	0.50	0.69
Ho	0.09	0.11	0.20	0.23	0.20	0.12	0.10	0.10	0.11
Er	0.29	0.41	0.66	0.66	0.64	0.33	0.32	0.44	0.29
Tm	0.05	0.08	0.09	0.12	0.11	0.08	0.06	0.10	0.06
Yb	0.30	0.43	0.59	0.75	0.67	0.45	0.41	0.43	0.39
Lu	0.05	0.07	0.11	0.11	0.11	0.08	0.07	0.06	0.06
Ta	0.11	0.06	0.05	0.09	0.09	0.20	0.13	0.04	bdl
Tl	2.63	3.64	2.27	2.59	2.37	1.61	1.99	6.84	9.70
Pb	248.1	173.3	174.9	90.9	83.1	14.5	44.4	69.9	157.1
Bi	0.65	0.19	0.20	0.49	0.60	1.08	1.27	1.36	1.90
Th	0.81	1.19	1.99	1.96	1.77	1.84	1.61	1.43	2.23
U	1.03	1.57	1.11	1.43	1.34	1.44	1.62	0.83	1.91
V	128.8	62.7	77.4	98.4	90.7	85.4	150.8	61.4	87.3
Cr	95.3	51.6	32.8	67.9	64.0	62.6	111.0	54.8	122.2
Co	1.4	8.2	9.7	14.8	14.1	14.7	36.7	24.0	59.2
Ni	9.8	30.3	10.7	18.8	13.6	14.8	30.1	15.3	20.6
Cu	1570	332	741	3093	3222	993	830	5107	2517
Zn	93	1798	497	241	226	62	170	233	314
As	26.8	336.2	214.8	24.4	9.2	22.2	269.0	57.7	246.7
Ag	4.0	0.6	0.8	1.4	1.7	0.6	0.7	1.6	2.5
Sn	1.5	0.6	4.4	2.4	2.0	2.1	2.0	2.2	3.8
Sb	5.3	20.7	2.9	2.1	1.9	1.1	4.4	5.7	10.4
Hg (ppb)	388	998	283	251	270	136	457	882	599
AI[2]	85.50	45.51	91.10	33.64	32.87	82.31	88.08	75.26	73.11
CCPI[3]	71.68	81.00	78.16	67.69	68.15	67.76	81.27	63.11	69.10
Mg#[4]	12.10	5.65	4.52	28.99	28.74	17.10	7.65	12.35	9.32
Ba/Sr	12.39	1.31	15.16	4.21	3.64	40.54	21.44	17.26	50.67
Eu/Eu*[5]	0.56	0.86	0.75	0.78	0.73	0.27	0.40	0.45	0.38
2200W	2207.54	2209.45	2201.51	2202.15	2204.49	2206.10	2204.49	2206.18	2205.03
2250W					2251.72				

[1]Calculated from Fe_2O_{3t}, assuming all iron is present as FeO

[2]Alteration Index: $AI = 100 \times (K_2O+MgO)/(K_2O+MgO+Na_2O+CaO)$

[3]Chlorite-carbonate-pyrite index: $CCPI = 100 \times (MgO + FeO_t)/(MgO+FeO_t+Na_2O+K_2O)$

[4]$Mg\# = Mg^{2+}/(Mg^{2+} + Fe^{2+})$ (molar %)

[5]$Eu/Eu^* = Eu_n/(Gd_n + Sm_n)^{0.5}$ (n = Normalized to Primitive Mantle; Sun and McDonough, 1989)

bdl = Below detection limit

Table A5. Complete Dataset of Altered Samples from the Rambler Rhyolite Formation *(continued)*

Sample ID	106403	106414	29833	29870	60506	60507	60508	60519	60520
Alteration	Quartz-sericite -sulfides	Quartz-sericite -sulfides	Sericite-calcite ±spessartine	Sericite-calcite ±spessartine	Sericite-calcite ±spessartine	Sericite-calcite ±spessartine	Sericite-calcite ±spessartine	Sericite-calcite ±spessartine	Sericite-calcite ±spessartine
DDH-Level	RM09-22	1450	RMUG08-140	RM07-8F	329	329	444	434	434
Zone	1806	Ming South	1806	Ming South	1807	1807	1807	1807	1807
Depth	199.5	300	7.3	986.3	329	329	444	434	434
Unit	Unit 1.2	Unit 1.2	Unit 1.2	Unit 1.2	Unit 1.2	Unit 1.2	Unit 1.2	Unit 1.2	Unit 1.2
SiO_2 (wt. %)	66.15	69.96	69.11	79.91	66.53	68.80	65.17	60.80	67.78
Al_2O_3	12.95	10.16	12.67	9.92	13.50	12.45	13.84	15.93	12.06
Fe_2O_{3t}	6.77	9.53	3.30	1.33	5.18	4.99	5.09	6.85	3.58
FeO_t[1]	6.09	8.58	2.97	1.20	4.66	4.49	4.58	6.16	3.22
MnO	0.149	0.040	0.064	0.022	0.748	0.204	1.058	0.096	2.632
MgO	5.03	2.27	1.36	0.33	1.33	1.28	1.33	3.19	0.99
CaO	0.88	0.70	5.03	2.62	3.61	2.70	5.14	2.83	5.32
Na_2O	1.39	1.17	2.74	4.33	3.01	3.39	4.43	4.29	2.89
K_2O	1.39	1.58	1.57	0.23	2.34	2.08	1.37	1.92	1.19
TiO_2	0.153	0.136	0.234	0.105	0.249	0.232	0.206	0.276	0.182
P_2O_5	0.04	0.03	0.04	0.04	0.29	0.30	0.07	0.02	0.07
LOI	4.53	5.12	4.61	1.80	2.02	2.14	3.09	3.63	4.05
Total	99.43	100.70	100.70	100.60	98.80	98.57	100.80	99.82	100.70
Sr (ppm)	40	41	132	127	84	65	161	217	85
Sc	29	19	16	9	21	20	18	26	15
Zr	42	40	65	46	63	58	57	63	54
Ba	103.4	374.6	99.9	34.0	807.2	709.8	848.1	1440.1	1024.6
Y	4.05	3.15	6.75	3.37	18.15	14.85	8.24	10.78	10.23
Nb	0.99	1.25	1.63	1.17	4.63	3.15	3.60	3.51	2.42
Cs	0.47	0.40	1.03	0.35	0.59	0.64	0.74	0.74	0.32
La	5.84	5.58	7.10	4.95	8.53	7.94	10.73	9.11	9.68
Ce	11.82	11.22	14.16	9.50	16.33	14.34	20.22	17.84	16.58
Pr	1.33	1.29	1.70	1.04	1.96	1.72	2.34	2.12	2.12
Nd	4.94	4.62	6.26	3.64	7.11	6.30	8.25	7.93	7.77
Sm	0.90	0.86	1.35	0.67	1.53	1.38	1.82	1.65	1.60
Eu	0.26	0.11	0.43	0.20	0.36	0.35	0.61	0.55	0.43
Gd	0.78	0.68	1.23	0.54	1.64	1.49	1.70	1.56	1.81
Tb	0.13	0.11	0.20	0.09	0.30	0.28	0.25	0.26	0.27
Dy	0.76	0.58	1.26	0.51	2.24	2.01	1.59	1.76	1.71
Ho	0.16	0.13	0.26	0.11	0.58	0.49	0.34	0.40	0.38
Er	0.46	0.39	0.77	0.38	1.96	1.78	0.93	1.37	1.28
Tm	0.10	0.07	0.15	0.07	0.40	0.32	0.16	0.24	0.20
Yb	0.54	0.42	0.77	0.48	2.78	2.37	1.02	1.51	1.34
Lu	0.10	0.07	0.13	0.07	0.52	0.42	0.17	0.24	0.26
Ta	bdl	bdl	bdl	0.11	bdl	bdl	bdl	bdl	bdl
Tl	0.79	0.72	1.52	0.20	2.91	2.85	1.09	4.43	1.54
Pb	26.3	21.2	45.3	21.5	21.8	18.7	11.5	34.7	15.8
Bi	0.09	1.25	0.16	0.10	0.19	0.18	0.14	1.31	0.15
Th	2.13	1.86	2.88	1.80	2.85	3.12	2.94	2.84	2.75
U	1.05	0.91	1.94	0.99	0.62	0.77	0.35	0.71	0.39
V	144.9	144.0	61.2	35.1	140.6	72.9	98.9	60.9	76.4
Cr	81.9	23.5	47.8	110.0	72.1	62.4	20.7	24.2	23.8
Co	14.1	13.4	9.7	3.3	77.9	12.2	36.9	14.6	44.3
Ni	23.6	7.1	bdl	7.0	21.6	15.2	11.0	11.4	10.0
Cu	65	270	84	46	800	378	45	341	60
Zn	1313	67	57	32	96	114	95	86	110
As	25.8	58.3	10.4	1.8	42.2	10.2	2.9	2.1	5.1
Ag	0.3	0.1	0.5	0.2	0.1	0.1	bdl	0.1	bdl
Sn	0.7	1.7	0.8	bdl	0.7	0.7	0.7	0.8	0.7
Sb	0.6	0.6	1.4	0.3	0.4	0.6	0.5	0.9	1.0
Hg (ppb)	197	9	95	bdl	235	1180	6	353	140
AI[2]	73.88	67.31	27.38	7.46	35.67	35.56	22.00	41.78	20.98
CCPI[3]	80.93	81.10	51.95	26.69	54.89	53.41	52.54	61.78	52.83
Mg#[4]	59.54	32.06	44.95	32.95	33.71	33.69	34.11	47.99	35.39
Ba/Sr	2.59	9.14	0.76	0.27	9.61	10.92	5.27	6.64	12.05
Eu/Eu*[5]	0.84	0.37	1.12	0.75	0.87	0.88	1.38	1.31	0.99
2200W	2202.82		2207.64		2209.56			2209.91	2213.32
2250W	2252.23		2251.49	2249.93	2232.66	2251.34			

[1]Calculated from Fe_2O_{3t}, assuming all iron is present as FeO

[2]Alteration Index: $AI = 100 \times (K_2O+MgO)/(K_2O+MgO+Na_2O+CaO)$

[3]Chlorite-carbonate-pyrite index: $CCPI = 100 \times (MgO + FeO_t)/(MgO+FeO_t+Na_2O+K_2O)$

[4]$Mg\# = Mg^{2+}/(Mg^{2+} + Fe^{2+})$ (molar %)

[5]$Eu/Eu^* = Eu_n/(Gd_n + Sm_n)^{0.5}$ (n = Normalized to Primitive Mantle; Sun and McDonough, 1989)

bdl = Below detection limit

Table A5. Complete Dataset of Altered Samples from the Rambler Rhyolite Formation *(continued)*

Sample ID	60586	62187	62525	29820	29825	29837	29876	29884	29891	62185	62056
Alteration	Sericite-calcite ±spessartine	Sericite-calcite ±spessartine	Sericite-calcite ±spessartine	Silica-rich horizon	Silica-rich horizon	Silica-rich horizon	Silica-rich horizon	Silica-rich horizon	Silica-rich horizon	Silica-rich fragment	Mn-Ca-rich assemblage
DDH-Level	RM07-20M	389	RM06-04C	RM08-145	RM08-123	RMUG08-140	RM08-123	RM08-159	RM08-151	375	375
Zone	1807	1807	Ming South	1806	1806	1806	1806	1806	1806	1807	1807
Depth	672.25	389	880	66.22	63.77	35.93	66.26	68.06	82.06	375	375
Unit	Unit 1.2	Unit 1.2	Unit 1.3						Unit 1.2		Unit 1.2
SiO_2 (wt. %)	69.55	71.61	74.15	92.87	88.24	92.13	89.41	93.88	57.45	86.29	41.63
Al_2O_3	10.07	11.60	12.84	0.29	1.61	0.24	0.36	0.28	0.58	1.79	11.97
Fe_2O_{3t}	7.87	4.61	3.27	6.65	2.33	4.43	5.79	4.17	7.84	4.67	4.50
FeO_t[1]	7.08	4.15	2.94	5.98	2.10	3.99	5.21	3.75	7.05	4.20	4.05
MnO	0.044	0.020	0.010	0.024	0.009	0.010	0.016	0.005	0.179	0.035	13.930
MgO	0.67	0.78	0.29	0.05	0.08	0.05	0.08	0.04	0.76	0.29	1.30
CaO	4.46	1.93	2.19	0.36	3.26	0.29	1.03	0.30	15.82	1.65	15.36
Na_2O	2.75	4.65	3.86	0.11	0.05	0.03	0.02	0.04	0.02	0.66	0.63
K_2O	1.41	0.07	1.02	0.01	0.47	0.04	0.08	0.06	0.03	0.11	0.15
TiO_2	0.149	0.219	0.145	0.004	0.010	0.007	0.019	0.006	0.010	0.254	0.132
P_2O_5	0.07	0.07	0.03	0.04	2.39	0.03	0.02	0.02	0.08	0.03	0.08
LOI	2.48	2.39	2.24	0.49	1.35	1.53	3.81	1.96	10.96	2.63	8.88
Total	99.52	97.94	100.10	100.90	99.80	98.80	100.60	100.80	93.72	98.41	98.58
Sr (ppm)	72	114	94	8	20	2	3	3	36	15	66
Sc	13	12	16	bdl	1	bdl	bdl	bdl	1	5	9
Zr	47	59	60	3	5	13	4	7	5	20	35
Ba	139.2	18.6	140.6	267.4	25.7	3.6	3.7	10.5	2.6	10.8	520.1
Y	8.88	7.49	4.27	14.23	27.26	0.57	0.77	0.45	4.50	1.86	6.64
Nb	2.52	0.52	1.09	3.22	0.36	0.23	0.30	0.24	0.18	1.33	1.37
Cs	0.57	0.08	0.37	4.00	0.12	0.06	bdl	bdl	0.06	0.07	0.23
La	7.81	8.64	6.57	13.53	11.00	0.59	0.65	0.59	3.30	1.06	4.90
Ce	14.65	16.94	12.94	27.75	8.95	1.13	1.62	1.03	5.39	2.59	13.82
Pr	1.74	2.04	1.38	3.35	1.72	0.18	0.17	0.14	0.79	0.37	1.13
Nd	6.20	7.34	4.78	12.80	7.23	0.61	0.61	0.49	2.99	1.43	4.16
Sm	1.39	1.50	0.89	2.66	1.47	0.11	0.07	bdl	0.63	0.37	1.16
Eu	0.38	0.39	0.25	0.95	0.48	0.03	0.04	bdl	0.18	0.10	0.29
Gd	1.32	1.52	0.72	2.75	2.15	0.11	0.13	bdl	0.69	0.37	1.15
Tb	0.21	0.24	0.12	0.44	0.31	0.02	0.02	bdl	0.11	0.06	0.20
Dy	1.42	1.42	0.76	2.85	2.21	0.09	0.16	0.11	0.64	0.37	1.33
Ho	0.31	0.28	0.16	0.57	0.55	0.02	0.02	0.01	0.14	0.07	0.30
Er	1.01	0.84	0.57	1.59	1.63	0.09	0.10	0.05	0.42	0.26	1.02
Tm	0.19	0.17	0.13	0.26	0.27	0.05	0.02	bdl	0.15	0.07	0.20
Yb	1.28	0.85	0.70	1.34	1.40	0.05	0.06	bdl	0.37	0.26	1.55
Lu	0.20	0.13	0.13	0.17	0.21	0.02	bdl	bdl	0.05	0.04	0.27
Ta	0.21	bdl	bdl	0.23	bdl	bdl	bdl	bdl	0.02	bdl	bdl
Tl	4.09	0.08	4.81	3.98	6.92	0.43	0.94	0.27	0.42	0.35	0.20
Pb	29.1	65.9	1900.6	27.3	2760.6	5.7	479.6	17.2	1348.4	166.6	7.1
Bi	0.51	0.37	0.12	0.20	0.56	0.23	10.98	0.64	6.83	19.39	1.11
Th	1.99	3.03	2.71	2.61	0.18	0.07	0.15	0.10	0.15	0.43	1.68
U	0.98	1.04	3.81	0.24	16.90	0.38	0.32	0.55	0.72	0.56	0.26
V	63.6	30.5	119.6	62.6	148.8	14.3	22.0	27.6	59.4	43.1	169.9
Cr	15.3	42.0	168.5	250.7	24.4	8.4	10.4	14.8	12.3	30.4	16.4
Co	6.1	10.1	7.1	28.1	0.9	0.9	3.4	1.0	48.0	7.1	114.0
Ni	11.1	bdl	14.3	91.8	9.6	9.2	bdl	bdl	11.4	bdl	bdl
Cu	60	773	120	45	2794	20418	5927	40	139	24671	224
Zn	247	51	92	189	148	739	297	18	798	229	43
As	2.6	3.8	8.9	8.4	69.2	19.1	274.6	24.4	142.6	78.4	7.1
Ag	bdl	0.4	1.3	0.3	26.8	39.8	16.9	bdl	4.8	5.1	0.2
Sn	0.6	0.3	0.6	1.0	6.7	1.0	0.7	0.3	0.3	2.6	3.4
Sb	0.8	0.7	3.5	1.3	48.7	10.7	11.7	2.1	2.9	38.7	4.4
Hg (ppb)	58	50	41	90	6260	5060	1840	203	727	2930	1120
AI[2]	22.39	11.44	17.80	11.32	14.25	21.95	13.22	22.73	4.75	14.76	8.31
CCPI[3]	67.24	53.31	42.18	98.24	82.25	98.46	98.32	97.68	99.42	86.56	88.15
Mg#[4]	14.43	25.10	14.94	1.47	6.37	2.19	2.66	1.86	16.11	10.95	36.40
Ba/Sr	1.93	0.16	1.50	33.43	1.28	1.80	1.23	3.51	0.07	0.72	7.88
Eu/Eu*[5]	0.98	0.96	0.84	1.74	1.07	0.30	0.40	bdl	0.65	0.51	0.82
2200W	2212.30		2212.70	2234.57	2199.69	2243.77	2209.45	2236.05	2243.80		
2250W				2249.10	2232.27	2249.97	2234.44	2236.05	2247.85		2251.20

[1]Calculated from Fe_2O_{3t}, assuming all iron is present as FeO

[2]Alteration Index: AI = 100 x (K_2O+MgO)/(K_2O+MgO+Na_2O+CaO)

[3]Chlorite-carbonate-pyrite index: CCPI = 100 x (MgO + FeO_t)/(MgO+FeO_t+Na_2O+K_2O)

[4]Mg# = $Mg^{2+}/(Mg^{2+} + Fe^{2+})$ (molar %)

[5]Eu/Eu* = $Eu_n/(Gd_n + Sm_n)^{0.5}$ (n = Normalized to Primitive Mantle; Sun and McDonough, 1989)

bdl = Below detection limit

Table A5. Complete Dataset of Altered Samples from the Rambler Rhyolite Formation *(continued)*

Sample ID	29832	29883	60599	62081	62195	62502	62503	62504	62506
Alteration	Weak alteration	Weak alteration	Weak alteration	Weak alteration	Weak alteration	Weak alteration	Weak alteration	Weak alteration	Weak alteration
DDH-Level	RMUG08-140	RM08-121	RM07-18	469	481	RM07-18	RM07-18	RM07-18	RM07-18
Zone	1806	1806	1807	1807	1807	1807	1807	1807	1807
Depth	2.32	77.3	627.8	469	481	618.1	638.57	647.38	660
Unit	Unit 1.2	Unit 1.2	Unit 1.2	Unit 1.2	Unit 1.2	Unit 1.2	Unit 1.2	Unit 1.2	Unit 1.2
SiO_2 (wt. %)	76.30	68.44	64.96	73.57	76.48	61.29	62.61	65.01	65.30
Al_2O_3	10.22	11.55	13.08	12.03	10.50	14.73	13.29	14.07	12.65
Fe_2O_{3t}	4.84	8.97	7.42	4.08	3.40	8.20	6.88	5.48	5.76
FeO_t[1]	4.36	8.07	6.68	3.67	3.06	7.38	6.19	4.93	5.18
MnO	0.011	0.080	0.074	0.024	0.031	0.084	0.091	0.070	0.087
MgO	0.56	1.36	4.06	0.75	0.35	4.91	4.34	2.58	2.89
CaO	1.30	1.60	5.02	2.79	3.32	4.58	5.27	5.61	5.74
Na_2O	3.26	3.05	1.71	4.10	3.11	2.93	1.43	4.87	2.76
K_2O	1.04	1.36	0.94	0.79	0.99	0.64	2.00	0.73	0.67
TiO_2	0.155	0.177	0.185	0.179	0.158	0.254	0.165	0.164	0.166
P_2O_5	0.03	0.15	0.03	0.04	0.04	0.04	0.04	0.06	0.04
LOI	2.86	4.18	2.05	0.32	1.41	2.06	3.53	2.25	2.68
Total	100.60	100.90	99.53	98.67	99.80	99.72	99.65	100.90	98.75
Sr (ppm)	149	60	167	149	125	195	85	212	182
Sc	19	18	30	15	13	31	29	33	25
Zr	40	53	51	53	47	66	49	47	51
Ba	80.3	342.9	128.0	53.1	147.2	116.7	103.7	98.7	73.4
Y	4.30	5.42	3.83	6.23	7.98	5.69	4.54	4.54	4.65
Nb	1.08	2.67	2.29	3.69	2.46	2.63	2.51	2.31	2.45
Cs	0.84	0.78	0.53	0.37	0.25	0.66	0.71	0.88	0.65
La	4.38	5.29	6.27	5.85	6.84	6.60	6.43	5.58	6.27
Ce	9.06	9.77	12.20	12.44	13.32	13.41	12.82	11.28	12.82
Pr	1.11	1.28	1.42	1.37	1.58	1.56	1.48	1.31	1.47
Nd	4.34	4.61	5.16	5.04	5.97	5.54	5.51	4.39	5.24
Sm	0.90	0.98	1.06	1.14	1.21	1.22	1.09	0.93	1.09
Eu	0.23	0.22	0.30	0.33	0.34	0.34	0.27	0.24	0.27
Gd	0.81	0.84	0.77	1.11	1.19	1.09	0.92	0.80	0.87
Tb	0.14	0.14	0.13	0.21	0.18	0.16	0.13	0.12	0.14
Dy	0.77	0.91	0.75	1.16	1.25	1.09	0.81	0.77	0.87
Ho	0.16	0.20	0.15	0.26	0.27	0.22	0.18	0.18	0.18
Er	0.52	0.66	0.46	0.74	0.95	0.67	0.54	0.56	0.49
Tm	0.11	0.13	0.10	0.11	0.16	0.11	0.13	0.09	0.10
Yb	0.64	0.70	0.56	0.73	1.03	0.74	0.63	0.69	0.65
Lu	0.10	0.11	0.08	0.11	0.15	0.12	0.11	0.13	0.11
Ta	bdl	0.21	0.21	bdl	0.21	0.27	0.24	0.21	0.21
Tl	0.90	6.38	0.16	1.50	0.81	0.09	0.22	0.16	0.16
Pb	294.7	37.4	7.5	18.8	11.6	8.3	3.9	7.0	9.6
Bi	0.42	0.43	0.13	0.22	0.15	0.13	0.10	0.14	0.17
Th	2.05	2.06	2.23	2.58	2.13	2.67	2.13	2.13	2.21
U	1.32	1.77	0.64	0.52	0.83	0.93	1.15	2.08	1.39
V	59.2	203.9	106.4	51.7	62.5	125.7	188.9	174.6	158.4
Cr	71.4	97.2	121.2	11.8	19.4	259.0	137.2	117.8	58.7
Co	10.4	22.4	15.3	5.2	3.5	18.5	20.1	14.8	14.6
Ni	20.1	40.3	24.1	bdl	5.1	48.0	46.1	28.9	34.7
Cu	63	173	56	31	28	161	159	96	983
Zn	1302	90	60	96	53	90	77	97	473
As	86.8	189.8	1.1	7.0	5.4	1.0	0.5	bdl	0.3
Ag	1.2	0.5	bdl	bdl	bdl	bdl	bdl	bdl	bdl
Sn	1.0	0.8	1.5	0.5	0.8	0.7	0.6	1.2	0.8
Sb	2.5	9.5	0.3	1.7	0.9	0.2	bdl	0.1	0.3
Hg (ppb)	960	270	bdl	bdl	7	bdl	bdl	bdl	bdl
AI[2]	25.97	36.91	42.63	18.27	17.25	42.50	48.62	24.00	29.52
CCPI[3]	55.67	70.08	81.25	49.69	47.77	78.60	76.59	59.00	71.61
Mg#[4]	18.65	23.10	52.01	26.69	16.94	54.26	55.55	48.26	49.85
Ba/Sr	0.54	5.72	0.77	0.36	1.18	0.60	1.22	0.47	0.40
Eu/Eu*[5]	0.73	0.68	0.92	0.93	0.94	0.94	0.80	0.76	0.82
2200W	2209.42	2213.84			2209.26				
2250W		2245.26	2253.49	2250.77	2254.01	2252.53	2252.75	2252.76	2253.70

[1]Calculated from Fe_2O_{3t}, assuming all iron is present as FeO

[2]Alteration Index: AI = 100 x (K_2O+MgO)/(K_2O+MgO+Na_2O+CaO)

[3]Chlorite-carbonate-pyrite index: CCPI = 100 x (MgO + FeO_t)/(MgO+FeO_t+Na_2O+K_2O)

[4]Mg# = $Mg^{2+}/(Mg^{2+} + Fe^{2+})$ (molar %)

[5]Eu/Eu* = $Eu_n/(Gd_n + Sm_n)^{0.5}$ (n = Normalized to Primitive Mantle; Sun and McDonough, 1989)

bdl = Below detection limit

Table A5. Complete Dataset of Altered Samples from the Rambler Rhyolite Formation *(continued)*

Sample ID	62507	62177
Alteration	Weak alteration	Weak alteration
DDH-Level	RM07-18	RM05-08
Zone	1807	Ming South
Depth	666.44	1000.75
Unit	Unit 1.2	Unit 1.3
SiO_2 (wt. %)	66.72	70.73
Al_2O_3	13.20	13.12
Fe_2O_{3t}	5.77	4.68
FeO_t[1]	5.19	4.21
MnO	0.079	0.021
MgO	3.10	1.76
CaO	5.99	1.97
Na_2O	1.27	3.20
K_2O	1.54	1.47
TiO_2	0.169	0.145
P_2O_5	0.05	0.03
LOI	2.38	2.30
Total	100.30	99.44
Sr (ppm)	152	111
Sc	26	19
Zr	51	62
Ba	125.2	161.6
Y	5.08	3.82
Nb	2.43	2.48
Cs	0.38	1.03
La	6.52	7.24
Ce	13.14	14.38
Pr	1.50	1.67
Nd	5.46	5.54
Sm	1.07	1.05
Eu	0.28	0.30
Gd	0.91	0.75
Tb	0.16	0.12
Dy	0.92	0.74
Ho	0.19	0.14
Er	0.59	0.49
Tm	0.10	0.11
Yb	0.64	0.49
Lu	0.12	0.07
Ta	0.22	bdl
Tl	0.13	1.86
Pb	10.7	77.7
Bi	0.17	0.15
Th	2.20	3.17
U	1.92	0.74
V	158.9	76.6
Cr	73.6	157.4
Co	13.1	10.6
Ni	22.6	30.5
Cu	493	16
Zn	75	87
As	0.5	6.4
Ag	bdl	bdl
Sn	1.4	0.8
Sb	0.4	0.4
Hg (ppb)	bdl	6
AI[2]	38.99	38.45
CCPI[3]	75.94	57.97
Mg#[4]	51.56	42.69
Ba/Sr	0.82	1.46
Eu/Eu*[5]	0.83	0.95
2200W		2207.16
2250W	2253.52	2250.66

[1]Calculated from Fe_2O_{3t}, assuming all iron is present as FeO

[2]Alteration Index: AI = 100 x $(K_2O+MgO)/(K_2O+MgO+Na_2O+CaO)$

[3]Chlorite-carbonate-pyrite index: CCPI = 100 x $(MgO + FeO_t)/(MgO+FeO_t+Na_2O+K_2O)$

[4]Mg# = $Mg^{2+}/(Mg^{2+} + Fe^{2+})$ (molar %)

[5]$Eu/Eu^* = Eu_n/(Gd_n + Sm_n)^{0.5}$ (n = Normalized to Primitive Mantle; Sun and McDonough, 1989)

bdl = Below detection limit

Appendix 6.
Complete Chlorite Dataset from the Ming Deposit

Table 6. Complete Chlorite Dataset from the Ming Deposit

	36637_Chl_05_01 Quartz-sericite-chlorite	36637_Chl_05_02 Quartz-sericite-chlorite	36637_Chl_03_01 Quartz-sericite-chlorite	36637_Chl_03_02 Quartz-sericite-chlorite	36637_Chl_02_03 Quartz-sericite-chlorite
SiO_2 (wt. %)	26.93	27.01	26.73	26.35	26.95
TiO_2	0.08	0.07	0.09	0.11	0.10
Al_2O_3	22.60	22.55	22.50	23.15	22.60
Cr_2O_3	bdl	bdl	bdl	bdl	bdl
V_2O_3	0.02	0.01	0.01	0.01	0.03
FeO[1]	20.59	19.40	19.72	19.73	19.48
MgO	18.08	17.91	17.74	17.81	17.97
MnO	0.25	0.23	0.22	0.23	0.21
CaO	0.00	0.00	0.01	0.01	0.02
BaO	0.02	bdl	bdl	bdl	0.01
Na_2O	0.01	0.03	0.02	bdl	0.03
K_2O	0.00	0.19	0.03	0.01	0.02
F	bdl	bdl	bdl	bdl	bdl
Cl	0.01	0.01	0.01	bdl	0.01
Total	88.40	87.25	86.90	87.19	87.26
Number of ions calculated on the basis of 28 (O):					
Si	5.45	5.51	5.48	5.38	5.49
Ti	0.01	0.01	0.01	0.02	0.01
Al	5.39	5.42	5.44	5.58	5.43
Cr	bdl	bdl	bdl	bdl	bdl
V	0.00	0.00	0.00	0.00	0.00
Fe^{2+}	3.49	3.31	3.38	3.37	3.32
Mg	5.45	5.45	5.42	5.42	5.46
Mn	0.04	0.04	0.04	0.04	0.04
Ca	0.00	0.00	0.00	0.00	0.00
Ba	0.00	bdl	bdl	bdl	0.00
Na	0.00	0.01	0.01	bdl	0.01
K	0.00	0.05	0.01	0.00	0.01
Total cations	19.84	19.80	19.79	19.82	19.78
Cl	0.00	0.00	0.00	bdl	0.00
F	bdl	bdl	bdl	bdl	bdl
Fe/(Fe+Mg)	0.39	0.38	0.38	0.38	0.38

[1]Assuming all Fe is Fe^{2+}

Table 6. Complete Chlorite Dataset from the Ming Deposit (*continued)*

	36637_Chl_01_01 Quartz-sericite-chlorite	36637_Chl_01_02 Quartz-sericite-chlorite	36637_Chl_01_03 Quartz-sericite-chlorite	106413_Chl_01_03 Quartz-chlorite-sulfides	106413_Chl_01_04 Quartz-chlorite-sulfides
SiO_2 (wt. %)	26.62	26.71	26.55	26.14	26.81
TiO_2	0.06	0.06	0.07	0.07	0.08
Al_2O_3	22.84	22.99	22.91	22.79	22.29
Cr_2O_3	0.08	0.10	0.08	0.10	0.10
V_2O_3	bdl	0.01	0.01	0.04	0.04
FeO[1]	20.19	19.91	19.95	20.77	20.87
MgO	17.68	17.90	17.84	16.50	16.99
MnO	0.24	0.24	0.23	0.27	0.27
CaO	bdl	0.01	0.01	0.02	0.04
BaO	0.01	bdl	bdl	bdl	0.01
Na_2O	bdl	bdl	0.02	0.08	0.22
K_2O	0.01	0.01	0.00	0.01	0.02
F	bdl	bdl	bdl	bdl	bdl
Cl	0.01	0.01	0.02	0.01	0.03
Total	87.57	87.73	87.51	86.62	87.60
Number of ions calculated on the basis of 28 (O):					
Si	5.43	5.43	5.41	5.42	5.50
Ti	0.01	0.01	0.01	0.01	0.01
Al	5.49	5.50	5.51	5.57	5.39
Cr	0.01	0.02	0.01	0.02	0.02
V	bdl	0.00	0.00	0.01	0.01
Fe^{2+}	3.44	3.38	3.40	3.60	3.58
Mg	5.38	5.42	5.42	5.10	5.19
Mn	0.04	0.04	0.04	0.05	0.05
Ca	bdl	0.00	0.00	0.00	0.01
Ba	0.00	bdl	bdl	bdl	0.00
Na	bdl	bdl	0.01	0.03	0.09
K	0.00	0.00	0.00	0.00	0.01
Total cations	19.81	19.80	19.82	19.80	19.83
Cl	0.00	0.00	0.01	0.00	0.01
F	bdl	bdl	bdl	bdl	bdl
Fe/(Fe+Mg)	0.39	0.38	0.39	0.41	0.41

[1]Assuming all Fe is Fe^{2+}

Table 6. Complete Chlorite Dataset from the Ming Deposit *(continued)*

	106413_Chl_02_04 Quartz-chlorite-sulfides	106413_Chl_02_05 Quartz-chlorite-sulfides	106413_Chl_03_01 Quartz-chlorite-sulfides	106413_Chl_03_02 Quartz-chlorite-sulfides	106413_Chl_04_03 Quartz-chlorite-sulfides
SiO_2 (wt. %)	26.31	26.61	26.81	26.59	26.38
TiO_2	0.07	0.09	0.08	0.07	0.10
Al_2O_3	22.53	22.49	22.72	22.85	22.95
Cr_2O_3	0.11	0.08	0.07	0.08	0.09
V_2O_3	0.04	0.05	0.05	0.04	0.05
FeO[1]	21.08	21.13	21.42	21.24	22.28
MgO	16.74	17.13	16.88	17.12	16.84
MnO	0.28	0.27	0.26	0.29	0.27
CaO	0.01	0.01	0.02	0.00	0.02
BaO	0.03	bdl	0.02	bdl	bdl
Na_2O	0.02	0.02	0.18	0.02	0.01
K_2O	0.01	0.03	0.01	bdl	0.01
F	bdl	bdl	bdl	bdl	bdl
Cl	bdl	0.02	0.04	0.01	0.01
Total	87.04	87.70	88.42	88.08	88.85
Number of ions calculated on the basis of 28 (O):					
Si	5.43	5.45	5.46	5.42	5.37
Ti	0.01	0.01	0.01	0.01	0.01
Al	5.48	5.43	5.45	5.49	5.50
Cr	0.02	0.01	0.01	0.01	0.01
V	0.01	0.01	0.01	0.01	0.01
Fe^{2+}	3.64	3.62	3.65	3.62	3.79
Mg	5.15	5.23	5.12	5.20	5.11
Mn	0.05	0.05	0.05	0.05	0.05
Ca	0.00	0.00	0.00	0.00	0.00
Ba	0.00	bdl	0.00	bdl	bdl
Na	0.01	0.01	0.07	0.01	0.00
K	0.00	0.01	0.00	bdl	0.00
Total cations	19.81	19.82	19.83	19.82	19.86
Cl	bdl	0.01	0.01	0.00	0.00
F	bdl	bdl	bdl	bdl	bdl
Fe/(Fe+Mg)	0.41	0.41	0.42	0.41	0.43

[1]Assuming all Fe is Fe^{2+}

Table 6. Complete Chlorite Dataset from the Ming Deposit *(continued)*

	106413_Chl_04_04 Quartz-chlorite-sulfides	62060_Chl_01_05 Quartz-chlorite	62060_Chl_01_06 Quartz-chlorite	62060_Chl_02_02 Quartz-chlorite	62060_Chl_02_01 Quartz-chlorite
SiO_2 (wt. %)	26.55	26.32	26.20	26.29	26.31
TiO_2	0.07	0.03	0.04	0.06	0.08
Al_2O_3	22.57	22.96	22.85	22.81	22.87
Cr_2O_3	0.05	0.14	0.15	0.08	0.06
V_2O_3	0.03	0.04	0.03	0.03	0.04
FeO[1]	21.21	21.54	21.86	21.73	21.45
MgO	17.05	16.65	16.60	16.42	16.30
MnO	0.30	0.17	0.17	0.18	0.18
CaO	0.01	0.00	0.01	0.01	0.02
BaO	bdl	0.02	bdl	bdl	0.01
Na_2O	0.01	0.02	0.01	bdl	0.01
K_2O	bdl	0.00	0.00	bdl	bdl
F	bdl	bdl	bdl	bdl	bdl
Cl	0.01	bdl	0.00	bdl	0.01
Total	87.68	87.70	87.69	87.42	87.16
Number of ions calculated on the basis of 28 (O):					
Si	5.44	5.40	5.38	5.41	5.43
Ti	0.01	0.01	0.01	0.01	0.01
Al	5.45	5.55	5.53	5.54	5.56
Cr	0.01	0.02	0.02	0.01	0.01
V	0.01	0.01	0.00	0.01	0.01
Fe^{2+}	3.63	3.69	3.76	3.74	3.70
Mg	5.21	5.09	5.09	5.04	5.01
Mn	0.05	0.03	0.03	0.03	0.03
Ca	0.00	0.00	0.00	0.00	0.00
Ba	bdl	0.00	bdl	bdl	0.00
Na	0.00	0.01	0.01	bdl	0.00
K	bdl	0.00	0.00	bdl	bdl
Total cations	19.82	19.81	19.83	19.80	19.77
Cl	0.00	bdl	0.00	bdl	0.00
F	bdl	bdl	bdl	bdl	bdl
Fe/(Fe+Mg)	0.41	0.42	0.42	0.43	0.42

[1]Assuming all Fe is Fe^{2+}

Table 6. Complete Chlorite Dataset from the Ming Deposit *(continued)*

	62060_Chl_03_05	62060_Chl_03_06	62060_Chl_04_01	62060_Chl_04_02	62060_Chl_05_01
	Quartz-chlorite	Quartz-chlorite	Quartz-chlorite	Quartz-chlorite	Quartz-chlorite
SiO_2 (wt. %)	26.09	26.14	26.11	26.00	25.66
TiO_2	0.03	0.04	0.05	0.05	0.07
Al_2O_3	23.03	23.07	22.80	23.05	22.95
Cr_2O_3	0.09	0.11	0.08	0.06	0.07
V_2O_3	0.03	0.05	0.04	0.04	0.03
FeO[1]	21.87	21.98	22.00	22.42	22.18
MgO	16.34	16.31	16.45	16.14	16.01
MnO	0.19	0.18	0.16	0.16	0.16
CaO	0.01	0.01	0.01	0.01	0.01
BaO	bdl	bdl	bdl	bdl	bdl
Na_2O	bdl	0.01	0.01	0.02	0.02
K_2O	bdl	bdl	0.01	0.00	0.01
F	bdl	bdl	bdl	bdl	bdl
Cl	0.01	0.00	0.00	0.02	0.01
Total	87.52	87.69	87.55	87.77	87.02
Number of ions calculated on the basis of 28 (O):					
Si	5.38	5.38	5.38	5.36	5.33
Ti	0.00	0.01	0.01	0.01	0.01
Al	5.59	5.59	5.54	5.60	5.62
Cr	0.02	0.02	0.01	0.01	0.01
V	0.01	0.01	0.01	0.01	0.01
Fe^{2+}	3.77	3.78	3.79	3.86	3.86
Mg	5.02	5.00	5.05	4.96	4.96
Mn	0.03	0.03	0.03	0.03	0.03
Ca	0.00	0.00	0.00	0.00	0.00
Ba	bdl	bdl	bdl	bdl	bdl
Na	bdl	0.01	0.01	0.01	0.01
K	bdl	bdl	0.00	0.00	0.00
Total cations	19.82	19.81	19.83	19.83	19.84
Cl	0.00	0.00	0.00	0.01	0.00
F	bdl	bdl	bdl	bdl	bdl
Fe/(Fe+Mg)	0.43	0.43	0.43	0.44	0.44

[1]Assuming all Fe is Fe^{2+}

Table 6. Complete Chlorite Dataset from the Ming Deposit *(continued)*

	62060_Chl_05_02	62524_Chl_04_01	62524_Chl_04_02	62524_Chl_04_03	62524_Chl_05_01
	Quartz-chlorite	Quartz-sericite	Quartz-sericite	Quartz-sericite	Quartz-sericite
SiO_2 (wt. %)	26.14	26.43	26.70	26.26	26.85
TiO_2	0.07	0.06	0.05	0.07	0.06
Al_2O_3	22.43	23.15	23.42	23.10	23.83
Cr_2O_3	0.08	0.05	0.02	0.02	0.01
V_2O_3	0.05	0.01	bdl	0.02	0.01
FeO[1]	22.02	17.93	18.08	18.03	18.34
MgO	16.59	18.81	19.07	18.80	18.45
MnO	0.17	0.11	0.12	0.13	0.11
CaO	0.01	0.00	0.01	0.02	0.02
BaO	bdl	0.04	bdl	0.04	0.02
Na_2O	bdl	0.02	0.02	bdl	0.01
K_2O	0.02	0.00	0.02	0.01	0.01
F	bdl	bdl	bdl	bdl	bdl
Cl	bdl	0.01	0.01	0.02	bdl
Total	87.35	86.54	87.49	86.43	87.61
Number of ions calculated on the basis of 28 (O):					
Si	5.40	5.40	5.39	5.38	5.41
Ti	0.01	0.01	0.01	0.01	0.01
Al	5.46	5.57	5.58	5.57	5.66
Cr	0.01	0.01	0.00	0.00	0.00
V	0.01	0.00	bdl	0.00	0.00
Fe^{2+}	3.81	3.06	3.06	3.09	3.09
Mg	5.11	5.73	5.74	5.74	5.54
Mn	0.03	0.02	0.02	0.02	0.02
Ca	0.00	0.00	0.00	0.00	0.00
Ba	bdl	0.00	bdl	0.00	0.00
Na	bdl	0.01	0.01	bdl	0.00
K	0.00	0.00	0.01	0.00	0.00
Total cations	19.85	19.81	19.81	19.83	19.75
Cl	bdl	0.00	0.00	0.01	bdl
F	bdl	bdl	bdl	bdl	bdl
Fe/(Fe+Mg)	0.43	0.35	0.35	0.35	0.36

[1]Assuming all Fe is Fe^{2+}

Table 6. Complete Chlorite Dataset from the Ming Deposit *(continued)*

	62524_Chl_05_02	62524_Chl_05_03	62524_Chl_07_01	62524_Chl_07_02	36634_Chl_01_03
	Quartz-sericite	Quartz-sericite	Quartz-sericite	Quartz-sericite	Quartz-sericite-chlorite
SiO_2 (wt. %)	26.40	26.66	26.64	26.58	26.07
TiO_2	0.07	0.06	0.08	0.06	0.07
Al_2O_3	23.41	23.45	23.28	23.56	22.36
Cr_2O_3	0.02	0.02	0.02	0.01	0.02
V_2O_3	0.01	0.02	0.01	0.01	0.04
FeO[1]	18.70	18.44	18.21	18.65	22.14
MgO	18.34	18.66	18.73	18.80	15.79
MnO	0.09	0.12	0.10	0.09	0.25
CaO	0.04	0.01	0.00	0.00	0.00
BaO	0.01	0.02	bdl	0.03	bdl
Na_2O	0.03	bdl	0.02	0.02	bdl
K_2O	0.02	0.00	0.00	0.01	0.03
F	bdl	bdl	bdl	bdl	bdl
Cl	0.01	bdl	bdl	0.00	0.02
Total	87.05	87.41	86.97	87.75	86.64
Number of ions calculated on the basis of 28 (O):					
Si	5.38	5.40	5.41	5.37	5.44
Ti	0.01	0.01	0.01	0.01	0.01
Al	5.62	5.60	5.57	5.61	5.50
Cr	0.00	0.00	0.00	0.00	0.00
V	0.00	0.00	0.00	0.00	0.01
Fe^{2+}	3.19	3.12	3.09	3.15	3.87
Mg	5.57	5.63	5.67	5.66	4.91
Mn	0.02	0.02	0.02	0.02	0.04
Ca	0.01	0.00	0.00	0.00	0.00
Ba	0.00	0.00	bdl	0.00	bdl
Na	0.01	bdl	0.01	0.01	bdl
K	0.00	0.00	0.00	0.00	0.01
Total cations	19.81	19.79	19.79	19.82	19.80
Cl	0.00	bdl	bdl	0.00	0.01
F	bdl	bdl	bdl	bdl	bdl
Fe/(Fe+Mg)	0.36	0.36	0.35	0.36	0.44

[1]Assuming all Fe is Fe^{2+}

Table 6. Complete Chlorite Dataset from the Ming Deposit *(continued)*

	36634_Chl_01_04 Quartz-sericite-chlorite	36634_Chl_02_01 Quartz-sericite-chlorite	36634_Chl_02_02 Quartz-sericite-chlorite	36634_Chl_03_03 Quartz-sericite-chlorite	36634_Chl_03_04 Quartz-sericite-chlorite
SiO_2 (wt. %)	25.94	26.07	26.02	26.02	26.08
TiO_2	0.08	0.06	0.05	0.06	0.05
Al_2O_3	22.81	22.72	22.63	22.74	22.83
Cr_2O_3	0.01	0.07	0.06	0.02	0.02
V_2O_3	0.03	0.04	0.03	0.04	0.03
FeO[1]	22.66	22.44	22.44	22.49	22.86
MgO	15.64	16.04	15.88	15.95	15.83
MnO	0.24	0.28	0.25	0.25	0.26
CaO	0.01	0.00	0.01	0.00	bdl
BaO	0.02	bdl	bdl	0.01	0.04
Na_2O	bdl	0.02	0.02	0.01	0.01
K_2O	0.03	bdl	bdl	0.01	0.00
F	bdl	bdl	bdl	bdl	bdl
Cl	0.01	0.00	0.02	0.01	0.01
Total	87.30	87.55	87.21	87.42	87.84
Number of ions calculated on the basis of 28 (O):					
Si	5.39	5.39	5.40	5.39	5.38
Ti	0.01	0.01	0.01	0.01	0.01
Al	5.58	5.53	5.54	5.55	5.56
Cr	0.00	0.01	0.01	0.00	0.00
V	0.01	0.01	0.01	0.01	0.01
Fe^{2+}	3.93	3.88	3.90	3.89	3.95
Mg	4.84	4.94	4.91	4.92	4.87
Mn	0.04	0.05	0.04	0.04	0.05
Ca	0.00	0.00	0.00	0.00	bdl
Ba	0.00	bdl	bdl	0.00	0.00
Na	bdl	0.01	0.01	0.00	0.00
K	0.01	bdl	bdl	0.00	0.00
Total cations	19.81	19.83	19.82	19.83	19.83
Cl	0.00	0.00	0.01	0.00	0.00
F	bdl	bdl	bdl	bdl	bdl
Fe/(Fe+Mg)	0.45	0.44	0.44	0.44	0.45

[1]Assuming all Fe is Fe^{2+}

Table 6. Complete Chlorite Dataset from the Ming Deposit *(continued)*

	36634_Chl_04_01 Quartz-sericite-chlorite	36634_Chl_04_02 Quartz-sericite-chlorite	36634_Chl_04_03 Quartz-sericite-chlorite	29815_Chl_01_03 Quartz-sericite-sulfides	29815_Chl_03_01 Quartz-sericite-sulfides
SiO_2 (wt. %)	25.55	26.23	25.97	28.79	28.61
TiO_2	0.06	0.06	0.06	0.07	0.04
Al_2O_3	22.84	22.51	22.65	23.31	22.93
Cr_2O_3	0.08	0.05	0.12	0.04	0.02
V_2O_3	0.05	0.04	0.03	0.00	0.03
FeO[1]	22.45	22.20	22.38	8.96	8.93
MgO	15.57	15.90	15.88	25.62	25.30
MnO	0.27	0.29	0.25	0.40	0.35
CaO	0.01	0.01	0.01	0.02	0.02
BaO	0.02	0.02	bdl	bdl	bdl
Na_2O	0.02	0.01	bdl	0.03	0.03
K_2O	0.00	0.01	0.01	0.01	0.01
F	bdl	bdl	bdl	bdl	bdl
Cl	0.00	0.02	0.02	bdl	bdl
Total	86.77	87.18	87.19	87.21	86.26
Number of ions calculated on the basis of 28 (O):					
Si	5.34	5.44	5.39	5.56	5.59
Ti	0.01	0.01	0.01	0.01	0.01
Al	5.63	5.50	5.54	5.30	5.28
Cr	0.01	0.01	0.02	0.01	0.00
V	0.01	0.01	0.01	0.00	0.00
Fe^{2+}	3.92	3.85	3.89	1.45	1.46
Mg	4.85	4.92	4.91	7.37	7.36
Mn	0.05	0.05	0.04	0.06	0.06
Ca	0.00	0.00	0.00	0.00	0.00
Ba	0.00	0.00	bdl	bdl	bdl
Na	0.01	0.01	bdl	0.01	0.01
K	0.00	0.00	0.00	0.00	0.00
Total cations	19.83	19.80	19.82	19.78	19.77
Cl	0.00	0.01	0.01	bdl	bdl
F	bdl	bdl	bdl	bdl	bdl
Fe/(Fe+Mg)	0.45	0.44	0.44	0.16	0.17

[1]Assuming all Fe is Fe^{2+}

Table 6. Complete Chlorite Dataset from the Ming Deposit *(continued)*

	29815_Chl_03_02 Quartz-sericite-sulfides	29815_Chl_03_03 Quartz-sericite-sulfides	29815_Chl_05_01 Quartz-sericite-sulfides	29815_Chl_05_02 Quartz-sericite-sulfides
SiO_2 (wt. %)	29.12	28.92	28.80	28.98
TiO_2	0.06	0.05	0.04	0.02
Al_2O_3	23.04	23.18	23.47	23.15
Cr_2O_3	0.03	0.03	0.04	0.04
V_2O_3	bdl	0.02	0.03	0.01
FeO[1]	8.96	9.15	9.07	9.16
MgO	25.46	25.54	25.58	25.31
MnO	0.37	0.38	0.39	0.38
CaO	0.01	0.02	0.02	0.01
BaO	0.01	bdl	bdl	0.02
Na_2O	0.01	bdl	bdl	0.01
K_2O	0.01	bdl	0.01	0.01
F	bdl	bdl	bdl	bdl
Cl	0.02	0.01	0.01	bdl
Total	87.06	87.25	87.37	87.10
Number of ions calculated on the basis of 28 (O):				
Si	5.63	5.58	5.55	5.61
Ti	0.01	0.01	0.01	0.00
Al	5.25	5.28	5.33	5.28
Cr	0.01	0.01	0.01	0.01
V	bdl	0.00	0.00	0.00
Fe^{2+}	1.45	1.48	1.46	1.48
Mg	7.33	7.35	7.35	7.30
Mn	0.06	0.06	0.06	0.06
Ca	0.00	0.00	0.00	0.00
Ba	0.00	bdl	bdl	0.00
Na	0.00	bdl	bdl	0.00
K	0.00	bdl	0.00	0.00
Total cations	19.74	19.77	19.78	19.75
Cl	0.01	0.00	0.00	bdl
F	bdl	bdl	bdl	bdl
Fe/(Fe+Mg)	0.16	0.17	0.17	0.17

[1]Assuming all Fe is Fe^{2+}

Appendix 7.
Complete Sericite Dataset from the Ming Deposit

Table 7. Complete Sericite Dataset from the Ming Deposit

	60507_Ser_03_03 Sericite-calcite±spessartine	60507_Ser_03_04 Sericite-calcite±spessartine	60507_Ser_03_05 Sericite-calcite±spessartine	60507_Ser_03_06 Sericite-calcite±spessartine	60507_Ser_04_05 Sericite-calcite±spessartine
SiO_2 (wt. %)	50.33	49.87	49.09	49.29	49.89
TiO_2	0.36	0.38	0.43	0.34	0.42
Al_2O_3	32.33	32.82	32.55	32.87	33.02
Cr_2O_3	0.01	0.03	0.01	0.03	0.02
V_2O_3	0.06	0.05	0.06	0.07	0.05
FeO[1]	4.03	4.02	4.14	4.02	4.10
MgO	1.89	1.85	1.75	1.70	1.82
MnO	0.03	0.04	0.02	0.05	0.05
CaO	0.07	0.00	0.00	0.01	0.01
BaO	0.39	0.38	0.36	0.40	0.34
Na_2O	1.65	0.35	0.35	0.32	0.37
K_2O	9.41	9.86	9.95	9.86	9.68
F	bdl	bdl	bdl	bdl	bdl
Cl	bdl	bdl	bdl	bdl	bdl
Total	100.48	99.59	98.61	98.86	99.65
Number of ions calculated on the basis of 22 (O):					
Si	6.42	6.40	6.38	6.38	6.39
Ti	0.03	0.04	0.04	0.03	0.04
Al	4.86	4.97	4.98	5.01	4.99
Cr	0.00	0.00	0.00	0.00	0.00
V	0.01	0.01	0.01	0.01	0.00
Fe^{2+}	0.43	0.43	0.45	0.44	0.44
Mg	0.36	0.35	0.34	0.33	0.35
Mn	0.00	0.00	0.00	0.01	0.01
Ca	0.01	0.00	0.00	0.00	0.00
Ba	0.02	0.02	0.02	0.02	0.02
Na	0.41	0.09	0.09	0.08	0.09
K	1.53	1.61	1.65	1.63	1.58
Total cations	14.08	13.92	13.96	13.93	13.91
Cl	bdl	bdl	bdl	bdl	bdl
F	bdl	bdl	bdl	bdl	bdl
Fe/(Fe+Mg)	0.54	0.55	0.57	0.57	0.56

[1]Assuming all Fe is Fe^{2+}

Table 7. Complete Sericite Dataset from the Ming Deposit *(continued)*

	60507_Ser_04_06 Sericite-calcite±spessartine	60507_Ser_04_07 Sericite-calcite±spessartine	RM03-01_01_01 Quartz-sericite-sulfides	RM03-01_01_02 Quartz-sericite-sulfides	RM03-01_01_03 Quartz-sericite-sulfides
SiO_2 (wt. %)	49.44	49.79	50.04	50.16	50.16
TiO_2	0.45	0.43	0.24	0.27	0.34
Al_2O_3	32.50	32.86	34.96	34.71	34.82
Cr_2O_3	0.02	0.02	0.15	0.32	0.36
V_2O_3	0.06	0.05	0.09	0.06	0.07
FeO[1]	4.18	4.20	1.33	1.30	1.34
MgO	1.85	1.87	1.62	1.55	1.59
MnO	0.05	0.04	0.01	0.02	0.01
CaO	0.01	0.01	0.00	0.00	0.01
BaO	0.37	0.38	0.10	0.11	0.11
Na_2O	0.35	0.38	0.58	0.57	0.63
K_2O	9.61	9.47	10.00	9.98	9.95
F	bdl	bdl	bdl	bdl	bdl
Cl	bdl	0.01	bdl	0.00	0.01
Total	98.77	99.42	99.05	99.00	99.31
Number of ions calculated on the basis of 22 (O):					
Si	6.40	6.39	6.36	6.38	6.36
Ti	0.04	0.04	0.02	0.03	0.03
Al	4.96	4.97	5.24	5.20	5.21
Cr	0.00	0.00	0.01	0.03	0.04
V	0.01	0.01	0.01	0.01	0.01
Fe^{2+}	0.45	0.45	0.14	0.14	0.14
Mg	0.36	0.36	0.31	0.29	0.30
Mn	0.00	0.00	0.00	0.00	0.00
Ca	0.00	0.00	0.00	0.00	0.00
Ba	0.02	0.02	0.00	0.01	0.01
Na	0.09	0.10	0.14	0.14	0.15
K	1.59	1.55	1.62	1.62	1.61
Total cations	13.91	13.90	13.87	13.85	13.86
Cl	bdl	0.00	bdl	0.00	0.00
F	bdl	bdl	bdl	bdl	bdl
Fe/(Fe+Mg)	0.56	0.56	0.32	0.32	0.32

[1]Assuming all Fe is Fe^{2+}

Table 7. Complete Sericite Dataset from the Ming Deposit *(continued)*

	RM03-01_02_01 Quartz-sericite-sulfides	RM03-01_02_02 Quartz-sericite-sulfides	RM03-01_02_03 Quartz-sericite-sulfides	RM03-01_02_04 Quartz-sericite-sulfides	RM03-01_03_01 Quartz-sericite-sulfides
SiO_2 (wt. %)	50.08	50.77	49.97	50.40	50.27
TiO_2	0.36	0.44	0.42	0.14	0.52
Al_2O_3	35.02	35.76	34.54	35.65	35.18
Cr_2O_3	0.27	0.14	0.12	0.04	0.04
V_2O_3	0.07	0.07	0.08	0.06	0.07
FeO[1]	1.46	1.48	1.47	1.33	1.42
MgO	1.70	1.60	1.70	1.52	1.66
MnO	0.01	0.01	0.01	0.03	0.03
CaO	0.04	0.05	0.02	0.02	0.00
BaO	0.12	0.09	0.15	0.10	0.11
Na_2O	0.62	0.59	0.65	0.67	0.64
K_2O	9.69	9.09	9.64	9.85	9.78
F	bdl	bdl	bdl	bdl	bdl
Cl	0.00	0.00	0.02	0.00	bdl
Total	99.40	100.02	98.70	99.74	99.66
Number of ions calculated on the basis of 22 (O):					
Si	6.34	6.35	6.37	6.35	6.35
Ti	0.03	0.04	0.04	0.01	0.05
Al	5.23	5.28	5.19	5.30	5.24
Cr	0.03	0.01	0.01	0.00	0.00
V	0.01	0.01	0.01	0.01	0.01
Fe^{2+}	0.16	0.16	0.16	0.14	0.15
Mg	0.32	0.30	0.32	0.29	0.31
Mn	0.00	0.00	0.00	0.00	0.00
Ca	0.01	0.01	0.00	0.00	0.00
Ba	0.01	0.00	0.01	0.00	0.01
Na	0.15	0.14	0.16	0.16	0.16
K	1.57	1.45	1.57	1.58	1.57
Total cations	13.85	13.75	13.85	13.85	13.85
Cl	0.00	0.00	0.00	0.00	bdl
F	bdl	bdl	bdl	bdl	bdl
Fe/(Fe+Mg)	0.33	0.34	0.33	0.33	0.32

[1]Assuming all Fe is Fe^{2+}

Table 7. Complete Sericite Dataset from the Ming Deposit *(continued)*

	RM03-01_03_02 Quartz-sericite-sulfides	RM03-01_03_03 Quartz-sericite-sulfides	29890_Ser_01_01 Quartz-sericite-sulfides	29890_Ser_01_02 Quartz-sericite-sulfides	29890_Ser_01_03 Quartz-sericite-sulfides
SiO_2 (wt. %)	49.81	49.73	49.26	49.83	49.41
TiO_2	0.32	0.15	0.41	0.39	0.38
Al_2O_3	35.09	35.47	34.22	34.35	34.25
Cr_2O_3	0.03	0.02	0.10	0.10	0.07
V_2O_3	0.07	0.06	0.11	0.12	0.09
FeO[1]	1.36	1.41	1.73	1.25	1.51
MgO	1.62	1.54	1.72	1.77	1.83
MnO	0.01	0.02	0.02	0.01	0.01
CaO	0.05	0.04	0.02	0.01	0.03
BaO	0.12	0.08	0.07	0.08	0.06
Na_2O	0.71	0.60	0.52	0.57	0.54
K_2O	9.61	9.19	10.23	10.14	9.89
F	bdl	bdl	bdl	bdl	0.02
Cl	0.01	bdl	0.01	0.01	0.01
Total	98.75	98.20	98.41	98.65	98.08
Number of ions calculated on the basis of 22 (O):					
Si	6.34	6.34	6.34	6.37	6.36
Ti	0.03	0.01	0.04	0.04	0.04
Al	5.27	5.33	5.19	5.18	5.19
Cr	0.00	0.00	0.01	0.01	0.01
V	0.01	0.01	0.01	0.01	0.01
Fe^{2+}	0.14	0.15	0.19	0.13	0.16
Mg	0.31	0.29	0.33	0.34	0.35
Mn	0.00	0.00	0.00	0.00	0.00
Ca	0.01	0.01	0.00	0.00	0.00
Ba	0.01	0.00	0.00	0.00	0.00
Na	0.18	0.15	0.13	0.14	0.13
K	1.56	1.49	1.68	1.66	1.62
Total cations	13.86	13.79	13.92	13.89	13.88
Cl	0.00	bdl	0.00	0.00	0.00
F	bdl	bdl	bdl	bdl	0.01
Fe/(Fe+Mg)	0.32	0.34	0.36	0.28	0.32

[1]Assuming all Fe is Fe^{2+}

Table 7. Complete Sericite Dataset from the Ming Deposit *(continued)*

	29815_Ser_04_01 Quartz-sericite-sulfides	29815_Ser_04_02 Quartz-sericite-sulfides	29815_Ser_04_03 Quartz-sericite-sulfides	29815_Ser_04_04 Quartz-sericite-sulfides	29815_Ser_07_01 Quartz-sericite-sulfides
SiO_2 (wt. %)	50.54	49.28	48.65	49.54	50.00
TiO_2	0.42	0.44	0.59	0.26	0.36
Al_2O_3	35.67	34.32	34.88	34.55	34.88
Cr_2O_3	0.07	0.07	0.04	0.07	0.06
V_2O_3	0.08	0.09	0.08	0.06	0.04
FeO[1]	1.27	1.21	1.45	1.28	1.23
MgO	2.01	1.85	2.13	2.00	1.85
MnO	0.01	0.02	0.03	0.02	0.01
CaO	0.01	0.02	0.02	0.04	0.01
BaO	0.09	0.05	0.11	0.08	0.10
Na_2O	0.49	0.51	0.51	0.53	0.57
K_2O	9.87	10.27	9.98	9.92	10.07
F	0.04	0.04	bdl	bdl	bdl
Cl	bdl	0.01	0.01	0.01	bdl
Total	100.56	98.14	98.46	98.34	99.14
Number of ions calculated on the basis of 22 (O):					
Si	6.32	6.34	6.25	6.35	6.35
Ti	0.04	0.04	0.06	0.02	0.03
Al	5.26	5.21	5.28	5.22	5.22
Cr	0.01	0.01	0.00	0.01	0.01
V	0.01	0.01	0.01	0.01	0.00
Fe^{2+}	0.13	0.13	0.16	0.14	0.13
Mg	0.38	0.36	0.41	0.38	0.35
Mn	0.00	0.00	0.00	0.00	0.00
Ca	0.00	0.00	0.00	0.01	0.00
Ba	0.00	0.00	0.01	0.00	0.00
Na	0.12	0.13	0.13	0.13	0.14
K	1.58	1.69	1.64	1.62	1.63
Total cations	13.85	13.91	13.93	13.89	13.88
Cl	bdl	0.00	0.00	0.00	bdl
F	0.01	0.02	bdl	bdl	bdl
Fe/(Fe+Mg)	0.26	0.27	0.28	0.26	0.27

[1]Assuming all Fe is Fe^{2+}

Table 7. Complete Sericite Dataset from the Ming Deposit *(continued)*

	29815_Ser_07_02 Quartz-sericite-sulfides	29815_Ser_07_03 Quartz-sericite-sulfides	29815_Ser_07_04 Quartz-sericite-sulfides	62524_Ser_06_01 Quartz-sericite	62524_Ser_06_04 Quartz-sericite
SiO_2 (wt. %)	50.01	49.49	50.41	47.17	49.12
TiO_2	0.29	0.32	0.47	0.29	0.31
Al_2O_3	34.97	35.07	35.41	34.89	37.21
Cr_2O_3	0.07	0.08	0.03	0.06	0.08
V_2O_3	0.03	0.06	0.05	0.03	0.02
FeO[1]	1.25	1.30	1.26	1.79	1.75
MgO	1.99	1.73	1.54	0.95	0.96
MnO	0.01	0.01	0.01	0.01	bdl
CaO	0.01	0.01	0.01	0.01	0.02
BaO	0.08	0.09	0.08	0.07	0.04
Na_2O	0.53	0.44	0.55	0.62	0.78
K_2O	10.10	10.26	9.95	9.81	9.43
F	bdl	0.02	bdl	0.07	bdl
Cl	0.01	0.00	0.01	0.03	bdl
Total	99.33	98.87	99.74	95.74	99.72
Number of ions calculated on the basis of 22 (O):					
Si	6.34	6.32	6.35	6.24	6.20
Ti	0.03	0.03	0.04	0.03	0.03
Al	5.23	5.28	5.26	5.44	5.53
Cr	0.01	0.01	0.00	0.01	0.01
V	0.00	0.01	0.00	0.00	0.00
Fe^{2+}	0.13	0.14	0.13	0.20	0.18
Mg	0.38	0.33	0.29	0.19	0.18
Mn	0.00	0.00	0.00	0.00	bdl
Ca	0.00	0.00	0.00	0.00	0.00
Ba	0.00	0.00	0.00	0.00	0.00
Na	0.13	0.11	0.13	0.16	0.19
K	1.63	1.67	1.60	1.65	1.52
Total cations	13.89	13.90	13.83	13.92	13.86
Cl	0.00	0.00	0.00	0.01	bdl
F	bdl	0.01	bdl	0.03	bdl
Fe/(Fe+Mg)	0.26	0.30	0.31	0.52	0.50

[1]Assuming all Fe is Fe^{2+}

Table 7. Complete Sericite Dataset from the Ming Deposit *(continued)*

	62524_Ser_06_02	62524_Ser_06_03	62524_Ser_06_05	62524_Ser_06_06	62524_Ser_08_04
	Quartz-sericite	Quartz-sericite	Quartz-sericite	Quartz-sericite	Quartz-sericite
SiO_2 (wt. %)	49.85	49.68	48.73	48.91	49.09
TiO_2	0.36	0.26	0.25	0.31	0.38
Al_2O_3	37.39	37.18	36.19	36.53	36.02
Cr_2O_3	0.08	0.04	0.01	0.07	0.06
V_2O_3	0.02	0.04	0.03	0.02	0.04
FeO[1]	1.85	1.88	1.68	1.83	1.80
MgO	1.03	1.07	1.05	0.94	1.11
MnO	bdl	bdl	bdl	0.01	0.01
CaO	0.04	0.01	bdl	0.01	0.01
BaO	0.03	0.02	0.05	0.04	0.04
Na_2O	0.65	0.72	0.78	0.68	0.71
K_2O	9.28	9.51	10.02	10.13	9.79
F	0.08	0.08	0.05	0.02	0.09
Cl	0.02	0.00	bdl	0.01	bdl
Total	100.63	100.45	98.82	99.49	99.08
Number of ions calculated on the basis of 22 (O):					
Si	6.23	6.23	6.23	6.22	6.25
Ti	0.03	0.02	0.02	0.03	0.04
Al	5.50	5.49	5.46	5.47	5.41
Cr	0.01	0.00	0.00	0.01	0.01
V	0.00	0.00	0.00	0.00	0.00
Fe^{2+}	0.19	0.20	0.18	0.19	0.19
Mg	0.19	0.20	0.20	0.18	0.21
Mn	bdl	bdl	bdl	0.00	0.00
Ca	0.01	0.00	bdl	0.00	0.00
Ba	0.00	0.00	0.00	0.00	0.00
Na	0.16	0.17	0.19	0.17	0.17
K	1.48	1.52	1.63	1.64	1.59
Total cations	13.80	13.85	13.93	13.92	13.88
Cl	0.00	0.00	bdl	0.00	bdl
F	0.03	0.03	0.02	0.01	0.04
Fe/(Fe+Mg)	0.50	0.50	0.47	0.52	0.48

[1]Assuming all Fe is Fe^{2+}

Table 7. Complete Sericite Dataset from the Ming Deposit *(continued)*

	62524_Ser_08_01	62524_Ser_08_02	62524_Ser_08_03	62524_Ser_09_01	62524_Ser_09_02
	Quartz-sericite	Quartz-sericite	Quartz-sericite	Quartz-sericite	Quartz-sericite
SiO_2 (wt. %)	49.42	49.47	48.18	49.58	48.43
TiO_2	0.33	0.32	0.38	0.32	0.36
Al_2O_3	37.21	36.77	35.30	37.53	35.68
Cr_2O_3	0.10	0.12	0.06	0.04	0.04
V_2O_3	0.03	0.02	0.04	0.05	0.04
FeO[1]	1.87	2.00	1.85	1.89	1.74
MgO	1.00	1.13	1.09	1.02	1.02
MnO	bdl	0.02	bdl	bdl	0.02
CaO	0.00	0.01	0.02	0.02	0.06
BaO	0.03	0.03	0.08	0.05	0.05
Na_2O	0.65	0.56	0.54	0.64	0.60
K_2O	9.75	9.77	10.06	9.54	9.14
F	0.03	0.07	0.06	0.02	0.06
Cl	0.00	0.02	0.03	0.01	0.05
Total	100.41	100.26	97.65	100.69	97.26
Number of ions calculated on the basis of 22 (O):					
Si	6.21	6.23	6.25	6.20	6.26
Ti	0.03	0.03	0.04	0.03	0.04
Al	5.51	5.46	5.40	5.53	5.44
Cr	0.01	0.01	0.01	0.00	0.00
V	0.00	0.00	0.00	0.00	0.00
Fe^{2+}	0.20	0.21	0.20	0.20	0.19
Mg	0.19	0.21	0.21	0.19	0.20
Mn	bdl	0.00	bdl	bdl	0.00
Ca	0.00	0.00	0.00	0.00	0.01
Ba	0.00	0.00	0.00	0.00	0.00
Na	0.16	0.14	0.14	0.16	0.15
K	1.56	1.57	1.66	1.52	1.51
Total cations	13.86	13.86	13.91	13.84	13.81
Cl	0.00	0.00	0.01	0.00	0.01
F	0.01	0.03	0.03	0.01	0.02
Fe/(Fe+Mg)	0.51	0.50	0.49	0.51	0.49

[1]Assuming all Fe is Fe^{2+}

Table 7. Complete Sericite Dataset from the Ming Deposit *(continued)*

	62524_Ser_09_03 Quartz-sericite	36634_Ser_01_01 Quartz-chlorite-sericite	36634_Ser_03_01 Quartz-chlorite-sericite	36634_Ser_03_02 Quartz-chlorite-sericite	36634_Ser_05_01 Quartz-chlorite-sericite
SiO_2 (wt. %)	48.43	48.50	48.69	49.00	49.01
TiO_2	0.31	0.35	0.48	0.44	0.37
Al_2O_3	36.32	34.53	34.30	34.50	36.08
Cr_2O_3	0.04	bdl	0.03	0.03	0.02
V_2O_3	0.02	0.10	0.11	0.11	0.11
FeO[1]	1.81	2.86	3.11	2.91	2.87
MgO	0.95	1.15	1.18	1.19	1.00
MnO	bdl	0.02	bdl	bdl	bdl
CaO	0.00	0.00	bdl	0.00	0.00
BaO	0.04	0.20	0.17	0.16	0.18
Na_2O	0.73	0.54	0.54	0.52	0.69
K_2O	9.85	9.95	10.18	9.98	9.26
F	0.02	bdl	bdl	bdl	bdl
Cl	0.01	0.01	0.01	0.05	0.02
Total	98.53	98.12	98.72	98.81	99.49
Number of ions calculated on the basis of 22 (O):					
Si	6.21	6.29	6.29	6.31	6.23
Ti	0.03	0.03	0.05	0.04	0.04
Al	5.49	5.27	5.22	5.23	5.41
Cr	0.00	bdl	0.00	0.00	0.00
V	0.00	0.01	0.01	0.01	0.01
Fe^{2+}	0.19	0.31	0.34	0.31	0.31
Mg	0.18	0.22	0.23	0.23	0.19
Mn	bdl	0.00	bdl	bdl	bdl
Ca	0.00	0.00	bdl	0.00	0.00
Ba	0.00	0.01	0.01	0.01	0.01
Na	0.18	0.13	0.13	0.13	0.17
K	1.61	1.65	1.68	1.64	1.50
Total cations	13.91	13.93	13.95	13.91	13.86
Cl	0.00	0.00	0.00	0.01	0.00
F	0.01	bdl	bdl	bdl	bdl
Fe/(Fe+Mg)	0.52	0.58	0.60	0.58	0.62

[1]Assuming all Fe is Fe^{2+}

Table 7. Complete Sericite Dataset from the Ming Deposit *(continued)*

	36634_Ser_05_02 Quartz-chlorite-sericite	36634_Ser_06_01 Quartz-chlorite-sericite	36637_06_01 Quartz-sericite-chlorite	36637_05_03 Quartz-sericite-chlorite	36637_07_04 Quartz-sericite-chlorite
SiO_2 (wt. %)	49.24	48.51	49.86	48.95	49.39
TiO_2	0.42	0.40	0.43	0.47	0.41
Al_2O_3	35.18	34.63	33.58	33.25	32.64
Cr_2O_3	0.02	0.05	0.02	0.02	0.01
V_2O_3	0.09	0.10	0.04	0.03	0.04
FeO[1]	2.78	3.84	3.00	3.04	3.48
MgO	1.20	1.30	1.64	1.55	1.62
MnO	0.02	0.02	bdl	0.01	bdl
CaO	0.00	0.02	0.01	0.01	bdl
BaO	0.17	0.17	0.23	0.33	0.25
Na_2O	0.80	0.48	0.66	0.45	0.74
K_2O	8.85	9.16	9.36	9.99	9.97
F	bdl	bdl	bdl	bdl	bdl
Cl	0.04	0.04	bdl	0.02	0.01
Total	98.75	98.63	98.73	98.02	98.49
Number of ions calculated on the basis of 22 (O):					
Si	6.30	6.26	6.40	6.36	6.40
Ti	0.04	0.04	0.04	0.05	0.04
Al	5.30	5.26	5.08	5.09	4.99
Cr	0.00	0.00	0.00	0.00	0.00
V	0.01	0.01	0.00	0.00	0.00
Fe^{2+}	0.30	0.41	0.32	0.33	0.38
Mg	0.23	0.25	0.31	0.30	0.31
Mn	0.00	0.00	bdl	0.00	bdl
Ca	0.00	0.00	0.00	0.00	bdl
Ba	0.01	0.01	0.01	0.02	0.01
Na	0.20	0.12	0.16	0.11	0.19
K	1.44	1.51	1.53	1.66	1.65
Total cations	13.83	13.88	13.87	13.93	13.98
Cl	0.01	0.01	bdl	0.00	0.00
F	bdl	bdl	bdl	bdl	bdl
Fe/(Fe+Mg)	0.57	0.62	0.51	0.52	0.55

[1]Assuming all Fe is Fe^{2+}

Table 7. Complete Sericite Dataset from the Ming Deposit *(continued)*

	36637_07_03 Quartz-sericite-chlorite	36637_04_01 Quartz-sericite-chlorite	36637_04_02 Quartz-sericite-chlorite	36637_01_03 Quartz-sericite-chlorite	36637_01_04 Quartz-sericite-chlorite	36637_02_05 Quartz-sericite-chlorite
SiO_2 (wt. %)	49.44	49.53	48.81	49.62	48.59	49.59
TiO_2	0.44	0.50	0.51	0.13	0.38	0.58
Al_2O_3	32.99	32.67	33.88	34.16	32.96	34.28
Cr_2O_3	0.01	0.02	bdl	0.03	0.23	0.00
V_2O_3	0.04	0.03	0.04	0.05	0.03	0.03
FeO[1]	3.13	3.06	3.10	2.70	3.04	3.05
MgO	1.55	1.71	1.39	1.42	1.55	1.36
MnO	bdl	0.01	0.01	0.00	0.01	0.01
CaO	0.01	bdl	0.00	0.01	0.01	bdl
BaO	0.25	0.24	0.38	0.09	0.23	0.32
Na_2O	0.57	0.71	0.73	0.60	0.54	0.70
K_2O	9.56	9.78	9.65	10.11	9.94	9.49
F	bdl	bdl	bdl	bdl	bdl	bdl
Cl	0.01	bdl	0.00	bdl	bdl	0.01
Total	97.93	98.21	98.44	98.84	97.43	99.32
Number of ions calculated on the basis of 22 (O):						
Si	6.41	6.42	6.32	6.37	6.36	6.34
Ti	0.04	0.05	0.05	0.01	0.04	0.06
Al	5.04	4.99	5.17	5.17	5.08	5.16
Cr	0.00	0.00	bdl	0.00	0.02	0.00
V	0.00	0.00	0.00	0.00	0.00	0.00
Fe^{2+}	0.34	0.33	0.34	0.29	0.33	0.33
Mg	0.30	0.33	0.27	0.27	0.30	0.26
Mn	bdl	0.00	0.00	0.00	0.00	0.00
Ca	0.00	bdl	0.00	0.00	0.00	bdl
Ba	0.01	0.01	0.02	0.00	0.01	0.02
Na	0.14	0.18	0.18	0.15	0.14	0.17
K	1.58	1.62	1.59	1.66	1.66	1.55
Total cations	13.88	13.93	13.94	13.93	13.95	13.88
Cl	0.00	bdl	0.00	bdl	bdl	0.00
F	bdl	bdl	bdl	bdl	bdl	bdl
Fe/(Fe+Mg)	0.53	0.50	0.56	0.52	0.52	0.56

[1]Assuming all Fe is Fe^{2+}

Table 7. Complete Sericite Dataset from the Ming Deposit *(continued)*

	106413_02_01 Quartz-chlorite-sulfides	106413_02_02 Quartz-chlorite-sulfides	106413_02_03 Quartz-chlorite-sulfides	106413_05_02 Quartz-chlorite-sulfides	106413_05_03 Quartz-chlorite-sulfides	106413_05_04 Quartz-chlorite-sulfides
SiO_2 (wt. %)	48.96	49.37	48.65	49.26	49.75	50.01
TiO_2	0.48	0.53	0.52	0.22	0.41	0.44
Al_2O_3	34.10	33.47	34.11	34.13	33.75	34.13
Cr_2O_3	0.11	0.14	0.14	0.16	0.15	0.09
V_2O_3	0.13	0.13	0.15	0.14	0.17	0.15
FeO[1]	3.02	3.04	3.64	2.56	2.86	2.94
MgO	1.29	1.43	1.44	1.37	1.40	1.53
MnO	bdl	bdl	0.01	bdl	0.01	0.02
CaO	bdl	bdl	0.02	0.01	0.02	0.01
BaO	0.25	0.18	0.26	0.21	0.15	0.19
Na_2O	0.60	0.66	0.53	0.83	0.73	0.53
K_2O	9.85	10.10	8.85	9.34	8.46	9.41
F	bdl	bdl	bdl	bdl	bdl	bdl
Cl	0.01	bdl	0.02	0.00	0.01	bdl
Total	98.68	98.97	98.26	98.13	97.80	99.39
Number of ions calculated on the basis of 22 (O):						
Si	6.31	6.36	6.29	6.35	6.41	6.37
Ti	0.05	0.05	0.05	0.02	0.04	0.04
Al	5.18	5.08	5.20	5.19	5.12	5.13
Cr	0.01	0.01	0.01	0.02	0.02	0.01
V	0.01	0.01	0.02	0.01	0.02	0.01
Fe^{2+}	0.33	0.33	0.39	0.28	0.31	0.31
Mg	0.25	0.28	0.28	0.26	0.27	0.29
Mn	bdl	bdl	0.00	bdl	0.00	0.00
Ca	bdl	bdl	0.00	0.00	0.00	0.00
Ba	0.01	0.01	0.01	0.01	0.01	0.01
Na	0.15	0.17	0.13	0.21	0.18	0.13
K	1.62	1.66	1.46	1.54	1.39	1.53
Total cations	13.92	13.95	13.84	13.89	13.76	13.84
Cl	0.00	bdl	0.00	0.00	0.00	bdl
F	bdl	bdl	bdl	bdl	bdl	bdl
Fe/(Fe+Mg)	0.57	0.54	0.59	0.51	0.53	0.52

[1]Assuming all Fe is Fe^{2+}

Table 7. Complete Sericite Dataset from the Ming Deposit *(continued)*

	106413_05_01 Quartz-chlorite-sulfides	106413_06_01 Quartz-chlorite-sulfides	106413_06_02 Quartz-chlorite-sulfides	106413_06_03 Quartz-chlorite-sulfides	62060_01_03 Quartz-chlorite	62060_01_04 Quartz-chlorite
SiO_2 (wt. %)	49.73	50.07	49.84	50.24	49.27	49.00
TiO_2	0.49	0.44	0.08	0.36	0.33	0.30
Al_2O_3	34.59	34.39	35.64	35.01	36.26	36.16
Cr_2O_3	0.09	0.07	0.00	0.09	0.16	0.17
V_2O_3	0.14	0.14	0.13	0.15	0.12	0.12
FeO[1]	2.86	2.97	2.50	2.75	3.23	3.11
MgO	1.35	1.42	1.23	1.41	0.88	0.82
MnO	bdl	0.02	bdl	0.03	bdl	bdl
CaO	0.01	0.01	bdl	0.02	0.01	0.00
BaO	0.19	0.19	0.17	0.22	0.08	0.06
Na_2O	0.51	0.50	0.70	0.47	1.31	1.33
K_2O	9.16	9.57	9.52	9.83	8.98	8.88
F	bdl	bdl	bdl	bdl	bdl	bdl
Cl	0.04	0.01	bdl	bdl	0.00	0.01
Total	99.08	99.71	99.73	100.49	100.57	99.89
Number of ions calculated on the basis of 22 (O):						
Si	6.34	6.36	6.31	6.34	6.21	6.21
Ti	0.05	0.04	0.01	0.03	0.03	0.03
Al	5.20	5.15	5.32	5.20	5.39	5.40
Cr	0.01	0.01	0.00	0.01	0.02	0.02
V	0.01	0.01	0.01	0.01	0.01	0.01
Fe^{2+}	0.31	0.32	0.26	0.29	0.34	0.33
Mg	0.26	0.27	0.23	0.26	0.17	0.15
Mn	bdl	0.00	bdl	0.00	bdl	bdl
Ca	0.00	0.00	bdl	0.00	0.00	0.00
Ba	0.01	0.01	0.01	0.01	0.00	0.00
Na	0.13	0.12	0.17	0.11	0.32	0.33
K	1.49	1.55	1.54	1.58	1.44	1.44
Total cations	13.80	13.85	13.87	13.86	13.93	13.92
Cl	0.01	0.00	bdl	bdl	0.00	0.00
F	bdl	bdl	bdl	bdl	bdl	bdl
Fe/(Fe+Mg)	0.54	0.54	0.53	0.52	0.67	0.68

[1]Assuming all Fe is Fe^{2+}

Table 7. Complete Sericite Dataset from the Ming Deposit *(continued)*

	62060_03_03	62060_03_04	62060_04_05	62060_04_06	62060_05_06	62060_05_05
	Quartz-chlorite	Quartz-chlorite	Quartz-chlorite	Quartz-chlorite	Quartz-chlorite	Quartz-chlorite
SiO_2 (wt. %)	49.53	48.06	48.81	48.52	49.06	49.45
TiO_2	0.30	0.29	0.31	0.31	0.29	0.36
Al_2O_3	36.21	36.18	36.33	35.61	35.53	36.13
Cr_2O_3	0.12	0.14	0.09	0.08	0.09	0.10
V_2O_3	0.10	0.08	0.09	0.11	0.12	0.15
FeO[1]	2.87	2.60	2.83	2.84	2.71	2.89
MgO	0.84	0.60	0.75	0.78	0.73	1.01
MnO	0.02	bdl	bdl	0.01	bdl	0.02
CaO	0.01	0.00	0.01	bdl	0.01	0.01
BaO	0.09	0.07	0.10	0.10	0.04	0.14
Na_2O	1.30	1.54	1.37	1.32	1.35	0.82
K_2O	8.59	8.72	8.84	9.13	8.78	9.49
F	bdl	bdl	bdl	bdl	bdl	bdl
Cl	0.01	0.00	bdl	0.01	0.01	0.00
Total	99.94	98.18	99.42	98.74	98.65	100.47
Number of ions calculated on the basis of 22 (O):						
Si	6.25	6.19	6.21	6.23	6.28	6.24
Ti	0.03	0.03	0.03	0.03	0.03	0.03
Al	5.39	5.49	5.44	5.39	5.36	5.37
Cr	0.01	0.01	0.01	0.01	0.01	0.01
V	0.01	0.01	0.01	0.01	0.01	0.02
Fe^{2+}	0.30	0.28	0.30	0.30	0.29	0.30
Mg	0.16	0.11	0.14	0.15	0.14	0.19
Mn	0.00	bdl	bdl	0.00	bdl	0.00
Ca	0.00	0.00	0.00	bdl	0.00	0.00
Ba	0.00	0.00	0.00	0.00	0.00	0.01
Na	0.32	0.38	0.34	0.33	0.33	0.20
K	1.38	1.43	1.43	1.49	1.43	1.53
Total cations	13.86	13.94	13.92	13.95	13.89	13.90
Cl	0.00	0.00	bdl	0.00	0.00	0.00
F	bdl	bdl	bdl	bdl	bdl	bdl
Fe/(Fe+Mg)	0.66	0.71	0.68	0.67	0.68	0.62

[1]Assuming all Fe is Fe^{2+}

Table 7. Complete Sericite Dataset from the Ming Deposit *(continued)*

	62060_06_01	62060_06_02
	Quartz-chlorite	Quartz-chlorite
SiO_2 (wt. %)	48.82	48.41
TiO_2	0.35	0.31
Al_2O_3	35.41	36.09
Cr_2O_3	0.12	0.09
V_2O_3	0.12	0.11
FeO[1]	2.93	3.09
MgO	0.85	0.76
MnO	0.01	bdl
CaO	0.01	0.01
BaO	0.12	0.05
Na_2O	1.21	1.34
K_2O	8.98	8.91
F	bdl	bdl
Cl	0.01	0.01
Total	98.82	99.07
Number of ions calculated on the basis of 22 (O):		
Si	6.25	6.19
Ti	0.03	0.03
Al	5.35	5.44
Cr	0.01	0.01
V	0.01	0.01
Fe^{2+}	0.31	0.33
Mg	0.16	0.14
Mn	0.00	bdl
Ca	0.00	0.00
Ba	0.01	0.00
Na	0.30	0.33
K	1.47	1.45
Total cations	13.91	13.94
Cl	0.00	0.00
F	bdl	bdl
Fe/(Fe+Mg)	0.66	0.70

[1]Assuming all Fe is Fe^{2+}

Appendix 8.
Complete Calcite Dataset from the Ming Deposit

Table A8. Complete Calcite Dataset from the Ming Deposit

	62199_Cal_01_01 Mn-Ca-rich assemblage	62199_Cal_01_02 Mn-Ca-rich assemblage	62199_Cal_01_03 Mn-Ca-rich assemblage	62199_Cal_02_01 Mn-Ca-rich assemblage	62199_Cal_02_02 Mn-Ca-rich assemblage
FeO[1] (wt. %)	0.99	1.21	0.91	0.95	0.95
MnO	5.35	4.59	5.07	5.27	4.89
ZnO	bdl	bdl	0.03	bdl	bdl
MgO	1.68	1.70	1.75	1.76	1.60
CaO	45.67	45.87	45.93	45.35	46.08
SrO	bdl	0.01	bdl	bdl	bdl
BaO	bdl	bdl	bdl	bdl	bdl
Total[2]	53.65	53.38	53.67	53.32	53.49
Number of ions calculated on the basis of 6 (O):					
Fe^{2+}	0.09	0.11	0.08	0.08	0.08
Mn	0.48	0.41	0.45	0.47	0.44
Zn	bdl	bdl	0.00	bdl	bdl
Mg	0.26	0.27	0.27	0.28	0.25
Ca	5.17	5.21	5.19	5.16	5.23
Sr	bdl	0.00	bdl	bdl	bdl
Ba	bdl	bdl	bdl	bdl	bdl
Total cations	6.00	6.00	6.00	6.00	6.00

[1]Assuming all Fe is Fe^{2+}

[2]CO_2 was not analyzed

Table A8. Complete Calcite Dataset from the Ming Deposit *(continued)*

	62199_Cal_02_03 Mn-Ca-rich assemblage	62199_Cal_03_04 Mn-Ca-rich assemblage	62199_Cal_03_05 Mn-Ca-rich assemblage	62199_Cal_03_06 Mn-Ca-rich assemblage	62199_Cal_04_01 Mn-Ca-rich assemblage
FeO[1] (wt. %)	1.18	1.05	1.04	0.99	1.16
MnO	4.75	6.02	5.86	5.97	4.95
ZnO	bdl	0.02	bdl	0.01	0.02
MgO	1.76	1.88	1.83	1.89	1.88
CaO	45.62	45.10	45.10	45.10	46.11
SrO	0.04	bdl	0.04	bdl	0.06
BaO	0.03	0.02	0.01	bdl	bdl
Total[2]	53.37	54.10	53.88	53.95	54.14
Number of ions calculated on the basis of 6 (O):					
Fe^{2+}	0.10	0.09	0.09	0.09	0.10
Mn	0.43	0.54	0.52	0.53	0.44
Zn	bdl	0.00	bdl	0.00	0.00
Mg	0.28	0.29	0.29	0.30	0.29
Ca	5.19	5.07	5.09	5.08	5.16
Sr	0.00	bdl	0.00	bdl	0.00
Ba	0.00	0.00	0.00	bdl	bdl
Total cations	6.00	6.00	6.00	6.00	6.00

[1]Assuming all Fe is Fe^{2+}

[2]CO_2 was not analyzed

Table A8. Complete Calcite Dataset from the Ming Deposit *(continued)*

	62199_Cal_04_02 Mn-Ca-rich assemblage	62199_Cal_04_03 Mn-Ca-rich assemblage	62199_Cal_04_04 Mn-Ca-rich assemblage	29891_Carb_01_01 Silica-rich horizon	29891_Carb_01_02 Silica-rich horizon
FeO[1] (wt. %)	1.18	0.99	1.00	0.03	0.89
MnO	4.86	6.07	5.52	0.07	0.84
ZnO	bdl	0.01	0.01	bdl	bdl
MgO	1.80	1.82	1.85	bdl	1.40
CaO	45.82	45.22	45.08	53.38	49.40
SrO	bdl	0.09	0.06	0.01	0.03
BaO	bdl	bdl	0.03	0.05	bdl
Total[2]	53.62	54.20	53.55	53.51	52.56
Number of ions calculated on the basis of 6 (O):					
Fe^{2+}	0.10	0.09	0.09	0.00	0.08
Mn	0.43	0.54	0.50	0.01	0.08
Zn	bdl	0.00	0.00	bdl	bdl
Mg	0.28	0.29	0.29	bdl	0.22
Ca	5.18	5.08	5.12	5.99	5.62
Sr	bdl	0.01	0.00	0.00	0.00
Ba	bdl	bdl	0.00	0.00	bdl
Total cations	6.00	6.00	6.00	6.00	6.00

[1]Assuming all Fe is Fe^{2+}

[2]CO_2 was not analyzed

Table A8. Complete Calcite Dataset from the Ming Deposit *(continued)*

	29891_Carb_01_03	29891_Carb_01_04	29891_Carb_02_01	29891_Carb_02_02
	Silica-rich horizon	Silica-rich horizon	Silica-rich horizon	Silica-rich horizon
FeO^{1} (wt. %)	0.94	0.72	0.03	0.76
MnO	0.81	0.82	0.19	0.84
ZnO	bdl	bdl	bdl	bdl
MgO	1.44	1.17	0.03	1.17
CaO	49.52	49.80	53.34	50.68
SrO	bdl	0.02	0.03	0.01
BaO	bdl	bdl	bdl	bdl
$Total^{2}$	52.65	52.53	53.59	53.46
Number of ions calculated on the basis of 6 (O):				
Fe^{2+}	0.08	0.06	0.00	0.07
Mn	0.07	0.07	0.02	0.07
Zn	bdl	bdl	bdl	bdl
Mg	0.23	0.19	0.00	0.18
Ca	5.62	5.68	5.98	5.68
Sr	bdl	0.00	0.00	0.00
Ba	bdl	bdl	bdl	bdl
Total cations	6.00	6.00	6.00	6.00

[1]Assuming all Fe is Fe^{2+}

[2]CO_2 was not analyzed

Table A8. Complete Calcite Dataset from the Ming Deposit *(continued)*

	29891_Carb_02_03	29891_Carb_03_01	29891_Carb_03_02	29891_Carb_04_01
	Silica-rich horizon	Silica-rich horizon	Silica-rich horizon	Silica-rich horizon
FeO^{1} (wt. %)	0.06	0.83	0.92	0.91
MnO	0.44	0.84	0.84	0.88
ZnO	bdl	bdl	0.01	bdl
MgO	0.04	1.48	1.47	1.49
CaO	52.35	49.09	49.89	49.91
SrO	bdl	0.02	bdl	0.04
BaO	bdl	0.02	bdl	0.03
$Total^{2}$	52.85	52.27	53.11	53.26
Number of ions calculated on the basis of 6 (O):				
Fe^{2+}	0.01	0.07	0.08	0.08
Mn	0.04	0.08	0.07	0.08
Zn	bdl	bdl	0.00	bdl
Mg	0.01	0.24	0.23	0.23
Ca	5.95	5.61	5.61	5.61
Sr	bdl	0.00	bdl	0.00
Ba	bdl	0.00	bdl	0.00
Total cations	6.00	6.00	6.00	6.00

[1]Assuming all Fe is Fe^{2+}

[2]CO_2 was not analyzed

Table A8. Complete Calcite Dataset from the Ming Deposit *(continued)*

	29891_Carb_04_02	29891_Carb_04_03
	Silica-rich horizon	Silica-rich horizon
FeO[1] (wt. %)	0.88	0.87
MnO	0.77	0.72
ZnO	bdl	bdl
MgO	1.53	1.47
CaO	49.61	49.94
SrO	0.06	0.02
BaO	bdl	bdl
Total[2]	52.80	53.00
Number of ions calculated on the basis of 6 (O):		
Fe^{2+}	0.08	0.08
Mn	0.07	0.06
Zn	bdl	bdl
Mg	0.24	0.23
Ca	5.61	5.63
Sr	0.00	0.00
Ba	bdl	bdl
Total cations	6.00	6.00

[1]Assuming all Fe is Fe^{2+}

[2]CO_2 was not analyzed

Appendix 9.
Complete Biotite Dataset from the Ming Deposit

Table A9. Complete Biotite Dataset from the Ming Deposit

Sample	36637_Biot_02_01	36637_Biot_02_02	36637_Biot_03_03	36637_Biot_07_01	36637_Biot_07_02
Kcode	Quartz-sericite-chlorite	Quartz-sericite-chlorite	Quartz-sericite-chlorite	Quartz-sericite-chlorite	Quartz-sericite-chlorite
SiO_2 (wt. %)	37.04	38.48	38.09	38.30	38.00
TiO_2	1.87	2.22	1.79	1.88	2.06
Al_2O_3	18.25	18.00	18.29	18.24	18.61
FeO[1]	16.23	16.50	16.49	16.38	15.98
MgO	11.52	11.83	12.03	11.88	11.48
MnO	0.12	0.12	0.15	0.13	0.12
CaO	0.01	0.00	0.02	bdl	0.02
BaO	0.10	0.05	0.06	0.04	0.09
Na_2O	0.12	0.10	0.11	0.11	0.09
K_2O	9.58	9.82	9.22	9.65	9.63
F	bdl	bdl	bdl	bdl	bdl
Cl	0.02	0.02	0.02	0.01	0.01
Total	94.86	97.11	96.24	96.56	96.05
Number of ions calculated on the basis of 22 (O):					
Si	5.57	5.64	5.62	5.64	5.62
Ti	0.21	0.24	0.20	0.21	0.23
Al	3.24	3.11	3.18	3.16	3.24
Fe^{2+}	2.04	2.02	2.04	2.02	1.97
Mg	2.58	2.59	2.65	2.61	2.53
Mn	0.02	0.01	0.02	0.02	0.02
Ca	0.00	0.00	0.00	bdl	0.00
Ba	0.01	0.00	0.00	0.00	0.01
Na	0.04	0.03	0.03	0.03	0.02
K	1.84	1.84	1.74	1.81	1.82
Total cations	15.54	15.49	15.47	15.49	15.46
Cl	0.01	0.00	0.00	0.00	0.00
F	bdl	bdl	bdl	bdl	bdl
Mg/Mg+Fe	0.56	0.56	0.57	0.56	0.56
Si/Al	1.72	1.81	1.77	1.78	1.73

[1]Assuming all Fe is Fe^{2+}

Table A9. Complete Biotite Dataset from the Ming Deposit *(continued)*

Sample	106413_Biot_01_01	106413_Biot_01_02	106413_Biot_03_03	106413_Biot_03_04	106413_Biot_04_01
Kcode	Quartz-chlorite-sulfides	Quartz-chlorite-sulfides	Quartz-chlorite-sulfides	Quartz-chlorite-sulfides	Quartz-chlorite-sulfides
SiO_2 (wt. %)	37.96	38.20	37.43	37.94	35.50
TiO_2	1.77	1.86	1.72	1.97	2.34
Al_2O_3	18.71	18.55	18.41	18.87	17.53
FeO[1]	17.10	17.11	16.78	17.22	21.10
MgO	11.41	11.19	11.12	11.18	10.15
MnO	0.16	0.13	0.16	0.15	0.19
CaO	0.01	0.00	0.00	bdl	0.05
BaO	0.03	bdl	0.04	0.05	0.07
Na_2O	0.14	0.13	0.13	0.10	0.10
K_2O	9.65	9.62	9.54	9.74	8.06
F	bdl	bdl	bdl	bdl	bdl
Cl	0.02	0.02	0.01	0.01	0.02
Total	96.91	96.83	95.32	97.22	95.03
Number of ions calculated on the basis of 22 (O):					
Si	5.59	5.63	5.60	5.57	5.43
Ti	0.20	0.21	0.19	0.22	0.27
Al	3.25	3.22	3.25	3.27	3.16
Fe^{2+}	2.11	2.11	2.10	2.12	2.70
Mg	2.50	2.46	2.48	2.45	2.32
Mn	0.02	0.02	0.02	0.02	0.02
Ca	0.00	0.00	0.00	bdl	0.01
Ba	0.00	bdl	0.00	0.00	0.00
Na	0.04	0.04	0.04	0.03	0.03
K	1.81	1.81	1.82	1.83	1.57
Total cations	15.52	15.48	15.51	15.50	15.52
Cl	0.00	0.01	0.00	0.00	0.00
F	bdl	bdl	bdl	bdl	bdl
Mg/Mg+Fe	0.54	0.54	0.54	0.54	0.46
Si/Al	1.72	1.75	1.73	1.71	1.72

[1]Assuming all Fe is Fe^{2+}

Table A9. Complete Biotite Dataset from the Ming Deposit *(continued)*

Sample	106413_Biot_04_02	106413_Biot_06_04	106413_Biot_06_05	2060_Biot_01_0	62060_Biot_01_02
Kcode	Quartz-chlorite-sulfides	Quartz-chlorite-sulfides	Quartz-chlorite-sulfides	Quartz-chlorite	Quartz-chlorite
SiO_2 (wt. %)	37.96	37.62	37.86	37.26	37.24
TiO_2	2.06	1.64	1.61	1.44	1.49
Al_2O_3	18.76	18.65	18.55	18.25	18.12
FeO[1]	16.38	17.06	17.51	17.90	17.83
MgO	11.07	11.22	11.15	11.50	11.41
MnO	0.14	0.16	0.16	0.10	0.12
CaO	0.01	0.01	bdl	0.01	0.00
BaO	bdl	0.02	0.05	0.12	0.06
Na_2O	0.10	0.12	0.17	0.17	0.17
K_2O	9.76	9.60	9.34	9.55	9.63
F	bdl	bdl	bdl	bdl	bdl
Cl	0.01	bdl	bdl	0.04	0.02
Total	96.22	96.05	96.36	96.33	96.09
Number of ions calculated on the basis of 22 (O):					
Si	5.61	5.59	5.61	5.56	5.57
Ti	0.23	0.18	0.18	0.16	0.17
Al	3.27	3.27	3.24	3.21	3.19
Fe^{2+}	2.03	2.12	2.17	2.23	2.23
Mg	2.44	2.48	2.46	2.56	2.54
Mn	0.02	0.02	0.02	0.01	0.01
Ca	0.00	0.00	bdl	0.00	0.00
Ba	bdl	0.00	0.00	0.01	0.00
Na	0.03	0.04	0.05	0.05	0.05
K	1.84	1.82	1.76	1.82	1.84
Total cations	15.46	15.52	15.50	15.61	15.61
Cl	0.00	bdl	bdl	0.01	0.00
F	bdl	bdl	bdl	bdl	bdl
Mg/Mg+Fe	0.55	0.54	0.53	0.53	0.53
Si/Al	1.72	1.71	1.73	1.73	1.74

[1]Assuming all Fe is Fe^{2+}

Table A9. Complete Biotite Dataset from the Ming Deposit *(continued)*

Sample	62060_Biot_03_01	62060_Biot_03_02	62060_Biot_04_03	62060_Biot_04_04	62060_Biot_05_03
Kcode	Quartz-chlorite	Quartz-chlorite	Quartz-chlorite	Quartz-chlorite	Quartz-chlorite
SiO_2 (wt. %)	37.25	37.34	36.69	37.13	37.26
TiO_2	1.41	1.44	1.63	1.50	1.43
Al_2O_3	18.56	18.64	17.67	18.02	18.41
FeO[1]	17.54	18.04	18.01	18.08	17.87
MgO	11.33	11.33	11.22	11.11	11.20
MnO	0.10	0.12	0.11	0.10	0.10
CaO	0.02	0.02	0.01	0.01	0.02
BaO	0.07	0.04	0.05	0.06	0.05
Na_2O	0.18	0.15	0.11	0.14	0.18
K_2O	9.49	9.40	9.46	9.36	9.52
F	bdl	bdl	0.06	bdl	bdl
Cl	0.02	0.03	0.02	0.02	0.03
Total	95.98	96.53	95.01	95.51	96.05
Number of ions calculated on the basis of 22 (O):					
Si	5.56	5.55	5.56	5.58	5.57
Ti	0.16	0.16	0.19	0.17	0.16
Al	3.27	3.26	3.16	3.19	3.24
Fe^{2+}	2.19	2.24	2.28	2.27	2.23
Mg	2.52	2.51	2.54	2.49	2.50
Mn	0.01	0.01	0.01	0.01	0.01
Ca	0.00	0.00	0.00	0.00	0.00
Ba	0.00	0.00	0.00	0.00	0.00
Na	0.05	0.04	0.03	0.04	0.05
K	1.81	1.78	1.83	1.80	1.82
Total cations	15.58	15.57	15.60	15.57	15.59
Cl	0.00	0.01	0.00	0.01	0.01
F	bdl	bdl	0.03	bdl	bdl
Mg/Mg+Fe	0.54	0.53	0.53	0.52	0.53
Si/Al	1.70	1.70	1.76	1.75	1.72

[1]Assuming all Fe is Fe^{2+}

Table A9. Complete Biotite Dataset from the Ming Deposit *(continued)*

Sample	62060_Biot_05_04	62524_Biot_01_01	62524_Biot_01_02	62524_Biot_02_01	62524_Biot_02_02
Kcode	Quartz-chlorite	Quartz-sericite	Quartz-sericite	Quartz-sericite	Quartz-sericite
SiO_2 (wt. %)	37.62	39.19	39.54	40.27	40.04
TiO_2	1.49	1.01	1.05	1.00	1.00
Al_2O_3	18.66	18.47	18.46	18.06	17.95
FeO[1]	17.78	13.22	13.01	12.90	12.88
MgO	11.07	14.12	14.34	14.63	14.58
MnO	0.11	0.06	0.04	0.05	0.07
CaO	0.02	0.02	0.00	0.00	0.00
BaO	0.08	0.02	bdl	bdl	0.02
Na_2O	0.19	0.24	0.26	0.19	0.17
K_2O	9.43	8.93	9.07	9.26	9.26
F	bdl	1.07	1.11	1.24	1.13
Cl	0.03	0.02	0.02	0.01	0.00
Total	96.44	95.91	96.43	97.09	96.63
Number of ions calculated on the basis of 22 (O):					
Si	5.59	5.72	5.74	5.80	5.80
Ti	0.17	0.11	0.11	0.11	0.11
Al	3.27	3.18	3.16	3.07	3.06
Fe^{2+}	2.21	1.61	1.58	1.55	1.56
Mg	2.45	3.07	3.10	3.14	3.15
Mn	0.01	0.01	0.01	0.01	0.01
Ca	0.00	0.00	0.00	0.00	0.00
Ba	0.00	0.00	bdl	bdl	0.00
Na	0.06	0.07	0.07	0.05	0.05
K	1.79	1.66	1.68	1.70	1.71
Total cations	15.54	15.44	15.45	15.43	15.44
Cl	0.01	0.00	0.01	0.00	0.00
F	bdl	0.48	0.50	0.55	0.51
Mg/Mg+Fe	0.53	0.66	0.66	0.67	0.67
Si/Al	1.71	1.80	1.82	1.89	1.89

[1]Assuming all Fe is Fe^{2+}

Table A9. Complete Biotite Dataset from the Ming Deposit *(continued)*

Sample	62524_Biot_03_01	29815_Biot_01_01	29815_Biot_01_02	29815_Biot_02_01	29815_Biot_03_04
Kcode	Quartz-sericite	Quartz-sericite-sulfides	Quartz-sericite-sulfides	Quartz-sericite-sulfides	Quartz-sericite-sulfides
SiO_2 (wt. %)	40.16	41.11	41.48	41.32	41.25
TiO_2	1.05	0.92	1.25	0.92	0.94
Al_2O_3	17.95	17.99	18.01	19.02	18.23
FeO[1]	13.10	6.99	7.15	6.86	7.18
MgO	14.70	18.65	18.22	18.70	18.52
MnO	0.05	0.23	0.24	0.24	0.22
CaO	0.01	0.03	0.00	0.04	0.01
BaO	bdl	0.04	bdl	bdl	bdl
Na_2O	0.18	0.17	0.19	0.18	0.16
K_2O	9.17	9.49	9.61	9.42	9.77
F	1.30	1.04	0.87	0.90	1.05
Cl	0.01	0.02	bdl	0.03	bdl
Total	97.11	96.24	96.66	97.22	96.89
Number of ions calculated on the basis of 22 (O):					
Si	5.79	5.82	5.84	5.77	5.80
Ti	0.11	0.10	0.13	0.10	0.10
Al	3.05	3.00	2.99	3.13	3.02
Fe^{2+}	1.58	0.83	0.84	0.80	0.85
Mg	3.16	3.93	3.82	3.89	3.88
Mn	0.01	0.03	0.03	0.03	0.03
Ca	0.00	0.00	0.00	0.01	0.00
Ba	bdl	0.00	bdl	bdl	bdl
Na	0.05	0.05	0.05	0.05	0.04
K	1.69	1.71	1.73	1.68	1.75
Total cations	15.44	15.47	15.43	15.44	15.48
Cl	0.00	0.01	bdl	0.01	bdl
F	0.58	0.46	0.38	0.39	0.46
Mg/Mg+Fe	0.67	0.83	0.82	0.83	0.82
Si/Al	1.90	1.94	1.95	1.84	1.92

[1]Assuming all Fe is Fe^{2+}

Table A9. Complete Biotite Dataset from the Ming Deposit *(continued)*

Sample	29815_Biot_06_01	62199_Biot_05_01	62199_Biot_05_02	62199_Biot_06_01	62199_Biot_06_02
Kcode	Quartz-sericite-sulfides	Mn-Ca-rich assemblage	Mn-Ca-rich assemblage	Mn-Ca-rich assemblage	Mn-Ca-rich assemblage
SiO_2 (wt. %)	41.75	39.93	39.95	40.41	39.98
TiO_2	0.97	1.53	1.39	1.22	1.17
Al_2O_3	18.12	17.72	17.67	17.85	17.38
FeO[1]	7.11	9.42	9.49	9.61	9.68
MgO	18.33	16.08	16.25	16.38	16.41
MnO	0.23	0.83	0.87	0.80	0.86
CaO	0.04	0.03	0.03	0.07	0.01
BaO	bdl	0.69	0.40	0.72	0.63
Na_2O	0.18	0.14	0.13	0.15	0.12
K_2O	9.42	9.00	8.95	8.94	9.20
F	1.02	0.32	0.33	0.33	0.38
Cl	0.00	0.00	0.01	0.02	bdl
Total	96.73	95.56	95.34	96.36	95.65
Number of ions calculated on the basis of 22 (O):					
Si	5.86	5.77	5.78	5.79	5.79
Ti	0.10	0.17	0.15	0.13	0.13
Al	3.00	3.02	3.01	3.01	2.97
Fe^{2+}	0.83	1.14	1.15	1.15	1.17
Mg	3.84	3.46	3.50	3.50	3.54
Mn	0.03	0.10	0.11	0.10	0.10
Ca	0.01	0.00	0.01	0.01	0.00
Ba	bdl	0.04	0.02	0.04	0.04
Na	0.05	0.04	0.04	0.04	0.03
K	1.69	1.66	1.65	1.63	1.70
Total cations	15.40	15.40	15.41	15.41	15.47
Cl	0.00	0.00	0.00	0.00	bdl
F	0.45	0.15	0.15	0.15	0.17
Mg/Mg+Fe	0.82	0.75	0.75	0.75	0.75
Si/Al	1.95	1.91	1.92	1.92	1.95

[1]Assuming all Fe is Fe^{2+}

Table A9. Complete Biotite Dataset from the Ming Deposit *(continued)*

Sample	62199_Biot_06_03	60507_Biot_01_07	60507_Biot_01_08	60507_Biot_01_09	60507_Biot_02_3
Kcode	Mn-Ca-rich assemblage	Sericite-calcite±spessartine	Sericite-calcite±spessartine	Sericite-calcite±spessartine	Sericite-calcite±spessartine
SiO_2 (wt. %)	39.87	38.40	38.19	37.54	38.26
TiO_2	1.32	1.35	1.34	1.32	1.68
Al_2O_3	17.63	17.76	18.07	17.64	17.43
FeO[1]	9.81	17.71	17.20	17.64	17.23
MgO	16.29	11.39	11.25	11.51	11.37
MnO	0.87	0.60	0.60	0.67	0.69
CaO	0.00	bdl	0.00	0.01	0.01
BaO	0.74	0.07	0.10	0.14	0.09
Na_2O	0.10	0.10	0.10	0.10	0.10
K_2O	9.13	9.40	9.35	9.15	9.49
F	0.29	bdl	bdl	bdl	0.06
Cl	0.01	0.01	bdl	0.02	0.00
Total	95.94	96.77	96.19	95.72	96.37
Number of ions calculated on the basis of 22 (O):					
Si	5.76	5.68	5.67	5.63	5.69
Ti	0.14	0.15	0.15	0.15	0.19
Al	3.00	3.10	3.16	3.12	3.05
Fe^{2+}	1.18	2.19	2.14	2.21	2.14
Mg	3.51	2.51	2.49	2.57	2.52
Mn	0.11	0.08	0.08	0.09	0.09
Ca	0.00	bdl	0.00	0.00	0.00
Ba	0.04	0.00	0.01	0.01	0.01
Na	0.03	0.03	0.03	0.03	0.03
K	1.68	1.77	1.77	1.75	1.80
Total cations	15.45	15.52	15.50	15.55	15.51
Cl	0.00	0.00	bdl	0.00	0.00
F	0.13	bdl	bdl	bdl	0.03
Mg/Mg+Fe	0.75	0.53	0.54	0.54	0.54
Si/Al	1.92	1.83	1.79	1.81	1.86

[1]Assuming all Fe is Fe^{2+}

Table A9. Complete Biotite Dataset from the Ming Deposit *(continued)*

Sample	60507_Biot_02_4	60507_Biot_02_5	60507_Biot_03_1	60507_Biot_03_2	60507_Biot_04_1	60507_Biot_04_2
Kcode	Sericite-calcite±spessartine	Sericite-calcite±spessartine	Sericite-calcite±spessartine	Sericite-calcite±spessartine	Sericite-calcite±spessartine	Sericite-calcite±spessartine
SiO_2 (wt. %)	38.32	38.05	37.82	38.26	38.18	38.15
TiO_2	1.67	1.58	1.62	1.62	1.82	1.69
Al_2O_3	17.75	17.65	17.50	17.58	17.68	17.48
FeO[1]	17.25	17.12	17.42	17.30	16.91	17.29
MgO	11.24	11.30	11.01	11.26	11.16	11.30
MnO	0.67	0.67	0.65	0.67	0.67	0.66
CaO	bdl	bdl	0.00	0.00	0.00	0.00
BaO	0.12	0.07	0.14	0.09	0.11	0.07
Na_2O	0.09	0.12	0.09	0.10	0.08	0.11
K_2O	9.42	9.56	9.33	9.44	9.39	9.46
F	bdl	bdl	bdl	bdl	bdl	bdl
Cl	0.01	0.01	0.02	bdl	bdl	0.01
Total	96.50	96.08	95.55	96.31	95.98	96.19
Number of ions calculated on the basis of 22 (O):						
Si	5.68	5.67	5.67	5.69	5.68	5.68
Ti	0.19	0.18	0.18	0.18	0.20	0.19
Al	3.10	3.10	3.10	3.08	3.10	3.07
Fe^{2+}	2.14	2.13	2.19	2.15	2.11	2.15
Mg	2.48	2.51	2.46	2.50	2.47	2.51
Mn	0.08	0.08	0.08	0.08	0.08	0.08
Ca	bdl	bdl	0.00	0.00	0.00	0.00
Ba	0.01	0.00	0.01	0.01	0.01	0.00
Na	0.03	0.03	0.03	0.03	0.02	0.03
K	1.78	1.82	1.79	1.79	1.78	1.80
Total cations	15.49	15.53	15.50	15.50	15.47	15.51
Cl	0.00	0.00	0.01	bdl	bdl	0.00
F	bdl	bdl	bdl	bdl	bdl	bdl
Mg/Mg+Fe	0.54	0.54	0.53	0.54	0.54	0.54
Si/Al	1.83	1.83	1.83	1.85	1.83	1.85

[1]Assuming all Fe is Fe^{2+}